



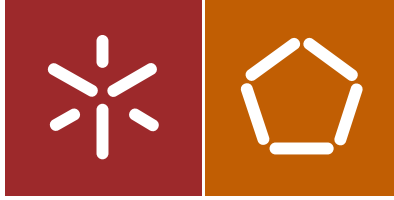
Anthony Michael Fernandes Pimentel

Caracterização Experimental e Modelação  
Numérica do Comportamento Mecânico de  
Chapas Multi-Camada e Multi-Material:  
Aplicação à Indústria Automóvel

Universidade do Minho  
Escola de Engenharia







Universidade do Minho  
Escola de Engenharia

Anthony Michael Fernandes Pimentel

Caracterização Experimental e Modelação  
Numérica do Comportamento Mecânico de  
Chapas Multi-Camada e Multi-Material:  
Aplicação à Indústria Automóvel

Tese de Doutoramento  
Engenharia Mecânica

Trabalho efetuado sob a orientação do  
Professor Doutor José Luís de Carvalho Martins Alves

## **Declaração**

Nome: Anthony Michael Fernandes Pimentel

Correio eletrónico: anthonypimentel@gmail.com

Telemóvel: 968490066

Número do Cartão de Cidadão: 12871297

Título da tese de doutoramento: Caracterização Experimental e Modelação Numérica do Comportamento Mecânico de Chapas Multi-Camada e Multi-Material: Aplicação à Indústria Automóvel

Orientador: Professor José Luís de Carvalho Martins Alves

Ano de conclusão: 2018

Designação do Doutoramento: Doutoramento em Engenharia Mecânica

Área de Especialização: Engenharia Mecânica

Escola: Escola de Engenharia

Departamento: Departamento de Engenharia Mecânica

Declaro que concedo à Universidade do Minho o direito não-exclusivo e irrevogável de arquivar, reproduzir, comunicar e/ou distribuir através do seu repositório institucional, nas condições abaixo indicadas, a versão final da minha dissertação/tese em suporte digital, aprovada após a realização das provas de defesa pública e, quando for caso disso, após confirmação pelo orientador e homologação pelo presidente do júri<sup>1</sup> da introdução das alterações solicitadas.

Declaro que autorizo a Universidade do Minho a arquivar mais de uma cópia da dissertação ou tese e a, sem alterar o seu conteúdo, convertê-la para qualquer formato de ficheiro, meio ou suporte, para efeitos de preservação e acesso.

Declaro que a dissertação ou tese agora entregue é um trabalho original e que, contendo material do qual não detenho direitos de autor, obtive autorização prévia do detentor dos referidos direitos para conceder à Universidade do Minho os termos requeridos por esta licença.

Declaro também que a entrega do documento não infringe, tanto quanto me é possível saber, os direitos de qualquer outra pessoa ou entidade.

Concordo que a minha tese ou dissertação seja colocada no repositório da Universidade do Minho com o seguinte estatuto:

3. Disponibilização do conjunto do trabalho para acesso exclusivo na Universidade do Minho.

Guimarães, junho 2018

Assinatura:

Anthony Michael Fernandes Pimentel

## DECLARAÇÃO DE INTEGRIDADE

Declaro ter atuado com integridade na elaboração da presente tese. Confirmando que em todo o trabalho conducente à sua elaboração não recorri à prática de plágio ou a qualquer forma de falsificação de resultados.

Mais declaro que tomei conhecimento integral do Código de Conduta Ética da Universidade do Minho.

Universidade do Minho,

Nome completo: Anthony Michael Fernandes Pimentel

Assinatura: Anthony Michael Fernandes Pimentel

## AGRADECIMENTOS

Desejo exprimir o meu mais sincero apreço e gratidão

Ao Professor Doutor José Luís de Carvalho Alves,  
*pela oportunidade de investigação concedida numa área científica tão interessante e desafiadora, pelas elevadas competências e profundo conhecimento que possui e procurou me infundir no decorrer de toda a investigação, pela disponibilidade altruísta e empatia demonstrada, pelas palavras de encorajamento, constante incentivo e apoio prestado, pelas conversas esclarecedoras e os indeléveis momentos de partilha pessoal, sem os quais todo esse trabalho não poderia se concretizar. Muito obrigado.*

Ao DEM, Escola de Engenharia da Universidade do Minho e às empresas Sodecia, Lamera AB, Thyssenkrupp AG, AutoForm AG e ESI Group  
*Pela disponibilização dos recursos necessários à realização desse trabalho*

À Fundação para a Ciência e Tecnologia (FCT)  
*pela atribuição da bolsa com referência*  
*SFRH/BDE/51189/2010*



## RESUMO

Na indústria automóvel, a redução de massa e um design leve e compacto são uma tendência contínua que não mostra sinais de declínio. A pressão para projetar veículos capazes de enfrentar desafios cada vez mais exigentes, como maior economia de combustível, maior segurança e controle eficaz de emissões é constante. Novos materiais avançados reduzem o peso total do veículo, aumentando a eficiência e, assim, reduzindo o consumo geral de combustível. Assim, os fabricantes de automóveis - OEM (Original Equipment Manufacturer) - são obrigados a empregar materiais avançados para garantir que os veículos atendam a normas de emissões cada vez mais rigorosas. Materiais monolíticos metálicos, cerâmicos ou poliméricos não podem satisfazer todas as necessidades tecnológicas para uma variedade de aplicações. Investigadores nas áreas da química e física, bem como engenheiros, entendem que, para obter materiais com propriedades superiores, precisam combinar materiais monolíticos produzindo materiais híbridos. Assim, um tipo de material híbrido especialmente desenvolvido para aplicações industriais, denominado *micro-sandwich*, tem sido amplamente estudado nas duas últimas décadas. Tratam-se de materiais laminados com duas ou mais camadas de, no mínimo, dois materiais diferentes - chamadas lâminas (lâmina: camada única ou camada) - ligados. A partir destas combinações em estrutura sandwich, é possível "projetar" as propriedades de certo componente ao escolher os materiais monolíticos certos, proporcionando assim a funcionalidade exigida pelos elevados requisitos impostos aos materiais e estruturas modernas. Embora a implementação de materiais sandwich possa contribuir para um bom compromisso entre a redução de peso e o custo do veículo, existem uma série de desafios que precisam ser ultrapassados. Um aspecto fundamental é que, na maior parte das vezes, estes materiais são idealizados e concebidos apenas do ponto de vista de produto final ou aplicação industrial. Porém, as maiores dificuldades relacionam-se com os processos de produção e transformação destes materiais. Por exemplo, os processos de conformação de chapa amplamente utilizados na indústria automóvel requerem um conhecimento profundo da conformabilidade dos materiais. No caso das chapas micro-sandwich, o domínio da conformabilidade é fortemente condicionado pela natureza multi-camada e multi-material do material. Uma tarefa desafiadora relacionada com a caracterização experimental da maioria dos materiais micro-sandwich é a determinação das propriedades desconhecidas do núcleo compósito. As chapas micro-sandwich não são fornecidas com as respectivas propriedades mecânicas e/ou químicas, pelo menos, para todas as camadas. Portanto, falta uma metodologia, simples e robusta, capaz auxiliar a determinação e fornecimento de



propriedades mecânicas de chapas micro-sandwich para a indústria. Além disso, não existe nenhum estudo sobre as diferentes abordagens numéricas disponíveis nas ferramentas FEA comerciais de estampagem para modelação e simulação de materiais micro-sandwich. No que diz respeito à análise de cascas 3D para processos de deformação de chapas metálicas, diferentes abordagens FEM podem ser utilizadas, como, por exemplo, elementos casca 2D, elementos casca 3D, elementos sólido-casca e elementos sólidos 3D. Todas estas formulações FE apresentam características próprias que afetam os resultados numéricos em termos de eficiência, precisão e confiabilidade. Não existe um consenso claro na indústria sobre a melhor estratégia FEM para a simulação de processos de conformação de materiais compósitos multi-camada. Para poderem ser usados em produtos industriais, as características relacionadas com a sua estampabilidade devem ser determinadas. Por isso, processos de conformação otimizados, novos materiais e modelos de simulação de processamento de chapas metálicas melhorados estão a tornar-se cada vez mais importantes e necessários para o desenvolvimento bem-sucedido de novos produtos conformados. A presente tese de doutoramento focaliza a caracterização experimental e modelação numérica do comportamento mecânico de chapas multi-camada e multi-material visando a sua implementação em processos de estampagem na indústria automóvel. Todo o trabalho realizado foi desenvolvido em estreita parceria com um dos maiores fornecedores portugueses de produtos estampados para a indústria automóvel, o Grupo SODECIA. As empresas Lamera AB e Thyssenkrupp AG também contribuíram com seus produtos, Hybrix e Litecore S, para os testes experimentais. Além disso, dois dos códigos FE de estampagem comerciais mais comumente usados na indústria automóvel, AutoForm e PAM-STAMP 2G, são profundamente avaliados e comparados antes de serem usados nas simulações de conformação de chapas micro-sandwich. Ao longo desta tese, vários desafios relacionados com a produção e fabricação são discutidos, e diferentes áreas, onde os requisitos de ferramentas de engenharia de projeto precisam ser avaliados em relação aos materiais micro-sandwich e decisões de design, são destacadas para que os fabricantes garantam a competitividade futura do mercado automóvel.

---

#### PALAVRAS-CHAVE

CONFORMAÇÃO PLÁSTICA; CHAPAS *MICRO-SANDWICH*; CARACTERIZAÇÃO EXPERIMENTAL  
SIMULAÇÃO NÚMERICA; FERRAMENTAS DE ELEMENTOS FINITOS; INDÚSTRIA AUTOMÓVEL

---

## ABSTRACT

In the automotive industry, mass reduction and lightweight design is a continuing trend that does not show signs of declining. The automotive industry is under constant pressure to design vehicles capable of meeting increasingly demanding challenges such as improved fuel economy, enhanced safety and effective emission control. Advanced automotive materials reduce the overall weight of the vehicle, increasing the efficiency and thereby reducing the overall fuel consumption. Automotive OEM (Original Equipment Manufacturer) are compelled to employ advanced automotive materials to ensure that the vehicles meet the increasingly stringent emission norms. Metals, ceramics, or polymers as mono materials cannot fulfill all technological needs for a variety of original applications. Researchers in chemistry and materials, as well as engineers, understand that to obtain materials with superior properties, they have to combine mono materials to hybrids. For industrial applications, the development of a special hybrid material, the *micro-sandwich*, has been one of the most studied in the last two decades. There are laminates with two or more layers of minimum two different materials—called *laminae* (lamina: single ply or layer)—bonded together. With these combinations in a sandwich material, it is possible to “design” the properties of particular components with the right choice of mono materials, thus providing the functionality to fulfill the high demands on modern materials and structures. But while implement sandwich materials may contribute to a good compromise between weight reduction and vehicle cost, it also proposes a number of challenges that need to be addressed.

A fundamental aspect is that, for the most part, these materials are designed and conceived only from the point of view of final product or industrial application. However, the greatest difficulties are related to the production and transformation processes. For instance, the sheet forming processes widely used in the automotive industry require a deep knowledge of the material’s formability. In the case of the micro-sandwich sheets, the understanding and mastery of the formability is strongly affected by its multi-layer and multi-material nature. A challenging task related with the experimental characterization for most micro-sandwich materials is the determination of the unknown properties of the composite core. The micro-sandwich sheets are not provided with this mechanical and chemical data, at least, for all layers. Therefore, it is missing a simple and robust methodology to supply the mechanical properties of the total micro-sandwich sheet to the industry. Furthermore, there is no study about the different numerical approaches available in the commercial stamping FEA tools to modelling and simulate micro-sandwich materials. Concerning the 3D shell

analysis of sheet metal forming processes, different FEM approaches can be used, such as, 2D shell elements, 3D shell elements, solid-shell elements and 3D solid elements. All these FE formulations have particular characteristics which affects the numerical results in terms of efficiency, accuracy and reliability. Therefore, there is not yet a clear consensus in the industry about the most suitable FEM strategy to the sheet metal forming simulation of layered materials. In order to use these layered materials, deep drawing characteristics must be determined before applying them to industrial products. Thus, optimized forming processes, new materials and improved simulation models in sheet metal processing are becoming increasingly important for the successful development of sheet metal parts. The current Phd thesis focuses the experimental characterization and numerical modelling of the mechanical behavior of multi-layer and multi-material sheets, aiming its implementation in industrial automotive stamping processes. All the work carried out was developed in close collaboration with one of the largest portuguese suppliers of automotive stamped products, the SODECIA Group. The companies Lamera AB and Thyssenkrupp AG also contributed with their products, the micro-sandwich materials Hybrix and Litecore S, for the experimental tests. In addition, two of the most popular stamping commercial FE codes in the automotive industry, AutoForm and PAM-STAMP 2G, are deeply evaluated and compared before being used to perform micro-sandwich sheet forming simulations. Throughout this thesis, a number of production and manufacturing related challenges are discussed, and different areas where the requirements of design engineering tools needs to be evaluated concerning the micro-sandwich materials and design decisions are highlighted in order for automotive manufacturers to ensure future market competitiveness.

---

#### **KEYWORDS**

SHEET METAL FORMING; MICRO-SANDWICH SHEETS; EXPERIMENTAL CHARACTERIZATION  
NUMERICAL SIMULATION; FINITE ELEMENT ANALYSIS TOOLS; AUTOMOTIVE INDUSTRY

---

# ÍNDICE

AGRADECIMENTOS .....	iii
RESUMO.....	v
ABSTRACT.....	vii
ÍNDICE.....	ix
ÍNDICE DE FIGURAS.....	xi
ÍNDICE DE TABELAS .....	xxiii
NOTAÇÕES E CONVENÇÕES.....	xxvii
NOMENCLATURA .....	xxxi
SIGLAS, ABREVIATURAS E ACRÓNIMOS .....	xxxv
1. INTRODUÇÃO .....	1
2. ARTIGO 1: “Comprehensive Benchmark Study of Commercial Sheet Metal Forming Simulation Software Used in the Automotive Industry” .....	13
3. ARTIGO 2: “Role of Process and Numerical Parameters on the Virtual Manufacturing of Automotive Deep-Drawn Parts” .....	49
4. ARTIGO 3: “Hybrix: Experimental Characterization of a Micro-Sandwich Sheet” .....	85
5. ARTIGO 4: “Modelling Strategies and FEM Approaches to Characterize Micro-Sandwich Sheets with Unknown Core Properties” .....	111
6. ARTIGO 5: “Experimental Validation Against Different FEM Models in the Simulation of Micro-Sandwich Sheets Forming Under Complex Strain Paths” .....	157
7. CONTRIBUIÇÃO PARA O CENTRO DE COMPETÊNCIAS DE PRODUTO SODECIA E PARA A INDÚSTRIA AUTOMÓVEL EM GERAL.....	211
8. REFERÊNCIAS.....	225
A. Anexo A – CINEMÁTICA DO MEIO CONTÍNUO .....	231
B. Anexo B – TEORIA DA PLASTICIDADE.....	241



## ÍNDICE DE FIGURAS

Fig. 1.1 – Componentes estampados produzidos pelo grupo Sodécia .....	1
Fig. 1.2 – Detalhe representativo da constituição de uma chapa multi-camada Hybrix desenvolvida e produzida pela empresa Lamera AB ( <i>Hybrix Brochure</i> , 2009).....	2
Fig. 1.3 – Empresas que participaram no projeto de investigação e apoiaram o PCC-S a desenvolver ferramentas e metodologias para a implementação de chapas multi-camada em componentes estampados. ....	3
Fig. 1.4 – Utilização de aços avançados de elevada resistência no <i>body</i> da pick-up Chevrolet Colorado 2015 (Wendy, 2015). ....	4
Fig. 1.5 – Diagrama representativo da estrutura da tese de doutoramento, baseada em cinco áreas de estudo, sobre as quais se produziu publicação científica. ....	9
Fig. 2.1 – S-Rail topology after the drawing operation (intermediate state) for the case of smooth beads [17]. ....	19
Fig. 2.2 – Numisheet 2008 BM 02 Stamping Tools: Blankholder, Drawbeads and Die [17]. ....	19
Fig. 2.3 - Section cuts of tools in initial position: a) without beads and b) with smooth beads (bead height = 3.6 mm) [17]. ....	19
Fig. 2.4 - Tools and blank in initial position before drawing [17]. ....	22
Fig. 2.5 - Tools and blank in home position after drawing [17]. ....	22
Fig. 2.6 – Comparison of experimental and numerical punch forces during the drawing operation, with the respective mean deviations, to the load cases without drawbeads. ....	22
Fig. 2.7 – Comparison of experimental and numerical punch forces during the drawing operation, with the respective mean deviations, to the load cases with drawbeads. ....	23
Fig. 2.8 – Variation of punch force in the experimental setup with no beads wrt. changing blankholder force (HC260LAD) [15]. ....	25
Fig. 2.9 - Variation of punch force in the experimental setup with no beads wrt. changing blankholder force (AC170) [15]. ....	25
Fig. 2.10 – Position and naming of the draw-in sections with the respect to the S-rail geometry. [17]. ....	26
Fig. 2.11 – Comparison of experimental and numerical section’s displacements during the drawing operation, with the respective mean deviations, to the load case AC170 LC1. ....	27

Fig. 2.12 – Comparison of experimental and numerical section’s displacements during the drawing operation, with the respective to mean deviations, to the load case HC260LAD LC1. ....	27
Fig. 2.13 – Comparison of experimental and numerical section’s displacements during the drawing operation, with the respective to mean deviations, to the load case AC170 LC3. ....	28
Fig. 2.14 – Comparison of experimental and numerical section’s displacements during the drawing operation, with the respective mean deviations, to the load case HC260LAD LC3. ....	28
Fig. 2.15 – Sections A2D – D2D for the evaluation of major/minor strains [17]. ....	30
Fig. 2.16 – Comparison of experimental and numerical principal strains over the arc-length distance of the section cut B2D, after springback, to the load cases without drawbeads. ....	30
Fig. 2.17 – Peak levels of numerical major strains localized at the inner top radius curvature of the geometry. [17]. ....	31
Fig. 2.18 – Comparison of experimental and numerical principal strains over the arc-length distance of the section cut B2D, after springback, to the load cases with drawbeads. ....	32
Fig. 2.19 – Comparison of experimental and numerical principal strains over the arc-length distance of the section cut C2D, after springback, to the load cases without drawbeads. ....	32
Fig. 2.20 – Comparison of experimental and numerical principal strains over the arc-length distance of the section cut B2D, after springback, to the load cases with drawbeads. ....	33
Fig. 2.21 – Direction of strain paths variation when drawbeads are introduced in the S-Rail drawing operation. ....	34
Fig. 2.22 – Comparison of Autoform’s FLD and Pam-Stamp’s FLD with the respective state of the material points in the part, at the end of the drawing operation, to the load case AC170 LC1. ...	35
Fig. 2.23 – Comparison of Autoform’s FLD and Pam-Stamp’s FLD with the respective state of the material points in the part, at the end of the drawing operation, to the load case HC260LAD LC1. ....	36
Fig. 2.24 – Comparison of Autoform’s FLD and Pam-Stamp’s FLD with the respective state of the material points in the part, at the end of the drawing operation, to the load case AC170 LC3. ...	36
Fig. 2.25 – Comparison of Autoform’s FLD and Pam-Stamp’s FLD with the respective state of the material points in the part, at the end of the drawing operation, to the load case HC260LAD LC3. ....	37
Fig. 2.26 – Part with grid for the optical measurement [17]. ....	38
Fig. 2.27 – Location of holes in S-Rail for fixing in measurement device [17]. ....	38
Fig. 2.28 – Presentation of the profile for springback measurements based on the deviation’s angles ( $\theta_1$ , $\theta_2$ , $\alpha_1$ , $\alpha_2$ ) of the reference section X = -90 [17]. ....	39

Fig. 2.29 – Comparison of experimental and numerical S-rail geometries without drawbeads after springback at the reference section $X = -90$ . .....	39
Fig. 2.30 – Comparison of experimental and numerical S-rail geometries with drawbeads after springback at the reference section $X = -90$ . .....	40
Fig. 2.31 – Comparison of Autoform and Pam-Stamp run time simulations for all the load cases studied. ....	42
Fig. 3.1 – S-Rail topology after the drawing operation (intermediate state) for the case of smooth beads [63]. .....	55
Fig. 3.2 - Numisheet 2008 BM 02 Stamping Tools: Blankholder, Drawbeads and Die [63]. .....	55
Fig. 3.3 - Section cuts of tools in initial position: a) without beads and b) with smooth beads (bead height = 3.6 mm) [63]. .....	55
Fig. 3.4 - Section cuts of tools in initial position: drawbead channel with clearance (Original CAD); drawbead channel without clearance (Modified CAD) [63]. .....	57
Fig. 3.5 – Mechanical and constitutive parameters of the yield criteria and hardening models used in the variability study [63]. .....	59
Fig. 3.6 – Comparison of experimental and numerical forming forces during the drawing operation, with the respective mean deviations, to the set of simulations related with the variability of the material model. ....	61
Fig. 3.7– Comparison of experimental and numerical forming forces during the drawing operation, with the respective mean deviations, to the set of simulations related with the variability of the friction conditions. ....	62
Fig. 3.8 – Comparison of experimental and numerical forming forces during the drawing operation, with the respective mean deviations, to the set of simulations related with the variability of the drawbead geometry. ....	63
Fig. 3.9 – Comparison of the maximum deviation between the numerical results obtained to each parameter (set of simulations), with and without drawbeads. ....	64
Fig. 3.10 – Position and naming of the draw-in sections with the respect to the S-rail geometry. [63]. .....	64
Fig. 3.11 – Comparison of experimental and numerical section’s displacements during the drawing operation, with the respective mean deviations, to the set of simulations related with the variability of the material model, when no drawbeads are present. ....	65
Fig. 3.12 – Comparison of experimental and numerical section’s displacements during the drawing operation, with the respective mean deviations, to the set of simulations related with the variability of the friction conditions, when no drawbeads are present. ....	66



Fig. 3.13 – Comparison of the mean values of the maximum deviations [mm] of all sections, for the simulation parameters of the case without drawbeads.....	67
Fig. 3.14 – Comparison of experimental and numerical section’s displacements during the drawing operation, with the respective mean deviations, to the set of simulations related with the variability of the material model, when drawbeads are present. ....	68
Fig. 3.15 – Comparison of experimental and numerical section’s displacements during the drawing operation, with the respective mean deviations, to the set of simulations related with the variability of the friction conditions, when drawbeads are present. ....	69
Fig. 3.16 – Comparison of experimental and numerical section’s displacements during the drawing operation, with the respective mean deviations, to the set of simulations related with the variability of the drawbead clearance. ....	70
Fig. 3.17 – Comparison of the mean values of the maximum deviations [mm] of all sections, for the simulation parameters of the case with drawbeads.....	71
Fig. 3.18 – Presentation of the profile for springback measurements based on the deviation’s angles [°] ( $\theta_1$ , $\theta_2$ , $\alpha_1$ , $\alpha_2$ ) of the reference section $X = -90$ and springback points constraint.....	72
Fig. 3.19 – Comparison of experimental and numerical S-rail geometries after springback, at the reference section $X = -90$ , to the set of simulations related with the variability of the material model. ....	73
Fig. 3.20 – Comparison of experimental and numerical S-rail geometries after springback, at the reference section $X = -90$ , to the set of simulations related with the variability of the friction conditions. ....	73
Fig. 3.21 – Comparison of experimental and numerical S-rail geometries after springback, at the reference section $X = -90$ , to the set of simulations related with the variability of the drawbead clearance. ....	74
Fig. 3.22 – Comparison of the mean values of the maximum deviations [°], obtained for each simulation parameter, with and without drawbeads. ....	76
Fig. 4.1 – Scheme of the Hybrix micro-sandwich sheet material, comprising two stainless steel layers and an intermediate composite core (metallic stainless-steel fibers embedded in an epoxy resin). The total nominal thickness of 1.6mm can be decomposed in two skin layers of 0.15 mm and a core with 1.3 mm. ....	88
Fig. 4.2 – Experimental force-displacement curves, with error bars, and correspondent stress-strain curves, for orientations of $0^\circ$ , $45^\circ$ and $90^\circ$ , for the Hybrix sheet. Average values of Young modulus ( $E$ ), yield stress ( $Y$ ) and ultimate tensile strength ( $UTS$ ) with the respective uncertainty. 91	

Fig. 4.3 – Experimental force-displacement curves, with error bars, and correspondent stress-strain curves, for orientations of 0°, 45° and 90°, for the metallic skins only. Average values of Young modulus ( $E$ ), yield stress ( $Y$ ) and ultimate tensile strength ( $UTS$ ) with the respective uncertainty.	92
Fig. 4.4 – Experimental Hybrix Forming Limit Curve (FLC), defined with 4 experimental points, with error bars and respective uncertainty.....	93
Fig. 4.5 – Decomposition load strategy. The 3 layers (2 metallic skins plus the core) are loaded in parallel during the uniaxial tensile test, and thus the total uniaxial tensile force can be decomposed in two components, the forces supported by the two metallic skins plus the force supported by the core. ....	94
Fig. 4.6 – Deducted core’s force-displacement curve and stress-strain curve. ....	95
Fig. 4.7 – Resultant core hardening curve identified for the core from the <i>true</i> stress-strain curve. ....	98
Fig. 4.8 – Swift parameters for the skin hardening curve definition. Comparison with the experimental stress-strain curve.....	98
Fig. 4.9 – Comparison between Hybrix experimental force-displacement curve and Hybrix numerical force-displacement curve.....	99
Fig. 4.10 – Finite element mesh with 3D Solid multilayer configuration. ....	100
Fig. 4.11 – Control Nodes used to mimic the displacement of the physical extensometer and determine the strain in the specimens after the tensile test. ....	100
Fig. 4.12 – Comparison of real and numerical punch forces during Nakazima test to each specimen geometry. ....	101
Fig. 4.13 – Cross-section for major strain evaluation of all Nakazima specimens. ....	102
Fig. 4.14 – Different evaluation stages.....	102
Fig. 4.15 – Comparison between experimental and numerical major strain distribution, in the same cross-section, to all specimen’s geometries. ....	104
Fig. 4.16 – Comparison between numerical and real formability results in the specimen b180 to 44mm of punch displacement.....	105
Fig. 4.17 – Comparison between numerical and real formability results in the specimen b100 to 32mm of punch displacement.....	105
Fig. 4.18 – Comparison between numerical and real formability results in the specimen b65 to 32mm of punch displacement.....	106
Fig. 4.19 – Comparison between numerical and real formability results in the specimen b30 to 31mm of punch displacement.....	106

Fig. 4.20 – Comparison between numerical and real formability results in the specimen b20 to 27mm of punch displacement. ....	107
Fig. 5.1 – Different mesh structures (Single fiber angle $\theta$ [°], Single fiber diameter $D$ [ $\mu\text{m}$ ] and fiber volume fraction $f$ [%]). a) CAMBOSS, b) CAMBOSS, c) CAMBRASS. ....	114
Fig. 5.2 – Scheme of the Hybrix micro-sandwich sheet material, comprising two stainless steel layers and an intermediate composite core (metallic/polymeric fibers embedded in an epoxy resin). ....	115
Fig. 5.3 – Presentation of the different strategies and approaches used in this study to characterize, modelling and simulate micro-sandwich Hybrix sheets with unknown core properties. ....	118
Fig. 5.4 – Decomposition load strategy of Hybrix. The 3 layers (2 metallic skins plus the core) are loaded in parallel during the uniaxial tensile test, and thus the total uniaxial tensile force can be decomposed in two components, the forces supported by the two metallic skins plus the force supported by the core. ....	120
Fig. 5.5 – Experimental average force-displacement curves of Hybrix 1mm, AISI 304L 0.10mm (2 skins sum), and deduced core of 0.80mm at the rolling direction. ....	121
Fig. 5.6 – Experimental average force-displacement curves of Hybrix 1mm, AISI 304L 0.10mm (2 skins sum), and deduced core of 0.80mm at 45° with the rolling direction. ....	121
Fig. 5.7 – Experimental average force-displacement curves of Hybrix 1mm, AISI 304L 0.10mm (2 skins sum), and deduced core of 0.80mm at 90° with the rolling direction. ....	121
Fig. 5.8 – Engineering stress-strain curves and the true stress-strain curves of the Hybrix 1mm, AISI 304L 0.10mm skin and deduced core of 0.80mm at the rolling direction. ....	123
Fig. 5.9 – Presentation of the graphical method (linear regression) to obtain the Young's Modulus $E$ and the hardening index $n$ from the linear trendline equation applied to the true stress-strain curve and the logarithmic true stress-strain curve at rolling direction. ....	124
Fig. 5.10 – Yield proof strength determined from the intersection of the true stress-strain curve (rolling direction) and proportional limit curve with an offset strain of 0.2%. ....	125
Fig. 5.11 – Experimental hardening curves of Hybrix micro-sandwich and AISI 304L skin, and deduced Hybrix core stress-strain curve, with respective Swift-Voce hardening curves. ....	127
Fig. 5.12 – Hybrix tensile specimen meshes based on <i>3D Brick Multilayer Model</i> and <i>2D Shell Multilayer Model</i> . ....	129
Fig. 5.13 – Control Nodes used to mimic the displacement of the physical extensometer and measure the strain in the specimens after the virtual tensile test. ....	130

Fig. 5.14 – Comparison between the experimental force-displacement curves and the numerical force-displacement curves based on 2D Shell approach and 3D brick approach. ....	130
Fig. 5.15 – Presence of 2 core types: a) glue epoxy resin with metallic fibers (asymmetric Hybrix). b) rubberized epoxy with polymeric fibers (symmetric Hybrix). ....	132
Fig. 5.16 – Experimental and numerical force-displacement curves to the orientations 0°, 45° and 90° for both symmetric and asymmetric Hybrix configurations. ....	133
Fig. 5.17 – Due to the different plastic behavior of the metallic skins, in the asymmetric configuration, the tensile specimens tend to bend after the rupture. ....	134
Fig. 5.18 – Experimental Nakazima tests conditions: a) Dimensions and shape of the dog bone geometries according ISO 12004:2008 b) Erichsen (model 142-40) universal testing machine c) Speckle pattern for strain measurements d) Position of the GOM ARAMIS cameras. ....	135
Fig. 5.19 – Post-treatment of the recorded strain data through the cross-section method. ....	136
Fig. 5.20 – Experimental Hybrix Forming Limit Curve (FLC) of each Hybrix configuration, defined with the averaged principal strains optically measured and the respective uncertainty. .	137
Fig. 5.21 – Presentation of the Nakazima tool set and Blank at FE meshes. ....	138
Fig. 5.22 – Comparison of the numerical punch forces, delivered by all the FEM approaches, and the experimental results during Nakazima tests for both, symmetric and asymmetric Hybrix configurations, of the specimen's geometries B180, B100, B65 and B30. ....	140
Fig. 5.23 – Comparison of the experimental Nakazima forces and the numerical Nakazima forces of AutoForm R5.2 and PAM-STAMP 2G 2015.1 using 2D shell multilayer approaches. ....	141
Fig. 5.24 – Comparison of experimental and numerical force-displacement curves of the asymmetric B180 specimen with both Hill48 and Hill48 + biaxial factor = 0.75 ....	142
Fig. 5.25 – Cross-section for major strain evaluation of all Nakazima specimens. ....	143
Fig. 5.26 – Different evaluation stages. ....	143
Fig. 5.27 – Comparison between experimental and numerical major strain distribution, in the same cross-section, to all specimen's geometries tested using different modelling strategies and FEM approaches. ....	144
Fig. 5.28 – Representation of 1 quarter of the B180 symmetric (at 30mm of punch displacement) and B180 asymmetric specimens (at 25mm of punch displacement) in AutoForm and PAM-STAMP 2G with the major strain variable displayed for the top skin. The maximum values are presented and compared. ....	146
Fig. 5.29 – Principal types of failure observed in the Nakazima specimens: Asymmetric Hybrix – Delamination and Wrinkles; Symmetric Hybrix – Tearing. ....	148

Fig. 6.1 – Stamped Prototype of an aluminium automotive fuel filling system designed by Sodectia.....	162
Fig. 6.2 – Set of stamping tools (Die, Blank-Holder and Punches) to the concave shell (a and d) and the convex shell (b and c). Blank in the initial position (d).....	163
Fig. 6.3 – Dimensions of the original rectangular blank.....	163
Fig. 6.4 – Presentation of the virtual stamping process in 2 forming operations. a) Closing of the tool pair Die/Blank-Holder to bend the Blank. b) Deep-drawing of the concave shell. ....	164
Fig. 6.5 – Presentation of true stress/strain curves of the metallic skins and polymeric core of the Litecore S .....	165
Fig. 6.6 – Presentation of the 3 FE mesh multilayer configurations compared in this study. ...	166
Fig. 6.7 – Position and naming of the draw-in sections with the respect to the part geometry. ....	168
Fig. 6.8 – Experimental measurements of the y-distances in cross sections defined in the study and marked in the part .....	168
Fig. 6.9 – Comparison of numerical and experimental wrinkling tendencies. Areas of material accumulation are highlighted with blue dotted circles, while areas with visible wrinkles are highlighted with red dotted circles. Black outline highlights the FEM model that failed to predict all areas of material accumulation or wrinkles identified in the real parts. ....	170
Fig. 6.10 – Presentation of a tools section cut at position $x=160$ . The acumulation material zone is represented by a gray circle. ....	171
Fig. 6.11 – Comparison of the Litecore S sheet behavior in the accumulation zone, predicted by the different FEM models and observed in the real part at the final of deep-drawing operation...	172
Fig. 6.12 – Position of the FLC of CR300IF+ZE, corresponding to the metallic skins of the micro-sandwich Litecore S, in FLD. ....	173
Fig. 6.13 – Cloud of the material points, and the respective strain state, predicted by the 2D/3D model, in the upper skin of the stamped part and in the FLD at 12mm, 6mm and 2mm.....	174
Fig. 6.14 – Cloud of the material points, and the respective strain state, predicted by the 2D/3D model, in the lower skin of the stamped part and in the FLD at 12mm, 6mm and 2mm. ....	175
Fig. 6.15 – Picture of the real part at the instant 2mm. ....	175
Fig. 6.16 – a) Tools and blank in initial position before deep-drawing operation. b) Tools and blank in home-position after deep-drawing operation.....	176
Fig. 6.17 – Comparison of the evolution of the numerical punch forces to all the FEM approaches during the deep-drawing operation. ....	176

Fig. 6.18 – Comparison of the principal strain profile of section 0, obtained from each FEM model, at 12mm of the end of the die stroke. Thickness profiles for the 2D Shell and 2D/3D model are also compared. The results are presented for lower and upper skin.....	179
Fig. 6.19 – Comparison of the principal strain profile of section -60, obtained from each FEM model, at 12mm of the end of the die stroke. Thickness profiles for the 2D Shell and 2D/3D model are also compared. The results are presented for lower and upper skin.....	181
Fig. 6.20 – Comparison of the principal strain profile of section +80, obtained from each FEM model, at 12mm of the end of the die stroke. Thickness profiles for the 2D Shell and 2D/3D model are also compared. The results are presented for lower and upper skin.....	182
Fig. 6.21 – Comparison of the principal strain profile of section 0, obtained from each FEM model, at 6mm of the end of the die stroke. Thickness profiles for the 2D Shell and 2D/3D model are also compared. The results are presented for lower and upper skin. ....	184
Fig. 6.22 – Comparison of the principal strain profile of section -60, obtained from each FEM model, at 6mm of the end of the die stroke. Thickness profiles for the 2D Shell and 2D/3D model are also compared. The results are presented for lower and upper skin. ....	185
Fig. 6.23 – Comparison of the principal strain profile of section +80, obtained from each FEM model, at 6mm of the end of the die stroke. Thickness profiles for the 2D Shell and 2D/3D model are also compared. The results are presented for lower and upper skin. ....	187
Fig. 6.24 – Comparison of the principal strain profile of section 0, obtained from each FEM model, at 2mm of the end of the die stroke. Thickness profiles for the 2D Shell and 2D/3D model are also compared. The results are presented for lower and upper skin. ....	189
Fig. 6.25 – Comparison of the principal strain profile of section -60, obtained from each FEM model, at 2mm of the end of the die stroke. Thickness profiles for the 2D Shell and 2D/3D model are also compared. The results are presented for lower and upper skin. ....	190
Fig. 6.26 – Comparison of the principal strain profile of section +80, obtained from each FEM model, at 2mm of the end of the die stroke. Thickness profiles for the 2D Shell and 2D/3D model are also compared. The results are presented for lower and upper skin. ....	192
Fig. 6.27 – Comparison between the principal strain profiles predicted by 2D Shell model, with 2 element sizes (0.5x0.5 and 2x2), and the principal strain profiles predicted by the 3D Solid model, to the section 0, at 2mm of the end of the die stroke. Thickness profiles for the 2D Shell models (0.5x0.5 and 2x2) and 2D/3D model are also compared. The results are presented for lower and upper skin. ....	195

Fig. 6.28 – Comparison of the evolution of the maximum principal stresses value across the section 0 predicted from each FEM model (2D Shell, 2D/3D and 3D Solid), at the 3 stages of the deep-drawing operation (12mm, 6mm and 2mm). The results are presented for lower and upper skin.	197
Fig. 6.29 – Comparison of the evolution of the maximum principal stresses value across the section -60 predicted from each FEM model (2D Shell, 2D/3D and 3D Solid), at the 3 stages of the deep-drawing operation (12mm, 6mm and 2mm). The results are presented for lower and upper skin.	198
Fig. 6.30 – Comparison of the evolution of the maximum principal stresses value across the section +80 predicted from each FEM model (2D Shell, 2D/3D and 3D Solid), at the 3 stages of the deep-drawing operation (12mm, 6mm and 2mm). The results are presented for lower and upper skin.	199
Fig. 6.31 – Comparison of the evolution of the maximum principal stresses value across the sections 0 and -60 at instant 6mm. Four FEM models are compared – the 2D Shell model, with 2 element sizes (0.5x0.5 and 2x2), the 2D/3D model and the 3D Solid model. The results are presented for lower and upper skin.	200
Fig. 6.32 – Modifications to the shape and dimensions of the original blank.	202
Fig. 6.33 – Comparison between the original and the modified blank - Cloud of the material points, and the respective strain state, predicted by the 2D/3D model, in the upper skin of the stamped part and in the FLD at 2mm.	203
Fig. 6.34 – Comparison between the original and the modified blank - Cloud of the material points, and the respective strain state, predicted by the 2D/3D model, in the lower skin of the stamped part and in the FLD at 2mm.	204
Fig. A.1 – Fenómenos de rotação de corpo rígido e deformação pura (Bittencourt, 2002).	233
Fig. A.2 – Trajetória de deformação até configuração final (Bittencourt, 2002).	233
Fig. A.3 – Representação da configuração intermédia $C^R$ (Alves, 2003).	237
Fig. B.1 – Representação do espaço das tensões de Haig-Westergaard (Natal, 2004).	243
Fig. B.2 – Representação do plano desviador (Natal, 2004).	244
Fig. B.3 – Condição de ortogonalidade no espaço das tensões de $\sigma_1 - \sigma_2$ (Natal, 2004).	244
Fig. B.4 – Representação das superfícies limite de elasticidade no espaço de Haig-Westergaard (Natal, 2004).	246
Fig. B.5 Influência dos coeficientes de anisotropia $r_0$ e $r_{90}$ sobre a superfície de plasticidade definida pelo critério de Hill 1948 (Banabic, 2010).	250
Fig. B.6 – Influência dos coeficientes de anisotropia $r$ e $\sigma_u$ sobre a superfície de plasticidade definida pelo critério de Hill 1948 (Banabic, 2010).	251

Fig. B.7 – Representação esquemática das superfícies plasticidade anisotrópica e “isotrópica equivalente” (Alves, 2003).....	254
Fig. B.8 – Representação geométrica da superfície de plasticidade de von Mises com os respectivos limites, superior e inferior (Alves, 2003; Karafillis and Boyce, 1993).....	256
Fig. B.9 – Representação das diferentes superfícies de plasticidade existentes entre a) von Mises e a fronteira inferior e b) von Mises e a fronteira superior (Alves, 2003; Karafillis and Boyce, 1993). .....	256
Fig. B.10 – escoamento plástico fazendo uso duma lei a) associada b) não-associada (Natal, 2004).....	277





## ÍNDICE DE TABELAS

Tab. 2.1 – Description of the Numisheet 2008 BM 02 load cases considered in this study. ....	19
Tab. 2.2 – Description of the mechanical model’s assumptions (Yield Criteria, Hardening Law, Flow Stress Model, Friction Coefficient) of each FE code. ....	20
Tab. 2.3 – Description of the numerical model’s assumptions (FE Formulation, FE Type, FE Integration, Mesh Refinement) of each FE code. ....	20
Tab. 2.4 – Friction coefficients of HC260LAD and AC170 measured in strip drawing tests at different values of contact pressure [17]. ....	24
Tab. 3.1 – Description of the Numisheet 2008 BM 02 load cases considered in this study. ....	55
Tab. 3.2 – Description of the standard mechanical model assumptions (Drawbead Geometry, Friction Coefficient, Yield Criteria, Hardening Law, Flow Stress Model,) used in deep-drawing process simulation. ....	56
Tab. 3.3 – Description of the standard mechanical model assumptions (Yield Criteria, Hardening Law, Flow Stress Model, Friction Coefficient) used in deep-drawing process simulation. ....	59
Tab. 3.4 – Description of the numerical model’s assumptions (FE Formulation, FE Type, FE Integration, Mesh Refinement) of Autoform R5.2. ....	60
Tab. 3.5 – Comparison of the maximum deviations [mm] between the numerical draw-in, in each section, for the simulation parameters of the case HC260LAD LC1. ....	66
Tab. 3.6 – Comparison of the maximum deviations [mm] between the numerical draw-in, in each section, for the simulation parameters of the case HC260LAD LC3. ....	70
Tab. 3.7 – Comparison of the maximum deviations [°] between the numerical springback, to the reference section, for the simulation parameters of the case HC260LAD LC1. ....	75
Tab. 3.8 – Comparison of the maximum deviations [°] between the numerical springback, to the reference section, for the simulation parameters of the case HC260LAD LC3. ....	75
Tab. 4.1 – Experimental yield forces from: total Hybrix uniaxial tensile test, isotropic core deduction and metallic skin deduction. ....	96
Tab. 4.2 – Experimental yield stresses from: total Hybrix uniaxial tensile test, isotropic core deduction and metallic skin deduction. ....	96
Tab. 4.3 – HILL48 constitutive parameters for the total Hybrix, the metallic skins and core. ..	97

Tab. 4.4 – Experimental tensile values and adjusted Nakazima values of the Young modulus. .....	99
Tab. 5.1 – Presentation of the experimental and deduced values of Young’s Modulus $E$ , Yield Stress $Y_s$ , Ultimate Tensile Strength $T_s$ , percentage of Elongation $A_{50}$ and Hardening Index $n$ , for Hybrix micro-sandwich and its independent layers, at the orientations $0^\circ$ , $45^\circ$ and $90^\circ$ . ....	125
Tab. 5.2 – Presentation of the six material parameters and the weighting factor used to generate the Swift-Voce hardening curves of the micro-sandwich Hybrix and its layers. ....	127
Tab. 5.3 – Presentation of the HILL48 parameters for the 1mm thick Hybrix micro-sandwich and its layers, core and skins.....	128
Tab. 5.4 – Presentation of the details of the FEM meshes topology for both 3D Brick multilayer model and 2D Shell multilayer model with the respective information of Cpu/Solver and Run Time simulation.....	131
Tab. 5.5 – Presentation of the mass, volumes and density to the core and total micro-sandwich for the both symmetric and asymmetric Hybrix and its nominal dimensions. ....	132
Tab. 6.1 – Description of the mechanical model’s assumptions (Yield Criteria, Young’s Modulus, Specific Weight) of each Litecore S layer. ....	165
Tab. 6.2 – Description of the numerical model’s assumptions (FE Type, FE Integration Rule, Gauss points over Thickness, Element Size) of each FEM approach and the respective run time simulation.....	166
Tab. 6.3 – Presentation of the experimental and numerical y-distance measured in each cross section. ....	168
Tab. 6.4 - Comparison between the highest predicted values of principal strains, thickening and thinning in the section 0, at 12mm of the end of the die stroke, and the values of the same variable predicted by the other FEM models at the same distance point.....	179
Tab. 6.5 - Comparison between the highest predicted values of principal strains, thickening and thinning in the section -60, at 12mm of the end of the die stroke, and the values of the same variable predicted by the other FEM models at the same distance point.....	181
Tab. 6.6 - Comparison between the highest predicted values of principal strains, thickening and thinning in the section +80, at 12mm of the end of the die stroke, and the values of the same variable predicted by the other FEM models at the same distance point.....	183
Tab. 6.7 - Comparison between the highest predicted values of principal strains, thickening and thinning in the section 0, at 6mm of the end of the die stroke, and the values of the same variable predicted by the other FEM models at the same distance point.....	184

Tab. 6.8 - Comparison between the highest predicted values of principal strains, thickening and thinning in the section -60, at 6mm of the end of the die stroke, and the values of the same variable predicted by the other FEM models at the same distance point. ....	186
Tab. 6.9 - Comparison between the highest predicted values of principal strains, thickening and thinning in the section +80, at 6mm of the end of the die stroke, and the values of the same variable predicted by the other FEM models at the same distance point. ....	187
Tab. 6.10 - Comparison between the highest predicted values of principal strains, thickening and thinning in the section 0, at 2mm of the end of the die stroke, and the values of the same variable predicted by the other FEM models at the same distance point. ....	189
Tab. 6.11 - Comparison between the highest predicted values of principal strains, thickening and thinning in the section -60, at 2mm of the end of the die stroke, and the values of the same variable predicted by the other FEM models at the same distance point. ....	191
Tab. 6.12 - Comparison between the highest predicted values of principal strains, thickening and thinning in the section +80, at 2mm of the end of the die stroke, and the values of the same variable predicted by the other FEM models at the same distance point. ....	192
Tab. 6.13 - Comparison of the maximum value of thickening and thinning [%] predicted by 2D Shell model and the 2D/3D model throughout the section 0 during the deep-drawing operation (12mm, 6mm and 2mm). ....	193
Tab. 6.14 - Comparison of the maximum value of thickening and thinning [%] predicted by 2D Shell model and the 2D/3D model throughout the section -60 during the deep-drawing operation (12mm, 6mm and 2mm). ....	193
Tab. 6.15 - Comparison of the maximum value of thickening and thinning [%] predicted by 2D Shell model and the 2D/3D model throughout the section +80 during the deep-drawing operation (12mm, 6mm and 2mm). ....	194
Tab. B.1 – Critérios de cedência implementados nos códigos FE comerciais mais utilizados.	273



## NOTAÇÕES E CONVENÇÕES

Utiliza-se neste texto uma notação mista tensorial – indicial. Como elementos da notação vetorial, os vetores serão representados por letras (latinas ou gregas) minúsculas a negrito ( $\mathbf{v}$ ) enquanto os tensores por letras (latinas ou gregas) maiúsculas a negrito ( $\mathbf{T}$ ). Na notação indicial para as componentes considera-se que os índices representam as três direcções cartesianas e que se verifica sempre uma soma implícita entre os índices repetidos (a menos que o contrário seja especificado). Assim,

$$A_{ij}$$

representa um dos 9 termos possíveis numa matriz 3 por 3,  $A_{11}, A_{12}, A_{13}, A_{21}, A_{22}, A_{23}, A_{31}, A_{32}, A_{33}$ . A expressão abaixo representa um dos 27 produtos possíveis

$$A_{ij}v_k$$

Contudo, considerando a existência de índices repetidos e a regra da soma implícita, a expressão

$$A_{ij}v_j$$

Passa a representar um dos apenas 3 termos possíveis, a saber

$$A_{ij}v_j = \sum_{j=1}^3 A_{ij}v_j = A_{i1}v_1 + A_{i2}v_2 + A_{i3}v_3$$

Ou seja

$$A_{ij}v_j = \begin{bmatrix} A_{11}v_1 + A_{12}v_2 + A_{13}v_3 \\ A_{21}v_1 + A_{22}v_2 + A_{23}v_3 \\ A_{31}v_1 + A_{32}v_2 + A_{33}v_3 \end{bmatrix}$$

O índice repetido no qual se realiza a soma é chamado de *índice mudo* e pode ser trocado por outra letra.

$$A_{ij}v_j = A_{ik}v_k = A_{il}v_l$$

Um símbolo importante na notação indicial é o *delta de Kronecker*

$$\delta_{ij} = \begin{cases} 0 & \text{se } i \neq j \\ 1 & \text{se } i = j \end{cases}$$

Como exemplo de aplicação deste símbolo, pode-se imaginar que a matriz identidade  $\mathbf{I}$  se escreve directamente como  $\delta_{ij}$ , isto é, uma matriz na qual as componentes na diagonal ( $i = j$ ) valem 1 e as componentes restantes são nulas.

Na convenção da notação indicial, um termo com soma implícita não pode conter mais de dois índices repetidos; termos como  $G_{ijk}F_{jj}$  estão incorrectos (para esta notação).

### Tensores

O produto entre dois tensores é identificado pelo símbolo " $\cdot$ ",

$$\mathbf{C} = \mathbf{A} \cdot \mathbf{B} \Leftrightarrow C_{ij} = A_{ik}B_{kj}$$

O produto tensorial é

$$\mathbf{S} = \mathbf{A} \otimes \mathbf{B} \Leftrightarrow S_{ijkl} = A_{ij}B_{kl}$$

A dupla contração de tensores (ou produto interno tensorial), identificada pelo símbolo " $:$ ", é:

$$s = \mathbf{A} : \mathbf{B} \Leftrightarrow s = A_{ij}B_{ij}, \quad \mathbf{C} = \mathbf{S} : \mathbf{B} \Leftrightarrow C_{ij} = S_{ijkl}B_{kl}$$

$$s = \mathbf{A} : \mathbf{S} : \mathbf{B} \Leftrightarrow s = A_{ij}S_{ijkl}B_{kl}$$

A norma dos tensores é dada por:

$$\|\mathbf{A}\| = \sqrt{\mathbf{A} : \mathbf{A}} = \sqrt{A_{ij}A_{ij}}, \quad \|\mathbf{S}\| = \sqrt{\mathbf{S} : \mathbf{S}} = \sqrt{S_{ijkl}S_{ijkl}}$$

Os super-índices  $T, S, A$  e  $'$ , quando associados a um tensor  $\mathbf{T}$  representam, respectivamente:

- O tensor transposto de  $\mathbf{T}$ ,  $(\mathbf{T}^T)_{ij} = T_{ji}$
- A parte simétrica do tensor  $\mathbf{T}$ ,  $\mathbf{T}^S = \frac{1}{2}(\mathbf{T} + \mathbf{T}^T) \Leftrightarrow T_{ij}^S = \frac{1}{2}(T_{ij} + T_{ji})$ ;
- A parte anti-simétrica do tensor  $\mathbf{T}$ ,  $\mathbf{T}^A = \frac{1}{2}(\mathbf{T} - \mathbf{T}^T) \Leftrightarrow T_{ij}^A = \frac{1}{2}(T_{ij} - T_{ji})$ ;
- A parte desviadora do tensor  $\mathbf{T}$ ,  $(\mathbf{T}')_{ij} = (\mathbf{T})_{ij} - \frac{T_{kk}}{3}\delta_{ij}$

A inversa do tensor é definida pelo índice  $^{-1}$  sobrescrito, sendo  $\mathbf{I}$  (ou  $\mathbf{I}$ ) o tensor unidade e  $\delta_{ij}$  o símbolo de *Kronecker*

$$\mathbf{A}^{-1}\mathbf{A} = \mathbf{I} \Leftrightarrow A_{ik}^{-1}A_{kj} = \delta_{ij}$$

### Vetores

As operações definidas entre os vetores são:

- O produto escalar,  $s = \mathbf{v} \cdot \mathbf{u} = \mathbf{v}\mathbf{u} \Leftrightarrow s = v_i u_i$
- O produto vetorial,  $\mathbf{C} = \mathbf{v} \otimes \mathbf{u} \Leftrightarrow C_{ij} = v_i u_j$ ;
- A norma,  $\|\mathbf{v}\| = \sqrt{\mathbf{v} : \mathbf{v}} = \sqrt{v_i v_i}$ ;

Por último, destacam-se os seguintes símbolos:

- $\mathbf{0}$  O tensor nulo sendo  $\mathbf{0}\mathbf{0} = [0]$ ;
- $(x_1, x_2, x_3)$  O sistema de eixos cartesiano global;
- $[A]$  A matriz  $\mathbf{A}$  representada num sistema cartesiano;
- $\{\mathbf{a}\}$  O vetor  $\mathbf{a}$  representado num sistema cartesiano;

div	O operador divergente;
grad, $\nabla$	O operador vetorial gradiente;
tr	O traço do tensor, $\text{tr}(\mathbf{AA}) = A_{ii}A_{ii}$ ;
(.)	O ponto é utilizado como separador decimal.





# NOMENCLATURA

## Mecânica dos Meios Contínuos

Símbolo	Descrição
$\mathbb{R}^3$	Domínio do espaço tridimensional;
$\varrho$	Ponto material
$C_0$	Configuração de referência da estrutura deformável;
$\Omega_0$	Região do espaço ocupada no instante inicial pela estrutura deformável;
$C$	Configuração corrente da estrutura deformável;
$C^R$	Configuração relaxada local;
$\Omega$	Região do espaço ocupada no instante final pela estrutura deformável;
$\dot{\alpha}$	Derivada temporal da grandeza escalar ou tensorial $\alpha$ ;
$\hat{\alpha}$	Derivada temporal objectiva da grandeza escalar ou tensorial $\alpha$ ;
$\hat{\alpha}^J$	Derivada objectiva de Jaumann do tensor $\alpha$ ;
$\hat{\alpha}$	Tensor $\alpha$ rodado para o sistema de ortotropia;
$\alpha^*$	Grandeza escalar ou vetorial conhecida no espaço e no tempo;
$\mathbf{F}$	Gradiente da transformação;
$\mathbf{F}^e$	Parte elástica do gradiente da transformação $\mathbf{F}$ ;
$\mathbf{F}^p$	Parte plástica do gradiente da transformação $\mathbf{F}$ ;
$\mathbf{L}$	Gradiente da velocidade;
$\mathbf{L}^e$	Parte elástica do gradiente da velocidade $\mathbf{L}$ ;
$\mathbf{L}^p$	Parte plástica do gradiente da velocidade $\mathbf{L}$ ;
$\mathbf{D}$	Velocidade de deformação, parte simétrica de $\mathbf{L}$ ;
$\mathbf{D}^e$	Parte elástica da velocidade de deformação;
$\mathbf{D}^p$	Parte plástica da velocidade de deformação;
$\mathbf{W}$	Velocidade de rotação, parte anti-simétrica de $\mathbf{L}$ ;

$\mathbf{W}^e$	Parte elástica da velocidade de rotação $\mathbf{W}$ ;
$\mathbf{W}^p$	Parte plástica da velocidade de rotação $\mathbf{W}$ ;
$\mathbf{R}$	Rotação elástica;
$\mathbf{U}, \mathbf{V}$	Tensor de deformação pura à direita e à esquerda;
$\mathbf{C}$	Tensor de Cauchy-Green direito;
$\mathbf{E}$	Tensor das deformações de Green-Lagrange;
$\boldsymbol{\varepsilon}, \boldsymbol{\varepsilon}_e, \boldsymbol{\varepsilon}_p$	Tensor das deformações total, elástica e plástica;
$\mathbf{v}$	Vetor velocidade de um ponto material da estrutura deformável;
$\mathbf{u}$	Vetor deslocamento de um ponto material da estrutura deformável;
$\mathbf{x}_0$	Vetor posição de um ponto material da estrutura deformável no instante inicial;
$\mathbf{x}$	Vetor posição de um ponto material da estrutura deformável no instante corrente $t$ ;

## Teoria da Plasticidade

Símbolo	Descrição
$\mathcal{F}$	Superfície de plasticidade e potencial plástico;
$\mathbf{C}^e$	Módulo elástico;
$\mathbf{C}^{ep}$	Módulo elastoplástico (tangente ou consistente);
$\boldsymbol{\sigma}$	Tensor das tensões de Cauchy;
$\sigma_1, \sigma_2, \sigma_3$	Tensões principais do tensor das tensões de Cauchy, $\boldsymbol{\sigma}'$ ;
$\sigma_\theta$	Tensão de cedência para o ângulo $\theta$ em relação à direção de laminagem;
$\sigma_b$	Tensão de cedência equibiaxial;
$\bar{\sigma}, \sigma_e$	Tensão equivalente;
$\boldsymbol{\Sigma}$	Tensor das tensões efectivo, $\boldsymbol{\Sigma} = \boldsymbol{\sigma} - \mathbf{X}$ ;
$\mathbf{X}$	Tensor das tensões inversas ou <i>back-stress</i> ;
$s_1, s_2, s_3$	Tensões principais do tensor das tensões efectivo transformado, $\mathbf{s} = \mathbf{L} : (\boldsymbol{\sigma} - \mathbf{X})$ ;

$I_1, I_2, I_3$	Primeiro, segundo e terceiro invariantes do tensor das tensões $\boldsymbol{\sigma}$ ;
$J_1, J_2, J_3$	Primeiro, segundo e terceiro invariantes do tensor das tensões desviador $\boldsymbol{\sigma}'$ ;
$\lambda$	Multiplicador plástico;
$\bar{\epsilon}^p$	Deformação plástica equivalente;
$\hat{\mathbf{V}}$	Primeira derivada da tensão equivalente $\bar{\sigma}$ em ordem ao tensor das tensões efectivo, $\boldsymbol{\Sigma}$ ;
$r_\theta$	Coefficiente de anisotropia para o ângulo $\theta$ em relação à direção de laminagem;
$\bar{r}$	Valor médio dos coeficientes de anisotropia;
$r_b$	Coefficiente de anisotropia $r$ em tração biaxial;
$\nu$	Coefficiente de Poisson;
$\lambda, \mu$	Coefficientes de Lamé;
$E$	Módulo de elasticidade ou módulo de Young;
$G$	Módulo de rigidez ou módulo de corte ( $G = \mu$ );
$K$	Módulo de compressibilidade;
$\rho$	Massa volúmica;
$h$	Parâmetro escalar de encruamento isotrópico;
$H'$	Módulo de encruamento isotrópico;
$Y$	Tensão limite de elasticidade em tração uniaxial;
$Y_0$	Tensão limite de elasticidade inicial em tração uniaxial;
$\mathbf{s}$	Tensor das tensões obtido a partir da transformação linear do tensor das tensões efectivo, $\mathbf{s} = \mathbf{L} : (\boldsymbol{\sigma} - X)$ ;
$\mathbf{t}$	Vetor tensão de Cauchy;
$\mathbf{S}$	Primeiro tensor das tensões de Piola-Kirchhoff;
$\mathbf{\Pi}$	Segundo tensor das tensões de Piola-Kirchhoff;

## Parâmetros constitutivos

Símbolo	Descrição
$F G H L M N$	Parâmetros de anisotropia do critério Hill48;
$\mathbf{M}$	Tensor de anisotropia de Hill48;
$f g h a b c m$	Parâmetros de anisotropia do critério Hill79;
$F G H a$	Parâmetros de anisotropia do critério Hosford 1979;
$c_1 c_2 c_3 c_4 c_5 c_6 a$	Parâmetros de anisotropia do critério Yld91;
$c_1 c_2 c_3 c_4 c_5 c_6 c k$	Parâmetros de anisotropia dos critérios KB93;
$\mathbf{L}$	Transformação linear, tensor de anisotropia (Yld91, KB93);
$a_1 \dots a_6 b_1 \dots b_{11} c$	Parâmetros de anisotropia do critério CB2001;
$\alpha_1 \dots \alpha_8$	Parâmetros de anisotropia do critério Yld2000;
$\mathbf{T}$	Matrix de transformação no critério Yld2000;
$\mathbf{X}$	Tensor de tensão de transformação linear do critério Yld2000;
$\lambda$	Parâmetros da função de Bézier usado no critério Vegter 2006;
$a b c k M N P Q R$	Parâmetros de anisotropia do critério BBC2000;
$a k M N P Q R S T$	Parâmetros de anisotropia do critério BBC2003;
$a b k L M N P Q R$	Parâmetros de anisotropia do critério BBC2005;
$C, \varepsilon_0, n$	Parâmetros da lei de Swift (encruamento isotrópico);
$Y_{sat}, C_Y, Y_0$	Parâmetros da lei de Voce (encruamento isotrópico);
$k$	Parâmetro da lei de Prager (encruamento cinemático linear);
$X_{sat}, C_X$	Parâmetros da lei de Lemaître & Chaboche 1985 (encruamento cinemático não-linear com saturação).

## SIGLAS, ABREVIATURAS E ACRÓNIMOS

Símbolo	Descrição
PCC-S	Centro de competências de produto – Sodécia;
R&D	Investigação e desenvolvimento;
OEM	Fabricantes ou construtores originais;
FEM	Método de elementos finitos;
FEA	Análise por elementos finitos;
CAE	Engenharia assistida por computador;
DD3IMP	Contração de “Deep Drawing 3D IMPLICIT finite element code”;
RD/TD/ND	Direção de laminagem, direção transversa e direção normal ao plano da chapa;
TBH	Modelo de plasticidade de policristais de Taylor-Bishop-Hill;
CFC	Estrutura cristalina cúbica de faces centradas
CCC	Estrutura cristalina cúbica do corpo centrado
HC	Estrutura cristalina hexagonal compacta
Hill48	Critério de plasticidade de Hill 1948;
Hill79	Critério de plasticidade de Hill 1979;
Yld89	Critério de plasticidade de Barlat <i>et al.</i> 1989;
Yld91	Critério de plasticidade de Barlat <i>et al.</i> 1991;
Yld2000	Critério de plasticidade de Barlat <i>et al.</i> 2000;
IPE	Estado plástico isotrópico equivalente;
KB93	Critério de Karafilis & Boyce 1993;
CB2001	Critério de Cazacu & Barlat 2001.
BBC2000	Critério de plasticidade de Banabic <i>et al.</i> 2000;
BBC2003	Critério de plasticidade de Banabic <i>et al.</i> 2003;
BBC2005	Critério de plasticidade de Banabic <i>et al.</i> 2005;



# 1. INTRODUÇÃO

## Motivação

A Sodecia SGPS é um grupo industrial português que atua no mercado automóvel há cerca de trinta anos e que consolidou a sua experiência, sobretudo, no desenvolvimento e produção de componentes estampados. O Centro de Competências de Produto Sodecia (PCC-S), empresa do grupo Sodecia SGPS, é uma empresa criada em 2005 com a finalidade de conceber e projectar componentes para veículos, automóveis ou motocicletas, e criar e desenvolver novos produtos e processos, respondendo às solicitações das unidades industriais do Grupo e dos seus Clientes.

Desde a sua criação que o Centro de Competências de Produto Sodecia participa ativamente no desenvolvimento de novos produtos e novas soluções de engenharia para a indústria automóvel, encontrando-se particularmente focado na concepção de produtos estampados [Fig. 1.1].

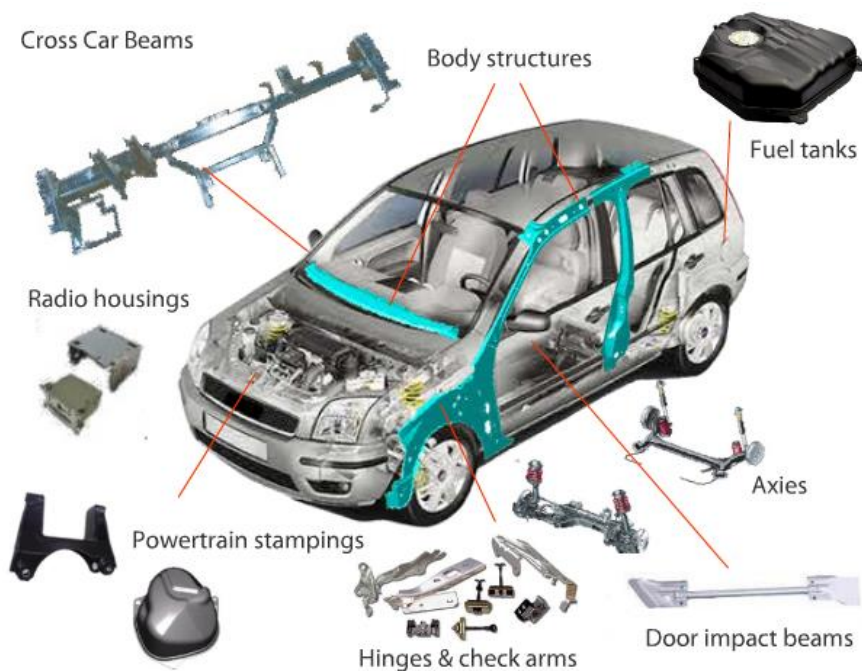


Fig. 1.1 – Componentes estampados produzidos pelo grupo Sodecia

Nos últimos anos, têm sido várias as parcerias de R&D estabelecidas pelo PCC-S com vista ao desenvolvimento de novos produtos e novas soluções para a indústria automóvel. Tais estudos envolvem, em geral, a utilização de novos materiais, novas tecnologias e novos processos de manufatura, que exigem as mais recentes e avançadas ferramentas de simulação.



Em 2010 foi estabelecida uma parceria entre o PCC-S e a empresa Lamera AB com o intuito de desenvolver uma aplicação automóvel para um material multi-camada denominado Hybrix [Fig. 1.2].

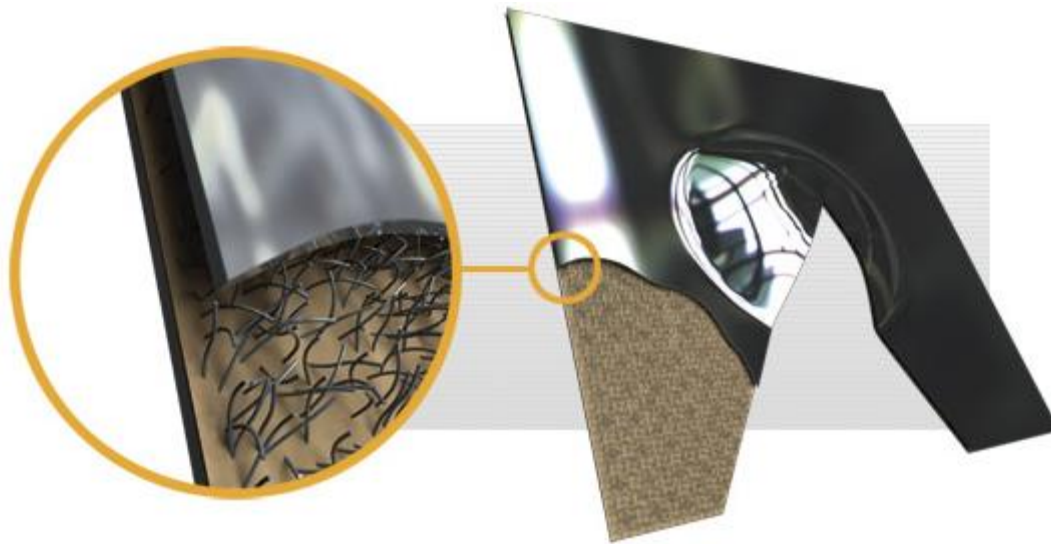


Fig. 1.2 – Detalhe representativo da constituição de uma chapa multi-camada Hybrix desenvolvida e produzida pela empresa Lamera AB (*Hybrix Brochure*, 2009)

O Hybrix um é *micro-sandwich* de aço inoxidável de elevada rigidez, baixo peso e espessura reduzida, utilizado em vários produtos, nomeadamente, aplicações interiores em aviões. Este material é constituído por uma camada intermédia de fibras metálicas/poliméricas impregnadas em uma resina epoxídica e duas camadas externas de aço inoxidável. Contrariamente a outros materiais multi-camada disponíveis no mercado, o Hybrix pode ser processado e conformado como as chapas metálicas convencionais. Por isso, é possível utilizar este material como substituto direto das chapas de aço ou de alumínio na maioria das aplicações.

O primeiro contacto com este material surgiu em 2008 no âmbito de um projeto denominado “*New Generation Hybrid Fuel Tank*” (NGHFT). O objetivo inicial deste projeto era a conceção de um tanque de combustível com materiais híbridos, isto é, não exclusivamente metálico, mas que pudesse ser produzido a partir de processos de estampagem convencional e competir com as atuais soluções poliméricas que recorrem a processos de moldação por injeção e dominam o mercado automóvel. A conceção do processo de estampagem e o desenvolvimento do projeto da ferramenta ficaram, em parte, comprometidos pela impossibilidade de modelar e simular processos de deformação plástica de materiais multi-camada com os softwares de simulação numérica utilizados até então (PAM-STAMP 2G e AutoForm). Após este projeto, os desenvolvedores destas ferramentas comerciais

começaram a incorporar os primeiros módulos dedicados à simulação de processos de estampagem com materiais multi-camada. Em primeiro lugar o PAM-STAMP 2G, no início de 2010, e depois o AutoForm, em 2013. Este esforço surgiu para suportar o desenvolvimento de novos materiais deste tipo, como foi o caso do *Litecore* da gigante Thyssenkrupp, e a aposta de fabricantes reconhecidos, como a Volkswagen, na sua aplicação tanto em automóveis de competição como de série. É, portanto, do interesse conjunto da Sodécia, em ultrapassar as limitações encontradas ao seu trajeto de inovação, da Lamera, em ampliar o leque de aplicações do seu material e posicionar-se no mercado automóvel, e dos desenvolvedores das ferramentas comerciais PAM-STAMP 2G e AutoForm, em testar a eficiência, exactidão e robustez dos seus novos módulos multi-camada, que nascem as condições para a referida parceria Sodécia/Lamera em um estudo mais profundo e detalhado deste tipo de materiais, ao qual se juntou posteriormente uma colaboração da Thyssenkrupp [Fig. 1.3].

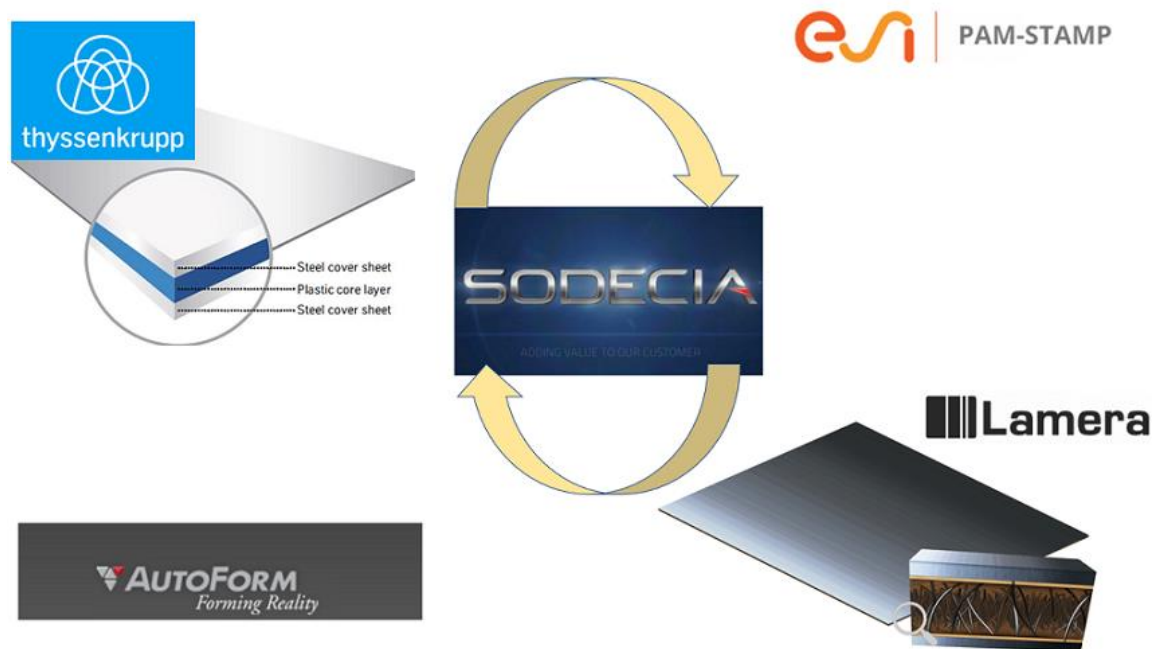


Fig. 1.3 – Empresas que participaram no projeto de investigação e apoiaram o PCC-S a desenvolver ferramentas e metodologias para a implementação de chapas multi-camada em componentes estampados.

## Estado da Arte

A crescente utilização de novos materiais avançados, em particular novos aços, ligas de alumínio e magnésio e, com elevado potencial, os materiais multi-camada e multi-material, no *body-in-white* automóvel, com vista a aumentar a sua rigidez estrutural, melhorar a segurança passiva e reduzir o consumo por via da redução do peso, tem tornado a simulação numérica dos processos de

conformação de chapas um desafio de crescente complexidade, no qual a obtenção de resultados numéricos rigorosos e precisos é cada mais difícil.

De facto, no decorrer das últimas décadas tem-se assistido a um contínuo desenvolvimento e surgimento de novos materiais metálicos monolíticos, tais como, entre outros, os aços Dual-Phase (DP), os aços de alta e ultra resistência e baixa liga (HSLA, TRIP, etc.) e as ligas de alumínio e magnésio, hoje de utilização quase universal na indústria automóvel, dadas as suas claras vantagens em termos de aumento da rigidez estrutural e segurança passiva dos meios de transporte actuais e redução do seu consumo energético por via da redução do peso [Fig. 1.4].

Por outro lado, outros materiais, denominados por *sandwich* e constituídos por multi-camadas e multi-materiais, estão a ser exaustivamente desenvolvidos e estudados para serem introduzidos no mercado automóvel, apresentando-se como dos mais promissores para integrar os futuros *bodies*, ultra leves e super resistentes.

Os materiais *sandwich*, como princípio de construção, não são novos, encontrando-se vários exemplos da sua aplicação na indústria aeronáutica. O que é de facto novo e inovador é a conformação deste tipo de chapas com vista à sua aplicação na indústria automóvel. Componentes construídos com esse tipo de material podem ser até 50% mais leves, mantendo as mesmas propriedades geométricas e funcionais quanto comparados com os clássicos aços convencionais (Kim *et al.*, 2003; Moreira *et al.*, 2010).

No estado actual, ser-se capaz de descrever e simular numericamente o processo de conformação de chapas *sandwich* é absolutamente fundamental. Para modelar e simular este tipo de materiais adequadamente, três campos específicos no desenvolvimento do modelo numérico tem recebido especial atenção na literatura científica, nomeadamente, o tipo de elemento finito, o modelo espacial e as técnicas de tratamento numérico.

A formulação do elemento finito deve permitir descrever, com precisão, os esforços de corte presentes no núcleo e nas interfaces entre camadas/materiais, a deformação do núcleo ao longo da



Fig. 1.4 – Utilização de aços avançados de elevada resistência no *body* da pick-up Chevrolet Colorado 2015 (Wendy, 2015).

espessura e o contacto em ambas as faces. Para isso, o elemento finito seleccionado deve ser capaz de responder a trajetórias de deformação tri-dimensionais. Visto que os componentes reais são, por definição, tridimensionais, parece natural que a escolha do tipo de elemento a usar na simulação recaia preferencialmente sobre os elementos sólidos (Valente *et al.*, 2009). Os elementos de casca não conseguem comportar leis constitutivas 3D essenciais à correcta modelação do comportamento do material nem tão pouco prever com precisão a redução de espessura final resultante do estiramento durante o processo de conformação (Schwarze *et al.*, 2009). Contudo, quando as espessuras são reduzidas e o material é sujeito a trajetórias de deformação complexas, os elementos sólidos, devido a sua elevada rigidez, apresentam um fraco desempenho tornando-se vulneráveis a comportamentos numéricos parasitas denominados efeitos de *locking*. Este comportamento pode levar à degradação completa do elemento finito. Para evitar os inconvenientes associados às formulações dos elementos finitos casca e sólido, é comum recorrer a uma formulação híbrida sólido-casca capaz de combinar o comportamento casca à modelação tridimensional.

Os elementos sólido-casca têm ganho especial notoriedade na simulação de materiais compósitos multicamada. Apesar da elevada resistência e rigidez específica, os compósitos lamelados são susceptíveis ao dano. A delaminação é um tipo de dano interlamelar que ocorre nos materiais compósitos lamelados, quase sempre acompanhado de dano intralamelar, conduzindo ao colapso da estrutura. Neste campo, Rah *et al.* (2009) investigaram uma série de conceitos FE avançados para o estudo detalhado do campo de tensões nos materiais multicamada e concluíram que nenhuma formulação baseada em deslocamentos sólido-casca poderia prever com precisão as tensões interlamelares e, conseqüentemente, a delaminação do compósito. Por outro lado, as formulações para elementos de tensão híbrida assumem as tensões como variáveis independentes na configuração variacional inicial o que se traduz em um grau de precisão de tensões igual aos deslocamentos. Assim, os autores propuseram a integração da formulação dos deslocamentos sólido-casca e da formulação da tensão parcial híbrida para o desenvolvimento de um elemento sólido-casca robusto adequado ao cálculo detalhado e eficiente da tensão interlamelar. Abed-Meraim *et al.* (2011) apresentam o desenvolvimento de um novo elemento sólido-casca prismático de seis nós, SHB6, que, combinado com o elemento sólido-casca hexaédrico, SHB8PS, torna-se uma opção interessante para a geração de malhas de geometrias complexas.

Além do tipo de elemento escolhido, outro aspecto essencial na simulação de materiais compósitos multicamada relaciona-se com o modelo espacial. As estruturas *sandwich* com núcleos macios, como por exemplo finas camadas viscoelásticas ou espumas entre duas camadas rígidas, não são simples de simular devido às dificuldades relacionadas com o modelo espacial do conjunto empilhado, que deve ser capaz de representar com precisão o padrão de corte e o gradiente de

deformação do núcleo. As abordagens mais usuais, consistem em um conjunto empilhado de elementos finitos sólidos e casca com ligações nodais ou elementos de ligação rígidos (Jonhson *et al.*, 1982; Kilian *et al.*, 1984; Moreira *et al.*, 2004; citados em Moreira *et al.*, 2010). Contudo, tais abordagens são muito sensíveis a patologias numéricas além de consumirem muito tempo (Moreira *et al.*, 2004; citado em Moreira *et al.*, 2010). Cada reconfiguração da estrutura lamelar requer a modificação total da malha de elementos finitos. Por isso, abordagens dedicadas à modelação de estruturas lameladas foram desenvolvidas. Os modelos ESL (Equivalent Single Layer), FSDT (First-order Shear Deformation Theory) e HSDT (Higher-order Shear Deformation Theory), podem ser facilmente implementados e o número de graus de liberdade requerido não depende do número de camadas. Ainda assim, tais modelos não conseguem descrever adequadamente o campo de deslocamentos ao longo da espessura (Pandya *et al.*, 1988; Kant, *et al.*, 2001; Kant, *et al.*, 2008; Zhen *et al.*, 2008; citados em Moreira *et al.*, 2010). Os modelos espaciais capazes de fornecer soluções mais confiáveis e precisos são os modelos *zig-zag* e *layerwise* (Moreira *et al.*, 2010). Os modelos *zig-zag* satisfazem a condição de continuidade nas interfaces e conseguem prever tensões de corte transversas. Contudo, requerem funções de forma  $C_1$  para a implementação dos elementos finitos. Assim, é difícil implementar um elemento especial *zig-zag* com os elementos isoparamétricos comuns nos códigos de ferramentas de análise por elementos finitos (FEA) comerciais (Cho *et al.*, 2008). Os elementos finitos *layerwise* (Suzuki *et al.*, 2003; Moreira *et al.*, 2006; citados em Moreira *et al.*, 2010) tornaram-se populares pela sua simplicidade e facilidade de implementação em configurações complexas por meio de geradores de malha de elementos casca.

Para evitar o surgimento de efeitos de *locking* nos elementos sólido-casca é comum recorrer a técnicas de tratamento numérico específicas. A abordagem mais simples consiste em procedimentos de integração reduzida. Contudo, tais procedimentos podem conduzir a modos de energia zero que requerem métodos de estabilização. Assim, as técnicas mais bem sucedidas para aliviar os efeitos de *locking* são classificadas de métodos mistos. Nestas formulações considerações de campos independentes são adoptadas para as deformações, as tensões e/ou os deslocamentos. Destes métodos destacam-se as abordagens ANS (Assumed Natural Strain) e EAS (Enhanced Assumed Strain) (Rah *et al.*, 2009; Valente *et al.*, 2009; Schwarze *et al.*, 2009; Moreira *et al.*, 2010; Abed-Meraim *et al.*, 2011). Moreira *et al.* (2010) propõem uma abordagem inovadora para as formulações *layerwise* para estruturas compósitas multicamada, baseada no uso de elementos sólido casca e uma formulação EAS.

Recentemente, a Volvo Technology desenvolveu um novo material *micro-sandwich* denominado *Hybrix*, o qual consiste em duas chapas finas de aço inoxidável e um núcleo contendo resina e fibras microscópicas de aço ou poliméricas. O desenvolvimento deste novo material valeu à Lamera AB,

empresa responsável pela produção e comercialização deste novo produto, o primeiro prémio no ACES Awards 2009.

Vários estudos e trabalhos de investigação foram realizados, em parceria com a Lamera, no sentido de melhorar as propriedades e o comportamento deste material, com vista à sua introdução no mercado automóvel. Engelmark (2009) realizou ensaios de embutidura com chapas Hybrix para diferentes geometrias de peças automóvel. Os resultados experimentais evidenciaram um elevado risco para enrugamento com um impacto directo sobre a robustez do processo de estampagem. Por volta da mesma altura, Jackson *et al.* (2008) tentavam também produzir peças factíveis com este material recorrendo à conformação incremental. Ainda assim, depararam-se com problemas de delaminação, isto é, a separação entre o núcleo compósito e as camadas de revestimento metálicas. Depois disto, muitos elementos de base referentes ao núcleo compósito foram melhorados. Mulone (2015) realizou ensaios de análise dinâmica termo-mecânica (DMTA) a diferentes versões de Hybrix. Os resultados demonstraram que, face às versões anteriores, a versão mais recente não apresentava delaminação melhorando em muito a rigidez à flexão do material. Contudo, nenhum destes estudos prevê o comportamento do material com base na simulação numérica.

Assim, embora o Hybrix apresenta um enorme potencial para ser introduzido na indústria automóvel, contudo, a modelação numérica do comportamento mecânico destes materiais e a forma de os poder simular ainda se encontram num estado de evolução embrionário. Dada a natureza complexa das chapas multi-camada e multi-material, o comportamento mecânico destes materiais avançados é muito mais sensível às variações dos parâmetros de material e dos parâmetros de processo. Estes materiais também apresentam novos modos de falha, que geralmente não são contemplados nos módulos multi-camada das ferramentas numéricas comerciais vocacionados para a estampagem, como é o caso da delaminação. Por outro lado, a construção do modelo constitutivo depende da informação experimental do núcleo compósito que não pode ser optida pelas metodologias de testes comuns. Este é talvez o maior *handicap* à caracterização experimental deste micro-sandwich. Existe, portanto, a necessidade de uma metodologia de teste robusta que permita aceder a esta informação experimental para modelar corretamente testes materiais e gerar mais conhecimento sobre o seu comportamento até agora mal descrito e mal dominado. Tentativas de se reproduzirem peças complexas com Hybrix têm resultado, na maior parte dos casos, em produtos não conformes e processos pouco robustos. Portanto, tais limitações existentes ao nível da correta caracterização e modelação destes materiais e simulação dos processos de conformação dos mesmos, traduzem-se num obstáculo à capacidade de inovação de empresas como o PCC-S.

## Âmbito e Estrutura da Tese

Em 2010, a Lamera AB convidou o PCC-S para participar como parceiro industrial num projecto que visa a correta modelação do comportamento mecânico deste material e a simulação numérica do seu processamento por conformação plástica, de modo a factibilizar geometrias e processos compatíveis com as propriedades do Hybrix e com as exigências da indústria automóvel.

O trabalho desenvolvido no âmbito deste projecto, procura aumentar a capacidade de projecto do PCC-S com vista ao desenvolvimento de novos produtos e, conseqüentemente, aumentar a sua competitividade e das empresas do Grupo Sodécia, por meio da aquisição de conhecimentos e competências internas associadas à caracterização experimental, modelação e simulação numérica de materiais micro-sandwich. No final do projecto pretende-se ser capaz de:

- Desenvolver uma metodologia robusta, e suficientemente expedita para ser implementada em ambiente industrial, que permita caracterizar experimentalmente um micro-sandwich.
- Modelar corretamente e simular o processamento de materiais multi-camadas;
- Aumentar a robustez dos processos de conformação de novos materiais avançados, e assim contribuir para um maior rigor numérico dos resultados;
- Utilizar ferramentas comerciais de simulação numérica já disponíveis no PCC-S para a adaptar processos de estampagem convencionais ao Hybrix.

O foco deste estudo preliminar baseou-se em 3 aspetos essenciais: materiais, processo e ferramentas CAE. O conhecimento crítico sobre materiais multi-camada obtido nestas 3 áreas permitiu a criação de planos de ação para tarefas de desenvolvimento. Estes planos estiveram na base das decisões das soluções a investigar e a desenvolver experimentalmente antes da aplicação ao produto.

A colaboração com empresas fornecedoras de materiais multi-camada (Lamera AB e Thyssenkrupp), de ferramentas CAE de simulação de estampagem (AutoForm e ESI Group) e de componentes para a indústria automóvel (Quantal Group), nesta fase inicial do projeto também contribuiu para alicerçar o percurso escolhido.

Assim sendo, definiu-se como um dos objetivos deste projeto produzir um componente automóvel com um material micro-sandwich. As ferramentas CAE de simulação de estampagem utilizadas foram o AutoForm e o PAM-STAMP 2G. A peça escolhida foi desenvolvida pelo departamento de R&D do PCC-S e conformada nas instalações da Quantal.

Os próximos capítulos compreendem o trabalho de investigação realizado em cada uma das etapas do projeto, apresentado sob a forma de artigos submetidos em revista científica. Assim sendo, esta tese compreende 5 artigos, cada qual correspondendo a 1 capítulo, e encontra-se, no total, dividida em 8 capítulos:

- O **Capítulo 1** introduz a *pergunta de investigação* e apresenta o enquadramento geral do projeto. A temática da simulação numérica de processos de conformação de materiais avançados multi-camada e multi-material na indústria automóvel é introduzida e correlacionada com as necessidades do Centro de Competências de Produto Sodectia, das empresas associadas ao grupo Grupo Sodectia e dos seus clientes. Esta visão geral define o ponto de partida da investigação e as etapas necessárias à sua execução que, por sua vez, constituem os tópicos de estudo que estruturam o corpo da presente tese de doutoramento [Fig. 1.5].

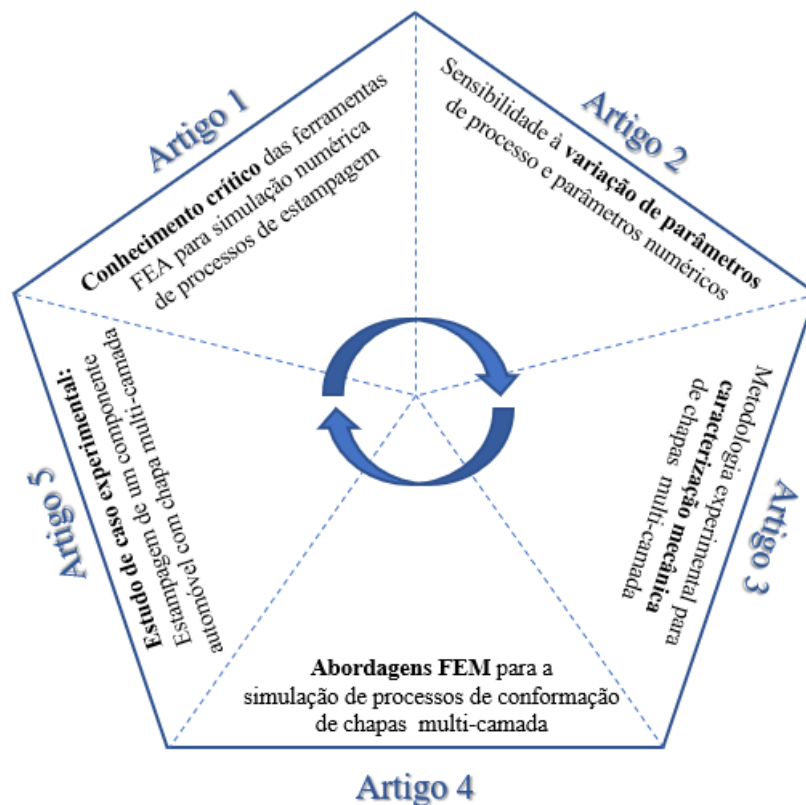


Fig. 1.5 – Diagrama representativo da estrutura da tese de doutoramento, baseada em cinco áreas de estudo, sobre as quais se produziu publicação científica.

Com esta metodologia pretende-se trazer mais luz sobre a pergunta de investigação que suporta todo o trabalho desenvolvido:

*“Como simular correctamente processos de conformação robustos, convencionais ou não convencionais, de chapas metálicas multi-camada e multi-material, recorrendo aos programas FEA comerciais disponíveis no Centro de Competências de Produto Sodectia, incrementando a sua capacidade competitiva no desenvolvimento de novos produtos?”*



- O **Capítulo 2** (Artigo 1) apresenta *o ponto de partida*. Segue-se um estudo comparativo das ferramentas FEA comerciais, vocacionadas para a simulação de processos de estampagem, mais comumente utilizadas na indústria automóvel (AutoForm e PAM-STAMP 2G) e o software académico DD3Imp. Este estudo é essencial para o desenvolvimento de conhecimento crítico em torno destas ferramentas de apoio à decisão, permitindo retirar conclusões abalizadas sobre a sua eficiência, exatidão e robustez. Para este efeito, reproduziu-se um estudo de caso bem conhecido e publicado na plataforma das conferências Numisheet. O Numisheet 2008 #BM02, proposto pela Daimler, envolve a estampagem de um perfil S-Rail em aço HC260LAD ou em uma liga de alumínio AC170, sendo que as ferramentas podem ou não apresentar freios. Realizadas as simulações em cada um dos softwares compararam-se os resultados numéricos com os resultados reais para as variáveis: Força do Punção, Escoamento, Maior Deformação Principal, Menor Deformação Principal e Retorno Elástico. As provas dadas destes softwares na descrição do comportamento mecânico de materiais mono-camada, sujeitos a processos de conformação plástica, estabelece uma base confiável para se poder avaliar o comportamento numérico exibido por materiais multi-material em condições semelhantes, os quais são constituídos por camadas de diferentes materiais monolíticos.

- O **Capítulo 3** (Artigo 2) expõe os resultados de um estudo de variabilidade de parâmetros de processo e parâmetros numéricos, tendo como base o estudo de caso do **Capítulo 2**. Embora os materiais avançados multi-camada e monolíticos apresentem diferentes especificidades e níveis de maturação, partilham em comum esta necessidade de se entender como a variabilidade dos parâmetros associados à simulação afeta o rigor e utilidade dos resultados numéricos. Este estudo investiga a influência dos critérios de plasticidade, leis de encruamento, coeficiente de atrito e alterações à geometria das ferramentas na exatidão e robustez dos resultados obtidos na simulação numérica. As simulações foram realizadas todas no mesmo software (AutForm R5.2) para o caso da estampagem do perfil S-Rail em aço HC260LAD.

- O **Capítulo 4** (Artigo 3) descreve uma metodologia para a caracterização mecânica de chapas micro-sandwich, tendo por base o material Hybrix. Do ponto de vista da modelação constitutiva e simulação numérica, a caracterização mecânica dos materiais é um passo fundamental já que permite a obtenção dos parâmetros mecânicos necessários à identificação dos parâmetros constitutivos. Contudo, não existem testes experimentais que permitam quantificar diretamente as propriedades mecânicas do núcleo compósito. Por isso, é essencial recorrer a uma metodologia robusta que permita obter a informação experimental necessária correspondente a cada uma das camadas do micro-sandwich. Para validar esta metodologia, ensaios de tração uniaxial e Nakazima foram realizados experimentalmente e, depois, reproduzidos virtualmente no software PAM-STAMP 2G 2012.2, comparando-se posteriormente os resultados numéricos e experimentais.

- O **Capítulo 5** (Artigo 4) foca diferentes abordagens FEM (Finite Element Method) para modelar chapas micro-sandwich. Depois de construir-se o modelo constitutivo, tendo em conta os parâmetros de material para cada camada, várias estratégias FEM podem ser adotadas no modelo numérico com base no tipo de elemento finito. Utilizando a metodologia descrita anteriormente, (**Capítulo 4**) e para os mesmos ensaios experimentais, comparam-se os resultados obtidos para duas configurações de Hybrix diferentes, uma cuja a espessura nominal das camadas metálicas externas é igual, a que se denominou simétrica, e outra com espessuras diferentes, portanto, assimétrica. Neste estudo testam-se modelos numéricos baseados em elementos casca e elementos sólidos e comparam-se os resultados devolvidos pelo AutoForm R5.2 e PAM-STAMP 2G 2012.2.

- O **Capítulo 6** apresenta um estudo de caso experimental para a estampagem de um dos semi-corpos pertencentes a um sistema de enchimento de combustível protótipo. Para isso, utilizaram-se chapas micro-sandwich Litecore cedidas pela Thyssenkrupp. Os testes experimentais foram realizados na empresa Quantal (fornecedora de protótipos da Sodecia). Os mesmos foram, posteriormente, reproduzidos em ambiente virtual com a ferramenta PAM-STAMP 2015.1. Com base em todos os pressupostos anteriores, comparam-se os resultados obtidos para diferentes abordagens FEM para validar o melhor modelo numérico.

- O **Capítulo 7** faz uma breve dissertação sobre a contribuição deste projeto no reforço da competitividade do PCC-S e das empresas ligadas ao grupo Sodecia, bem como da sua importância e enquadramento nas necessidades da indústria automóvel global, concluindo com linhas de investigação para trabalhos futuros.

- Adicionalmente, incorporaram-se no final desta tese os **Anexos A e B**, que apresentam de forma abrangente, detalhada e profunda os fundamentos teóricos da cinemática dos meios contínuos e da teoria da plasticidade envolvidos na simulação numérica dos processos de conformação plástica de chapas metálicas. Esta secção pode ser consultada pelo leitor como texto de apoio na análise deste documento ou para aquisição de novos conhecimentos na área da mecânica computacional. Assim, tanto utilizadores de ferramentas numéricas que desenvolvem o seu trabalho junto da indústria, como investigadores mais ligados ao ciclo académico, podem beneficiar desta leitura.



## **2. ARTIGO 1: “Comprehensive Benchmark Study of Commercial Sheet Metal Forming Simulation Software Used in the Automotive Industry”**

**A.M. Pimentel, J.L. Alves, N.M. Merendeiro, D. Vieira**

Anthony Michael Fernandes Pimentel<sup>a,b,\*</sup>

\*E-mail: anthony.pimentel@ct.sodecia.com \ anthony.pimentel@dep.uminho.pt

José Luís de Carvalho Martins Alves<sup>b</sup>

Nuno Miguel de Seabra Merendeiro<sup>a,1</sup>

Diana Maria Faria Vieira<sup>a</sup>

<sup>a</sup> Product Competence Center Sodecia, Rua Eng.º Frederico Ulrich, 2650, 4470-605 Maia, Portugal

<sup>b</sup> CMEMS, Universidade do Minho, Campus de Azurém 4800-058 Guimarães, Portugal

---

<sup>1</sup> Present Adress - Sodecia-participações Sociais Sgps Sa, Rua do Espido, 164-F, Edifício Via Norte, 4470-177 Maia – Portugal

## **ABSTRACT**

There are currently several commercial Finite Element Analysis (FEA) softwares available, and it is not clear for a company the differences between them, mostly in terms of results accuracy, reliability and usability. International conferences were created to promote a world-class forum in which, simulation engineers and automakers, can exchange their knowledge in the sheet metal forming field and evaluate stamping simulation softwares, through benchmarking exercises. However, a comparison of FEA tools based in such methodology is not truly reliable, since each participant can choose its own strategy to build the numerical model based on the experimental data delivered.

In this study, the authors use a different approach to achieve a more reasonable and fair comparison between three different sheet metal forming FEA tools: AUTOFORM R5.2, PAM-STAMP 2G 2012.2 and DD3IMP. Although the existence of substantial differences in the Finite Element (FE) formulations and element types, the material laws and process parameters adopted were kept as close as possible, making the constitutive models essentially identical. This benchmark was carried out using the Numisheet 2008 Benchmark #2, which is well specified and for which there are a set of experimental results available. The numerical results and experimental results were compared in terms of: punch forces, draw-in, principal strains, formability, geometry after springback and computational cost. The usage of equivalent constitutive models shows that the accuracy of the FEA tools are roughly the same. This study also highlights the true meaning of the differences between the numerical results in the industrial competitiveness of a company.

## **KEYWORDS**

Commercial Stamping Simulation Softwares; Springback Accuracy; Numisheet Benchmarks; Computational Cost

## INTRODUCTION

Today FEA tools play a main role in the automotive stamping. New advanced materials and new sheet forming technologies challenge constantly the stamping simulation market to develop more robust, efficient, reliable and accurate FEA tools. The commercial FE codes existent today are based in different formulations. They can be *static* or *dynamic*, in terms of the mathematical formulation of the equilibrium equations, and *explicit* or *implicit*, regarding the time integration method. During the last 30 years, FE code developers based on implicit formulations or explicit formulations and wrestle each other to offer to automotive industry the best sheet stamping simulation CAE tool.

As observed by Banabic [1] in his "*Historical Review of Sheet Forming Simulation*", the *static-implicit* codes were the first to be developed. However, this method did not seem promising at the time. Due to very unstable numerical procedures and an excessive computational cost practical application of sheet forming simulation were restrict to small problems. In the 80s, the idea of using this kind of FE codes as a decision support tool to develop stamping parts, sheet forming processes and stamping tools in the automotive industry was almost science fiction. As an example of state-of-the-art at the time, Tang et al. [2] published results from practical applications of a code, developed at Ford, to the simulation of the stamping of real 3D automotive parts. Models with up to 400 higher shell elements were analyzed, and reported computing time was about 20h on a super-computer.

In the other hand, Banabic [1] also refers that some authors have used an alternative *static-explicit* approach, in which no iteration at all are performed. In this method, the updating geometry is just based on the tangent moduli in the previous step. This implies that equilibrium is never satisfied. To reduce the errors involved, very small steps must be taken. Differently from the hundreds incremental steps that we have in static-implicit ordinary simulation, several thousand steps are common with this method. The advantage of this approach is that it is quite robust, since there are no iterative processes that have to converge. According to the author, even instability phenomena like wrinkling have been simulated by means of this procedure.

Honecker and Matiasson [3] presented results from a study, in which the *dynamic-explicit* approach was evaluated in application to sheet metal stamping. The results from this study were very promising. Problems with up to 10,000 shell elements could be solved within 1.5h on a super computer. Also, the robustness of this approach was found to be widely superior to that of any other method.

Thus, explicit FE codes began to be in advantage thanks to their higher robustness – no convergence problems associated to the iterative process – higher simplicity and ease of adapting to a parallel computation.

From the beginning of the 1990s there was an explosive increase of the practical utilization of sheet forming simulations within the industry, and from the middle of this decade most companies within the automotive industry were performing sheet stamping simulations on a regular basis. As stated by Banabic [1], the *dynamic-explicit* codes were dominating the software market. General purpose codes like LS-DYNA and ABAQUS/Explicit, and specialized codes such as PAM-STAMP and OPTRIS are examples of codes in use. Apart from few exceptions, as INDEED in the German automotive industry and MTLFORM at FORD Motor Company, the *static-implicit* FE codes were more commonly used in the academic circles. Contrary to the trend, the highly specialized code for stamping simulations, AutoForm emerged from a research project at ETH in Zurich in the early 1990s. Based on the *static-implicit* approach, this FE code uses some innovative algorithms to enhance stability and computational efficiency, which make it competitive with the best-in-class *dynamic-explicit* codes.

At the end of the 1990s, the development of the massive parallel computing (MPP) allows a greater exploitation of the explicit codes efficiency in the automotive simulation industry. In 1998, Hyperform was launched as part of the multi-physics application HYPERWORKS. Three years later, in 2001, Quantech presents the first commercial version release of STAMPAK, which was developed in collaboration with the International Center for Numerical Methods in Engineering (CIMNE). Today (2017), DYNAFORM (LS-DYNA), PAM-STAMP 2G, HYPERFORM (RADIOSS), ABAQUS/Explicit and STAMPAK are the main *dynamic-explicit* codes available in the market. Despite being considered *dynamic-explicit* codes, it is worth noting that springback simulation is *static-implicit*. Lenard and Schey [4] explain that in an implicit solution the final step will represent an equilibrium state, but in an explicit solution the part will be oscillating dynamically after removal of the tooling elements and contact. This vibration after forming will not affect the part's plastic strains, so the part formability can still be assessed based on predicted strains. However, to solve for the springback after the tooling is removed an explicit solution would require a large time period for the oscillation to damp out. Therefore, the preferred approach is often an explicit forming solution coupled with an implicit springback analysis. On the other hand, AutoForm, which is probably the most commonly used code in the automotive industry for stamping simulation, is always *static-implicit*. The use of other types of codes is now only marginal.

In the last 15 years, these commercial stamping softwares have been continuously improved to deliver more reliable and robust results. Thanks to the work of many authors, such as Cazacu and Barlat [5], Banabic et al. [6], Aretz and Barlat [7], Banabic et al. [8], Vegter and Boogard [9], Comsa and Banabic [10], new material laws have been implemented in the stamping FE codes. The graphical user interfaces (GUI) have also improved significantly from over the years. A good example is the patent work of Hillmann and Kubli [11], Kubli and Krainer [12-14] to make AutoForm more

attractive and user-friendly. In addition, new features (as blank design, die design, process planning, cost estimating), were incorporated to meet the evolving needs and expectation of the modern automotive industry.

After 30 years of intense development in the FE codes to stamping simulation application, is it true that *explicit* codes are the most robust and efficient in the market? Or, is it true that *implicit* codes are more accurate and provide more reliable results? More important, what is the real competitive advantage to an automotive company which uses one instead of the other?

In this work, two of the most popular stamping FE codes in the automotive industry, AUTOFORM R5.2 (*static-implicit* code) and PAM-STAMP 2G 2012.2 (*dynamic-explicit* code), are compared. In addition, the academic FE code DD3IMP (*static-implicit* code) is also put to the test. The stamping part evaluate is an S-Rail proposed by Daimler at the 2008 Numisheet Conference. This benchmark exercise is suitable to the aim of this work because it focuses on the most meaning and challenging process variables of stamping automotive applications.

The Numisheet Conferences series are widely known to promote a world-class forum in which simulation engineers and automakers can exchange their knowledge in the sheet metal forming field. In addition, these conferences are a great opportunity to evaluate the stamping simulation softwares and demonstrate their ability to provide reliable results. The industrial problems proposed in these conferences are carefully prepared and delivered with a list of proceedings to help all the participants to build their virtual models with the same level of data. However, a comparison of FEA codes based in such methodology is not truly reliable, since the methods and models adopted by the participants are different. As an example, at the 2008 Numisheet Conference 12 participants contributed to the benchmark #02 [15], of which:

- 7 solved the problem using the standard approach (which considers the springback effect after the trimming operation) whereas the remaining 5 preferred using the advanced approach (which considers the springback effect after the drawing operation and after the trimming operation).
- 3 computed using LS-Dyna, 4 AutoForm, 1 Abaqus, 1 ASU/P-form, 1 DD3IMP, 1 Stampack V 6.2.1 and 1 Sheet3 FE codes.
- Except one, all participants preferred to use an implicit formulation to compute springback. Whereas for drawing simulation 6 used explicit and 6 implicit codes.
- 2 delivered results computed with solid finite elements. The remaining used shell elements with different integration characteristics.
- Fully integrated shell formulations have been largely preferred, with number of through thickness integration points ranging from 4 to 15.
- All participant used an isotropic hardening law



In this benchmark, each participant could choose its own strategy to build the most suitable numerical model based on the experimental data delivered in the conference. For instance, different assumptions could be adopted concerning the material laws and process parameters affecting directly the numerical results [16]. Therefore, this context does not seem to be the most suitable to compare the numerical accuracy of different sheet metal FEA tools. This study presents the results of the benchmark #02 performed in 3 different stamping simulation softwares by the same user. To reduce the discrepancies between the FE models as much as possible equivalent constitutive models were considered, i.e, the same constitutive laws or constitutive laws with an equivalent level of flexibility and accuracy (Yield Criterion, Hardening Law, Power Law, Stress-Strain relationship) were used to treat the experimental data making the comparison more reasonable and fair.

The benchmark # 02 was brought to the Numisheet conference by Daimler and proposes the study of a stamped component with special interest for the scientific community and the automotive industry. Therefore, this component already has 2 participations in Numisheet conferences (1996, 2008). During the sheet metal forming of the S-rail geometry, complex strain paths hinder a uniform stretching. When using aluminum alloys and high strength steels, springback effects appear making it even more difficult ensure the stamping process robustness and the stamped part quality. In addition, the costs with tool & die design and manufacturability engineering increases considerably. Therefore, the springback prediction accuracy is still one of the most studied themes in the stamping simulation and one of the most desired inputs in the current automotive industry. As an example, from the last 10 years, the springback effect has been subject of international study at the Numisheet conferences (BM02 at Numisheet 2008, BM04 at Numisheet 2011, BM02 at Numisheet 2014 and BM02 and BM03 at Numisheet 2016). In this particular study, it is demonstrated how far the commercial softwares can go and what are the best options available to supply the automotive market needs.

## **BENCHMARK DEFINITION: NUMISHEET2008 BM02**

In this benchmark study, the influence of 2 different drawbead geometries (smooth bead or locking bead) on the springback behavior for steel and aluminum were examined. For this purpose, the well-known S-Rail geometry is used [Fig. 2.1]. The S-Rail tool contains two different blank-holders. One can be equipped with different drawbeads [Fig. 2.2]; the other offers a complete plane surface. Depending on which drawbead geometry is applied an adequate die can be adopted.



Fig. 2.1 – S-Rail topology after the drawing operation (intermediate state) for the case of smooth beads [17].

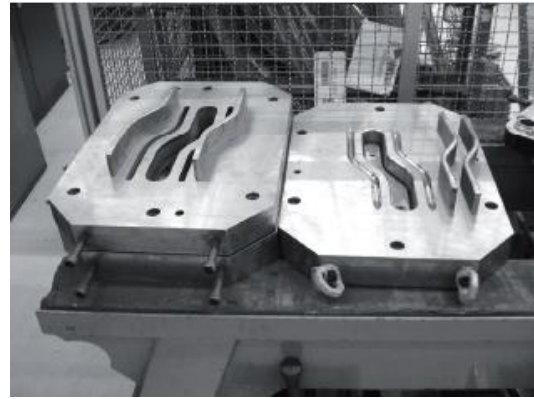


Fig. 2.2 – Numisheet 2008 BM 02 Stamping Tools: Blankholder, Drawbeads and Die [17].

In this approach, the focus will be the difference between the numerical results of stamping simulation softwares and its meaning to the competitiveness of automotive industry companies. Therefore, only 2 geometries of tools, for each material, were considerate in this study as shown in Fig. 2.3.

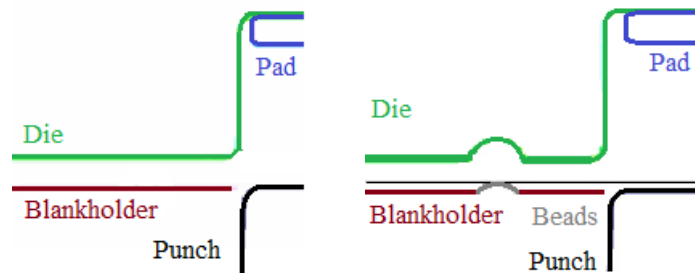


Fig. 2.3 - Section cuts of tools in initial position: a) without beads and b) with smooth beads (bead height = 3.6 mm) [17].

The resultant load cases, presented in Tab. 2.1, are enough to achieve intended purpose.

Tab. 2.1 – Description of the Numisheet 2008 BM 02 load cases considered in this study.

Material / Load Case ID	Drawbead	Blankholder Force
HC260LAD – LC1	Without beads	400 kN
HC260LAD – LC3	Smooth beads	400 kN
AC170 – LC1	Without beads	90 kN
AC170 – LC3	Smooth beads	90 kN

Regarding the process steps, a standard approach was followed: closing, drawing, trimming and springback. The stamping tools and blank geometries were provided to the Numisheet participants in IGES format. For the cases with drawbeads, its physical profile was directly included in the 3D CAD geometries of both die and blank-holder. In addition, Daimler has also provided all the experimental data tests strictly necessary to build the HC260LAD and AC170 mechanical models.

Since the mechanical model drove the material behavior during the sheet forming simulation, it is absolutely necessary to ensure the same, or almost the same, numerical characterization in the different FE codes. Tab. 2.2 presents the mechanical models assumptions used in each FE code.

Tab. 2.2 – Description of the mechanical model’s assumptions (Yield Criteria, Hardening Law, Flow Stress Model, Friction Coefficient) of each FE code.

MECHANICAL MODEL				
FE Code	Yield Criteria HC260LAD / AC170	Hardening Law	Stress-Strain HC260LAD / AC170	Friction Coefficient
AutoForm R5.2	HILL48 / BBC2005	Isotropic	Swift / Hockett-Sherby	0.04
Pam-Stamp 2G 2012.2	HILL48 / Yld2000	Isotropic	Swift / Hockett-Sherby	0.04
DD3Imp	HILL48 / CB2001	Isotropic	Swift / Voce	0.04

It must be noted that it might not always be possible to use exactly the same mathematical descriptions in the different FE codes, in such cases, it is necessary to resort to the more closely comparable. As shown in Tab. 2, different advanced yield criteria (**Autoform** – *Banabic-Balan-Comsa (BBC) 2005*, **Pam-Stamp** – *Barlat (Yld) 2000*, **DD3Imp** - *Cazacu-Barlat (CB) 2001*) with nearly the same flexibility are used to describe the AC170 mechanical behavior. Likewise, *Hockett-Sherby* and *Voce* equations are chosen to describe the aluminum alloy stress-strain curve because they are both comparable saturated models. Tab. 2.3 presents some important assumptions of the numerical model in each FE code.

Tab. 2.3 – Description of the numerical model’s assumptions (FE Formulation, FE Type, FE Integration, Mesh Refinement) of each FE code.

NUMERICAL MODEL				
FE Code	FE Formulation	FE Type	FE Integration	Mesh Refinement
AutoForm R5.2	Static-Implicit	2D Triangular Shell Elements	Fully-Integrated with 11 Gauss Pts	Adaptive
Pam-Stamp 2G 2012.2	Dynamic-Explicit Dynamic-Implicit	2D Quadrilateral Shell Elements	Fully-Integrated with 11 Gauss Pts	Adaptive
DD3IMP	Static-Implicit	3D Hexaedral Solid Elements	Selective Reduced	Non-Adaptive

Concerning the space-time FE formulation, Autoform and DD3Imp are both *Static-Implicit*.

Pam-Stamp is *Dynamic-Explicit* during drawing simulation but becomes *Dynamic-Implicit* in the springback phase. In stamping simulations, Autoform and Pam-Stamp use 2D shell elements with adaptive mesh refinement algorithms, while DD3Imp work with 3D hexaedral elements. The same number of integration points is defined for the triangular elements of Autoform and the quadrilateral elements of Pam-Stamp during the setup.

## **RESULTS: COMPARISON AND DISCUSSION**

After running the simulations, the numerical results and experimental results are compared in terms of:

- Punch forces
- Draw-in (closed tools)
- Principal strains
- Formability
- Geometry after springback
- Computacional Cost

The objective of this comparison consists in evaluating the accuracy of each FE codes in providing realistic restraining forces and reliable springback values.

### **Punch Forces:**

Industrial meaning: An accurate prediction of the stamping tools forces is fundamental to the stamping press selection at the beginning of a project. In the automotive industry, the stamping press capacity is a major concern especially when advanced high strength steels are considered. During the forming sequence, a simple shape calibration step can significantly increase the tonnage needed for the press. When progressive dies are considered, several operations occur simultaneously, so, the required load can vary a lot along the press stroke. Therefore, find a stamping press which meets the load and energy requirements is strongly dependent of the correct prediction of all forming and cutting forces involved in each step. The wrong definition of the stamping press capacity, the press tool elements (such as springs and hydraulic cylinders) or the hydraulic circuit pressure leads to “unfeasible” parts and/or lack of robustness in the stamping process with huge losses for the companies.

During a common deep-drawing operation, the punch force must be enough to deform plastically the blank and overcome the restraining forces (drawbead and friction forces) allowing the metal to flow into the die cavity. Assuming the mechanical equilibrium in the press, the RAM forces are equal to the BED forces. If the upper die moves against the punch and the blank-holder, the sum of the punch force and blank-holder force is equivalent to the tonnage needed for the stamping press.

Since the blank-holder force is always constant in this benchmark load cases, the focus will only remain upon the evolution of the punch force.

The Fig. 2.4 and Fig. 2.5 presents, respectively, a cross section view of the closed tools with the blank in the initial position and in the final position of the drawing operation.

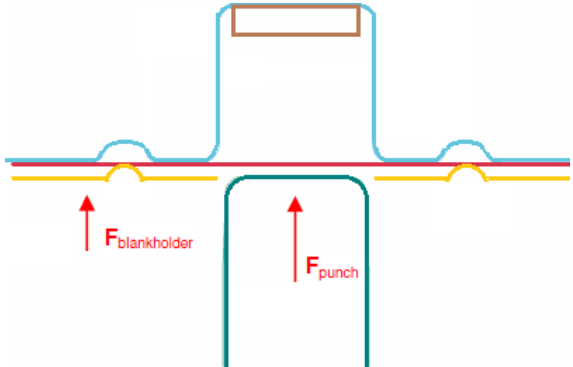


Fig. 2.4 - Tools and blank in initial position before drawing [17].

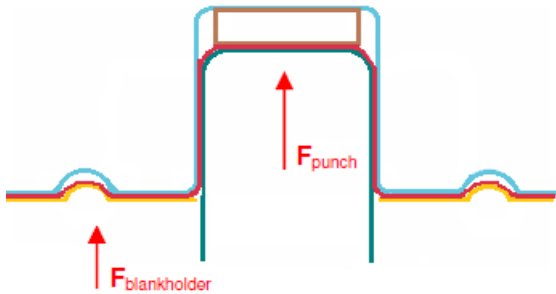
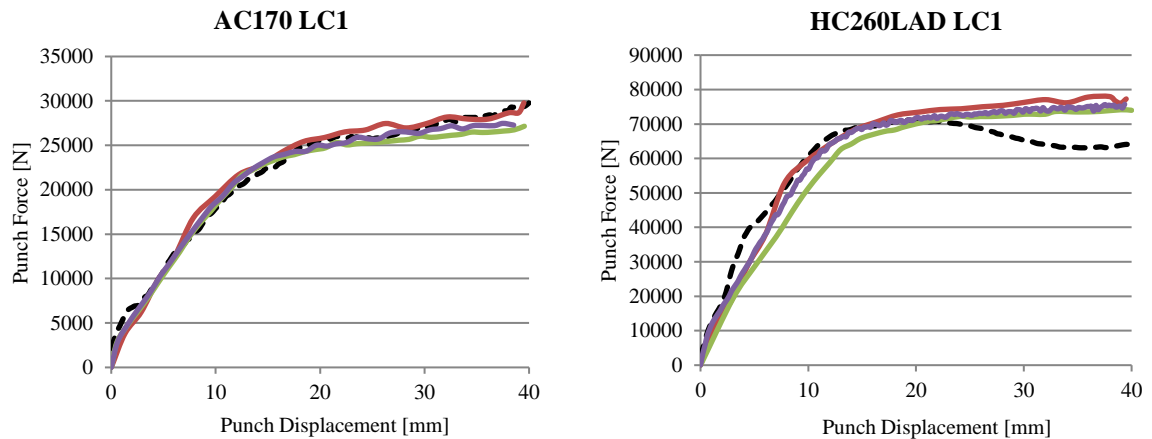


Fig. 2.5 - Tools and blank in home position after drawing [17].

The punch forces were recorded throughout the deep-drawing operation, for all the load cases, in each FE code. These have been plotted together with the experimentally obtained Punch Force vs. Punch Displacement curves and the Fig. 2.6 and Fig. 2.7 have been computed.

Fig. 2.6 presents the evolution of the experimental and numerical punch forces to the without bead cases.



AC170 LC1	Mean Deviation
AF R5.2	0.03
PAM 2012.2	0.03
DD3Imp	0.04

- AUTOFORM
- PAMSTAMP
- DD3IMP
- - - EXPERIMENTAL

HC260LAD LC1	Mean Deviation
AF R5.2	0.12
PAM 2012.2	0.10
DD3Imp	0.09

Fig. 2.6 – Comparison of experimental and numerical punch forces during the drawing operation, with the

respective mean deviations, to the load cases without drawbeads.

As it can be seen from the Fig. 2.6, all the numerical punch forces are very similar. For these load cases, the FE codes exhibited the same level of accuracy as indicated by the small difference between the mean deviation values (about 1% for the AC170 LC1 and 2% for the HC260LAD LC1). Moreover, the numerical and experimental results are in excellent agreement. The mean deviations are around 3% for the aluminum alloy and 10% for the high strength steel. The larger mean deviation for steel is the result of the drop in the experimental punch force at the end of the drawing stage.

The Fig. 2.7 presents the evolution of the experimental and numerical punch forces to the with bead cases.

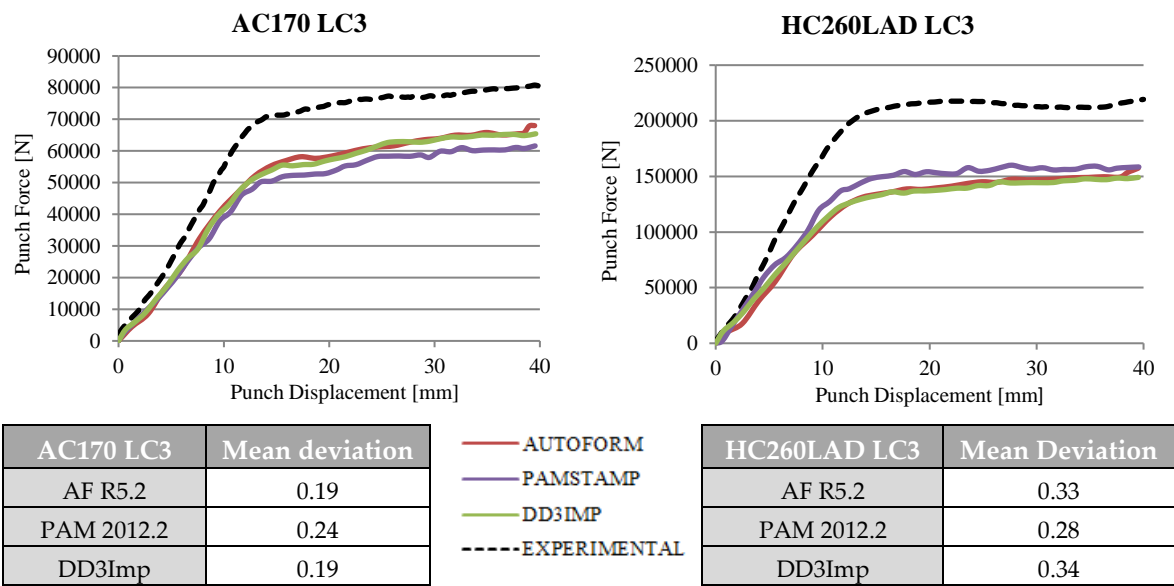


Fig. 2.7 – Comparison of experimental and numerical punch forces during the drawing operation, with the respective mean deviations, to the load cases with drawbeads.

As demonstrated in Fig. 2.7, even with drawbeads the numerical punch force curves still present the same behavior. The small difference existent between Pam-Stamp and the other softwares represents around 5% of mean deviation. The major concerning in these load cases is the difference between the numerical curves and the experimental curve (about 20% for the AC170 LC1 and 30% for the HC260LAD LC1). None of the FE codes tested came close of the experimental values. In both cases, the predicted punch forces are too much underestimated. The utilization of this information, as input data, to support the tools project, can lead to high costs associated to the wrong stamping press definition and/or wrong process design. Therefore, it would be important to understand why this difference is so big. In general, simulation engineers working with sheet metal forming processes

are accustomed with overestimated predictions and not the opposite. In Fig. 2.7 it is also noted that the drop effect in the punch force almost disappeared in the drawbead presence.

Padmanabhan et al. [18] have noted that this drop effect can be related with the profile of the draw die radius. In such cases, the drop effect can be easily predicted in the numerical simulation, which does not happen in this benchmark study. From the Fig. 2.6 and Fig. 2.7, it is clear that the drop effect is intrinsically connected to the blank material and the material flow during the forming operation. In the case HC260LAD LC1, all the restraining force supported by the punch results from the friction generated between blank and tools, whereas in the case HC260LAD LC3, is almost totally dependent of the plastic deformation when the blank flows through the drawbeads. Therefore, the restraining force tends to maintain stable while there is material to go through the drawbeads. However, in the absence of drawbeads, the restraining force tends to decrease, as the material flows into the die cavity, if the hardening work was not enough to compensate the friction force decrease. In addition, as the contact area decreases the contact pressure also increases. As a consequence, depending on the material, the friction coefficient may also decrease. As presented in Tab. 2.4, the preliminary strip drawing tests performed for this benchmark shows that this dependency is much stronger for the AC170 than for the HC260LAD, which means the drop effect should be perceived up to a much lower blankholder forces.

Tab. 2.4 – Friction coefficients of HC260LAD and AC170 measured in strip drawing tests at different values of contact pressure [17].

Contact Pressure [N/mm <sup>2</sup> ]	Friction Coefficient [-]	
	HC260LAD	AC 170
2	0.047	0.068
5	0.042	0.040
8	0.042	0.030
11	0.041	0.025
14	0.041	0.023

This conclusion appears to be in line with the experimental results delivered at Numisheet 2008 Conference, where other load cases were also studied, as depicted in the Fig. 2.8 and Fig. 2.9.

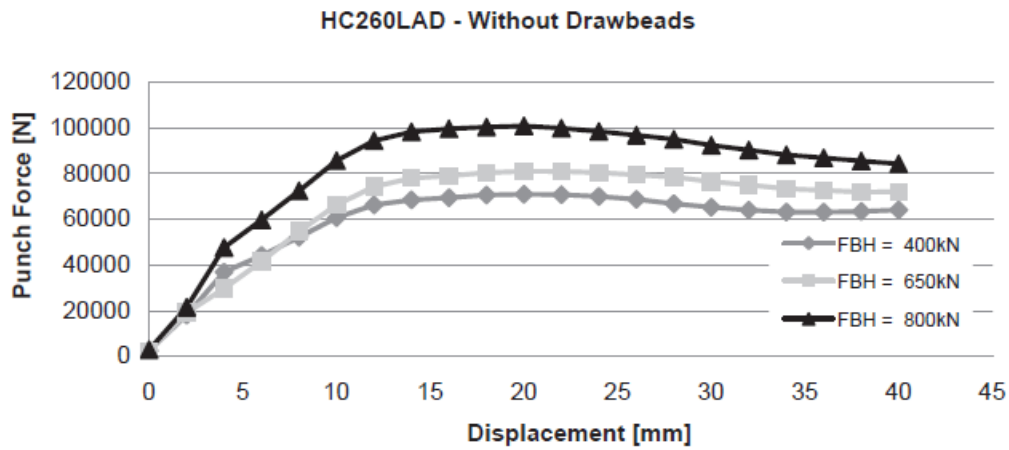


Fig. 2.8 – Variation of punch force in the experimental setup with no beads wrt. changing blankholder force (HC260LAD) [15].

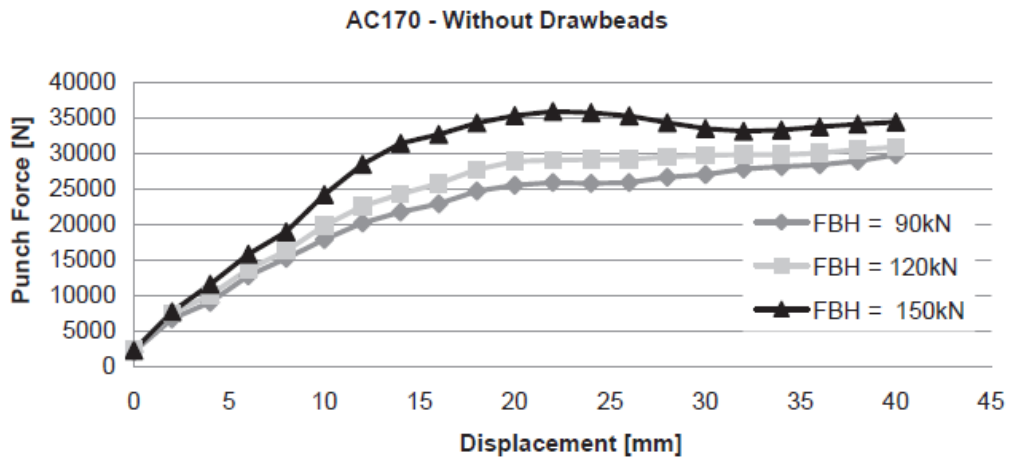


Fig. 2.9 - Variation of punch force in the experimental setup with no beads wrt. changing blankholder force (AC170) [15].

It is also important to keep in mind that the experimental values of the strip drawing test were obtained always for the same specific direction. However, the magnitude and direction of friction forces acting on a body moving over a machined surface are often found to vary with the direction of sliding. As stated by Walker and Leine [19], machining or finishing of a tool surface can lead to an anisotropic surface roughness which in turn causes anisotropic friction. Therefore, as already have been observed by Trzepieciński, and Lemu, [20], the Coulomb's friction coefficients are dependent of the slip directions. In this case, the blank tends to rotate due to the geometry of the S-rail and, therefore, the material's flow direction changes during the drawing operation. Additionally, Lemu and Trzepieciński [21] also verified the influence of the plastic deformation in the friction coefficients in dry and lubricated conditions. In order to deal with the complex nature of the anisotropic friction, Trzepieciński et al. [22] conducted three tribological tests, i.e. a strip drawing test, a draw bead test and a pin-on-disc tribometer, to determine the friction coefficient with more accuracy. Despite all



these issues, the friction coefficients adopted in the numerical models were always assumed as constant, therefore the drop effect was not predicted in the simulations.

**Draw-in:**

Industrial meaning: A good prediction of the draw-in is highly desirable. A correct estimation of the blank consumption during the stamping process contributes to cost savings with the raw material, and prevent process instabilities like wrinkles and ruptures improving the quality of the stamping part. The draw-in optimization will allow to define the best size and shape to the blank. Before negotiations begin, OEM’s use to send a request for quotation to all potential suppliers. In this phase, the definition of the most economic process to produce a feasible part is a competitive advantage to win the project.

According to the benchmark definition the participants were required to provide y-displacements in 8 sections across the blank at the end of the forming process. Due to difficulties in positioning the measurement equipment during the experiments, the number of sections were reduced to 5, as depicted in the Fig. 2.10.

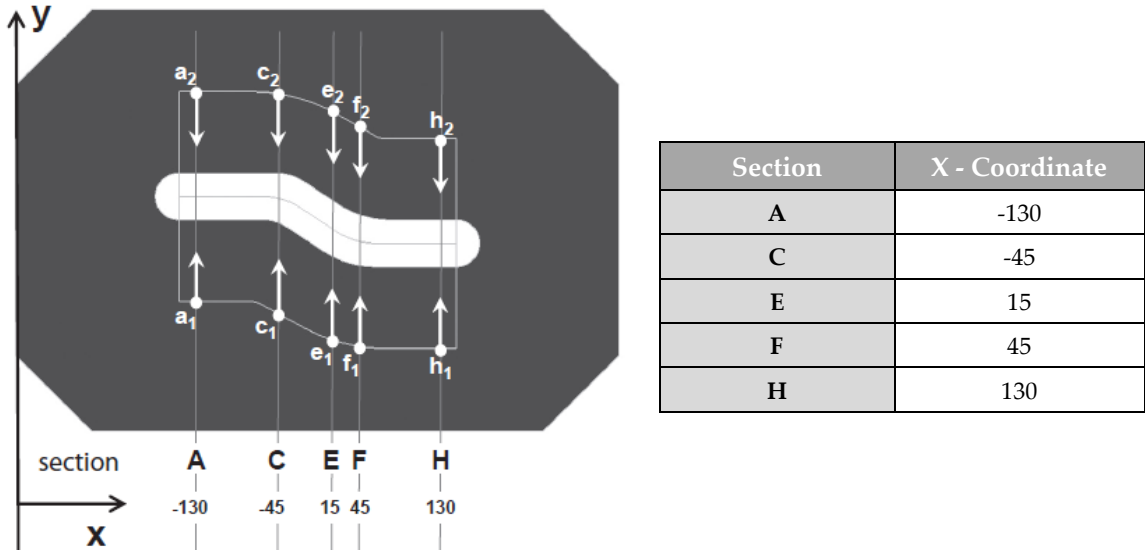


Fig. 2.10 – Position and naming of the draw-in sections with the respect to the S-rail geometry. [17]

Fig. 2.11 to Fig. 2.14 represent the comparison between the virtual draw-in and experimental draw-in. Draw-in levels have been plotted for each material and drawbead model. Each plot contains draw-in levels as a bar chart for each FE code and the average value of the experimental section displacements. In addition, the correspondent numerical deviations are also presented.

From the Fig. 2.11 to Fig. 2.14 it can be seen that the numerical draw-in always follows the same trend of the experimental draw-in.

Since the S-Rail geometry is very complex, the blank shape was previously studied to facilitate the flow material making it more uniform. Even so, the drawing operation tends to favor certain section displacements. Looking at the end sections (A and H) [Fig. 2.10], it can be noted in all cases that the section's displacement at  $h_2$  is higher than at  $a_2$  and  $a_1$  higher than  $h_1$ . In addition, the blank contour segments [ $a_2 - c_2$ ] and [ $h_1 - f_1$ ] [Fig. 2.10] always present the lower y-displacements. On the other hand,  $e_2$ ,  $f_2$  and  $c_1$  achieve always the higher y-displacements.

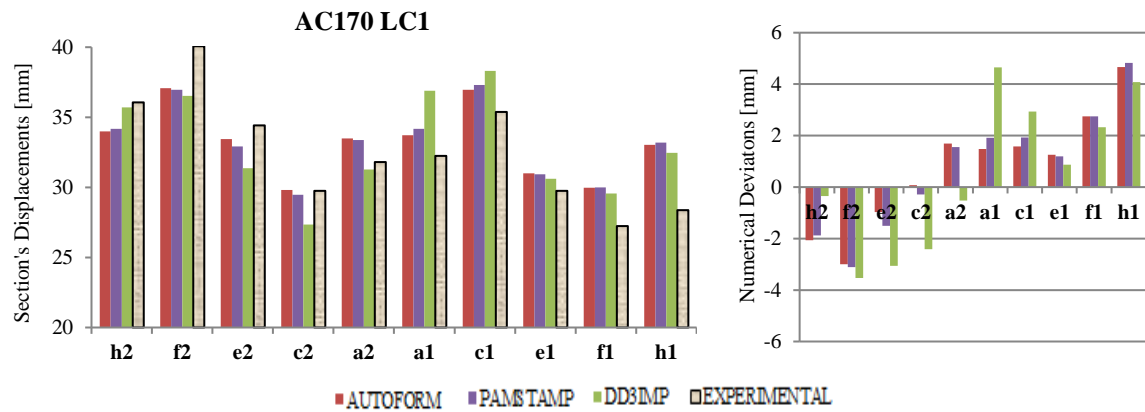


Fig. 2.11 – Comparison of experimental and numerical section's displacements during the drawing operation, with the respective mean deviations, to the load case AC170 LC1.

As shown in the numerical deviations chart of the Fig. 2.11, for the case AC170 LC1, when compared with the experimental values, the numerical draw-in is higher in the side [ $a_1 - h_1$ ] but lower in the side [ $a_2 - h_2$ ]. In this case, the maximum numerical deviations are about 4mm.

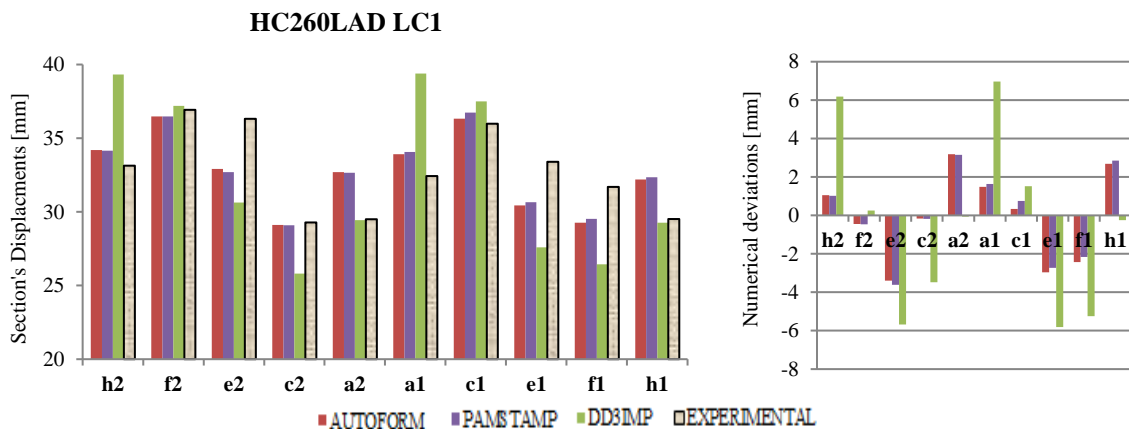


Fig. 2.12 – Comparison of experimental and numerical section's displacements during the drawing operation, with the respective to mean deviations, to the load case HC260LAD LC1.

In the case HC260LAD LC1, presented in Fig. 2.12, the numerical deviations have not a preferential side. Considering the section's displacements predicted by the commercial FEA codes,

Autoform and Pam-Stamp, the numerical deviations are very similar and do not reach the 4mm. But in the case of DD3Imp the maximum deviations are around 7mm. Comparing the experimental displacements with AC170 LC1, the standard deviation decreases from 3.8 to 2.7, which means a lower dispersion.

Looking at the Fig. 2.11 and Fig. 2.12, the draw-in variation range is mainly located between [30,35] mm. Regarding the numerical predictions, the differences between Autoform and Pam-Stamp are minimal and DD3Imp presents the higher deviations.

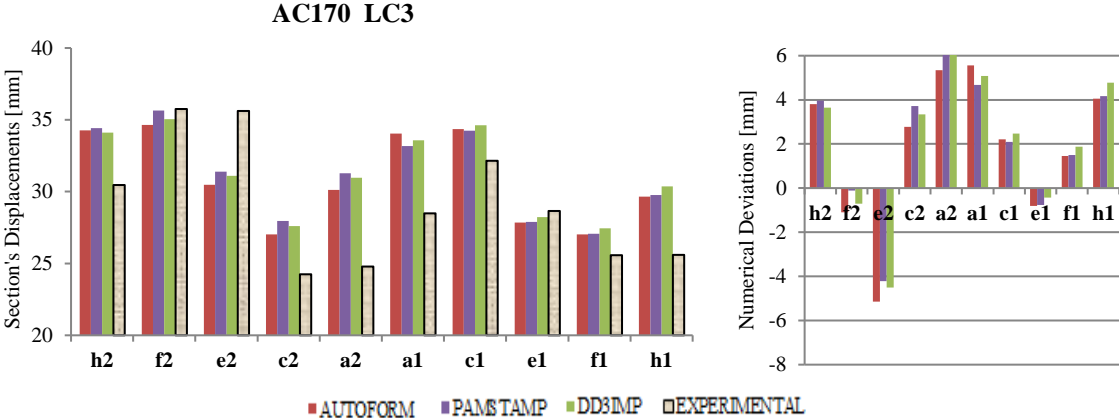


Fig. 2.13 – Comparison of experimental and numerical section’s displacements during the drawing operation, with the respective to mean deviations, to the load case AC170 LC3.

With respect to AC170 LC3, Fig. 2.13 shows an extension of the draw-in variation range ([25, 35] mm) when drawbeads are used. Thus, the maximum numerical deviations increased from 4mm to 6mm.

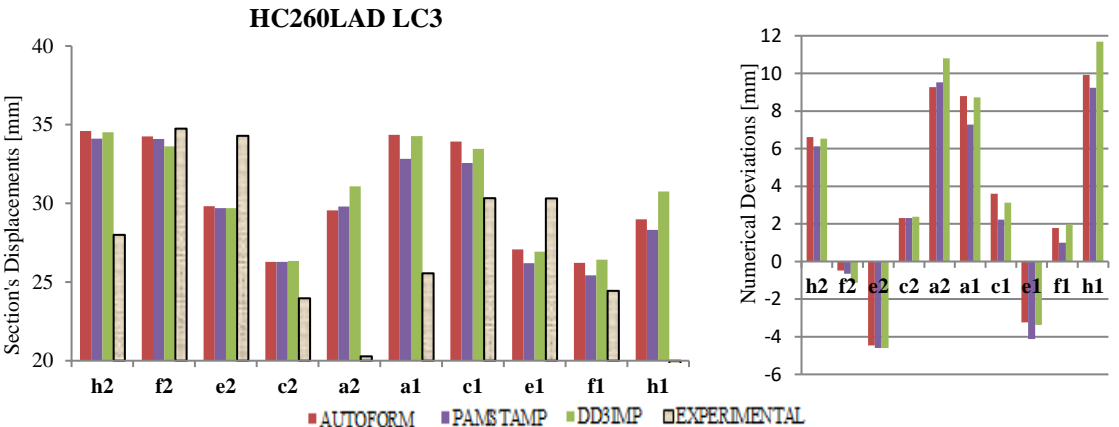


Fig. 2.14 – Comparison of experimental and numerical section’s displacements during the drawing operation, with the respective mean deviations, to the load case HC260LAD LC3.

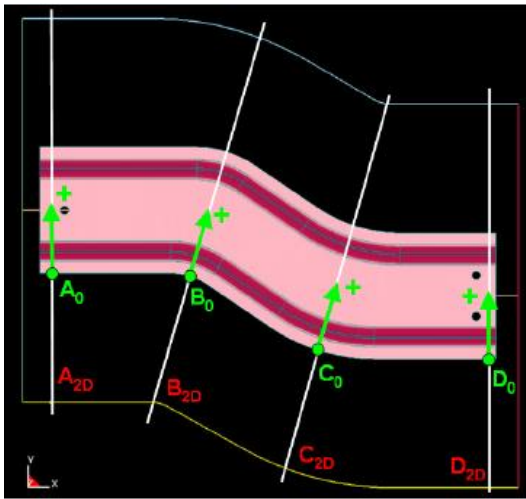
As depicted in the Fig. 2.14, HC260LAD LC3 follows the same tendency of AC170 LC3. In this case, the range of draw-in variation has increased to [20,35]mm and the maximum numerical deviations from 7mm to almost 12mm. Moreover, in these cases, the deviations are often positive, which means that the numerical draw-in is significantly higher than the experimental draw-in. Nevertheless, looking to the numerical deviation charts the same pattern for both materials can be noticed [Fig. 2.13 and Fig. 2.14]. In addition, the numerical results of all FEA codes became much closer.

Without drawbeads, the material flow is more unstable and finite elements can experience greater distortions, making the behavior of the 3D meshes (DD3Imp) very different from the 2D meshes (Autoform and Pam-Stamp), which benefit from an adaptive refinement. So, the introduction of drawbeads reduces this instability making the stamping process more robust and the numerical results more reliable.

### **Principal Strains distribution:**

Industrial meaning: The principal strains and thickness distribution is strongly related with the general formability of a stamping part. The quantification of these variables allows to predict lower or higher stretched areas, splits, compression areas and wrinkles. The amount and distribution of the equivalent plastic strain are also determinative to the springback effect. A correct prediction of these variables is essential to evaluate the feasibility of the stamping part, considering material and geometry, the stamping tools design and the stamping processes robustness.

According to the benchmark, the evaluation of true major and minor strain was required in 4 section cuts after springback. The 4 sections A2D, B2D, C2D and D2D are defined in Fig. 2.15. In this study, the authors decided to focus in the sections B2D and C2D to avoid the presentation of too much results. For the evaluation of the strain the upper side (die side) results were considered. The resulting curves were output as strain over the arc-length distance of the section cut. The zero points for the arclength distances B0 and C0 for sections B2D and C2D are defined by the trimming line and corresponds to the points 1 (see Fig. 2.15). The points 2 correspond to the end of the trimming line. The numerical and experimental strain profiles are plotted in the charts below to the 2 materials and the 4 load cases. The strains are dimensionless and the arc-length in millimeter [Fig. 2.16 and Fig. 2.18 to Fig. 2.20].



Section	Coordinates	Point 1	Point 2
B2D	X	-60.5	-13.0
	Y	-55.5	101.5
	Z	-39	-39
C2D	X	15.5	63.0
	Y	-102.0	54.5
	Z	-39	-39

Fig. 2.15 – Sections A2D – D2D for the evaluation of major/minor strains [17].

All the numerical results presented below (Fig. 2.16 and Fig. 2.18 to Fig. 2.20) follow the same trend of the experimental results, except for the minor strain of the B2D section.

### B2D SECTION

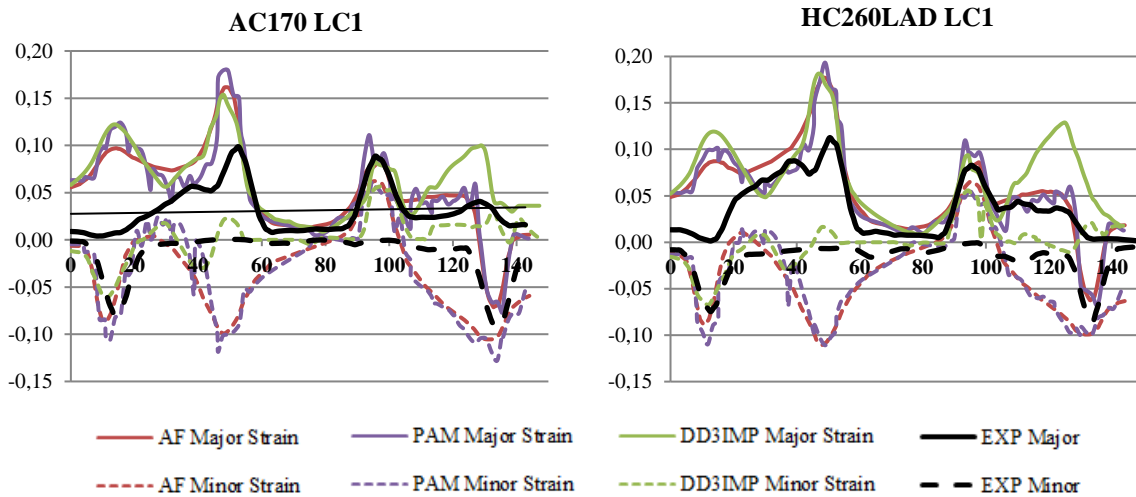


Fig. 2.16 – Comparison of experimental and numerical principal strains over the arc-length distance of the section cut B2D, after springback, to the load cases without drawbeads.

As it can be seen in Fig. 2.16, the profile of principal strains at B2D section is very similar to both

materials. This indicates that the tools geometry has the greater influence in the strain path definition. At the flat top of the drawn part [60-85]mm the deformation is residual, while most of stretched material is located in the top radii [50 and 95]mm and vertical wall [40 and 105]mm (*Plane Strain* - Major Strains  $> 0$ , Minor Strains = 0). The experimental values also present some compression tendency at the bottom radii (*Uniaxial Compression* = Major Strains  $> 0$ , Minor Strains  $< 0$ ,  $|Major Strains| < |Minor Strains|$ ). In terms of major strains, the numerical values reach peak levels always at the inner top radius curvature [50 and 95]mm, in both sections (B2D and C2D) Fig. 2.17.

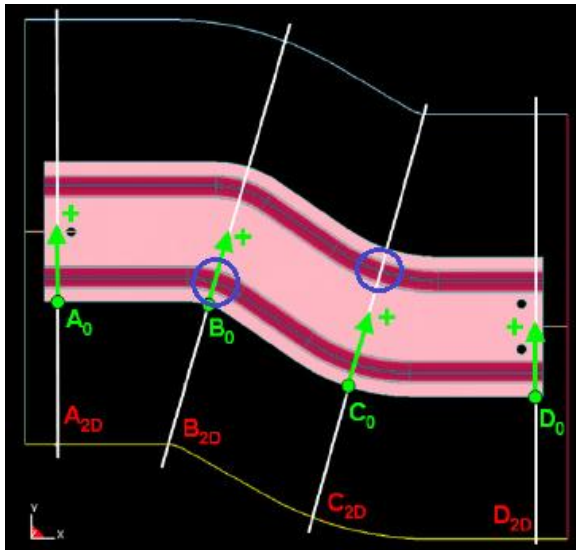


Fig. 2.17 – Peak levels of numerical major strains localized at the inner top radius curvature of the geometry. [17]

At this geometric zone (50mm and 95mm), the commercial FEA codes, Autoform and Pam-Stamp, has also predicted negative peak values to the minor strains, and consequently, a *Uniaxial Tension State* (Major Strain  $> 0$ , Minor Strain  $< 0$ , Major Strain  $> |Minor Strain|$ ), which could not be verified experimentally. Comparing numerical and experimental results, the major strain peak values in the simulations are higher.

## B2D SECTION

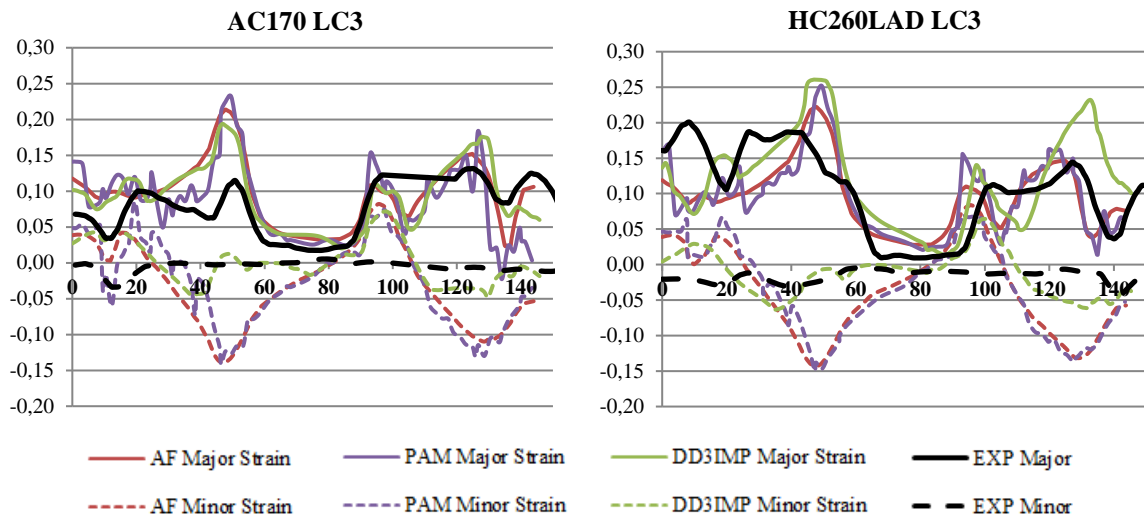


Fig. 2.18 – Comparison of experimental and numerical principal strains over the arc-length distance of the section cut B2D, after springback, to the load cases with drawbeads.

With the drawbeads the amount and level of stretching in the vertical walls [40 and 105]mm increase, but the minor strain remains close to 0, predominating the *Plane Strain State* [Fig. 2.18]. In this case, the compression tendency at the bottom radius almost disappear.

#### C2D SECTION

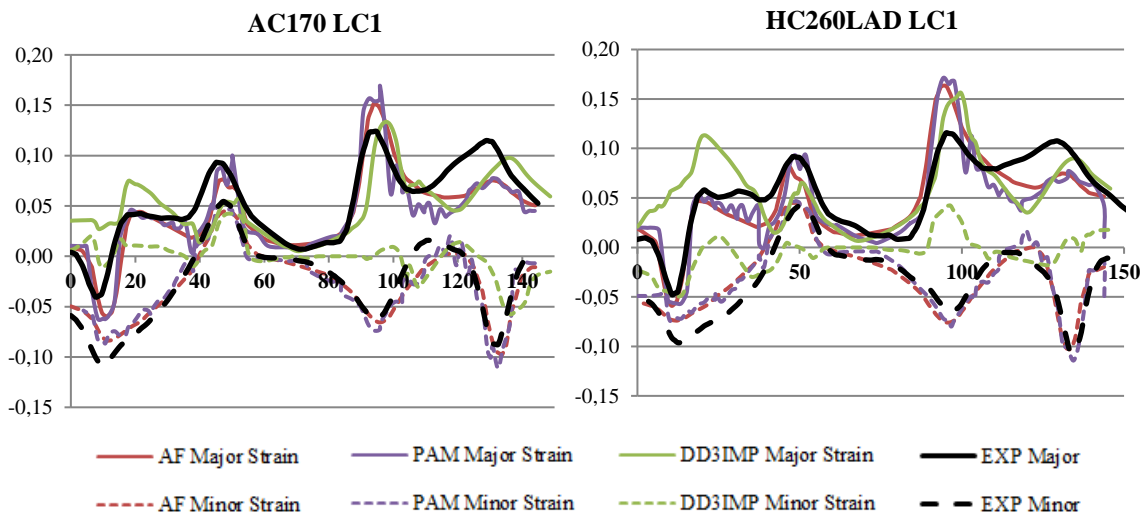


Fig. 2.19 – Comparison of experimental and numerical principal strains over the arc-length distance of the section cut C2D, after springback, to the load cases without drawbeads.

Due to the symmetry conditions of the geometry, the numerical profiles of major and minor strains to the section B2D and C2D are very similar, whether the drawbeads are present or not. However, this symmetry is not perceptible in the experimental minor strains. While the predicted profile of minor strains is quite different from the experimental values at section B2D [Fig. 2.16 e Fig.

2.18], the real tendency is very well described by the numerical values at the section C2D [Fig. 2.19 e Fig. 2.20].

According to the experimental values, all the material points at the top radii of section B2D [50 and 95]mm, are under *Plane Strain State*, but, at the section C2D, the material points located in the outer top radius of the curvature (about 50mm of length) are under *Biaxial Stretching* (Major Strain > Minor Strain > 0), while the material points located in the inner top radius of the curvature (about 95mm of length) are under *Uniaxial Tension State*. In the vertical wall of the outer radius at C2D (around 30mm of length) the thickness should be constant (Major Strains > 0, Minor Strains < 0, Major Strains = |Minor Strains|). In the opposite wall (around 115mm of length), the material points are under *Biaxial Stretching*. Concerning the 2 bottom radii, one (around 10mm of length) is under excessive compression paths, while the opposite (around 130mm of length) is near the *Uniaxial Tension State*. The strains profiles are practically the same for both materials [Fig. 2.19].

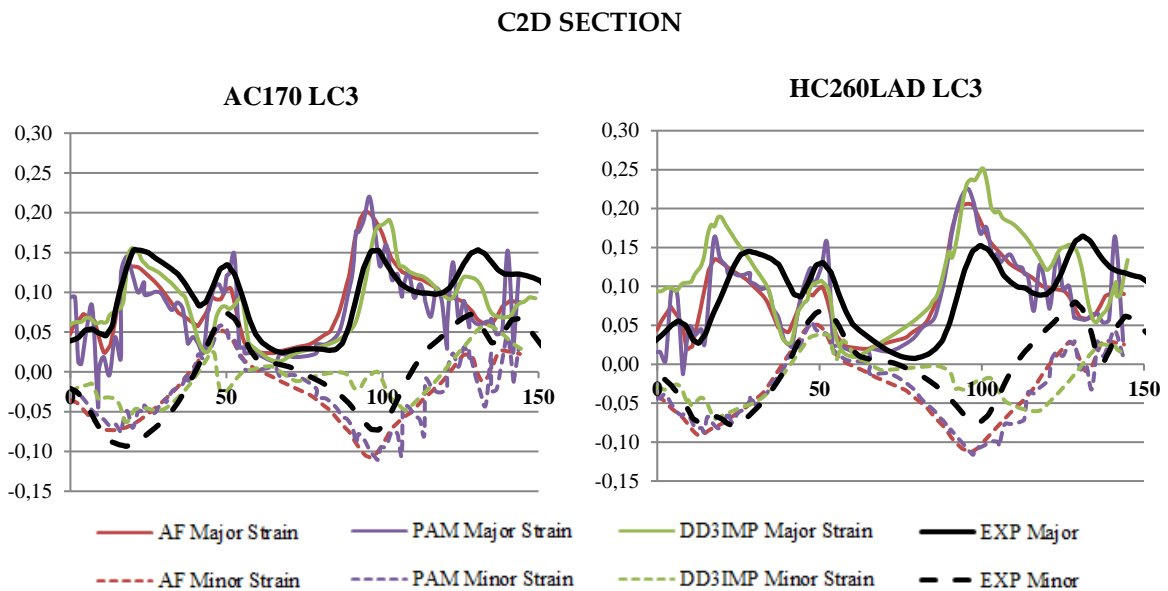


Fig. 2.20 – Comparison of experimental and numerical principal strains over the arc-length distance of the section cut B2D, after springback, to the load cases with drawbeads.

As previously stated for the section B2D, the introduction of drawbeads increased the amount and level of stretching. Looking at Fig. 2.20, the strain path in the bottom radius, at 10mm, change from the excessive compression to *Uniaxial Tension*, the vertical wall, at 30mm, change from the constant thickness state to the *Uniaxial Tension*, the top radius, at 50mm, increases its level of *Biaxial Stretching*. In the opposite side, at 95mm, the other top radius increases its level of *Uniaxial Tension*. At 115mm, the level of *Biaxial Stretching* present in the vertical wall, increases. Finally, in the second bottom radius, at 130mm, the material's state change from the *Uniaxial Tension* to *Biaxial Stretching*.

The analysis of the principal strains profiles, at sections B2D and C2D, puts in evidence a strain



path variation when drawbeads are introduced in the S-Rail drawing operation. The direction of this variation is depicted in Fig. 2.21.

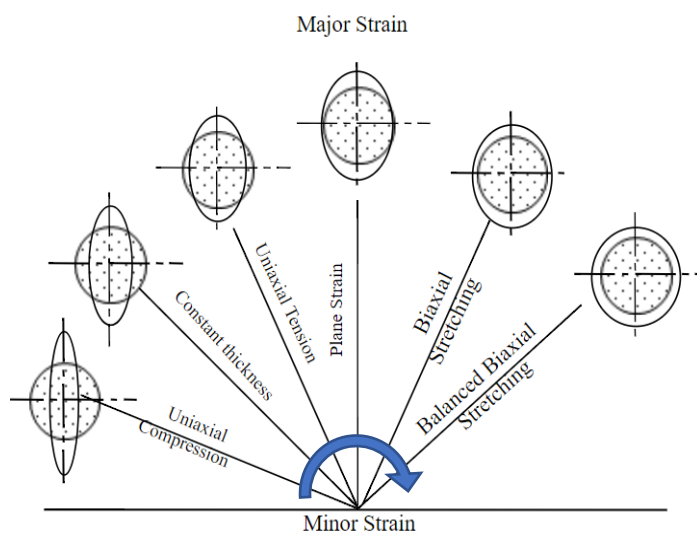


Fig. 2.21 – Direction of strain paths variation when drawbeads are introduced in the S-Rail drawing operation.

### Formability:

One of the most consulted and indispensable results in any stamping simulation report is the Forming Limit Diagram (FLD). The FLD consists of two orthogonal axes, which account the major strain level in the ordinate axis and the minor strain level in the abscissa axis, and presents the plastic deformation history of all the sheet material points during the forming process. The visualization of the materials points cloud at the end of the stamping process, allows to get the big picture of the most requested strain paths. Thus, it is possible to have an idea of the amount and distribution of stretch in the part. So, the FLD is a very useful tool to predict formability defects related with the stamping process and/or the product geometry.

To take advantage of this diagram it is necessary to introduce the Forming Limit Curve (FLC), which will define the limits until the cloud points can move, or material can be plastically deformed, without necking occurrence. The FLC is a distinguished feature of each material and can be obtained through a Nakazima test. Considering that the strain paths during the stamping process are not always linear, a non-linear FLD must be used instead of a linear FLD, to get a correct evaluation of the deformation history.

The clouds of the material points in the FLD and its location in the part for each load case, at the end of the drawing operation and with the tools still closed, are presented below (Fig. 2.22 to Fig. 2.25). In this section, only the numerical results of the comercial FEA tools (Autoform and Pam-

Stamp) were compared.

*LOAD CASE AC170 LC1*

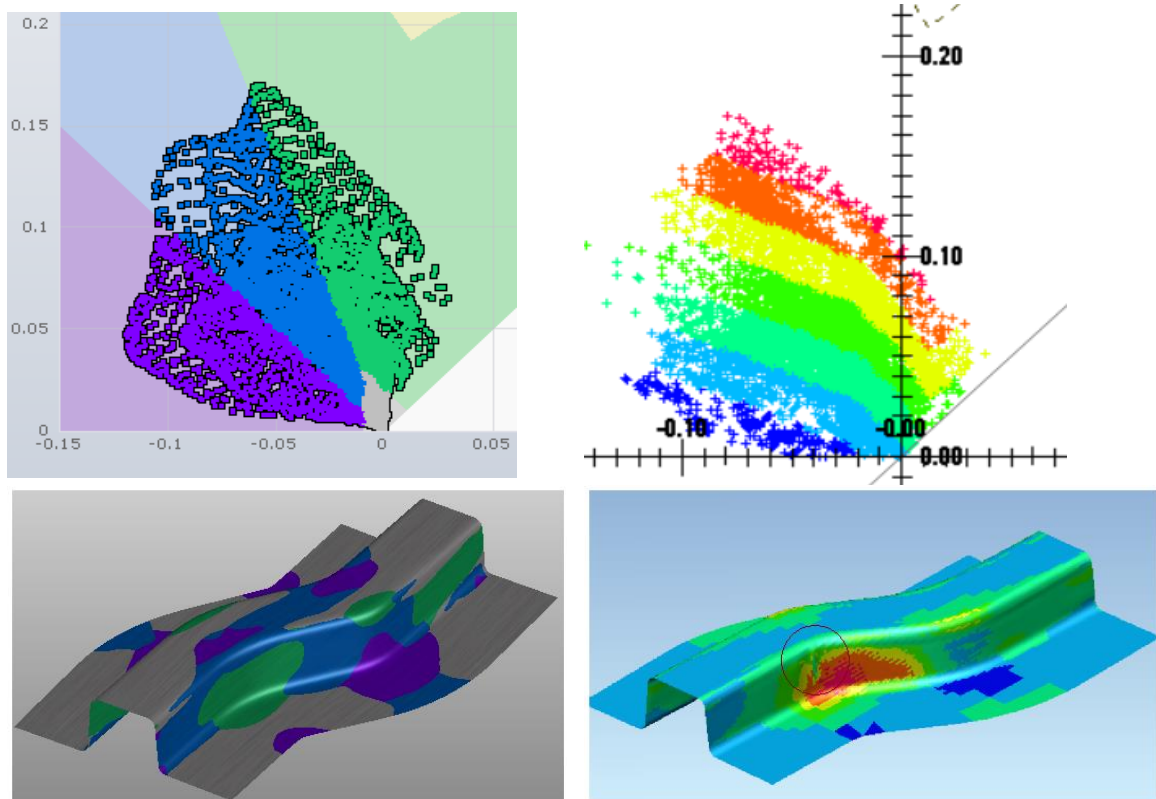
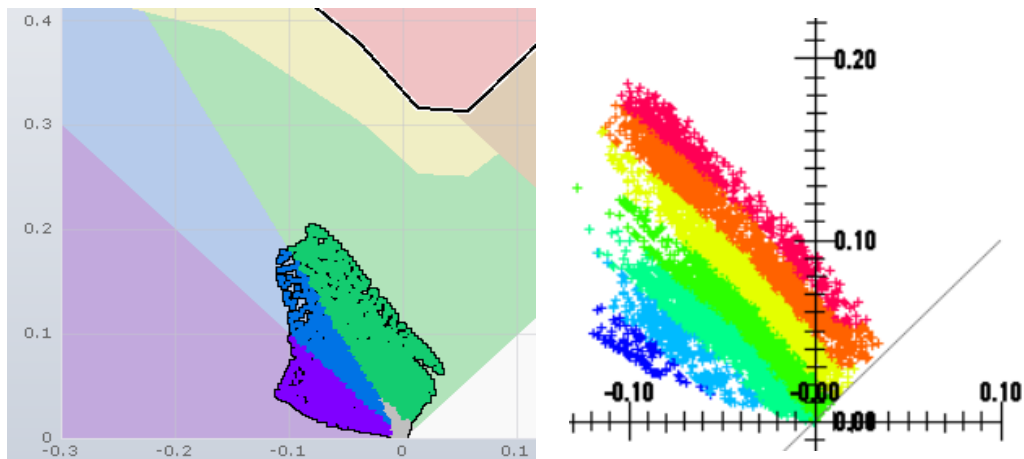


Fig. 2.22 – Comparison of Autoform's FLD and Pam-Stamp's FLD with the respective state of the material points in the part, at the end of the drawing operation, to the load case AC170 LC1.

*LOAD CASE HC260LAD LC1*



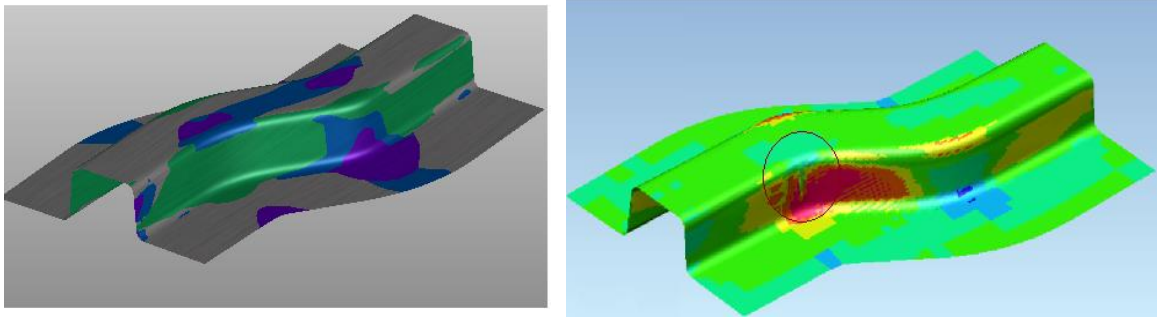


Fig. 2.23 – Comparison of Autoform’s FLD and Pam-Stamp’s FLD with the respective state of the material points in the part, at the end of the drawing operation, to the load case HC260LAD LC1.

*LOAD CASE AC170 LC3*

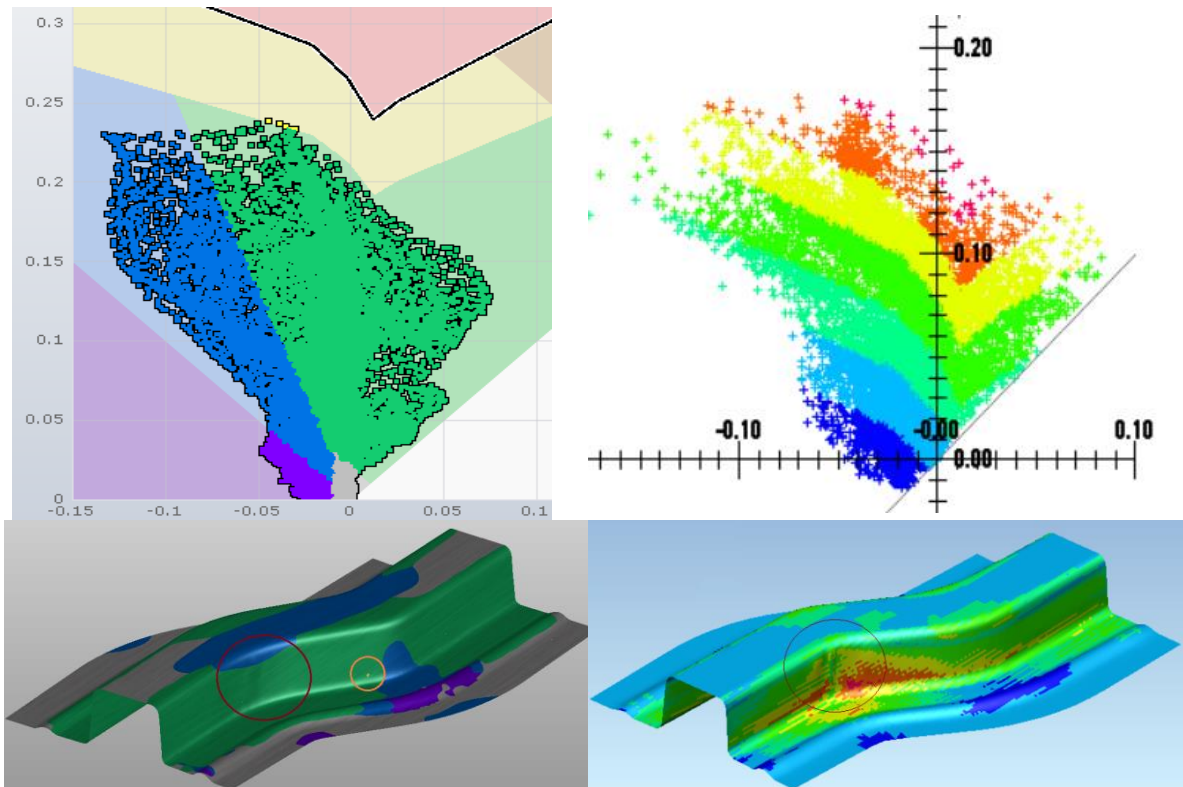


Fig. 2.24 – Comparison of Autoform’s FLD and Pam-Stamp’s FLD with the respective state of the material points in the part, at the end of the drawing operation, to the load case AC170 LC3.

*LOAD CASE HC260LAD LC3*

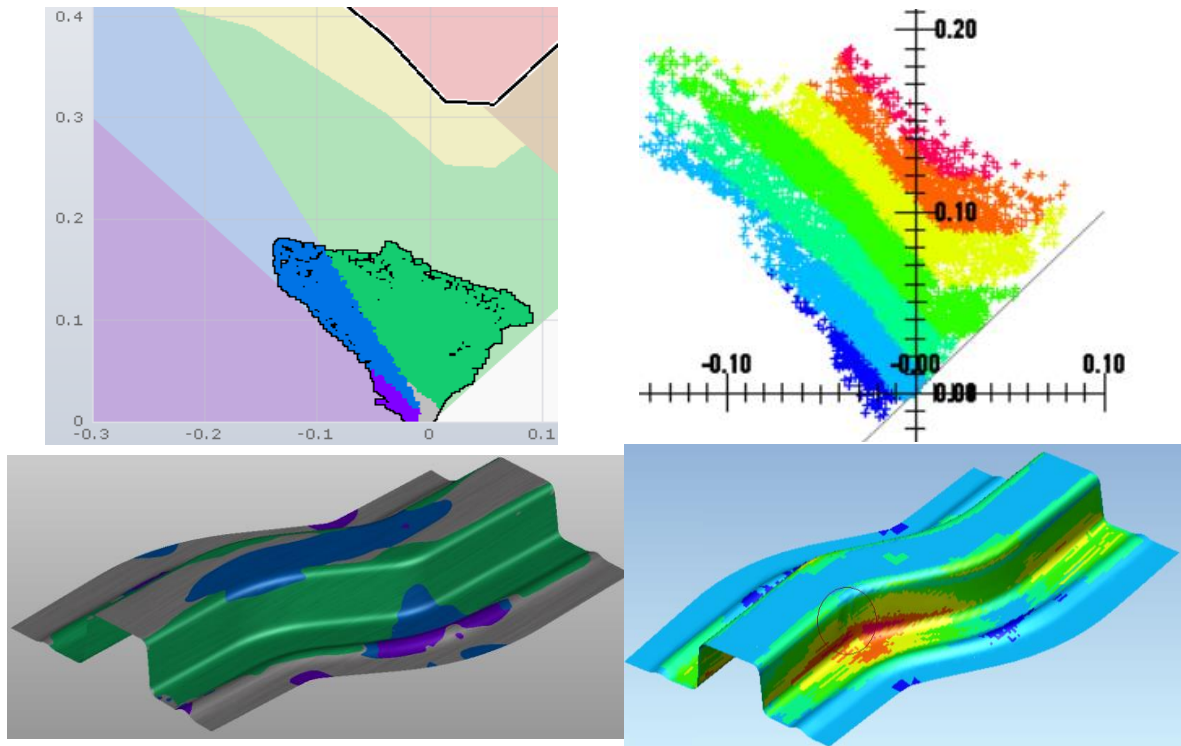


Fig. 2.25 – Comparison of Autoform’s FLD and Pam-Stamp’s FLD with the respective state of the material points in the part, at the end of the drawing operation, to the load case HC260LAD LC3.

As it can be seen (Fig. 2.22 to Fig. 2.25), there are no significant differences in the FLD prediction between Pam-Stamp and Autoform. In almost all the cases, the material points distribution is similar for both softwares. The only exception is the case AC170 LC3 [Fig. 2.24], where the cloud of material points described by Autoform reaches almost 0.25 of major strain, while Pam-Stamp is at 0.19. However, this isn’t a significant difference, since both point clouds are into the safe zone. The Pam-Stamp wrinkles are only seen in Autoform for the case AC170 LC3 (wrinkles indicated with a brown circle). The wrinkling prediction in sheet metal forming simulation is very important because it impacts directly on the product quality. The accurate prediction of this kind of instability is hard task. In general, dynamic FE codes, like Pam-Stamp, are more effective on the wrinkling prediction than the static FE codes. In this case, the wrinkle is vertical and appears consistently in a transition zone with a good level of stretching. It was noticed the presence of wrinkles in some stamped parts. However, the wrinkling tendency was not included in the scope of this benchmark study. Therefore, no measurements of the wrinkles amplitude or real pictures of the parts, to estimate the wrinkles location and extension, were provided.

### Springback:

Industrial meaning: Currently, one of the highest concerns of the automotive stamping industry is achieved an accurate and reliable springback prediction through the sheet metal forming

simulation. This springback effect needs to be minimized and controlled within a certain range of tolerances to ensure the quality of stamped parts. Thus, the springback must be considered during the tool and process design. Reliable predictions of this effect contribute to significantly reduce the tooling costs and increase the stamping process robustness.

To evaluate the springback topology all parts were covered with point grids [Fig. 2.26] and measured with an optical system. For fixing the part within the measurement device 3 material points were used [Fig. 2.27].

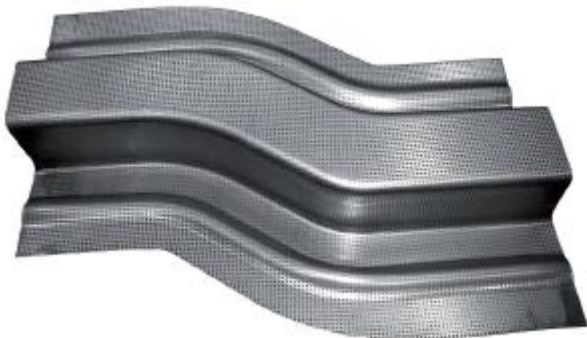


Fig. 2.26 – Part with grid for the optical measurement [17].

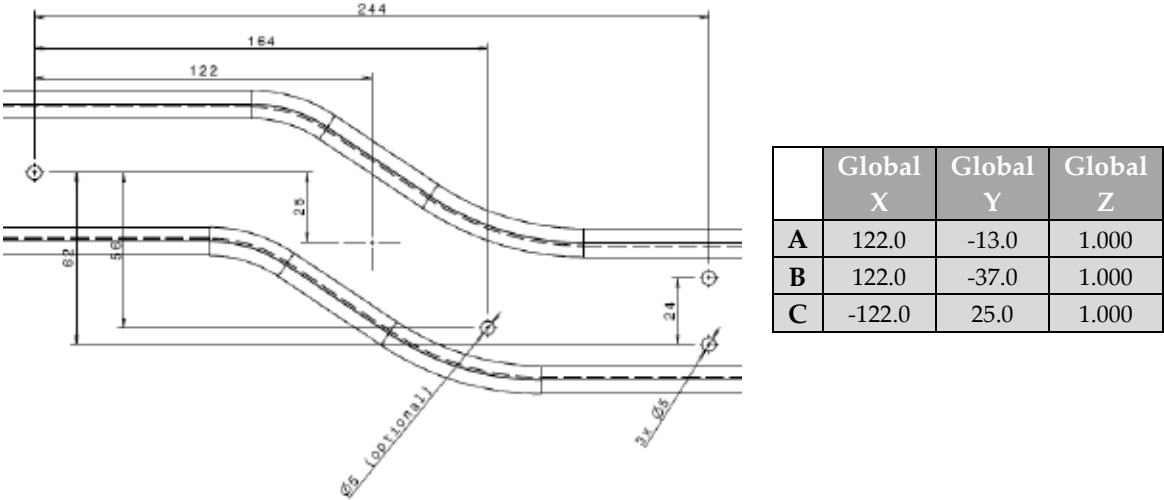


Fig. 2.27 – Location of holes in S-Rail for fixing in measurement device [17].

These 3 points also correspond to the exact support points where simulations meshes were constrained to allows the springback comparison. All the meshes were compared after trimming and springback. This comparison was based on the section’s cut profile  $X = -90$ . Thus, each profile was

compared with the reference part profile measuring the respective deviation angles  $\theta_1$ ,  $\theta_2$ ,  $\alpha_1$  and  $\alpha_2$  [Fig. 2.28].

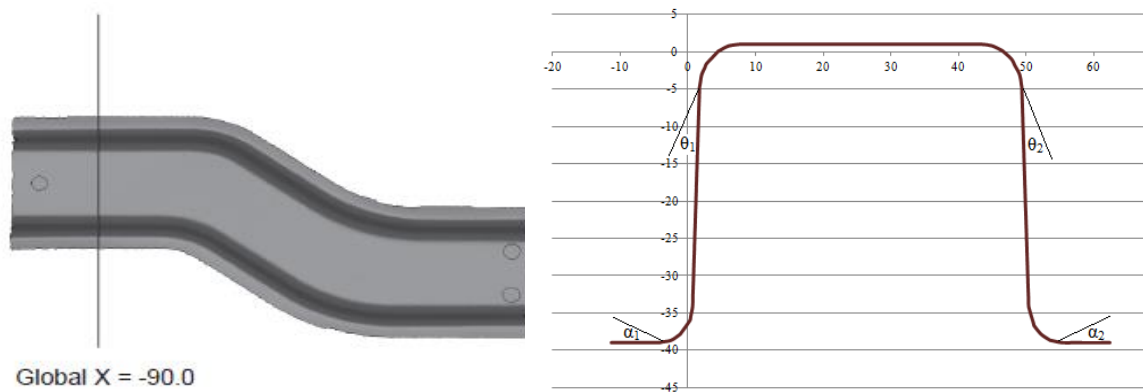


Fig. 2.28 – Presentation of the profile for springback measurements based on the deviation's angles ( $\theta_1$ ,  $\theta_2$ ,  $\alpha_1$ ,  $\alpha_2$ ) of the reference section  $X = -90$  [17].

The experimental and numerical results of each material and drawbead model are presented in Fig. 2.29 and Fig. 2.30.

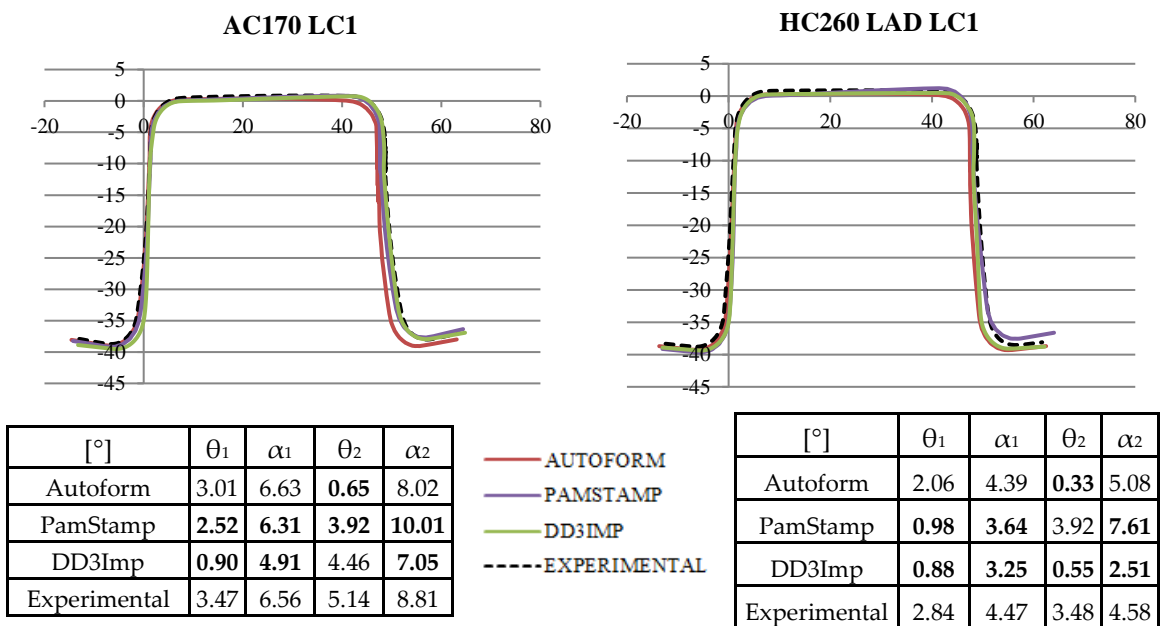


Fig. 2.29 – Comparison of experimental and numerical S-rail geometries without drawbeads after springback at the reference section  $X = -90$ .

Due to the process conditions, the springback effect is not symmetric, in most cases,  $\theta_1 < \theta_2$  and  $\alpha_1 < \alpha_2$ . The evaluation showed later that the overlapping of the experimental and theoretical meshes was not sufficient due to rigid body translations. So, it would be necessary to add additional constraint points to avoid these parasitic displacements. Even so, since the reference mesh and the

constraint points are always the same, it is possible to use these results for comparison purposes. Furthermore, it is worth noting that the profile side which present higher deviations  $[\theta_2, \alpha_2]$  it is related with the blank contour segment  $[a_1, c_1]$  which present the higher draw-in values, whereas the lower deviations side  $[\theta_1, \alpha_1]$  is related with the blank contour segment  $[a_2, c_2]$  which present lower draw-in values [Fig. 2.11 and Fig. 2.12]. Naturally, an unbalanced material flow leads to an unbalanced stretching state and, consequently, to an unbalanced springback effect.

Looking at Fig. 2.29, it is clear that, except for  $\theta_2$ , Autoform meshes always presents the closest numerical deviations from experimental meshes. Nevertheless, the accuracy and reliability of these deviations are compromised by the measurement methodology and, mainly, by the process robustness.

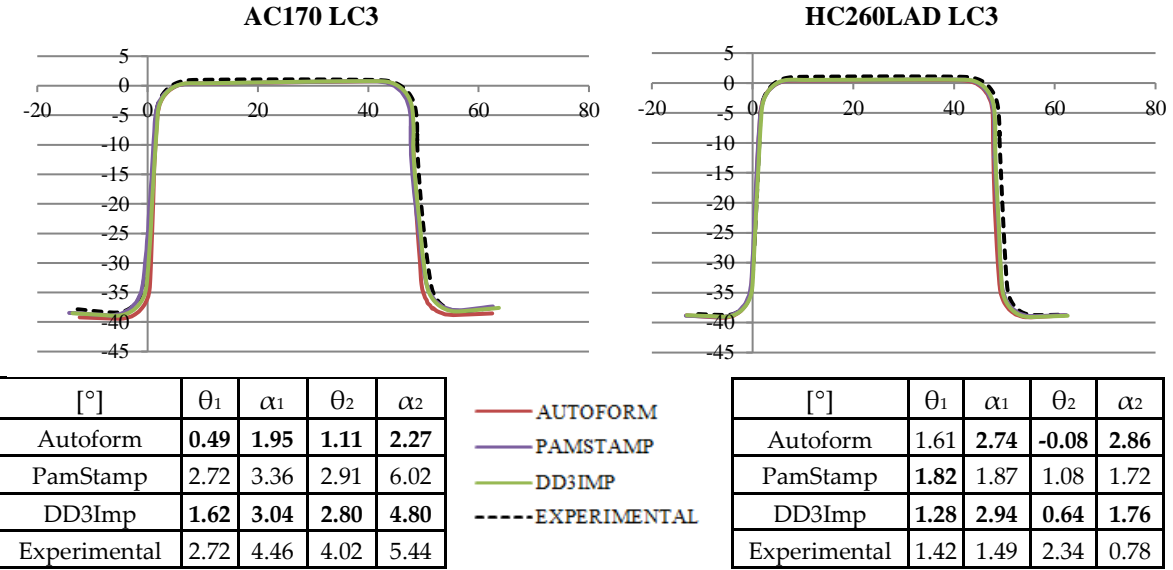


Fig. 2.30 – Comparison of experimental and numerical S-rail geometries with drawbeads after springback at the reference section  $X = -90$ .

In the other hand, it can be noted that the presence of drawbeads reduces the amount of springback deviation [Fig. 2.30]. Comparing with the draw-in measurements [Fig. 2.13 and Fig. 2.14], it is easy to see how the displacement's decrease of the blank contour segments  $[a_1, c_1]$  and  $[a_2, c_2]$  affects the springback deviations  $[\theta_2, \alpha_2]$  and  $[\theta_1, \alpha_1]$ . The lower is the draw-in, smaller are the springback deviations. This happens because the decrease of the draw-in level is related with a higher level of restraining force and, consequently, a higher level and better distribution of the stretching in the part. In this case, the lowest section displacements  $[a_1, c_1, a_2, c_2]$  are observed to HC260LAD LC3 [Fig. 2.14 and Fig. 2.30], which also presents the smaller springback deviations.

In the presence of drawbeads, Pam-Stamp meshes presents the closest numerical deviations from experimental meshes [Fig. 2.30]. In this case, the process robustness is much higher, however, it should be not forgotten that significant differences between numerical and experimental forming

forces and draw-in where also observed. With such differences, it is hard to draw valid conclusions about the accuracy and reliability of the numerical springback deviations.

On the whole, the numerical springback simulations delivered results which qualitatively follow reality, and are able to represent the sensitivities correctly. So, to use the numerical simulations to include the springback compensation in the stamping dies design it is necessary to minimize the deviations range. If the deviations range is too large, the springback repeatability and accuracy may be not enough to allow a reliable comparison with the numerical predictions. Concerning the springback compensation, the most effective procedure consists in a stochastic analysis to find the appropriate set of process parameters which minimize the springback deviations. Then, the compensated geometry tools can be manufactured or modified if the deviations range is within the allowed tolerances. Where possible, tools and dies makers also incorporates variable geometry systems which allows to tune the compensation level during the try-out or even in the production phase. Autoform-Sigma software module is a great help in this kind of study since it includes statistical process control techniques, taking into account the noise and variability that are inherent in the forming process. Then, Autoform-Compensator helps to generate the compensated surfaces of the stamping dies based on the robust springback analysis.

### **Computational Cost:**

Industrial meaning: Produce a car is a very complex process that requires an extremely meticulous planning between OEM's and their suppliers. In the automotive industry, the project, design and development of stamping tools deadlines are becoming tighter. Moreover, all the problems that arise in the production line must be solved quickly. Thus, the requirement for effectiveness of the FE codes is increasing. The computational cost (calculation time and the necessary computing resources) needs to be minimized. Of course, the amazing processing power of current computers and the ability to perform simulations in parallel calculation greatly increased the efficiency of the codes. Even so, the complexity of the models associated with the material laws, interaction with tools, stochastic analysis, among others, also increase considerably. Furthermore, stamping simulation softwares need become more and more automated and intuitive for the process virtual design and facilitate the access and evaluation of numerical results. In fact, the effective cost of a simulation should also include the pre/post – processing.

After design the virtual stamping processes to each case, and built the respective numerical models, the simulations were executed in the same machine with the following characteristics:

- Number of Threads: 1
- Windows Version: Windows 7 Ultimate
- Windows Type: Architecture Intel64, Version 6.1.7601



- Processor Type: Intel(R) Xeon(R) CPU X5650 @ 2.67GHz (12 cores)

The elapsed time of each simulation is presented, in minutes, in the bar charts below [Fig. 2.31]

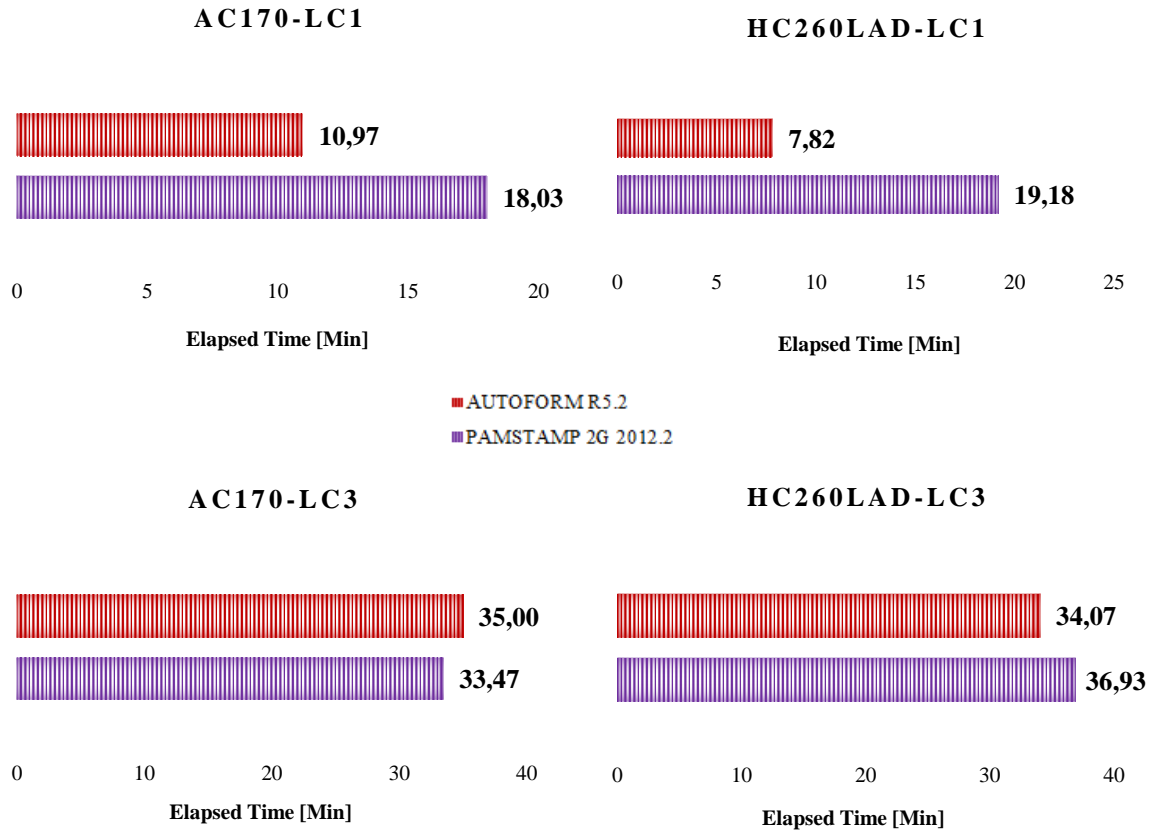


Fig. 2.31 – Comparison of Autoform and Pam-Stamp run time simulations for all the load cases studied.

In the cases without drawbeads, Autoform is twice as faster as Pam-Stamp. However, in the presence of drawbeads, both FE codes end the simulation job at the same time. Looking at these results, it seems that the combination of the robust solver of Autoform with the implicit FE formulation, which allows much larger time-steps, and the 2D triangular elements are the key to obtain the best numerical accuracy at minimal computational cost. But, as shown, when complex strain path (like drawbeads) are introduced in the stamping process and the level of plastic strain and stretching increase, the computing time of implicit FE codes may increase much more than the explicit FE codes to satisfy the equilibrium equations.

These 2 FE codes are extremely fast even with 1 thread. However, both softwares can use multiple processing cores to speed up single run or multi-step run executions. Therefore, it is possible to shorten run times of large designs present in progressive stamping simulations or run several stamping simulations at the same time. Depending of the design complexity of the stamping process, multi-threaded execution allows to run progressive stamping simulations, with 5 or 6 steps,

in 15 minutes or less, which is perfectly in line with the industrial needs. Thus, the simulation run-time is no longer the biggest concern of the automotive stamping industry.

Instead, the key aspect which affects the productivity of the CAE process engineer is the time spent with Pre/Post processing. In this regard, the virtual productivity of Autoform is, with no doubt, unbeatable. The Autoform DieDesigner module allows to generate automatically the tools required for try-out simulations from the selected die face. This module is based on a fully associatively linked model of the entire die layout, which allows the user to easily modify intermediate operations as well as the final part geometry. When such modifications are made, the tooling geometries of all operations and the input for simulation are automatically and instantly updated. Pam-Stamp also include a clear and logical structure to help users to work step-by-step, from the import of CAD part geometry to the complete die design. However, the available features to enable a precise geometry modelling are much more limited. Furthermore, the post processing tools are not so powerful, and each process step have to be analyzed in a different file, which makes the numerical data treatment a tedious work. Autoform presents sophisticated post processing tools which automate a large part of the numerical data treatment and the simulation report generation, making it the most suitable for progressive stamping.

## CONCLUSIONS

Based on the Numisheet 2008 Benchmark #2, it was made a comprehensive study of the sheet metal forming simulation softwares used today in the automotive industry. This study highlights the differences between the numerical results and its impact on the industrial competitiveness of a company.

**Concerning the forming forces, all the FEA codes present the same level of accuracy in both cases, with or without drawbeads.** In the cases without drawbeads, where the constraint forces are mainly driven by friction, the punch forces drop effect cannot be described if the Coulomb friction coefficient is assumed constant. A contact pressure dependent law must be considered in the FEM model. Despite the lack of accuracy in the description of this phenomenon, the slightly overestimated predicted forming forces are still reliable for industrial purposes as the stamping press selection. In the presence of drawbeads, the predicted punch forces are very underestimated (around 25% for the AC170 and 35% for the HC260LAD). This huge difference between numerical and experimental forces is not common in the automotive stamping simulation. A further study regarding the influence of numerical and process parameters is required to clarify this issue.

**Concerning the draw-in analysis, the numerical values always follows the same trend of the experimental values, in all the FEA codes. However, it was noticed that the numerical draw-in can be strongly FE mesh dependent.** In the cases without drawbeads, the material flow is more unstable

and the FE mesh can experiment greater distortions. Comparing the commercial FE codes with DD3Imp, it was noted that, if the material flow during the process is not stable (progressive stamping, tandem stamping without drawbeads, crashforming, etc.), the numerical results can diverge between FE codes which use 2D meshes and 3D meshes, in terms of draw-in and principal strain distribution. These differences may affect the blank contour optimization and the process feasibility. Therefore, special attention should be given to the FE mesh refinement and finite element integration rule, particularly if 3D solid elements are used. The introduction of drawbeads, make the stamping process more robust and the numerical results of 2D mesh and 3D mesh closer.

**Regarding the principal strains profiles, the numerical results delivered by the FEA codes tested present a good description of the experimental pattern.** The principal strains are mostly affected by the tools geometries since they define the strain paths forward by the material points during the drawing operation. Therefore, as the draw-in, the numerical principal strains are also very dependent of the FE mesh. Since Autoform and Pam-Stamp work with shell elements and 2D FE meshes, the numerical strain profiles are practically the same. Comparing with DD3Imp, the numerical profiles are a bit different due to the 3D FE mesh, especially in the case of the minor strains. In the presence of drawbeads, the material flow tends to be more stable, and the numerical profiles become closer.

**In terms of the general formability, the results were very similar.** However, Pam-Stamp predicts wrinkles that cannot be seen in the Autoform meshes. These instabilities are quite difficult to predict and an important advantage in numerical studies of part feasibility and stamping process robustness.

**Concerning the benchmark results, the numerical springback present the highest variability between the FEA codes.** The higher deviations were observed to the case without drawbeads and to the side that presented higher levels of draw-in, whereas, the lower springback values were achieved with drawbeads to the side with lower draw-in. This means that drawbeads plays a paramount role in control the material flow, ensuring a uniform stretching distribution, and, consequently, decrease and stabilize the springback. From the comparison made between the numerical and experimental springback, Autoform present the most accurate and reliable values without drawbeads, whereas, Pam-Stamp present better results in the presence of drawbeads. However, this assumption may not be entirely true. In the cases without drawbeads, the stamping process may not be stable enough to guarantee the springback robustness. This means that the experimental springback can vary so much that the numerical predictions become unreliable. In the cases with drawbeads, important differences were detected between the experimental and numerical forming forces and draw-in values. These differences affect the state of residual strains, residual stresses and stretching distribution present in the part after the drawing operation. Since the springback effect is essentially

dependent of these state variables, a comparison between experimental and numerical quantification may not be effective.

**Looking at the computational cost, only the commercial FEA codes were compared.** In the case without drawbeads, Autoform was 2 times faster than Pam-Stamp. However, in the cases with drawbeads, Autoform and Pam-Stamp ends the calculus more or less at the same time. These 2 stamping simulation softwares prove to be extremely fast even with 1 thread. However, both FEA codes are able to use multiple processing cores to speed up single run or multi-step run executions. Therefore, it is possible to shorten run times of large designs present in progressive stamping simulations or run several stamping simulations at the same time. The key aspect which affects the productivity of the CAE process engineer is the time spent with Pre/Post processing. In this regard, the virtual productivity of Autoform is, with no doubt, unbeatable.

So, it was shown that, beyond the fundamental differences in their FE formulation, Autoform and Pam-Stamp delivery very similar numerical results, which are, in general, in good agreement with the real results. This means that the stamping companies may choose freely, between these softwares, without be extremely concerned about the impact of the numerical results accuracy in their competitiveness. However, Autoform can provide extra modules, as Autoform Sigma and Autoform Compensator, to improve stamping die design with an accurate springback compensation and presents a better virtual productivity due to its pre/post processing environment and features.

## ACKNOWLEDGMENTS

The authors greatly acknowledge the financial support of “Fundação para a Ciência e Tecnologia” (FCT – Portugal), through the research project SFRH/BDE/51189/2010 (“Development FEA Tools Applied to Sheet Forming Special Cases. Application to the Automotive Industry, Advanced Metallic Materials and Multi-Layer and Multi-Material Sheets”) in partnership with Sodecia Product Competence Center (Maia, Portugal). The authors would also like to thank the companies AutoForm and ESI GROUP to the technical support and collaboration in this study.

## COMPLIANCE WITH ETHICAL STANDARDS:

Funding: This study was funded by SFRH/BDE/51189/2010.  
No conflict exists: The authors declare that they have no conflict of interest.

## REFERENCES

1. Banabic D (2010). Sheet Metal Forming Processes: Constitutive Modelling and Numerical Simulation, first Ed., Springer, ISBN: 978-3-540-88112-4, pp. 21-25, 45-52. DOI: 10.1007/978-3-540-88113-1
2. Tang SC, Ilankamban R, Ling P (1988) “A finite element modeling of the stretch-draw forming process.” SAE Paper 880527
3. Honecker A, Mattiasson K (1989) “Finite element procedures for 3D sheet forming simulation.” In: Thompson EG, Wood RD, Zienkiewicz OC, Samuelsson A (eds) NUMIFORM’89, AA Balkema, Sophia Antipolis.
4. Lenard JG, Schey JA (2002) Metal Forming Science and Practice: A State-of-the-Art Volume in Honour of Professor J.A. Schey's 80th Birthday. Chapter 8: Numerical Simulation of Sheet Metal, pp. 143.
5. Cazacu O and Barlat F (2001) “Generalization of Drucker’s yield criterion in orthotropy.” Mathematics and Mechanics of Solids. Vol 6, Issue 6, pp. 613 – 630
6. Banabic D, Kuwabara T, Balan T, Comsa DS, Julean D (2003) “Non-quadratic yield criterion for orthotropic sheet metals under plane-stress conditions.” Proceedings of the 7<sup>th</sup> Conference ‘TPR2000’. Cluj Napoca, Romania, pp. 217-224
7. Aretz H, Barlat F (2004) “General orthotropic yield function based on linear stress deviator transformations.” In: Ghosh, S. Castro, G. C. Lee, J. K. (eds) Materials processing and design: Modelling, simulation and applications. Proceedings of the NUMIFORM 2004 Conference, Columbus, O. H. pp.147-151

8. Banabic D, Aretz H, Comsa DS, Paraianu L (2005) "An improved analytical description of orthotropy in metallic sheets." *International Journal of Plasticity*. Vol 21, pp. 493-512. DOI: 10.1016/j.ijplas.2004.04.003
9. Vegter D, van den Boogaard AH (2006) "A plane stress yield function for anisotropic sheet material by interpolation of biaxial stress states." *International Journal of Plasticity*. Vol 22, pp. 557-580, DOI: 10.1016/j.ijplas.2005.04.009
10. Comsa DS, Banabic D (2008) "Plane-stress yield criterion for highly-anisotropic sheet metals." In: Hora, P. (ed) *Proceedings of the 7<sup>th</sup> International Conference and Workshop on Numerical Simulation of 3D Sheet Metal Forming Processes, NUMISHEET 2008, Interlaken, Switzerland*, pp. 43-48
11. Hillmann M, Kubli W (2009) *Method for designing a tool for deep drawing and tool for deep drawing of sheet metal*" US 7623939 B2.
12. Kubli W, Krainer A (2012) "Method and computing system for designing a sheet-metal-forming process" US 20120123579 A1.
13. Kubli W, Krainer A (2013) "Method and system for processing and displaying sheet-metal-forming simulation parameters" US 8478572 B2.
14. Kubli W, Krainer A (2013) "Method and computing system for designing a sheet-metal-forming process" US 8560103 B2.
15. Roll K, Wiegand K, Hora P, Manopulo N, Clausmeyer T (2008) "Benchmark 2 – Influence of drawbeads on the Springback Behavior («S-Rail») Part B: Benchmark Analysis" in *Proceeding of the 7th International Conference and Workshop on Numerical Simulation of 3d Sheet Metal Forming Processes, Interlaken, Switzerland, September 2008*.
16. Hora P, Peters P, Manopulo N, Gorji M (2015) "Challenges in the accurate modeling of sheet metal forming processes" in the *Proceedings of 8<sup>th</sup> Forming Technology Forum Zurich 2015 – Advanced Constitutive Models in Sheet Metal Forming*. June 2015
17. Roll K, Wiegand K, Hora P (2008) "Benchmark 2 – Influence of drawbeads on the Springback Behavior («S-Rail») Part A: Physical Tryout Report" in *Proceeding of the 7th International Conference and Workshop on Numerical Simulation of 3d Sheet Metal Forming Processes, Interlaken, Switzerland, September 2008*.
18. Padmanabhan R, Oliveira MC, Alves JL, Menezes LF (2007) "Influence of process parameters on the deep drawing of stainless steel". *Finite Elements in Analysis and Design*; Volume 43, Issue 14, pp. 1062-1067, DOI: 10.1016/j.finel.2007.06.011
19. Walker SV, Leine RI (2016) *Modeling and numerical simulation of anisotropic dry friction with non-convex friction force reservoir*. in *Proc. IMSD, Montréal*.

20. Trzepieciński T, Lemu H (2011) "Investigation of anisotropy problems in sheet metal forming using finite element method". *International Journal of Material Forming*; Volume 4, Issue 4, pp. 357–369, DOI: 10.1007/s12289-010-0994-7
21. Lemu, H, Trzepieciński T (2013) "Numerical and Experimental Study of Frictional Behavior in Bending Under Tension Test". *Journal of Mechanical Engineering*, Volume 59, Issue 1, pp. 41-49
22. Trzepieciński T, Bazan A, Lemu H (2015) "Frictional characteristics of steel sheets used in automotive industry". *International Journal of Automotive Technology*; Volume 16, Issue 5, pp. 849–863, DOI: 10.1007/s12239-015-0087-1

### **3. ARTIGO 2: “Role of Process and Numerical Parameters on the Virtual Manufacturing of Automotive Deep-Drawn Parts”**

**A.M. Pimentel, J.L. Alves, N.M. Merendeiro**

Anthony Michael Fernandes Pimentel<sup>a,b,\*</sup>

\*E-mail: anthony.pimentel@ct.sodecia.com \ anthony.pimentel@dep.uminho.pt

José Luís de Carvalho Martins Alves<sup>b</sup>

Nuno Miguel de Seabra Merendeiro<sup>a,2</sup>

<sup>a</sup> Centro Tecnológico Sodecia, Rua Eng.º Frederico Ulrich, 2650, 4470-605 Maia, Portugal

<sup>b</sup> CMEMS, Universidade do Minho, Campus de Azurém 4800-058 Guimarães, Portugal

---

<sup>2</sup> Present Adress - Sodecia-participações Sociais Sgps Sa, Rua do Espido, 164-F, Edifício Via Norte, 4470-177 Maia – Portugal



## **ABSTRACT**

Deep drawing process has become an important manufacturing process to produce automotive parts of good strength and light weight. Numerical modeling is nowadays an indispensable step in the design process of formed parts. This is especially the case for sheet metal forming operations where simulation techniques continue to generate substantial savings. However, although the large variety of FE codes available on the market reached substantial maturation in terms of reliability and user-friendliness, the industrialists still report problems and defects that are not predicted by the virtual manufacturing. In these cases, the measurement of certain state variables in the industrial environment reveals some discrepancies with the numerical predictions. In general, these discrepancies are related with the variation of process or/and numerical parameters, which have been studied separately by many authors.

The present paper aims at analyzing the root cause of numerical vs experimental discrepancies in sheet metal forming simulation based in a variability study of process and numerical parameters. The sheet forming process of the well-known S-Rail geometry proposed at Benchmark #02 of Numisheet 2008 is investigated. The influence of the variation of the material model, friction conditions and drawbead geometry on the forming and springback FE simulations is deeply evaluated and discussed. The contribution will open the discussion about the industrial benefit of the variability study in sheet forming simulation with higher efforts to reach a tight control of the process parameters and more accurate experimental data.

## **KEYWORDS**

Sheet Metal Forming Simulation; Process and Numerical Parameters; Springback; Material Models; Friction

## INTRODUCTION

Numerical modeling is nowadays an indispensable step in the design process of formed parts. This is especially the case for sheet metal forming operations where simulation techniques continue to generate substantial savings. Surprisingly, discrepancies between experimental and numerical are still encountered in relatively simple and well-studied geometries.

The sheet forming process simulation of the S-Rail profile is an either academic or industrial case of study well known in the automotive industry, which has received wide prominence in the Numisheet conferences over the past 20 years. The comparison between experimental and numerical results has provided valuable outputs to control instabilities such as wrinkles and springback, thus making the sheet forming processes more robust. On the other hand, the analysis of the virtual sheet forming process of the of the S-Rail geometry has allowed to understand some limitations of the FEM codes and to improve the numerical models, increasing its accuracy, efficiency and reliability. However, if such exchanges of information are to be truly effective, it is necessary to identify the root cause for the discrepancies between experimental and numerical results. This difference may increase or decrease depending on the control level of the variables associated with the process and of the domain level of the parameters associated with the numerical model. Therefore, the issue about the impact of the process and numerical parameters variability on the simulation results of sheet forming processes has been investigated by several authors. In recent years, the focus of this study has been given to the prediction of springback effects.

The growing trend towards the application of high strength steels and aluminum alloys in automotive components has greatly increased the severity of springback deviations due to the higher yield stress/modulus of elasticity ratio of these advanced materials. Thus, the biggest challenge related to the deep-drawing process with these new materials is to accurately predict and quantify this effect to define the compensated geometries of the stamping tools before its production.

It is well established that the springback simulation is sensitive to many numerical parameters. Numerical procedures that must be considered more critical for springback simulation include the spatial integration scheme, element type, and time integration scheme. Efficient and accurate numerical procedures were proposed to predict the springback using FE analysis including integration scheme [1], element type [2], through-thickness integration points [3, 4], yield stress and work hardening rate [5]. The degradation of the elastic modulus with increase of plastic strain and its influence on springback prediction were also reported [6-8]. One of the most important issues in material modeling is the description of anisotropy in terms of stress directionality and  $r$ -value, and for that purpose, many types of anisotropic yield functions have been proposed in the past [9-19]. Conventional plasticity models assume that the material parameters in the models remain fixed, and as a result, the anisotropy of the stress directionality and  $r$ -values are kept constant throughout

plastic deformation. [20] proposes a constitutive model that describes the evolution of anisotropy, both for the stress directionality and  $r$ -values, of sheet metals with increasing plastic strain. Furthermore, the springback was predicted more reliably after considering the effect of the strain-hardening behavior under strain-path changes. As such, properties associated with reverse loading, such as the Bauschinger effect, transient hardening with high rate or stagnation, and permanent softening were found to strongly influence the prediction of springback [5, 21,22]. In the kinematic-hardening models suggested by [23] and [24], the Bauschinger effect was considered; however, the hardening response was linear. Nonlinear hardening models incorporating kinematic hardening have been widely adopted to improve the accuracy of the sheet metal forming simulations. Three main nonlinear hardening models used to predict springback accurately are: (1) Armstrong-Frederick type hardening models, (2) multi-surface-type hardening models and (3) a novel hardening model without simple kinematic hardening. [25] and [26] proposed nonlinear kinematic-hardening models to characterize the Bauschinger effect and subsequent transient hardening. Armstrong–Frederick type non-nonlinear kinematic hardening models dominated before 2005 and remain prevalent, with new variations still being introduced [27-28]. [29] modified the Chaboche model to consider the permanent softening, using a form of kinematic hardening with a two-surface plasticity formulation. This hardening law has been implemented for plane-stress thin-shell elements in conjunction with three anisotropic yield criteria: Hill'48, Barlat's three-parameter yield function, and Barlat's Yld96. More recently, conventional two-surface models were integrated and extended in a unified mathematical context to incorporate anisotropy, the Bauschinger effect, transient behavior, and permanent softening [30]. [31] incorporated the work-hardening stagnation characteristic into the model. Among other hardening models based on two-surface schemes, the Yoshida–Uemori (Y–U) model gained popularity in part because it has relatively few parameters to be determined and it has been implemented into the commercial FE software Pam-Stamp (ESI/PSI, 1995). Numerous studies were conducted using nonlinear kinematic-hardening models, wherein the predicted springback results were in reasonable agreement with the predictions [8, 32-34]. Kinematic hardening models, whether involving one or two yield surfaces, still invoke the translation and expansion of a fixed surface shape, thus preserving the direction of normals at given locations. Recently, [35] proposed a new approach known as the homogenous yield function based anisotropic hardening (HAH) model as an alternative to the kinematic hardening model. The model is a distortional plasticity model that helps evaluate complex hardening responses without requiring the back stress or kinematic hardening components, i.e., without yield surface translation. Several versions of the HAH models were subsequently proposed to consider the latent hardening and Bauschinger-like effect under cross-loading conditions [36-39]. [40] studied the influence of hardening during non-linear strain-path, present in the double stage U-draw bending test, on

springback predictions. The advanced hardening models of Yoshida-Uemori (YU) and HAH models were compared with isotropic hardening models. Other authors also investigate the influence of the yield criterion and hardening models on the sheet metal forming limits [41, 42].

Equally important are the process parameters. Admittedly, one of the main limitations of the current numerical models is closely related to the lack of process data (press speed, effect of temperature variations, friction conditions, tool parallelism, etc.,). Thus, understanding how these variables are involved in the process and how its variability influences the results is the key to success. One of the process parameters that has received most attention in the literature regards the friction conditions. Despite its great influence on springback, the frictional behavior has been often simplified in numerical simulations by adopting the classical Coulomb's law. Experimental observations have revealed that the friction coefficients of sheet metals normally range between 0.1 and 0.2 in lubricated forming conditions [43-46]. Even this amount of deviation can significantly change the predicted springback; for instance, the sidewall curl changed about 24% in U-draw/bending according to [47]. The sensitivity study shown in [48] also implies that the friction coefficient is the major factor influencing the simulation accuracy. Therefore, a reasonable description of frictional behavior is essential in developing a reliable springback prediction model. Several experimental reports have shown that friction coefficient is not constant for a given set of contact bodies and lubricant but varies depending on loading condition and sliding velocity [49-52]. [53] suggested assigning different values of the friction coefficient on different contact regions in the U-draw/bending process. However, the calculated force-displacement data depend not only on the friction model but also on the constitutive model. [54] analyze the influences of the material and friction models and to suggest the optimum selection of the models for springback simulations. [55] conducted a study of friction behavior of sheet metal forming in bending under tension test. It was stated that the application of lubricant during tests of all of the sheet metal samples causes reduction of friction coefficient value, however, the use of tools with low surface roughness value to reduce the frictional resistance is unfounded because the increased real contact area increases the interatomic interaction of surfaces. This phenomenon increases frictional resistance. [56] has investigated the influence of the friction coefficient on the drawing load and the maximum drawing force for both the analytical and FE methods. [57] has studied influencing factors like the punch and die radii, the punch velocity, clamping force, friction and draw depth. Experimentally effect of various parameters has been observed then statistical analysis has been performed. The statistical treatment ANOVA has been applied to the results of the experiment to determine the percent contribution of each factor. [58] has presented the effect of process parameters such as die radius, blank holder force and friction coefficient on deep drawing of stainless steel. In this research FEM with ANOVA method has been used to determine the proportion of contribution of three important

process parameters in the deep-drawing process. The die radius (89.2%) has major influence on the deep-drawing process, followed by friction coefficient (6.3%) and blank holder force (4.5%). [59] carried out the tension/compression test of steel sheets in order to investigate the effect of the strain rate on the tension/compression hardening behaviour. It was found that the tension/compression hardening behaviour of steel sheets changes sensitively with the variation of the strain rate. Following this line, [60] conducted experimental and numerical investigation of the effect of the punch speed on the amount of springback in U-bending of auto-body steel sheets. U-bending tests and finite element analysis of SPCC and DP780 steel sheets were conducted for springback evaluation at different punch speeds with the geometry adopted from the NUMISHEET '93 benchmark problem. For its part, [61] simulated the sheet metal forming process with varying process parameters (dimensions of the blank, shape of the tools, mechanical properties of the blank material and type of forming process) using the adaptive finite element techniques. The effect of radial clearance percentage on the autographic record (punch load – punch travel), thickness strain distribution, the maximum amount of thinning and the maximum deep drawing force and the total consumed work were investigated by [62].

Concerning the issue of the springback compensation in the stamping automotive industry, the benchmark #02 presented at Numisheet 2008 aimed the investigation of the predictability of the springback for the S-rail geometry, where the stress state is influenced by drawbeads. In this study, the validation of the accuracy of drawbead modelling was based in stamping tools geometries with and without drawbeads. Two types of drawbeads geometry (smooth and locking) and two types of material (aluminum alloy and steel) were tested. In the Numisheet 2008 Conference, 12 participants contributed to the benchmark #02. While several FE codes, FE formulations and different process approaches were used in this benchmark, it was found significant discrepancies between the experimental and predicted forming forces, for the deep drawing process of the steel S-Rail with drawbeads. The numerical forming forces predicted by the FE codes were far below than expected level. This issue is particularly relevant since the main objective of this study was the accurate drawbeads modelling. In addition, the reliability in the springback outcomes were also affected. Until the date, no study was performed to understand the root cause of this difference. In this paper, the authors present a sensitivity study of the numerical results based on the variation of different parameters in the simulation. The impact of the variation of process and numerical parameters in the forming forces, draw-in and springback results were evaluated and discussed. This investigation highlights the importance of the parameters variability studies in the sheet forming simulation to minimize the difference between experimental and numerical results, to design more robust and optimized processes and to introduce successfully new advanced materials in automotive parts.

## **BENCHMARK DEFINITION: NUMISHEET2008 BM02**

In the original benchmark definition, the influence of two different drawbead geometries (smooth bead or locking bead) on the springback behavior for steel and aluminum were examined. For this purpose, the well-known S-Rail geometry is used [Fig. 3.1]. The S-Rail tool contains two different blank-holders. One can be equipped with different drawbeads [Fig. 3.2]; the other one offers a complete plane surface. Depending on which drawbead geometry is applied an adequate die can be adopted.



Fig. 3.1 – S-Rail topology after the drawing operation (intermediate state) for the case of smooth beads [63].



Fig. 3.2 - Numisheet 2008 BM 02 Stamping Tools: Blankholder, Drawbeads and Die [63].

As mentioned in the previous section, the focus will be the difference between the experimental and numerical forming forces noted to the steel drawn part, when drawbeads are used. Therefore, just two geometries of tools (without drawbeads and with smooth drawbeads), for steel material, were considered in this study as shown in Fig. 3.3.

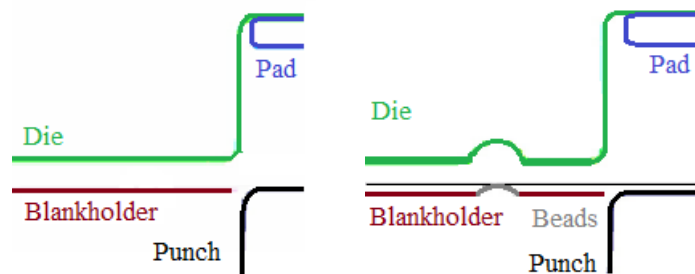


Fig. 3.3 - Section cuts of tools in initial position: a) without beads and b) with smooth beads (bead height = 3.6 mm) [63].

The resultant load cases, presented in Tab. 3.1, are enough to achieve intended purpose.

Tab. 3.1 – Description of the Numisheet 2008 BM 02 load cases considered in this study.

Material / Load Case ID	Drawbead	Blankholder Force
HC260LAD LC1	Without beads	400 kN
HC260LAD LC3	Smooth beads	400 kN

Regarding the process steps, a standard approach was followed: closing, drawing, trimming and springback. The stamping tools and blank geometries were provided to Numisheet participants in IGES format. For the cases with drawbeads, its physical profile was directly included in the 3D CAD geometries of both die and blank-holder. In addition, Daimler has also provided all the experimental data tests strictly necessary to build the HC260LAD mechanical model. Based on this data, Tab. 3.2 presents the standard mechanical model assumptions used in the numerical simulation of the deep-drawing process of the S-Rail with Autoform R5.2.

Tab. 3.2 – Description of the standard mechanical model assumptions (Drawbead Geometry, Friction Coefficient, Yield Criteria, Hardening Law, Flow Stress Model,) used in deep-drawing process simulation.

<b>STANDARD MECHANICAL MODEL</b>				
Process Parameters		Numerical Parameters		
Drawbead	Friction Coefficient	Yield Criterion	Hardening Law	Stress-Strain
Original CAD	0.04	HILL48	Isotropic Hardening	Gosh

As shown in Tab. 3.2, the main process parameters of the standard mechanical model used were based in the 3D CAD of the stamping tools geometries, which include the original geometry of the drawbeads (HC260LAD LC3) or not (HC260LAD LC1), and a constant friction coefficient of 0.04 at the interface blank/tools. The main numerical parameters were based in the classical Hill's quadratic anisotropic yield criterion (1948), which defines a yield surface that increases isotropically according to a non-saturated Gosh law.

### **Parameters Variation:**

As mentioned before, in order to find evidences about the root cause of the discrepancies observed between the experimental and numerical forming forces, a variability study of the simulation parameters was made. Furthermore, the sensitivity of the numerical springback to these changes is also analysed.

Regarding the process parameters, it was studied, separately, the influence of the drawbeads geometry and the friction conditions. Drawbeads are used for a long time in sheet metal forming processes to control the material flow under the blankholder. A drawbead consists of a convex rigid tool which soars above the blank sheet level, acting as an important restriction to its movement. So, it is necessary to include the concave geometry of the drawbead in the opposite tool

to ensure a perfect matching during the closing operation. Depending on the process characteristics and the blank thickness, the channel, in which the drawbead fits, is machined considering a certain clearance and tolerance values. Modifications to the position, length and strength of drawbeads are made during the process design phase to produce an optimal stamped part with minimum material usage. In industrial practice, drawbeads may also be manually modified during the tryout phase in order to obtain the desired process. Therefore, it is not unusual for the shape and dimensions of these optimized channels, and hence the clearance, to be different from the geometry specified during the design of the tool. To test the influence of this parameter on the simulation results, and especially on the forming forces, the tools CAD file was modified not to present any clearance in the drawbead channel, as presented in the Fig. 3.4, and compared with the original.

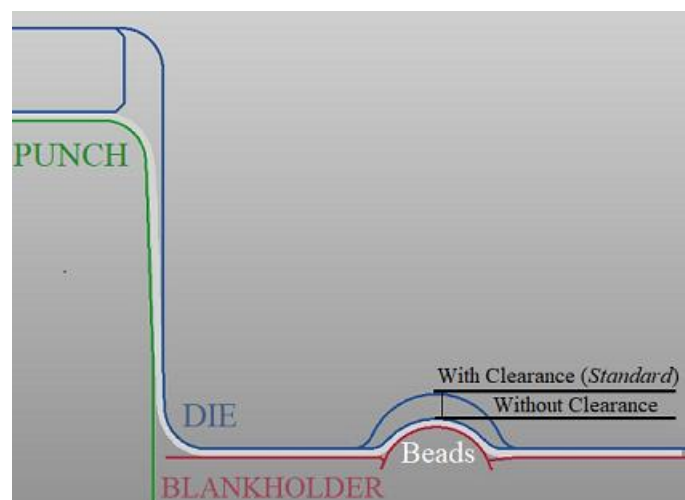


Fig. 3.4 - Section cuts of tools in initial position: drawbead channel with clearance (Original CAD); drawbead channel without clearance (Modified CAD) [63].

Since the most common approaches in the automotive stamping simulation present constant values of friction coefficient and the results are satisfactory from an industrial point of view, this same assumption was adopted in this study. Thus, a set of four mechanical models was prepared to evaluate the influence of the *friction conditions*. The first corresponds to the standard friction coefficient of 0.04 to all the tools surfaces. In the second, the friction coefficient was increased to 0.06. The third presents a friction coefficient of 0.08. In the last one, the friction coefficient of the punch surface was increased to 0.08 and the other tools surfaces kept the standard value of 0.04. To achieve more accurate results, the authors decided to use the an advanced BBC2005 yield criterion to all the mechanical models.

Regarding the numerical parameters, a set of three mechanical models were built to study the influence of *material model* (yield criteria + hardening law). The first mechanical model corresponds to the standard definition. The second mechanical model corresponds to the substitution of the



classical Hill48 yield criterion by the advanced *Banabic-Balan-Comsa* (BBC) 2005 yield criterion. In fact, the Hill 48 anisotropic yield criterion has been the most used in the automotive stamping simulation due to the small number of constitutive parameters and mechanical tests required, simple mathematical definition and ease numerical implementation. However, more advanced and flexible yield criteria, as BBC2005, have been developed and implemented in commercial stamping simulation softwares to deliver more accurate and reliable predictions. Here, an interesting comparison of these two yield criteria is presented. The last mechanical model, corresponds to the substitution of the isotropic hardening model by a combined isotropic-kinematic hardening model. This is also a very important comparison, since that all the 12 participants of the Benchmark #02, at the Numisheet 2008, used isotropic hardening models which cannot predict the bauschinger effect during the elastic springback phase. The modifications performed to the standard mechanical model related with the yield criterion and hardening model definition are presented in Fig. 3.5.

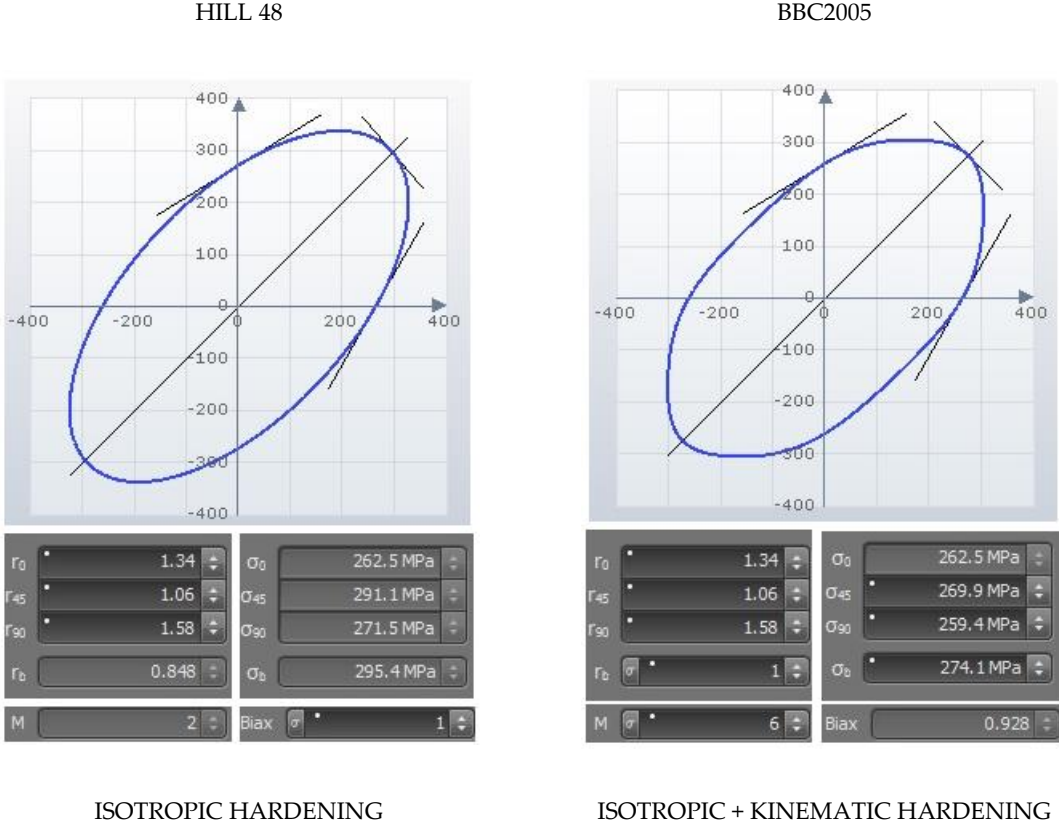




Fig. 3.5 – Mechanical and constitutive parameters of the yield criteria and hardening models used in the variability study [63].

All the alternative mechanical models built in this variability study of simulation parameters are presented in the Tab. 3.3.

Tab. 3.3 – Description of the standard mechanical model assumptions (Yield Criteria, Hardening Law, Flow Stress Model, Friction Coefficient) used in deep-drawing process simulation.

ALTERNATIVE MECHANICAL MODELS				
Process Parameters		Numerical Parameters		
With Drawbead	Friction Coefficient	Yield Criterion	Hardening Law	Stress-Strain
Original CAD	0.04	Hill48	Isotropic Hardening	Gosh
Modified CAD	0.04	Hill48	Isotropic Hardening	Gosh
Original CAD	0.04	BBC2005	Isotropic Hardening	Gosh
Original CAD	0.06	BBC2005	Isotropic Hardening	Gosh
Original CAD	0.08	BBC2005	Isotropic Hardening	Gosh
Original CAD	0.08 (only punch)	BBC2005	Isotropic Hardening	Gosh
Original CAD	0.04	BBC2005	Isotropic Hardening	Gosh
Original CAD	0.04	Hill48	Isotropic Hardening	Gosh
Original CAD	0.04	Hill48	Kinematic Hardening	Gosh

As shown in Tab. 3.3, this study includes two sets of alternative mechanical models for the process parameters and one set of numerical parameters. It must be noted that just one set of mechanical models is dedicated to the comparison of drawbead geometries (HC260LAD LC3), all the other sets of mechanical models will be applied to both cases, with and without drawbeads (HC260LAD LC1 and HC260LAD LC3). This means that it is necessary to run 10 simulations to consider all the alternative mechanical models of the process parameters and 6 simulations in the case of the numerical parameters. A total of 16 simulations for each variable studied in this benchmark. Therefore, a limited number of 3 variables were evaluated, i.e, the forming forces, the draw-in (closed tools) and the geometry after springback. Tab. 3.4 presents some important assumptions of the numerical model in Autoform R5.2.

Tab. 3.4 – Description of the numerical model’s assumptions (FE Formulation, FE Type, FE Integration, Mesh Refinement) of Autoform R5.2.

NUMERICAL MODEL				
FE Code	FE Formulation	FE Type	FE Integration	Mesh Refinement
AutoForm R5.2	Static-Implicit	2D Triangular Shell Elements	Fully-Integrated with 11 Gauss Pts	Adaptive

Concerning the space-time FE formulation, AutoForm is *Static-Implicit*. In stamping simulations, AutoForm uses 2D shell elements with adaptive mesh refinement algorithms and 11 integration points were defined for the triangular elements during the setup.

## RESULTS: COMPARISON AND DISCUSSION

As mentioned above, after running the 16 simulations, the numerical results and experimental results are compared in terms of:

- Forming forces
- Draw-in (closed tools)
- Geometry after springback

The objective of this comparison consists in evaluating the accuracy of each FE code in providing realistic restraining forces and reliable springback values.

### Forming Forces:

The forming forces were recorded throughout the deep-drawing operation, for all the simulations performed. These have been plotted together with the experimentally obtained Punch Force vs. Punch Displacement curves and Fig. 3.6 and Fig. 3.7 have been plotted.

Fig. 3.6 presents the evolution of the experimental and numerical forming forces which belongs to the set of simulations related with the variability of the material model (yield criterion + hardening law) in both cases, with or without drawbeads.

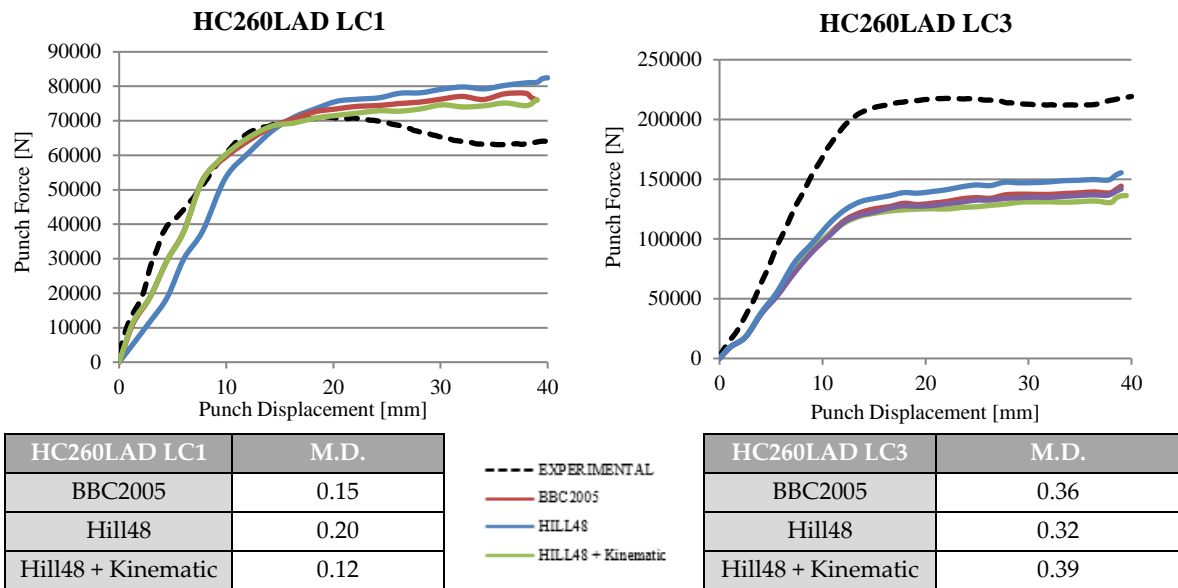


Fig. 3.6 – Comparison of experimental and numerical forming forces during the drawing operation, with the respective mean deviations, to the set of simulations related with the variability of the material model.

As it can be seen from the Fig. 3.6, the evolution of the numerical forming forces curves are very similar in both cases with and without drawbeads. Comparing with the experimental data, the predicted forming forces to the case HC260LAD LC1 tend to be overestimated within a range of 12% to 20%. In the other hand, the predicted forming forces to the case HC260LAD LC3 tend to be underestimated into a range between 32% and 39%. From the Fig. 3.6, it is possible to observe the existence of a drop effect in the punch force curve at the final of the stroke, which is much more pronounced to the case HC260LAD LC1. This effect is intrinsically connected to the blank material and the material flow during the forming operation. In the case HC260LAD LC1, all the restraining force supported by the punch results from the friction generated between blank and tools, whereas in the case HC260LAD LC3, is almost totally dependent of the plastic deformation when the blank flows through the drawbeads. During the forming process, as the contact area decreases the contact pressure increases. As a consequence, depending on the material, the friction coefficient may also decrease. If the drop effect was not present, the predicted forming forces, in the case HC260LAD LC1, would not be so overestimated. In both cases with and without drawbeads the numerical results do not differ significantly. The maximum deviation between the numerical forming forces is around 8%. The Hill48 punch force curve tends to reach the higher values in both cases. However, when the kinematic hardening law is considered in the numerical model, the Hill48 punch force curve drops 8% presenting then the lowest values. This was expected since the kinematic hardening predicts

lower reverse yield stress than isotropic hardening. Therefore, the combined isotropic-kinematic rule contributed to a slight improvement of the forming forces predictions in the cases without beads (HC260LAD LC1), but, worst forming forces prediction in the cases with drawbeads (HC260LAD LC3).

Fig. 3.7 shows the evolution of the experimental and numerical forming forces which belongs to the set of simulations related with the variability of the friction conditions in both cases, with or without drawbeads.

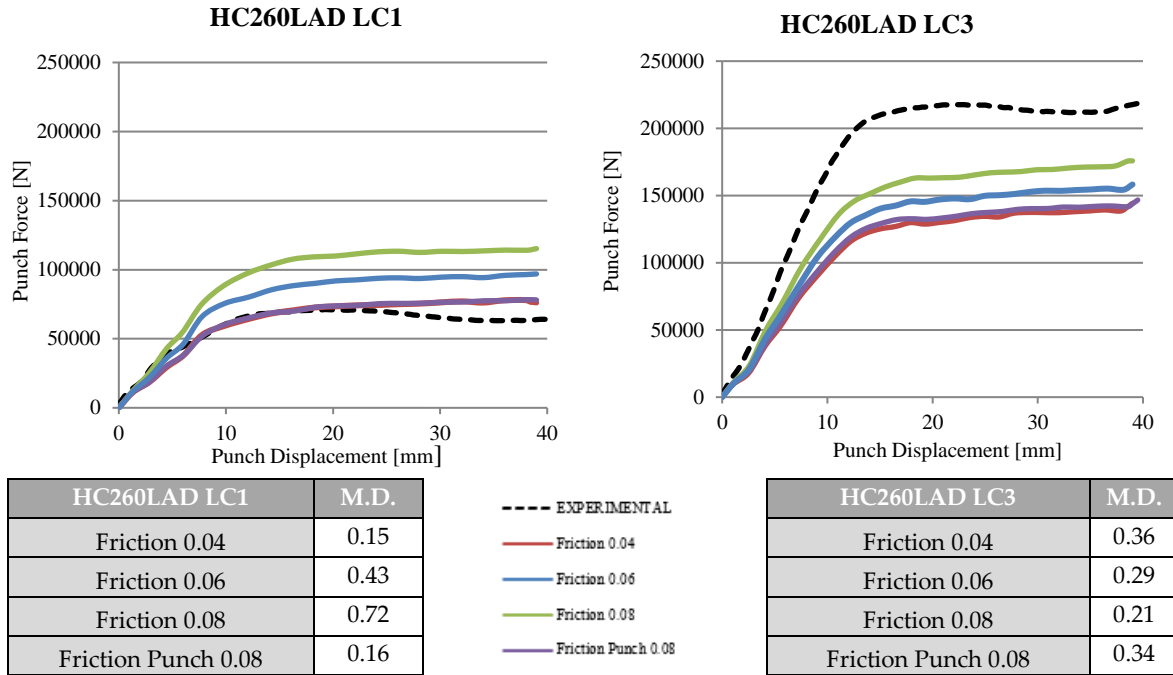


Fig. 3.7– Comparison of experimental and numerical forming forces during the drawing operation, with the respective mean deviations, to the set of simulations related with the variability of the friction conditions.

Looking at Fig. 3.7, it is clear that the numerical forming forces curves are very dependent on the friction conditions. In these cases, the predicted forming forces are also overestimated, varying within a range of 15% to 72%. In the presence of drawbeads, the numerical forming forces are underestimated and vary in a range of 21% to 36%. Since the forming forces are closely related with the restraining flow conditions, the increase of punch friction will not produce noticeable changes. On the other hand, when the friction conditions of the other tools (die and blankholder) are considered, the numerical punch force curves are strongly affected. As presented, when the lubrication coefficient was changed from 0.04 to 0.06, the forming forces increase 28% in the case HC260LAD LC1 and 7% in the case HC260LAD LC3. Additionally, the lubrication coefficient was also changed to 0.08 increasing the forming forces in 57% to HC260LAD LC1 and 15% to HC260LAD LC3. Thus, although the HC260LAD LC3 results seem to indicate that increased friction leads to

better forming forces predictions, when drawbeads are removed, the predicted forming forces reach values unrealistically overestimated.

The evolution of the experimental and numerical forming forces which belongs to the set of simulations related with the variability of the drawbead clearance is represented in Fig. 3.8.

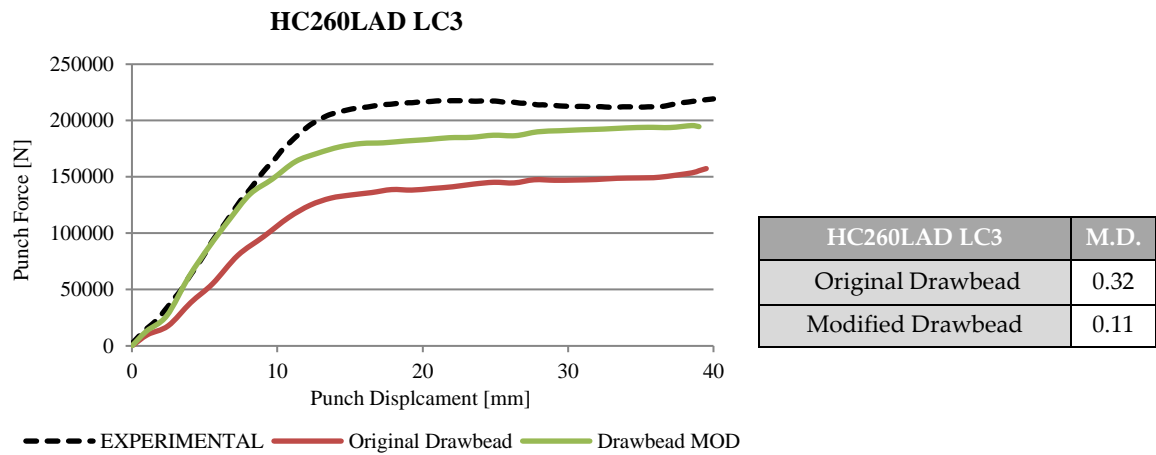


Fig. 3.8 – Comparison of experimental and numerical forming forces during the drawing operation, with the respective mean deviations, to the set of simulations related with the variability of the drawbead geometry.

As depicted in Fig. 3.8, even if the original assumptions like the classical yield criterion of Hill48 and the standard lubrication coefficient of 0.04 are kept, a simple modification in the drawbead channel geometry affects greatly the forming forces prediction. In this case, the mean deviation between the numerical forming forces and the experimental forming forces is around 11%, which represents an improvement of 20% when compared with the original geometry of the drawbead channel.

With the regard to the forming forces analysis, the Fig. 3.9 presents the maximum deviation between the numerical results obtained to each parameter (set of simulations), with and without drawbeads.

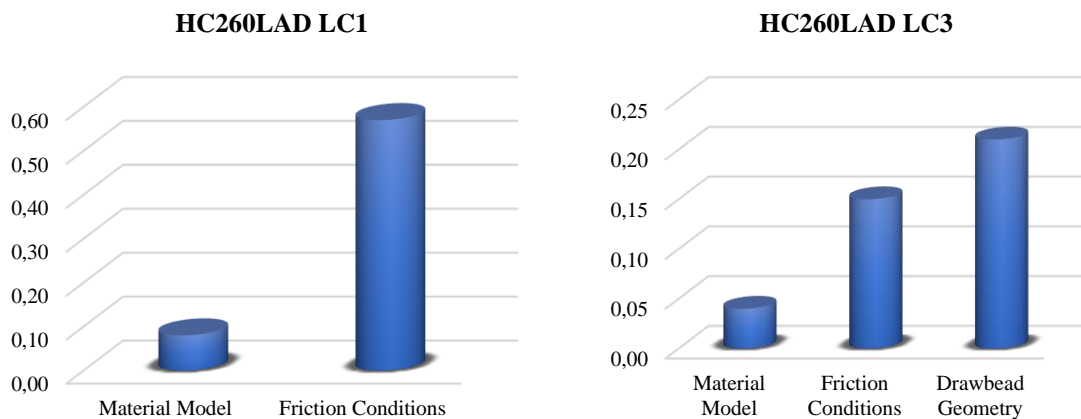


Fig. 3.9 – Comparison of the maximum deviation between the numerical results obtained to each parameter (set of simulations), with and without drawbeads.

As it can be seen from the charts in Fig. 3.9, the numerical forming forces response is very sensitive to changes on the *Friction Conditions* of the stamping tools, that restrain the material flow (Die/Blankholder), mainly in the cases without drawbeads. In the presence of drawbeads, the influence of the *Friction Conditions* in the numerical forces is still considerable but much lower. As represented in the HC260LAD LC3 chart, the most influent parameter is the *Drawbead Geometry*. In addition, it can be observed to both cases HC260LAD LC1 and HC260LAD LC3 that the numerical forming forces present low sensitivity to *Material Model* changes.

**Draw-in:**

According to the benchmark definition, y-displacements were provided to 5 sections across the blank at the end of the forming process, as depicted in the Fig. 3.10.

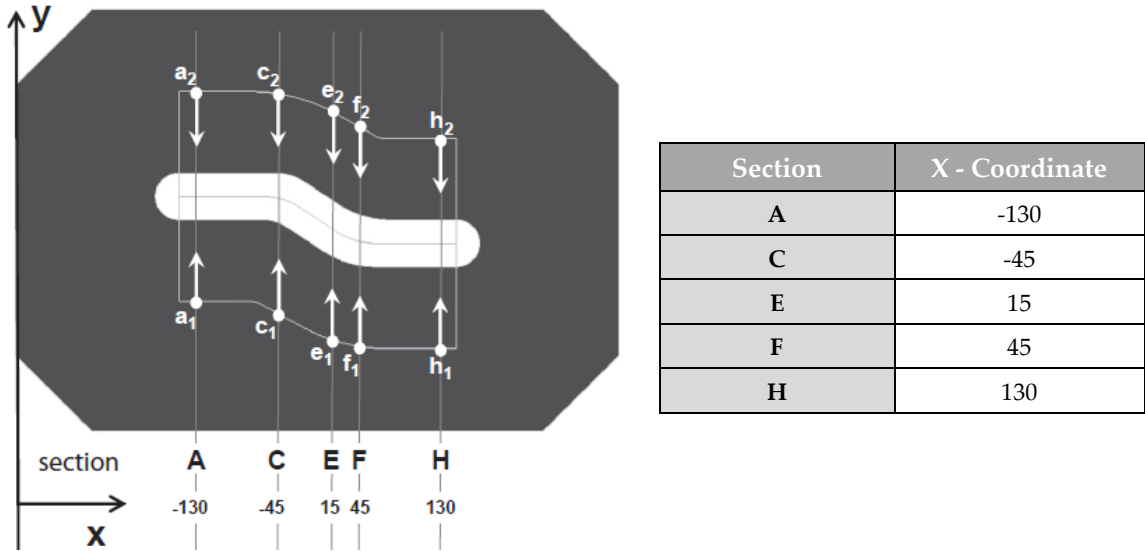


Fig. 3.10 – Position and naming of the draw-in sections with the respect to the S-rail geometry. [63]

Fig. 3.11, Fig. 3.12 and Fig. 3.14 to Fig. 3.16 represent the comparison between the virtual draw-in and experimental draw-in. Draw-in levels have been plotted for each set of simulations (Material Model, Friction Condition, Drawbead Geometry) and each drawbead model (HC260LAD LC1 / HC260LAD LC3). Each plot contains draw-in levels as a bar chart for each FE code and the average value of the experimental section displacements. In addition, the correspondent numerical deviations are also presented.

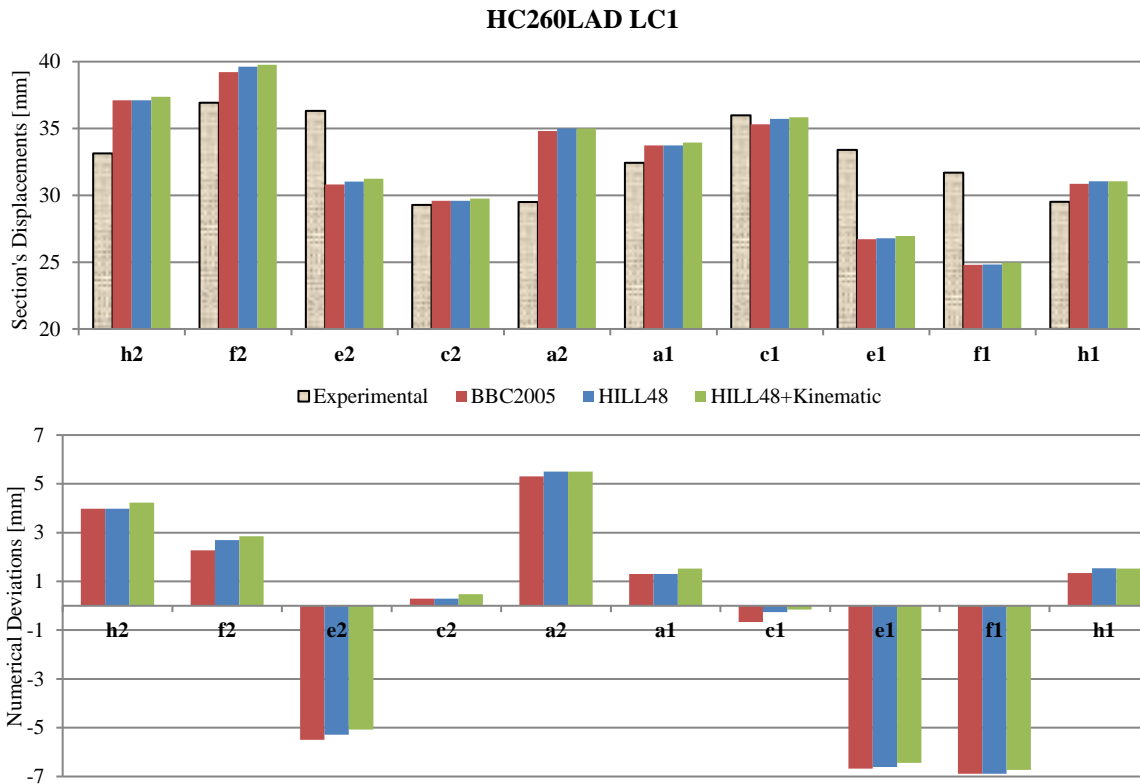


Fig. 3.11 – Comparison of experimental and numerical section's displacements during the drawing operation, with the respective mean deviations, to the set of simulations related with the variability of the material model, when no drawbeads are present.

Considering the HC260LAD LC1 section's displacements predicted by different *Material Models*, the Fig. 3.11 shows that the numerical deviations from the experimental results are very similar and do not reach the 7mm. As observed, the experimental draw-in variation range is mainly located between [30,35] mm.

The comparison of the numerical draw-in under different *Friction Conditions* for the case HC260LAD LC1 is presented below [Fig. 3.12]



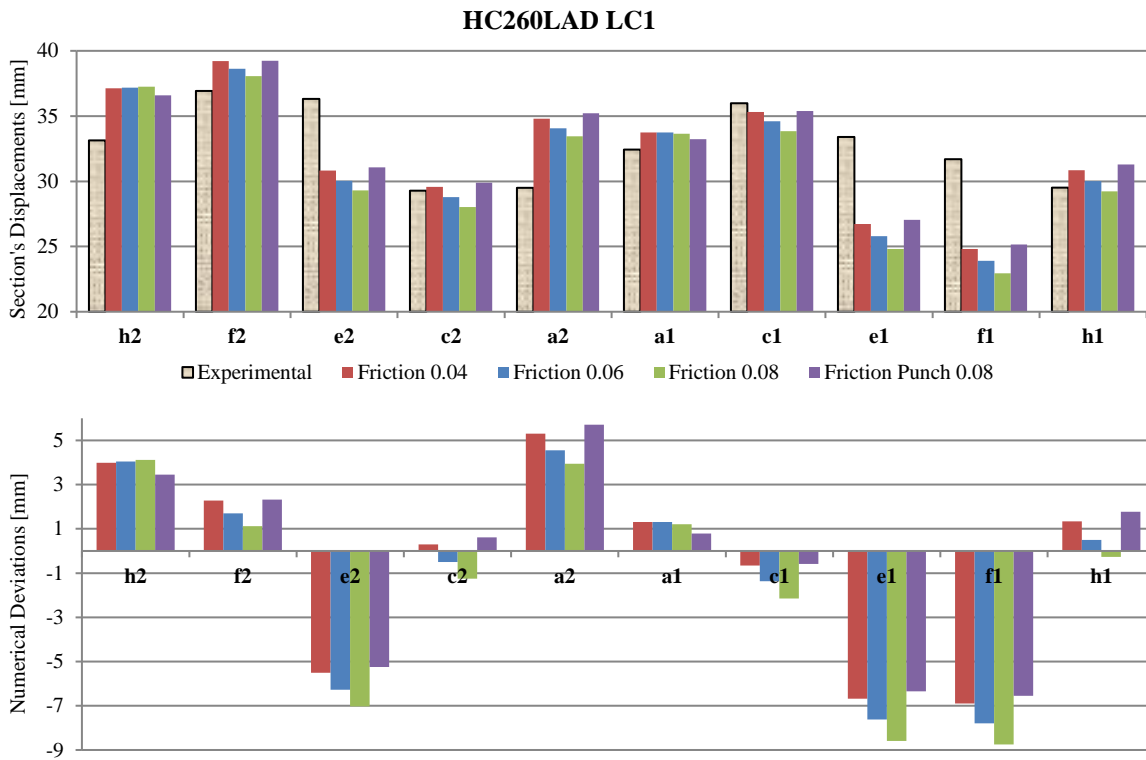


Fig. 3.12 – Comparison of experimental and numerical section’s displacements during the drawing operation, with the respective mean deviations, to the set of simulations related with the variability of the friction conditions, when no drawbeads are present.

As observed in Fig. 3.12, the HC260LAD LC1 section’s displacements predicted by different *Friction Conditions* shows slight differences in the numerical deviations. Despite increasing friction in punch only do not affect the numerical draw-in, doubling the overall lubrication coefficient (0.04 to 0.08) leads to differences around 2mm. The maximum numerical deviations from the experimental results do not exceed 9mm.

Tab. 3.5 presents a comparison of the maximum deviations between the numerical draw-in, in each section, for all the simulation parameters tested in the case HC260LAD LC1.

Tab. 3.5 – Comparison of the maximum deviations [mm] between the numerical draw-in, in each section, for the simulation parameters of the case HC260LAD LC1.

HC260LAD LC1	Maximum difference between the numerical results in each section.									
PARAMETERS	$h_2$	$f_2$	$e_2$	$c_2$	$a_2$	$a_1$	$c_1$	$e_1$	$f_1$	$h_1$
Material Model	0.28	0.57	0.42	0.18	0.19	0.23	0.51	0.23	0.16	0.22
Friction Conditions	<b>0.66</b>	<b>1.19</b>	<b>1.77</b>	<b>1.87</b>	<b>1.76</b>	<b>0.51</b>	<b>1.56</b>	<b>2.24</b>	<b>2.20</b>	<b>2.05</b>

As expected, the range of maximum deviations is higher to the parameter *Friction Conditions*. The graph below [Fig. 3.13] compares the mean values of the maximum deviations of all sections, for the simulation parameters of the case HC260LAD LC1.

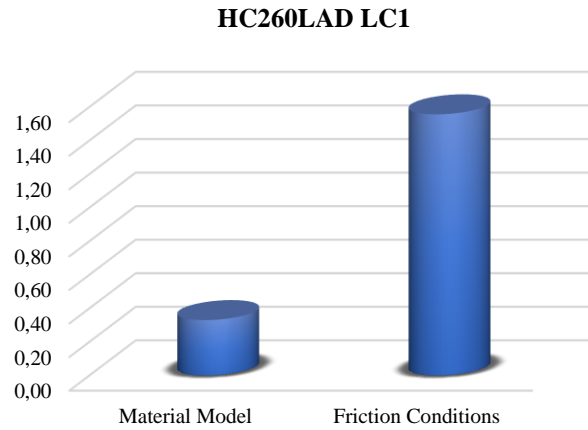


Fig. 3.13 – Comparison of the mean values of the maximum deviations [mm] of all sections, for the simulation parameters of the case without drawbeads.

Fig. 3.13 shows that the mean value of the friction parameter is 5.2 times higher than the mean value of the *Material Model* parameter. So, it is clear that, in the absence of drawbeads, the *Friction Conditions* play the paramount role in the predicted draw-in.

In the presence of drawbeads, the numerical draw-in predicted by different *Material Models*, to each section, is shown in the Fig. 3.14.

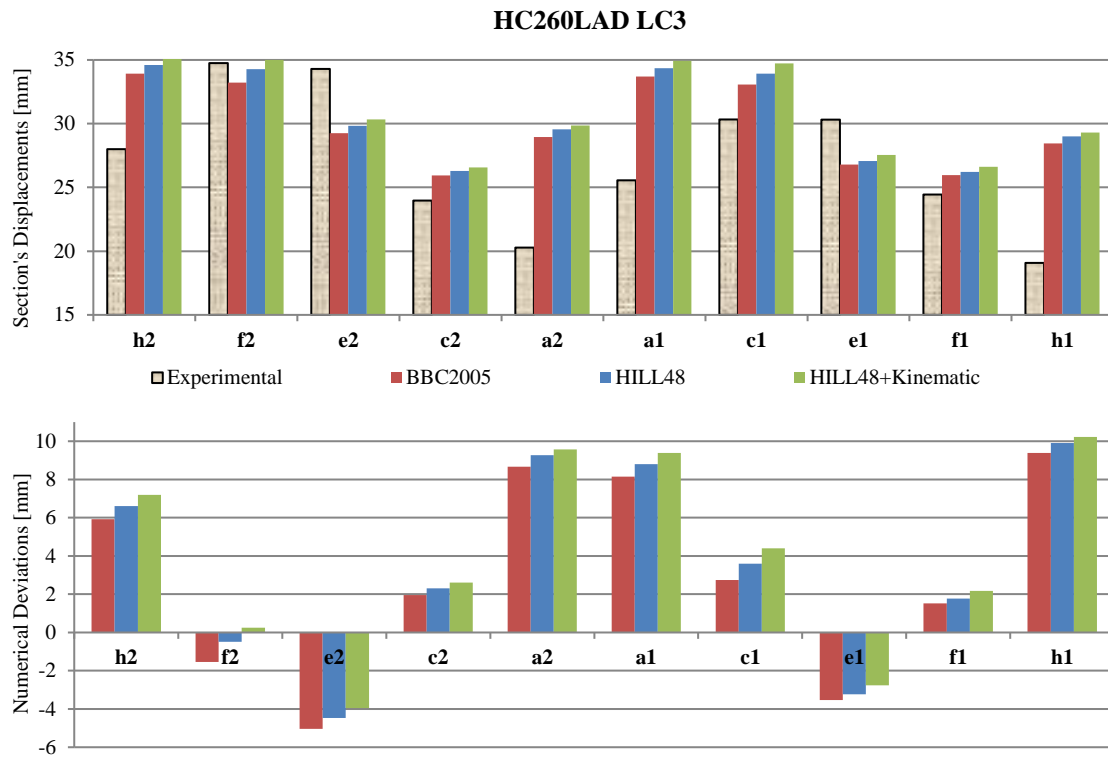


Fig. 3.14 – Comparison of experimental and numerical section’s displacements during the drawing operation, with the respective mean deviations, to the set of simulations related with the variability of the material model, when drawbeads are present.

Regarding the HC260LAD LC3 section’s displacements predicted by different *Material Models*, the Fig. 3.14 shows that the maximum numerical deviations from the experimental results are around 10mm. Since the restraining forces increases with the presence of drawbeads the experimental draw-in tends to decrease leading to a range of variation of [20,35] mm. In these case, the maximum deviations of the numerical draw-in remains under 2mm.

The Fig. 3.15 presents the comparison of the numerical draw-in under different *Friction Conditions* for the case HC260LAD LC3.

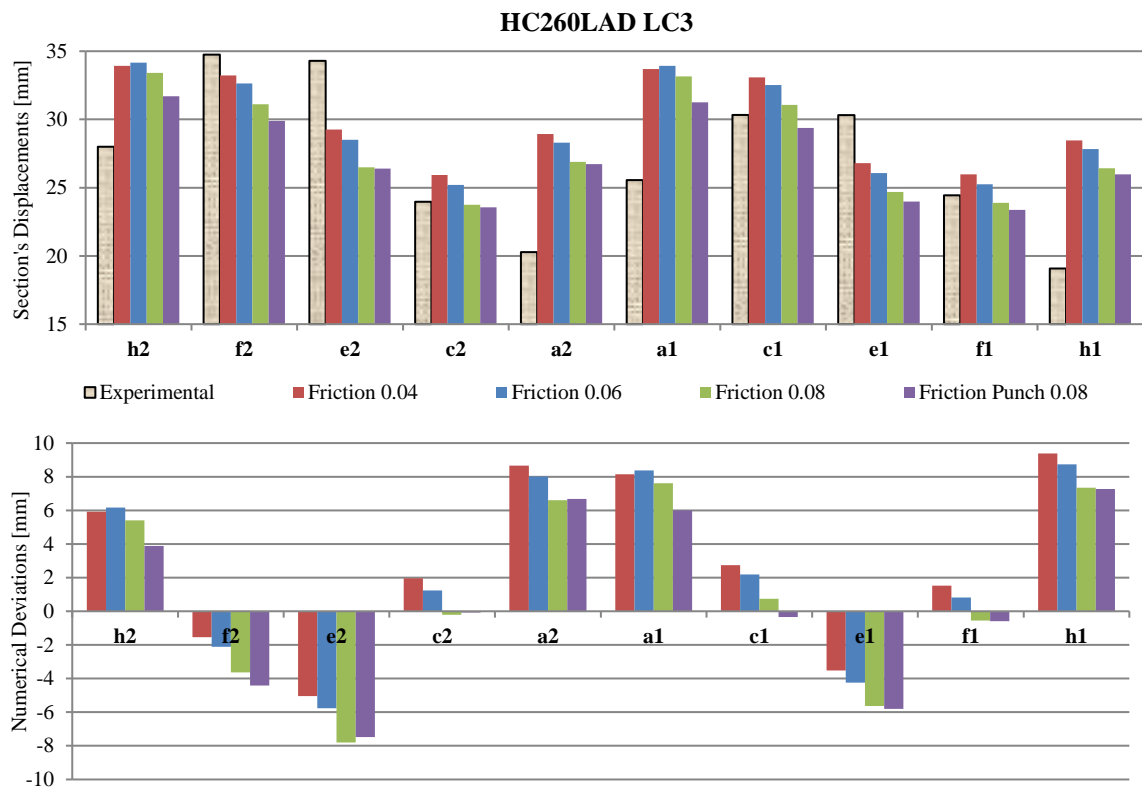


Fig. 3.15 – Comparison of experimental and numerical section’s displacements during the drawing operation, with the respective mean deviations, to the set of simulations related with the variability of the friction conditions, when drawbeads are present.

As it can be seen [Fig. 3.15], the HC260LAD LC3 section’s displacements predicted by different *Friction Conditions* are not the same. In the presence of drawbeads, the maximum deviations between the numerical results are around 3mm. As expected, the closest outcomes belong to the standard friction model and the model in which the punch lubrication coefficient was double. The maximum numerical deviations from the experimental results do not exceed 9mm.

Finally, the Fig. 3.16 presents the comparison of the numerical draw-in with the original drawbead channel and the modified drawbead channel.

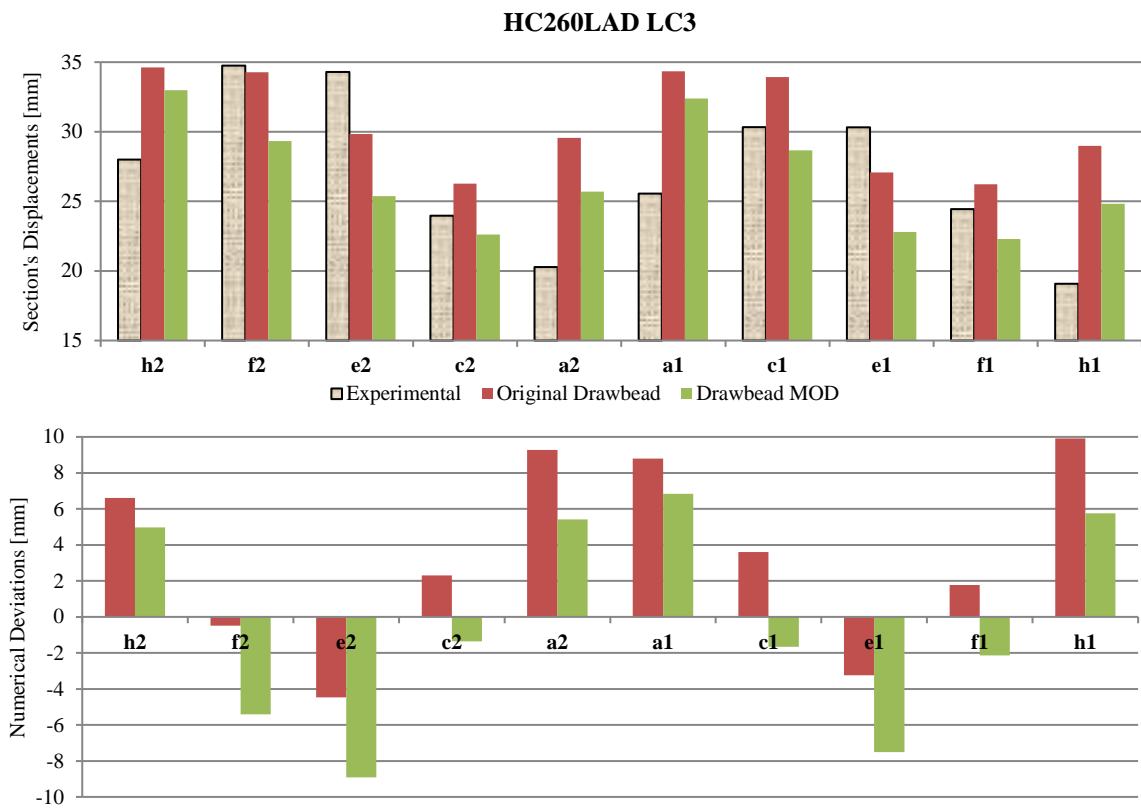


Fig. 3.16 – Comparison of experimental and numerical section's displacements during the drawing operation, with the respective mean deviations, to the set of simulations related with the variability of the drawbead clearance.

Since the modification of the drawbead channel geometry increases the restraining forces it contributes to higher forming forces and lower draw-in values. Looking at Fig. 3.16, it can be observed that the maximum numerical deviations from the experimental results are around 9mm. Furthermore, it is possible to see that the maximum deviations between the model with the original and the modified geometry is around 5mm.

For a full overview, the Tab. 3.6 presents a comparison of the maximum deviations between the numerical draw-in, in each section, for all the parameters tested in the case HC260LAD LC3.

Tab. 3.6 – Comparison of the maximum deviations [mm] between the numerical draw-in, in each section, for the simulation parameters of the case HC260LAD LC3.

HC260LAD LC3	Maximum difference between the numerical results in each section.									
PARAMETERS	$h_2$	$f_2$	$e_2$	$c_2$	$a_2$	$a_1$	$c_1$	$e_1$	$f_1$	$h_1$
Material Model	1.28	1.79	1.08	0.70	0.91	1.24	1.65	0.76	0.67	0.85
Friction Conditions	<b>2.28</b>	2.87	2.77	2.17	2.05	<b>2.37</b>	3.09	2.28	2.11	2.11
Drawbead Geometry	1.63	<b>4.93</b>	<b>4.45</b>	<b>3.67</b>	<b>3.85</b>	1.96	<b>5.26</b>	<b>4.28</b>	<b>3.92</b>	<b>4.16</b>

In the cases with drawbeads, the parameter *Drawbead Geometry* presents often the higher values of maximum deviations, which means that it has the major influence on the numerical draw-in robustness. The graph below [Fig. 3.17] compares the mean values of the maximum deviations of all sections for the studied parameters.

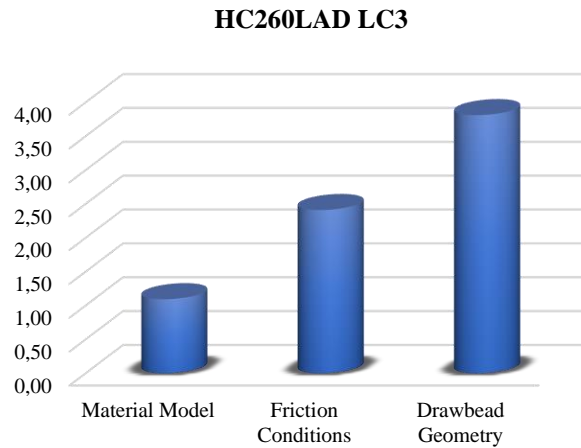


Fig. 3.17 – Comparison of the mean values of the maximum deviations [mm] of all sections, for the simulation parameters of the case with drawbeads.

The Fig. 3.17 shows that the mean value of the *Drawbead Geometry* parameter is around 3.5 times higher than the mean value of the *Material Model* parameter while the mean value of the *Friction Conditions* parameter is around 2.2 times higher than the mean value of the *Material Model* parameter. Thus, it is clear that the variable draw-in is more sensitive to the process parameters than numerical parameters, i.e., a small change in the process parameters (*Friction conditions* or *Drawbead Geometry*) has more influence than a small change in the numerical parameters (*Material Model*).

### Springback:

To evaluate the springback topology all parts were covered with point grids and measured with an optical system. For fixing the part within the measurement device 3 material points were used. These 3 points also correspond to the exact support points where simulations meshes were constrained to allows the springback comparison. All the meshes were compared after trimming and springback. This comparison was based on the section's cut profile  $X = -90$ . Thus, each profile was compared with the reference part profile measuring the respective deviation angles  $\theta_1$ ,  $\theta_2$ ,  $\alpha_1$  and  $\alpha_2$ , in degrees. The global coordinates of the springback points constraint, springback section cut and springback deviation angles are presented in Fig. 3.18.

	Global X	Global Y	Global Z
A	122.0	-13.0	1.000
B	122.0	-37.0	1.000
C	-122.0	25.0	1.000

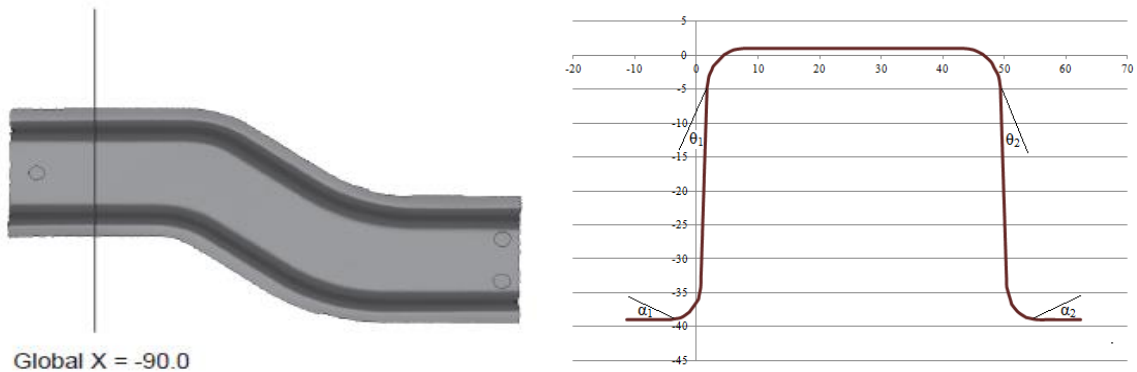
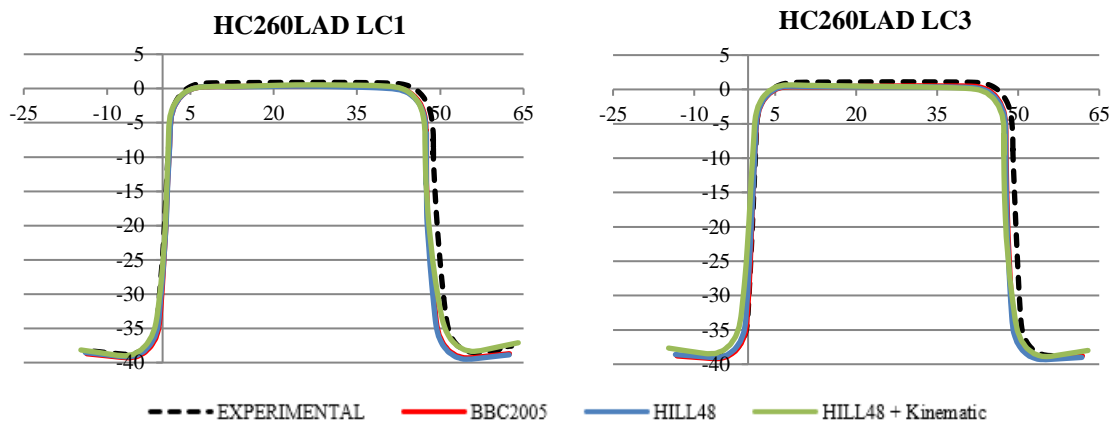


Fig. 3.18 – Presentation of the profile for springback measurements based on the deviation's angles [°] ( $\theta_1$ ,  $\theta_2$ ,  $\alpha_1$ ,  $\alpha_2$ ) of the reference section  $X = -90$  and springback points constraint.

The experimental and numerical results of each material and drawbead model are presented in Fig. 3.19 and Fig. 3.20.

The experimental results show that, overall, the springback effect is not symmetric throughout the specified cross-section since  $\theta_1 < \theta_2$  in both cases with and without drawbeads. Additionally, the springback deviations  $\theta_1$  and  $\theta_2$  are lower than  $\alpha_1$  and  $\alpha_2$  due to the amount and distribution of plastic strain and the level of residual stresses. Nevertheless, the presence of drawbeads has a significant effect on reducing springback deviations.

Fig. 3.19 present the cross-sections after springback predicted by different yield criteria and the experimental cross-section with the respective angular deviations [°] from the part reference.



Yield Criterion	$\theta_1$ [°]	$\alpha_1$ [°]	$\theta_2$ [°]	$\alpha_2$ [°]
BBC2005	2.06	4.39	0.33	4.21
Hill48	2.38	4.68	0.08	4.35
Hill48+Kinematic	3.25	6.36	2.59	8.76
EXPERIMENTAL	2.84	4.47	3.48	4.58

Yield Criterion	$\theta_1$ [°]	$\alpha_1$ [°]	$\theta_2$ [°]	$\alpha_2$ [°]
BBC2005	1.61	2.74	-0.08	2.86
Hill48	2.05	3.66	-0.35	2.81
Hill48+Kinematic	3.94	6.56	0.87	7.06
EXPERIMENTAL	1.42	1.49	2.34	0.78

Fig. 3.19 – Comparison of experimental and numerical S-rail geometries after springback, at the reference section  $X = -90$ , to the set of simulations related with the variability of the material model.

As shown in Fig. 3.19 the springback deviations predicted by the numerical cross-sections are, in general, very close of each other. The only exception is related with the springback predictions of the isotropic-kinematic hardening model which leads to higher angular deviations. Thus, the introduction of a kinematic hardening rule associated to the Hill48 yield criterion can reach better springback predictions when the stamping processes are less-robust and the deviations are higher. In the case HC260LAD LC1, the best springback predictions of the vertical walls  $\theta_1$  and  $\theta_2$  were achieved when the kinematic hardening was considered. However, the springback deviations  $\alpha_1$  and  $\alpha_2$  predicted by this model are largely overestimated. The most accurate springback deviations  $\alpha_1$  and  $\alpha_2$  were delivered by the non-kinematic hardening models BBC2005 and Hill48. In the case HC260LAD LC3, the most reliable springback deviations were delivered by the non-kinematic hardening models. Despite the springback deviations of the anisotropic yield criterion BBC2005 are overall better, the numerical predictions of the isotropic yield criterion Von Mises are also very close to the experimental results.

The next figure [Fig. 3.20] compares the numerical cross-sections predicted after the springback simulation, under different friction conditions, with the experimental cross section.

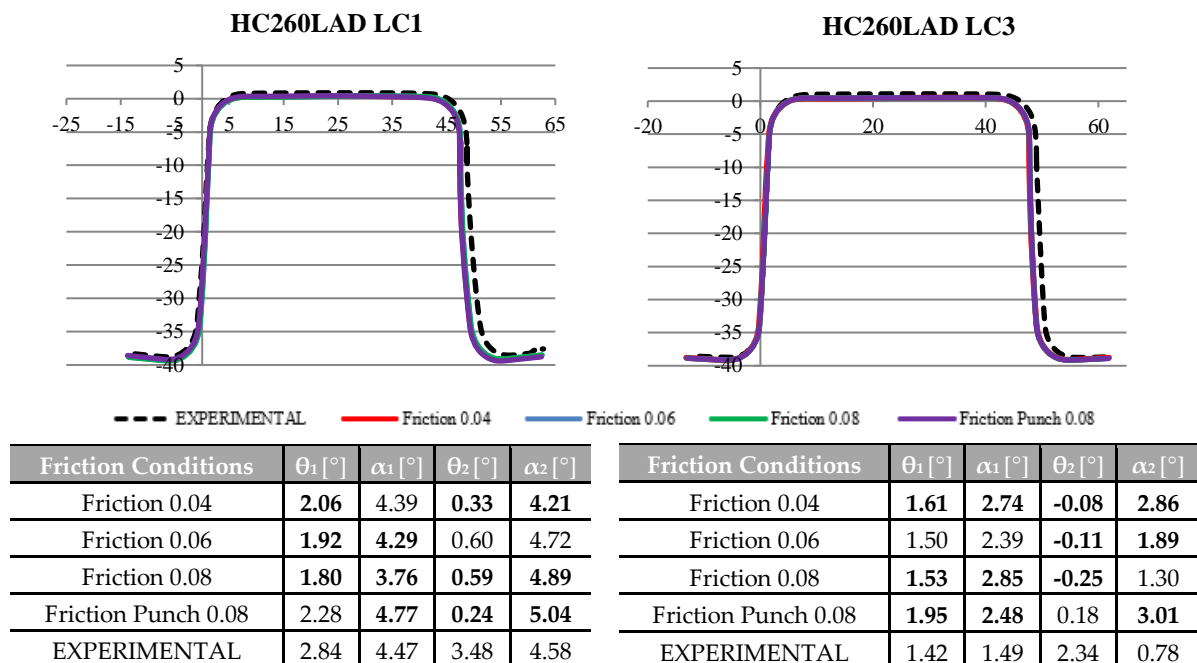
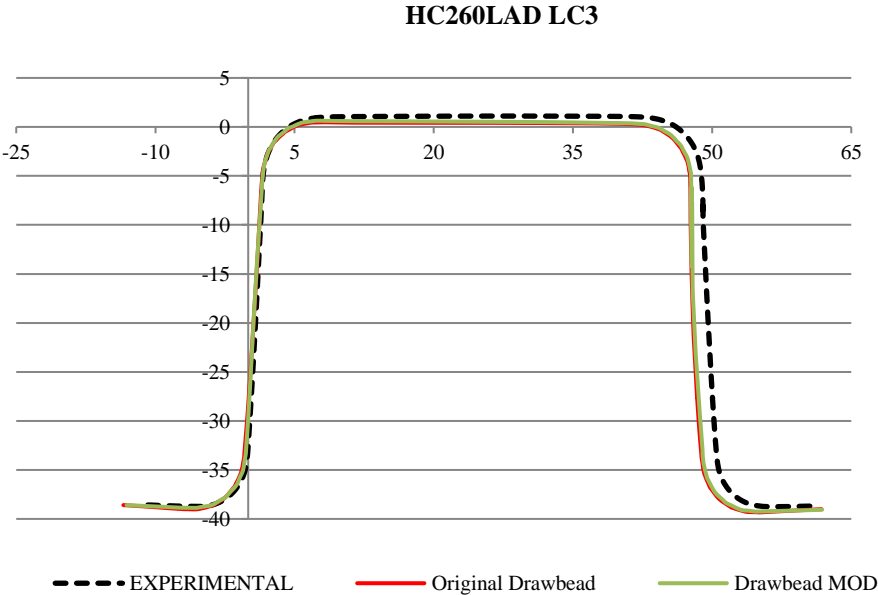


Fig. 3.20 – Comparison of experimental and numerical S-rail geometries after springback, at the reference section  $X = -90$ , to the set of simulations related with the variability of the friction conditions.



Concerning the *Friction Conditions*, it can be seen in Fig. 3.20 that the numerical springback deviations [°] are also affected by this parameter. In the case HC260LAD LC1, increasing the overall lubrication coefficient leads to successively smaller springback deviations at the right side of the cross-section profile [  $\theta_1$ ,  $\alpha_1$  ] and successively higher springback deviations at the left side of the cross-section profile [  $\theta_2$ ,  $\alpha_2$  ]. In the case HC260LAD LC3, the effect of increasing the overall lubrication coefficient is not very significant to the right side of the cross-section profile. However, it is quite clear that  $\theta_2$  increases and  $\alpha_2$  decreases on the left side of the cross-section profile. In addition, it is also possible to see that the augmentation of the lubrication coefficient only in the punch results in higher springback deviations for the both cases HC260LAD LC1 and HC260LAD LC3. Taking into the account the experimental results, the most suitable friction condition for the both cases is achieved when the lubrication coefficient is set at the value 0.06.

In the Fig. 3.21 the springback results with the original drawbead channel and the modified drawbead channel are presented.



Drawbead Geometry	$\theta_1$ [°]	$\alpha_1$ [°]	$\theta_2$ [°]	$\alpha_2$ [°]
Original Drawbead	2.05	3.66	-0.35	2.81
Drawbead MOD.	1.79	2.07	-0.09	1.52
EXPERIMENTAL	1.42	1.49	2.34	0.78

Fig. 3.21 – Comparison of experimental and numerical S-rail geometries after springback, at the reference section  $X = -90$ , to the set of simulations related with the variability of the drawbead clearance.

Comparing the cross-section profiles after springback with the original drawbead channel and the modified drawbead channel, it is evident that the numerical results are greatly affected by the

geometry. As shown in Fig. 3.21, the modification of the drawbead channel geometry in the tool CAD file leads to smaller springback deviations and more reliable results when compared with the experimental results.

From the results mentioned above [Fig. 3.19 to Fig. 3.21], it is possible to determine the maximum deviations between the numerical results obtained to each angle, getting a quick overview of the numerical springback sensitivity to the parameters considered in this study. These results are presented in table Tab. 3.7 to the case HC260LAD LC1 and Tab. 3.8 to the case HC260LAD LC3.

Tab. 3.7 – Comparison of the maximum deviations [°] between the numerical springback, to the reference section, for the simulation parameters of the case HC260LAD LC1.

<b>HC260LAD LC1</b>	Maximum deviation [°] between the numerical results in each section.			
Reference Angle	$\theta_1$	$\alpha_1$	$\theta_2$	$\alpha_2$
Material Model	1.19	2.08	<b>2.51</b>	<b>4.73</b>
Friction Conditions	0.48	1.01	0.57	0.83

As shown in Tab. 3.7, the value of the maximum deviation between numerical results is always higher for Material Model, which indicates that springback is more sensitive to *Material Model* variation than to *Friction Conditions* variation. In the case without drawbeads, it is also clear that the right side of the part is more affected by *Material Model* variation.

Tab. 3.8 – Comparison of the maximum deviations [°] between the numerical springback, to the reference section, for the simulation parameters of the case HC260LAD LC3.

<b>HC260LAD LC3</b>	Maximum deviation [°] between the numerical results in each section.			
Reference Angle	$\theta_1$	$\alpha_1$	$\theta_2$	$\alpha_2$
Material Model	2.33	<b>3.82</b>	1.22	<b>4.25</b>
Friction Conditions	0.45	<b>0.46</b>	0.43	<b>1.71</b>
Drawbead Geometry	0.26	<b>1.59</b>	0.26	<b>1.29</b>

Looking at the Tab. 3.8, the value of the maximum deviation between the numerical results is higher for the *Material Model*, which means that this parameter has a greater impact on the robustness of the predicted springback. Additionally, it can be noted that the angles [ $\alpha_1$ ,  $\alpha_2$ ] are the most sensitive to changes in the parameters under study to both cases, with and without drawbeads. From the results of Tab. 3.7 and Tab. 3.8, a comparison of the average values obtained for each parameter and drawbead model is presented in the Fig. 3.22.

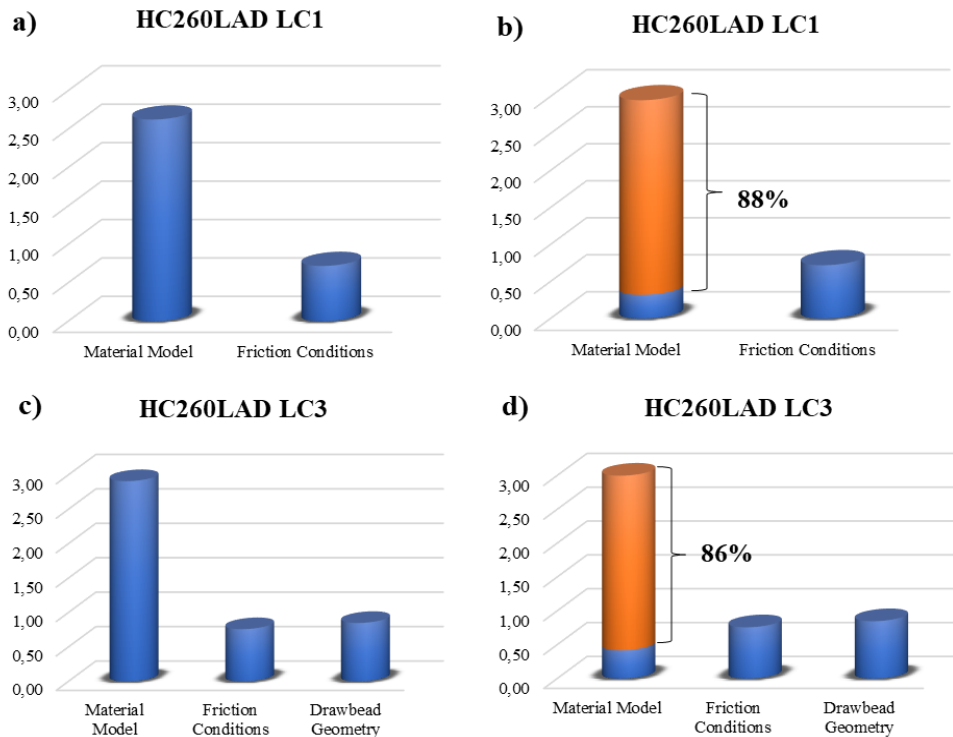


Fig. 3.22 – Comparison of the mean values of the maximum deviations [°], obtained for each simulation parameter, with and without drawbeads.

Fig. 3.22 shows that the mean value of the maximum deviations [°] between the numerical results is greater for the parameter *Material Model*. In case HC260LAD LC1, the *Material Model* mean value is 2.63 and the *Friction Condition* mean value is 0.72. In case HC260LAD LC3, the mean value is 2.91 for the *Yield Criterion* parameter, 0.85 for the *Drawbead Geometry* parameter and 0.76 for the *Friction Condition* parameter. However, it's worth noting that 88% of the *Material Model* mean value, in the case without drawbeads, and 86% of the *Material Model* mean value, in the case with drawbeads, are only dependent on the kinematic hardening rule. Taking the influence of kinematic hardening rule, the *Material Model* mean value decreases to 0.32, in the case without drawbeads, and 0.41, in the case with a drawbeads. Therefore, the definition of the kinematic hardening is undoubtedly the aspect of the numerical model which introduce more variability in the numerical springback. When a simple isotropic-kinematic model is considered, the predicted springback will be more sensitive to the *Friction Condition*, in the case without the drawbeads, and more sensitive to drawbead channel geometry, in the case with drawbeads.

## CONCLUSIONS

In this study, the sensitivity of the numerical results to the variation of process and numerical parameters in sheet metal forming simulation was considered. Taking into account the benchmark # 02 proposed in the Numisheet 2008 congress, the effect of variations of the material model, friction

conditions and drawbeads geometry, on the predicted results of forming and springback simulations were evaluated and analyzed.

**In terms of the predicted forming forces** it has been found that the numerical results tend to be overestimated in the case HC260LAD LC1 and underestimated in the case HC260LAD LC3. The variability study revealed that the process parameters are the most influential. In the case HC260LAD LC1, the most influential parameter was the "Friction Condition", which led to a variation of 57% in the predicted forming forces. In the case HC260LAD LC3, the most influential parameter was the "Drawbead Geometry", responsible for a variation of 21% in the predicted forming forces.

**Regarding the predicted draw-in** the same trend was observed. The variability study also indicated that the process parameters are more influential. In the case HC260LAD LC1, the variation of the predicted draw-in as a function of the variation of the parameter "Friction Condition" is 5.2 times higher than the variation of the predicted draw-in as a function of the variation of the parameter "Material Model". In the case HC260LAD LC3, the most influential parameter is "Drawbead Geometry" which generates a variation of the predicted draw-in almost 3.5 times higher than the "Material Model".

**Finally, the results obtained for the predicted springback** showed a greater dependence on the numerical parameters. In the case HC260LAD LC1, the variation of the parameter "Material Model" produced an average angular deviation 2.7 times higher than the variation of the parameter "Friction Model". In the case HC260LAD LC3, this ratio increased to 2.9 times. However, it is worth noting that 88% of the predicted springback variation generated by the parameter "Material Model", in the case HC260LAD LC1, and 86%, in the HC260LAD LC3 case, is exclusively due to the introduction of a kinematic hardening law in the mechanical model.

Therefore, the most probable root cause for the significant differences between the numerical and experimental forming forces are related to the drawbeads geometry. This is an important conclusion since this benchmark is directly related to the influence of the drawbeads on the control of the springback effect, so common in the sheet forming processes of the automotive industry. Thus, experimental results are often used by developers of stamping simulation FE codes to improve their numerical tools and, in this particular case, the accuracy of the drawbeads models. But, if these experimental results are not fully reliable, then the numerical models calibrated based on these may be not reliable too. Therefore, outcomes of numerical drawbead models based on the experimental data of this benchmark may lead to highly questionable conclusions. In fact, both in industry and academia, it is essential that the development and validation of numerical models rely on consistent and robust experimental tests able to deliver reliable results. Therefore, the priority must be given to the full control of the process parameters involved and their tuning. As shown in this study, the

variables forming forces and draw-in force are more sensitive to process parameters such as tool geometry and lubrication conditions. On the other hand, the FE simulation of springback, is much more sensitive to numerical tolerances and to material model than forming simulations.

## ACKNOWLEDGMENTS

The authors greatly acknowledge the financial support of “Fundação para a Ciência e Tecnologia” (FCT – Portugal), through the research project SFRH/BDE/51189/2010 (“Development FEA Tools Applied to Sheet Forming Special Cases. Application to the Automotive Industry, Advanced Metallic Materials and Multi-Layer and Multi-Material Sheets”) in partnership with Sodécia Product Competence Center (Maia, Portugal). The authors would also like to thank the company AutoForm to the technical support and collaboration in this study.

## COMPLIANCE WITH ETHICAL STANDARDS:

Funding: This study was funded by SFRH/BDE/51189/2010.  
No conflict exists: The authors declare that they have no conflict of interest.

## REFERENCES

1. Papeleux, L., Ponthot, J.-P., 2002. “Finite element simulation of springback in sheet metal forming.” *J. Mater. Process. Technol.* 125, 785–791. Doi: 10.1016/S0924-0136(02)00393-X.
2. Asgari, S., Pereira, M., Rolfe, B., Dingle, M., Hodgson, P., 2008. “Statistical analysis of finite element modeling in sheet metal forming and springback analysis.” *J. Mater. Process. Technol.* 203, 129–136. Doi: 10.1016/j.jmatprotec.2007.09.073.
3. Wagoner, R.H., Li, M., 2007. “Simulation of springback: Through-thickness integration.” *International Journal of Plasticity* 23 (3), 345–360. Doi: 10.1016/j.ijplas.2006.04.005.
4. Burchitz, I.A., Meinders, T., 2008. “Adaptive through-thickness integration for accurate springback prediction.” *International Journal for Numerical Methods in Engineering* 75 (5), 533–554. Doi: 10.1002/nme.2260
5. Oliveira, M., Alves, J., Chaparro, B., Menezes, L., 2007. “Study on the influence of work-hardening modeling in springback prediction.” *Int. J. Plastic.* 23, 516–543. Doi: 10.1016/j.ijplas.2006.07.003.
6. Cleveland, R., Ghosh, A., 2002. “Inelastic effects on springback in metals.” *Int. J. Plastic.* 18, 769–785. Doi: 10.1016/S0749-6419(01)00054-7.
7. Geng, L., Wagoner, R., 2002. “Role of plastic anisotropy and its evolution on springback.” *Int. J. Mech. Sci.* 44, 123–148. Doi: 10.1016/S0020-7403(01)00085-6.
8. Yoshida, F., Uemori, T., 2003. “A model of large-strain cyclic plasticity and its application to springback simulation.” *Int. J. Mech. Sci.* 45, 1687–1702. Doi: 10.1016/j.ijmecsci.2003.10.013.
9. Hill, R., 1948. “A theory of the yielding and plastic flow of anisotropic metals.” *Proc. Roy. Soc. London A*193, 281-297.

10. Hill, R., 1990. "Constitutive modeling of orthotropic plasticity in sheet metals." *J. Mech. Phys. Solids* 38, 405-417. Doi: 10.1016/0022-5096(90)90006-P.
11. Barlat, F., Brem, J. C., Yoon, J. W., Chung, K., Dick, R. E., Lege, D. J., Pourgoghrat, F., Choi, S. H., Chu, E., 2003. "Plane stress yield function for aluminum alloy sheets - part 1: theory." *Int. J. Plast.* 19, 1297-1319. Doi: 10.1016/S0749-6419(02)00019-0.
12. Barlat, F., Aretz, H., Yoon, J. W., Karabin, M. E., Brem, J. C., Dick, E., 2005. "Linear transformation-based anisotropic yield functions." *Int. J. Plast.* 21, 1009-1039. Doi: 10.1016/j.ijplas.2004.06.004.
13. Barlat, F., Yoon, J. W., Cazacu, O., 2007. "On linear transformations of stress tensors for the description of plastic anisotropy." *Int. J. Plast.* 23, 876-896. Doi: 10.1016/j.ijplas.2006.10.001.
14. Banabic, D., Aretz, H., Comsa, D. S., Paraianu L., 2005. "An improved analytical description of orthotropy in metallic sheets." *Int. J. Plast.* 21, 493-512. Doi: 10.1016/j.ijplas.2004.04.003.
15. Leacock, A. G., 2006. "A mathematical description of orthotropy in sheet metals." *J. Mech. Phys. Solids* 54, 425-444. Doi: 10.1016/j.jmps.2005.08.008.
16. Vegter, H., van den Boogaard, A. H., 2006. "A plane stress yield function for anisotropic sheet material by interpolation of biaxial stress states." *Int. J. Plast.* 22, 557-580. Doi: 10.1016/j.ijplas.2005.04.009.
17. Hu, W. L., 2007. "Constitutive modeling of orthotropic sheet metals by presenting hardening-induced anisotropy." *Int. J. Plast.* 23, 620-639. Doi: 10.1016/j.ijplas.2006.08.004.
18. Soare, S., Yoon, J. W., Cazacu, O., 2008. "On the use of homogeneous polynomials to develop anisotropic yield functions with applications to sheet forming." *Int. J. Plast.* 24, 915-944. Doi: 10.1016/j.ijplas.2007.07.016.
19. Yoshida, F., Hamasaki, H. and Uemori, T., 2013. "A user-friendly 3D yield function to describe anisotropy of steel sheets." *Int. J. Plast.* 45, 119- 139. Doi: 10.1016/j.ijplas.2013.01.010.
20. Yoshida, F., Hamasaki, H. and Uemori, T., 2014. "A model of anisotropy evolution of sheet metals." *Procedia Engineering* Vol.81 pp. 1216-1221. Doi: 10.1016/j.proeng.2014.10.100.
21. Chun, B., Jinn, J., Lee, J., 2002. "Modeling the Bauschinger effect for sheet metals, part I: theory." *Int. J. Plastic.* 18, 571-595. Doi: 10.1016/S0749-6419(01)00046-8.
22. Verma, R.K., Kuwabara, T., Chung, K., Haldar, A., 2011. "Experimental evaluation and constitutive modeling of non-proportional deformation for asymmetric steels." *Int. J. Plastic.* 27, 82-101. Doi: 10.1016/j.ijplas.2010.04.002.
23. Prager, W., 1956. "A new method of analyzing stresses and strains in work-hardening plastic solids." *Journal of Applied Mechanics*, 23, 493-496.
24. Ziegler, H., 1959. "A modification of Prager's hardening rule." *Q. Appl. Math.* 17, 55-65. Doi: 10.1090/qam/104405.

25. Armstrong, P.J., Frederick, C., 1966. "A Mathematical Representation of the Multiaxial Bauschinger Effect." Central Electricity Generating Board and Berkeley Nuclear Laboratories, Research & Development Department.
26. Chaboche, J.L., Rousselier, G., 1983. "On the plastic and viscoplastic constitutive equations - Part I: Rules developed with internal variable concept." *ASME Journal of Pressure Vessel Technology* 34, 153–158. Doi: 10.1115/1.3264257.
27. Choi, Y., Han, C.S., Lee, J.K., Wagoner, R.H., 2006. "Modeling multi-axial deformation of planar anisotropic elasto-plastic materials. Part I: Theory." *International Journal of Plasticity* 22 (9), 1745. Doi: 10.1016/j.ijplas.2006.02.002.
28. Chaboche, J.L., 2008. "A review of some plasticity and viscoplasticity constitutive theories." *International Journal of Plasticity* 24, 1642–1693. Doi: 10.1016/j.ijplas.2008.03.009.
29. Geng, L. and Wagoner, R., "Springback Analysis with a Modified Hardening Model," SAE Technical Paper 2000-01-0768, 2000. Doi: <https://doi.org/10.4271/2000-01-0768>.
30. Lee, M.G., Kim, D., Kim, C., Wenner, M.L., Wagoner, R.H., Chung, K., 2007. "A practical two-surface plasticity model and its application to spring-back prediction." *International Journal of Plasticity* 23 (7), 1189–1212. Doi: 10.1016/j.ijplas.2006.10.011.
31. Yoshida, F., Uemori, T., 2002. "A model of large-strain cyclic plasticity describing the Bauschinger effect and workhardening stagnation." *International Journal of Plasticity* 18, 661–686. Doi: 10.1016/S0749-6419(01)00050-X.
32. Eggertsen, P.-A., Mattiasson, K., 2010. "On constitutive modeling for springback analysis." *Int. J. Mech. Sci.* 52, 804–818. Doi: 10.1016/j.ijmecsci.2010.01.008.
33. Ghaei, A., Green, D., Taherizadeh, A., 2010. "Semi-implicit numerical integration of Yoshida–Uemori two-surface plasticity model." *Int. J. Mech. Sci.* 52, 531–540. Doi: 10.1016/j.ijmecsci.2009.11.018.
34. Yilamu, K., Hino, R., Hamasaki, H., Yoshida, F., 2010. "Air bending and springback of stainless steel clad aluminum sheet." *J. Mater. Process. Technol.* 210, 272–278. Doi: 10.1016/j.jmatprotec.2009.09.010.
35. Barlat, F., Gracio, J.J., Lee, M.-G., Rauch, E.F., Vincze, G., 2011. "An alternative to kinematic hardening in classical plasticity." *International Journal of Plasticity* 27 (9), 1309–1327. Doi: 10.1016/j.ijplas.2011.03.003.
36. Barlat, F., Ha, J., Grácio, J.J., Lee, M.-G., Rauch, E.F., Vincze, G., 2013. "Extension of homogeneous anisotropic hardening model to cross-loading with latent effects." *Int. J. Plastic.* 46, 130–142. Doi: 10.1016/j.ijplas.2012.07.002.



37. Barlat, F., Vincze, G., Grácio, J., Lee, M.-G., Rauch, E., Tomé, C., 2014. "Enhancements of homogenous anisotropic hardening model and application to mild and dual-phase steels." *Int. J. Plastic.* 58, 201–218. Doi: 10.1016/j.ijplas.2013.11.002.
38. Lee, J.-W., Lee, M.-G., Barlat, F., 2012. "Finite element modeling using homogeneous anisotropic hardening and application to springback prediction." *Int. J. Plastic.* 29, 13–41. Doi: 10.1016/j.ijplas.2011.07.007
39. Lee, J., Lee, J.-Y., Barlat, F., Wagoner, R., Chung, K., Lee, M.-G., 2013. "Extension of quasi-plastic–elastic approach to incorporate complex plastic flow behavior - application to springback of advanced high-strength steels." *Int. J. Plastic.* 45, 140–159. Doi: 10.1016/j.ijplas.2013.01.011
40. Choi, J., Lee, J., Bong, H.J., Lee, M.G. and Barlat, F., 2017. "Advanced constitutive modeling of advanced high strength steel sheets for springback prediction after double stage U-draw bending." *International Journal of Solids and Structures*, In Press, 1–13. Doi: 10.1016/j.ijsolstr.2017.09.030.
41. Butuc, M.C., Teodosiu, C., Barlat, F., Gracio, J., 2011. "Analysis of sheet metal formability through isotropic and kinematic hardening models." *European Journal of Mechanics / A Solids*, doi: 10.1016/j.euromechsol.2011.03.005.
42. S. Bruschi, T. Altan, D. Banabic, P. F. Bariani, A. Brosius, J. Cao, A. Ghiotti, M. Khraisheh, M. Merklein, A. E. Tekkaya 2014. "Testing and modelling of material behaviour and formability in sheet metal forming." *CIRP Annals - Manufacturing Technology*, vol. 63 issue 2, 727–749. Doi: 10.1016/j.cirp.2014.05.005.
43. Felder, E., Samper, V., 1994. "Experimental study and theoretical interpretation of the frictional mechanisms in steel sheet forming." *Wear* 178, 85-94. Doi: 10.1016/0043-1648(94)90132-5.
44. Gong, H., Lou, Z., Zhang, Z., 2004. "Studies on the friction and lubrication characteristics in the sheet steel drawing process." *J. Mater. Process. Tech.* 151, 328-333. Doi: 10.1016/j.jmatprotec.2004.04.082.
45. Keum, Y.T., Wagoner, R.H., Lee, J.K., 2004. "Friction model for FEM simulation of sheet metal forming operations." *AIP Conf. Proc.* 712, 989-994. Doi: 10.1063/1.1766656.
46. Saha, P.K., Wilson, W.R.D., 1994. "Influence of plastic strain on friction in sheet metal forming." *Wear* 172, 167-173. Doi: 10.1016/0043-1648(94)90284-4.
47. Lee, J.Y., 2011. "Evaluation of Constitutive Models for Springback Prediction in U-draw/bending of DP and TRIP Steel Sheets." Pohang University of Science and Technology, Pohang, Republic of Korea. Master Thesis. Doi: 10.1063/1.3623659.

48. Hora, P., Heingartner, J., Manopulo, N., Tong, L., 2011. "Zero failure production methods based on a process integrated virtual control." AIP Conf. Proc. 1383, 35-47. Doi: 10.1063/1.3623590.
49. Azushima, A., Kudo, H., 1995. "Direct observation of contact behaviour to interpret the pressure dependence of the coefficient of friction in sheet metal forming." CIRP Ann. Manufac. Tech. 44, 209-212. Doi: 10.1016/S0007-8506(07)62309-9.
50. Gruebler, R., Hora, P., 2009. "Temperature dependent friction modeling for sheet metal forming." Int. J. Mater. Form. 2, 251-254. Doi: 10.1007/s12289-009-0548-z.
51. Han, S.S., Kim, D.J., 2011. "Contact pressure effect on frictional characteristics of steel sheet for autobody." AIP Conf. Proc. 1383, 780-783. Doi: 10.1063/1.3623685.
52. Lanzon, J.M., Cardew-Hall, M.J., Hodgson, P.D., 1998. "Characterising frictional behaviour in sheet metal forming." J. Mater. Process. Tech. 80-81, 251-256. Doi: 10.1016/S0924-0136(98)00110-1
53. Santos, A.D., Teixeira, P., 2008. "A study on experimental benchmarks and simulation results in sheet metal forming." J. Mater. Process. Tech. 199, 327-336. Doi: 10.1016/j.jmatprotec.2007.08.039
54. Jeong-Yeon Lee., Barlat, F., Myoung-Gyu, Lee, 2015. "Constitutive and friction modeling for accurate springback analysis of advanced high strength steel sheets." International Journal of Plasticity 71 (2015) 113-135. Doi: 10.1016/j.ijplas.2015.04.005.
55. Hirpa, G., Lemu, T., Trzepiecinski, T. 2013. "Numerical and experimental study of Frictional behavior in bending under tension test." Strojnicki vestnik – Journal of Mechanical Engineering. 59, pp. 41-49. Doi: 10.5545/sv-jme.2012.383.
56. Saniee F. Fereshteh, Montazeran M.H., 2003. "A Comparative Estimation of the Forming Load in the Deep Drawing Process", Journal of Materials Processing Technology, vol. 140, pp 555–561, 2003. Doi: 10.1016/S0924-0136(03)00793-3.
57. Colgan M., Monaghan J., 2003. "Deep Drawing Process: Analysis and Experiment", Journal of Materials Processing Technology, vol. 132, pp 35-41. Doi: 10.1016/S0924-0136(02)00253-4.
58. Padmanabhan R., Oliveira M.C., Alves J.L., Menezes L.F. "Influence of Process Parameters on the Deep Drawing of Stainless Steel", Finite Elements in Analysis and Design, vol.43 pp 1062 – 1067, 2007. Doi: 10.1016/j.finel.2007.06.011.
59. G. H. Bae, H. Huh, 2011. "Tension/compression test of auto-body steel sheets with the variation of the pre-strain and the strain rate." In: Proc. 5<sup>th</sup> Int. Conf. on Computational Methods and Experiments in Materials Characterisation, Kos, Greece. Doi: 10.2495/MC110191.

60. Min Kuk Choi, Hoon Huh, 2014. "Effect of punch speed on amount of springback in U-bending process of auto-body steel sheets." *Procedia Engineering* 81, 963 – 968 Doi: 10.1016/j.proeng.2014.10.125.
61. Mohd Ahmed, 2018. "Adaptive finite element simulation of sheet forming process parameters." *Journal of King Saud University - Engineering Sciences* Volume 30, Issue 3, 259-265 Doi: 10.1016/j.jksues.2016.10.002.
62. Adnan I. O. Zaid, Fadhil A. Hashim, 2017. "Effect of Punch and Die Profile Radii on Deep Drawing of Galvanized Steel." *International Journal of Scientific & Engineering Research*, Volume 8, Issue 1.
63. Roll K, Wiegand K, Hora P (2008) "Benchmark 2 – Influence of drawbeads on the Springback Behavior («S-Rail») Part A: Physical Tryout Report" in *Proceeding of the 7th International Conference and Workshop on Numerical Simulation of 3d Sheet Metal Forming Processes*, Interlaken, Switzerland, September 2008.

## 4. ARTIGO 3: “Hybrix: Experimental Characterization of a Micro-Sandwich Sheet”

**A.M. Pimentel, J.L. Alves, N.M. Merendeiro, D. Oliveira**

Anthony Michael Fernandes Pimentel<sup>a,b,\*</sup>

\*E-mail: anthony.pimentel@ct.sodecia.com \ anthony.pimentel@dep.uminho.pt

José Luís de Carvalho Martins Alves<sup>b</sup>

Nuno Miguel de Seabra Merendeiro<sup>a,3</sup>

Daniel Casanova Pinto Martins de Oliveira<sup>a,4</sup>

<sup>a</sup> Centro Tecnológico Sodecia, Rua Eng.º Frederico Ulrich, 2650, 4470-605 Maia, Portugal

<sup>b</sup> CMEMS, Universidade do Minho, Campus de Azurém 4800-058 Guimarães, Portugal

---

<sup>3</sup> Present Adress - Sodecia-participações Sociais Sgps Sa, Rua do Espido, 164-F, Edifício Via Norte, 4470-177 Maia – Portugal

<sup>4</sup> Present Adress - Efacec-Sistemas de Electrónica SA, Rua Eng.º Frederico Ulrich, 4470-605 Maia, Portugal

## **ABSTRACT**

The development of new micro-sandwich sheets (i.e. two metallic skins separated by a composite core), which can be shaped by conventional sheet metal forming processes, became one of the most interesting materials and promising automotive applications in the past few years. However, due to the lack of understanding of certain fundamentals related with the mechanical behavior of micro-sandwich sheets during forming processes, the transfer and scale-up of this promising material to industry has been hindered. To overcome problems concerning the formability of these new materials and make the conventional sheet forming process more adapted, the experimental characterization of the micro-sandwich sheets is absolutely necessary. In this work, a new approach to experimentally characterize micro-sandwich sheets, with the mechanical properties of the core unknown, is presented. Firstly, for the characterization of stress-strain curves and anisotropy, uniaxial tensile tests in 3 different orientations with respect to rolling direction are performed on total micro-sandwich specimens and skin-only specimens. Secondly, the mechanical properties of the core are then deduced from micro-sandwich and skins' mechanical properties, and the constitutive parameters established. Additionally, 5 different Nakazima geometries were punched according to ISO 12004 for formability assessment. Experimental Forming Limit Curves (FLC), punch forces and principal strain data were recorded during the tests using high resolution cameras and system GOM ARAMIS. Finally, the experimental mechanical tests were numerically reproduced. The systematic excellent agreement between numerical and experimental results is a good validation of the methodology proposed in the present work to identify the constitutive properties of the micro-sandwich materials.

## **KEYWORDS**

Micro-Sandwich Sheets; Lamera, Hybrix; Uniaxial Tensile Test; Nakazima Test; Forming Limit Curve

## INTRODUCTION

Lighter vehicles, lower fuel consumption and easier recyclability is the new pragma of automotive industry due to the most recent environmental concerns. Such new framework has been the opportunity for the introduction of new lighter and challenging materials, such as alternative metals and composites, which have been at the heart of the research and innovation in order to develop and introduce in the market the lighter and more environmentally friendly future vehicles, as stated by Ghassemieh (2011).

In this context, multi-layer materials, usually known as sandwich materials, are currently one of the most promising technological solutions in terms of new advanced materials to be applied in automotive industry. As Moreira et al. (2010) refers, the main advantages of these materials are the excellent stiffness to weight and strength to weight ratios, ease of production and, when developed for this purpose, excellent ability to absorb vibrations and noise.

In the past few years, the sandwich concept has been applied to very thin metallic sheet layers, which can be transformed by conventional sheet forming processes. These sheet materials, also known as micro-sandwich, are usually made by a polymeric soft core (as epoxy resins or rubber) covered by two metallic skins. In certain cases, the soft core can also contain fibbers, metallic or not. Some of these materials have already been used with success in the automotive industry. For instance, the CORUS micro-sandwich *Hylite* was applied in automotive parts as bonnets, roof panels and hoods. Mann (1999) mentions the NedCar Aceso (1996), Palkowski and Lange (2005) refers the Ford e-Ka (2000), and the Hylite supplier Alcan Singen GmbH claims the successful applications on the Aixam 400 (1997) and Audi A2 (2000). Volkswagen is using the *LITECORE* micro-sandwich, developed and produced in a partnership with ThyssenKrupp Steel Europe, to the production of a super lightweight hood for the Polo R WRC, as revealed online by TSE (2014). Volvo was also involved in the development of a new micro-sandwich, called Hybrix, born out of a partnership between Lamera AB, a spin-off company from the Sweden OEM, and Chalmers University. The Hybrix core consists of millions of microscopic stainless-steel fibers vertically oriented against the AISI 304L stainless steel skins and bounded by an epoxy resin, as depicted in Fig. 4.1.



Fig. 4.1 – Scheme of the Hybrix micro-sandwich sheet material, comprising two stainless steel layers and an intermediate composite core (metallic stainless-steel fibers embedded in an epoxy resin). The total nominal thickness of 1.6mm can be decomposed in two skin layers of 0.15 mm and a core with 1.3 mm.

The Hybrix sandwich material can display several thickness combinations, with different nominal thicknesses and symmetric or asymmetric metallic skins, i.e. the two outside metallic skins can exhibit the same or different thicknesses. The experimental results presented in this work concern a symmetric Hybrix configuration, with the following nominal thicknesses: 1.3mm of the core and 0.15mm of each metallic skin. Because of its excellent strength and ductility, stainless steel is commonly used in deep drawing parts. So, using stainless steel skins, Hybrix sheets seem to be well adapted to be shaped in sheet forming operations, and very promising to be used in automotive industry.

To study Hybrix feasibility in automotive industry, several stamped case studies were experimentally tested by Engelmark (2009): the experimental results explored by this author put in to evidence a high risk of wrinkles in case of deep drawn parts, which is a major concern to the stamping process robustness. Moreover, Jackson et al. (2008) conducted some experimental tests in different types of sandwich materials in order to evaluate their formability behavior; in brief, authors claim that, using an incremental forming technique, the Hybrix sandwich material may exhibit some formability problems mainly due to delamination failure mode, i.e. separation between the composite polymeric core and the metallic skins. In summary, the previous works in this field have identified several drawbacks concerning the industrialization of micro-sandwich materials. Concerning the conventional cold stamping processes, a major issue is the general poor formability of these materials, and their trend to wrinkling and delamination.

The global mechanical behavior of sandwich materials is obviously related with the thicknesses and mechanical behavior of each layer. Moreover, Palkowski and Lange (2005) compared different sandwich materials and examined their formability, and claim that the difficulties in the deep drawing process of these sandwich system dwells from the different behavior of the layer materials. Nevertheless, it is not quite enough to understand the mechanical behavior of each layer individually given that the global behavior is also driven by the interaction between layers. Moreover, when very thin skins are considered, such as the ones on the micro-sandwich materials, the mechanical properties can change and new constitutive model parameters are needed to accurately describe the formability and springback phenomena, as claimed by Štok et al. (2014). Luzin et al. (2005) compare several experimental techniques to measure the Young Modulus of samples made from sub-

millimeter thickness layers, and observed that the elastic properties can no longer be measured with conventional mechanical tests. The manufacture process of multi-layer sheets, even if well controlled, always introduces some variability of material properties and bounding conditions that affects the quality of the stamped parts. Schreursa et al. (2009) also studied the relationship between the delamination in a polymer coated metal and the deep-drawing process parameters; the authors consider that both manufacture and stamping processes contributes to delamination and debonding of multi-layer materials affecting its formability.

Thus, to adapt the conventional sheet forming processes to the features and mechanical behavior of Hybrix sheets, it is absolutely paramount to carry out their experimental characterization beforehand. Such information is crucial to build robust numerical models to design the forming processes in order to provide reliable and accurate results.

However, the experimental characterization of the Hybrix materials is not a simple task. For instance, the chosen process to cut the testing specimens affects the experimental results. In case of laser cutting, one must consider the fusion and burning of the micro-sandwich polymeric cores, the heat affected zone in the metallic skins and the presence of burrs along the contour. In case of water jet cutting, the core adhesive properties can be seriously affected by the water and abrasive particles, particularly the epoxy cores. In order to avoid such drawbacks and obtain a better cutting quality surface, Pauchard (2009) suggests the Laser MicroJet technique. Moreover, on the one hand, the experimental tests to identify the mechanical properties of a composite core are very specific and still far from the current reality in industry; on the other hand, the constitutive models to model and describe the mechanical behavior of composite materials are complex and not yet completely implemented in the commercial FE codes dedicated to sheet forming simulation.

This work deals with the experimental characterization and numerical modeling of the mechanical behavior of a micro-sandwich sheets. The main goal is to present and validate a very simple and expedite methodology to characterize the mechanical behavior of an advanced micro-sandwich material. Uniaxial tensile tests were performed on specimens oriented along 3 different orientations with respect to the rolling direction, in order to characterize the isotropic hardening and anisotropy, and the Nakazima tests were performed to characterize the FLC and for preliminary validation test purposes. The numerical model to validate this methodology was created and tested in commercial software PAM-STAMP 2G 2012.2.

## **HYBRIX: EXPERIMENTAL CHARACTERIZATION**

The aim of this section is to present the results concerning the experimental characterization of the Hybrix sandwich material, in order to determine the constitutive parameters required for the numerical modelling and numerical simulation. The experimental data must be enough to define the



**hardening curve**, the **yield criterion** and the **forming limit curve (FLC)**. In case of a sandwich system as Hybrix, this information is needed for each layer. The material model is a paramount aspect to take in account in the numerical simulation of the sheet forming processes; since it rules the mechanical behavior of the micro-sandwich materials, the reliability and accuracy of the numerical results depend on it.

## Uniaxial Tensile Tests

Uniaxial tensile tests, commonly used in case of metallic sheets, are able to provide all the relevant experimental data to characterize the **hardening** and the **yield surface**. Through the force-displacement curves it is possible to establish the stress-strain relationship, and thus to characterize the isotropic hardening curve. Tensile tests carried out for several orientations with respect to the rolling direction are required to characterize the anisotropic behavior and the yield surface. Since Hybrix is a multi-layer material, uniaxial tensile tests can be performed either on the complete micro-sandwich structure or on only the external metallic skins: in what follows both cases, i.e. the complete and skin-only specimens, will be presented and analyzed. Such procedure was adopted in order to isolate and understand the contribution of the fiber /polymeric CORE to the overall mechanical behavior of the Hybrix sandwich material.

The tensile test was conducted according to EN 10002-1: 2009, using a universal testing machine Tinius Olsen and 5 tensile specimens for each orientation with respect to the rolling axis: 0°, 45° and 90°. During the tests, the deformation was measured with a 50mm gauge extensometer. All experimental force-displacement curves were recorded. Based on a simple arithmetic average, the force-displacement curves and the correspondent stress-strain curves were averaged for each orientation, and the result are shown in Fig. 4.2 for the complete Hybrix sheet, and in Fig. 4.3 for the metallic skins only.

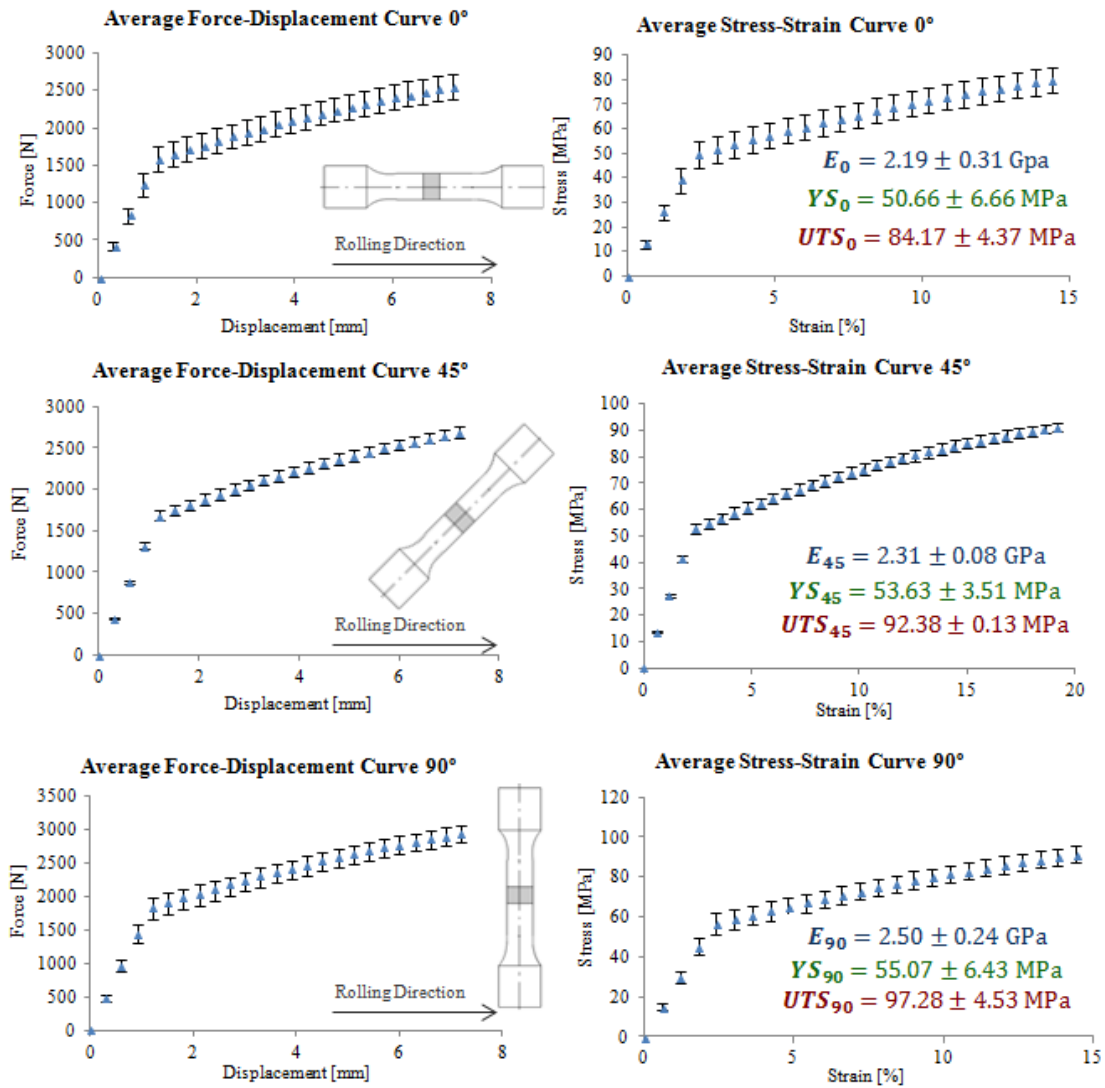


Fig. 4.2 – Experimental force-displacement curves, with error bars, and correspondent stress-strain curves, for orientations of 0°, 45° and 90°, for the Hybrix sheet. Average values of Young modulus ( $E$ ), yield stress ( $Y$ ) and ultimate tensile strength ( $UTS$ ) with the respective uncertainty.

The experimental results of the uniaxial tensile tests with the total Hybrix specimens at Fig. 4.2 show that the average yield stress and the average ultimate tensile strength increase with the orientation from 0° to 90°. The error bars show that the lowest deviations between the tests were achieved for the orientation of 45°. The elastic behavior and the total elongation between the different orientations are very similar. A final remark concerning the value of the Young modulus, of about 2.3 GPa.

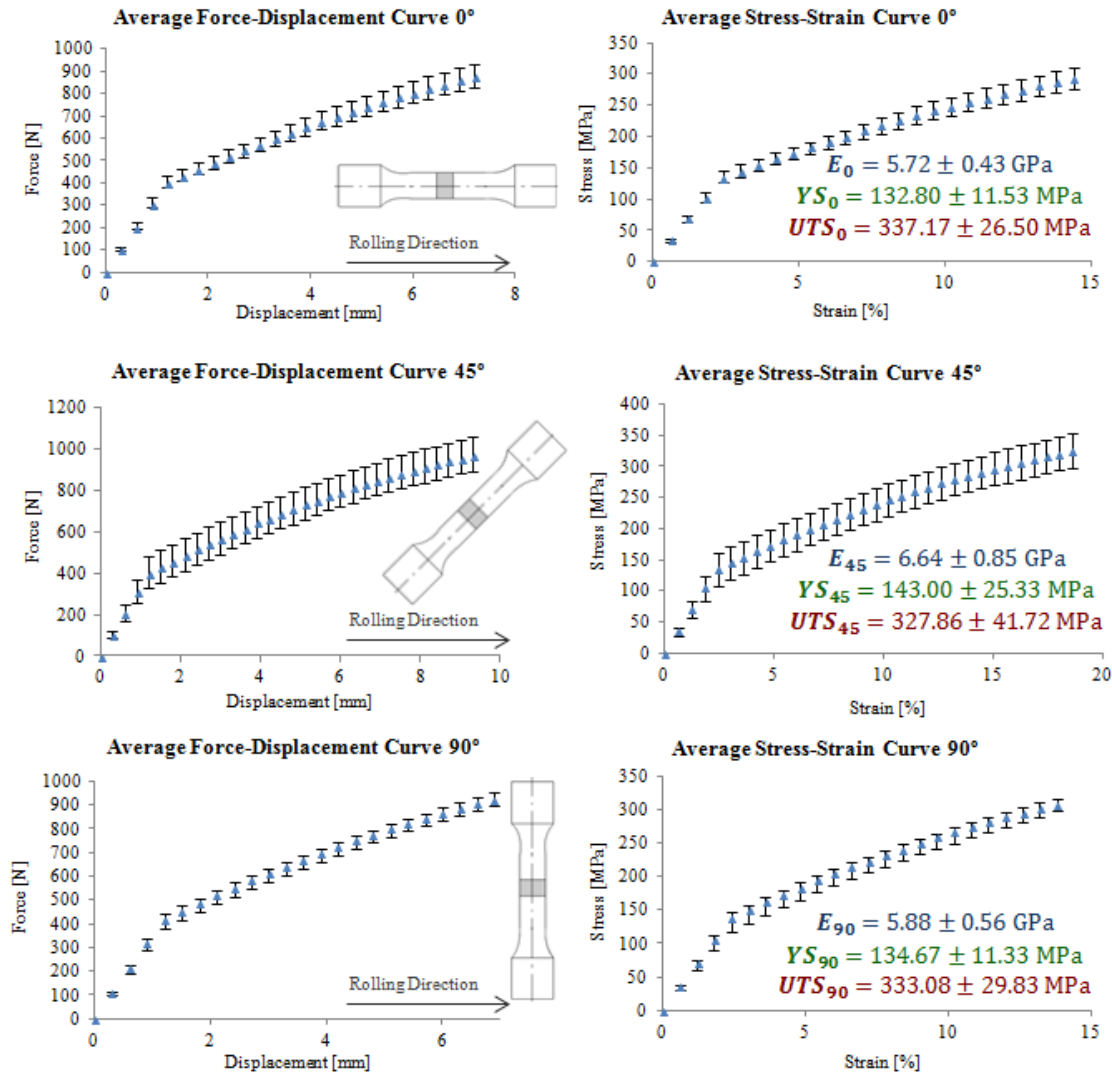


Fig. 4.3 – Experimental force-displacement curves, with error bars, and correspondent stress-strain curves, for orientations of 0°, 45° and 90°, for the metallic skins only. Average values of Young modulus ( $E$ ), yield stress ( $Y$ ) and ultimate tensile strength ( $UTS$ ) with the respective uncertainty.

The experimental results of the uniaxial tensile tests performed on the metallic skins specimens at Fig. 4.3 put in evidence the anisotropic behavior of the metallic skins. In fact, the initial yield stress is higher for 45° (143.0 MPa), being of 132.8 MPa and 134.7 MPa for 0° and 90°, respectively. However, it is also true that the highest variation was determined for 45° specimens, with an uncertainty of about 18%. The elastic strains of the metallic skins and of the total Hybric specimens are very similar, because the elastic strains are mainly driven by the elastic behavior of the metallic skins. The ductility of the metallic skins tends to be lower than expected for a stainless steel. However, due to the small thickness of the metallic skins it can be expected that the metallic skins are supplied with a pre-hardening treatment, with almost all ductility already consumed by the rolling process due to cold reduction. Finally, the experimentally measured Young modulus of around 6 GPa is too low,

mainly if compared with the typical value of the Young modulus for AISI 304 stainless steels (193 GPa, matweb.com).

## Nakazima Tests

Nakazima tests are often used for general formability limits evaluation of metallic materials. With the experimental data of Nakazima test it is possible to draw the **Forming Limit Curve (FLC)** of the characterized material. The experimental tests were carried out in an Erichsen (model 142-40) universal testing machine, punching 5 different specimen's geometries (20-30-65-100-180), according to ISO 12004. Each Nakazima specimen refers to a different strain path on the *Forming Limit Diagram*. To optical 3D deformation measurement purposes, all specimens were painted to display a random speckled pattern. The overall movement of the random speckle pattern was captured during the test by high resolution cameras and treated with the GOM ARAMIS system. The punch velocity was fixed at 20 mm/min and the blankholder force fixed at 150kN. The obtained FLC curve is shown in Fig. 4.4.

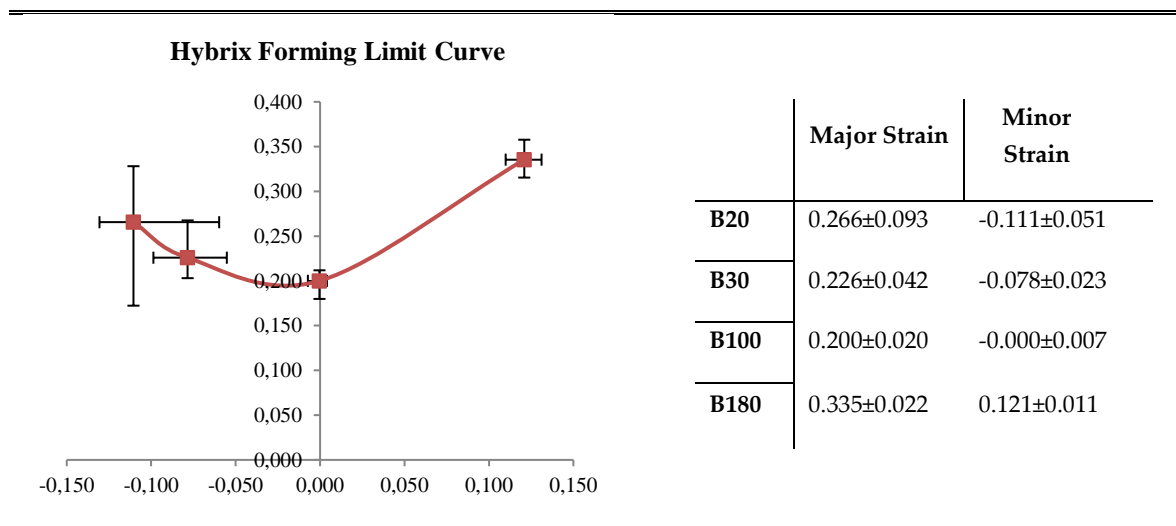


Fig. 4.4 – Experimental Hybrix Forming Limit Curve (FLC), defined with 4 experimental points, with error bars and respective uncertainty.

Several experimental issues like lens focusing, cameras calibration or the speckle pattern capture, amongst others, can often affect seriously the speckle pattern measurements and mesh generation, and thus invalidate the FLC determination. In the present study, problems with the experimental measurements of the B65 specimens have made impossible its usage. On the other hand, a high variability of the experimentally measured values of both the maximum punch force and principal strains were observed in the narrower specimens, i.e. B20 and B30. Finally, it was found that some specimens started failing unexpectedly too early by the geometry contour nearby the die

radius, which is not usually seen in case of monolithic materials. The more stable and robust experimental results were determined for the geometries B100 and B180.

## HYBRIX: CONSTITUTIVE MODELLING METHODOLOGY

### Core’s Stress-Strain Curves Deduction

To describe numerically the mechanical behavior of a given material it is mandatory to use suitable constitutive models, i.e. flexible enough physically-based laws, and to identify a set of appropriate constitutive parameters. When it concerns micro-sandwich materials, to know beforehand the constitutive parameters for each material layer, may not be enough or possible. Thus, it is necessary to follow a different strategy which will allow “determining” the unknown constitutive parameters of the composite material. In case of the Hybrix material, two AISI 304 stainless steel skins are spaced and bonded by an adhesive epoxy resin impregnated with stainless steel micro fibers, which constitutes the core material. The core material is a complex composite material, and no experimental data is available for it. The new strategy followed in this work aims at deducing the mechanical properties of the core material from the previously identified experimental behavior of the total Hybrix material and the single metallic skins, whose results of the uniaxial tensile tests are shown in Fig. 4.2 and Fig. 4.3. The assumption behind this strategy is that the total force measured during the uniaxial tensile test of the Hybrix material is the sum of the forces supported by the two skins plus the force supported by the core, as schematically shown in Fig. 4.5.

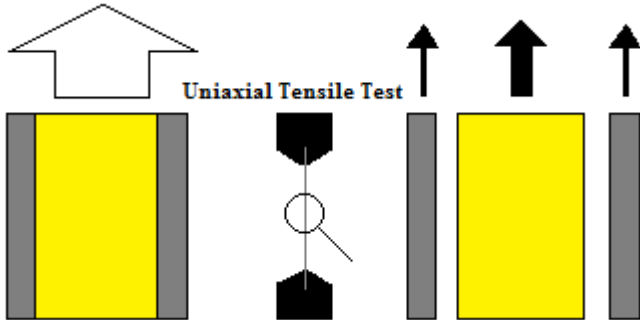


Fig. 4.5 – Decomposition load strategy. The 3 layers (2 metallic skins plus the core) are loaded in parallel during the uniaxial tensile test, and thus the total uniaxial tensile force can be decomposed in two components, the forces supported by the two metallic skins plus the force supported by the core.

The composite fibrous core is hereafter assumed as an isotropic homogeneous material with unknown mechanical properties. Then, it is possible to use the experimental tensile data of both total

Hybrix and metallic skins to deduct the force-displacement and stress-strain curves of the Hybrix core [Fig. 4.6], considering that

$$\vec{F}_{Core} = \vec{F}_{Hybrix} - \vec{F}_{Skin} \quad (1)$$

The resultant force-displacement curve and stress-strain curve concerning the core material are plotted in Fig. 4.6. It is worth noting at flow stress of about 30MPa displays almost no hardening, and to compare this value with the one of the metallic skins, of about 132MPa to 337MPa (see Fig. 4.3).

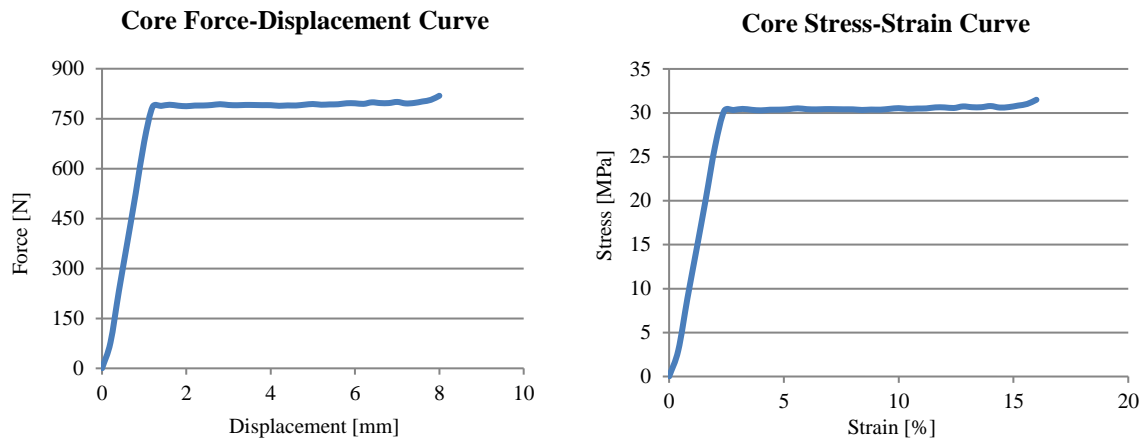


Fig. 4.6 – Deducted core's force-displacement curve and stress-strain curve.

## Anisotropy and Yield Criterion

After determining the stress-strain relationship it is also necessary to define the **yield criterion** for each layer and for the total Hybrix. Due to the anisotropic behavior of the metallic skins, an **anisotropic yield criterion** must be used. Therefore, the methodology presented can be followed to deduct and characterize the Hybrix anisotropy, as well as to establish a basic analysis to identify the elastic behavior. The experimental force-displacement curves and the global dimensions of the two specimens (metallic skins only and the total Hybrix) are the only data available for the abovementioned deduction.

As previously mentioned, the Hybrix core consists of millions of microscopic stainless-steel fibers preferably oriented vertically against the AISI 304L stainless steel skins and bounded by an epoxy resin. Since the stainless-steel fibers are assumed vertically oriented in the epoxy matrix, the core mechanical behavior can be assumed as isotropic in the rolling plane, i.e. the same in-plane mechanical behavior irrespective the loading orientation with respect to the rolling direction; in the through-thickness direction, the vertical fibers do not change the compressive behavior. So, the yielding force of the core is considered invariant with the specimens' orientation and equal to 790N.

To maintain the same global behavior, Tab. 4.1 displays a new set of skin values for 1 single skin.

Tab. 4.1 – Experimental yield forces from: total Hybrix uniaxial tensile test, isotropic core deduction and metallic skin deduction.

	Yield Force [N]			Section Area (mm)	Gauge Length (mm)	Elongation d (mm)		
	0°	45°	90°			0°	45°	90°
<b>Total Hybrix</b>	1583	1676	1721	32	50	1.2	1.2	1.2
<b>Skin (1 Layer)</b>	397	443	466	3	50	1.2	1.2	1.2
<b>Core</b>	790	790	790	26	50	1.2	1.2	1.2

Next, it is possible to determine the yield stresses for each orientation from the following expression,

$$\sigma_{\theta} = \frac{F_{\theta}}{A} \times \left( 1 + \left( \frac{d}{50} \right) \right) \quad (2)$$

The values obtained are depicted in Tab. 4.2.

Tab. 4.2 – Experimental yield stresses from: total Hybrix uniaxial tensile test, isotropic core deduction and metallic skin deduction.

Yield Stresses [MPa]	$\sigma_0$	$\sigma_{45}$	$\sigma_{90}$
<b>Total Hybrix</b>	51	54	55
<b>Skin (1 Layer)</b>	135	151	159
<b>Core</b>	31	31	31

In general, the anisotropy coefficients are determined from the Lankford coefficients, which are experimentally determined from the width and thickness strains measured during the uniaxial tensile tests. However, due to either the small thickness or the small elongation and ductility of the metallic skins, one was not able of measuring the experimental strain, and thus of determining the Lankford coefficients. Therefore, the anisotropy characterization was carried out taking into account the anisotropy of the yield stresses instead of the anisotropy of the strains. Moreover, the multi-layer character of the total Hybrix material also justifies this option, given that there is no relation between the in-plane strains measured on the metallic skins and the total thickness strain measured on a total Hybrix specimen.

To the description of the surface of plasticity of the metallic skins the HILL48 anisotropic yield criterion was adopted. This yield criterion is expressed by the following quadratic function,

$$\bar{\sigma}^2 = F(\sigma_{22} - \sigma_{33})^2 + G(\sigma_{33} - \sigma_{11})^2 + H(\sigma_{11} - \sigma_{22})^2 + 2L\sigma_{23}^2 + 2M\sigma_{31}^2 + 2N\sigma_{12}^2 \quad (3)$$

where  $\bar{\sigma}$  is the equivalent tensile stress;  $F$ ,  $G$ ,  $H$ ,  $L$ ,  $M$  and  $N$  are constants specific to the anisotropy

of the material, and  $\sigma_{ij}, i, j = 1, 3$  are the stress component of the Cauchy stress tensor. In case of sheet metals, axis 1 is the rolling direction, 2 is the transverse direction and 3 is the normal direction.

As referred by Banabic (2010) it is possible to establish the following mathematical relations between the tensile yield stresses (*normalized* by the tensile uniaxial yield stress in the RD - rolling direction) and the anisotropy parameters

$$\frac{1}{\sigma_0^2} = G + H; \quad \frac{1}{\sigma_{45}^2} = H + F; \quad \frac{1}{\sigma_{90}^2} = F + G \quad (2)$$

and thus to determine the values of the anisotropy parameters  $F$ ,  $G$  and  $H$ . Tab. 4.3 presents the HILL48 parameters for the Hybrix micro-sandwich and their two layers, core and skins. Because there is no experimental data to determine parameter  $N$ , the isotropic case was considered.

Tab. 4.3 – HILL48 constitutive parameters for the total Hybrix, the metallic skins and core.

HILL 48	$H$	$F$	$G$	$N$
Total Hybrix	0.50	0.35	0.50	1.50
Skin (1 Layer)	0.50	0.23	0.50	1.50
Core	0.50	0.25	0.50	1.50

With all the constitutive parameters identified and the “unknown” core stress-strain curve deduced, the material model can be built. This new strategy was effective in providing the missing data to model the mechanical behavior of the Hybrix micro-sandwich as a multilayer material.

## HYBRIX: NUMERICAL SIMULATIONS AND VALIDATION

In the previous sections, the experimental FLC was defined and the constitutive parameters of the **yield criterion** for each layer were identified. Now, the hardening laws must be identified from the stress-strain data. The **hardening curve** identified for the **core** is graphically shown in Fig. 4.7.



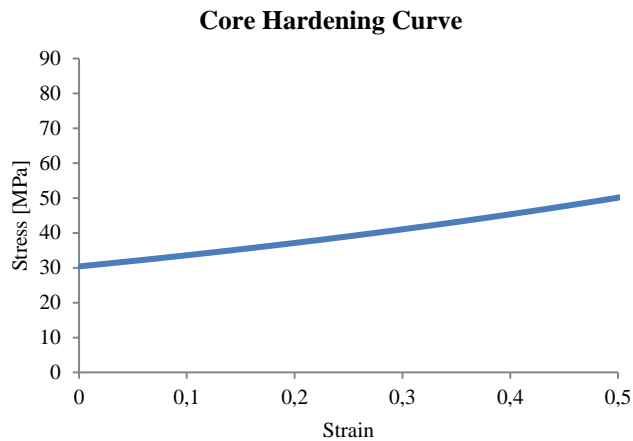


Fig. 4.7 – Resultant core hardening curve identified for the core from the *true* stress-strain curve.

The swift law was chosen to model the isotropic **hardening curve** of the stainless-steel **skins**, and the parameters identified as graphically shown in Fig. 4.8.

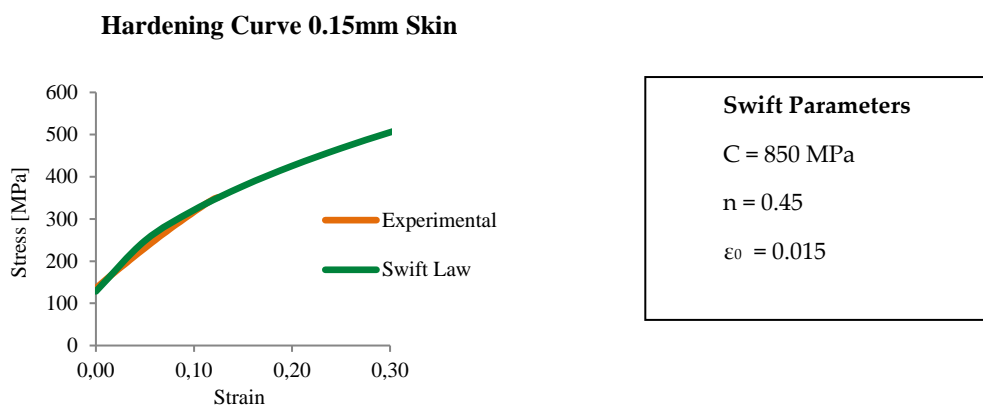


Fig. 4.8 – Swift parameters for the skin hardening curve definition. Comparison with the experimental stress-strain curve.

Taking into account the hardening curves of the core [plotted in Fig. 4.7] and of the metallic skins [plotted on Fig. 4.8] the hardening behavior of the total Hybrix can be simulated. The Swift parameters of the skin were adjusted until the best fit between the Hybrix average force-displacement curve experimentally measured for  $0^\circ$  [Fig. 4.2] and the one determined numerically. The comparison between experimental and numerical curves is shown in Fig. 4.9.

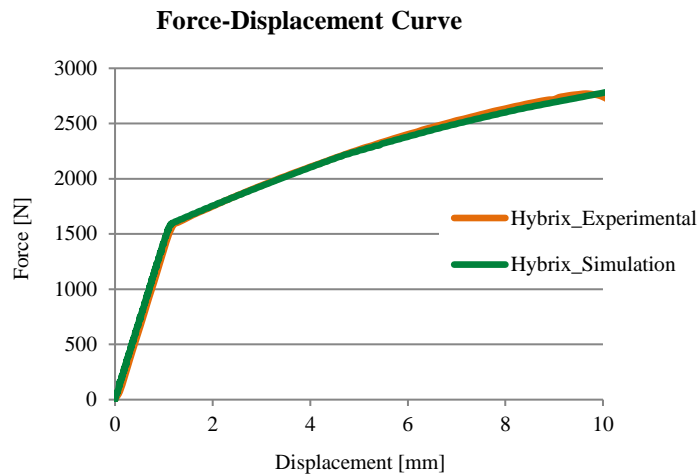


Fig. 4.9 – Comparison between Hybrix experimental force-displacement curve and Hybrix numerical force-displacement curve.

Comparing the standard yield stress values of the AISI 304L steel, i.e. between 260 MPa and 280 MPa, with the values experimentally measured from the skin's tensile samples with a nominal thickness of 0.15mm, i.e. around 135 MPa, the main conclusion is that the values experimentally determined are much lower than the expected (or standard) ones. However, such conclusion is in good agreement with uniaxial tensile tests performed on very thin stainless steel samples (nominal thicknesses smaller than 0.3 mm), for which the stress-strain curves are systematically under the ones obtained for samples with larger thicknesses. Besides, the role of even small edge defects increases when the nominal thicknesses decreases. This so-called "size effect", i.e. the variation of the mechanical properties of the stainless steel when the sheet's nominal thickness decreases was well described and documented by Engel et al. (1997) in micro-forming, and Chen et al. (2009) in micro-bending. Hoffmann and Hong (2006) also investigated the grain size effect in copper foils whereas Diehl et al. (2008) focused upon aluminium sheets. Since it has been proven that degradation of mechanical properties for very thin sheets, it is not recommended to use stress-strain curves of tensile samples with higher thicknesses to characterize the mechanical behavior of the very thin skins.

Concerning the elastic properties, and given that the punch forces determined numerically for the Nakazima test were very low, the value of the Young modulus was adjusted until a good fit between experimental and numerical forces was attained. The main results are shown in Tab. 4.4, i.e. the values of the Young modulus determined from the experimental uniaxial tensile tests and the ones determined from the adjustment between numerical and experimental Nakazima tests

Tab. 4.4 – Experimental tensile values and adjusted Nakazima values of the Young modulus.

YOUNG MODULUS	SKIN [GPa]	CORE [GPa]
Tensile Test	6.3	1.3
Adjusted to Nakazima test	22	4.5

The values of the experimental Young modulus is also very far from the theoretical value usually adopted for the steel, i.e. 210 GPa. Even considering a degradation of the elastic properties for very small thicknesses, it seems that conventional tensile tests are unreliable to measure the Young modulus in case of micro-sandwich materials. However, the skin to core Young modulus ratio obeys to the *rule of mixtures* and it is a key-parameter to adjust the elastic properties of the micro-sandwich sheet as stated in Crolla (2015).

For modeling the multi-layer Hybrix material, 3D 8-node hexagonal solid finite element meshes were used [Fig. 4.10]. The FE mesh comprises 4 layers of elements, 2 layers for the two exterior metallic skins and 2 layers for the composite core.

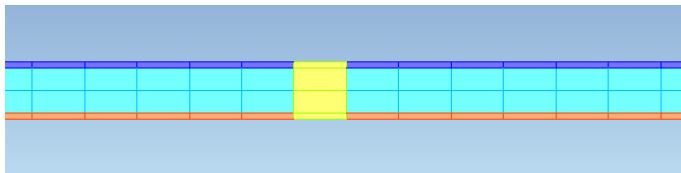


Fig. 4.10 – Finite element mesh with 3D Solid multilayer configuration.

In the virtual tensile test, the experimental 50 mm length gauge was mimicked by following the displacement of 2 nodes initially at the same relative distance, as schematically shown in Fig. 4.11.

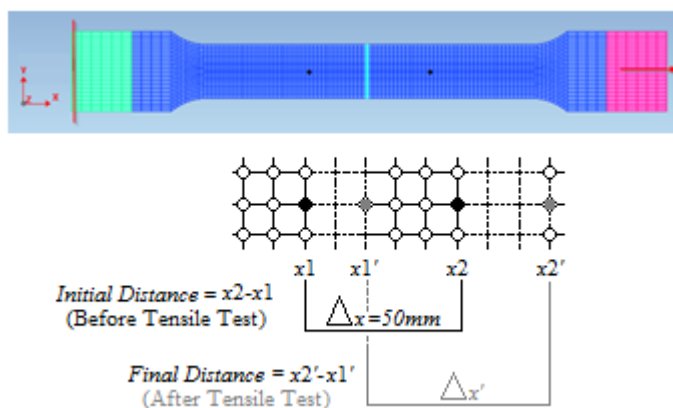


Fig. 4.11 – Control Nodes used to mimic the displacement of the physical extensometer and determine the strain in the specimens after the tensile test.

The CAD geometry of the Nakazima tools were obtained with a 3D scanner and converted in IGES format to PAM-STAMP.

## DISCUSSION AND COMPARISON

In this section experimental and numerical results are analyzed and compared. To validate the accuracy of the numerical model, the results of Nakazima tests, namely the forming forces, the major strain distribution and the formability are compared.

### Forming Forces

Punch displacement and punch force were recorded during Nakazima tests. The comparison between experimental and simulation results is presented in Fig. 4.12 for several geometries of the Nakazima specimen.

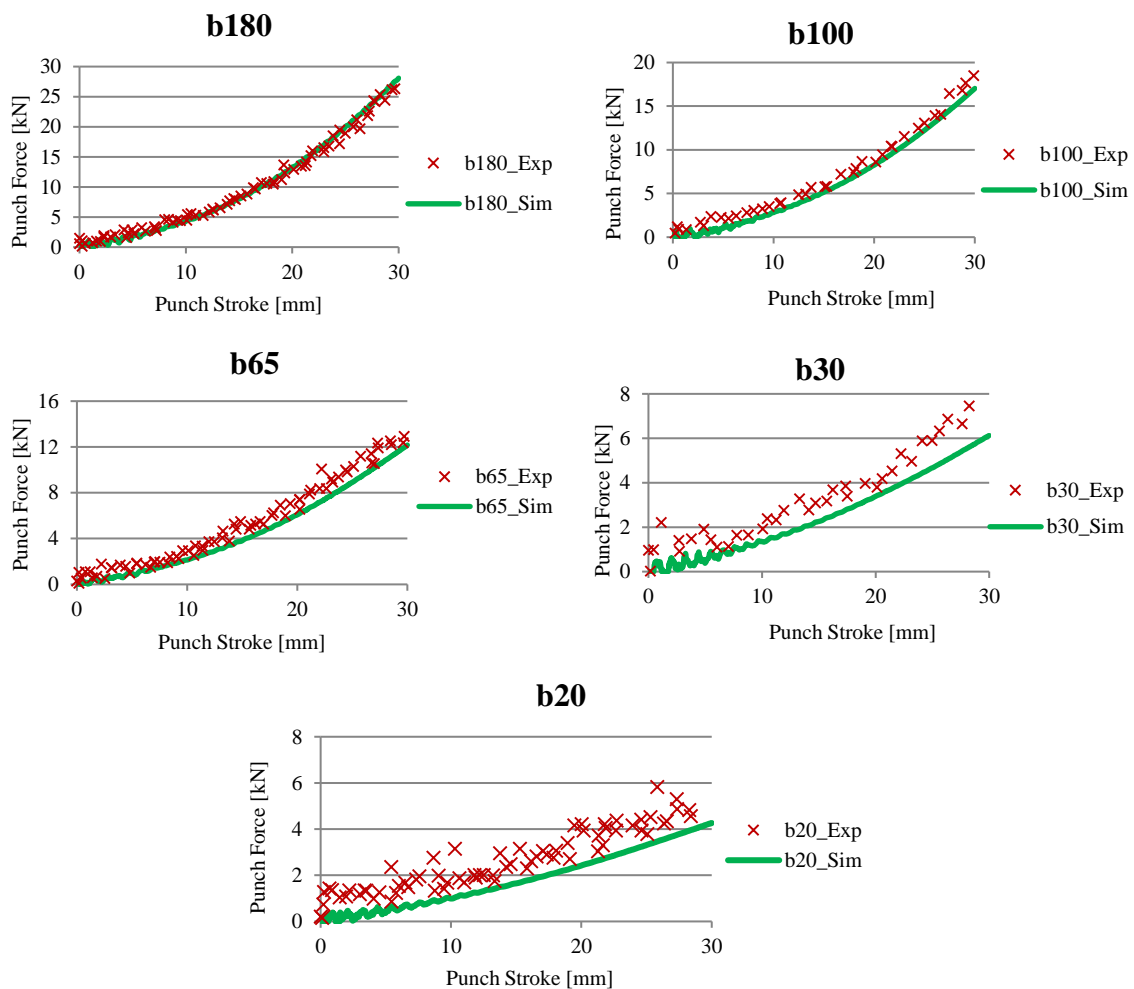


Fig. 4.12 – Comparison of real and numerical punch forces during Nakazima test to each specimen geometry.

In case of Nakazima tests, the specimen geometries with higher values of the punch force,

namely the b180, b100 and b65 geometries, exhibit smaller oscillations in terms of the experimental punch force evolution. On the contrary, noisy curves can be seen in case of b30 and b20 specimen geometries, as shown in Fig. 4.12. The reason for this behavior can be related with the load cell sensitivity. Therefore, in order to minimize the contribution of the noisy curves, the adjustment procedure between experimental and numerical curves was focused mainly on the noisiless curves.

### Major Strain Distribution

Major strain field distribution was also analyzed in the outer surface (the outside surface of the metallic skin not in contact with the punch) along the well-defined line identified in Fig. 4.13. The major strain fields are determined from ARAMIS software. The same line was defined and used in PAM-STAMP 2G in order to allow the comparison between experimental and numerical results.

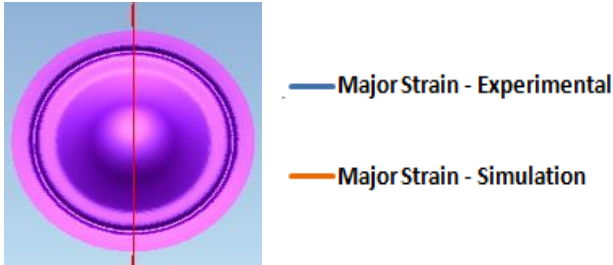
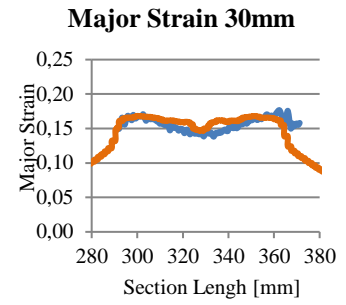
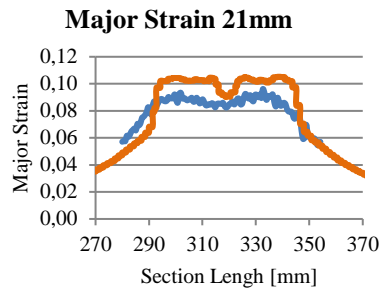
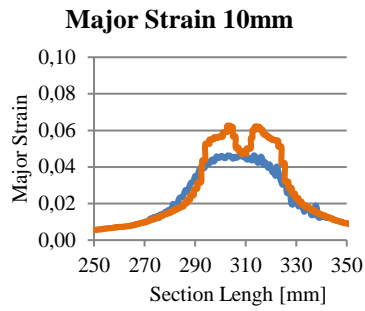


Fig. 4.13 – Cross-section for major strain evaluation of all Nakazima specimens.

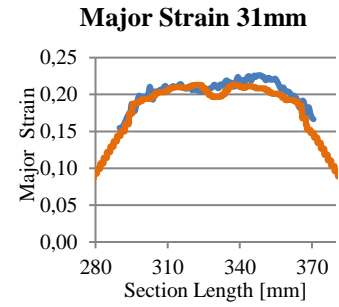
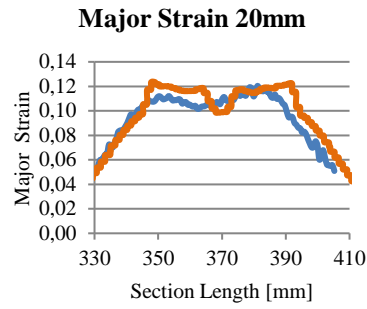
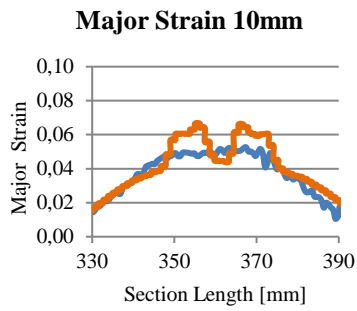
Three time steps were selected for comparison purposes, corresponding to a punch displacement of around 10 mm, 20 mm and 30 mm, as identified in Fig. 4.14 and Fig. 4.15.



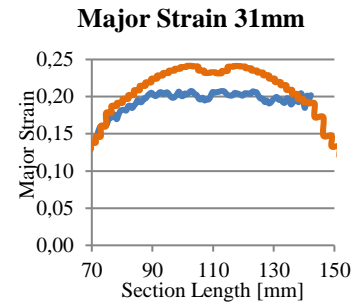
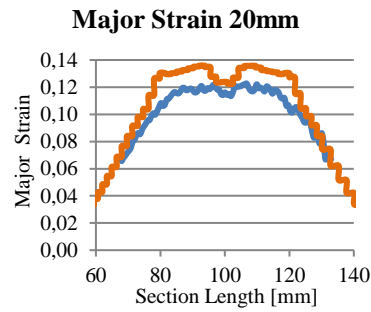
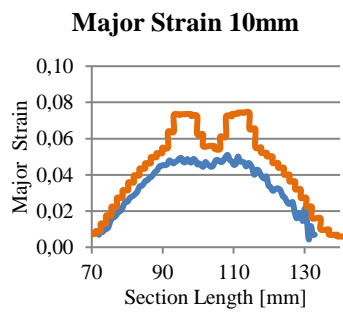
Fig. 4.14 – Different evaluation stages.



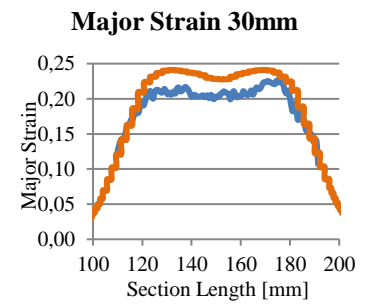
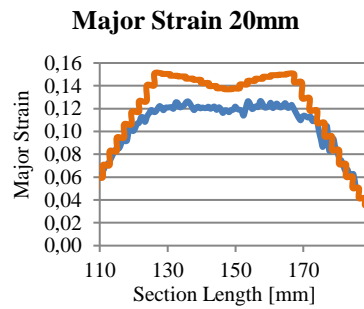
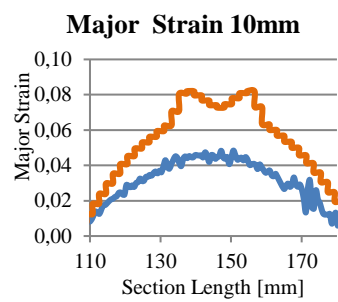
B100



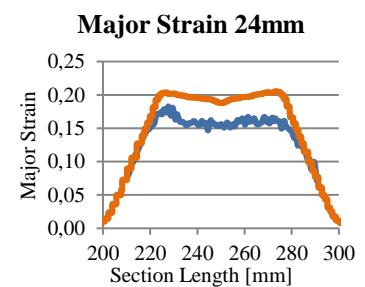
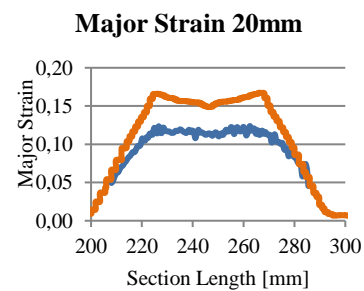
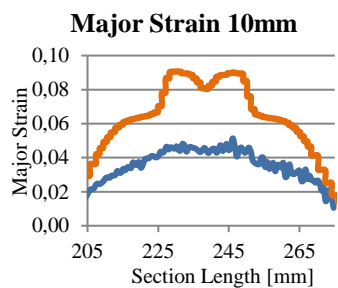
B65



B30



B20



— Numerical Major Strain Profile      — Experimental Major Strain Profile

Fig. 4.15 – Comparison between experimental and numerical major strain distribution, in the same cross-section, to all specimen's geometries.

At the first time step (i.e. at about 10 mm of punch displacement) the experimental major strains are always lower than the numerical major strains. Moreover, this difference is larger for the narrower specimens b30 and b20. Such behavior can be explained by the existence of pre-strain that is not taken into account equally in the experimental and numerical simulations. In fact, the cameras just began recording the Nakazima test after the blankholder closing, and so the reference configuration was not effectively the initially one. In fact, the blankholder closing introduces some pre-strains in the sample, which is more pronounced in case of the narrower samples. As the punch displacement increases the experimental and numerical values close up. The better correlation is achieved for the larger punch displacement.

## Formability

Sheet metal forming simulation is undoubtedly a valuable support for the development of manufacturable sheet metal parts. During this process, the evaluation of part and process feasibility is strongly dependent on the formability study, which can predict the risk of ruptures and/or splits, the wrinkling tendency and zones of insufficient stretching. However, this study can only be done with the Forming Limit Diagram if the FLC is available. In general, experimental FLC's are more reliable than mathematical FLC's. As mentioned before, because of the phenomenon of progressive tearing failure in the narrower specimens, the experimental results were unstable. This failure mode is caused by the combination of sheet thickness and the position of the edge of the specimen according to the die radius. As observed by Pepelnjak and Barisic (2009), for sheet thicknesses below 0.4mm the undesired tearing take place in the specimens defining the left-hand side of the FLD. Therefore, a mathematical FLC was used for the formability assessment of Hybrix. For each layer, the FLC was automatically generated by the software based on the thickness and the hardening coefficient of the material. The analytical method behind this FLC approximation was developed by Keeler and Brazier (1977).

The average of maximal punch displacements in the experimental Nakazima tests is used as a reference for each geometry, and compared with numerical results for the same conditions. The real critical points were compared with the critical zones in the simulation and marked in blue. Other critical zones in the simulation were marked in red [ Fig. 4.16-Fig. 4.20].

Upper Skin

FLD

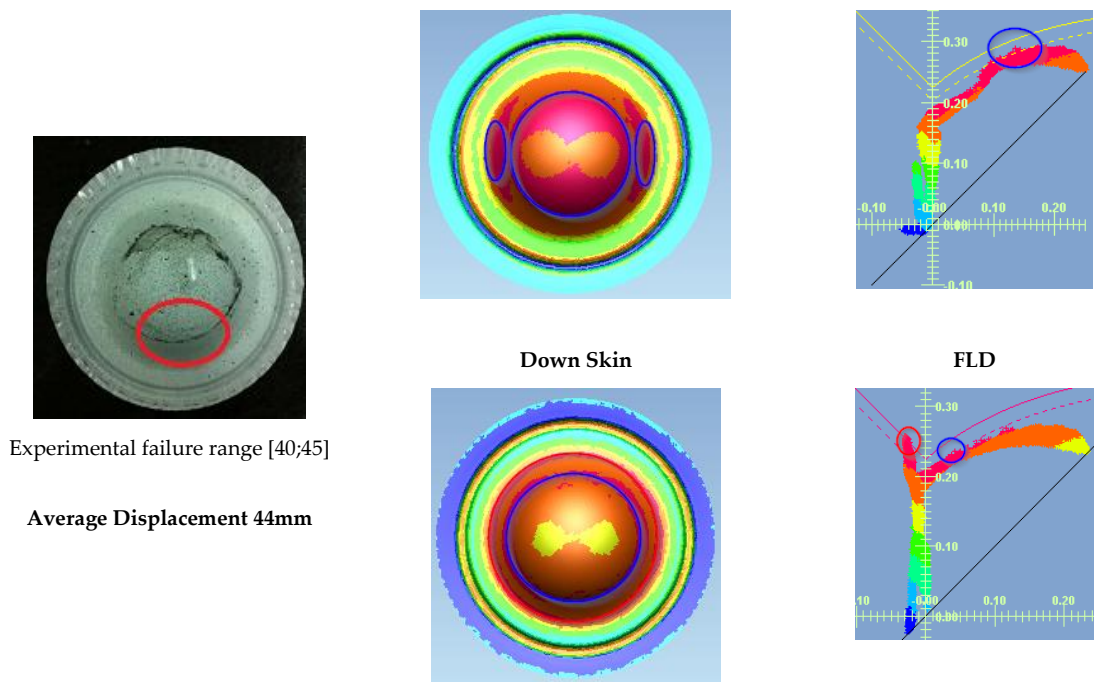


Fig. 4.16 – Comparison between numerical and real formability results in the specimen b180 to 44mm of punch displacement.

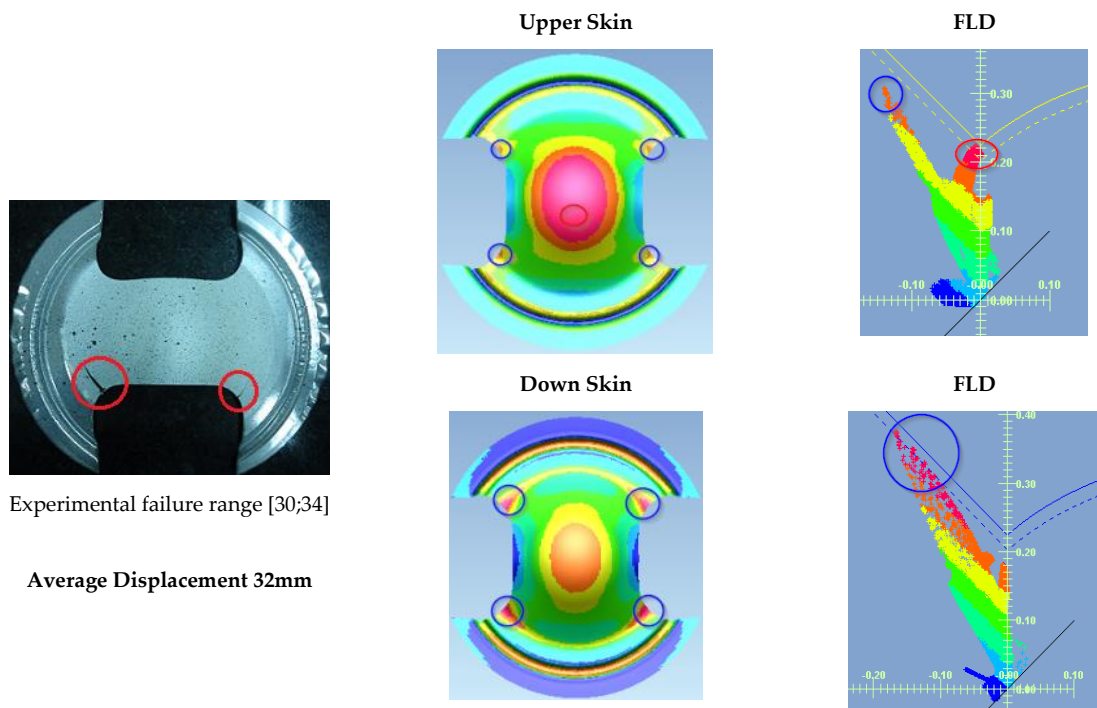
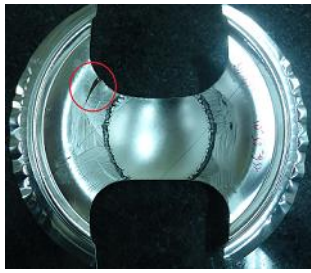


Fig. 4.17 – Comparison between numerical and real formability results in the specimen b100 to 32mm of punch displacement.

Upper Skin

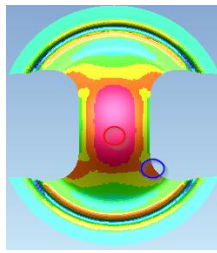
FLD



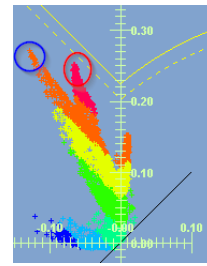
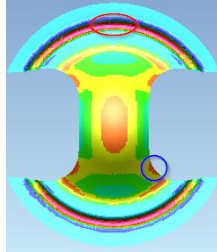


Experimental failure range [30;33]

Average Displacement 32mm



Down Skin



FLD

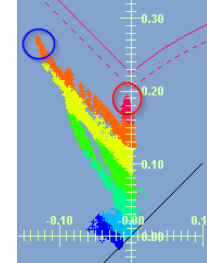


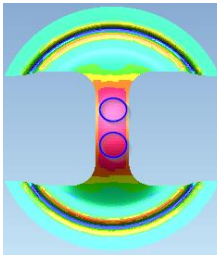
Fig. 4.18 – Comparison between numerical and real formability results in the specimen b65 to 32mm of punch displacement.



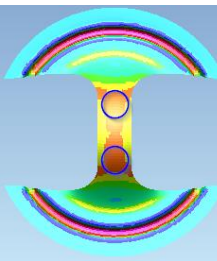
Experimental failure range [30;33]

Average Displacement 31mm

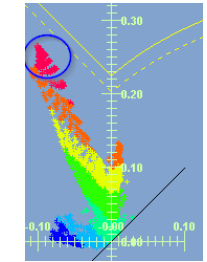
Upper Skin



Down Skin



FLD



FLD

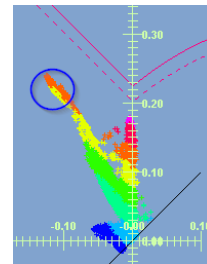


Fig. 4.19 – Comparison between numerical and real formability results in the specimen b30 to 31mm of punch displacement.

Upper Skin

FLD

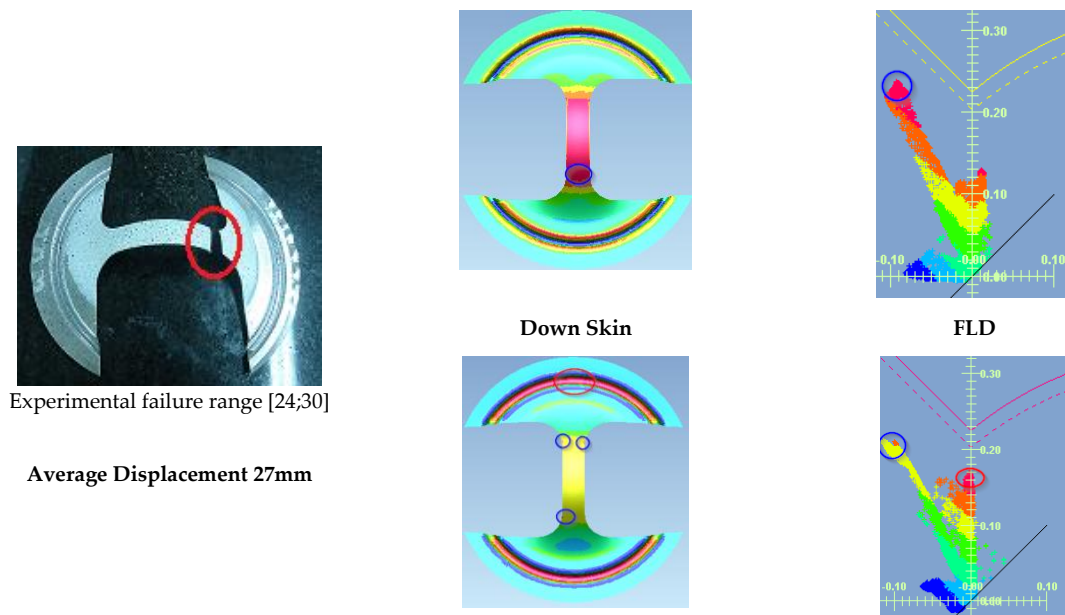


Fig. 4.20 – Comparison between numerical and real formability results in the specimen b20 to 27mm of punch displacement.

Hot spots can be easily detected in the FLD. The critical zones must be analyzed in both upper and bottom skins in order to obtain an accurate prediction of the specimen failure. In case of specimens b20 and b30, the FLC cannot predict the exact moment (punch displacement) of the specimens' failure. As shown in Fig. 4.19 and Fig. 4.20, the cloud of points is still above the FLC, i.e. on the safety region, at the maximum experimental punch displacement. However, in these cases the tearing phenomenon is the mechanism responsible for failure. For these very thin sheets, the geometry of the specimens, the size effects and any micro-defect in the contour (due to the specimens cutting process, for example) can lead to a micro-crack, and early propagation and rupture. So, this Keeler FLC can be still correct and useful. In fact, for many stamping processes, cutting and trimming operations occur only after the stamping operations.

In summary, for general applications, the results shown above shows that this numerical model predicts accurately critical zones and points of rupture.

## HYBRIX: CONCLUSIONS

A simple methodology for experimental characterization of an advanced micro-sandwich material was presented. The method is based on uniaxial tensile tests commonly used for the characterization of metallic sheets. The unknown mechanical behavior of the core was deduced from the overall mechanical behavior of both the Hybrix and of the single metallic skins.

The uniaxial tests performed with total Hybrix specimens did not lead to reliable elastic properties. Nakazima tests allowed to adjust the Hybrix's Young modulus to achieve better results. However, Nakazima tests were not very effective to obtain Hybrix FLC. The fact that metallic skins

are too thin, combined with the shape of the specimens, result in tearing failure outside the central area of the specimens, which define the left-hand side of the FLD. In order to eliminate the tearing effect observed in Hybrix the specimens redesign should be considered.

Conclusively, the good correlation between the numerical results and the experimental results in terms of forming forces, major strain distribution and general formability, proves that the proposed methodology is appropriate and functional to develop accurate numerical models for the modeling and simulation of micro-sandwich materials.

## ACKNOWLEDGMENTS

The authors greatly acknowledge the financial support of “Fundação para a Ciência e Tecnologia” (FCT – Portugal), through the research project SFRH/BDE/51189/2010 (“Development FEA Tools Applied to Sheet Forming Special Cases. Application to the Automotive Industry, Advanced Metallic Materials and Multi-Layer and Multi-Material Sheets”) in partnership with Sodécia Tecnical Center (Maia, Portugal). The authors would also like to thank the company Lamera AB (Sweden), for providing the Hybrix material, and ESI GROUP to the technical support with PamStamp 2G 2012.2 and collaboration in this study.

## REFERENCES

1. Banabic, D. (2010). *Sheet Metal Forming Processes: Constitutive Modelling and Numerical Simulation*, first Ed., Springer, ISBN: 978-3-540-88112-4, pp.45-52. Doi: 10.1007/978-3-540-88113-1
2. Chen, F.K. Shih, W.C. Tu, K.Y. (2009), “Micro-bending of thin stainless steel sheets”, *6<sup>th</sup> International Conference on Multi-Material Micro Manufacture*, pp. 337 – 340. Doi:10.3850/4M2009RP001\_9070
3. Crolla, D. (2015). *Encyclopedia of Automotive Engineering*. In: Palkowski, H. Sokolova, O.A. Carradó, A. “Materials and Manufacturing” - Sandwich Materials, pp.1-17. Online © 2014 John Wiley & Sons, Ltd. Doi: 10.1002/9781118354179.auto163
4. Diehl, A. Staud, D. Engel, U. (2008) “Investigation of the mechanical behaviour of thin metal sheets using the hydraulic bulge test” *Proceedings of the 4th International Conference “Multi-Material Micro Manufacture” 4M’2008*, Cardiff, 2008, pp. 195-198.
5. Elaheh Ghassemieh (2011). “Materials in Automotive Application, State of the Art and Prospects, New Trends and Developments in Automotive Industry”, Prof. Marcello Chiaberge (Ed.), ISBN: 978-953-307-999-8, InTech, Doi: 10.5772/13286.
6. Engelmark, M. (2009) “Usability Evaluation of the Fibrous Core Sandwich Material Hybrix for Automobile Body Applications”. *Master of Science Thesis Stockholm, Sweden*, pp.5,6
7. Geiger, M. Mebner, A. and Engel, U. (1997), “Production of microparts-size effects in bulk metal forming”, *Similarity theory, Production Engineering*, Vol. 4 (1), pp. 55–58.
8. Hoffmann, H. and Hong, S. (2006) “Tensile test of very thin sheet metal and determination of flow stress considering the scaling effect”. *CIRP Annals - Manufacturing Technology*, Vol.55 (1), 263–266
9. Jackson, K.P. Allwood, J.M. Landert, M. (2008) “Incremental forming of sandwich panels”. *Journal of Materials Processing Technology*, vol. 204, pp. 290–303
10. Keeler, S.P., Brazier, W.G., (1977) “Relationship between laboratory material characterization and press-shop formability.” *Microalloying*, vol. 75, Union Carbide, pp. 517–530

11. Luzin, V. Banovic, S. Gnäupel-Herold, T. Prask, H. Ricker, R.E. (2005) "Measurement and Calculation of Elastic Properties in Low Carbon Steel Sheet", *Materials Science Forum*, Vol 495-497, pp. 1591-1596.
12. Mann, D. (1999). "Automotive Plastics & Composites - Worldwide Markets & Trends to 2007", second ed. Elsevier, pp. 90
13. Moreira, RAS. Sousa, RJA. Valente, RAF. (2010) "A solid shell layerwise finite element for non-linear geometric and material analysis". *Composite Structures*; 92:15 7–23.
14. Palkowski, H. and Lange, G. (2005) "Ame Austenitic Sandwich Materials in the Focus of Research", *Metallurgija – Journal of Metallurgy*, vol. 11, pp. 215-224
15. Pauchard, A. (2009) "Precise thin metal cutting using the Laser MicroJet" *Laser in der Elektronikproduktion & Feinwerkstechnik*, 15 (2009), pp. 145–156
16. Pepelnjak, T. and Barisic, B. (2009) "Computer-assisted engineering determination of the formability limit for thin sheet metals by a modified Marciniak method," *J. Strain Analysis*, 44 (1), 459-472. Doi:10.1243/03093247JSA503
17. Starman, B. Vrh, M. Halilovič, M. Štok, B., (2014) "Advanced Modelling of Sheet Metal Forming Considering Anisotropy and Young's Modulus Evolution" *Journal of Mechanical Engineering* Vol.60, No 2, 84-92, Doi:10.5545/sv-jme.2013.1349.
18. Van Den Boscha, M.J. Schreursa, P.J.G. Geersa, M.G.D. (2009) "On the prediction of delamination during deep-drawing of polymer coated metal sheet", *Journal of Materials Processing Technology*, vol. 209 pp. 297–302. Doi: 10.1016/j.jmatprotec.2008.02.024

#### WEB REFERENCES

1. jtmconsultancy, 2015. <https://www.jtmconsultancy.nl>
2. TSE, 2014. <https://www.thyssenkrupp-steel-europe.com/en/press/press-releases/press-release-6552.html>

## 5. ARTIGO 4: “Modelling Strategies and FEM Approaches to Characterize Micro-Sandwich Sheets with Unknown Core Properties”

**A.M. Pimentel, J.L. Alves, N.M. Merendeiro, T. Soares**

Anthony Michael Fernandes Pimentel<sup>a,b,\*</sup>

\*E-mail: anthony.pimentel@ct.sodecia.com \ anthony.pimentel@dep.uminho.pt

José Luís de Carvalho Martins Alves<sup>b</sup>

Nuno Miguel de Seabra Merendeiro<sup>a, 5</sup>

Tiago Soares<sup>a</sup>

<sup>a</sup> Sodecia Product Competence Center, Rua Eng.º Frederico Ulrich, 2650, 4470-605 Maia, Portugal

<sup>b</sup> Departamento de Engenharia Mecânica, Escola de Engenharia da Universidade do Minho, Campus de Azurém 4800-058 Guimarães, Portugal

---

<sup>5</sup> Present Adress - Sodecia-participações Sociais Sgps Sa, Rua do Espido, 164-F, Edifício Via Norte, 4470-177 Maia – Portugal

## **ABSTRACT**

The micro-sandwich sheets with metallic/polymer fibrous core have been pointed out as one of the most promising technological solutions to the automotive industry. However, due to the lack of understanding of certain fundamentals related with the mechanical behavior of micro-sandwich sheets during forming processes, the transfer and scale-up of this promising technology to industry has been limited. A challenging aspect in the experimental characterization of these materials is related with the unknown properties of the composition of the core which consist of metallic (polymer) fibers and adhesive. In general, the suppliers of monolithic metal sheets also make available the respective datasheets with the mechanical and chemical properties. These datasheets use to refer the minimum, maximum or a specific tolerance range (dependent of the grade material) to the mechanical properties. However, the micro-sandwich sheets are not provided with this mechanical and chemical data, at least, for all layers. Therefore, it is missing a simple and robust methodology to supply the mechanical properties of the total micro-sandwich sheet to the industry. Furthermore, there is no study about the different numerical approaches available in the commercial stamping softwares to modelling and simulate micro-sandwich materials.

In this work, a strategy to deduce the unknown mechanical properties of the fibrous core from symmetric or asymmetric micro-sandwich sheets, i.e, with the same or different skin thickness, is presented. For true stress-strain curves and anisotropy purposes, uniaxial tensile tests in 3 different directions, according ISO 6892-1:2009 standard, were performed. Total micro-sandwich specimens and skin specimens were tested. The mechanical properties of the core were deduced from micro-sandwich and skin's mechanical properties. Based on this data, the constitutive model was established. Additionally, 6 different Nakazima geometries were punched according to ISO 12004 for formability assessment. Experimental Forming Limit Curves (FLC) and principal strains data were recorded during the tests thanks to a high-resolution cameras and software GOM ARAMIS. Finally, the experimental mechanical tests were virtually reproduced with both commercial codes AutoForm R5.2 and PAM-STAMP 2G 2015.1. Thus, different modelling strategies and Finite Element Method (FEM) approaches were compared. The excellent agreement between numerical and experimental results demonstrate the accuracy of the applied methodology.

## **KEYWORDS**

Micro-Sandwich Sheets; Formability; AutoForm R5.2; PAM-STAMP 2015.1; Automotive Industry

## INTRODUCTION

Lighter vehicles, lower fuel consumption and cost-efficient recyclability are the major guidelines of the today's automotive industry. Such new framework has been the opportunity for the introduction of new lighter and challenging materials, such as alternative metals and composites, which have been at the heart of the research and innovation in order to develop and introduce in the market the lighter and more environmentally friendly future vehicles [1, 2].

In terms of new advanced materials, multilayer materials, usually known as sandwich, are currently one of the most promising technological solutions [3]. Due to its multilayer structure and multi-material nature, this kind of material can be designed with unique mechanical properties, and optimized for very special applications [4-7]. The sandwich concept is not new since it has been used for years in the aeronautic and construction industries for lightweight structures as presented by [8]. However, the fact that this concept has been applied to very thin metallic sheet layers, which can be shaped by conventional stamping processes, makes their application very attractive and technologically challenging. These multilayer materials are also called as micro-sandwich, since they are usually much thinner and lighter than the traditional sandwich materials.

These sheets are usually made by a polymeric soft core (as epoxy, polyethylene and polypropylene resins or rubber) covered by two metallic skins (commonly, steel or aluminum alloys). The research of micro-sandwich sheets in fields such Numerical Simulation in [4, 9], Experimental Characterization in [10-14]; Forming Processes in [15-17]; Structural Mechanics in [5,6]; has grown a lot lately contributing to the success in the development of some automotive parts. For instance, the aluminum micro-sandwich *Hylite* was applied in automotive parts as bonnets, roof panels and hoods. Some examples are the NedCar Access (1996), the Aixam 400 (1997), the Ford e-Ka (2000) and the Audi A2 (2000) ([8, 18, 19]). Concerning the steel micro-sandwiches, Volkswagen is using the *LITECORE* micro-sandwich, developed and produced in partnership with ThyssenKrupp Steel Europe, to the production of a super lightweight hood for the Polo R WRC (2014) ([20]).

As referred by [21], the soft core can also contain fibers, metallic or not. In the metallic fibers family, many types have been developed, e.g. stainless-steel fibers, nickel fibers, aluminum alloys fibers, and iron inter metallic fibers, *etc.* The latest development in micro-sandwich materials is related with metal fibers porous materials. Volvo Car Corporation is the first institute to research and apply metal fiber porous sandwich structure, which developed the ultra-light stainless-steel sheet using sandwich structure (HSSA – Hybrid Stainless Steel Assembly) ([22, 23]).

HSSA is lighter and has higher stiffness than aluminium, as stated in [24] its energy absorption capacity is 50% - 60% higher than solid metal plates and is about 10 times that of aluminum foam at



the same porosity. According to [25], its formability and weldability are comparable with those of conventional monolithic metallic sheets

In the preparation of metal fiber sandwich material research, Massachusetts Institute of Technology and Cambridge have developed two kinds of sandwich preparation methods: CAMBOSS (Cambridge Bonded Steel Sheets) and CAMBRASS (Cambridge Brazed Steel Sheets). The difference between CAMBOSS and CAMBRASS is the combination method of plates and metal fiber material, the former uses bonding method and the latter uses brazing method, as explained in [26]. The result is different core structures as depicted in Fig. 5.1.

Several authors such as [26] and [27] investigated mechanical behavior of HSSA. [28] presented 3 different HSSA core structures and demonstrated their relationship with the mechanical and electrical properties of the micro-sandwich [30].

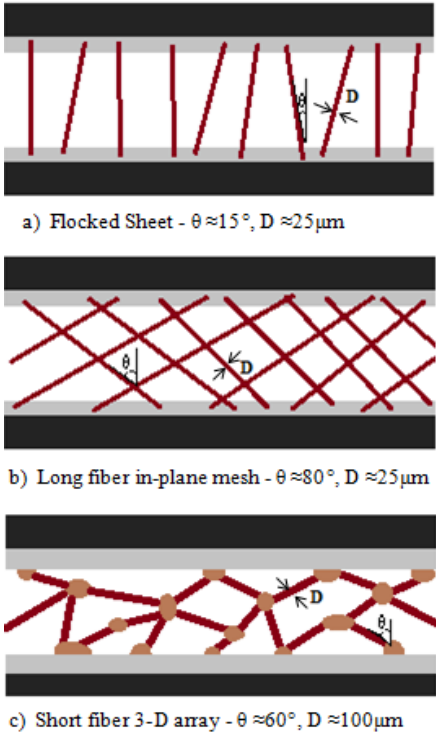


Fig. 5.1 – Different mesh structures (Single fiber angle  $\theta$  [°], Single fiber diameter  $D$  [ $\mu\text{m}$ ] and fiber volume fraction  $f$  [%]). a) CAMBOSS, b) CAMBOSS, c) CAMBRASS.

The fiber volume fraction of the core structure and the characteristics of each single fiber (diameter, angle and length) play an important role in the through-thickness stiffness, through-thickness yield stress and interfacial fracture energy. But, these mechanical parameters need very specific experimental equipments and procedures to be measured [28]. On the other hand, considering a numerical model that includes the fiber core of the micro-sandwich sheet in the

stamping simulation of an automotive part would be too much expensive. These aspects render difficult to understand the mechanical behavior of HSSA's.

In this study, *Hybrix* was taken as an example of HSSA. *Hybrix* was born out of a partnership between Lamera AB, a spin-off company from Volvo, and Chalmers University. The *Hybrix* core consists of millions of microscopic metallic/polymeric fibers vertically oriented against the stainless-steel skins and bounded by an epoxy resin. Regarding the metallic skins, the most common stainless-steel grades are the 301 and 304. In this case, AISI 304L covers were included in the micro-sandwich system as depicted in Fig. 5.2.



Fig. 5.2 – Scheme of the *Hybrix* micro-sandwich sheet material, comprising two stainless steel layers and an intermediate composite core (metallic/polymeric fibers embedded in an epoxy resin).

The *Hybrix* micro-sandwich sheets can display several skin/core thickness combinations, with symmetric or asymmetric configurations, depending on whether or not the nominal skin thickness is the same. The experimental results presented in this work includes 3 different sets of *Hybrix* with different nominal thicknesses (1mm and 1.6mm) and different configurations (symmetric and asymmetric). Because of its excellent strength and ductility, stainless steel is commonly used in deep drawing parts. Therefore, micro-sandwich covers made of austenitic stainless-steel grades make *Hybrix* sheets well suited to be shaped in sheet forming operations, and very promising to be used in automotive industry.

Several sheet metal stamping cases were experimentally tested by [29]: the experimental results explored by this author put in to evidence a high risk of wrinkles in case of deep drawn parts, which is a major concern to the stamping process robustness. [30] Also tried to shape *Hybrix* sheets with incremental forming, but the fibrous core did not resist to delamination mode failure, i.e. separation between the composite polymeric core and the metallic skins. Thus, the trend to wrinkling and the delamination failure have been pointed as the major concerns of the formability of these micro-sandwiches. Meanwhile, many ground elements of *Hybrix* were improved. [31] conducted some dynamic mechanical thermal analysis (DMTA) tests on different versions of *Hybrix*, regarding the adhesive core composition. Comparing with the older versions, no delamination was observed to

the newer version of Hybrix, which presented a significant improvement of the bending stiffness.

The global mechanical behavior of sandwich materials is obviously related with the thicknesses and mechanical behavior of each layer. Moreover, [8] observed that the difficulties in the deep drawing process of sandwich system dwells from the different behavior of the layer materials. Nevertheless, it is not quite enough to understand the mechanical behavior of each layer individually given that the global behavior is also driven by the interaction between layers. Moreover, when very thin skins are considered, such as the ones on the micro-sandwich materials, the mechanical properties can change and new constitutive model parameters are needed to accurately describe the formability and springback phenomena as mentioned in [32]. [33] compared several experimental techniques to measure the Young's modulus of very thin specimens and it was observed that the conventional mechanical tests are not suited to measure accurately the elastic properties. On the other hand, the manufacture process of multilayer sheets, even if well controlled, always introduces some variability of material properties and bounding conditions that affects the quality of the stamped parts. As observed by [34], both manufacture and stamping processes contributes to delamination and debonding of multilayer materials affecting its formability.

Thus, to adapt the conventional sheet forming processes to the features and mechanical behavior of Hybrix sheets, it is absolutely paramount to carry out their experimental characterization beforehand. Such information is crucial to build robust numerical models to design the forming processes in order to provide reliable and accurate results.

However, the experimental characterization of the Hybrix materials is not a simple task. For instance, the chosen process to cut the testing specimens affects the experimental results. In case of laser cutting, one must consider the fusion and burning of the micro-sandwich polymeric cores, the heat affected zone in the metallic skins and the presence of burrs along the contour. In case of water jet cutting, the core adhesive properties can be seriously affected by the process due to the epoxy resin hygroscopicity. In order to avoid such drawbacks and obtain a better cutting quality surface the Laser Microjet technique could be a very feasible option as referred in [35]. Moreover, the experimental tests to identify the mechanical properties of a composite core are very specific. In these cases, [36] mentions that the formability is strongly dependent of intrinsic properties (as macroscopic structure, bond type, crystalline structure) or extrinsic properties (such microporous size and distribution, microcracks, initial stress states, etc) which are not easy to measure when compared with the common mechanical properties (as the elongation, yield strength, tensile strength, hardness, etc.) of the monolithic metal sheets. In addition, the constitutive models to model and describe the mechanical behavior of composite materials are complex and not yet completely implemented in the commercial FE codes dedicated to sheet forming simulation. The description of the non-linear mechanical behavior of the composite materials is much more complex than the ordinary monolithic

sheets (so common in the automotive industry). The behavior of the composite is a function of the proportion of the total volume and morphologic distribution of the compounding substances. So, microscopic constitutive models are more suitable to describe correctly the mechanical behavior of this kind of materials. In the case of phenomenological constitutive models, the mixing theory is also commonly used to simulate the behavior of composite materials. However, this model requires input parameters that are experimentally determined via large number of time-consuming tests. As mentioned by [37] if, for example, the volume fraction of fibers is changed we have a different material and new series of experiments on this new material are required. The fiber/matrix composites show a non-linear behavior, sometimes, with significant strain softening under cyclic loading. Moreover, the debonding effects that take place into the composite core or the delamination effect that take place between the layers of the composite are not always easy to define through experimental parameters that can be converted into constitutive parameters. Concerning the stamping simulation, commercial FE codes like AutoForm and PAM-STAMP are only just getting off the ground with the multilayer materials.

This work deals with the experimental characterization and numerical modeling of the mechanical behavior of micro-sandwich sheets. The main goal is to present and validate a very simple and expedite methodology to characterize the mechanical behavior of an advanced micro-sandwich material. The formability of symmetric and asymmetric configurations is compared. Uniaxial tensile tests were performed on specimens oriented along 3 different orientations with respect to the rolling direction, in order to characterize the isotropic hardening and anisotropy, and the Nakazima tests were performed to characterize the FLC for preliminary validation test purposes. Multilayer and Monolayer models based in both, 2D and 3D, FEM approaches are compared. In the multilayer modelling strategy, different mechanical properties are assumed for the skins and the core. On the other hand, the monolayer modelling strategy considers a single-layer with macro-mechanical properties estimated as a weighted average of the core's and skin's mechanical properties. Thus, single-layered meshes of 3D Bricks or 2D Shells can be used, considering a homogeneous material equivalent to the sandwich system. To include the mechanical properties of each layer separately, multilayer finite element meshes must be built with 3D Bricks or 2D Shells. If allowed by the FE code, the 2D Shells finite mesh is defined in the plane and the number of layers through the thickness. The numerical models to validate this methodology were created and tested with the commercial softwares PAM-STAMP 2G 2015.1 (2D and 3D models) and AutoForm R5.2 (only 2D models). For a deep understanding of geometric asymmetries in the formability of micro-sandwich sheets, the experimental and numerical results to both geometric configurations, symmetric and asymmetric, are exhaustively compared in this study. The different modelling strategies and FEM approaches developed in this study to describe the mechanical behavior of the

Hybrix micro-sandwich sheets are depicted in the Fig. 5.3.


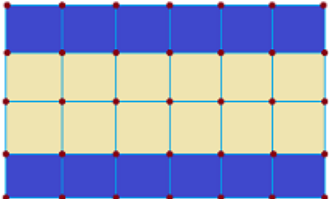
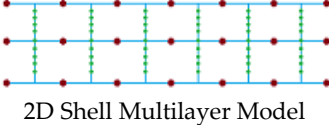



Micro-Sandwich	Modelling Strategy	FEM Approach	FEA CODE
HYBRIX	 Multilayer Multi-Material	 3D Bricks Multilayer Model	PAM-STAMP 2G 2015.1
		 2D Shell Multilayer Model	PAM-STAMP 2G 2015.1 AutoForm R5.2
	 Monolayer Monolithic	 3D Bricks Monolithic Model	PAM-STAMP 2G 2015.1
		 2D Shell Monolithic Model	PAM-STAMP 2G 2015.1 AutoForm R5.2

Fig. 5.3 – Presentation of the different strategies and approaches used in this study to characterize, modelling and simulate micro-sandwich Hybrix sheets with unknown core properties.

**HYBRIX: EXPERIMENTAL CHARACTERIZATION AND CONSTITUTIVE MODELLING METHODOLOGY**

The aim of this section is to present the results concerning the experimental characterization of the Hybrix sandwich material, in order to determine the constitutive parameters required for the numerical modeling and numerical simulation. The experimental data must be enough to define the **hardening curve**, the **yield criterion** and the **forming limit curve (FLC)**. The material model is a paramount aspect to take into account in the numerical simulation of the sheet forming processes; since it rules the mechanical behavior of the micro-sandwich materials, the reliability and accuracy of the numerical results depend on it. As mentioned above, for comparison purposes, two modelling strategies were adopted. In this study, the first is called “monolithic” and assumes that all the micro-sandwich is compound by an homogeneous and continuous material. The other is called “multilayer” because it assumes different materials for the skins and the core, however, the composite fibrous core is considered itself as monolithic [Fig. 5.3].

**Uniaxial Tensile Tests**

Uniaxial tensile tests, commonly used in case of metallic sheets, are able to provide all the relevant experimental data to characterize the **hardening curve** and the **yield surface**. Through the

force-displacement curves it is possible to establish the true stress-strain relationship, and thus to characterize the isotropic hardening curve. Tensile tests carried out for several orientations with respect to the rolling direction are required to characterize the anisotropic behavior and the yield surface. Since Hybrix is a multilayer material, uniaxial tensile tests can be performed either on the complete micro-sandwich structure or on only the external metallic skins: in what follows both cases, i.e. the complete and skin-only specimens, will be presented and analyzed. Such procedure was adopted in order to isolate and understand the contribution of the fiber /polymeric core to the overall mechanical behavior of the Hybrix sandwich material.

To describe numerically the mechanical behavior of a given material it is mandatory to use suitable constitutive models, i.e. flexible enough physically-based laws, and to identify a set of appropriate constitutive parameters. When it concerns to micro-sandwich materials, to know beforehand the constitutive parameters for each material layer, may not be enough or possible. Even when the fiber/matrix composite core is assumed as homogenous and suitable constitutive models (elastoplastic, viscoelastic, hyperelastic, etc.,) exist to describe its mechanical behavior, identifying the correct constitutive parameters through experimental tests can be very challenging. In certain cases, the experimental characterization of skins and composite core, separately, is not enough to guarantee that the mechanical behavior of the sandwich accurately described (since the mechanical behavior in the bonded interfaces and the effect of the interaction on each other are unknown). Thus, it is necessary to follow a different strategy which will allow “determining” the unknown constitutive parameters of the composite material. In case of the Hybrix material, two AISI 304L stainless steel skins are spaced and bonded by an adhesive epoxy resin impregnated with metallic/polymeric micro fibers, which constitutes the core’s material. The core’s material is a complex composite material, and no experimental data is available for it. The new strategy followed in this work aims at deducting the mechanical properties of the core’s material from the previously identified experimental behavior of the total Hybrix material and the single metallic skins. The assumption behind this strategy is that the total force measured during the uniaxial tensile test of the Hybrix material is the sum of the forces supported by the two skins plus the force supported by the core, as schematically shown in Fig. 5.4.

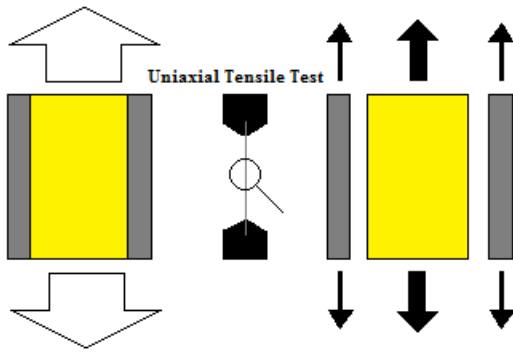


Fig. 5.4 – Decomposition load strategy of Hybrix. The 3 layers (2 metallic skins plus the core) are loaded in parallel during the uniaxial tensile test, and thus the total uniaxial tensile force can be decomposed in two components, the forces supported by the two metallic skins plus the force supported by the core.

The composite fibrous core is hereafter assumed as a non-isotropic homogeneous material with unknown mechanical properties. Then, it is possible to use the experimental tensile data of both the total Hybrix and the metallic skins to deduce the force-displacement and true stress-strain curves of the Hybrix core, considering the following relationship

$$F_{Core} = F_{Hybrix} - F_{Skins} \quad (5.1)$$

### Force-Displacement Curves

Taking into account the orientations  $0^\circ$ ,  $45^\circ$  and  $90^\circ$ , with respect to the rolling direction, 5 tensile specimens, of both materials (Hybrix micro-sandwich and AISI 304L skins), were prepared by laser cutting. The Hybrix sheets presented a symmetric configuration with 1mm of nominal thickness, i.e. 0.10mm for each skin and 0.80mm for the composite core. The tensile tests were performed on a conventional screw-driven tension-compression testing machine, following the ISO 6892-1:2009 standard. The length of the uniform zone of the sample was 80mm for a sample width of 12.5mm. The strain was determined from the displacements measured during the uniaxial tensile test by a 50mm gauge extensometer. All experimental force-displacement curves were recorded. Since the experimental measurements showed an excellent repeatability, the uncertainty can be neglected, and the averages values considered reliable. The force-displacement curves were averaged for each orientation and core force-displacement curves deduced using the equation (5.1). The results are presented in the Fig. 5.5 to Fig. 5.7.

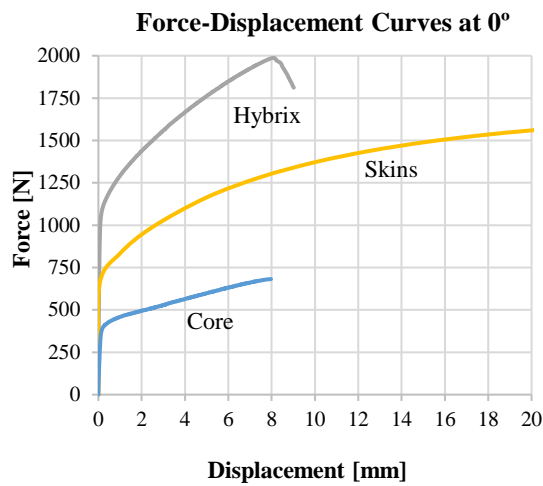


Fig. 5.5 – Experimental average force-displacement curves of Hybrix 1mm, AISI 304L 0.10mm (2 skins sum), and deduced core of 0.80mm at the rolling direction.

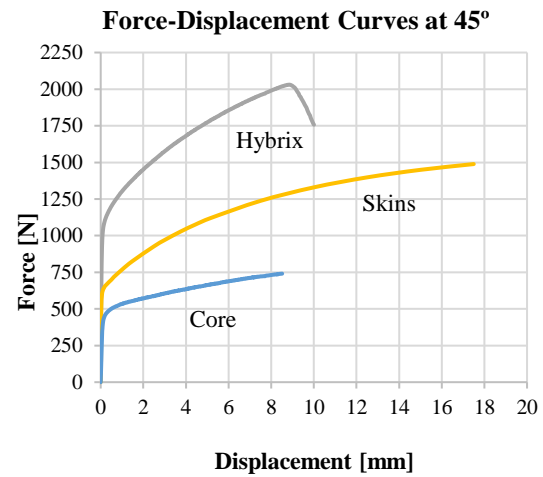


Fig. 5.6 – Experimental average force-displacement curves of Hybrix 1mm, AISI 304L 0.10mm (2 skins sum), and deduced core of 0.80mm at 45° with the rolling direction.

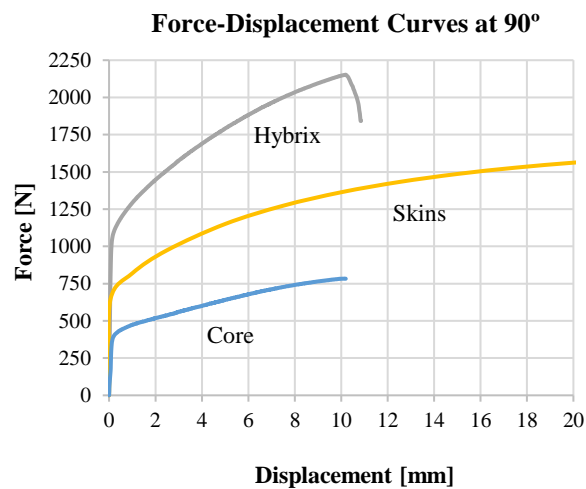


Fig. 5.7 – Experimental average force-displacement curves of Hybrix 1mm, AISI 304L 0.10mm (2 skins sum), and deduced core of 0.80mm at 90° with the rolling direction.

The experimental average force-displacement curves displayed in Fig. 5.5 to Fig. 5.7 shows that the mechanical behavior of the micro-sandwich Hybrix, in large part driven by the AISI304L skins, does not actually vary much with the orientation of the sheet. Even so, the maximum tensile force and its displacement point successively increase from the orientation 0° to 90°.

### True Stress-Strain Curves

Based on the force-displacement curves, the stress-strain relationships were determined as well as the most important tensile properties.



First, the engineering stresses ( $\sigma_\theta$ ) and engineering strains ( $\varepsilon_\theta$ ) are calculated using

$$\sigma_\theta = \frac{F_\theta}{A_0} \quad (5.2)$$

$$\varepsilon_\theta = \frac{\delta_\theta}{L_0} \quad (5.3)$$

where  $F_\theta$  is the load,  $A_0$  is the initial cross-sectional area,  $\delta_\theta$  total elongation,  $L_0$  is the original gauge length and  $\theta$  is the orientation angle related with the rolling direction.

Then, the true stresses ( $\sigma_{T_\theta}$ ) and true strains ( $\varepsilon_{T_\theta}$ )

$$\sigma_{T_\theta} = \sigma_\theta(1 + \varepsilon_\theta) \quad (5.4)$$

$$\varepsilon_{T_\theta} = \ln(1 + \varepsilon_\theta) \quad (5.5)$$

A quick look on the engineering stress–strain curves allows to know some of the most important mechanical properties like the yield strength, ultimate tensile strength and the material elongation. However, these curves haven't a real meaning since they do not consider the cross-section area reduction of the tensile specimen. To that end, the true stress–strain curves are needed. Since the true stress–strain curves are obtained from the engineering stress–strain curves, these are only valid as long as the plastic deformation is uniform, namely, until the ultimate tensile strength.

Fig. 5.8 presents the engineering stress-strain curves and the true stress-strain curves obtained for the Hybrix 1mm, the AISI 304L 0.10mm skin and the deduced core of 0.80mm at the rolling direction.

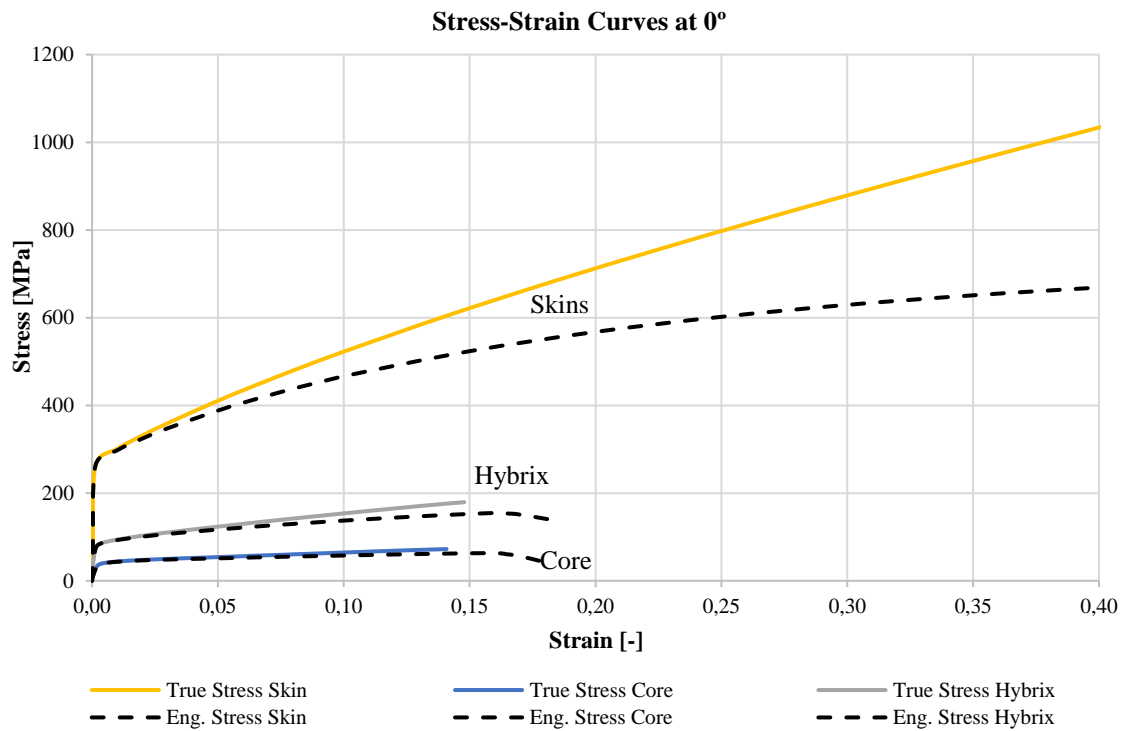
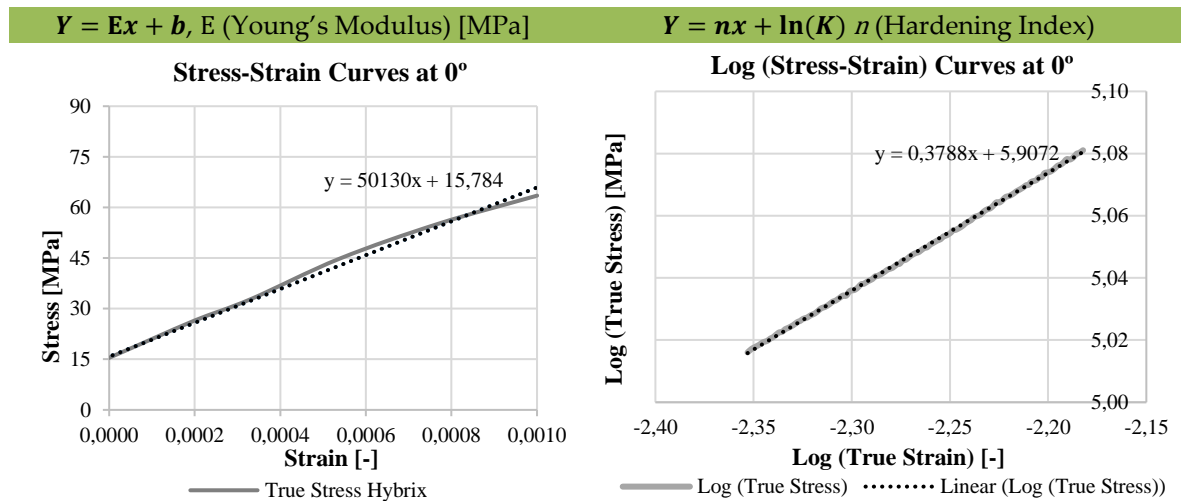


Fig. 5.8 – Engineering stress-strain curves and the true stress-strain curves of the Hybrix 1mm, AISI 304L 0.10mm skin and deduced core of 0.80mm at the rolling direction.

Looking at Fig. 5.8, it is possible to note that the elongation of the micro-sandwich Hybrix (15%) is much less than the stainless skins (around 50%), therefore it is only possible to deduce the behavior of the core to a maximum of 15% of elongation. Since the core matrix is made from an epoxy resin, which has, in general, a very low elongation, it is expected that the total elongation of the micro-sandwich is lower than the annealed stainless skins. Furthermore, it should be taken into account that the cutting process can also result in stress concentration points or even microfissures on the specimen's edges free surfaces that seriously jeopardize the tensile elongation.

Generally, the stress-strain curves can be directly output by the tests machine software when an appropriate extensometer is used. In such cases, the *Young's Modulus*, *Hardening Index*, *Yield* and *Ultimate Tensile Strength* can be automatically obtained. However, this is not possible for the core, since its stress-strain curve was deduced. As such, these properties must be numerically determined. The Young's Modulus  $E$  and Hardening Index  $n$  identification procedure is based on the least squares method. The method is applied to the elastic region of the rolling direction true stress-strain curve to determine  $E$  and applied to the plastic region of the logarithmic form of the rolling direction true stress-strain curve, to obtain the hardening index  $n$  [Fig. 5.9].



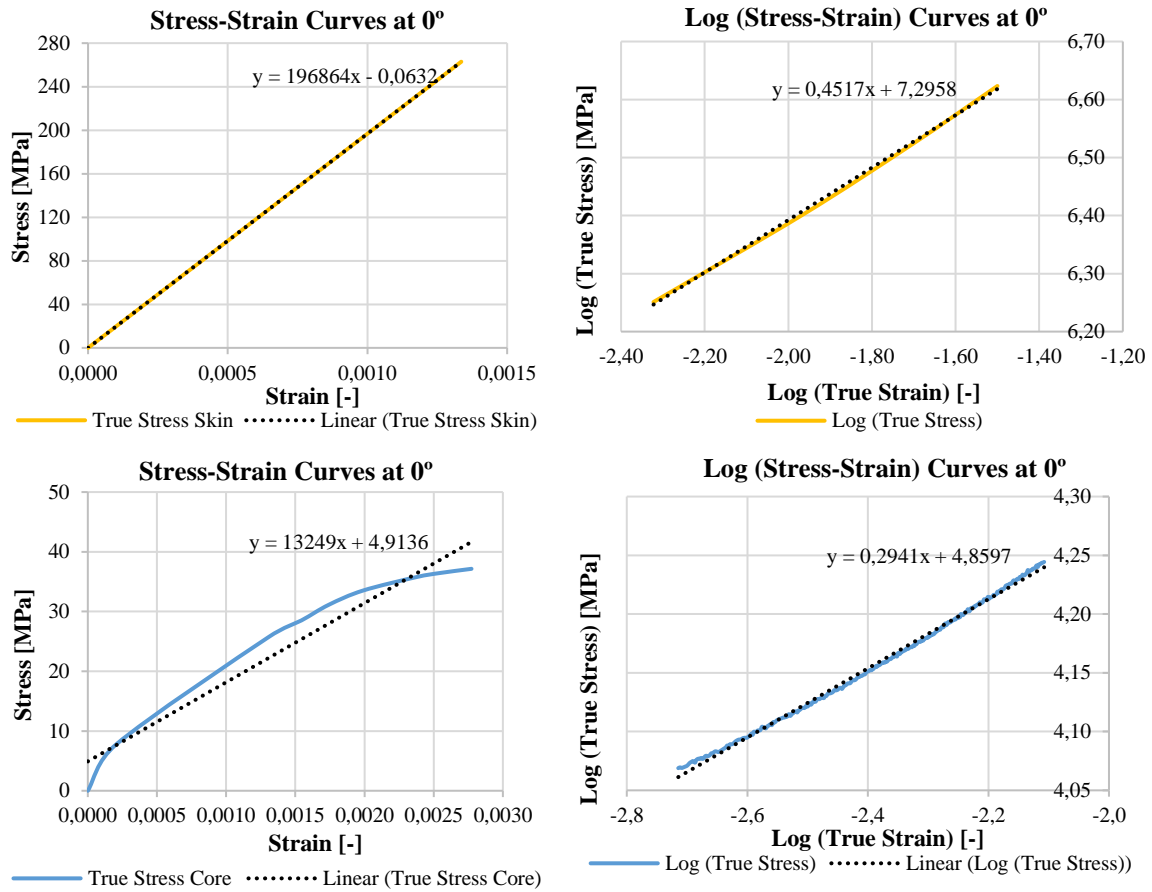


Fig. 5.9 – Presentation of the graphical method (linear regression) to obtain the Young’s Modulus  $E$  and the hardening index  $n$  from the linear trendline equation applied to the true stress-strain curve and the logarithmic true stress-strain curve at rolling direction.

From Fig. 5.9, it should be stressed that the Young’s Modulus obtained from the experimental (Hybrix and skin) and deduced (core) stress–strain curves are very consistent and in line with “the *rule of mixtures*”, frequently used to determine the elastic properties of composite materials [16].

For the core yield stress, a yield proof strength at 0.2% was used as reference, as seen in Fig. 5.10.

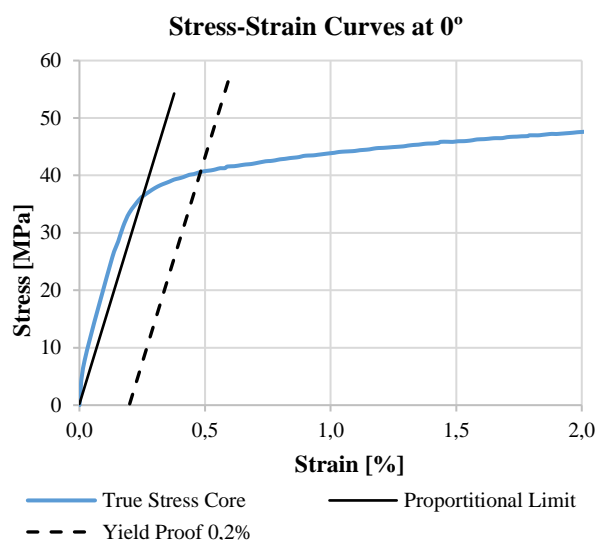


Fig. 5.10 – Yield proof strength determined from the intersection of the true stress-strain curve (rolling direction) and proportional limit curve with an offset strain of 0.2%.

Following the same procedure for the orientations 0°, 45° and 90°, the mechanical properties of the Hybrix micro-sandwich and its layers were determined as presented in Tab. 5.1.

Tab. 5.1 – Presentation of the experimental and deduced values of Young’s Modulus  $E$ , Yield Stress  $Y_s$ , Ultimate Tensile Strength  $T_s$ , percentage of Elongation  $A_{50}$  and Hardening Index  $n$ , for Hybrix micro-sandwich and its independent layers, at the orientations 0°, 45° and 90°.

Layer	Properties in different directions	$Y_s$ , MPa	$T_s$ , MPa	$A_{50}$ , %	$E$ , GPa	$n$
Hybrix	$X_0$	86	153	16	50.1	0.38
	$X_{45}$	94	170	18	58.3	0.39
	$X_{90}$	88	171	21	51.9	0.42
Skin	$X_0$	262	697	52	196.8	0.45
	$X_{45}$	241	629	57	196.1	0.42
	$X_{90}$	258	648	61	197.2	0.41
Core	$X_0$	41	62	-----	13.3	0.29
	$X_{45}$	45	72	-----	18.8	0.25
	$X_{90}$	39	76	-----	14.3	0.33

Once the true stress–strain curves of the Hybrix micro-sandwich and its layers, showed in Fig. 5.8, are valid only for a limited percentage of elongation, a stress-strain relationship able to predict the mechanical behavior for higher levels is needed. This relationship is established by a hardening law.

## Hardening Curves

Several work-hardening constitutive models can be used in order to allow the different

materials' mechanical behavior to be better described: the Swift law or a Voce saturation law to describe the classical isotropic work hardening; a Lemaître and Chaboche type law to model the non-linear kinematic hardening; and Teodosiu's microstructural work-hardening model. The isotropic work hardening models usually provide a good prediction of the true stress–strain curves, demand less experimental data and present less complex material parameter identification procedures. When high strength steels or non-ferrous metallic alloys are considered, non-linear kinematic hardening laws deliver more reliable springback predictions.

The Swift law [38] is expressed by

$$\sigma_S = K(\varepsilon + \varepsilon_0)^n \quad (5.6)$$

where  $K$ ,  $n$ ,  $\varepsilon_0$  are material parameters,  $\sigma_S$  the true stress  $\varepsilon$  the true plastic strain.

When fitted to data for annealed metals or aluminium alloys, power laws can lead to overestimated values, at large strains, since it does not fall away sufficiently rapidly [39]. Thus, Voce type saturation law are commonly preferred to austenitic stainless steels.

The strain hardening law interrelating true stress ( $\sigma_V$ ) and true plastic strain ( $\varepsilon$ ) proposed by Voce [40] is expressed as

$$\sigma_V = B + (B - A)Exp(-p\varepsilon) \quad (5.7)$$

where  $B$  is the saturation stress,  $A$  the true stress at the onset of plastic deformation, and  $p$  is a constant.

Since the annealed metallic skins have a major influence on the mechanical behavior of the Hybrix micro-sandwich, the authors opted for a law that combines Voce and Swift with 6 parameters, such as [41], giving a weight of 80% to the Voce law. The same weighting factor was assigned to the independent layers. This combined law is given by

$$\sigma_{VS} = \alpha \cdot \sigma_V + (1 - \alpha) \cdot \sigma_S \quad (5.8)$$

$\sigma_V$  and  $\sigma_S$  are, respectively, the flow stresses from Voce and Swift. The parameter  $\alpha$  is the weighting factor.

The material parameters  $K$  and  $n$  of the Swift law can be obtained using the logarithmic form of the true stress–strain curve, as shown in Fig. 5.9, while  $\varepsilon_0$  is an estimated pre-strain constant.

The Voce law (Eq. 5.7) can be rearranged to give

$$\text{Ln}(\sigma_V - B) = \text{Ln}(B - A) - p\varepsilon \quad (5.9)$$

which is again a linear expression when  $A$  and  $B$  are constants, and permits the determination of  $p$  from the experimental data by the iterative least squares method when both  $A$  and  $B$  are estimated [42].

The parameters used to generate the Swift-Voce hardening curves are showed below [Tab. 5.2].

Tab. 5.2 – Presentation of the six material parameters and the weighting factor used to generate the Swift-Voce hardening curves of the micro-sandwich Hybrix and its layers.

Layer	Hardening Law Parameters						Weighting Factor $\alpha$
	$K$	Swift $n$	$\epsilon_0$	$A$	Voce $B$	$p$	
Hybrix	370	0.38	0.022	86	300	4.0	0.8
Hybrix Skin	1475	0.45	0.021	262	1500	2.4	0.8
Hybrix Core	129	0.29	0.019	39	120	4.0	0.8

The hardening curves used in the constitutive model of the micro-sandwich Hybrix, of the AISI 304L 0.10mm skins and the 0.80mm deduced core are showed below [Fig. 5.11].

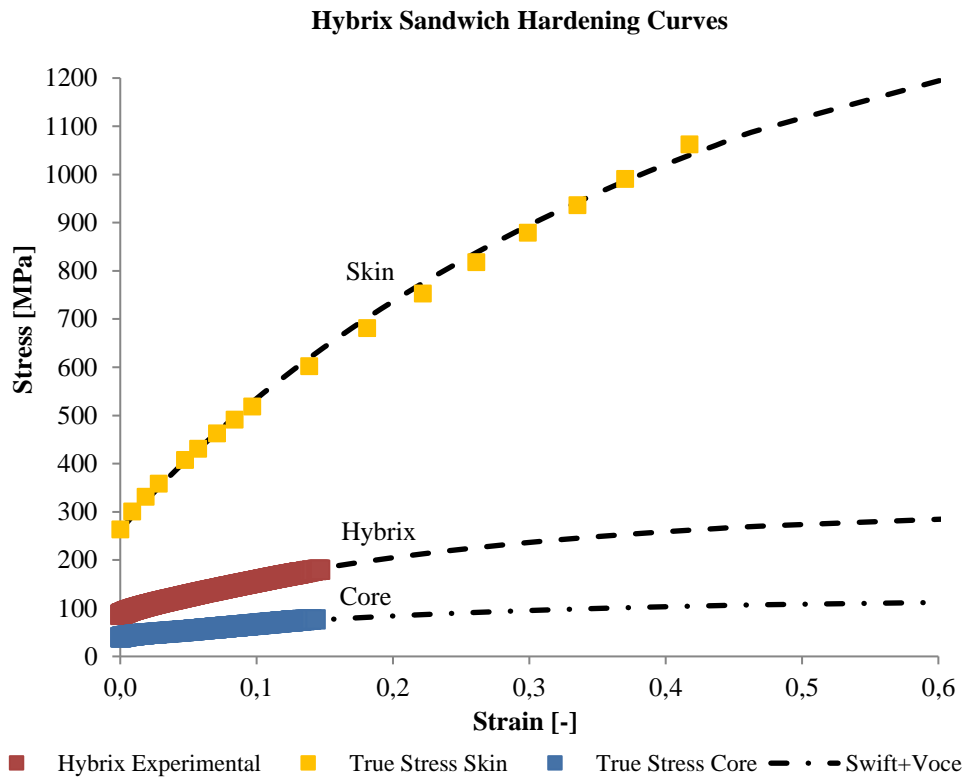


Fig. 5.11 – Experimental hardening curves of Hybrix micro-sandwich and AISI 304L skin, and deduced Hybrix core stress-strain curve, with respective Swift-Voce hardening curves.

## Anisotropy

After determining the true stress-strain relationship it is also necessary to define the **yield criterion** for each layer and for the total Hybrix. Due to the anisotropic behavior of micro-sandwich

[see Tab. 5.1], an **anisotropic yield criterion** must be used. In general, the anisotropy coefficients are determined from the Lankford coefficients, which are experimentally determined from the in-plane strains in the transverse direction and rolling direction. Alternatively, as suggested in the literature [43, 44] the anisotropy characterization was carried out taking into account the anisotropy of the yield stresses instead of the anisotropy of the strains. The multilayer character of the total Hybrix material also justifies this option, given that there is no relation between the in-plane strains measured on the metallic skins and the total thickness strain measured on a total Hybrix specimen.

To the description of the surface of plasticity of the metallic skins the HILL48 anisotropic yield criterion was adopted. This yield criterion is expressed by the following quadratic function,

$$\bar{\sigma}^2 = F(\sigma_{22} - \sigma_{33})^2 + G(\sigma_{33} - \sigma_{11})^2 + H(\sigma_{11} - \sigma_{22})^2 + 2L\sigma_{23}^2 + 2M\sigma_{31}^2 + 2N\sigma_{12}^2 \quad (5.10)$$

where  $\bar{\sigma}$  is the equivalent tensile stress;  $F, G, H, L, M$  and  $N$  are constants specific to the anisotropy of the material, and  $\sigma_{ij}, i, j = 1, 3$  are the stress component of the Cauchy stress tensor. In case of sheet metals, axis 1 is the rolling direction, 2 is the transverse direction and 3 is the normal direction.

Then, it is possible to establish the following mathematical relations between the tensile yield stresses (*normalized* by the tensile uniaxial yield stress in the RD - rolling direction) and the anisotropy parameters [45, 46]

$$\frac{1}{\sigma_0^2} = G + H; \quad \frac{1}{\sigma_{45}^2} = H + F; \quad \frac{1}{\sigma_{90}^2} = F + G; \quad \frac{2}{\sigma_{45}^2} - \frac{1}{2\sigma_{90}^2} = N \quad (5.11)$$

and thus to determine the values of the anisotropy parameters  $F, G, H$  and  $N$ . Tab. 5.3 presents the HILL48 parameters for the Hybrix micro-sandwich and its layers, core and skins.

Tab. 5.3 – Presentation of the HILL48 parameters for the 1mm thick Hybrix micro-sandwich and its layers, core and skins.

Layer	HILL 48 Constitutive Parameters			
	$H$	$F$	$G$	$N$
<i>Hybrix</i>	0.50	0.46	0.50	1.20
<i>Skin</i>	0.50	0.53	0.50	1.85
<i>Core</i>	0.50	0.61	0.50	1.11

This methodology was effective in providing the missing data to model the mechanical behavior of the Hybrix micro-sandwich as a multilayer material. With all the constitutive parameters identified and the “unknown” core stress-strain curve deduced, the material model can be built. At this point, two modelling strategies can be taken: assuming the micro-sandwich sheet as monolayer monolithic or multilayer multi-material [Fig. 5.3]. The next section shows different FEM approaches

(based on 2D or 3D FEM formulations), available in PAM-STAMP 2G 2015.1, to modelling a micro-sandwich Hybrix, simulate the uniaxial tensile test and validate the experimental methodology.

## FEM Models

PAM-STAMP 2G 2015.1 allows to create multilayer meshes and modelling micro-sandwiches materials. Two FEM models were created to build the mesh Hybrix tensile specimen: one based on 3D brick/solid finite elements and the other based in 2D shell finite elements. For the *3D Brick Multilayer Model*, 3D 8-node hexahedral solid finite elements were used. The FE mesh comprises 6 layers of elements, 2 layers for the two exterior metallic skins and 4 layers for the composite core. For the *2D Shell Multilayer Model*, 4-node quadrilateral shell finite elements were used. The two meshes created are represented in the Fig. 5.12.

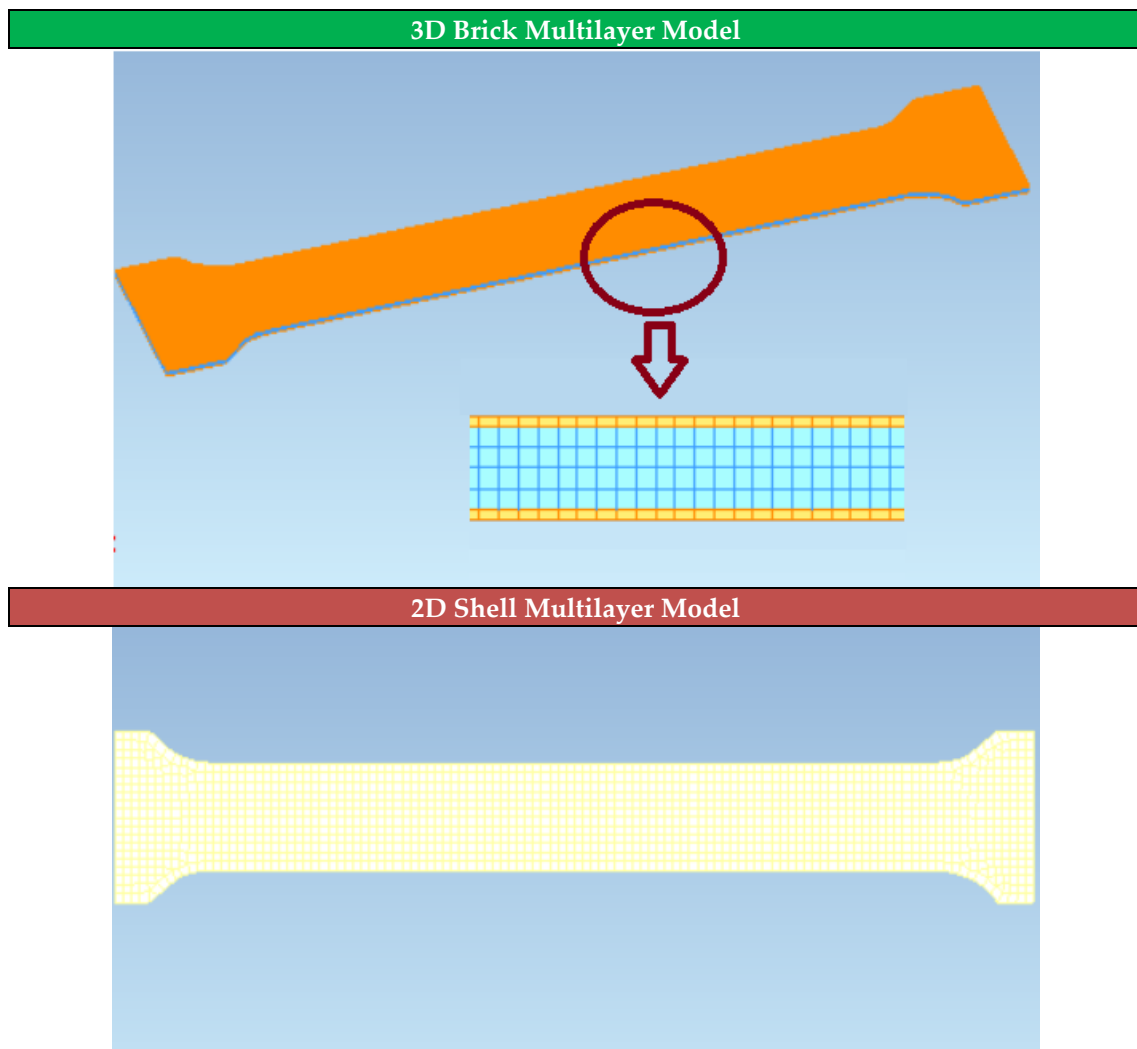


Fig. 5.12 – Hybrix tensile specimen meshes based on *3D Brick Multilayer Model* and *2D Shell Multilayer Model*.

In the virtual tensile test, the experimental 50 mm length gauge was mimicked by following the



displacement of 2 nodes initially at the same relative distance, as schematically shown in Fig. 5.13. Boundary conditions and forces were applied on the model in order to simulate the same conditions applied during the tests. Fixed grip was simulated by using an encastre condition in the other side of the sample:  $u_x = u_y = u_z = 0$  and  $u_{rx} = u_{ry} = u_{rz} = 0$ . In the opposite side, prescribed displacement of 20mm was applied on the nodes of the finite elements in order to simulate the action of the movable grip in x-direction, but restrictions of displacements were applied in y-direction and z-direction. Based on the displacements of control nodes  $X_1$  and  $X_2$  (which mimic the action of the extensometer) before and after the virtual test, it is possible to calculate the elongation of the specimen and then to determine the respective strains. After the virtual tensile tests, the numerical force-displacement curves, of each model, were compared with the experimental Hybrix 1mm force-displacement curve at the rolling direction [Fig. 5.5]. The results are presented in the Fig. 5.14.

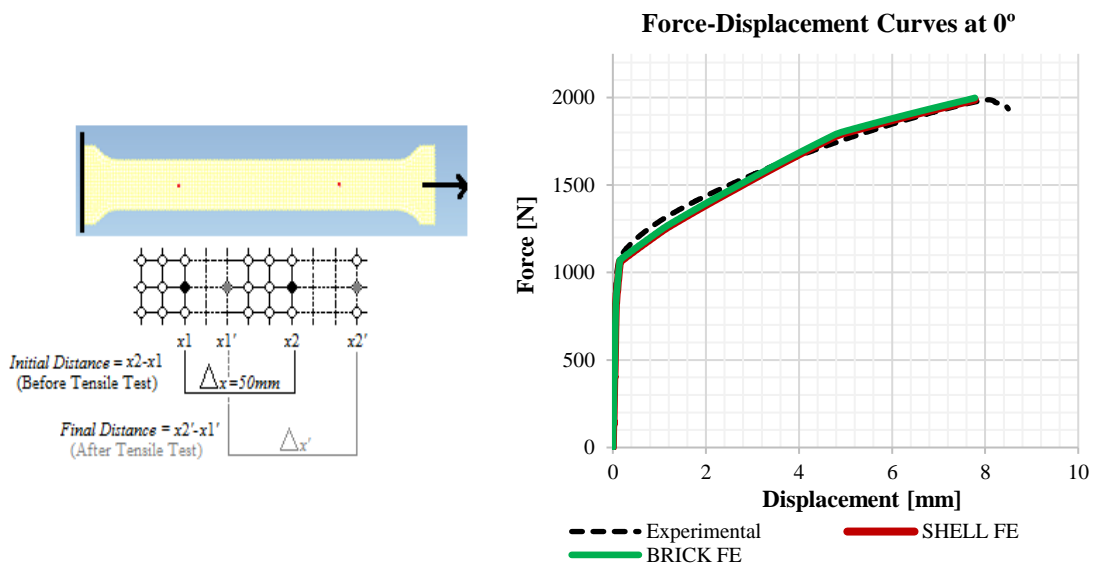


Fig. 5.13 – Control Nodes used to mimic the displacement of the physical extensometer and measure the strain in the specimens after the virtual tensile test.

Fig. 5.14 – Comparison between the experimental force-displacement curves and the numerical force-displacement curves based on 2D Shell approach and 3D brick approach.

Fig. 5.14 shows a very good approximation between the numerical and experimental force-displacement curves, which demonstrates that the methodology presented to characterize the unknown core properties experimentally works-well. In addition, it is clearly seen that both FEM models present the same force-displacement curve accuracy. Due to the uniaxial tensile test being limited to the membrane action it is understandable that shell elements and brick elements exhibit a similar level of performance. This is interesting when the computational cost of the two approaches are compared. Since the micro-sandwich skins are very thin (0.1mm) the 3D brick elements are also

very small (ideally the length/thickness ratio must be 1). To save some computational cost, it was assumed a length/thickness ratio equal to 1 for the core layers and 2 for the skin layers. Even so, the simulation took 10.5 hours to run. On the other hand, PAM-STAMP 2G 2015.1 allows to modelling multilayer materials using 2D shell elements with different through-thickness properties. In addition of halving the number of nodes by replacing a 3D hexaedral by a 2D quadrilateral, it was possible to use much larger finite elements (1mm) maintaining the same length/thickness ratio (1). As a result, the total number of finite elements and nodes was drastically reduced allowing to run the tensile simulation in 6 minutes. Both models run in the same machine (CPU I7 6700HQ – 8 Cores) and using the same solver (*SMP* – Shared Memory Parallel). The details of each FEM model are presented in Tab. 5.4.

Tab. 5.4 – Presentation of the details of the FEM meshes topology for both 3D Brick multilayer model and 2D Shell multilayer model with the respective information of Cpu/Solver and Run Time simulation.

3D Brick Multilayer Model						
Layer	Thickness (mm)	Element Type	Elements	Nodes	Cpu/Solver	Run Time [hours]
Skins	0.10 /0.10	8 Node	256.368	303.772	8 Cores / <i>SMP</i>	10.5
Core	0.80	Hexahedral				
2D Shell Multilayer Model						
Layer	Thickness (mm)	Element Type	Elements	Nodes	Cpu/Solver	Run Time [hours]
Skins	0.10 /0.10	4 Node	1.457	1.582	8 Core/ <i>SMP</i>	0.1
Core	0.80	Quadrilateral				

## Symmetric and Asymmetric issues

The methodology presented previously was applied to the experimental characterization of a standard version of Hybrix. However, the supplier of this micro-sandwich (Lamera) can also provide customized versions adapted to the customer’s need. Sometimes, specific requirements associated to the design of new products such as minimum thickness (ex: welding purposes), different stretching (ex: springback control) or stiffness levels in the opposite faceplates, among others, make the asymmetric micro-sandwich sheets preferable. In such cases, how is the formability affected by the asymmetric structure? And, what is the numerical behavior of the asymmetric models?

In order to answer to these questions the authors investigated and compared the mechanical behavior of symmetric and asymmetric Hybrix configurations. In both cases the Hybrix nominal thickness is 1.6mm. In the symmetric configuration skins are 0.15mm thick, while in the asymmetric configuration, one skin is 0.15mm thick and the other is 0.30mm thick. The stainless steel of the face material is also 304L grade.

Tab. 5.5 presents, respectively, the mass, volume and density to the core and total micro-sandwich for both configurations, asymmetric and symmetric Hybrix. These values were determined taking into account 3 measurements to the tensile specimens' mass, i.e. total micro-sandwich and skins. The volumes were calculated from the nominal measures.

Tab. 5.5 – Presentation of the mass, volumes and density to the core and total micro-sandwich for the both symmetric and asymmetric Hybrix and its nominal dimensions.

Measurements Average						
Hybrix	Mass (g)		Volume (cm <sup>3</sup> )		Density (g/cm <sup>3</sup> )	
	Total	Core	Total	Core	Total	Core
Symmetric	16.32	3.90	8.32	6.76	<b>1.96</b>	<b>0.58</b>
Asymmetric	23.99	5.36	8.32	5.98	<b>2.88</b>	<b>0.90</b>

These values reveal a significant difference between the 2 Hybrix configurations. The asymmetric Hybrix is around 1.5 times denser than the symmetric Hybrix. It is clear that this difference is related with the thicker stainless steel faceplate. However, the Hybrix core in the asymmetric configuration is also 1.6 time denser. In this case, the explanation is related with the nature of the micro-sandwich adhesive and fibers. It was noted that the asymmetric configuration seems to present a glue epoxy adhesive and metallic fibers while the symmetric configuration a rubberized epoxy adhesive impregnated with polymeric fibers Fig. 5.15.

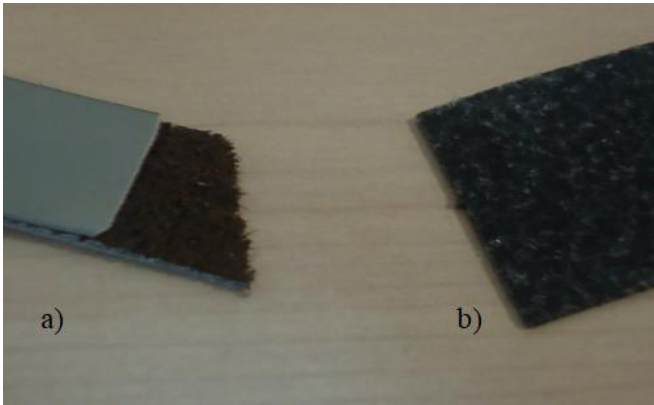


Fig. 5.15 – Presence of 2 core types: a) glue epoxy resin with metallic fibers (asymmetric Hybrix). b) rubberized epoxy with polymeric fibers (symmetric Hybrix).

The same methodology was used to characterize the mechanical behavior of the symmetric and

asymmetric Hybrix micro-sandwich sheets. The experimental and numerical force displacement curves to the orientations  $0^\circ$ ,  $45^\circ$  and  $90^\circ$  are presented below Fig. 5.16.

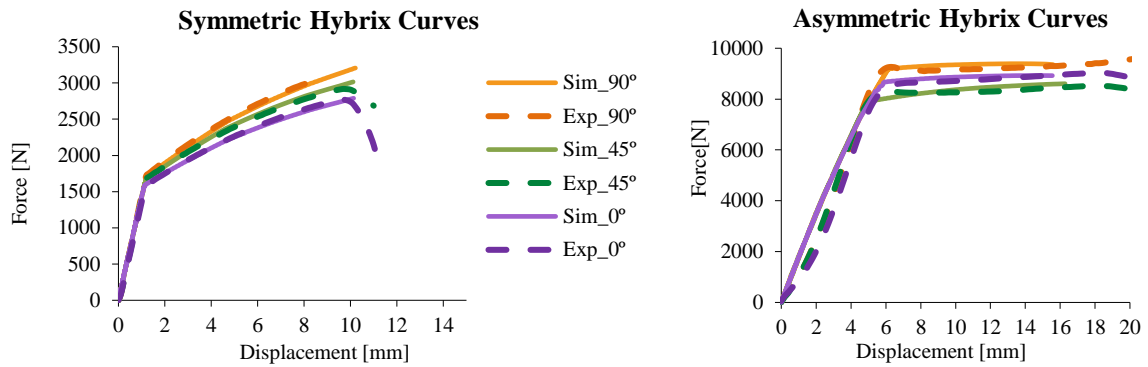


Fig. 5.16 – Experimental and numerical force-displacement curves to the orientations  $0^\circ$ ,  $45^\circ$  and  $90^\circ$  for both symmetric and asymmetric Hybrix configurations.

As for the first version of Hybrix, the experimental results of the uniaxial tensile tests with the symmetric and asymmetric Hybrix specimens show that the higher force-displacement curve is always related with the transversal direction. The lower force-displacement curves were recorded to the rolling direction, for the symmetric specimens, and  $45^\circ$  for the asymmetric specimens. In terms of maximum load, Fig. 5.16 also shows that the asymmetric configuration can support around 3 times of the maximum load of the symmetric configuration. This remarkable difference is obviously related with the 50% extra of stainless steel in the asymmetric configuration, which proves the huge influence of the skins thickness in the strength of the Hybrix micro-sandwich sheets. On the other hand, it cannot be ignored the paramount role of the composite core. As mentioned above, while the asymmetric specimens presented an epoxy core with impregnated metallic fibers, the symmetric specimens presented a most recent rubberized epoxy core with polymeric fibers, the asymmetric configuration. The nature and amount of fibers also affect the mechanical properties of the micro-sandwich sheets, in this case the metallic fibers ensure a higher strength. Lastly, the different amount of stretching, plastic strain and residual stresses in the opposite skins makes that all the asymmetric specimens bend after the rupture as shown in the Fig. 5.17.

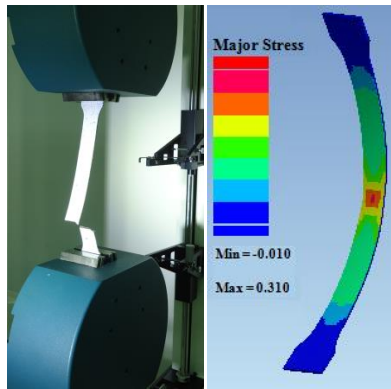


Fig. 5.17 – Due to the different plastic behavior of the metallic skins, in the asymmetric configuration, the tensile specimens tend to bend after the rupture.

In this case, with a monolithic modelling strategy, regardless of the FEM approach (3D or 2D), is not possible describe the springback effect. The only way is follow a multilayer modelling strategy and characterize the mechanical behavior of each micro-sandwich layer.

## **HYBRIX: MICRO-SANDWICH SHEETS FORMABILITY**

The forming limit diagram (FLD) has been widely applied in analysis of sheet metal forming. The FLDs have enabled the prediction of which deformation can lead to the failure of the material for different strain paths and, as referred in [45], are considered an important tool in the die project as well as to optimize and correct problems in the line production. To assess formability in sheet forming, experimentally determined Forming Limit Curves (FLC) are often used. The FLC is affected by many factors, such as the forming speed, the lubrication conditions, the thickness, among others. The standard EN ISO 12004-2:2008 [47] presents the methodology for determine the FLC for a sheet of thickness between 0.3 mm and 4 mm. Since the metallic skins of Hybrix micro-sandwich are out of this specification the results in this section must be viewed as qualitative forming comparison instead of a quantitative forming assessment.

In this study, the limit strains for deep drawing quality sheet metal of symmetric and asymmetric Hybrix micro-sandwich made by Lamera with nominal thickness of 1.6mm are investigated. The experimental tests were carried out in an Erichsen (model 142-40) universal testing machine [Fig. 5.18 b)], according to ISO 12004:2008, punching 6 different specimen geometries. The values of the width parameter  $w$  adopted by authors are 20, 30, 45, 65, 100 and 180mm, the last of them corresponding to a fully circular specimen [Fig. 5.18 a)]. The faceplate in contact with the punch (inner skin) is always the thicker, in the opposite side (outer skin), the thinner. Waisted blanks with parallel shaft length  $l$  of 50 mm and fillet  $R$  of 25 mm have been prepared by waterjet cutting. Before each test the punch was lubricated with graphite grease. The punch velocity was fixed at 20 mm/min

and the blankholder force fixed at 150kN. For optical 3D deformation measurement purposes, all specimens were painted to display a random speckled pattern [Fig. 5.18 c)]. The overall movement of the random speckle pattern was captured during the test by high resolution cameras and treated with the GOM ARAMIS system [Fig. 5.18 d)].

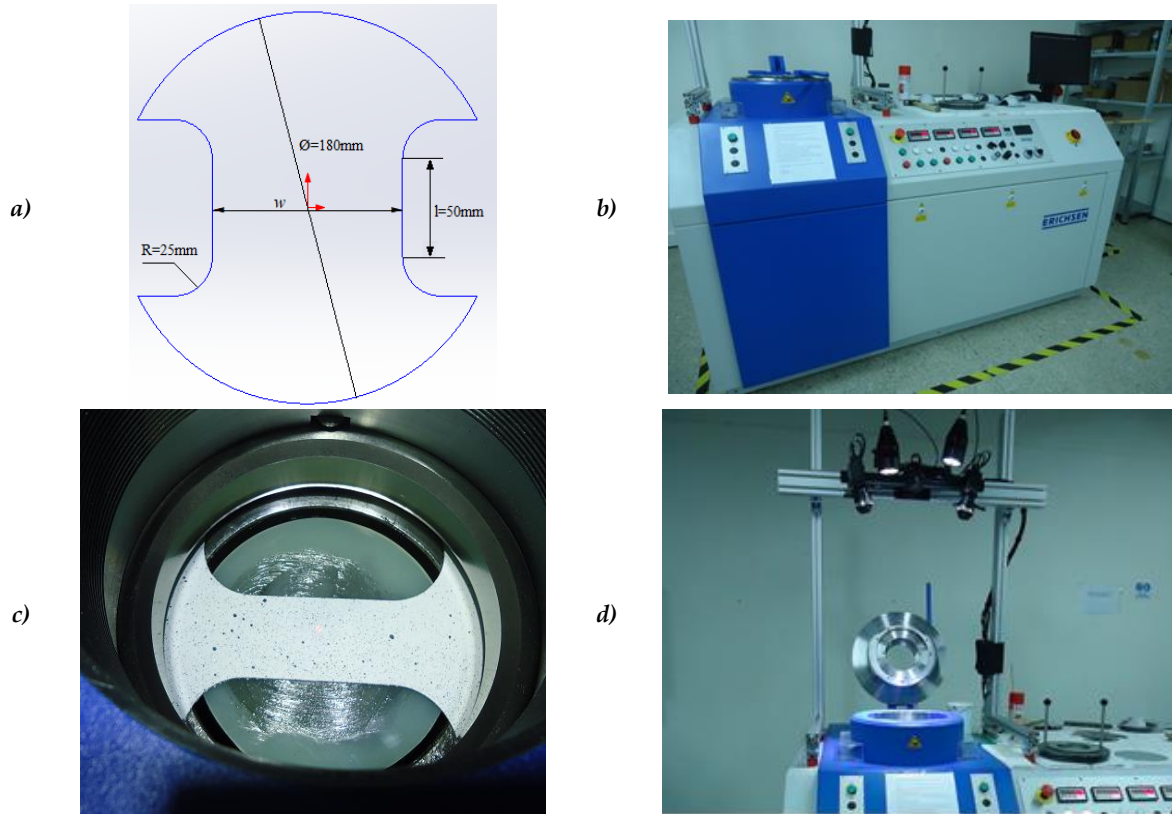


Fig. 5.18 – Experimental Nakazima tests conditions: *a)* Dimensions and shape of the dog bone geometries according ISO 12004:2008 *b)* Erichsen (model 142-40) universal testing machine *c)* Speckle pattern for strain measurements *d)* Position of the GOM ARAMIS cameras.

The strain measurement was performed in the central test piece zone, close to the crack of the material. The frame for evaluation of major and minor strains has been chosen a few steps before fracture occurred. After the project is calculated and evaluated, it is necessary to define positioning of three parallel cross sections [Fig. 5.19] and subsequent determination of limit strains in *forming limit diagram* (FLD). From each test piece shape, several tests were carried out.

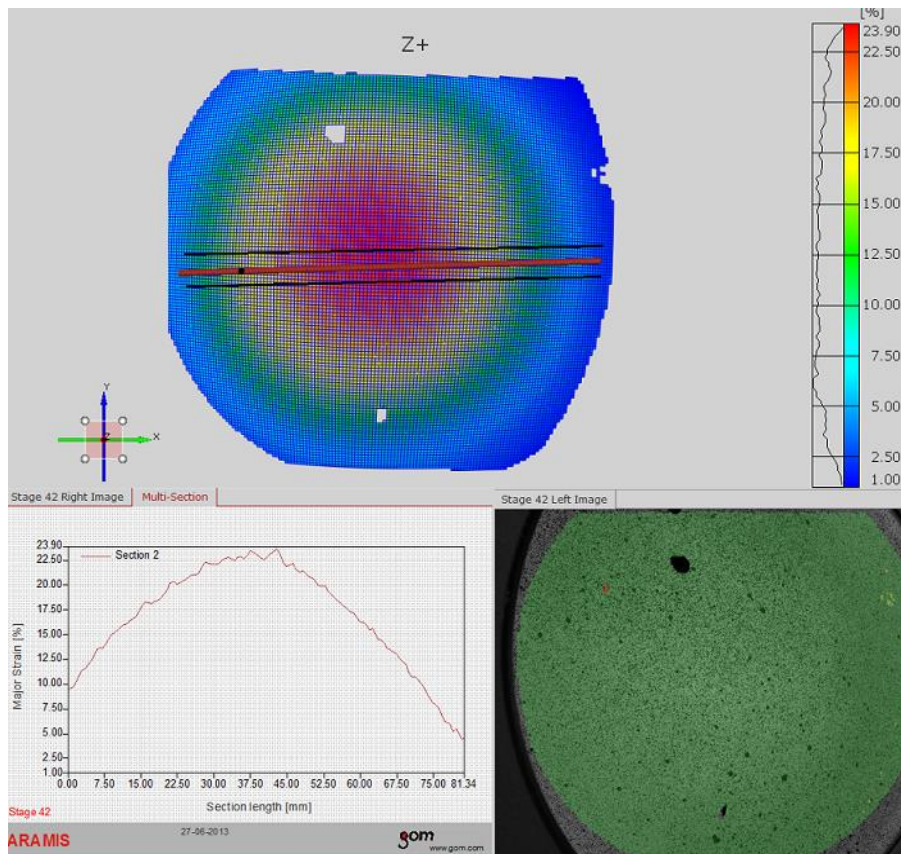
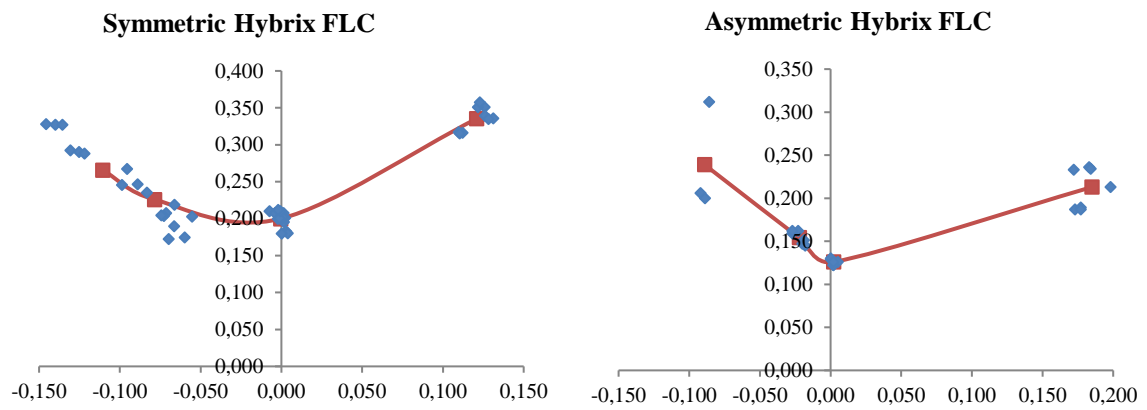


Fig. 5.19 – Post-treatment of the recorded strain data through the cross-section method.

The obtained FLC's are presented in Fig. 5.20.



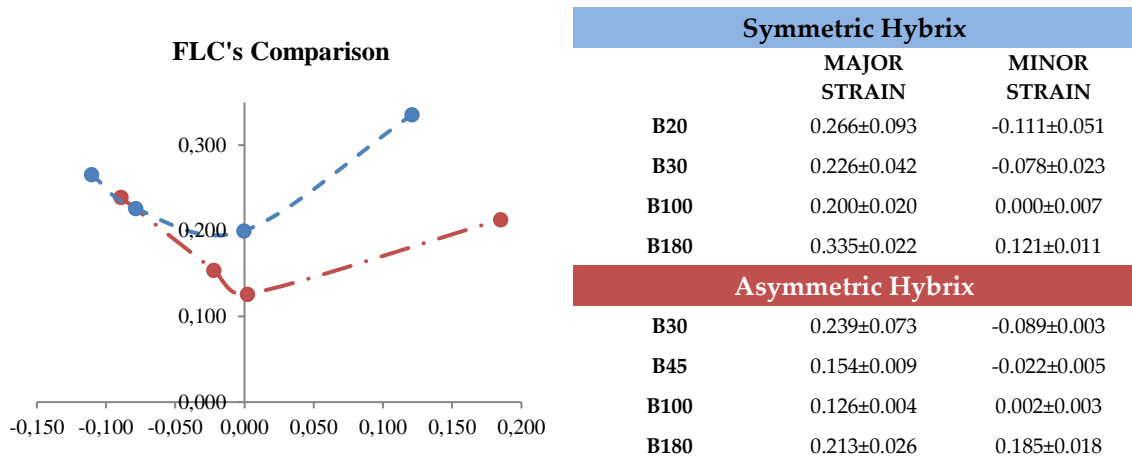


Fig. 5.20 – Experimental Hybrix Forming Limit Curve (FLC) of each Hybrix configuration, defined with the averaged principal strains optically measured and the respective uncertainty.

Several experimental issues like lens focusing, cameras calibration, speckle pattern capture, tools lubrication, amongst others, can affect seriously the speckle pattern measurements and mesh generation, and thus invalidate the FLC determination. In the present study, problems with strain optical measurements did not allow the usage of all specimens in the FLC comparison. Only 4 geometries to each Hybrix configuration could be used. On the other hand, a high variability of the experimentally measured values of both the maximum punch force and principal strains were observed in the narrower specimens, i.e. B20 and B30. Finally, it was found that some specimens started failing unexpectedly too early by the geometry contour nearby the die radius due to tearing. The more stable and robust experimental results were determined for the geometries B100 and B180. On the other hand, there is a significant difference between symmetric and asymmetric Hybrix results for these 2 geometries. The asymmetric specimen B180 followed an almost equibiaxial strain path and the largest major strains are located in the top of the specimen. For its parts, symmetric specimens present the largest major strains close to the die radius. These results are not valid and may happen due to the lack of lubrication or the excess of clamping force. The micro-sandwich skins are very thin and sensitive to the friction conditions, so it can easily localize the strains out of the dome. Typically, in the Nakazima tests the largest major strains must be distributed between the top and the die radius. Looking at the principal strain values in the table (Fig. 5.20) it can be seen Major Strain = 0.335 and Minor Strain = 0.121, but the expected here was a more balanced ratio between these values. In general, a fracture closer to the dome represents also a more homogenous distribution of the strains. In this case, the Major Strain is too high (overestimated) and the Minor Strain is too low (underestimated). This means that, if the test were valid, the point of the FLC, for the symmetric B180 specimen, would be lower and more shifted to the right. So, concerning the right side of the FLC, it is possible that the major strains are overestimated in the symmetric configuration. In the asymmetric case, the fracture is localized at the top of the dome. In addition, the principal



strains ratio is more balanced (Major Strain = 0.213 and Minor Strain = 0.185). However, the thicker skin (face in contact with punch) presented wrinkles after the test. It seems, that the core has collapsed. This can justify the low values obtained to the asymmetric Hybrix. While the B180 symmetric specimen fail at a maximum punch displacement of 47mm, the B180 asymmetric specimen only reached 28mm. So, it can be stated that both, the configuration type (Symmetric or Asymmetric) and the core type (epoxy resin with metallic fibers or rubberized epoxy with polymeric fibers) affect the micro-sandwich sheet formability. From the experimental FLC's comparison, in the Fig. 5.20, the symmetric micro-sandwich sheet seems to be more formable and adapted to deep drawing processes.

### **HYBRIX: VALIDATION AND COMPARISON OF FEM APPROACHES**

In this section experimental and numerical results are analyzed and compared. The main goals are to validate the micro-sandwich characterization methodology presented, and compare the accuracy of the different FEM approaches available in the commercial FEA tools PAM-STAMP 2G 2015.1 and AutoForm R5.2. For this purpose, virtual Nakazima tests were prepared, based on the real geometry tools, which were captured with a 3D scanner and converted to IGES format. Then, the CAD file geometries were used to create into PAM-STAMP 2G and AutoForm an appropriate set of Nakazima tool meshes [Fig. 5.21].

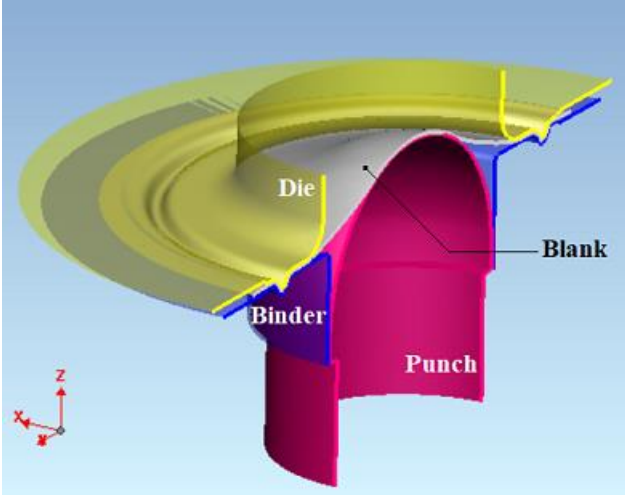
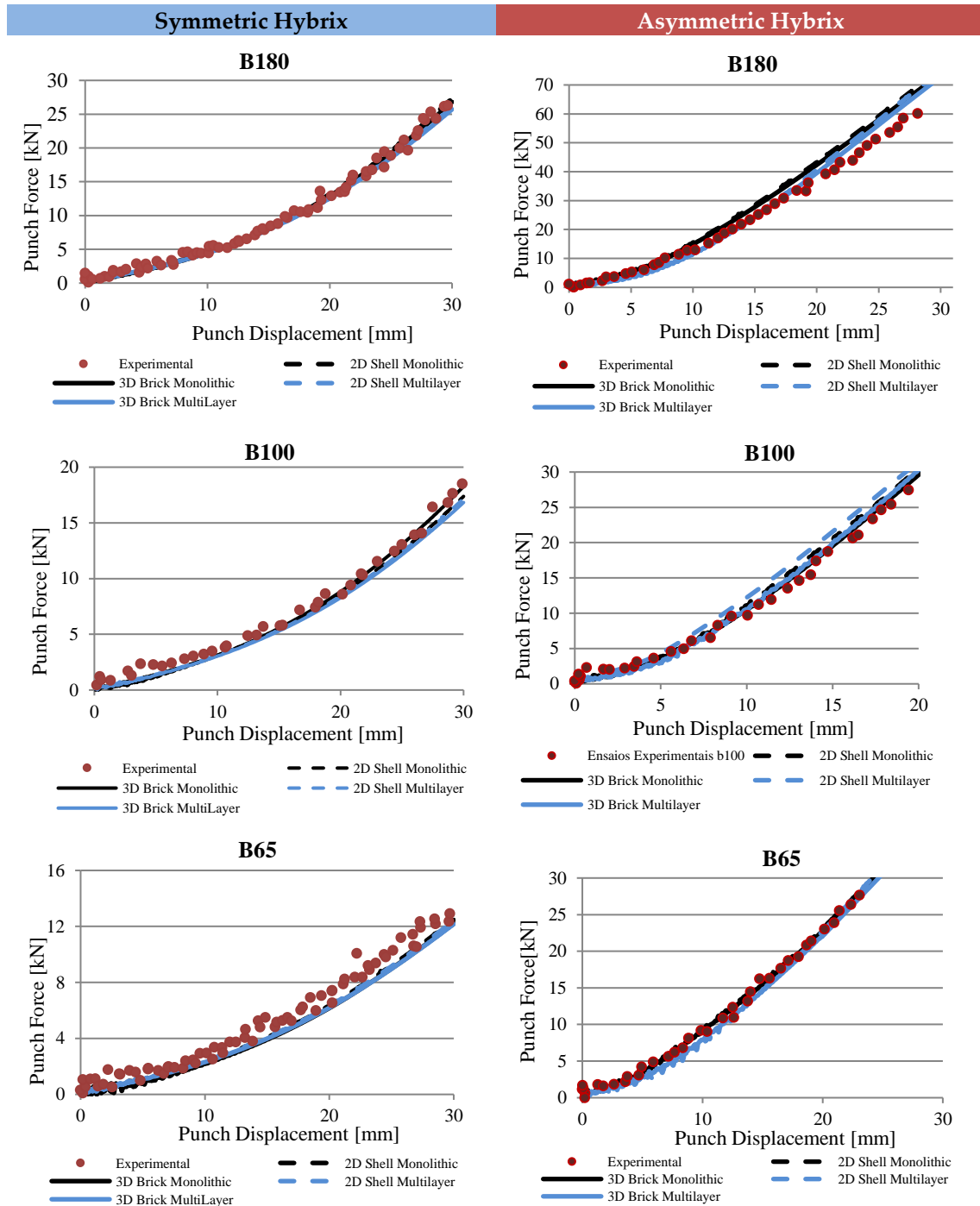


Fig. 5.21 – Presentation of the Nakazima tool set and Blank at FE meshes.

After running the simulations, the numerical and experimental results were compared in terms of forming forces and the major strain distribution.

### **Forming Forces**

Punch displacement and punch force were recorded during physical Nakazima tests and imported as .txt\* files. The same material and process parameters were used in both PAM-STAMP 2G and AutoForm to reproduce the Nakazima tests and obtain comparable results. The numerical punch force displacement curves were imported as .xls\* files. The comparison between the experimental and numerical results is presented in Fig. 5.22 for the Nakazima specimens B30, B65, B100 and B180. In order to compare all the FEM approaches, the numerical results presented below were obtained from the FEA tool PAM-STAMP 2G 2015.1.



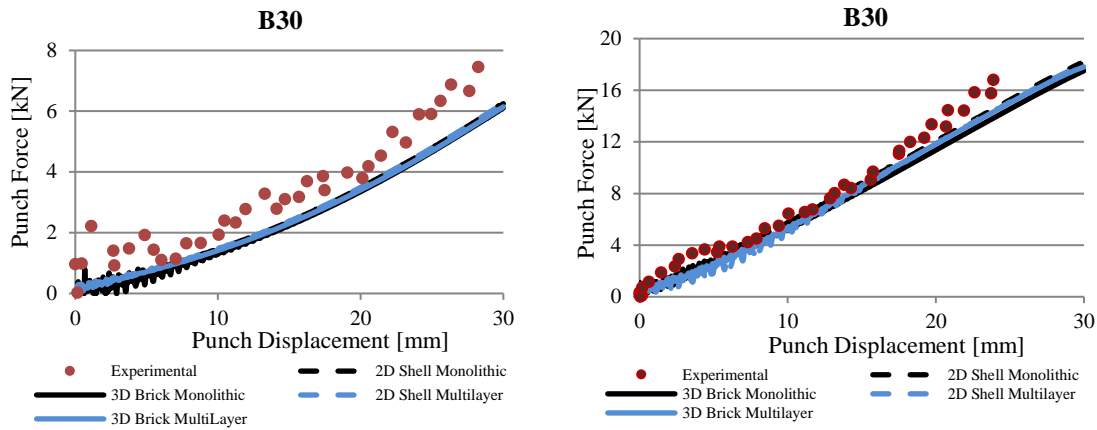


Fig. 5.22 – Comparison of the numerical punch forces, delivered by all the FEM approaches, and the experimental results during Nakazima tests for both, symmetric and asymmetric Hybrid configurations, of the specimen’s geometries B180, B100, B65 and B30.

Concerning the experimental Nakazima tests, the specimen geometries with higher values of punch force, exhibit smaller oscillations in terms of the experimental punch force evolution. On the contrary, the B30 symmetric Hybrid specimen reveals some noisy trend, as shown in Fig. 5.22. The reason for this behavior can be related with the load cell sensitivity. Obviously, the bigger the punch displacement, the greater the punch force required. Comparing the 2 micro-sandwich sheets, the symmetric Hybrid always reach much higher displacements at low punch forces, which means it is more formable and less power consuming. For its part, the asymmetric Hybrid offers more tensile and flexural strength. With regards to that, a closer look at the punch-force curves puts in evidence that the load forming is 3 times greater in the case of the asymmetric specimens (B180 – 25mm; B100 – 20mm; B65 – 20mm; B30 – 20mm), the same proportion identified previously in the uniaxial tensile tests.

The numerical results are in excellent agreement with the experimental values to all specimen geometries tested. For the B180 geometry, the numerical punch forces of the asymmetric Hybrid seems to be a little bit overestimated. However, all the other specimen geometries are very well described so this is not particularly worrying. For both configurations, symmetric and asymmetric, all the FEM models tested, monolithic or multilayer, 2D or 3D, present the same level of accuracy.

The numerical forming forces delivered by the 2D shell multilayer models of AutoForm R5.2 and PAM-STAMP 2G 2015.1 were also compared. Instead of an exhaustive presentation of all results, the geometries B180 and B30 were assumed as representative of this comparison as depicted below [Fig. 5.23].



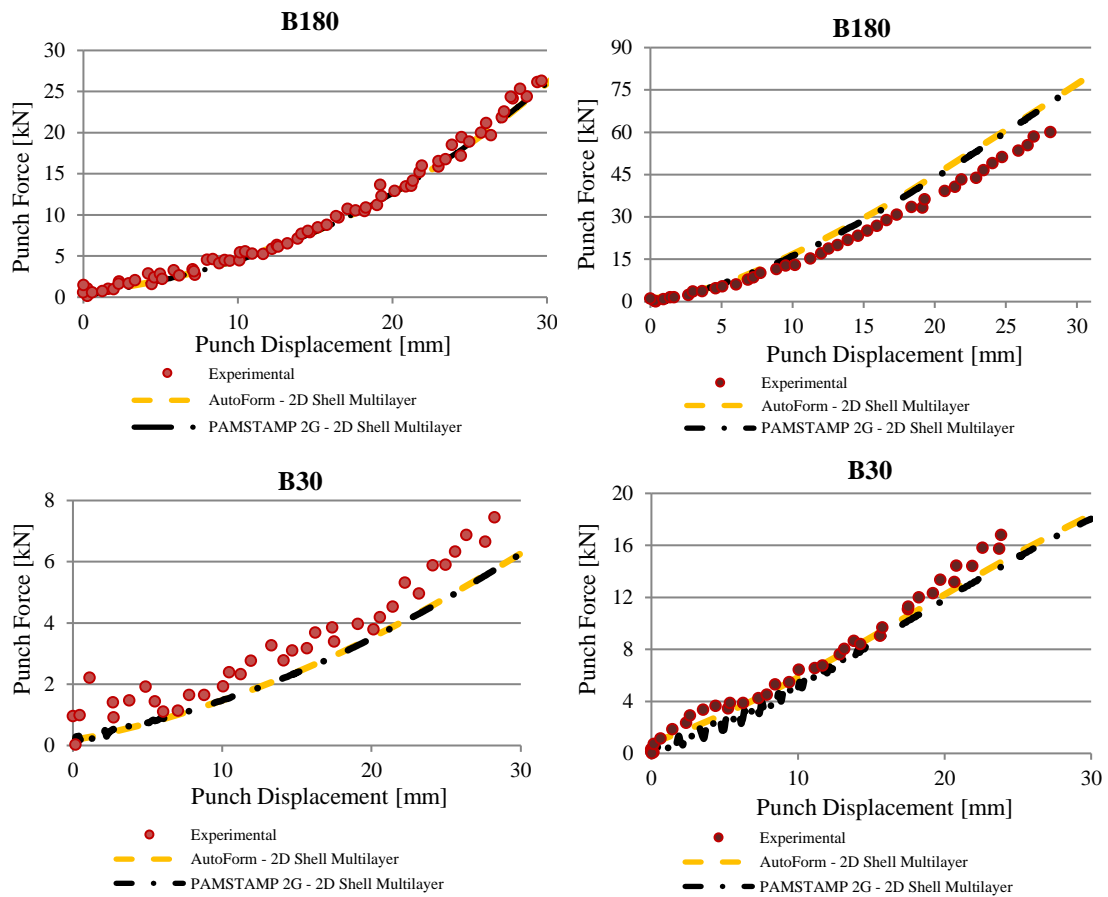


Fig. 5.23 – Comparison of the experimental Nakazima forces and the numerical Nakazima forces of AutoForm R5.2 and PAM-STAMP 2G 2015.1 using 2D shell multilayer approaches.

As shown in Fig. 5.23 the force-displacement curves delivered by AutoForm and PAM-STAMP 2G are closely similar to the specimens B180 and B30 for both configurations, symmetric and asymmetric. The other geometries also exhibited the same trend. In spite of this, it can be stated that 2D shell monolithic models are the most efficient to predict the Nakazima forming forces without compromising on accuracy [Fig. 5.22]. If preferred, 2D shell multilayer models can be used in either AutoForm or PAM-STAMP 2G with the same level of accuracy [Fig. 5.23].

Due to the axisymmetric geometry of the B180 specimen, biaxial strain paths predominate. Uniaxial tensile tests performed do not allow obtaining biaxial yield stress or biaxial anisotropy coefficient. Moreover, the criterion of plasticity hill 48 does not incorporate, by definition, the biaxial anisotropy. To obtain a better correlation between experimental and numerical results, it is necessary to use a criterion of plasticity that takes into account the biaxial anisotropy. Regarding plasticity criteria available in 2D multilayer model, only AutoForm allows the incorporation of biaxial anisotropy with Hill 48. In AutoForm, the theoretical  $R_b$  is given by a relationship between  $R_0$  and  $R_{90}$  (Eq. 12) while the theoretical biaxial stress  $\sigma_b$  is obtained from  $\sigma_{90}$  and a biaxial factor  $F_b$  (Eq. 13). In this case no experimental biaxial data are available, however it can be possible tuning the  $F_b$  factor

until achieving the best correlation with experimental results. PAM-STAMP 2G 2015.1 also has a yield criterion with biaxial anisotropy (Vegter Lite), that take into account only the mechanical parameters of uniaxial tensile test. However, it cannot be used in multilayer module. To illustrate this point, Fig. 5.24 shows the force-displacement curve of the asymmetric B180 with both Hill48 (biaxial factor = 1) and Hill48 + biaxial factor = 0.75.

$$R_b = \frac{R_0}{R_{90}} \tag{5.12}$$

$$\sigma_b = \sigma_{90} \times F_b \tag{5.13}$$

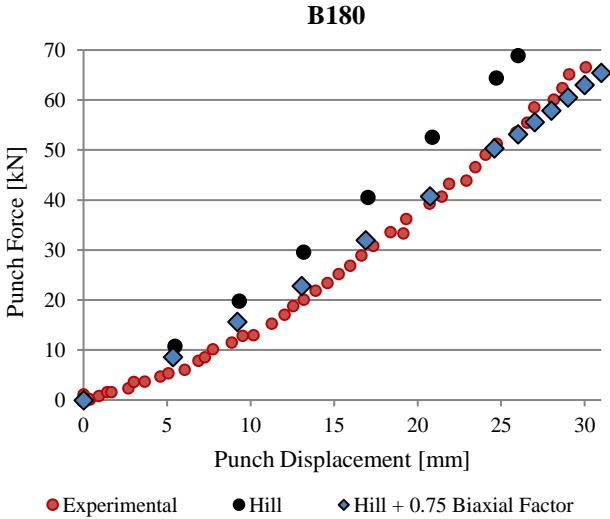


Fig. 5.24 – Comparison of experimental and numerical force-displacement curves of the asymmetric B180 specimen with both Hill48 and Hill48 + biaxial factor = 0.75

Fig. 5.24 shows a significant impact of the biaxial factor  $F_b$  on the evolution of the numerical punch force during the axisymmetric forming of a Nakazima’s specimen. Thus, it becomes clear that the mechanical characterization of Hybrix sheets, which includes experimental biaxial data, leads to more accurate and reliable numerical results.

### Major Strain Distribution

Major strain field distribution was always analyzed in the outer skin (the metallic skin which is not in contact with the punch) along the well-defined line identified in Fig. 5.25. The major strain fields are determined from ARAMIS software. The same line was defined and used in PAM-STAMP 2G 2015.1 (since 2D models and 3D models can be built) in order to allow the comparison between experimental and numerical results.

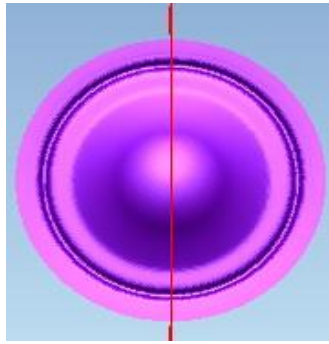


Fig. 5.25 – Cross-section for major strain evaluation of all Nakazima specimens.

Three time-steps were selected for comparison purposes, corresponding to a punch displacement of around 10 mm, 20 mm and 30 mm, as identified in Fig. 5.26 and Fig. 5.27.

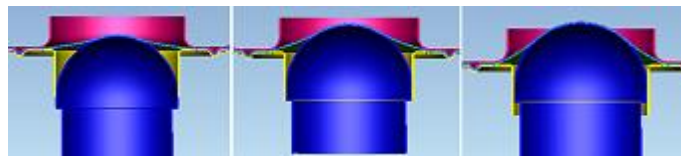
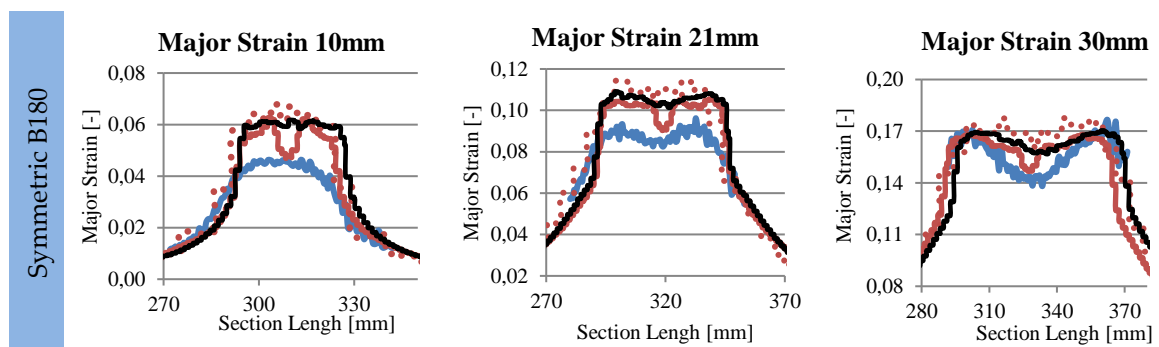


Fig. 5.26 – Different evaluation stages.

The experimental data recorded during the Nakazima tests were compared with the numerical major strain profiles obtained with monolithic or multilayer modelling strategies and 2D or 3D FEM in the same cross-section to the geometries B30, B100, B180.



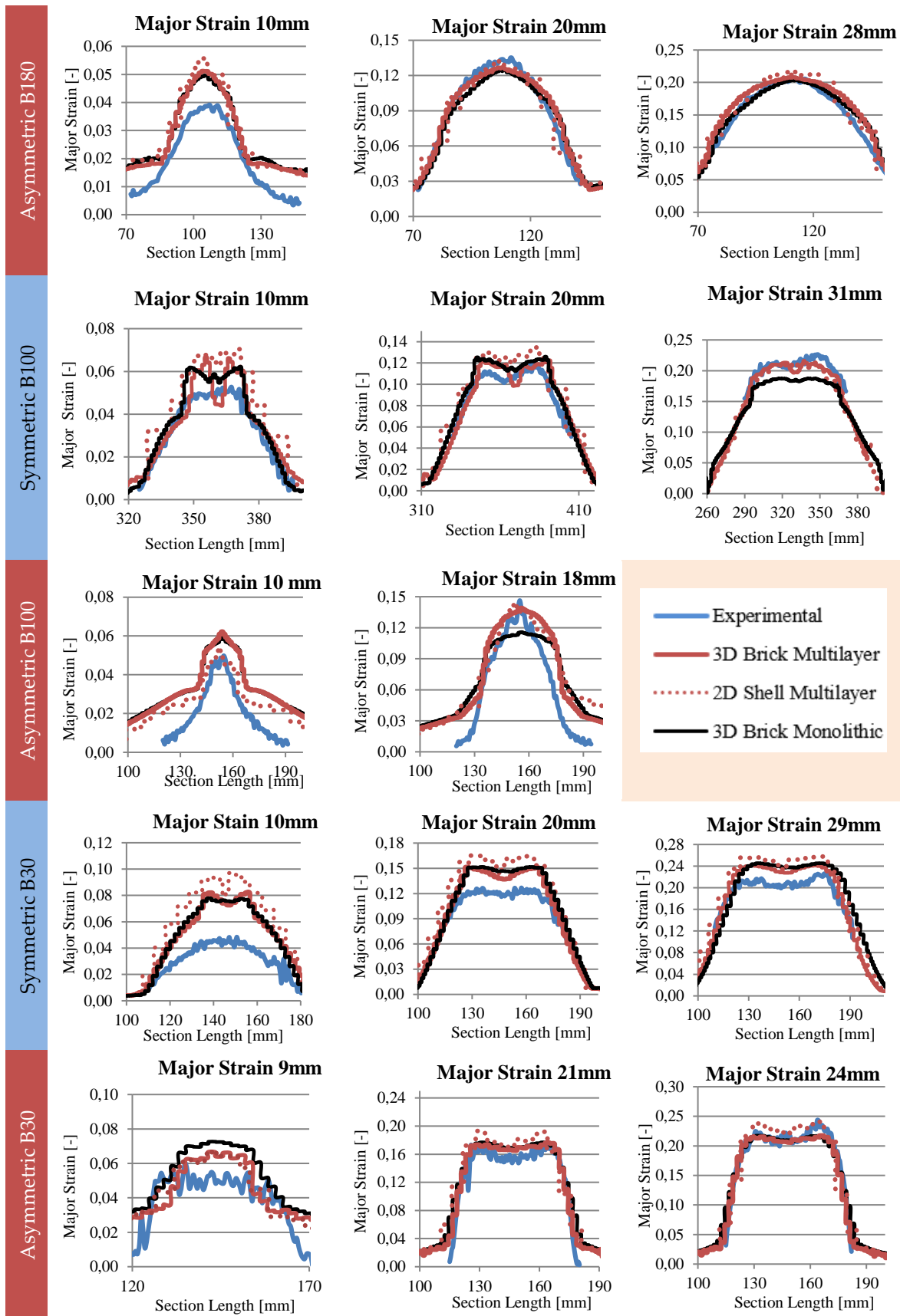


Fig. 5.27 – Comparison between experimental and numerical major strain distribution, in the same cross-section, to all specimen's geometries tested using different modelling strategies and FEM approaches.

At the first time-step (i.e. at about 10 mm of punch displacement) the experimental major strains are always higher than the numerical major strains. Moreover, this difference is larger for the narrower specimens. Such behavior can be explained by the existence of pre-strain that is not taken into account equally in the experimental and numerical simulations. In fact, the cameras just began recording the Nakazima test after the blankholder closing, and so the reference configuration was not effectively the initially one. In fact, the blankholder closing introduces some pre-strains in the sample, what is more pronounced in case of the narrower samples. Comparing the symmetric Hybrix with the asymmetric configuration, the narrower sample, b30, presents a higher level of major strain at the first time-step (0.08 against 0.06) which also indicates a higher level of pre-strain. The strain path is closer to the uniaxial tensile test, so, the tensile strength and tensile stiffness assume a key role. From the strain profiles of the B180 specimens, it seems that the lubricant conditions were better to the asymmetric case, since the higher major strain is in the top of the dome while in the symmetric case is shifted from the center. This could be true. However, the lubrication conditions were the same in the virtual tests to both cases, symmetric and asymmetric, and curiously the numerical profiles also present the same trend. Therefore, it is more probable that this difference is related with the through-thickness mechanical properties. In the symmetric configuration, the same flexural and tensile strength of the inner and outer skin leads to the expected behavior in Nakazima tests in which the largest values of major strain localized in a region below the top of the dome. On the other hand, the much higher strength layers below the top skin, which contact with the punch, in the asymmetric Hybrix configuration contributes to a different behavior. As observed, the largest values of the major strain localized at the top of the specimen and the transition to the lower values is smooth.

The differences between the numerical profiles are slight. Concerning the 3D models, it can be seen that the multilayer and monolithic profiles are often very close to each other. It must be remembered, however, that the in-plane strains of the monolithic model are related with the total thickness reduction rather than the outer skin reduction. Since the material is considered homogenous and continuous in these models, the thinning percentage of each individual layer, which plays a paramount role in the micro-sandwich failure, cannot be computed.

Looking at the first time-step considered, the strain profile of the 2D shell multilayer model is higher than the others and have more noise. But, as the punch moves up the 2D multilayer profiles tends to fit the 3D models. Taking into account the performance of each finite element, differences between the 2D and 3D model were expected. Even so, it was found that both models present a comparable level of accuracy, which is in good agreement with the experimental values.

Still regarding the accuracy of the 2D multilayer models, AutoForm and PAM-STAMP 2G were also compared in terms of major strain distribution [Fig. 5.28] to the B180 case. The range of values and color pallet definition are the same to both softwares. Due to specimen symmetry, just a quarter



is represented (black square – PAM-STAMP 2G; Yellow square – AutoForm). In order to providing an easy and effective visual checking of the differences, the quarters were joined and the maximum values displayed.

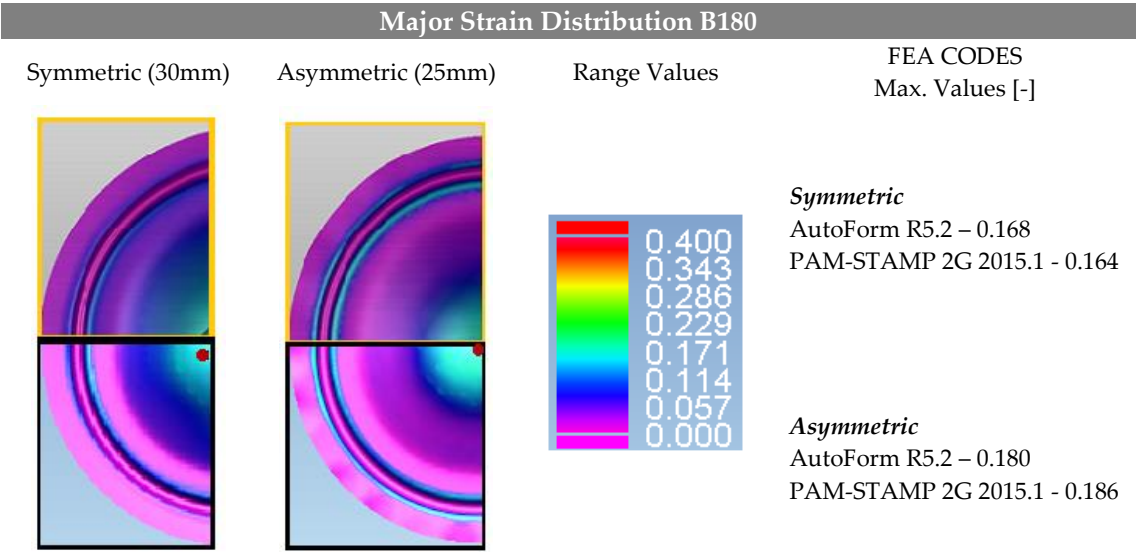


Fig. 5.28 – Representation of 1 quarter of the B180 symmetric (at 30mm of punch displacement) and B180 asymmetric specimens (at 25mm of punch displacement) in AutoForm and PAM-STAMP 2G with the major strain variable displayed for the top skin. The maximum values are presented and compared.

As shown in Fig. 5.28, the major stress distribution patterns of AutoForm and PAM-STAMP 2G are almost the same to both Hybrix configurations. The maximum values are also located in the same positions (near to the top of the dome). In the symmetric configuration, the maximum values reached were 16.8% to AutoForm and 16.4% to PAM-STAMP 2G at a punch stroke of 30mm. In the asymmetric configuration, the maximum values reached were 18.0% to AutoForm and 18.6% to PAM-STAMP 2G at a punch stroke of 25mm. So, the accuracy of AutoForm and PAM-STAMP 2G in terms of major strains distribution is also very similar. In addition, Fig. 5.28 also present wrinkles on the whole border perimeter of the asymmetric B180 specimens. Due to PAM-STAMP 2G be based on a dynamic formulation (instead of an implicit formulation as AutoForm), it can predict the micro-sandwich wrinkles with a greater ease.

**SYMMETRIC AND ASYMMETRIC HYBRIX – FINAL REMARKS**

The experimental mechanical tests conducted in this study were fundamental to characterize the Hybrix multilayer material and, thus, understand more about its mechanical behavior under sheet metal forming processes. That’s because materials formability, i.e. the ability to transform them by plastic deformation, is a driver parameter to produce manufacturable sheet metal parts.

Concerning Hybrix micro-sandwich sheets, this study reveals very big differences between the formability of the symmetric and asymmetric configurations. However, it should also be included that influence of the core type in these differences. At first glance, they are perfect in terms of lightweight product conception. Nevertheless, understanding its formability is the true challenge.

The micro-sandwich strength and formability are mostly driven by the very thin metallic skins. So, thinking in automotive applications, it will not be considered for crashworthiness purposes, but only in applications with low strength requirements. During the geometry part design, it is necessary to take into account that these metallic skins cannot admit almost any thickness reduction. All edges, radii, geometry features and transitions from the top to the bottom have to be smooth to avoid excessive thinning, splits or rupture. Another caution to be taken is with the compressive stresses which cause easy wrinkles and, consequently, the micro-sandwich delamination. To achieve the best results and take advantage of the good formability of symmetric Hybrix, the plastic deformation needs to be dominated by the biaxial stretching mode as demonstrated by the punching of the Nakazima specimen b180. Whenever possible, cutting and/or trimming operations have to be done after all forming operations. These thin metallic skins have a great tendency to the tearing failure [46] as observed in the narrower Nakazima specimens [Fig. 5.29].

As mentioned above, the change of the core type, from rubberized epoxy/polymeric fibers (most recent version) to glue epoxy resin/metallic fibers (old version), and the change of one metallic skin, from 0.15mm to 0.30mm, had a deep impact in the formability of the micro-sandwich sheet as demonstrated by the experimental results of asymmetric Hybrix sheet. The maximum tensile force increased around 3 times. Additionally, the thicker metallic skin allows the asymmetric Hybrix tensile specimen to support a higher level of plastic deformation before fracture. After the specimen fracture, the straight tensile specimens become slightly curved due to the different equivalent strain state and equivalent stress state of the 2 external skins. The curvature is dependent of the thickness and mechanical properties of each layer. Concerning the formability, the experimental Nakazima tests results were not so satisfactory. An unusual unstable behavior was observed. Some Nakazima specimens began to present wrinkles in the metallic skins during the punching operation. In few cases, a micro-sandwich delamination is clearly seen. Thus, the core degradation suspicion is confirmed. Since the core fails first, the wrinkle tendency and delamination take place. In general, the wrinkles were localized just in the thicker skin and next to die radius [Fig. 5.29].



Fig. 5.29 – Principal types of failure observed in the Nakazima specimens: Asymmetric Hybrix – Delamination and Wrinkles; Symmetric Hybrix – Tearing.

Furthermore, comparing the two configurations it was found that the asymmetric specimens presented a higher level of major strain in the top of the dome for the same punch displacement. This seems to be related with the higher strength of the adjacent layers.

All these experimental considerations give assent to the utilization of Hybrix, as a micro-sandwich material, to produce automotive parts. It was demonstrated how to characterize and modeling this multilayer material. With strong metalworking knowledge, it is possible to design manufacturable geometry parts and robust stamping processes based on reliable numerical simulations. Its mechanical properties and forming behavior make it suitable to aesthetically interior components and body shells. Body shells in automotive industry are mainly produced by deep drawing. Due to the low work hardening of the process, especially in areas with low strain contents, a pre-stretching operation is commonly introduced [48]. The use of micro-sandwich sheets would reduce the unstretched areas (due to the very thin skins) and improve the stiffness part (due to the higher global thickness). The asymmetric configurations tested bring many problems to the micro-sandwich formability and process robustness. However, it should be noted that this asymmetric configuration presented an old version of the Hybrix core. No delamination evidences were observed in the symmetric specimens with the newer core.

## **HYBRIX: CONCLUSIONS**

A simple methodology for experimental characterization of an advanced micro-sandwich material was presented. The method is based on uniaxial tensile tests commonly used for the characterization of metallic sheets. The unknown mechanical behavior of the core was deduced from the overall mechanical behavior of both the Hybrix and of the single metallic skins.

**The experimental methodology** proved efficient in the experimental characterization of Hybrix micro-sandwich. The fact that the core is considered monolithic make the experimental characterization more expeditious and the numerical implementation easier. In this regard, this methodology is particularly suitable to metallic/polymeric fibrous cores, since the mechanical properties are highly dependent on the manufacturing process robustness. Therefore, even the most robust characterization procedures (which include fiber's mechanical properties, dimensions, orientation, percentage volume, mechanical behavior of the adhesive, etc.,) can fail. Due to this, the most reliable procedure is to repeat the methodology for each configuration of micro-sandwich sheets, instead of trying to extrapolate the results of one configuration to another.

**Concerning the modelling strategies**, both models, monolithic and multilayer, presented a good approximation to the experimental forces obtained in the uniaxial tensile tests and Nakazima tests. In terms of major strain distribution, the same level of accuracy can also be addressed to both models. Despite this, the monolithic models cannot describe the mechanical behavior of each layer. Therefore, the skin's thinning level, which defines the limits of the micro-sandwich formability, cannot be computed, moreover, springback effect cannot be predicted. Thus, monolithic models cannot be used to assess the part feasibility on Hybrix sheet forming processes. Despite this, it can be used to determine the global mechanical parameters of Hybrix sheets and could be explored to identify constitutive parameters with inverse analysis methods.

**In terms of FEM approaches**, both 2D and 3D models presented a good approximation to the experimental forces and the same level of accuracy in the uniaxial tensile tests and Nakazima tests. In terms of major strain distribution, the 2D models generated a little bit of noise in the early stages and present a slightly tendency to overestimate the Nakazima strains. Even so, the accuracy of the 2D models in the Nakazima tests were quite reasonable. Although the 3D models are more accurate, they are too much expensive to an industrial use, specially when micro-sandwich with very thin skins are considered (if hexahedral elements are used, its size must be directly proportional to the thickness layer).

**Comparing the commercial FEA tools**, the 2D multilayer modules of AutoForm R5.2 and PAM-STAMP 2G 2015.1 present always very similar numerical predictions to all the variables considered in this study (forces and strains). AutoForm allows to introduce experimental biaxial data into the material model and therefore improve the numerical prediction. PAM-STAMP 2G was more effective in the wrinkling prediction, which is one of the most common sheet stamping defect and particularly important to assess in the micro-sandwich, since it can lead to the delamination compromising the structural integrity of the sandwich system.

**With respect to the micro-sandwich configurations**, the Nakazima tests were not effective to obtain reliable Hybrix FLC, due to the tearing mode failure present in the narrower symmetric specimens and the early core failure in some asymmetric specimens. However, Nakazima tests a pretty good purpose for a qualitatively formability. In terms of general Hybrix formability, as an example of an ultra-lightweight micro-sandwich with metallic/polymeric fibrous core, it was proved:

- The good formability of the micro-sandwich sheet under biaxial strain paths.
- The influence of the metallic skins thickness on the micro-sandwich mechanical behavior.
- The formability is deeply affected by asymmetries and the core type. The symmetric configuration with the rubberized epoxy/polymeric fibers presented a much better formability than the asymmetric configuration with epoxy resin/metallic fibers.

Conclusively, the good correlation between the numerical results and the experimental results in terms of forming forces and major strain distribution proves that the proposed methodology is appropriate and functional to develop accurate numerical models for the modeling and simulation of micro-sandwich materials. In this work a preliminary validation of different FEM models to modelling the mechanical behavior of micro-sandwich sheets was done. However, the accuracy, efficiency and reliability of these FEM models must be evaluated and compared under complex strain paths. Therefore, the future perspectives of this work aim an experimental case of study of the deep drawing process of a real automotive part. Since the delamination of the micro-sandwich sheet are, in many cases, related with the wrinkling phenomena, the accuracy of the FEM models in describe instabilities as wrinkles during the forming process must be highlighted. Specific constitutive and numerical considerations must be included in the FEM models to perform this kind of formability assessment.

## ACKNOWLEDGMENTS

The authors greatly acknowledge the financial support of “Fundação para a Ciência e Tecnologia” (FCT – Portugal), through the research project SFRH/BDE/51189/2010 (“Development FEA Tools Applied to Sheet Forming Special Cases. Application to the Automotive Industry, Advanced Metallic Materials and Multilayer and Multi-Material Sheets”) in partnership with Sodécia Product Competence Center (Maia, Portugal). The authors would also like to thank the company Lamera AB (Sweden), for providing the Hybrix material, ESI GROUP and AutoForm to the technical support and collaboration in this study.

## COMPLIANCE WITH ETHICAL STANDARDS:

Funding: This study was funded by SFRH/BDE/51189/2010.  
No conflict exists: The authors declare that they have no conflict of interest.

## REFERENCES

1. Ghassemieh, E. (2011). “Materials in Automotive Application, State of the Art and Prospects, New Trends and Developments in Automotive Industry”, Prof. Marcello Chiaberge (Ed.), ISBN: 978-953-307-999-8, InTech, doi: 10.5772/13286.
2. Ermolaeva, N., Castro, M. and Kandachar, P. (2004) “Materials selection for an automotive structure by integrating structural optimization with environmental impact assessment”. *Materials & Design*. Vol. 25, 689-698. doi: 10.1016/j.matdes.2004.02.021
3. Deshmukh, A.B Chaitanya, S.V Wagh, S. (2013) “Case Study on Sandwich steel Application in Automotive BIW for NVH Improvements”, *IOSR Journal of Mechanical and Civil Engineering*, 2nd National Conference on “Recent Developments in Mechanical Engineering”, Vol. 1, pp. 1-6
4. Moreira, RAS. Sousa, RJA. Valente, RAF. (2010) “A solid shell layerwise finite element for non-linear geometric and material analysis”. *Composite Structures*; 92:15 7–23.
5. Chen, L. and Zhang, Y. (2013) “A study on the application of material selection optimization approach for structural-acoustic optimization”. *Materials & Design*. Vol. 52, pp. 207-213 doi: 10.1016/j.matdes.2013.05.031
6. Wan, H. Bai, S. Li, S. Mo, J. Zhao, S. and Song, Z. (2013) “Shielding performances of the designed hybrid laminates impacted by hypervelocity flyer”. *Materials & Design*. Vol. 52, pp. 422-428 doi: 10.1016/j.matdes.2013.05.050
7. Sinmazçelik, T. Avcu, E. Bora, M. and Çoban, O. (2011) “A review: Fibre metal laminates, background, bonding types and applied test methods”. *Materials & Design*. Vol. 32, pp. 3671-3685. doi: 10.1016/j.matdes.2011.03.011

8. Palkowski, H. and Lange, G. (2005) "Ame Austenitic Sandwich Materials in the Focus of Research", *Metalurgija – Journal of Metallurgy*, vol. 11, pp. 215-224
9. Besse, C. (2012) *Development and Optimization of a Formable Sandwich Sheet*. Materials and Structures in Mechanics [physics. class-ph].
10. Parsa, M. H. Ettehad, M. Nasher, S. (2009) "FLD determination of AL 3105/Polypropylene/AL 3105 sandwich sheet using numerical calculation and experimental investigations". *International Journal of Material Forming*. Volume 2, Issue 1, pp. 407-410 doi:10.1007/s12289-009-0502-0
11. Kim K.J., Kim D., Choi S.H., Chunga K., Shin K.S., Barlat F., Oh K.H., Youn J.R. (2003) "Formability of AA5182/Polypropylene/AA5182 Sandwich Sheets", *Journal of Materials Processing Technology*, Vol. 139, pp. 1-7. doi:10.1016/S0924-0136(03)00173-0
12. Sokolova, O.A. Kühn, M. Palkowski, H. (2012) "Deep drawing properties of lightweight steel/polymer/steel sandwich composites" *Archives of Civil and Mechanical Engineering*, Vol. 12, pp. 105-112. doi: 10.1016/j.acme.2012.05.001
13. Liu, J. Xue, W. (2013) "Formability of AA5052/polyethylene/AA5052 sandwich sheets" *Transactions of Nonferrous Metals Society of China*, Vol. 23, pp. 964-969. doi:10.1016/S1003-6326(13)62553-4
14. Logesh, K. Raja, V.K.B. (2015) "Formability analysis for enhancing forming parameters in AA8011/PP/AA1100 sandwich materials", *The International Journal of Advanced Manufacturing Technology*, pp. 1-8. doi: 10.1007/s00170-015-7832-5
15. Mohammadi, S.V. Parsa, N.H. Aghchai, A.J. (2011) "Effect of the thickness distribution and setting condition on springback in multilayer sheet bending" *International Journal of Engineering, Science and Technology*, Vol. 3, No.4, pp. 225-235. doi: 10.4314/ijest.v3i4.68555
16. Crolla, D. (2015). *Encyclopedia of Automotive Engineering*. In: Palkowski, H. Sokolova, O.A. Carradó, A. "Materials and Manufacturing" - Sandwich Materials, pp.1-17. Online © 2014 John Wiley & Sons, Ltd. DOI: 10.1002/9781118354179.auto163
17. Engel, B. and Buhl, J. (2012). *Metal Forming – Process, Tools, Design*. Chapter 4 "Forming of Sandwich Sheets Considering Changing Damping Properties", pp.85-108. doi: 10.5772/50565
18. Mann, D. (1999). "Automotive Plastics & Composites - Worldwide Markets & Trends to 2007", second ed. Elsevier, pp. 90
19. A. Carrado, J. Faerber, S. Niemeyer, G. Ziegmann, H. Palkowski (2011) "Metal/polymer/metal hybrid systems: Towards potential formability applications." *Composite Structures*, 93: 715-721.
20. TSE, 2014. <https://www.thyssenkrupp-steel-europe.com/en/press/press-releases/press-release-6552.html>
21. Xi, Z. Zhu, J. Tang, H. Ao, Q. Zhi, H. Wang, J. Li, C. (2011) "Progress of application researches of porous fiber metals" *Materials*, Vol. 4, pp. 816-824. doi: 10.3390/ma4040816

22. R. Gustavsson, Formable Sandwich Construction Material and Use of the Material as Construction Material in Vehicles, Refrigerators, Boats etc., Patent WO A 9801295, 15 January 1998, AB Volvo, International.
23. T.W. Clyne, A.E. Markaki, Ultra Light Stainless Steel Sheet Material, US Patent 6764772, 20 July, 2004.
24. Markaki, A.E.; Westgate, S.A.; Clyne, T.W. The stiffness and weldability of an ultra-light steel sandwich sheet material with a fibrous metal core. In Processing and Properties of Lightweight Cellular Metals and Structures; Ghosh, A., Sanders, T., Claar, D., EdZhou, D.W.; Stronge, W.J. Mechanical properties of fibrous core sandwich panels. *Int. J. Mech. Sci.* 2005, 47, 4-5. s.; TMS: Seattle, DC, USA, 2002; pp. 15-24.
25. J.C. Tan, S.A. Westgate and T.W. Clyne, "Resistance Welding of Thin Stainless Steel Sandwich Sheets with Fibrous Metallic Cores: Experimental and Numerical Studies", *Science and Technology of Welding and Joining* 12(6), 490-504 (2007) doi: 10.1179/174329307X213666
26. A.E.; Markaki, T.W. Clyne mechanics of thin ultra-light stainless steel sandwich sheet material Part I. *Acta Mater.* 2003, 51, 1341–1350.
27. M.A. Azeem C. Shortall U. Ramamurty. Tensile properties of stainless steel sandwich sheets with fibrous cores. *Scripta Materialia* 57 (2007) 221–224 doi: 10.1016/j.scriptamat.2007.04.016
28. Cantor, B., Grant, P., & Johnston, C. (2008). *Automotive engineering: Lightweight, functional, and novel materials*. Chapter 14 "Stainless Steel Sandwich Sheets with Fibrous Metals Cores". New York: Taylor & Francis.
29. Engelmark, M. (2009) "Usability Evaluation of the Fibrous Core Sandwich Material Hybrix for Automobile Body Applications". *Master of Science Thesis Stockholm, Sweden*, pp.5,6
30. Jackson, K.P. Allwood, J.M. Landert, M. (2008) "Incremental forming of sandwich panels". *Journal of Materials Processing Technology*, vol. 204, pp. 290–303
31. Mulone, A. (2015) "Characterization of ultra-light metal-polymer sandwich composite material through dynamic mechanical thermal analysis and microstructural analysis of nickel metal coating obtained through pulse-electrodeposition", Unpublished master's thesis, *Master of Science in Materials Engineering and Nanotechnology*, POLITECNICO DI MILANO - School of Industrial Engineering and Information, Italy.
32. Starman, B. Vrh, M. Halilovič, M. Štok, B., (2014) "Advanced Modelling of Sheet Metal Forming Considering Anisotropy and Young's Modulus Evolution" *Journal of Mechanical Engineering* Vol.60, No 2, 84-92, doi:10.5545/sv-jme.2013.1349.
33. Luzin, V. Banovic, S. Gnäupel-Herold, T. Prask, H. Ricker, R.E. (2005) "Measurement and Calculation of Elastic Properties in Low Carbon Steel Sheet", *Materials Science Forum*, Vols 495-497, pp. 1591-1596.



34. Van Den Boscha, M.J. Schreursa, P.J.G. Geersa, M.G.D. (2009) "On the prediction of delamination during deep-drawing of polymer coated metal sheet", *Journal of Materials Processing Technology*, vol. 209 pp. 297–302. doi: 10.1016/j.jmatprotec.2008.02.024
35. Pauchard, A. (2009) "Precise thin metal cutting using the Laser MicroJet" *Laser in der Elektronikproduktion & Feinwerkstechnik*, 15 (2009), pp. 145–156
36. Car, E. Oller, S. Oñate, E. (2000) "An anisotropic elastoplastic constitutive model for large strain analysis of fiber reinforced composite materials", *Computer Methods in Applied Mechanics and Engineering*, vol. 185 pp. 245–277. doi: 10.1016/S0045-7825(99)00262-5
37. Pupure, L. Joffe, Varna, R. Nyström, J. (2013) "Development of constitutive model for composites exhibiting time dependent properties", *IOP Conference Series: Materials Science and Engineering*, vol. 48 012007.
38. Swift, H. W. (1952) "Plastic Instability under Plane Stress", *Journal of the Mechanics and Physics of Solids*, Vol. 1, No. 1, 1952, pp. 1-18. doi:10.1016/0022-5096(52)90002-1
39. Hill, R. (1998). *The mathematical theory of plasticity*. Oxford University Press Inc, New York, U.S.A
40. Voce, E. (1948) "The Relationship between Stress and Strain for Homogeneous Deformations", *Journal of the Institute of Metals*, Volume 74, pp. 537–562
41. Pipard, J-M. Balan, T. Abed-Meraim, F. Lemoine, X. (2013) "Elasto-visco-plastic modeling of mild steels for sheet forming applications over a large range of strain rates", *International Journal of Solids and Structures*, Vol. 50, issues 16-17, pp. 2691–2700.
42. Kleemola, H.J. and Nieminen, M.A. (1974) "On the strain-hardening parameters of metals", *Metallurgical Transactions, A*. 5. (1974) 1863-1866
43. Neto, D.M. Oliveira, M.C. Alves, J.L. Menezes, L.F (2014) "Influence of the plastic anisotropy modelling in the reverse deep drawing process simulation", *Journal of Materials and Design*, vol. 60 pp. 368–379. DOI:10.1016/j.matdes.2014.04.008
44. Banabic, D. (2010). *Sheet Metal Forming Processes: Constitutive Modelling and Numerical Simulation*, first Ed., Springer, ISBN: 978-3-540-88112-4, pp.45-52. DOI: 10.1007/978-3-540-88113-1
45. Slota, J. Jurčičin, M. Spišák, E. Tomáš, M. Šiser, M. (2015) "Experimental Determination of High strength steel sheet metal", *Acta Metallurgica Slovaca*, Vol. 21, No. 4, p. 269-277.
46. Pepelnjak, T. and Barisic, B. (2009) "Computer-assisted engineering determination of the formability limit for thin sheet metals by a modified Marciniak method," *J. Strain Analysis*, 44 (1), 459 – 472. DOI:10.1243/03093247JSA503.
47. EN ISO 12004-2:2008: Metallic materials, Sheet and strip, Determination of forming-limit curves, 2008.

48. Tekkaya, E.A. Homberg, W. Brosius A. (2015). *60 Excellent Inventions in Metal Forming*. In: Liewald, M. Schmid, P. Schneider, M. Papaioanu, A. "Short-Cycle-Stretch-Forming (SCS)", pp.95. © 2015 Springer Verlag - Berlin Heidelberg, Ltd. DOI: 10.1007/978-3-662-46312-3\_15



## 6. ARTIGO 5: “Experimental Validation Against Different FEM Models in the Simulation of Micro-Sandwich Sheets Forming Under Complex Strain Paths”

**A.M. Pimentel, J.L. Alves, N.M. Merendeiro, T. Soares**

Anthony Michael Fernandes Pimentel<sup>a,b,\*</sup>

\*E-mail: anthony.pimentel@ct.sodecia.com \ anthony.pimentel@dep.uminho.pt

José Luís de Carvalho Martins Alves<sup>b</sup>

Nuno Miguel de Seabra Merendeiro<sup>a, vi</sup>

Tiago Soares<sup>a</sup>

<sup>a</sup> Product Competence Center Sodecia, Rua Eng.<sup>o</sup> Frederico Ulrich, 2650, 4470-605 Maia, Portugal

<sup>b</sup> CMEMS, Universidade do Minho, Campus de Azurém 4800-058 Guimarães, Portugal

---

<sup>vi</sup> Present Adress - Sodecia-participações Sociais Sgps Sa, Rua do Espido, 164-F, Edificio Via Norte, 4470-177 Maia – Portugal

## **ABSTRACT**

Issues and challenges regarding new, continuous and progressive changes in consumer demands and global emission standards have forced European OEMs to develop and implement cost-effective multi-material solutions coupled with efficient and environmentally friendly manufacturing practices in the design and production of their lightweight cars.

In recent years, the interest of the automotive industry in the lightweight potential of laminate composites with metallic cover sheets has greatly increased. However, the industrial production of automotive stamped parts with these materials requires first the knowledge of its deep drawing characteristics. Therefore, the optimization of the manufacturing processes of these new materials and the development of accurate numerical models that are suitable for the multi-layer sheet forming simulation became absolutely fundamental to design feasible stamped parts. Concerning the 3D shell analysis of sheet metal forming processes different FEM approaches can be used, such as, 2D shell elements, 3D shell elements, solid-shell elements and 3D solid elements. All these FE formulations have particular characteristics which affects the numerical results in terms of efficiency, accuracy and reliability. Therefore, there is not yet a clear consensus in the industry about the most suitable FEM strategy to the sheet metal forming simulation of layered composites.

In this work, the current state-of-the-art of multilayer FE formulations available in the stamping simulation market is evaluated. In this regard, the software PAM-STAMP 2015.1 was used to compare 3 possible multilayer FEM approaches. The experimental case of study consists in the deep drawing process of an automotive fuel filling system geometry. To perform the experimental tests micro-sandwich sheets of a layered composite named Litecore S, from Thyssenkrupp, were used. The virtual stamping tests were based on the real tools/blank geometries and process parameters. In the end, the numerical results of each FE model were compared in terms of forming forces, principal strains, principal stresses and thicknesses. In order to validate the most suitable FE model, a formability assessment based in the detection of hot spots, such as wrinkles and splits, was also made. Additionally, some considerations about the deep drawing optimization to the new micro-sandwich material were included.

## **KEYWORDS**

Micro-Sandwich Sheets; Stamping Simulation; Automotive Parts Design; Lightweight Materials

## INTRODUCTION

The production of lightweight vehicles is currently an increasingly serious and unavoidable challenge for the worldwide car manufacturers. The Euro 6 standard, adopted by the European Union and introduced in September 2015, imposes the application of a high tax on vehicles exceeding 95 g/km of CO<sub>2</sub> emissions. In order to adapt to the new regulations, car manufacturers, particularly in Europe, have made a very significant effort to restructure several systems, include new technologies and equipment, and develop new materials to meet these emission requirements. In this context, Ishikawa et al. (2018) present a study showing that it is possible to reduce 20g/km of CO<sub>2</sub> emissions per 100kg of weight savings in a car.

As mentioned by Gándara (2013), the employment of new lightweight materials such as high-tensile steel, aluminum alloy, and composites is the most direct and effective means of weight reduction. Considering this, the concept of "Multiple-material designs", that supports the design of the latest lightweight bodies, promotes the proper application of any available materials that best perform the intended functions regardless of its nature (steel, aluminum, magnesium, plastic or composites).

Due to its low density, good formability, and corrosion resistance, aluminum is the material of choice for many automotive applications such as chassis, autobody and many structural components (Gándara, 2013). In this context, Hirsch (2014) presents some recent developments in aluminum for automotive applications. Henriksson and Johansen (2016) also emphasized the challenges of introducing lightweight materials, like aluminum, in automotive BIWs via part-by-part substitution projects. Material substitution in existing car bodies affects both product development and production processes in an integrated way. So, the improvement of lightweight construction aspects of present and future products must be supported by forming processes and taken into account even during the process developments.

The ongoing development of new materials and new manufacturing technologies has driven the ever-growing trend in the automotive industry to substitute material in existing products (Henriksson and Johansen, 2016). Due to its many advantages in terms of product performance, the micro-sandwich or fiber-reinforced materials are among the most promising candidates for these substitution projects. Nevertheless, there are still many open issues concerning its experimental characterization and numerical modeling, tribological conditions, requirements for manufacturing tools and manufacturing processes in terms of quality assurance. In these cases, numerical simulations studies play a paramount role.

The aim of this study concerns the substitution of the material of an automotive stamped product. The original part is made by aluminum, but the intention is to use a new micro-sandwich material called Litecore S, which exhibits higher stiffness and strength.

However, these micro-sandwich sheet materials, or multi-material sheets, behave very differently from the traditional homogenous aluminum sheets due to the huge difference between the mechanical properties of the polymeric core and the metallic skins. One of the main defects, related to the formability of these materials, is the high risk of wrinkling initiation and propagation during forming operations, together with

tearing, springback and other geometric and surface defects (Cao et al., 2004). Thus, the correct modeling and accurate simulation of micro-sandwich sheets still remains a complex and challenging problem.

Today, the most common finite element analyses (FEA) tools in the automotive stamping industry are based on the thin shell theory. The first shell theory was developed by Kirchhoff (1850) and then extended by Love (1888) as an attempt to construct a theory of the vibrations of bells. The fundamental assumption considered, is that the finite element cross section remains straight, unstretched and normal to the mid-surface, which is not true. So, the Kirchhoff theory can be used for the numerical modeling and treatment of several problems in solid structural mechanics, involving static bending, vibration and stability, but it is limited to thin plates (Ghugal and Shimpi, 2002). In the case of thick plates, Kirchhoff's theory is no longer valid because it neglects the transversal shear deformation.

Sandwich plates are frequently used because of their ability to provide high bending stiffness while presenting light weight. Typically, the core is made of materials with reduced stiffness, which results in the appearance of shear effects that need to be accounted for. The first order shear deformation theory (FSDT), commonly referred to as the Mindlin-Reissner's theory, is the most basic tool available to take into account such effects. Mindlin-Reissner's plate theory, proposed by Raymond Mindlin (1951), is an extension of Kirchhoff-Love's plate theory. As well as the Reissner's theory (1945), it also takes into account shear deformations through-the-thickness of thick plates. Yet Mindlin's theory assumes that there is a linear variation of displacement across the plate thickness, together with a plane stress condition, i.e. the normal stress across the thickness is neglected. For its part, Reissner's theory assumes a linear bending stress and a quadratic shear stress through the plate thickness, in which the plane stress condition is not fulfilled (Wang et al., 2001). Unlike Mindlin, whose assumptions impose a constant plate thickness during the deformation, Reissner's theory allows the non-linear variation of the through-the-thickness displacement and the variation of the plate thickness (Wang et al., 2001). Therefore, Reissner's theory is considered a stress-based plate theory while the Mindlin-Reissner's theory is considered a displacement-based plate theory. The Mindlin-Reissner's theory is widely used for the bending analysis of sandwich plates. It relaxes the normal segment hypothesis and takes into account a constant shear strain on the plate thickness. In order to correct the discrepancy between this constant distribution and the real parabolic distribution, the theory uses a shear correction factor. Naghdi (1957) also included the shear transverse strains to develop a second-order shear deformation theory.

In 1968, Ahmad, Irons and Zienkiewicz presented a method based on the 2D-discretization of the 3D-continuum named "degenerated solid approach" (Ahmed et al., 1968). As the name suggests, the method consists in degenerating a 3D finite element to obtain an equivalent 2D shell element, also known as 3D shell. Then, a 2D mesh is generated from geometrical discretization. In addition to the common 6 degrees of freedom (3 rotations and 3 translations) a 7th parameter for linear transverse normal strain distribution was included in this FEM model. Thus, the unstretched inconsistency is solved. However, the 7th parameter

shell model is not able to reproduce high order effects. Büchter and Ramm (1992) presented a method based on the 3D-discretization of the 3D-continuum. In this case, a 3D mesh is generated from the geometrical discretization. However, specific linear shape functions and additional assumptions are assigned to the finite elements in order to present a shell behavior. For that reason, these finite elements are known as solid-shell or shell-continuum. Even so, since only an average shape of some stress components through the thickness can be obtained, these elements are still considered straight. In fact, several methods, such as the multi-director shell formulations, have been developed to describe the local deformation behavior in non-homogeneous thin structures and to produce approximate solutions of the three-dimensional boundary value problem (Reddy, 2004).

The emergence of advanced micro-sandwich materials in the automotive industry, which can be shaped by conventional stamping processes, has raised the need of using 3D shell analysis rather than 2D shell theory in this area of computational mechanics. In this kind of large strain shell problem, classical shells are not effective to predict the 3D stress state present in micro-sandwich sheets. As referred in the literature, the main complicating effects connected with the use of multilayered structures are the in-plane anisotropy and the transverse anisotropy (Fung et al., 2001; Love, 1959). Brischetto (2017) explains that the high in-plane anisotropy is related with the different mechanical-physical properties in the in-plane directions and the higher transverse shear/normal flexibility with respect to in-plane deformability. While the in-plane anisotropy gives a coupling between shear and axial strains, hindering the solution procedure in the analysis of anisotropic structures, transverse anisotropy leads to different mechanical properties through the thickness direction (Brischetto, 2017). This discontinuity in terms of mechanical properties produces a variation of the in-plane displacements through the thickness that can be described by a piecewise nearly linear zigzag function. (Aitharaju and Averill, 1999)

Thus, the development of efficient and accurate 3D and refined 2D shell models able to describe the effects of planar anisotropy, transverse anisotropy and allowing the correct description of the load conditions in multilayered configurations has become a real challenge (Brischetto, 2017). Laminated and sandwich structure formulations are mainly classified according to the treatment of the variables in the normal direction of the plate/shell surface: equivalent single layer, zig-zag and layer-wise theories.

Sussman and Bathe (2013) mention 3 different approaches to model the large strain behavior of the shells. The simplest approach uses 2D shell elements, in which thickness is updated iteratively during the incremental solution (Dvorkin et al., 1995). In the second approach, a single layer made by 3D solid elements with 12 nodes or 27 nodes is used. The latter approach consists on the use of 3D-shell elements or solid-shell elements.

Concerning large strain shell problems, as the stamping simulation of micro-sandwich sheets, the usage of 3D solid elements, in practice, can be too expensive (Bathe and Wilson, 1974; Bathe, 1976). In addition, locking phenomena tends to appear with 3D solid or 3D-Shell displacement-based elements,



making them unsuitable for the mathematical model discretization (Sussman and Bathe, 2013). To overcome this problem, the ‘enhanced strain approach’ and the ‘reduced integration’ has been used by many researchers. But, the usage of these special treatment techniques results into severe numerical instabilities, which can only be suppressed using artificial numerical factors that at large strains may need to change with the deformation response (Daniel and Belytschko, 2005; Reese and Wriggers, 2000; Wall et al., 2000; Reese, 2005). As stated by Sussman and Bathe (2013), the use of any of these numerical factors is quite undesirable, in particular, when large deformations and large strains shall be predicted, since the solutions may contain physical instabilities that may be masked by artificial factors; hence the solutions can be unreliable and quite inaccurate. In order to suppress locking effects from the 3D-shell elements.

The 3D-continuum elements have been greatly investigated over the past 20 years, presenting itself as a very promising response to solve 3D large strain shell problems of laminated, such as the stamping simulation of micro-sandwich sheets. Still, the solutions available in the market relies essentially on the classical formulations of 2D shells or 3D solids elements. In this work, different FEM approaches based on 2D Shell and 3D Solid elements are compared to evaluate the feasibility of commercial FEA tools in the design of new products or substitution projects of conventional materials in complex geometry parts, throughout micro-sandwich sheet forming processes. The software chosen to perform this study is PAM-STAMP 2015.1.

## **EXPERIMENTAL CASE OF STUDY: GEOMETRY PART AND STAMPING PROCESS**

In this section, the original stamped part and stamping process conditions, in which this study is based, are presented.

- **Part Geometry**

The selected geometry is based in a stamped automotive fuel filling system which was designed and developed at the Product Competence Center of Sodecia in Portugal [Fig. 6.1].



Fig. 6.1 – Stamped Prototype of an aluminium automotive fuel filling system designed by Sodecia.

This prototype part is originally made by 2 shells of 1050 aluminum alloy, each one corresponding to

the half part of the fuel filling geometry, welded together by roll welding techniques.

- **Tools Geometries and Blank Dimensions**

As depicted below [Fig. 6.2], two sets of stamping tools are needed: a) and d) - to the concave shell; b) and c) - to the convex shell. Each stamping tool set includes 1 die, 1 blankholder and 2 punches.

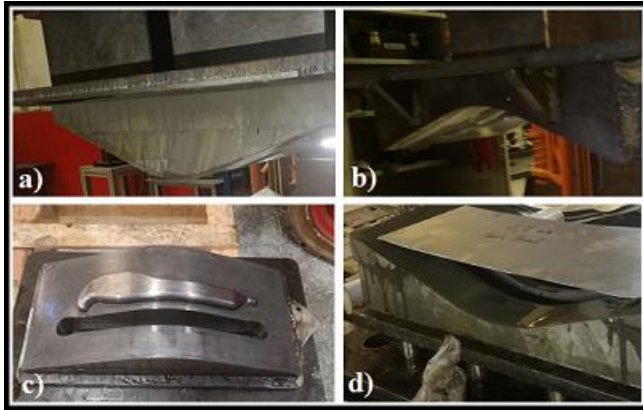


Fig. 6.2 – Set of stamping tools (Die, Blank-Holder and Punches) to the concave shell (a and d) and the convex shell (b and c). Blank in the initial position (d).

The blank considered in the stamping process is the same for both shells. The in-plane dimensions of the blank are presented below on Fig. 6.3.

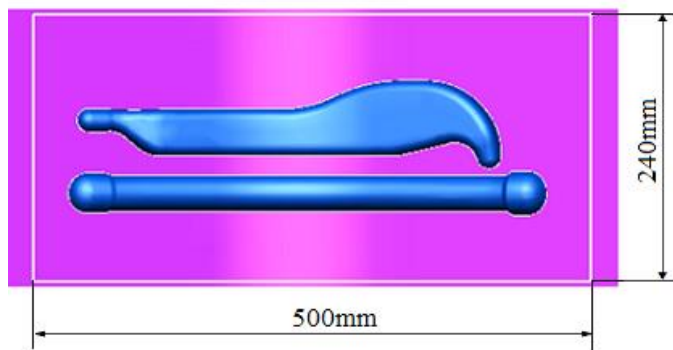


Fig. 6.3 – Dimensions of the original rectangular blank.

Therefore, the stamping complexity is roughly the same. In this study, the concave shell was chosen to perform the stamping tests with Litecore material. Since the stamping tool offset cannot be changed and the original aluminum blank was 1.5mm thickness, it would be recommended to use Litecore blanks with a nominal thickness of 1.5mm. In addition, it would be desirable that the maximum metallic thickness of the micro-sandwich sheet did not exceed 0.5mm to remain close of the original weight. Taking into account the commercial line of Litecore, the available product closer to these requirements was the Litecore S. The

Litecore S micro-sandwich sheets have 2 metallic skins, each one of 0.3mm, and a polymeric core with a thickness of 1mm.

- **Stamping Process Conditions**

The stamping process includes 2 forming operations. In the first forming operation, the blank is bent as the die moves vertically until it reaches the blankholder. The die stroke in the closing tools step is 80mm. In the second forming operation, the die moves against the punch and the blankholder until the closing position. In this deep-drawing step, the blank is shaped to the final part geometry. During this 25mm stroke, the die must overcome the punch force, necessary to deform plastically the blank, and the 10bar of blankholder pressure defined to control the flow material.

The 2 forming operations of the stamping process are depicted in the Fig. 6.4.

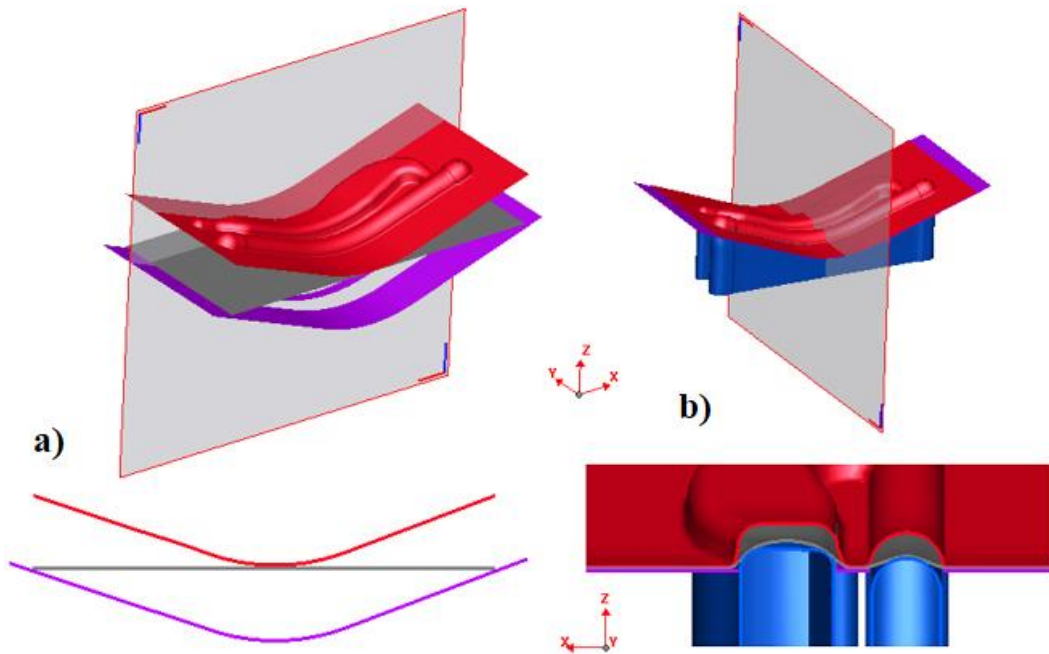


Fig. 6.4 – Presentation of the virtual stamping process in 2 forming operations. a) Closing of the tool pair Die/Blank-Holder to bend the Blank. b) Deep-drawing of the concave shell.

As mentioned before, the understanding of the carrying-load actions which dominates the deformation mode is very useful to build a suitable FEM model. In this case, a closer look to the tools kinematics reveals that the first forming operation is only driven by *bending deformation*, while the second forming operation is mainly driven by *membrane deformation*. The amount and distribution of plastic deformation is also related with lubrication conditions. To handle with high level of stretching during the forming process, the contact surface blank/stamping tools was smeared with oil and covered with a plastic film.

## CASE OF STUDY: NUMERICAL MODEL

The material model is a paramount aspect to consider in the numerical simulation of the sheet forming

processes; since it rules the mechanical behavior of the micro-sandwich sheets, the reliability and accuracy of the numerical results depend on it. In order to do so, this model must be based in the experimental characterization of the materials.

Fig. 6.5 presents the hardening curves used in this study to characterize the mechanical behavior of the metallic skins (CR300IF+ZE) and the polymeric core of the Litecore S micro-sandwich sheets.

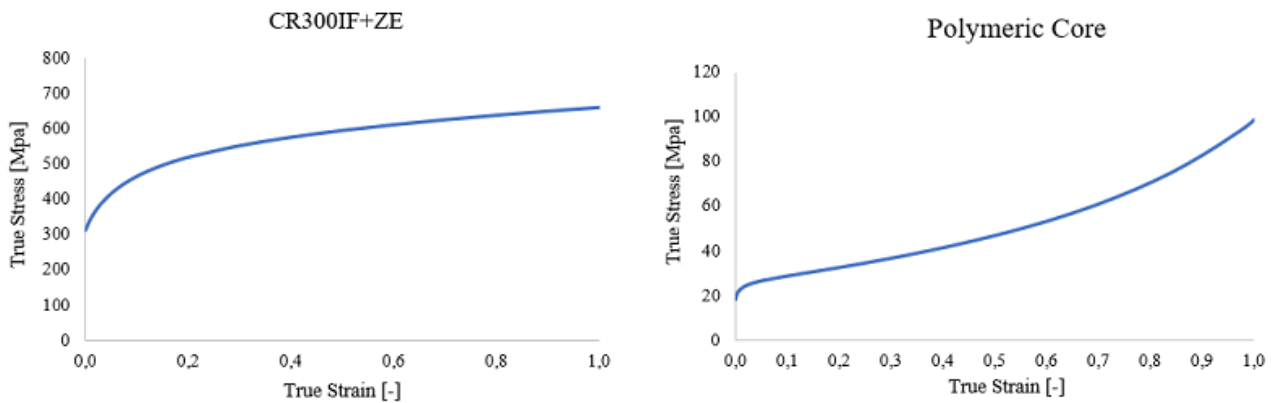


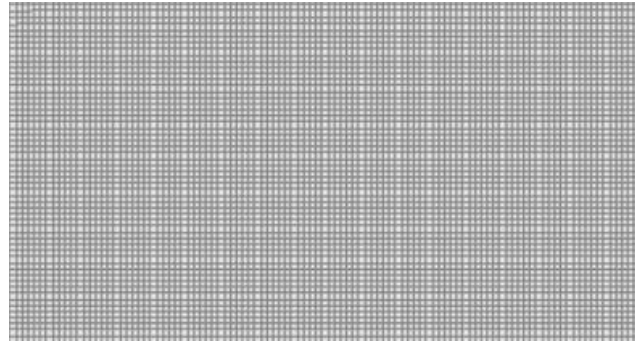
Fig. 6.5 – Presentation of true stress/strain curves of the metallic skins and polymeric core of the Litecore S

In addition to stress-strain relationship, the anisotropic behavior of the metallic sheets must be defined to complete the mechanical model. Thus, a quadratic yield criterion of Hill48 was considered in the elastoplastic constitutive model. The Lankford coefficients, Young modulus and specific weight of each Litecore S layer are presented in Tab. 6.1.

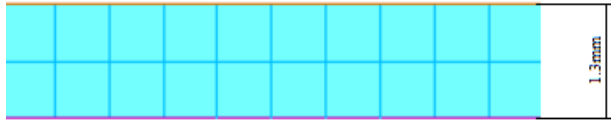
Tab. 6.1 – Description of the mechanical model’s assumptions (Yield Criteria, Young’s Modulus, Specific Weight) of each Litecore S layer.

MECHANICAL MODEL					
Layer	Yield Criteria Hill48			Young’s Modulus (GPa)	Specific Weight (kg/dm <sup>3</sup> )
	<i>r</i> <sub>0</sub>	<i>r</i> <sub>45</sub>	<i>r</i> <sub>90</sub>		
Skin	1.02	1.85	1.53	210	7.8
Core	1.00	1.00	1.00	0.65	1.5

As a result, different FEM approaches can be taken in the numerical model and fairly compared since it is considered the same FE code and constitutive description. The stamping software PAM-STAMP 2G 2015.1 allows modelling multilayer material with 2D shell elements and/or 3D solid elements. So, 3 different models based in the multilayer configuration of the FE mesh were built and compared in this study [Fig. 6.6].



a) 2D Shell model



b) 2D/3D model



c) 3D Solid model

Fig. 6.6 – Presentation of the 3 FE mesh multilayer configurations compared in this study.

The first FEM model, which is called throughout this paper **2D Shell model**, is based in a 2D shell finite elements mesh. This mesh is defined in the plane while the number, thickness and material properties of the layers is defined through thickness. Since the part presents a complex geometry with very small radii and the aspect ratio of the finite element should be comparable with the other FEM models, the element size defined was  $0.50 \times 0.50$  [mm].

The second FEM model, which is referred to as **2D/3D model** is based in a mesh, which combines 2D shell elements to model the metallic skins, with 3D Solid elements, to model the polymeric core. Due to the fact that the 2D shell elements are defined in the middle plane, the 2 metallic skins meshes had to be separated by a distance of 1.3mm, instead of 1.0mm, to match the nominal thickness (1.6mm) of the Litecore S micro-sandwich sheet. The resultant FE mesh is made by 2 inner layers of 3D solid elements with a size of  $0.65 \times 0.65 \times 0.65$  [mm] and 2 outer layers of 2D shell elements with  $0.65 \times 0.65$  [mm].

The third FEM model, which is called throughout this paper **3D Solid model**, is based in a 3D solid finite element mesh. This mesh is made by 2 inner layers of 3D solid elements with a size of  $0.50 \times 0.50 \times 0.50$  [mm] and 2 outer layers of 3D solid elements with  $0.50 \times 0.50 \times 0.30$  [mm].

All models run in the same machine (CPU I7 6700HQ – 8 Cores) and using the same solver (*DMP* – Distributed Memory Parallel). Tab. 6.2 presents some other important assumptions of the numerical model of each FEM approach like the FE type, FE integration rule, gauss points and the respective run time simulation.

Tab. 6.2 – Description of the numerical model's assumptions (FE Type, FE Integration Rule, Gauss points over Thickness, Element Size) of each FEM approach and the respective run time simulation.

NUMERICAL MODEL					
FEM Approach	FE Type	FE Integration Rule	Gauss points Thickness	Element Size [mm]	Run Time [sec]
2D Shell	2D Quadrilateral	BWC Full (4 pts)	11 pts	0.50x0.50	282
2D Shell 3D Solid	2D Quadrilateral 3D Hexahedral	BT Reduced (1pts) Selective Reduced (8 pts)	11pts -	0.65x0.65 0.65x0.65x0.65	1898
3D Solid	3D Hexahedral	Selective Reduced (8 pts)	-	0.50x0.50x0.50 0.50x0.50x0.30	7203

In all the FEM approaches considered, the meshes are based in first-order finite elements, independently of being 2D quadrilateral or 3D Hexahedral. All the 2D shell elements have 11 gauss points in the thickness direction and all the 3D solid elements use the selective reduced integration. However, different integration techniques were used concerning the shell finite elements of the 2D shell and 2D/3D FEM models. In the case of the 2D Shell FEM model, it was adopted a fully integrated Belytschko-Wong-Chiang formulation, which uses an in-plane integration scheme with 4 gauss points instead of 1 to obtain an exact integration of the internal forces. This results in a full rank element, i.e. no zero energy modes (hourglass modes) are present in the element. In addition, an assumed shear field based is used to avoid shear locking in the element due to full integration and an assumed membrane field is used to avoid membrane locking due to full integration. In the other hand, it was adopted a Belytschko-Tsay formulation in the case of the 2D/3D model, which is based on the concept of reduced uniform integration, making this element extremely simple, very efficient, and suitable to be combine with 3D solid elements.

## EXPERIMENTAL VS. NUMERICAL RESULTS: COMPARISON AND DISCUSSION

After running the numerical simulations, the results are compared in terms of:

- Draw-in
- Formability (Wrinkles Assessment, Forming Limit Diagram - FLD)
- Punch forces
- Principal strains and thickness distribution
- Maximum stress distribution

The aim of this study is to compare the accuracy and reliability of each FE model and determine the most suitable to model and simulate the stamping process of Litecore S micro-sandwich sheets.

### Draw-in:

The draw-in optimization helps to define the best size and shape of the blank, maximizing cost savings with the raw material and the quality of the stamping part (Pimentel et al., 2018).

To get a measurement representative of the variable draw-in, 3 sections across the blank, at the end of

the forming process, were defined, as depicted in the Fig. 6.7. Then, the y-distances from the edge of the blank to the die radius, were measured in each section and for both sides.

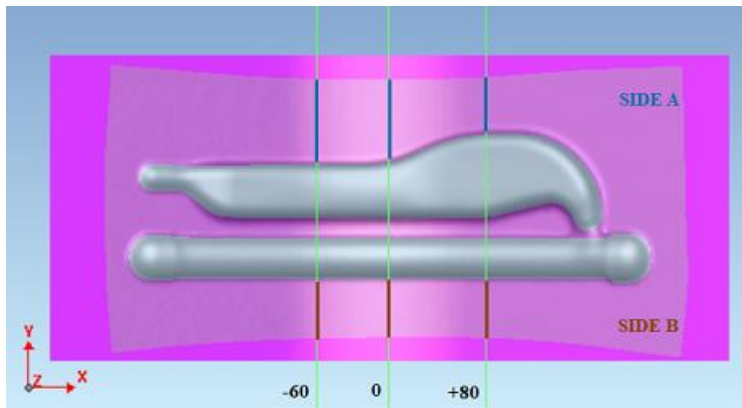


Fig. 6.7 – Position and naming of the draw-in sections with the respect to the part geometry.

The y-distances were measured from the section cuts made in the meshes for each FEM model and also in the experimental part, using a Mitutoyo digital pachymeter, duly calibrated [Fig. 6.8].



Fig. 6.8 – Experimental measurements of the y-distances in cross sections defined in the study and marked in the part.

The numerically predicted and experimentally measured y-distances are presented below [Tab. 6.3]. The numerical results that are furthest from the experimental value are highlighted in bold.

Tab. 6.3 – Presentation of the experimental and numerical y-distance measured in each cross section.

-60	2D Shell	2D Shell 3D Solid	3D Solid	Exp.
<b>SIDE A</b>	47.25	<b>45.31</b>	<b>45.38</b>	46.96
<b>SIDE B</b>	<b>64.97</b>	<b>63.01</b>	61.18	60.84

0	2D Shell	2D Shell 3D Solid	3D Solid	Exp.
<b>SIDE A</b>	45.30	45.28	45.35	45.85
<b>SIDE B</b>	59.19	59.10	61.18	59.98

80	2D Shell	2D Shell 3D Solid	3D Solid	Exp.
<b>SIDE A</b>	45.46	43.57	43.62	48.61
<b>SIDE B</b>	40.15	38.31	40.19	40.45

In general, the y-distances predicted in the stamping simulation showed a good correlation with the experimental measurements. The overall mean deviation between the numerical values and the experimental values was 1.54mm for the 2D Shell model, 2.08mm for the 2D/3D model and 1.48mm for the 3D Solid model, which is quite acceptable considering the dimensions and geometry of the part and the type of stamping process. Therefore, although the experimental friction coefficient was not measured, the results obtained in the stamping simulations suggest a good reproducibility of the experimental conditions. Comparing the numerical values of each section, the deviations between the different FEM models vary within the range [0.02-3.97] mm, where the overall mean value is 1.3mm if a distance of 50mm is considered, or 2.6%. In industrial practices, where so many factors affecting the tribological conditions such as lubrication, tool's wear and geometry, misalignments in the stamping press, etc., this difference is not so significant to change a conservative decision based in the FEA tool results. Therefore, it can be concluded that the element technology had a little impact on draw-in predictions.

### **Formability:**

This section attempts to evaluate the accuracy of the numerical simulations in the prediction of the part formability. In this regard, the authors defined two criteria:

- a) The sensitivity of FEM models to predict wrinkles tendencies.
- b) The Forming Limit Diagram (FLD) analysis.

- **Wrinkles Assessment**

The wrinkling prediction in sheet metal forming simulation is very important because it impacts directly on the product quality. The accurate prediction of this kind of instability in the stamping simulation is a challenging task.

The next figure [Fig. 6.9] compares the results predicted by the different FEM models and the experimental results at the 3 reference stages of the deep-drawing step (12mm, 6mm and 2mm). Areas where the material accumulation becomes apparent (excessive thickening) were highlighted with blue dotted circles, while areas with visible wrinkles were highlighted with red dotted circles. The black outline highlights the model that failed to predict all areas of material accumulation or wrinkles identified in the



real parts.

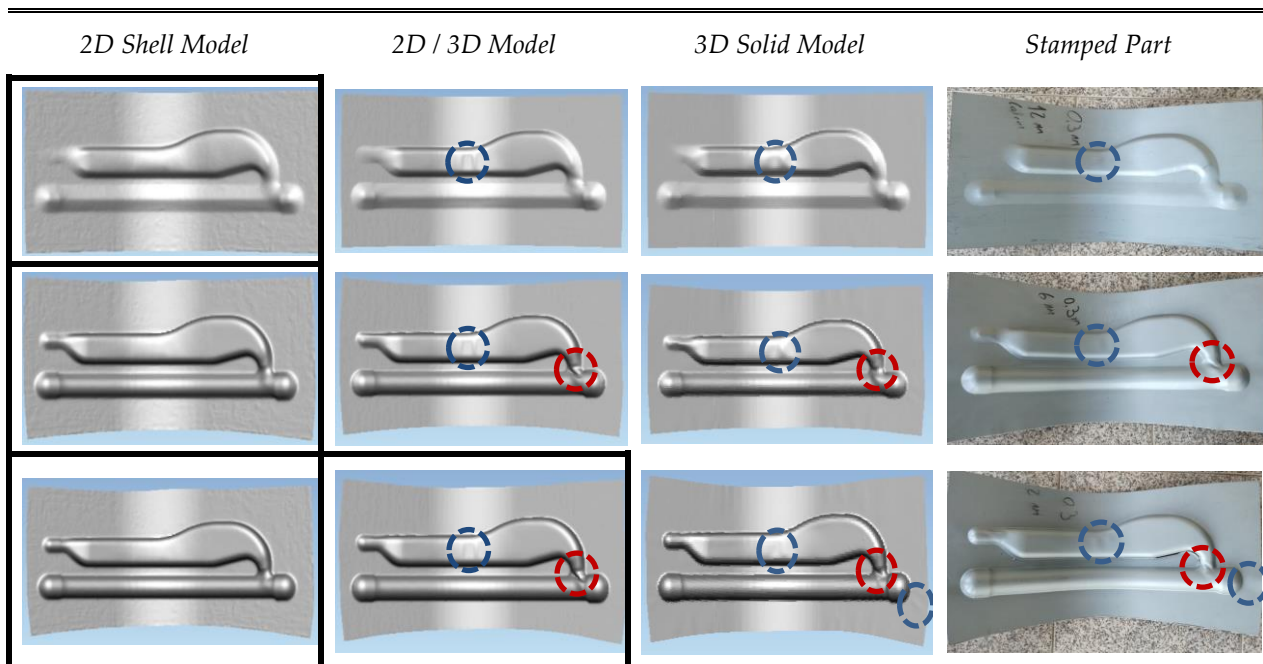


Fig. 6.9 – Comparison of numerical and experimental wrinkling tendencies. Areas of material accumulation are highlighted with blue dotted circles, while areas with visible wrinkles are highlighted with red dotted circles. Black outline highlights the FEM model that failed to predict all areas of material accumulation or wrinkles identified in the real parts.

As observed in Fig. 6.9, the 2D Shell model cannot predict the areas of material accumulation and wrinkles at any deep-drawing stage. In the 2D/3D model, no accumulation of material near the end of the part becomes apparent at the end of the stamping operation. The 3D Solid model showed to be the most accurate in the study, identifying all the hot spot zones during different stages of the deep-drawing step.

The initiation and growth of the most prominent wrinkle takes place in the punches transition zone due to the instability of the flow of material generated during the deep-drawing operation. A cross-section at position  $X = 160\text{mm}$ , which corresponds to the most problematic area of material accumulation, is represented [Fig. 6.10].

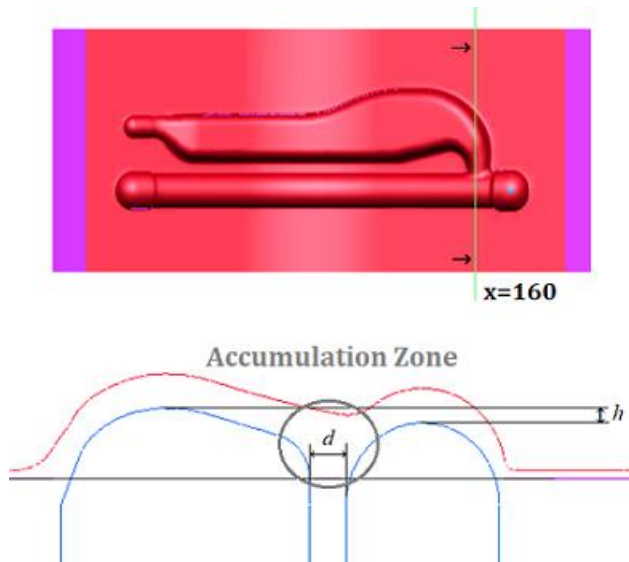
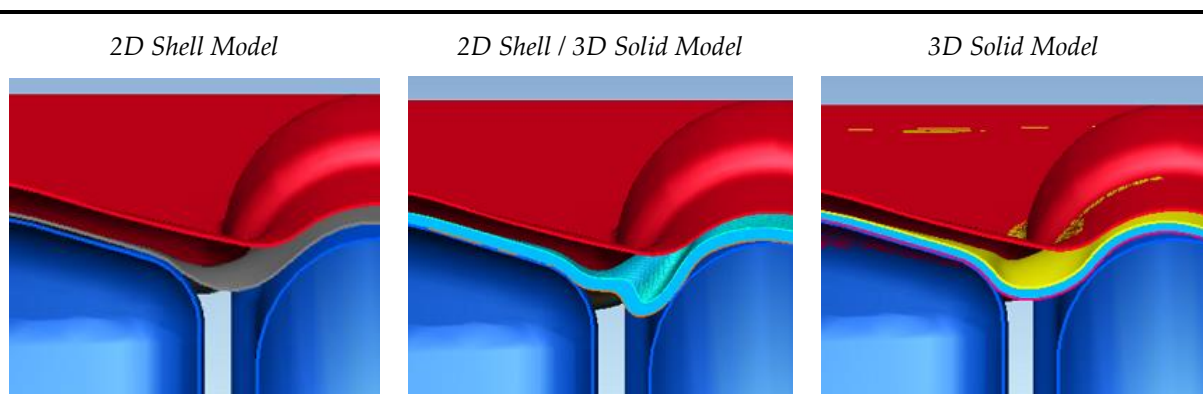


Fig. 6.10 – Presentation of a tools section cut at position  $x=160$ .  
The accumulation material zone is represented by a gray circle.

Here, the material accumulation zone, resultant from the combined effect of the height difference  $h$  between the punches and the total absence of support of the sheet along the distance  $d$ , is represented by the gray circle. This accumulation of material, induces in-plane compressive forces that lead to the wrinkle formation. In this case, the mechanical behavior of the micro-sandwich sheet is closely related with bending stiffness. Due to this fact, multilayer sheets with soft polymer cores are less buckling resistant to compressive forces and more susceptible to wrinkling than monolithic metal sheets with the same total thickness.

A comparison of the Litecore S sheet behavior in the accumulation zone, predicted by the different FEM models and observed in the real part at the final of deep-drawing operation, is presented at Fig. 6.11. For a better understanding, cross-section views of the FEM models, at distance  $X=160\text{mm}$ , are presented.



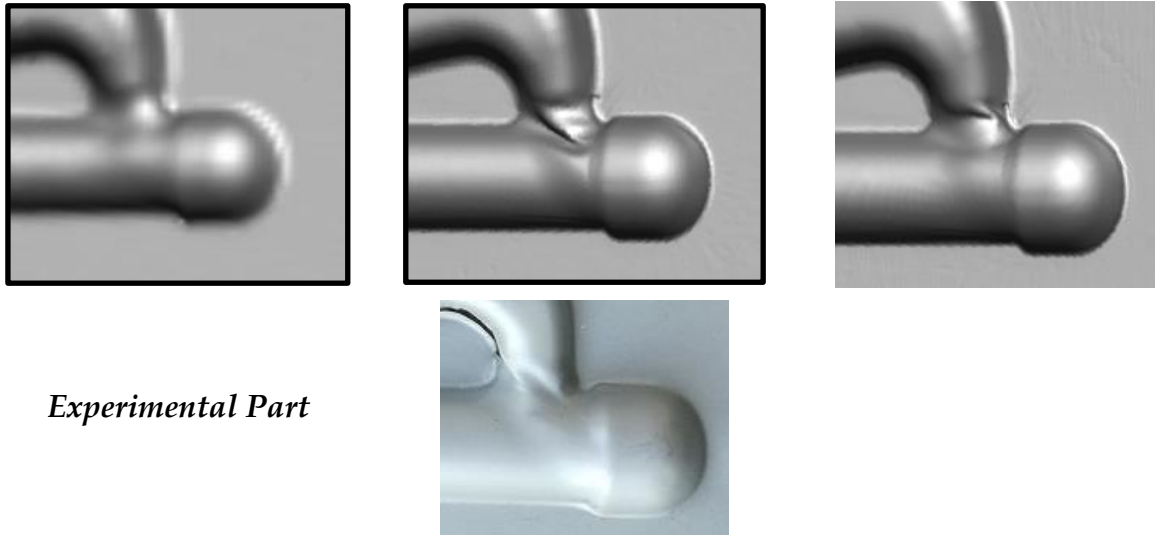


Fig. 6.11 – Comparison of the Litecore S sheet behavior in the accumulation zone, predicted by the different FEM models and observed in the real part at the final of deep-drawing operation.

Using the 2D Shell model it was not possible to reproduce numerically the formation of the wrinkle. On the other hand, the 2D/3D model and the 3D Solid model reproduce the wrinkle phenomenon. Comparing with the real part, the numerical wrinkle of the 3D Solid model is the one closest to the experimental. However, it should be noted that the location, shape and length of the experimental wrinkle was also affected by a relatively close rupture of the sheet. Thus, to achieve a more accurate comparison of the FEM model that best describes the initiation and collapse of the wrinkle it would be necessary to include the elimination of the finite elements of the mesh in the rupture zone. Nevertheless, the results obtained numerically are quite satisfactory for the 2D/3D and 3D models and sufficient to identify the measures necessary to make a feasible part and improve stamping process robustness.

- **Forming Limit Diagram - FLD**

The Forming Limit Diagram (FLD) is an absolutely necessary outcome in any stamping simulation report, since it is very useful to predict formability defects related with the stamping process and/or product geometry (Pimentel et al., 2018).

Fig. 6.12 shows the position of the FLC of CR300IF, corresponding to the metallic skins of the micro-sandwich Litecore S, in FLD.

### CR300IF+ZE Forming Limit Diagram

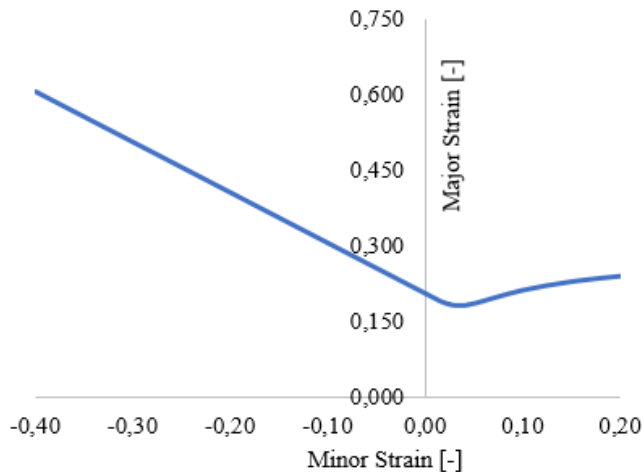


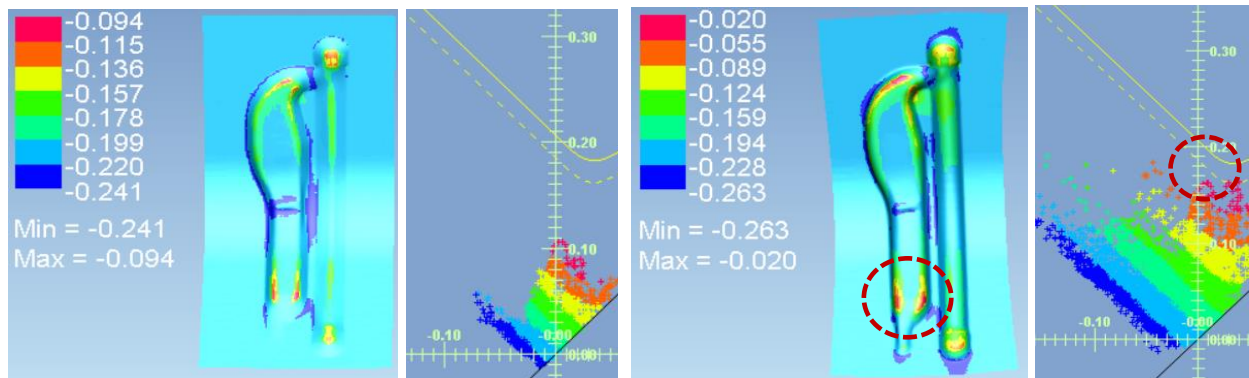
Fig. 6.12 – Position of the FLC of CR300IF+ZE, corresponding to the metallic skins of the micro-sandwich Litecore S, in FLD.

This study was based on the FLD of the metallic skins because the mechanical behavior of the Litecore S sheets is mainly ruled by them, which are much more resistant than the core. Additionally, the detection of defects with the naked eye can only be done in the outer layers. Since the strain paths during the stamping process are not always linear, the non-linear FLD must be used instead of a linear FLD, to get a correct evaluation of the deformation history.

To avoid a very thorough analysis and taking into account the conclusions that already have been drawn concerning the FEM model with the best accuracy/efficiency ratio, only the results predicted by the 2D/3D model are displayed. Thus, Fig. 6.13 shows the cloud of the material points, and the respective strain state, in the upper skin of the stamped part and in the FLD at 12mm, 6mm and 2mm.

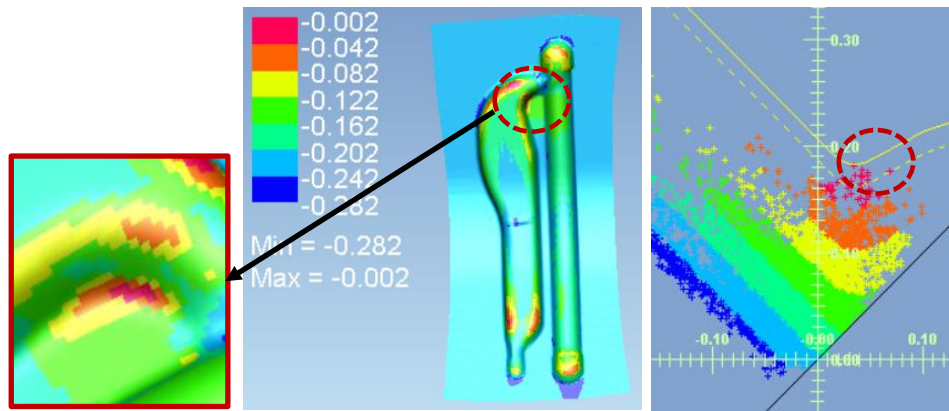
### 2D/3D Model

#### Upper Skin



At 12mm of the end

At 6mm of the end



At 2mm of the end

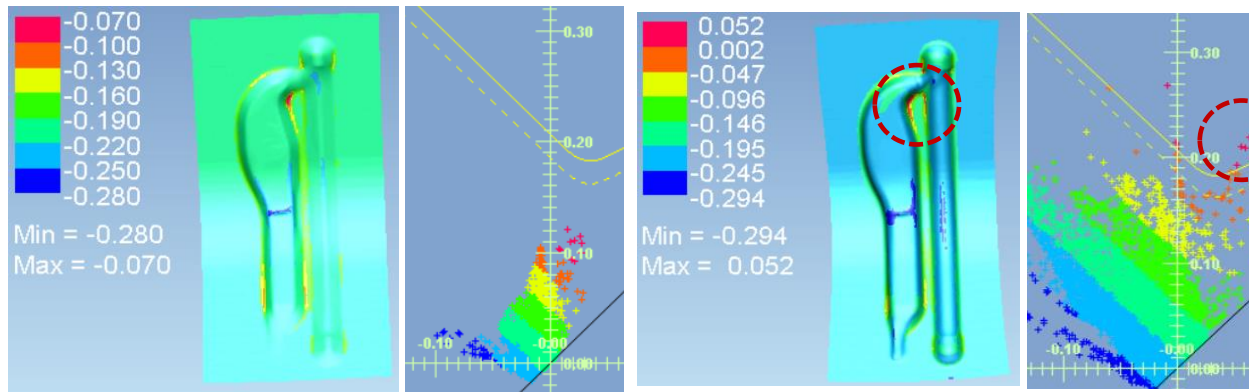
Fig. 6.13 – Cloud of the material points, and the respective strain state, predicted by the 2D/3D model, in the upper skin of the stamped part and in the FLD at 12mm, 6mm and 2mm.

From this analysis, it is expected that the upper skin splits between the punches near to the transition zone, since the material points reach the limit of admissible plastic strain. It is also possible to verify the existence of material points subjected to compression in the previously identified accumulation zones.

Fig. 6.14 shows the distribution of the material points, and the respective strain state, in the lower skin of the stamped part and in the FLD for the 2D/3D model at 12mm, 6mm and 2mm.

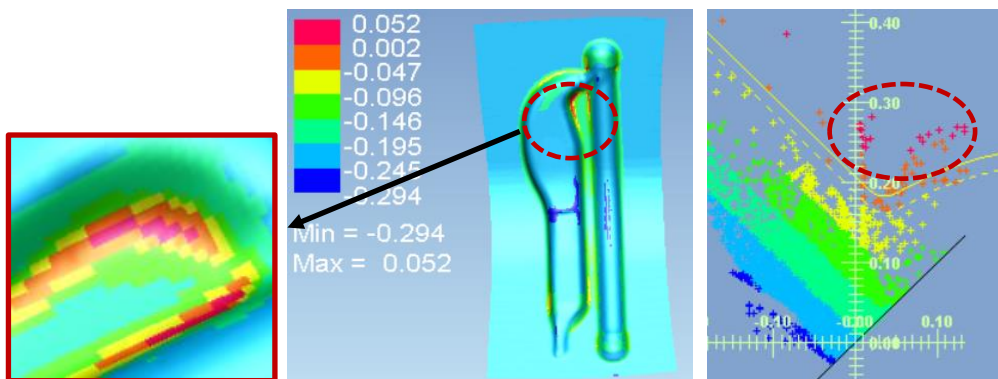
### 2D/3D Model

#### Lower Skin



At 12mm of the end

At 6mm of the end



#### At 2mm of the end

Fig. 6.14 – Cloud of the material points, and the respective strain state, predicted by the 2D/3D model, in the lower skin of the stamped part and in the FLD at 12mm, 6mm and 2mm.

In this case the conclusions are similar, the lower skin will split in the same zone but more severely, since the material points reach strain levels that widely exceed the FLC. On the other hand, less material points are subjected to compression in the lower skin.

A picture of the real part at the instant 2mm is shown below Fig. 6.15.

### *Experimental Part*



Fig. 6.15 – Picture of the real part at the instant 2mm.

Thus, it is also possible to confirm the existence of the numerically predicted rupture in the real stamped part and prove the accuracy of the 2D/3D FEM model to the simulation of stamping process using micro-sandwich sheets with polymeric cores, subjected to complex deformation paths.

### **Punch Forces:**

An accurate prediction of the stamping forces involved in the process is very useful to select a stamping press which meets the load and energy requirements (Pimentel et al., 2018).

As mentioned before, different FE models were considered to model and simulate the real stamping process of a complex geometry part with Litecore S. In this section, the influence of the FE model in the numerical forming forces will be evaluated.

Fig. 6.16 presents, respectively, a cross section of the closed tools with the blank in the initial position and the final position of the deep-drawing operation.

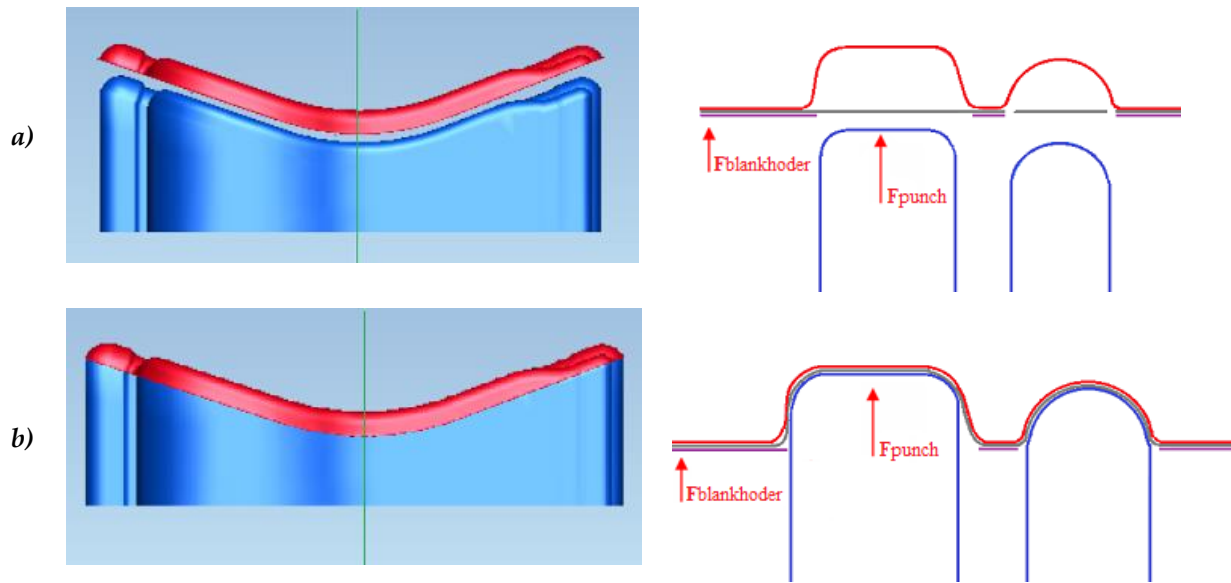


Fig. 6.16 – a) Tools and blank in initial position before deep-drawing operation. b) Tools and blank in home-position after deep-drawing operation.

The numerical punch forces of each FE model were recorded throughout the deep-drawing operation and plotted together. Fig. 6.17 presents the evolution of the numerical punch forces to all FEM approaches.

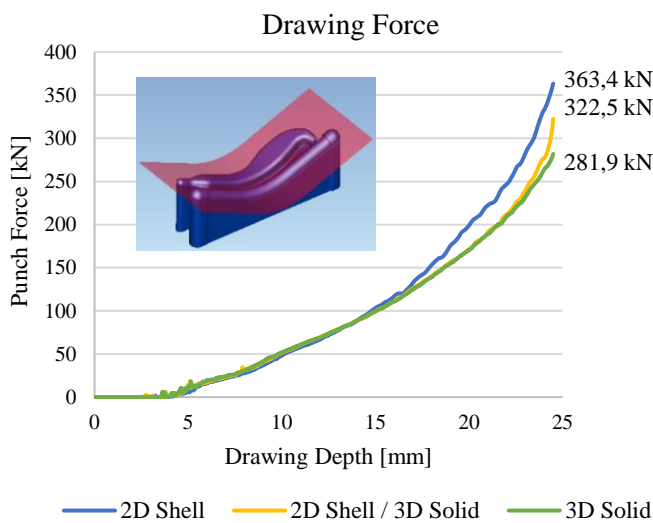


Fig. 6.17 – Comparison of the evolution of the numerical punch forces to all the FEM approaches during the deep-drawing operation.

As it can be seen from Fig. 6.17, the 2D Shell model predicts the higher final punch force, 363.4kN, which means, 22% more than the 2D/3D model and 11% more than the 3D solid model. From a practical point of view, a difference of 8tf (80kN) is not especially significant if considered a common press tonnage range of 200tf-1500tf in the automotive industry. However, this difference may take on a greater importance

when multiplied by several operations in a progressive tool. Therefore, it is necessary to understand how the FEM model influences the forming forces prediction.

Looking at the Fig. 6.17, it is possible to see that the numerical force-displacement curves present the same behavior up to 17mm of drawing depth, that is, almost 70% of the stroke. From there, there is a divergence of the force-displacement curve predicted by the 2D Shell model. The force-displacement curve of the 2D/3D model starts to diverge from the 3D solid model after reach 24mm of drawing depth, or, 96% of the stroke. Thus, it is evident that the finite element technology determines the numerical forming force results.

As the die moves towards the punch, the material is submitted to more and more complex 3D strain paths and increasingly higher plastic strain levels affecting the efficiency and performance of the 2D shell elements. In general, shell elements are very effective in the stamping simulation and delivers very good results in terms of forming forces for most of geometries. But, in the case of complex geometries with very small radii, these elements must be used carefully since they are no longer effective for a certain thickness/radius ratio. The stamping process of the fuel filling system is extremely demanding for the shells in terms of bending-unbending-stretching effects. In addition, the formulation of these shells also includes very different mechanical properties through the thickness related with the micro-sandwich layers. In such circumstances, the excessive deformation and distortion of the 2D shell elements leads to overestimated predictions of final forming force. On the other hand, the nodal displacements of the 2D shell elements are linked to the nodal displacements of the 3D solid elements in the 2D/3D model, so they are not affected by excessive deformation in this case. Moreover, the separation of 2D shell elements by 3D solid elements along the thickness also improves their bending behavior and consequent performance. The divergence of the 2D/3D model only occurs when the stamping tools are practically closed and the plastic strain already reaches values above the forming limits of the material.

### **Principal Strains and Thickness distribution:**

The principal strains and thickness distribution are strongly related with the general formability of a stamping part. Therefore, the evaluation of the stamping part feasibility, stamping tools design and stamping process robustness is highly dependent of a correct prediction of these variables (Pimentel et al., 2018).

The principal strains and thickness were evaluated in the 3 sections referred (-60, 0, +80). In addition, the upper skin (die side) and lower skin (punch side) results are detailed. The resulting curves were output as principal strain/thickness over the arc-length distance of the section cut. The strain and thickness profiles are plotted in Fig. 6.18 to Fig. 6.26. The variables were evaluated at 3 different drawing depths (12mm, 6mm and 2mm of the closing tools position). For analysis purposes, the final position was considered at 2mm of the end of the die stroke because the real part fails around this drawing depth. The peak values of major



strains are highlighted with red circles, whereas purple circles are used to the minor strain peaks. The thickness peaks are also identified using the red circles to the higher values and the purple circles to the lower values.

An overall look to the results put in to evidence:

- An excellent correlation between the 2D/3D and 3D Solid FEM models.
- A divergence from the results predicted by the 2D Shell model and the other FEM models.
- A relation between the principal strains and thickness distributions. The peaks of minor strains correspond to peaks of thickening whereas the peaks of major strains are related with the peaks of thinning.

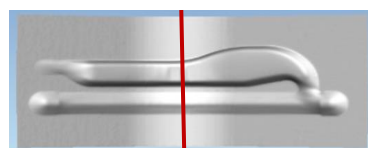
Further, a sequence of tables [Tab. 6.4 to Tab. 6.12] provides an overall view of the peak values of principal strains, thickening and thinning, predicted in the stamping simulation to each metallic skin. Between all the FEM models, the highest value throughout the section profile are highlighted in bold and becomes the reference value. Then, it is compared with the other FEM models predicted values *at the same distance point* of the section profile. All the values are presented in percentage. The main purpose of these tables is give an inside of the existent gap between the different FEM model predictions at the specific location of the cross section peak value. The focus was especially on the thickening and thinning of the 2D Shell and 2D/3D models, which are calculated from the predicted thickness and the nominal thickness of the metallic skins (0.30mm), and presented.

Later on, the tables [Tab. 6.13 to Tab. 6.15] present a comparison of the maximum values of thickening and thinning [%] predicted by the 2D Shell and 2D/3D models in each section. It must be noted that, unlike the previous analysis [Tab. 6.4 to Tab. 6.12], these values are *not necessarily related with the same distance point* but only with the same cross section. The main goal is to complement and reinforce the understanding of how much the shell element performance is affected by the spatial model and influences the maximum thickening and maximum thinning variables, which in turn are determinant to the micro-sandwich sheet failure.

Fig. 6.18 presents a comparison of the principal strain profiles of the section 0, predicted from all the FEM models at 12mm of the end of the die stroke. The thickness profiles predicted by the 2D Shell and 2D/3D model are also compared.

AT 12MM OF THE END

*Upper*



*Lower*

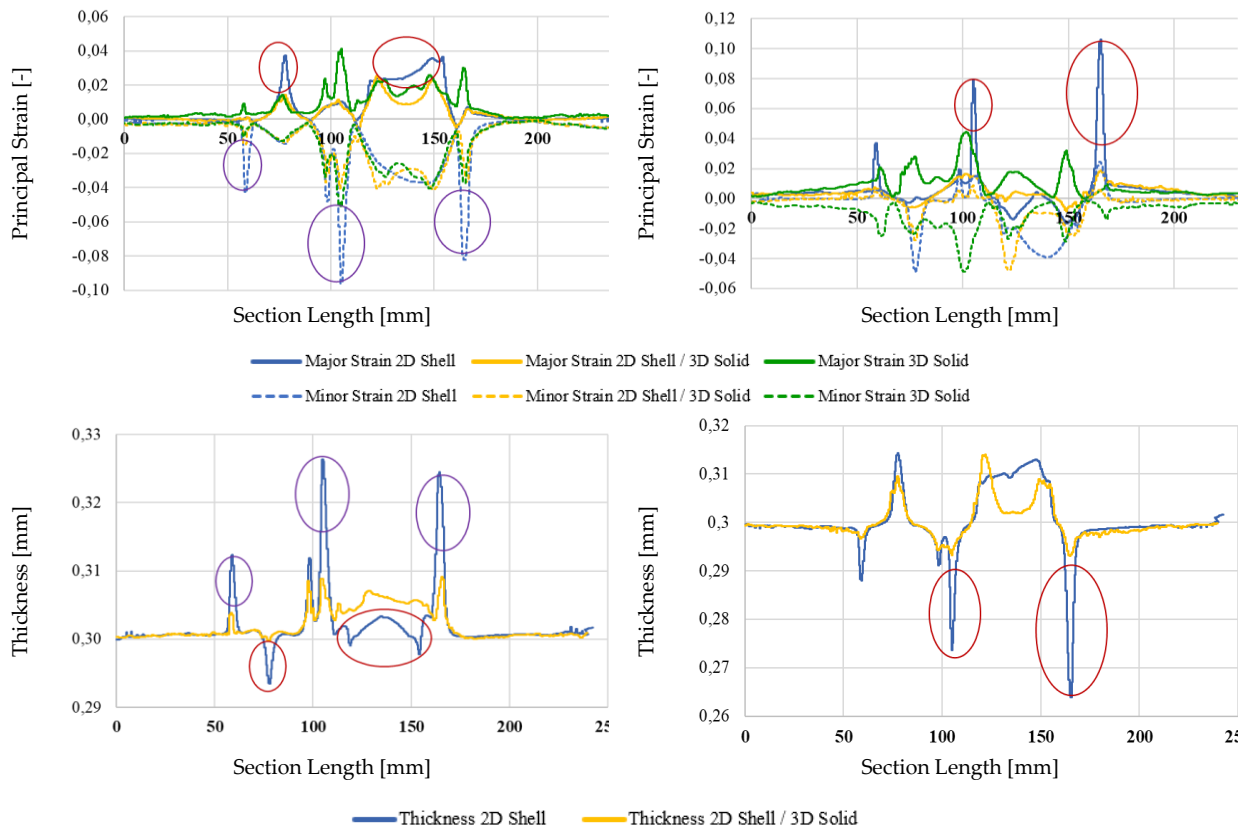


Fig. 6.18 – Comparison of the principal strain profile of section 0, obtained from each FEM model, at 12mm of the end of the die stroke. Thickness profiles for the 2D Shell and 2D/3D model are also compared. The results are presented for lower and upper skin.

In terms of principal strains, the 2D Shell model reach the highest values. In the upper skin, the biggest differences can be found at 77mm, where the 2D Shell major strain (3.8%) is 2.5 times higher than the other models, and at 105mm, where the 2D Shell minor strain (-9.8%) also exceed the double of the other models. In the lower skin, the biggest differences can be found at 165mm, where the major strain (10%) is 4 times higher in the 2D Shell model. An exception to the general trend, can be observed at 105mm, where the biggest differences between the numerical minor strains can be found. Here, the minor strain predicted by the 3D Solid (-4.2%) is about 2 times higher than the other FEM models.

Tab. 6.4 shows a clear image of the differences between the principal strain predictions in the location where peak values (highlighted in bold) to the section 0, at instant 12mm, occurs. As the Fig. 6.18, the thickening and thinning values are just presented to the 2D Shell and 2D/3D models.

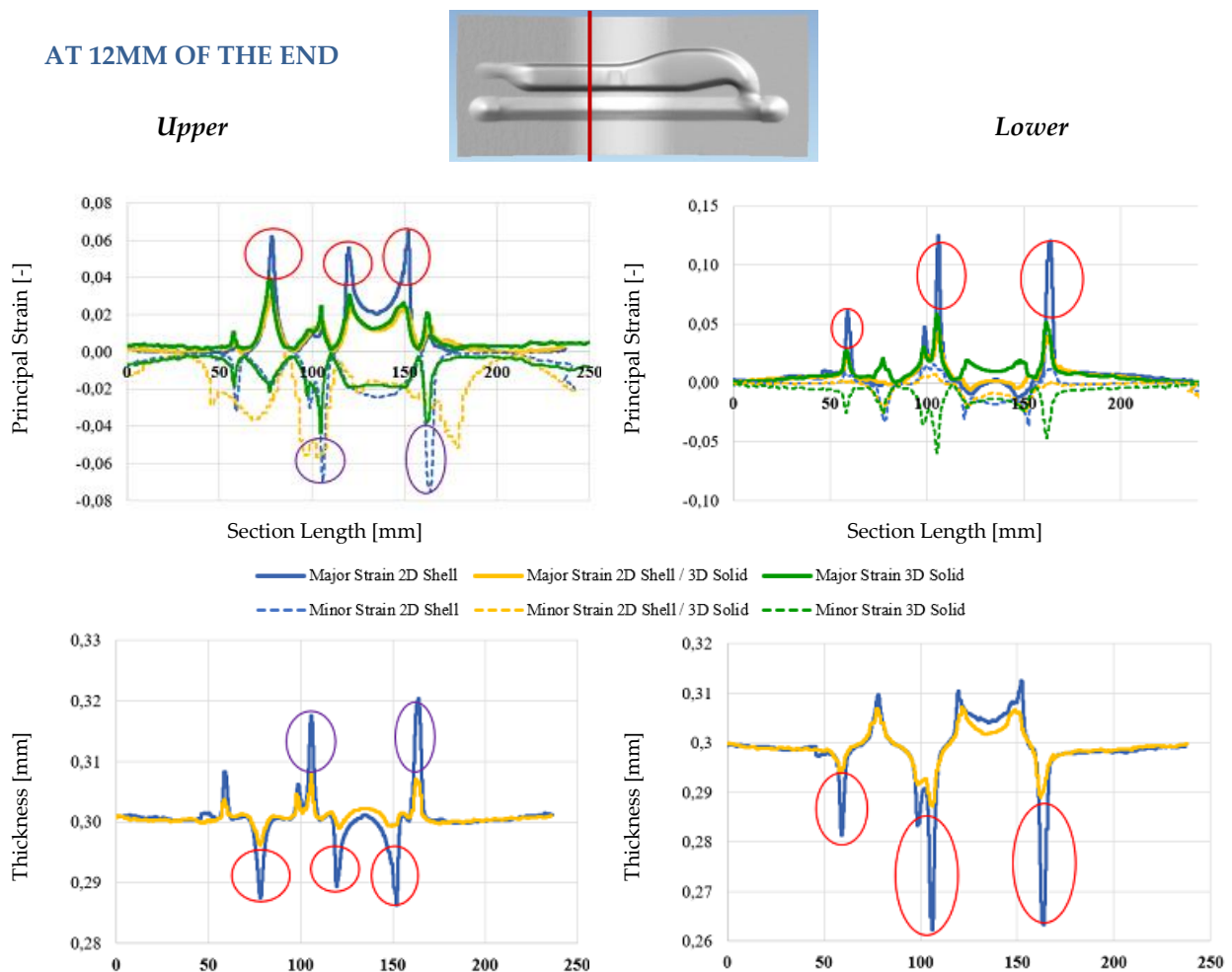
Tab. 6.4 - Comparison between the highest predicted values of principal strains, thickening and thinning in the section 0, at 12mm of the end of the die stroke, and the values of the same variable predicted by the other FEM models at the same distance point.

Peak Values [%] – Section 0								
12mm	Major Strain		Minor Strain		Thickening		Thinning	
	Upper	Lower	Upper	Lower	Upper	Lower	Upper	Lower

2D Shell	3.8	10.0	-9.8	-4.8	8.3	4.3	2.3	12.0
2D/3D	1.6	2.0	-4.0	-2.2	2.7	3.0	0.0	2.3
3D Solid	1.6	1.2	-5.0	-2.5	-	-	-	-

In the section 0 and at instant 12mm, the 2D Shell model predicts always the highest values of principal strains, thickening and thinning to both metallic skins. With regard to the upper skin, the maximum thickness predicted by the 2D Shell is 0.325mm against the 0.308mm predicted by the 2D/3D model, which represent a thickening difference of 5.7% at the distance point 105mm. The minimum thickness is found at the distance point 77mm where the 2D Shell model reach a value of 0.293 against the 0.300mm of the 2D/3D model, which represent a thinning difference of 2.3%. Regarding the lower skin, the maximum thickness predicted by the 2D Shell is 0.313mm against the 0.309mm predicted by the 2D/3D model, which represent a thickening difference of 1.3% at the distance point 77mm. The minimum thickness is found at the distance point 165mm where the 2D Shell model reach a value of 0.265 against the 0.297mm of the 2D/3D model, which represent a thinning difference of 9.7%.

In the next figure [Fig. 6.19], a comparison of the principal strain profiles of the section -60, predicted from all the FEM models, at 12mm of the end of the die stroke is presented. The thickness profiles predicted by the 2D Shell and 2D/3D model are also compared.



Section Length [mm]

Section Length [mm]

— Thickness 2D Shell      — Thickness 2D Shell / 3D Solid

Fig. 6.19 – Comparison of the principal strain profile of section -60, obtained from each FEM model, at 12mm of the end of the die stroke. Thickness profiles for the 2D Shell and 2D/3D model are also compared. The results are presented for lower and upper skin.

Looking at the results of the section -60 at 12mm [Fig. 6.19], in the upper skin, the highest differences in terms of principal strains can be found at 150mm, where the 2D Shell major strain (6.5%) is 2.5 times higher than the other models, and at 165mm, where the 2D Shell minor strain (-7.5%) is the double of the other models. In the lower skin, the biggest differences can be found at 105mm, where the major strain (12.5%) is 2 times higher in the 2D Shell model. An exception to the general trend, can be observed at 105mm, where the biggest differences between the numerical minor strains can be found. Here, the minor strain predicted by the 3D Solid is -5.9% while the other FEM models present a value around 1,5%.

Tab. 6.5 shows the numerical principal strains, thickening and thinning, obtained to peak values (highlighted in bold) location of the section -60, at 12mm.

Tab. 6.5 - Comparison between the highest predicted values of principal strains, thickening and thinning in the section -60, at 12mm of the end of the die stroke, and the values of the same variable predicted by the other FEM models at the same distance point.

Peak Values [%] – Section -60								
12mm	Major Strain		Minor Strain		Thickening		Thinning	
	Upper	Lower	Upper	Lower	Upper	Lower	Upper	Lower
2D Shell	<b>6.5</b>	<b>12.5</b>	<b>-7.5</b>	1.5	<b>6.7</b>	<b>4.0</b>	<b>4.3</b>	<b>12.7</b>
2D/3D	2.3	4.0	-3.8	2.2	2.3	2.3	0.3	4.3
3D Solid	2.6	6.0	-3.8	<b>-5.9</b>	-	-	-	-

As it can be seen [Tab. 6.5], the 2D Shell model predicts often the highest values of principal strains, thickening and thinning to both metallic skins. With regard to the upper skin, the maximum thickness predicted by the 2D Shell is 0.320mm against the 0.307mm predicted by the 2D/3D model, which represent a thickening difference of 4.3% at the distance point 165mm. The minimum thickness is found at the distance point 150mm where the 2D Shell model reach a value of 0.287 against the 0.299mm of the 2D/3D model, which represent a thinning difference of 4.0%. Regarding the lower skin, the maximum thickness predicted by the 2D Shell is 0.312mm against the 0.307mm predicted by the 2D/3D model, which represent a thickening difference of 1.7% at the distance point 152mm. The minimum thickness is found at the distance point 105mm where the 2D Shell model reach a value of 0.262 against the 0.287mm of the 2D/3D model, which represent a thinning difference of 8.3%.

Fig. 6.20 shows the comparison of the principal strain profiles of the section +80, predicted from all the FEM models, at 12mm of the end of the die stroke. The thickness profiles predicted by the 2D Shell and

2D/3D model are also compared.

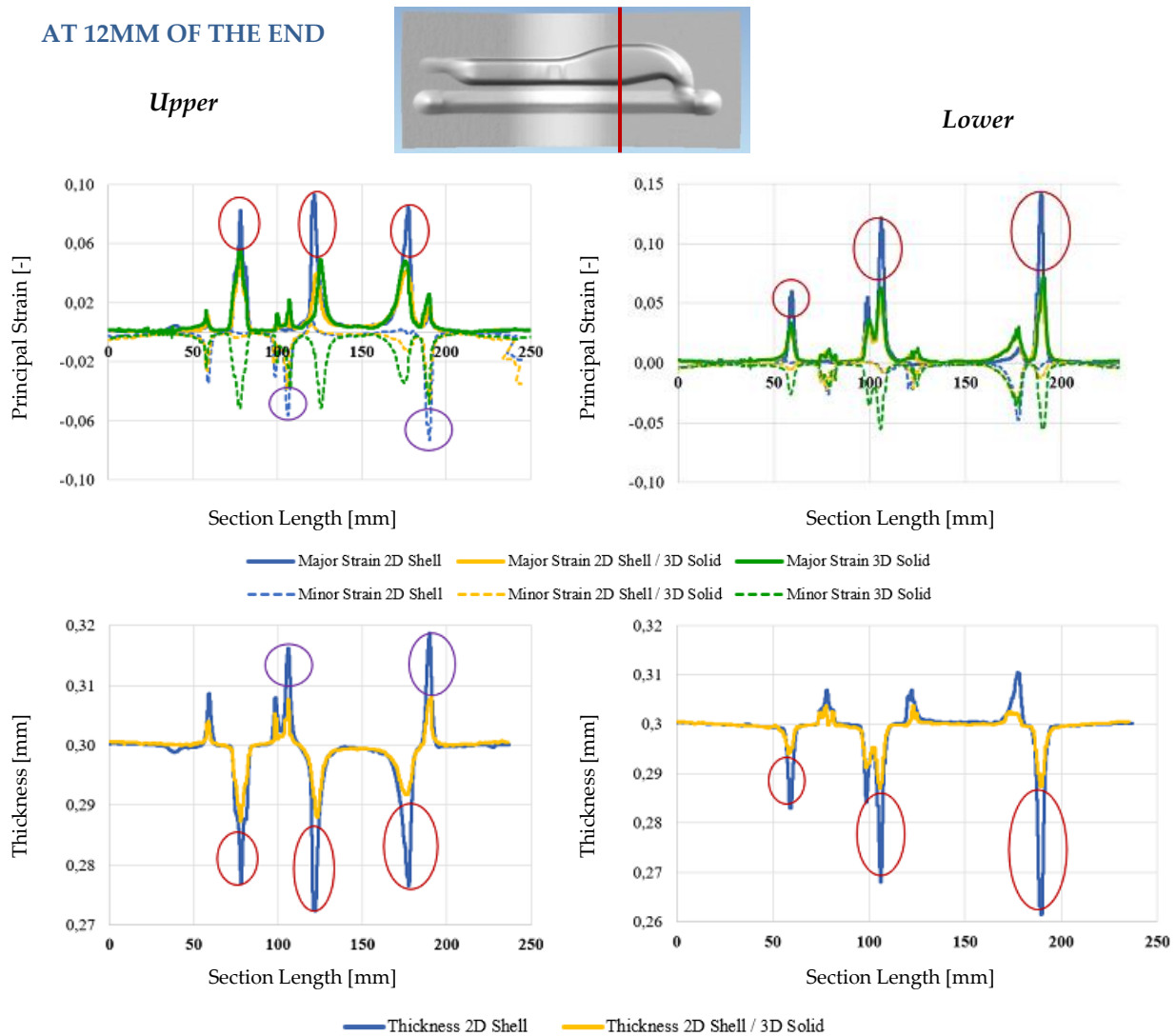


Fig. 6.20 – Comparison of the principal strain profile of section +80, obtained from each FEM model, at 12mm of the end of the die stroke. Thickness profiles for the 2D Shell and 2D/3D model are also compared. The results are presented for lower and upper skin.

Looking at the results of the section +80 at 12mm [Fig. 6.20], in the upper skin, the biggest differences in terms of principal strains can be found at 125mm, where the 2D Shell major strain (9.2%) is 1.9 times higher than the 3D Solid model and 2.3 times higher than the 2D/3D model, and at 190mm, where the 2D Shell minor strain (-7.0%) is 1.5 times higher than the other FEM models. In the lower skin, the 2D Shell major strain (14%) is 2 times higher than the 3D Solid model and 2.5 times higher than the 2D/3D model at distance point 190mm. The biggest differences between the numerical minor strains can be found at 105mm. Here, the minor strain predicted by the 3D Solid is -5.5% while the other FEM models a value near from 0%.

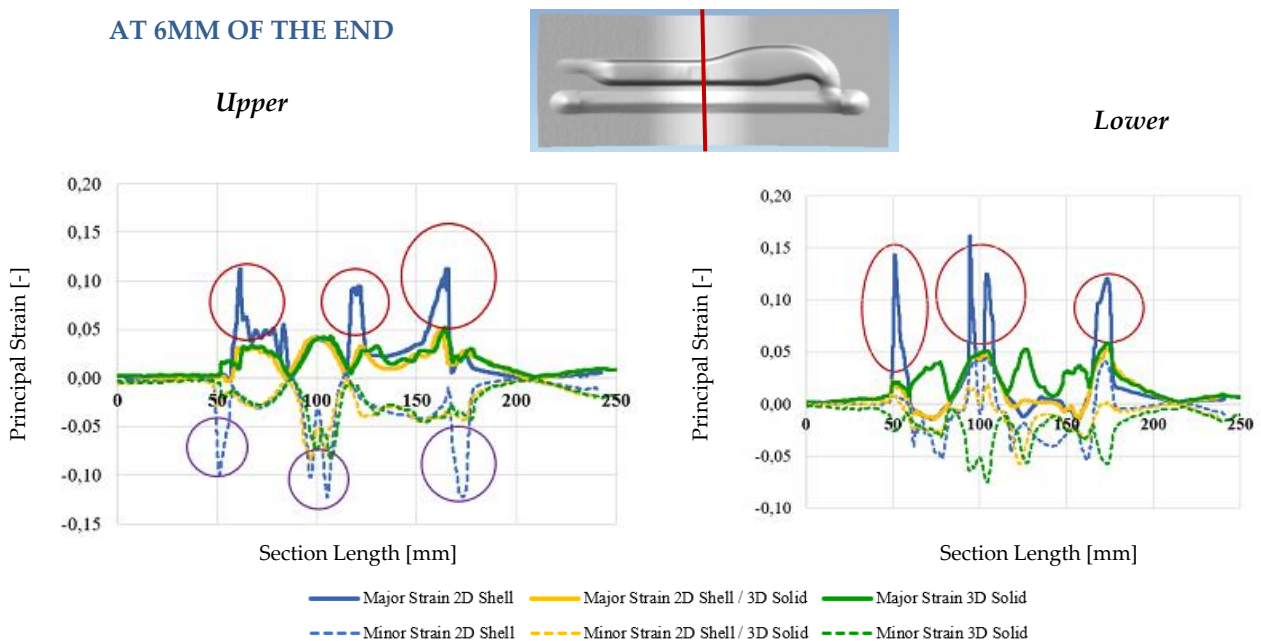
The peak values of principal strains, thickening and thinning, obtained to the section +80 at 12mm are presented in the table below [Tab. 6.6].

Tab. 6.6 - Comparison between the highest predicted values of principal strains, thickening and thinning in the section +80, at 12mm of the end of the die stroke, and the values of the same variable predicted by the other FEM models at the same distance point.

Peak Values [%] – Section +80								
12mm	Major Strain		Minor Strain		Thickening		Thinning	
	Upper	Lower	Upper	Lower	Upper	Lower	Upper	Lower
2D Shell	9.2	14.0	-7.0	-0.9	6.0	3.3	9.0	13.3
2D/3D	2.3	5.6	-3.8	-0.9	2.7	1.0	4.3	4.3
3D Solid	4.9	7.0	-4.5	-5.5	-	-	-	-

As it can be seen [Tab. 6.6], the 2D Shell model predicts often the highest values of principal strains, thickening and thinning to both metallic skins. With regard to the upper skin, the maximum thickness predicted by the 2D Shell is 0.318mm against the 0.308mm predicted by the 2D/3D model, which represent a thickening difference of 3.3% at the distance point 190mm. The minimum thickness is found at the distance point 125mm where the 2D Shell model reach a value of 0.273 against the 0.287mm of the 2D/3D model, which represent a thinning difference of 4.7%. Regarding the lower skin, the maximum thickness predicted by the 2D Shell is 0.310mm against the 0.303mm predicted by the 2D/3D model, which represent a thickening difference of 1.3% at the distance point 180mm. The minimum thickness is found at the distance point 190mm where the 2D Shell model reach a value of 0.260 against the 0.287mm of the 2D/3D model, which represent a thinning difference of 9.0%.

In the Fig. 6.21, the principal strain profiles of the section 0, predicted from all the FEM models, at 6mm of the end of the die stroke are compared. The thickness profiles predicted by the 2D Shell and 2D/3D model are also presented.



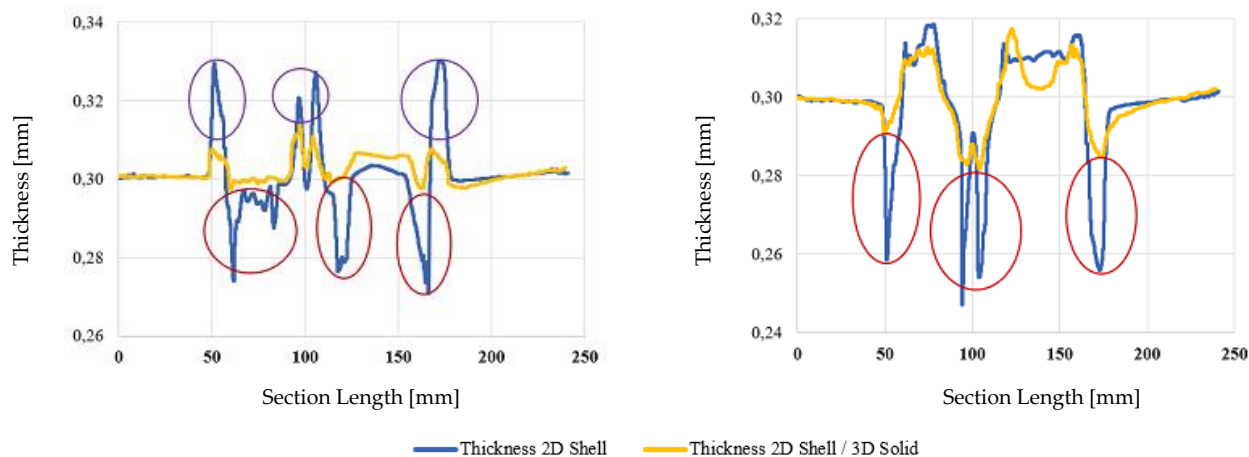


Fig. 6.21 – Comparison of the principal strain profile of section 0, obtained from each FEM model, at 6mm of the end of the die stroke. Thickness profiles for the 2D Shell and 2D/3D model are also compared. The results are presented for lower and upper skin.

Looking at the results of the section 0 at 6mm [Fig. 6.21], in the upper skin, the highest differences in terms of principal strains can be found at 166mm, where the 2D Shell major strain (11.0%) is 2.1 times higher than the other FEM models, and at 174mm, where the 2D Shell minor strain (-12.0%) is 3 times higher than the other FEM models. In the lower skin, the 2D Shell major strain (16.2%) is 3.4 times higher than the 3D Solid model and 3.7 times higher than the 2D/3D model at distance point 95mm. The biggest differences between the numerical minor strains can be found at 105mm. Here, the minor strain predicted by the 3D Solid is -7.2% while the 2D Shell minor strain is 4.0% and the 2D/3D minor strain is 2.0%.

Tab. 6.7 presents the peak values of principal strains, thickening and thinning, obtained to the section 0 at 6mm.

Tab. 6.7 - Comparison between the highest predicted values of principal strains, thickening and thinning in the section 0, at 6mm of the end of the die stroke, and the values of the same variable predicted by the other FEM models at the same distance point.

Peak Values [%] – Section 0								
6mm	Major Strain		Minor Strain		Thickening		Thinning	
	Upper	Lower	Upper	Lower	Upper	Lower	Upper	Lower
2D Shell	<b>11.0</b>	<b>16.2</b>	<b>-12.0</b>	4.8	<b>10.0</b>	<b>6.0</b>	<b>10.0</b>	<b>17.7</b>
2D/3D	5.2	4.8	-4.0	2.5	2.3	4.0	0.7	5.3
3D Solid	4.9	4.3	-4.1	<b>-7.2</b>	-	-	-	-

This table [Tab. 6.7] shows that the 2D Shell model predicts often the highest values of principal strains, thickening and thinning to both metallic skins. With regard to the upper skin, the maximum thickness predicted by the 2D Shell is 0.330mm against the 0.307mm predicted by the 2D/3D model, which represent a thickening difference of 7.7% at the distance point 174mm. The minimum thickness is found at the distance point 166mm where the 2D Shell model reach a value of 0.270 against the 0.298mm of the 2D/3D model,

which represent a thinning difference of 9.3%. Regarding the lower skin, the maximum thickness predicted by the 2D Shell is 0.318mm against the 0.312mm predicted by the 2D/3D model, which represent a thickening difference of 2.0% at the distance point 77mm. The minimum thickness is found at the distance point 95mm where the 2D Shell model reach a value of 0.247 against the 0.284mm of the 2D/3D model, which represent a thinning difference of 12.4%.

In the following image [Fig. 6.22], the principal strain profiles of the section -60, predicted from all the FEM models, at 6mm of the end of the die stroke are depicted. The thickness profiles predicted by the 2D Shell and 2D/3D model are also compared.

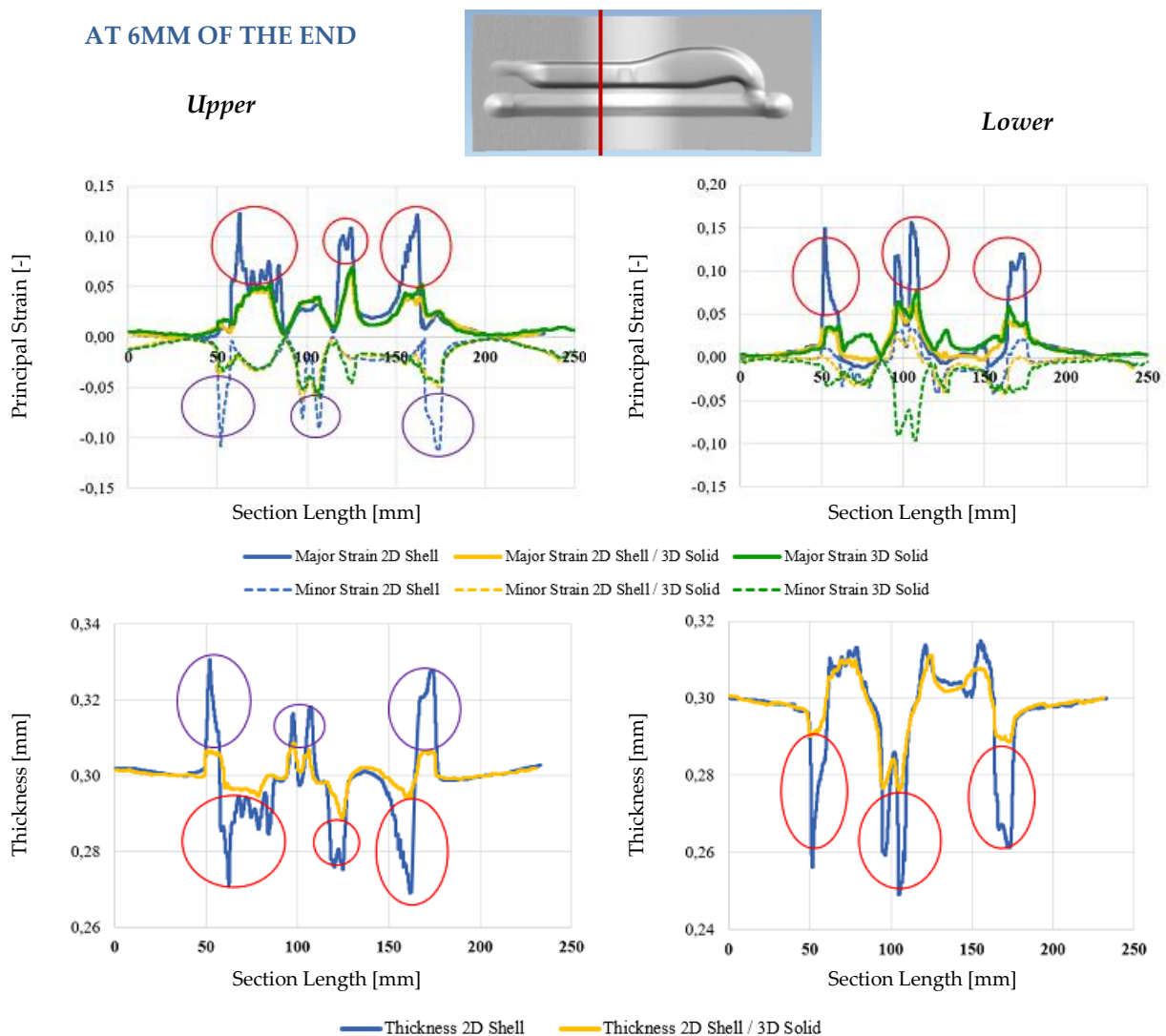


Fig. 6.22 – Comparison of the principal strain profile of section -60, obtained from each FEM model, at 6mm of the end of the die stroke. Thickness profiles for the 2D Shell and 2D/3D model are also compared. The results are presented for lower and upper skin.

Looking at the results of the section -60 at 6mm [Fig. 6.22], in the upper skin, the biggest differences in terms of principal strains can be found at 162mm, where the 2D Shell major strain (12.0%) is 3 times higher



than the other models, and at 174mm, where the 2D Shell minor strain (-11.0%) is 2.5 times higher than the other models. In the lower skin, the biggest differences can be found at 105mm, where the 2D Shell major strain (15.0%) is 2 times higher than the other models and the 3D Solid minor strain is -9.6%, while the 2D Shell minor strain is 3.3% and the 2D/3D minor strain is 3.0%.

Tab. 6.8 presents the peak values of principal strains, thickening and thinning, obtained to the section -60 at 6mm.

Tab. 6.8 - Comparison between the highest predicted values of principal strains, thickening and thinning in the section -60, at 6mm of the end of the die stroke, and the values of the same variable predicted by the other FEM models at the same distance point.

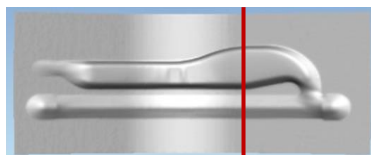
Peak Values [%] – Section -60								
6mm	Major Strain		Minor Strain		Thickening		Thinning	
	Upper	Lower	Upper	Lower	Upper	Lower	Upper	Lower
2D Shell	<b>12.0</b>	<b>15.0</b>	<b>-11.0</b>	3.2	<b>10.0</b>	<b>4.7</b>	<b>10.0</b>	<b>16.7</b>
2D/3D	4.0	6.1	-4.5	2.2	2.3	2.7	2.0	7.3
3D Solid	4.3	7.3	-4.4	<b>-9.6</b>	-	-	-	-

Regarding the upper skin, the maximum thickness predicted by the 2D Shell is 0.330mm against the 0.307mm predicted by the 2D/3D model, which represent a thickening difference of 7.7% at the distance point 52mm. The minimum thickness is found at the distance point 162mm where the 2D Shell model reach a value of 0.270 against the 0.294mm of the 2D/3D model, which represent a thinning difference of 8.0%. Regarding the lower skin, the maximum thickness predicted by the 2D Shell is 0.314mm against the 0.308mm predicted by the 2D/3D model, which represent a thickening difference of 2.0% at the distance point 155mm. The minimum thickness is found at the distance point 105mm where the 2D Shell model reach a value of 0.250 against the 0.278mm of the 2D/3D model, which represent a thinning difference of 9.4%.

The Fig. 6.23 shows the comparison of the principal strain profiles of the section +80, predicted from all the FEM models, at 6mm of the end of the die stroke. The thickness profiles predicted by the 2D Shell and 2D/3D model are also compared.

AT 6MM OF THE END

*Upper*



*Lower*

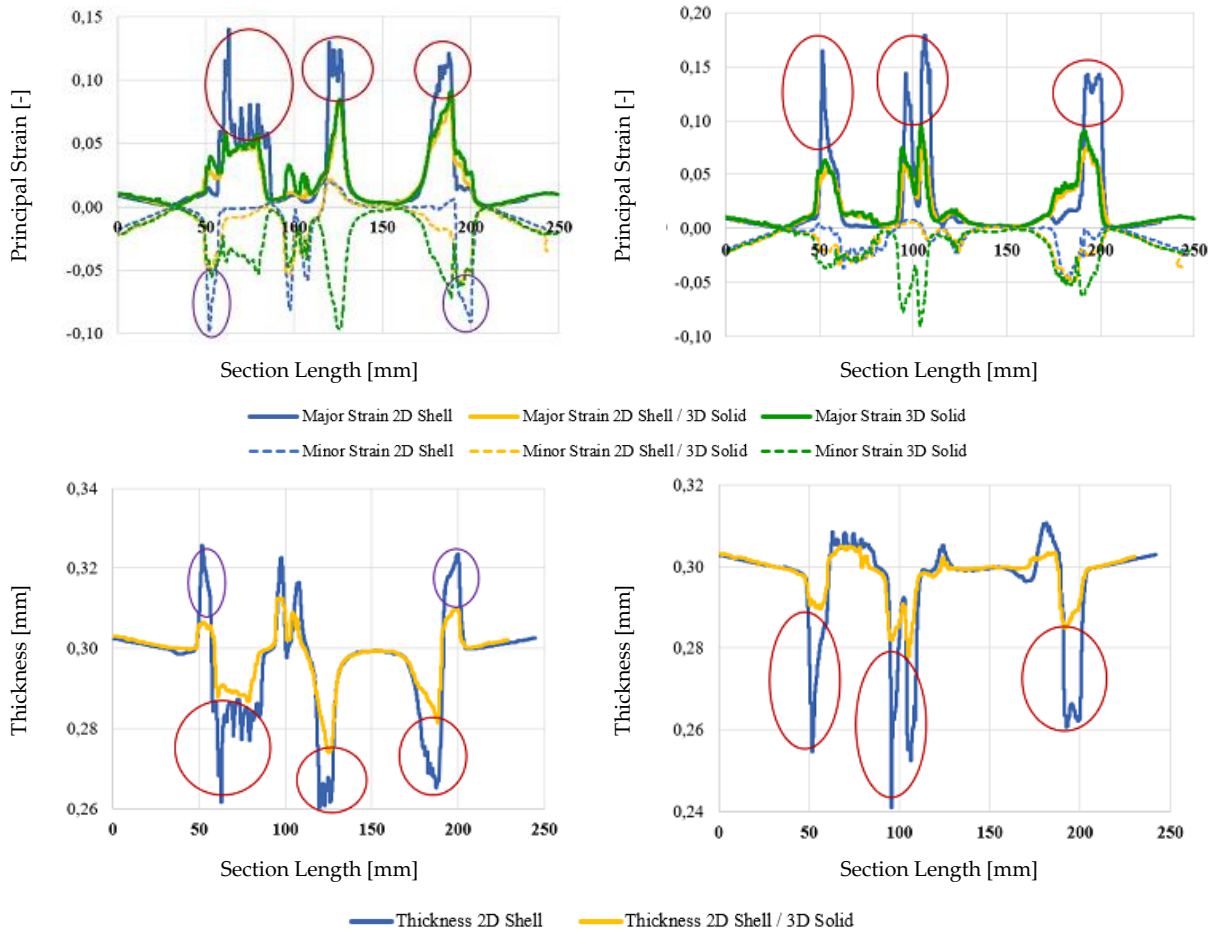


Fig. 6.23 – Comparison of the principal strain profile of section +80, obtained from each FEM model, at 6mm of the end of the die stroke. Thickness profiles for the 2D Shell and 2D/3D model are also compared. The results are presented for lower and upper skin.

The results of the section +80 at 6mm [Fig. 6.23], to the upper skin, present the biggest differences in terms of principal strains at distance point 60mm, where the 2D Shell major strain (13.0%) is 1.6 times higher than the other models, and at 105mm, where the 2D Shell minor strain (-18.0%) is 2.1 times higher than the other models. In the lower skin, the 2D Shell major strain (10%) is 2 times higher than the other models at distance point 50mm. In terms of minor strains, the biggest differences appear at distance point 105mm, where 3D Solid model prediction is about -9% while the other FEM models a value near from 0%.

The Tab. 6.9 present the peak values of principal strains, thickening and thinning, obtained to the section +80 at 6mm.

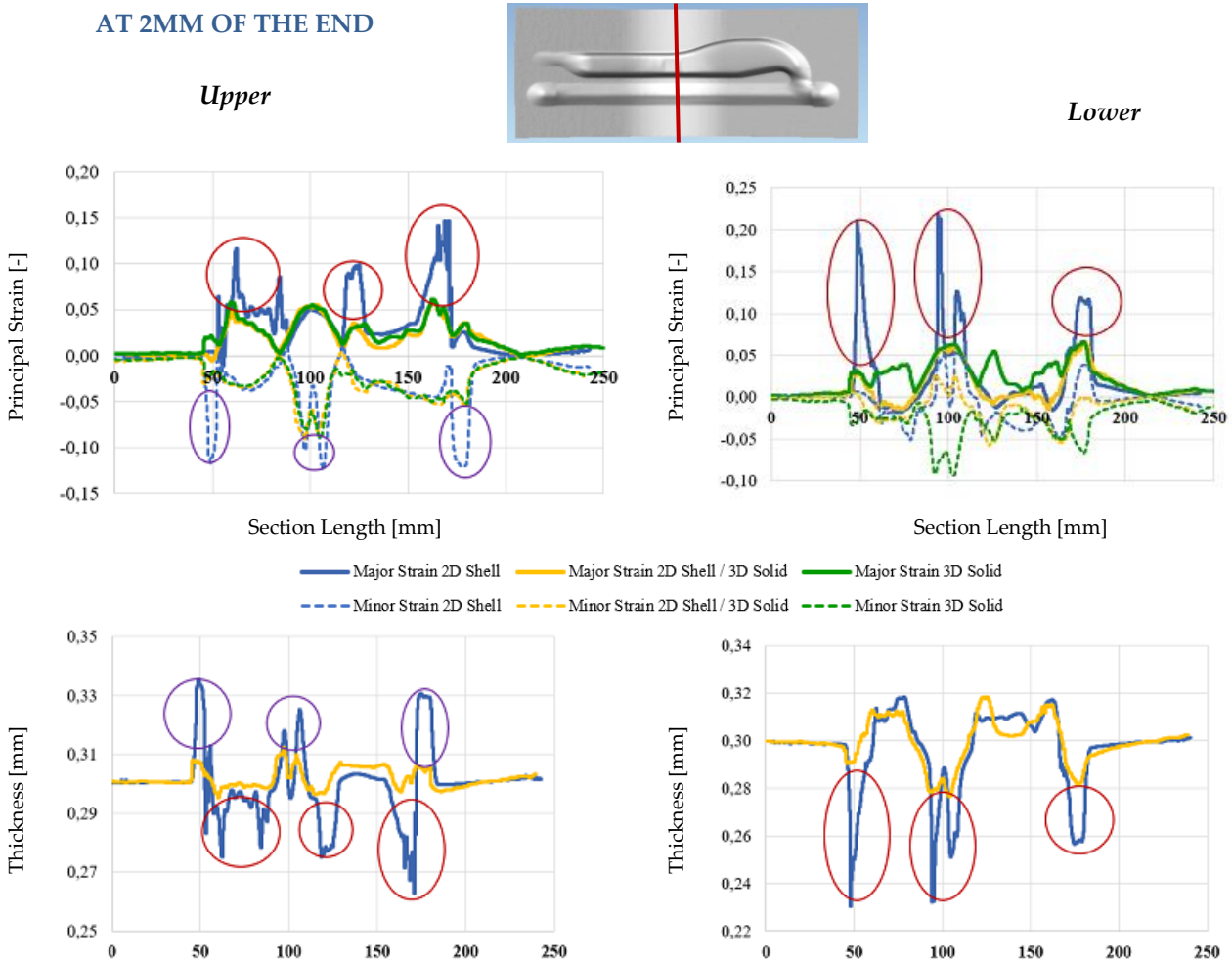
Tab. 6.9 - Comparison between the highest predicted values of principal strains, thickening and thinning in the section +80, at 6mm of the end of the die stroke, and the values of the same variable predicted by the other FEM models at the same distance point.

Peak Values [%] – Section +80								
6mm	Major Strain		Minor Strain		Thickening		Thinning	
	Upper	Lower	Upper	Lower	Upper	Lower	Upper	Lower

2D Shell	13.0	18.0	-10.0	0.4	8.3	3.3	13.3	20.0
2D/3D	8.0	8.5	-4.9	0.4	2.0	1.3	8.3	6.0
3D Solid	8.0	8.6	-5.0	-9.0	-	-	-	-

As it can be seen [Tab. 6.9], the 2D Shell model predicts often the highest values of principal strains, thickening and thinning to both metallic skins. Concerning the upper skin, the maximum thickness predicted by the 2D Shell is 0.325mm against the 0.306mm predicted by the 2D/3D model, which represent a thickening difference of 6.3% at the distance point 52mm. The minimum thickness is found at the distance point 125mm where the 2D Shell model reach a value of 0.260 against the 0.275mm of the 2D/3D model, which represent a thinning difference of 5.0%. Regarding the lower skin, the maximum thickness predicted by the 2D Shell is 0.310mm against the 0.304mm predicted by the 2D/3D model, which represent a thickening difference of 1.0% at the distance point 180mm. The minimum thickness is found at the distance point 100mm where the 2D Shell model reach a value of 0.240 against the 0.282mm of the 2D/3D model, which represent a thinning difference of 14.0%.

The comparison of the principal strain profiles of the section 0, predicted from all the FEM models, at 2mm of the end of the die stroke is shown below [Fig. 6.24]. The thickness profiles predicted by the 2D Shell and 2D/3D model are also compared.



Section Length [mm]

Section Length [mm]

— Thickness 2D Shell      — Thickness 2D Shell / 3D Solid

Fig. 6.24 – Comparison of the principal strain profile of section 0, obtained from each FEM model, at 2mm of the end of the die stroke. Thickness profiles for the 2D Shell and 2D/3D model are also compared. The results are presented for lower and upper skin.

As depicted above [Fig. 6.24] the biggest differences in terms of principal strains of the section 0 at the instant 2mm, in the upper skin, occurs at distance point 170mm, where the 2D Shell major strain (15.0%) is 2.5 times higher than the other FEM models, and at 180mm, where the 2D Shell minor strain (-12.0%) is 2.4 times higher than the other FEM models. In the lower skin, the 2D Shell major strain (22.0%) is 3.7 times higher than the other FEM models at distance point 95mm. The biggest differences between the numerical minor strains can be found at 105mm. Here, the minor strain predicted by the 3D Solid is -9.0% while the 2D Shell minor strain is 5.0% and the 2D/3D minor strain is 2.5%.

The Tab. 6.10 shows the peak values of principal strains, thickening and thinning, obtained to the section 0 at 2mm.

Tab. 6.10 - Comparison between the highest predicted values of principal strains, thickening and thinning in the section 0, at 2mm of the end of the die stroke, and the values of the same variable predicted by the other FEM models at the same distance point.

Peak Values [%] – Section 0								
2mm	Major Strain		Minor Strain		Thickening		Thinning	
	Upper	Lower	Upper	Lower	Upper	Lower	Upper	Lower
2D Shell	15.0	22.0	-12.0	5.0	11.7	6.3	12.7	22.7
2D/3D	6.0	6.0	-5.0	2.5	2.7	4.3	0	7.0
3D Solid	6.0	6.0	-5.0	-9.0	-	-	-	-

As usual the 2D Shell model predicts often the highest values of principal strains, thickening and thinning to both metallic skins. About the upper skin, the maximum thickness predicted by the 2D Shell is 0.335mm against the 0.308mm predicted by the 2D/3D model, which represent a thickening difference of 9.0% at the distance point 50mm. The minimum thickness is found at the distance point 170mm where the 2D Shell model reach a value of 0.262 against the 0.300mm of the 2D/3D model, which represent a thinning difference of 13.0%. Regarding the lower skin, the maximum thickness predicted by the 2D Shell is 0.319mm against the 0.313mm predicted by the 2D/3D model, which represent a thickening difference of 2.0% at the distance point 77mm. The minimum thickness is found at the distance point 95mm where the 2D Shell model reach a value of 0.232 against the 0.279mm of the 2D/3D model, which represent a thinning difference of 15.7%.

Next [Fig. 6.25], the principal strain profiles of the section -60, predicted from all the FEM models, at 2mm of the end of the die stroke are compared. The thickness profiles predicted by the 2D Shell and 2D/3D

model are also presented.

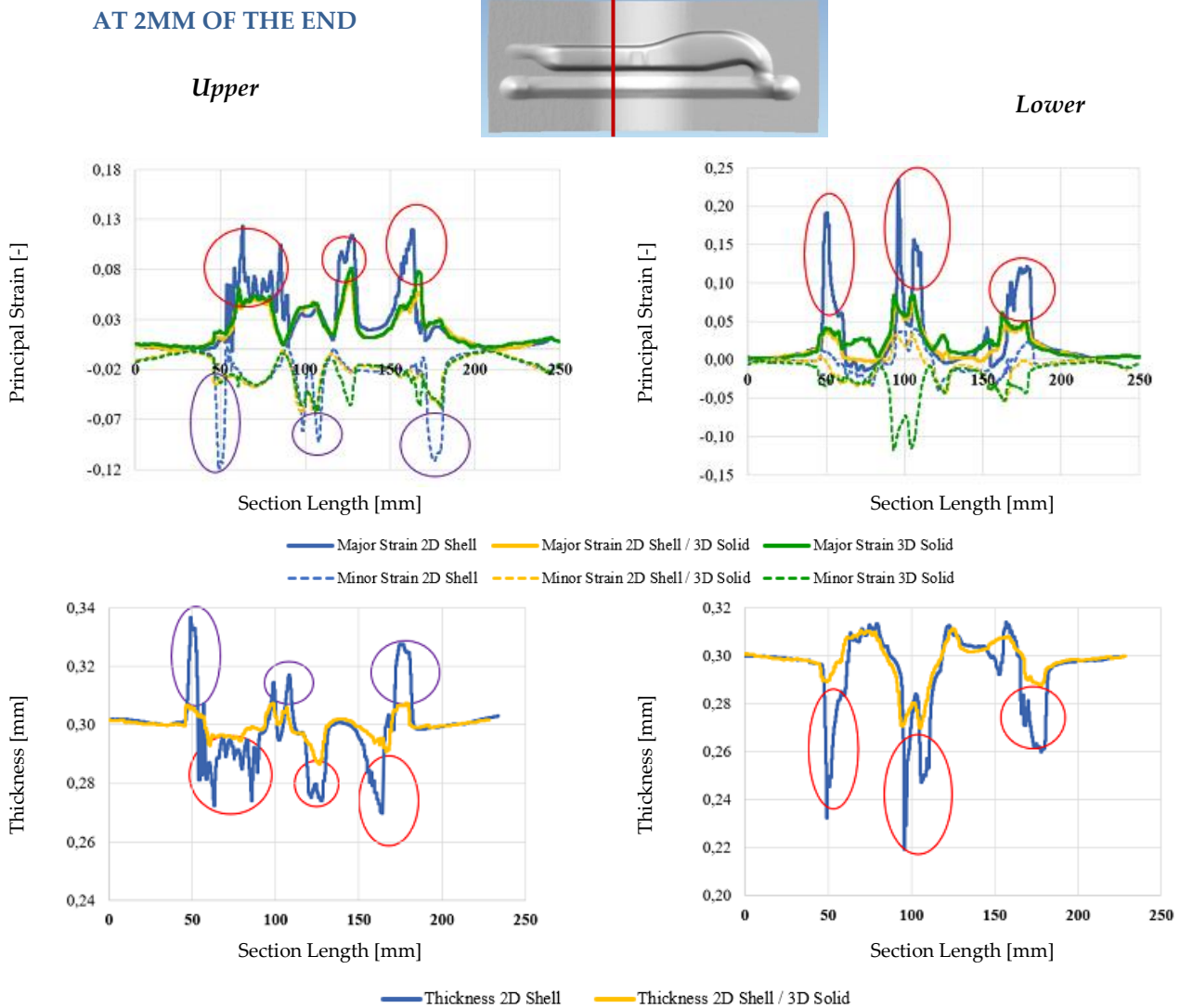


Fig. 6.25 – Comparison of the principal strain profile of section -60, obtained from each FEM model, at 2mm of the end of the die stroke. Thickness profiles for the 2D Shell and 2D/3D model are also compared. The results are presented for lower and upper skin.

Looking at the results of the section -60 at 2mm [Fig. 6.25], in the upper skin, the biggest differences in terms of principal strains can be found at 165mm, where the 2D Shell major strain (12.9%) is 1.6 times higher than the 3D Solid model and 2.2 times than the 2D/3D model, and at 50mm, where the 2D Shell minor strain (-12.0%) is 4.0 times higher than the other FEM models. In the lower skin, the biggest differences can be found at 95mm, where the major strain (24.0%) is 3 times higher in the 2D Shell model. In terms of minor strains, the biggest differences appear at distance point 105mm, where 3D Solid model prediction is about -12% while the other FEM models a value around 4%.

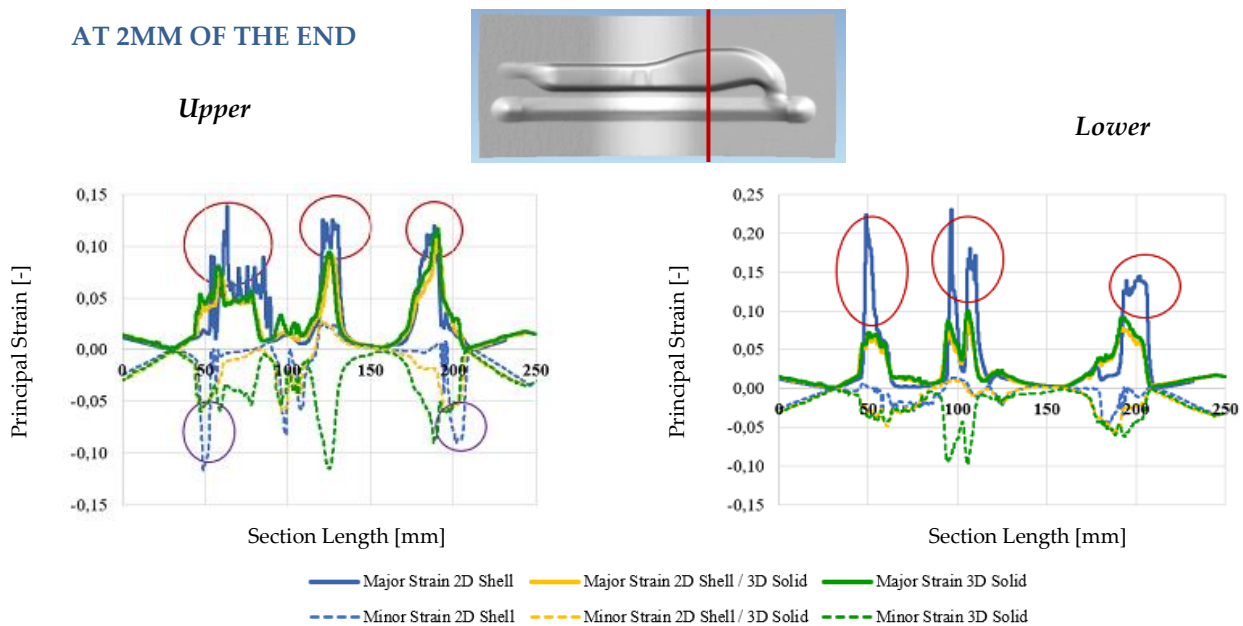
The peak values of principal strains, thickening and thinning, obtained to the section -60 at 2mm are presented below [Tab. 6.11]

Tab. 6.11 - Comparison between the highest predicted values of principal strains, thickening and thinning in the section -60, at 2mm of the end of the die stroke, and the values of the same variable predicted by the other FEM models at the same distance point.

Peak Values [%] – Section -60								
2mm	Major Strain		Minor Strain		Thickening		Thinning	
	Upper	Lower	Upper	Lower	Upper	Lower	Upper	Lower
2D Shell	12.9	24.0	-12.0	4.0	11.7	4.7	10.0	26.7
2D/3D	6.0	7.8	-3.0	3.8	2.7	3.0	3.3	10.0
3D Solid	7.9	8.0	-3.0	-12.0	-	-	-	-

With respect to the upper skin, the maximum thickness predicted by the 2D Shell is 0.335mm against the 0.308mm predicted by the 2D/3D model, which represent a thickening difference of 9.0% at the distance point 50mm. The minimum thickness is found at the distance point 165mm where the 2D Shell model reach a value of 0.270 against the 0.290mm of the 2D/3D model, which represent a thinning difference of 6.7%. Regarding the lower skin, the maximum thickness predicted by the 2D Shell is 0.314mm against the 0.309mm predicted by the 2D/3D model, which represent a thickening difference of 1.7% at the distance point 155mm. The minimum thickness is found at the distance point 95mm where the 2D Shell model reach a value of 0.220 against the 0.270mm of the 2D/3D model, which represent a thinning difference of 16.7%.

The Fig. 6.26 compares the principal strain profiles of the section +80, predicted from all the FEM models, at 2mm of the end of the die stroke. The thickness profiles predicted by the 2D Shell and 2D/3D model are also compared.



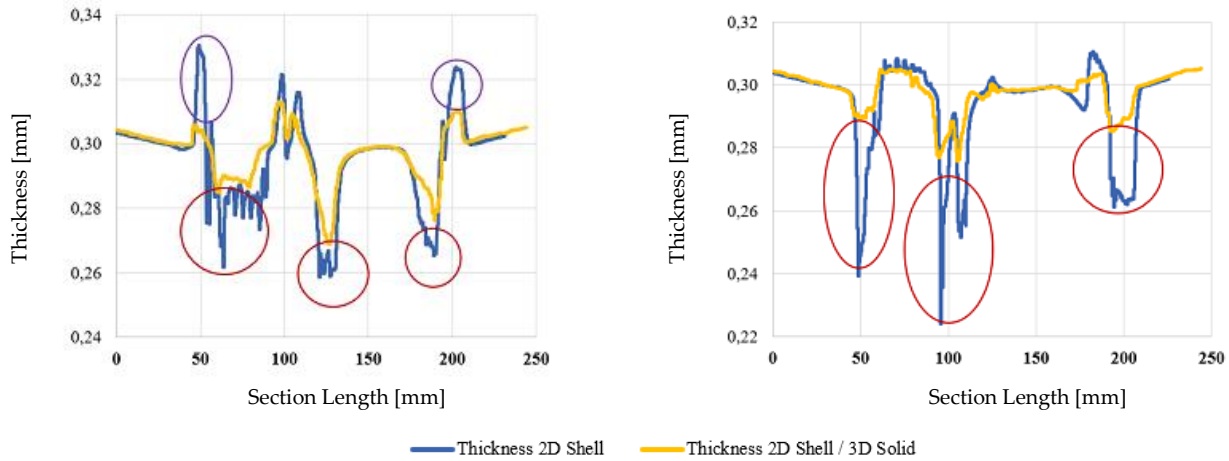


Fig. 6.26 – Comparison of the principal strain profile of section +80, obtained from each FEM model, at 2mm of the end of the die stroke. Thickness profiles for the 2D Shell and 2D/3D model are also compared. The results are presented for lower and upper skin.

The results of the section +80 at 2mm [Fig. 6.26], to the upper skin, present the biggest differences in terms of principal strains at distance point 60mm, where the 2D Shell major strain (14.0%) is 1.8 times higher than the other models, and at 125mm, where the 2D Shell minor strain (-11.0%) is 2.0 times higher than the other models. In the lower skin, the 2D Shell major strain (23.0%) is 2.6 times higher than the other models at distance point 95mm. In terms of minor strains, the biggest differences appear at distance point 105mm, where 3D Solid model prediction is about -10% while the other FEM models a value near from 0%.

The peak values of principal strains, thickening and thinning, obtained to the section +80 at 2mm are presented below [Tab. 6.12]

Tab. 6.12 - Comparison between the highest predicted values of principal strains, thickening and thinning in the section +80, at 2mm of the end of the die stroke, and the values of the same variable predicted by the other FEM models at the same distance point.

Peak Values [%] – Section +80								
2mm	Major Strain		Minor Strain		Thickening		Thinning	
	Upper	Lower	Upper	Lower	Upper	Lower	Upper	Lower
2D Shell	<b>14.0</b>	<b>23.0</b>	<b>-11.0</b>	0.7	<b>10.0</b>	<b>4.3</b>	<b>13.3</b>	<b>26.0</b>
2D/3D	8.0	8.8	-5.1	0.8	2.3	1.3	10.0	7.7
3D Solid	8.0	9.0	-5.3	<b>-10.0</b>	-	-	-	-

In the section +80 and at instant 2mm, the 2D Shell model predicts often the highest values of principal strains, thickening and thinning to both metallic skins. In the upper skin, the maximum thickness predicted by the 2D Shell is 0.330mm against the 0.307mm predicted by the 2D/3D model, which represent a thickening difference of 7.7% at the distance point 50mm. The minimum thickness is found at the distance point 125mm where the 2D Shell model reach a value of 0.260 against the 0.270mm of the 2D/3D model, which represent a thinning difference of 3.3%. Regarding the lower skin, the maximum thickness predicted

by the 2D Shell is 0.313mm against the 0.304mm predicted by the 2D/3D model, which represent a thickening difference of 3% at the distance point 180mm. The minimum thickness is found at the distance point 95mm where the 2D Shell model reach a value of 0.222 against the 0.277mm of the 2D/3D model, which represent a thinning difference of 18.3%.

As mentioned before, the tables present in Tab. 6.13 to Tab. 6.15 focus on the comparison between the maximum values of thickening and thinning [%] predicted by the 2D Shell and 2D/3D models in each section. The values highest values between the two models are always presented in bold. The variable  $\bar{R}$  refers to the average ratio between 2D Shell and 2D/3D models obtained for the instants 12mm, 6mm and 2mm. The maximum and minimum  $\bar{R}$  value are highlighted respectively in red and green. Thus, there is a greater convergence of the models when the ratio is green and a greater divergence when the ratio is red.

Overall, it is verified that the thickening and thinning predictions are larger in the 2D Shell model than in the 2D/3D model. Moreover, the 2D Shell model always shows an increase of thickening values from the lower to the upper skin and the opposite tendency for the thinning values. This consistency does not occur in the case of the 2D/3D model. These differences can be explained by the spatial FEM model. In the 2D Shell model the state variables in the outer layers are calculated from the same 2D mesh in the middle layer, whereas in the 2D/3D model the same calculation is based on two independent 2D meshes which are separated by the 3D solid mesh of the core.

Tab. 6.13 - Comparison of the maximum value of thickening and thinning [%] predicted by 2D Shell model and the 2D/3D model throughout the section 0 during the deep-drawing operation (12mm, 6mm and 2mm).

Max. Thickening [%]							Max. Thinning [%]						
0	Upper			Lower			0	Upper			Lower		
	2D Shell	2D/3D	$\bar{R}$	2D Shell	2D/3D	$\bar{R}$		2D Shell	2D/3D	$\bar{R}$	2D Shell	2D/3D	$\bar{R}$
12mm	<b>8.3</b>	2.9		4.3	<b>4.7</b>		12mm	<b>2.3</b>	0.0		<b>12.0</b>	2.3	
6mm	<b>10.0</b>	4.6	2.6	<b>6.0</b>	4.7	<b>1.0</b>	6mm	<b>10.0</b>	0.7	<b>11.9</b>	<b>17.7</b>	5.3	<b>3.9</b>
2mm	<b>11.7</b>	4.1		<b>6.3</b>	6.0		2mm	<b>12.7</b>	1.3		<b>22.7</b>	7.0	

The section 0 corresponds to the greatest compression zone with a higher tendency to accumulate material, therefore, it presents the highest percentages of maximum thickening and the lowest percentages of maximum thinning [Tab. 6.13]. Regarding the thickening variable, this section presents the lowest  $\bar{R}$  value to the lower layer. However, this section presents the highest  $\bar{R}$  value to the thinning variable.

Tab. 6.14 - Comparison of the maximum value of thickening and thinning [%] predicted by 2D Shell model and the 2D/3D model throughout the section -60 during the deep-drawing operation (12mm, 6mm and 2mm).

Max. Thickening [%]							Max. Thinning [%]						
-60	Upper			Lower			-60	Upper			Lower		
	2D Shell	2D/3D	$\bar{R}$	2D Shell	2D/3D	$\bar{R}$		2D Shell	2D/3D	$\bar{R}$	2D Shell	2D/3D	$\bar{R}$



12mm	<b>6.7</b>	2.3		<b>4.0</b>	2.3		12mm	<b>4.3</b>	1.3		<b>12.7</b>	4.3	
6mm	<b>10.0</b>	2.7	<b>3.9</b>	<b>4.7</b>	3.7	2.0	6mm	<b>10.0</b>	3.7	2.9	<b>16.7</b>	7.3	<b>2.6</b>
2mm	<b>11.7</b>	2.3		<b>4.7</b>	3.7		2mm	<b>10.0</b>	4.0		<b>26.7</b>	10.0	

The section -60 crosses a moderate stretching zone and therefore the maximum percentage of thinning tends to exceed the maximum percentage of thickening [Tab. 6.14]. This section obtained the highest thickening  $\bar{R}$  value to the upper skin and the lowest thinning  $\bar{R}$  value to the lower skin.

Tab. 6.15 - Comparison of the maximum value of thickening and thinning [%] predicted by 2D Shell model and the 2D/3D model throughout the section +80 during the deep-drawing operation (12mm, 6mm and 2mm).

Max. Thickening [%]							Max. Thinning [%]						
+80	Upper			Lower			+80	Upper			Lower		
	2D Shell	2D/3D	$\bar{R}$	2D Shell	2D/3D	$\bar{R}$		2D Shell	2D/3D	$\bar{R}$	2D Shell	2D/3D	$\bar{R}$
12mm	<b>6.0</b>	2.7		<b>3.3</b>	1.0		12mm	<b>9.0</b>	4.3		<b>13.3</b>	4.3	
6mm	<b>8.3</b>	4.0	<b>2.3</b>	<b>3.3</b>	1.7	<b>2.5</b>	6mm	<b>13.3</b>	8.3	<b>1.7</b>	<b>20.0</b>	7.3	3.0
2mm	<b>10.0</b>	4.0		<b>4.3</b>	1.7		2mm	<b>13.3</b>	10.0		<b>26.0</b>	8.3	

In section +80 the strain paths become more complex and the more severe stretching resulting in a maximum percentage of thinning clearly higher [Tab. 6.15]. In this section, the upper skin presents the lowest thickening and thinning  $\bar{R}$  values. In the other hand, the lower skin presents the higher thickening  $\bar{R}$  value.

This analysis shows that higher levels of stretching leads to closer numerical predictions of 2D Shell and 2D/3D FEM models. Nevertheless, even when the 2D Shell models are limited to stamping processes simulation with a suitable amount and distribution of stretching, where the results are more robust in terms of maximum thickening and maximum thinning, the predicted percentages are, in the best case, 2 times higher than the 2D/3D model. The main reason for this is that the 2D Shell model is based on 1 mesh of shell elements mesh with the total thickness of the micro-sandwich sheet, 1.6mm. On the other hand, the 2D/3D model has 2 independent meshes of shell elements, each with a thickness of 0.3mm. Therefore, when considering an approximate element size between the two models (0.5x0.5 vs. 0.65x0.65), the ratio between the element size and its thickness is much more favorable for the 2D/3D model. In fact, the mesh refinement needed to describe the tools geometry results in too small elements affecting the performance of the shell element. This means that by increasing the element size, it is possible to reduce the peaks observed in the principal strains, improving the numerical accuracy.

To demonstrate this effect, the Fig. 6.27 presents a comparison between the predicted principal strains and thickness profiles, in the upper and lower skins, for section 0, at the end of the deep-drawing operation (2mm). In this comparison an augmented 2D shell with an element size of 2x2 was used.

Upper 0

Lower 0

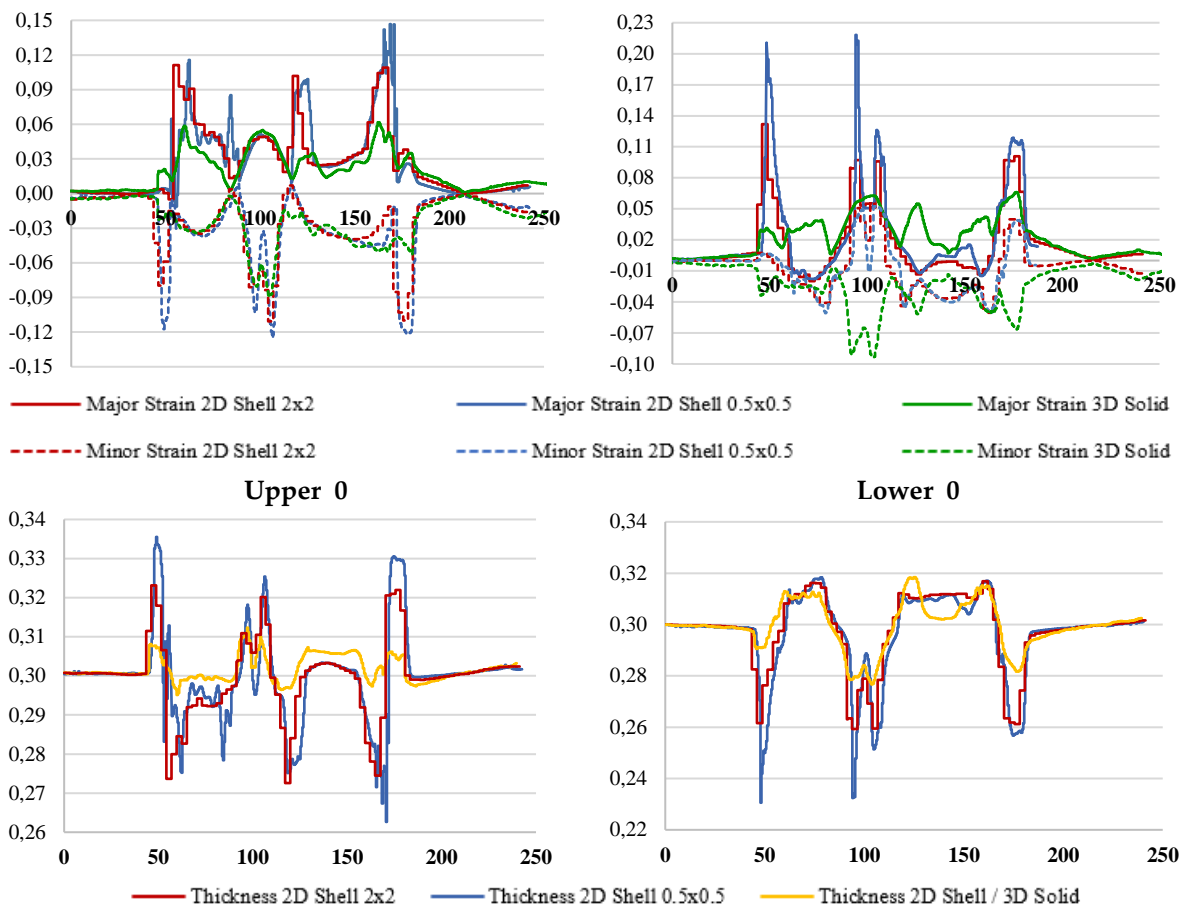


Fig. 6.27 – Comparison between the principal strain profiles predicted by 2D Shell model, with 2 element sizes (0.5x0.5 and 2x2), and the principal strain profiles predicted by the 3D Solid model, to the section 0, at 2mm of the end of the die stroke. Thickness profiles for the 2D Shell models (0.5x0.5 and 2x2) and 2D/3D model are also compared. The results are presented for lower and upper skin.

As it can be seen [Fig. 6.27], increasing the size of the element in the 2D Shell have a softening effect on the numerical results and leads to a reduction of the peak values in principal strain and thickness profiles. This effect is more noticeable in the lower skin than in the upper skin. In addition, the reduction of the maximum values is more evident for the major strains than for the minor strains, affecting more the thinning prediction of the micro-sandwich sheets. Even so, the increase in element size was not sufficient to reach an approximation to the results of the 3D Solid model as good as the 2D/3D model. It should also be noted that increasing the size of the 2D element leads to a lower resolution of the mesh and its ability to correctly describe the tools geometry. While using this method to soften values and eliminate spurious peaks improves certain results it does not bring tangible benefits and should be avoided.

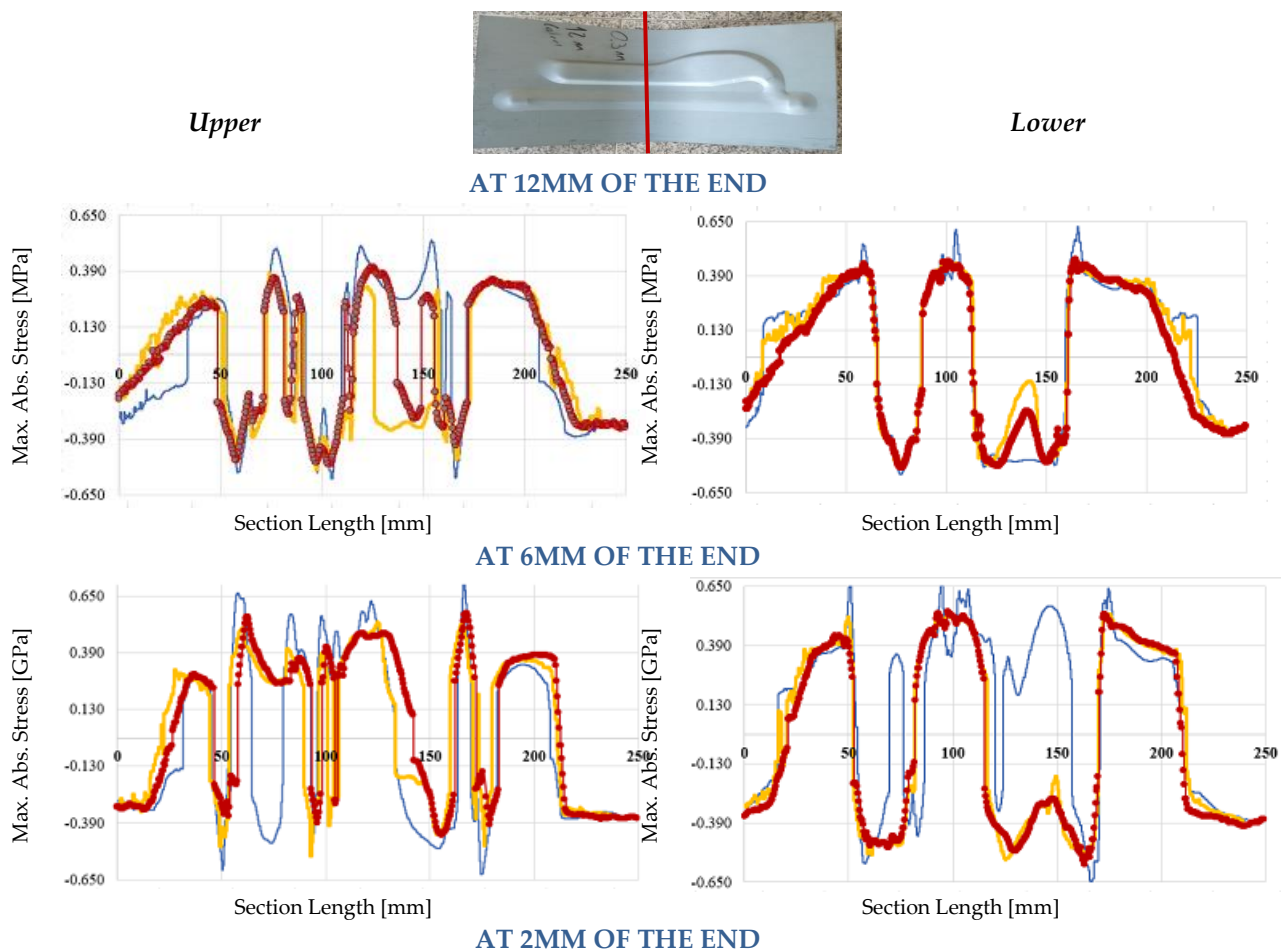
Therefore, the use of 2D Shell models to predict the feasibility of micro-sandwich stamped parts is strongly conditioned by the complexity of the geometry. On the one hand, small radii require higher mesh refinements; on the other hand, the efficiency of the 2D Shell element depends on the size/thickness ratio. Thus, when tool geometries present smooth shapes, large radii with good levels of uniformly distributed stretching, the 2D Shell models are highly efficient. However, in the case of stamping processes with

complex tool geometries and severe sheet deformation, such as the one presented in this study, the numerical results may be seriously compromised by element technology. The better compromise between efficiency and accuracy is reached by combining in the same FEM model 2D shell elements and 3D solid elements.

### Maximum Stress distribution:

The evaluation of the maximum stress distribution on the stamped part is very important to the prediction of metal-forming defects such as initiation and propagation of cracks, residual stresses and springback effect.

The evolution of the maximum absolute value of the principal stresses throughout the defined sections at 12mm, 6mm and 2mm of the tool's closed position (die/punch), is presented in Fig. 6.28 to Fig. 6.30. According to these, the excellent correlation between the 2D/3D model and the solid 3D model is confirmed again. Although the 2D Shell model following the same tendency, the results present a greater oscillation leading to a significant divergence from the other FEM models.



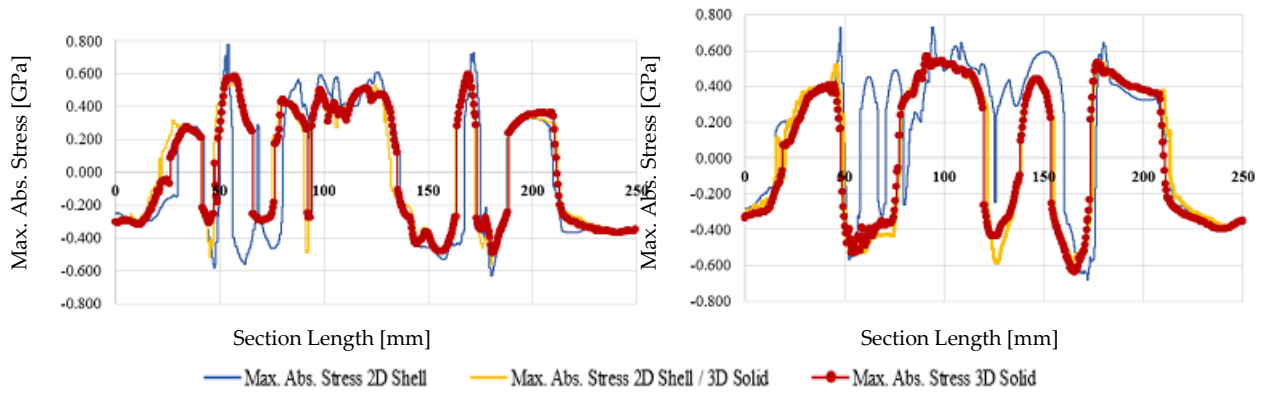
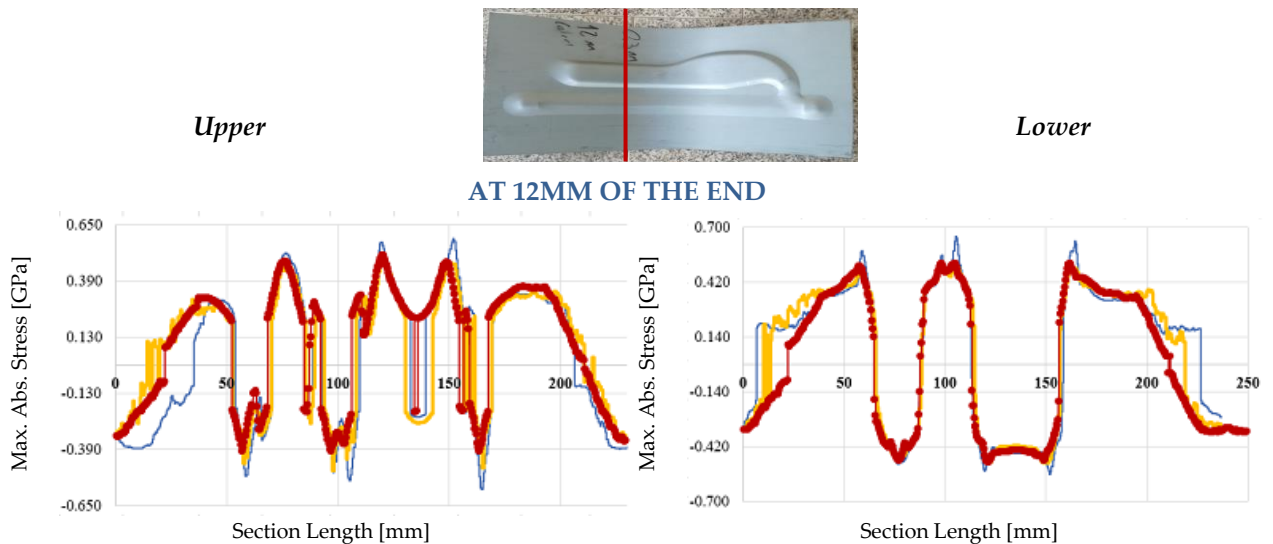


Fig. 6.28 – Comparison of the evolution of the maximum principal stresses value across the section 0 predicted from each FEM model (2D Shell, 2D/3D and 3D Solid), at the 3 stages of the deep-drawing operation (12mm, 6mm and 2mm). The results are presented for lower and upper skin.

The Fig. 6.28 shows the evolution of the maximum value of the principal stresses across the section 0. The 3D Solid model and 2D/3D exhibit an excellent correlation, which is closer in the lower skin at instants 6mm and 2mm. Regarding the 2D Shell model values, the correlation is not such a good, especially at instant 6mm, where the greatest divergence occurs. At this time, the 2D Shell model provides a maximum positive stress (tensile) of 560MPa, while the solid 3D Solid and 2D/3D models provide a maximum negative stress (compressive) of 265MPa and 197MPa, respectively, at the distance point 150mm measured in the lower skin. At 75mm distance, there is also a fluctuation of the maximum principal stress value, which in the case of the 2D Shell model reaches a positive value of 340MPa, while the 3D Solid and 2D/3D models register negative values of 455MPa. In the case of the upper skin, there is an inversion of the tendency towards the distance 75mm. Here, the 3D Solid and 2D/3D models predict a positive maximum value around 275MPa, while the 2D Shell model predicts a maximum negative value of 460MPa. At the instant 2mm, the predictions of the different FEM models tend to be closer, even so, the 2D Shell model presents some fluctuations that cause a significant divergence from the solid 2D/3D and 3D Solid models.



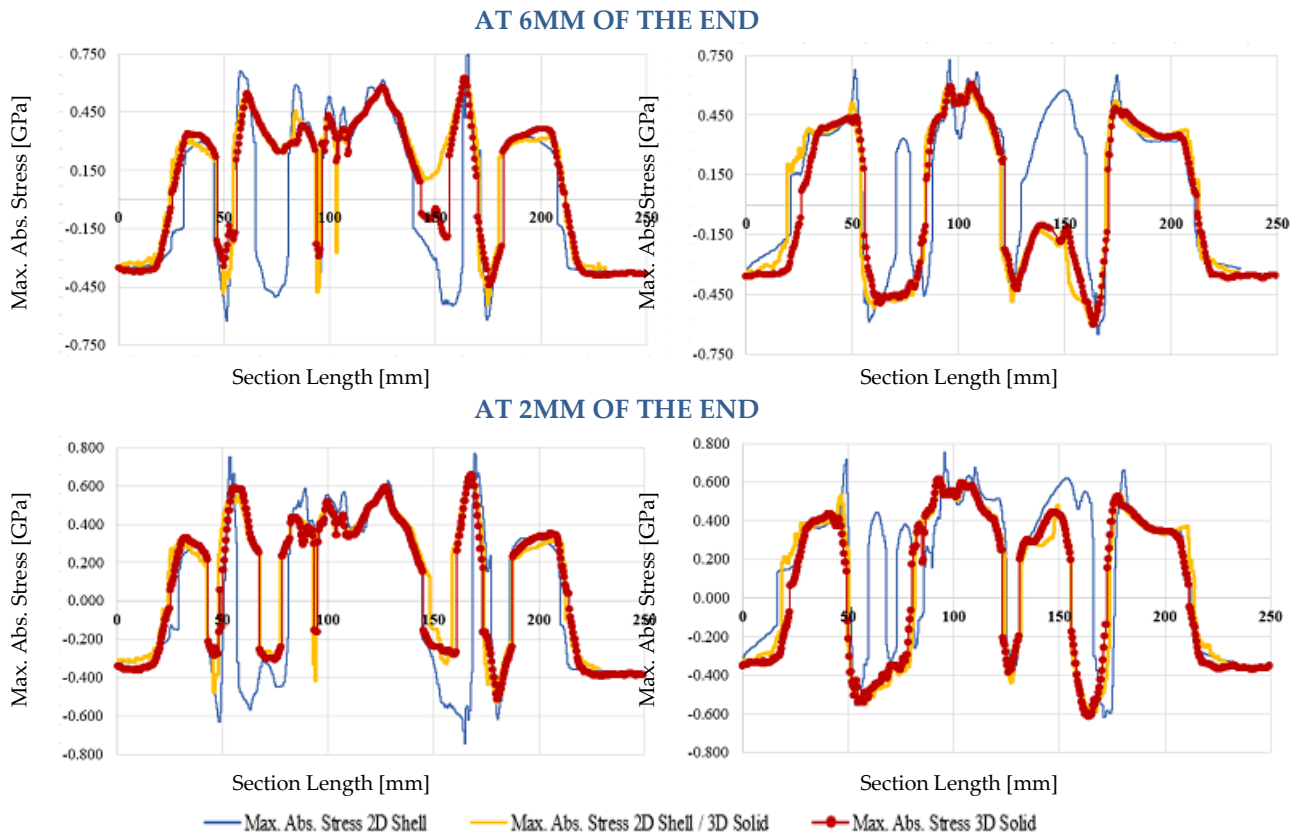


Fig. 6.29 – Comparison of the evolution of the maximum principal stresses value across the section -60 predicted from each FEM model (2D Shell, 2D/3D and 3D Solid), at the 3 stages of the deep-drawing operation (12mm, 6mm and 2mm). The results are presented for lower and upper skin.

The Fig. 6.29 shows the evolution of the maximum principal stress value along the section -60. In this section, the 3D Solid and 2D/3D models continue to present an excellent correlation. The conclusions are like those in section 0. The greatest divergence in the profile of the maximum principal stress value of the 2D Shell model, still occur at the intermediate state (6mm to the closing), with the largest fluctuations also occurring around 75mm and 150mm of distance. In the lower skin, the 2D Shell model predicts a maximum principal stress of 600MPa at 150mm, while the 3D Solid and 2D/3D models predict a maximum principal stress around 150MPa. At 75mm, the 2D Shell model reaches a positive value of 320MPa, while the 3D Solid and 2D/3D models give negative values close to 450MPa. Regarding the upper layer, the 3D Solid and 2D/3D models predict a positive maximum value around 300MPa at 75mm, while the 2D Shell model predicts a maximum negative value of 450MPa. At the instant 2mm, the numerical predictions of the different FEM models tend to approach again, but fluctuations persist.

*Upper*



*Lower*

**AT 12MM OF THE END**

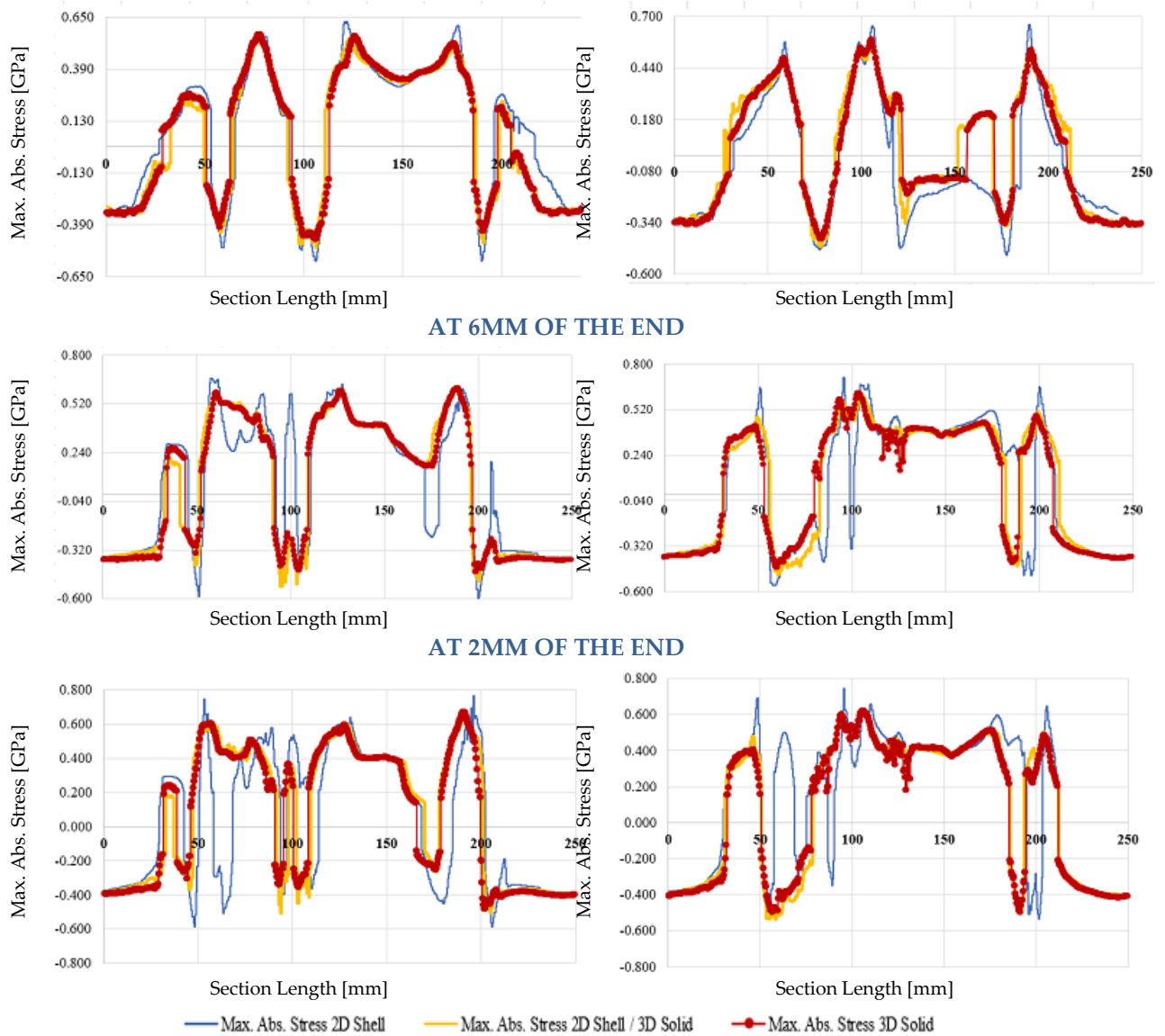


Fig. 6.30 – Comparison of the evolution of the maximum principal stresses value across the section +80 predicted from each FEM model (2D Shell, 2D/3D and 3D Solid), at the 3 stages of the deep-drawing operation (12mm, 6mm and 2mm). The results are presented for lower and upper skin.

The evolution of the maximum principal stresses value along the section -80 is shown at Fig. 6.30. This section presents the best correlation between all FEM models tested. The 2D Shell model continues to be prone to fluctuations regarding the evolution of the maximum principal stresses value. At the instant 6mm, these fluctuations are observed at 100mm and 175mm of distance. At point 100mm, the 2D Shell model predicts a negative value of maximum principal stress of 320MPa, to the lower skin, and a positive value of maximum principal stress of 570MPa, to the upper skin. The 3D Solid and 2D/3D models provide a positive value of maximum principal stress of 450MPa at the lower skin and negative value of maximum principal stress around 200MPa at the upper skin. At point 175mm, the 2D Shell model predicts a negative maximum value 200MPa to the upper skin, while the 3D Solid and 2D/3D models predict positive maximum value around 180MPa. At the instant 2mm, fluctuations are visible to 60mm of distance. Here, the 2D Shell model

provides a maximum value of 500MPa, positive to the lower skin and negative to the upper skin. The 3D Solid and 2D/3D models predict negative value of maximum principal stress around 380MPa, to the lower skin, and positive value of maximum principal stress around 420MPa, to the upper skin.

Considering all these results [Fig. 6.28 to Fig. 6.30], it is verified a greater oscillation in the maximum principal stresses value profile of the 2D Shell model. The largest deviations of this FEM model occur at instants 12mm and 6mm. In the peak values, the deviations between the 2D Shell and the other FEM models range from 700MPa to 950MPa. As noted earlier, in the case of principal strains, the very small size of the 2D Shell element affects its numerical performance, which is also reflected in the principal stresses analyze. The next figure [Fig. 6.31] shows what happens to the maximum value profile of the principal strains when the element size is increased to 2.0x2.0 [mm]. The profiles presented belongs to the sections 0 and -60, at the instant 6mm.

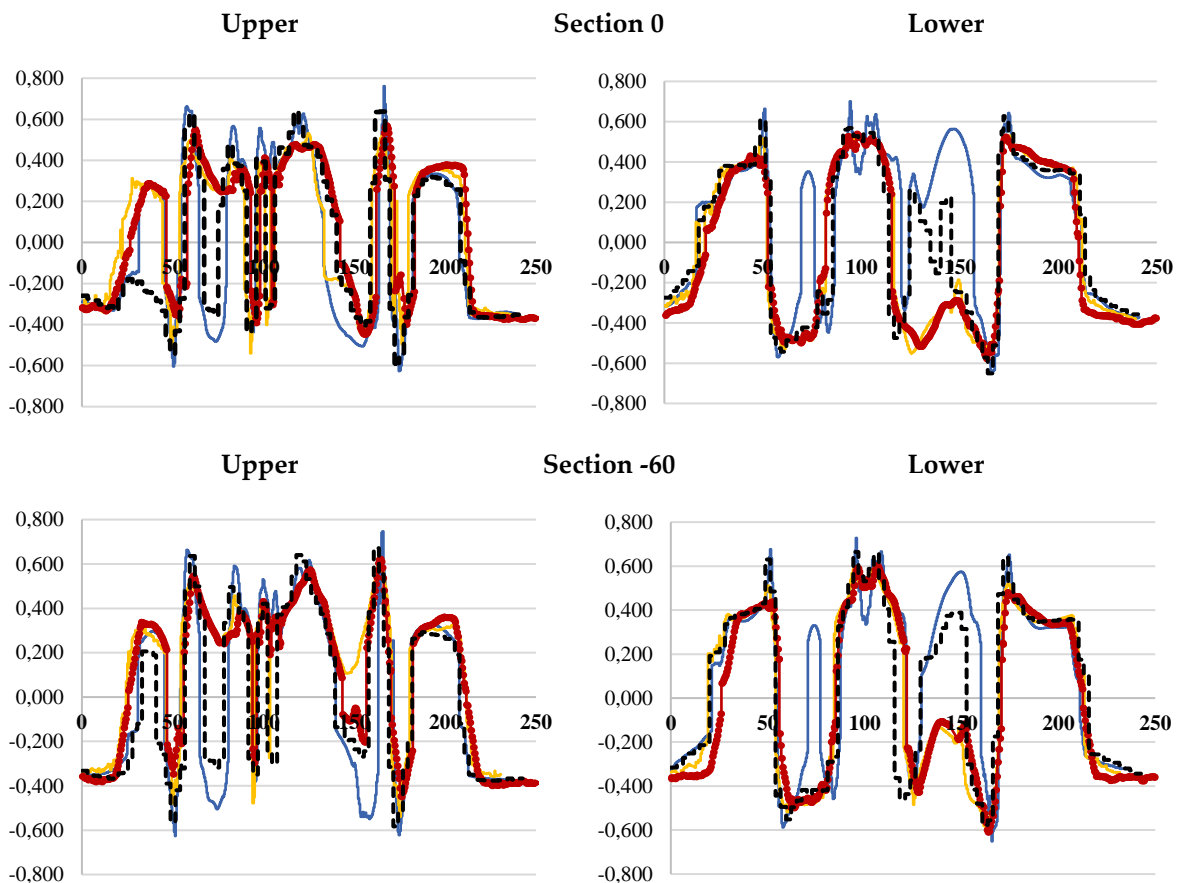


Fig. 6.31 – Comparison of the evolution of the maximum principal stresses value across the sections 0 and -60 at instant 6mm. Four FEM models are compared – the 2D Shell model, with 2 element sizes (0.5x0.5 and 2x2), the 2D/3D model and the 3D Solid model. The results are presented for lower and upper skin.

As it can be seen [Fig. 6.31], that increase of the element size of the FEM mesh contributes to reduce the peaks in the profile of the maximum principal stresses value. However, it should be noted that even after

increase the element area 16 times the fluctuations in the profile of the maximum principal stresses value are still present. Therefore, 2D Shell models are also not suitable for describing the stress state present in a stamped part when the micro-sandwich sheets are subjected to complex deformation trajectories.

## **CASE OF STUDY: PROCESS OPTIMIZATION CONSIDERATIONS**

Several measures can be taken to optimize a stamping process. These improvement actions depend on the type of defect and/or instability found and the respective failure mode. The actions taken to solve split issues may be different from the actions taken to solve a wrinkling issue. However, in certain cases, these forming problems can be related one to each other and solved by the same improvement action. On the other hand, the same type of forming defect may require different actions, especially when the failure modes are different. For instances, a fracture originated under tensile deformation in a severely stretched zone cannot be solved like a fracture originated under compression deformation in a material accumulation zone, since the stress states which defines the failure modes in each case are different. On the other hand, other constraints such as material properties (chemicals and mechanicals), tool modifications allowed, “quoted blank” size by the sales department, etc. In general, the optimization process always starts with the simplest, easiest to implement and cheaper actions, such as the change of the blank-holder force/pressure, the tools stroke, the press speed, the lubrication conditions, among others. One of the most common measures is the optimization of the blank shape.

Changing the shape of the blank modifies the material flow directions and may reduce the friction generated during the stamping process by relieving the forming forces involved. So, the optimization of the size and shape of the blank plays a paramount role to prevent splits, avoid material accumulation zones and wrinkles, increasing the robustness of the stamping process. In tandem tools, this procedure is especially useful when the geometries are very complex, the flow directions vary widely and the sliding distances are considerable. In the case of progressive tool stamping the optimization of the strip layout design is essential to make the product feasible, reduce the scrap and turn the process robust.

In this study, one of the main assumptions defined from the beginning was not to change the tools geometry and respect the maximum blank size defined in the original process. Therefore, it was decided to test the influence of blank shape in the stamping process.

The Fig. 6.32 shows the shape and dimensions of the modified blank considered in the numerical study.



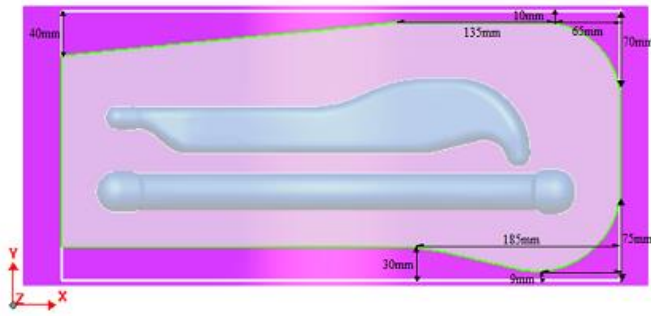
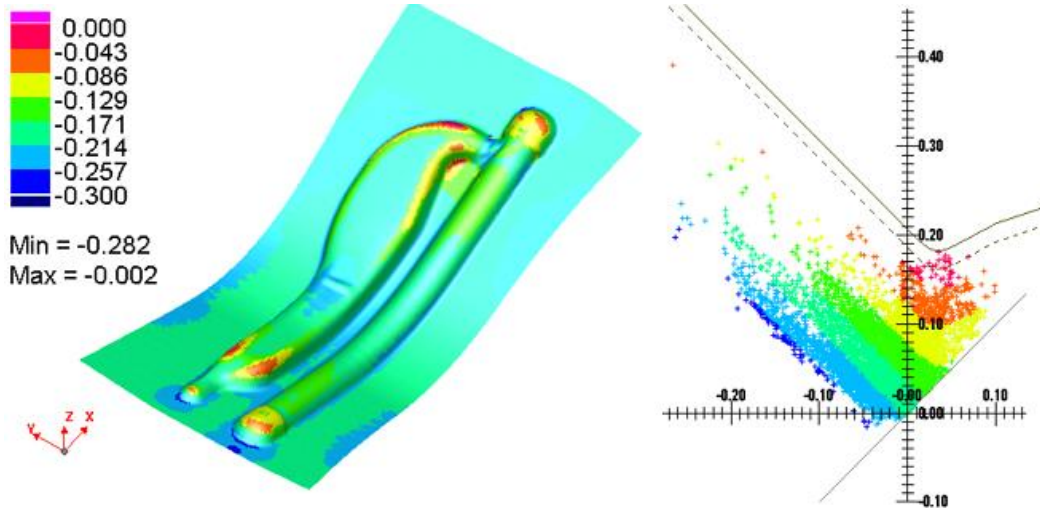


Fig. 6.32 – Modifications to the shape and dimensions of the original blank.

As shown in Fig. 6.32, the flat-blank flange area has been reduced in order to decrease the total friction force, facilitate the material flow and prevent the excessive stretching of the sheet. Moreover, the corners were rounded, allowing a more uniform flow in all directions of the blank plane and preventing compression paths.

A comparison of the FLD's results of the upper skin at the instant 2mm, before and after the virtual blank optimization, is presented in Fig. 6.33.

#### FLD – Upper Skin at 2mm of the end



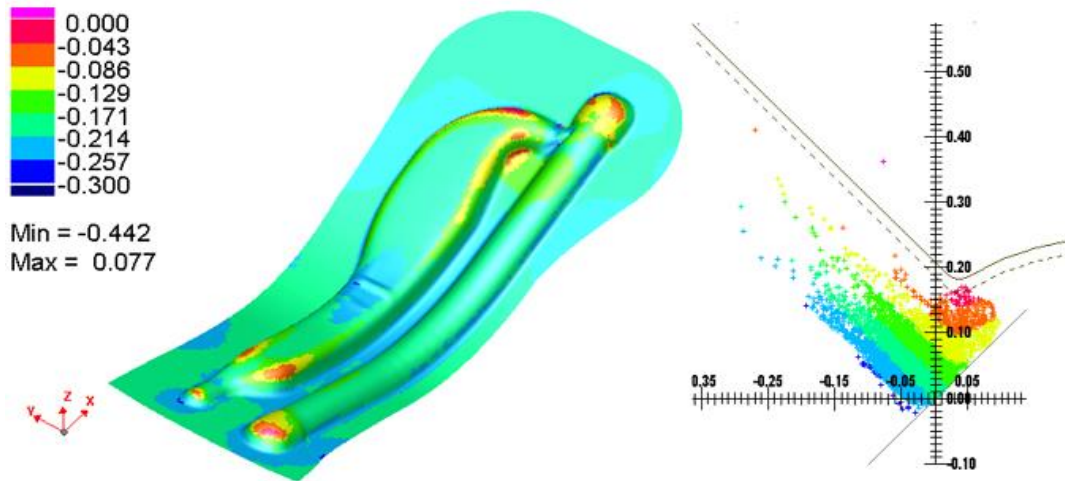
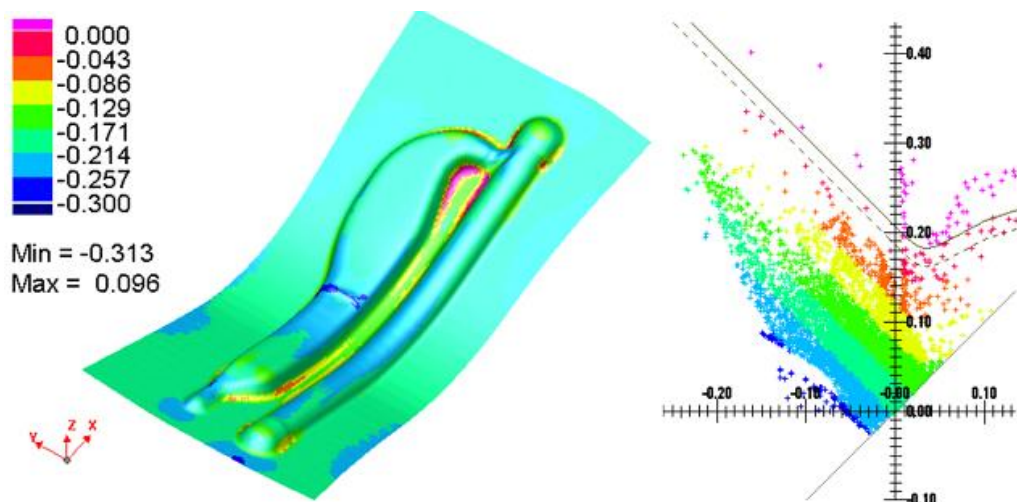


Fig. 6.33 – Comparison between the original and the modified blank - Cloud of the material points, and the respective strain state, predicted by the 2D/3D model, in the upper skin of the stamped part and in the FLD at 2mm.

As depicted, the numerical results in the upper layer remain very similar after blank shape optimization. The areas of excessive stretching and compression with wrinkles formation remain unchanged. The improvements are very faint and consist of a slightly setback of the material points near to FLC0 - the low point located on the 0 minor strain axis. The point with the higher value (7.7% above the FLC limit) should be disregarded in this analysis because it results from the penetration of a loose patch of the tool geometry outside the study blank area. Thus, all material points are below the FLC, but very close to the limit.

Fig. 6.34 presents a comparison of the FLD's results of the lower skin at the instant 2mm, before and after the virtual blank optimization.

#### FLD – Lower Skin at 2mm of the end



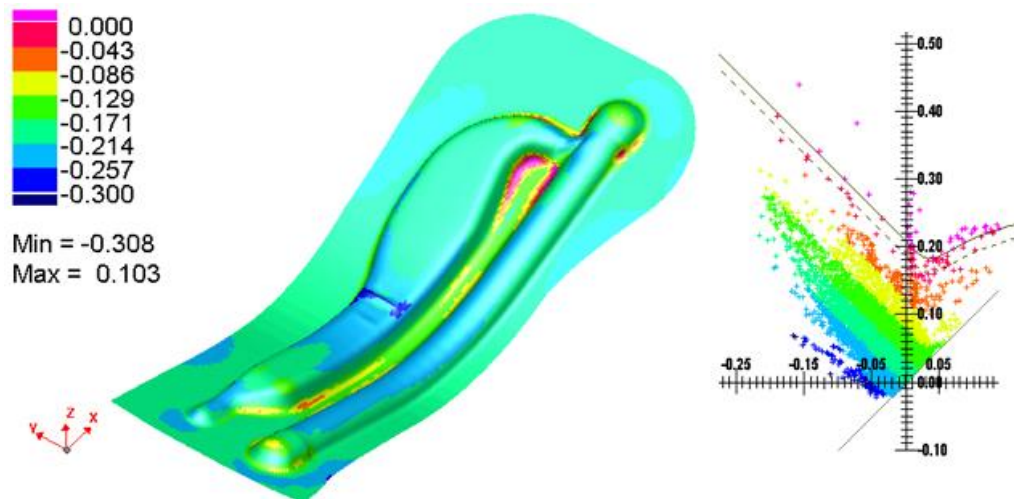


Fig. 6.34 – Comparison between the original and the modified blank - Cloud of the material points, and the respective strain state, predicted by the 2D/3D model, in the lower skin of the stamped part and in the FLD at 2mm.

Likewise, the blank shape modification did not bring significant improvements in the numerical results predicted to the lower skin. Although a slight decrease in the amount of material points above the FLC is perceptible, the risk of rupture is still incontestable.

Therefore, the results cannot be improved only through the blank shape modification. As previously mentioned, the blank shape modification intends to facilitate the flow of the material into the die. In this case, this is not possible since the material flow to the zone between punches is restricted by the tools geometry. During the tools closing, the flow of the material becomes less and less, increasing highly the sheet stretching. The plastic strain becomes more severe and tends to localize immediately before the tools closure, when the material flow is totally restricted, causing to the rupture of the part. Moreover, the blank shape modification was not effective to solve the wrinkling problem either. This is because the wrinkle formation is intrinsically linked to the strain path imposed by the tool geometry.

Given the above, it is concluded that the only way to solve the forming problems detected in the stamping process of this part is by modifying the geometries of the tools. Excessive stretching can be reduced by smoothing the tool shapes, increasing radii and wall opening angles. The tools must be redesigned in the transition zone between the punches to avoid the material accumulation and reduce the wrinkling tendency. This study demonstrates that, especially in the case of parts with complex geometries, it is not possible to perform a direct replacement of monolithic aluminum sheets by micro-sandwich Litecore sheets with the same overall thickness. The realization of a prior numerical simulation study, with an appropriate FEM model, that allows to identify and solve possible forming defects is absolutely essential. In some cases, the improvement actions may be relatively simple, allowing the introduction of innovative materials into automotive components with the same processes and technologies and resulting in a cost-benefit ratio more favorable to the industry.

## CONCLUSIONS

Based on a prototype geometry of an aluminum stamped fuel filling system, designed at Sodectia Product Competence Center, a benchmark study was drawn up to evaluate the accuracy and reliability of 3 different FEM approaches available to modelling and simulation of automotive stamping processes of micro-sandwich sheets. For this purpose, the Litecore S micro-sandwich, produced by Thyssenkrupp AG, was chosen and the commercial stamping simulation software PAM-STAMP 2015.1 was used.

Regarding the micro-sandwich stamping simulation, the 3D Solid models are highly accurate, however, because of its demanding of high computational cost and complex FE mesh generation they are not efficient to industrial practices. In the other hand, the 2D Shell models are highly efficient and can delivery good results when tool geometries present smooth shapes, large radii with good levels of uniformly distributed stretching. But, in the case of stamping processes with complex tool geometries and severe sheet deformation, such as the one presented here, the numerical results may be seriously compromised by element technology. Concerning the 2D Shell model, it was observed that:

- The forming forces predicted by the 2D Shell model at the final of the deep-drawing operation are 22% higher than the 3D Solid.
- Highly refined 2D Shell meshes under complex deformation trajectories leads to unrealistic peaks of principal strains and, consequently, unreliable predictions of thinning and thickening of the micro-sandwich sheet. Spurious fluctuations of the maximum principal stresses value where also detected.
- In this example, the 2D Shell model was not able to reproduce wrinkling tendencies.

Following a strategy that combines 2D shell elements and 3D solid elements the accuracy of the results was highly improved:

- The forming forces predicted by the 2D/3D model at the final of the deep-drawing operation are 11% higher than the 3D Solid.
- The principal strains profiles, thickness profiles and maximum principal stresses value profile of the 2D/3D model are in excellent agreement with the 3D solid model.
- The 2D/3D model was able to reproduce the formation of wrinkles and the location of micro-sandwich ruptures.

Therefore, despite of the 2D Shell multilayer modules present in commercial stamping simulation softwares being very effective and highly useful, for example, with inner and outer automotive skins (bonnets, fenders, interior door panels etc.,) they are not suitable to deep drawn parts with complex geometries. In these cases, 2D/3D models must be used to achieve a reliable feasibility study and improve the stamping process robustness. As demonstrated in this study, when the subject is develop and produce a new product based on innovative materials, using the right FEM model can make the difference between

success and failure.

## ACKNOWLEDGMENTS

The authors greatly acknowledge the financial support of “Fundação para a Ciência e Tecnologia” (FCT – Portugal), through the research project SFRH/BDE/51189/2010 (“Development FEA Tools Applied to Sheet Forming Special Cases. Application to the Automotive Industry, Advanced Metallic Materials and Multi-Layer and Multi-Material Sheets”) in partnership with Sodecia Product Competence Center (Maia, Portugal). The authors would also like to thank the company Thyssenkrupp AG, for providing the Litecore material, and ESI GROUP to the technical support with PAM-STAMP 2015.1 and collaboration in this study.

## COMPLIANCE WITH ETHICAL STANDARDS:

Funding: This study was funded by SFRH/BDE/51189/2010.  
No conflict exists: The authors declare that they have no conflict of interest.

## REFERENCES

1. Ishikawa, T., Amaoaka, K., Masubuchi, Y., Yamamoto, T., Yamanaka, A., Arai, M., & Takahashi, J. (2018). “Overview of automotive structural composites technology developments in Japan.” *Composites Science and Technology*, 155, 221-246. DOI: 10.1016/j.compscitech.2017.09.015
2. Gándara, M. (2013). “Aluminium: The metal of Choice.” *Materials and Technology*, 47, 261-265.
3. Hirsch, J. (2014). “Recent development in aluminum for automotive applications.” *Transactions of Nonferrous Metals Society of China*, 1995-2002. DOI: 10.1016/S1003-6326(14)63305-7
4. Henriksson, F. Johansen, K. (2016). “On material substitution in automotive BIWs - From steel to aluminum body sides.” *Procedia CIRP*, 50, 683-688. DOI: 10.1016/j.procir.2016.05.028
5. Cao, J. Cheng, H. S. Yao, H. Liu, S. D. Kinsey, B. (2004) “Wrinkling behavior of laminated steel sheets.” *Journal of Materials Processing Technology*, vol. 151, issue 1-3, pp.133-140. DOI: 10.1016/j.jmatprotec.2004.04.028
6. Ghugal, Y. M. Shimpi, R. P. (2002) “A Review of Refined Shear Deformation Theories of Isotropic and Anisotropic Laminated Plates.” *Journal of Reinforced Plastics and Composites*, vol. 20, issue 3, pp.255-272. DOI: 10.1106/073168402025748
7. Kirchhoff, G. R. (1850) “Über das Gleichgewicht und die Bewegung einer Elastischen Scheibe,” *J. Reine Angew. Math. (Crelle)*, Vol. 40, pp. 51–88.
8. Kirchhoff, G. R. (1850) “Über die Schwingungen Einer Kriesformigen Elastischen Scheibe,” *Poggendaorffs Annalen*, Vol. 81, pp. 258–264.
9. Love, A. E. H. (1888) “On the small free vibrations and deformations of elastic shells”, *Philosophical trans. of the Royal Society (London)*, Vol. série A, N° 17 p. 491–549
10. Mindlin, R. D. (1951) “Influence of rotatory inertia and shear on flexural motions of isotropic elastic plates”, *J. Appl. Mech.*, 18, pp. 31-38

11. Reissner, E. (1945) "The effect of transverse shear deformation on the bending of elastic plates", *J. Appl. Mech.*, 12, pp. 69-77
12. Wang, C. M. Lim, G. T. Reddy, J. N. Lee, K. H. (2001) "Relationships between bending solutions of Reissner and Mindlin plate theories." *Engineering Structures*, Vol 23, Issue 7, pp. 838-849. DOI: 10.1016/S0141-0296(00)00092-4
13. Naghdi, P. M. (1957) "On the Theory of Thin Elastic Shells", *Quarterly of Applied Mathematics*, Vol. 14, pp. 369–380.
14. Ahmed S., Irons B.M. and Zienkiewicz O.C. (1968) "Curved Thick Shell and Membrane Elements with Particular Reference to Axi-Symmetric Problems", *Proceeding of the second conferences on Matrix method in Structural Machines*, USA, pp. 539-572
15. Büchter, N. Ramm, E. (1992) "Shell theory versus degeneration – a comparison in large rotation finite element analysis", *International Journal for Numerical Methods in Engineering*, vol.37, pp. 55–62. DOI: 10.1002/nme.1620340105
16. Reddy, J.N "Mechanics of Laminated Composite Plates and Shells: Theory and Analysis", CRC Press, New York, 2004.
17. Fung, Y.C. Tong, P. Chen, X. "Classical and Computational Solid Mechanics, Advanced Series in Engineering Science", vols. 1 and 2, World Scientific Publishing Co. Pte. Ltd., Singapore, 2001.
18. Love, A.E.H. "A Treatise on the Mathematical Theory of Elasticity", fourth edition, World Cambridge University Press, USA, 1959.
19. Brischetto, S. (2017). "A closed-form 3D shell solution for multilayered structures subjected to different load combinations." *Aerospace Science and Technology*, vol. 70, pp. 26-46. DOI: 10.1016/j.ast.2017.07.040
20. Aitharaju, V. Averill, R. (1999) "C0 zigzag kinematic displacement models for the analysis of laminated composites." *Mechanics of Composite Materials and Structures*, Vol 6, Issue 1, pp.31-56
21. Sussman, T., & Bathe, K.J. (2013). "3D-shell elements for structures in large strains." *Computers and Structures*, 2-12. DOI: 10.1016/j.compstruc.2012.12.018
22. Dvorkin, E.N. Pantuso, D. Repetto, E.A. (1995) "A formulation of the MITC4 shell element for finite strain elasto-plastic analysis." *Comput Methods Appl Mech Eng*, vol. 125, pp. 17–40. DOI: 10.1016/0045-7825(95)00767-U
23. Bathe, K.J. Wilson, E.L. Thick shells. In: Pilkey WD, Saczalski K, Schaeffer HG, editors. *Chapter in Structural mechanics computer programs: surveys, assessments, and availability*. University of Virginia Press; 1974.
24. Bathe, KJ. "An assessment of current finite element analysis of nonlinear problems in solid mechanics." In: Hubbard B, editor. *Chapter in Numerical solution of partial differential equations – III*. Academic Press; 1976.

25. Daniel, W.J.T, Belytschko, T. (2005) "Suppression of spurious intermediate frequency modes in under-integrated elements by combined stiffness/viscous stabilization." *Int J Numer Methods Eng*, vol. 64, pp. 335–353. DOI: 10.1002/nme.1369
26. Reese, S. Wriggers, P. (2000) "A stabilization technique to avoid hourglassing in finite elasticity." *Int J Numer Methods Eng*, vol. 48, pp. 79–109. DOI: 10.1002/(SICI)1097-0207(20000510)48:1<79::AID-NME869>3.0.CO;2-D
27. Wall, W.A. Bischoff, M. Ramm, E. (2000) "A deformation dependent stabilization technique, exemplified by EAS elements at large strains." *Comput Methods Appl Mech Eng*, vol. 188, pp. 859–871. DOI: 10.1016/S0045-7825(99)00365-5
28. Reese S. (2005) "On a physically stabilized one point finite element formulation for three-dimensional finite elasto-plasticity." *Comput Methods Appl Mech Eng*, vol. 194, pp. 685–715. DOI: 10.1016/j.cma.2004.12.012
29. Pimentel, A. M. Alves, J. L. Merendeiro, N. Vieira, D. (2018) "Comprehensive benchmark study of commercial sheet metal forming simulation softwares used in the automotive industry." *International Journal of Material Forming*. DOI: 10.1007/s12289-018-1397-4





## 7. CONTRIBUIÇÃO PARA O CENTRO DE COMPETÊNCIAS DE PRODUTO SODECIA E PARA A INDÚSTRIA AUTOMÓVEL EM GERAL

Conforme apresentado no capítulo introdutório, as linhas de investigação traçadas neste trabalho tiveram como base a seguinte questão:

*“Como simular correctamente processos de conformação robustos, convencionais ou não convencionais, de chapas metálicas multi-camada e multi-material, recorrendo aos programas FEA comerciais disponíveis no Centro de Competências de Produto (PCC) Sodecia, incrementando a sua capacidade competitiva no desenvolvimento de novos produtos?”*

Assim, definiram-se 5 pilares essenciais para sustentar um estudo capaz de responder cabalmente a esta pergunta. Em seguida, apresentam-se um conjunto de observações e recomendações afetas a cada um destes pilares.

### ***Benchmarking de Ferramentas FEA - Observações:***

Em primeiro lugar, realizou-se uma análise comparativa dos programas FEA comerciais disponíveis no PCC Sodecia. No que concerne à simulação de processos de estampagem, o PCC Sodecia dispõe de 2 das ferramentas FEA mais comumente utilizadas na indústria automóvel, sendo que tanto o uma (AutoForm) como outra (PAM-STAMP 2G), incorporam módulos específicos para a utilização de materiais multi-camada e multi-material. Contudo, estes dois códigos FE baseiam-se em formulações diferentes. Enquanto o AutoForm é estático-implícito o PAM-STAMP 2G é dinâmico-explícito. Visto que a formulação FE e as especificações inerentes a cada código afetam os resultados numéricos, decidiu-se, antes de mais, comparar estas duas ferramentas. Este estudo foi fundamental não apenas para perceber qual o software capaz de devolver resultados numéricos mais próximos dos resultados reais, mas também para desenvolver um conhecimento crítico das ferramentas FEA, capaz de conferir ao PCC mais autonomia e independência face à propaganda dos fornecedores, e, ao mesmo tempo, eliminar ferramentas que partilhem as mesmas potencialidades reduzindo os custos inerentes às mesmas. A este estudo comparativo também foi adicionado o software académico DD3Imp, que é puramente implícito e utiliza elementos finitos sólidos. Consequentemente, reproduziu-se um caso de estudo bem conhecido e publicado das conferências Numisheet. O Numisheet 2008 #BM02 é um caso particularmente interessante, com uma geometria suficientemente complexa, e cujos resultados experimentais se encontram disponíveis. O Benchmark #02, proposto pela Daimler, envolve a estampagem de um perfil S-Rail em aço HC260LAD ou em uma liga de alumínio AC170, sendo que as ferramentas podem ou não apresentar freios. Realizadas as simulações em cada um dos softwares, comparam-se os resultados numéricos com os resultados experimentais para as

variáveis: *Força do Punção, Escoamento, Maior Deformação Principal, Menor Deformação Principal e Retorno Elástico*. Os resultados devolvidos pelas duas ferramentas FEA comerciais foram sempre muito aproximados, para quase todas as variáveis, com exceção do retorno elástico. Durante a análise da simulação do processo virtual de estampagem do S-Rail, é perceptível a formação de uma ruga, com o software PAM-STAMP 2G, que o AutoForm não prevê, mas que foi identificada em algumas peças experimentais. Assim, a formulação dinâmica-explicita do PAM-STAMP é mais sensível às instabilidades do processo de estampagem e uma mais-valia importante quando se procura aumentar a robustez do mesmo. O DD3IMP, também deu resultados sempre bastante consistentes e próximos dos outros softwares em praticamente todos os casos. Contudo, o tempo associado ao *setup* do processo e geração da malha 3D e o custo computacional associado à simulação com elementos sólidos, não tornam esta ferramenta eficiente para a prática industrial. Já o refinamento adaptativo das malhas 2D, em função das características geométricas das ferramentas e nível de precisão desejado, do AutoForm e PAM-STAMP 2G, no decurso do processo de estampagem, garantem uma descrição rigorosa da “história de deformação” e a obtenção de resultados numéricos confiáveis. Não se verificaram diferenças dignas de registo no que concerne ao tempo de cálculo das ferramentas FEA comerciais testadas. A maior dispersão de resultados verificou-se para a variável retorno elástico, mesmo com a utilização de modelos mecânicos e numéricos equiparáveis. O que indica que, neste caso, as formulações FE de cada código exercem um maior impacto. Quanto à exactidão das previsões do retorno elástico, o AutoForm apresentou resultados mais próximos dos obtidos experimentalmente para os casos de estampagem sem freios, já o PAM-STAMP 2G alcançou melhores resultados para os casos de estampagem com freios. Contudo, convém ser prudente na análise destes resultados, os quais podem não ser totalmente representativos do desempenho dos softwares avaliados. No caso sem freios, o processo de estampagem é mais instável o que prejudica a robustez do retorno elástico. Isto significa que o retorno elástico experimental pode variar tanto (dentro de uma determinada “janela de processo”) que as previsões numéricas obtidas podem não ser confiáveis. No caso com freios, verificaram-se diferenças significativas entre os resultados numéricos e os resultados experimentais das forças de conformação e escoamento. Estas diferenças afectam diretamente o estado de deformações residuais e tensões residuais, bem como a distribuição do estiramento presente na peça após a operação de estampagem. Visto que o efeito retorno elástico é essencialmente dependente destas variáveis de estado, a comparação entre os resultados experimentais e numéricos pode não ser efetiva.

#### ***Benchmarking de Ferramentas FEA - Recomendações:***

Apesar de diferenças fundamentais nas suas formulações FE, foi demonstrado que o AutoForm e o PAM-STAMP 2G geram resultados muito semelhantes, que geralmente, se aproximam muito bem dos resultados experimentais. Isto significa que as empresas não devem ficar demasiadamente preocupadas com o impacto das formulações FE na precisão dos resultados numéricos gerados pelas suas ferramentas

FEA e, conseqüentemente, na sua própria competitividade. Na verdade, a escolha das ferramentas FEA deve refletir sobretudo a estratégia e os objetivos da empresa. Neste âmbito, o principal *objetivo* da empresa pode ser a produtividade. Se este for o caso, é necessário ter em mente que um dos aspectos chave, que mais afeta a produtividade de um engenheiro CAE processo, é o tempo gasto com o pré/pós processamento das simulações. Neste quesito, deve reconhecer-se que a produtividade virtual do AutoForm é, sem dúvida, imbatível. Por ser uma ferramenta FEA concebida, desde o início, para apoiar exclusivamente indústria de estampagem automóvel, disponibiliza uma série de módulos que permitem rapidamente não só gerar as ferramentas virtuais e o respetivo processo, como também aceder e tratar os resultados de uma forma muito intuitiva. Por outro lado, também oferece módulos extras como o AutoForm Sigma e o AutoForm Compensator, que oferecem vantagens inequívocas que vão para além da validação da factibilidade de determinada peça ou processo visto que permitem avaliar a robustez do processo de estampagem concebido. Esta ferramenta é, portanto, a mais completa para apoiar as decisões de engenharia dentro das unidades de fabrico de peças estampadas ou de produção de ferramentas de estampagem. Ainda assim, nem todas as empresas estabelecem o seu *objetivo* em torno da produção. Empresas e centros de pesquisa que se dedicam, por exemplo, ao desenvolvimento de novos produtos ou processos inovadores, não baseiam a sua geração de valor em torno da quantidade de peças produzidas. Neste caso, as soluções oferecidas por um software dedicado, como é o caso do AutoForm, podem ser insuficientes para as exigências e necessidades destas empresas. A aposta destas empresas recai normalmente sobre plataformas de simulação multi-domínio que permitem cobrir várias áreas da engenharia. Altair, LS-Dyna e ESI Group, são alguns dos fornecedores mais conhecidos presentes neste mercado. As suas plataformas integram diferentes módulos FEA, que permitem modelar e simular diferentes fenómenos, usando os resultados obtidos de forma intercambiável. Assim, é possível, por exemplo, modelar e simular o processo de conformação de chapa para obter um determinado produto. Após isso, o histórico de variáveis de estado como deformação plástica e tensão equivalentes, quantidade e distribuição de estiramento e variação da espessura pode ser preservado e utilizado como ponto de partida para uma nova simulação, por exemplo, de um processo de soldadura. Neste caso, as tensões térmicas induzidas neste último, terão um efeito cumulativo sobre as tensões residuais do processo de transformação de chapa, influenciando significativamente os resultados obtidos para outras análises FEM costumeiramente realizadas para atestar a performance do produto (estrutural, fadiga, impacto, acústica, etc.). Embora o AutoForm permita o mapeamento de algumas variáveis de estado, o seu uso é limitado e a compatibilidade com outros softwares nem sempre é garantida. Enquanto isso, o PAM-STAMP 2G foi concebido para trabalhar dentro de uma filosofia de simulação multi-domínio onde a informação gerada pode ser facilmente e rapidamente partilhada com as outras ferramentas FEA pertencentes à família ESI Group.

*Estudo de Variabilidade dos Parâmetros de Simulação - Observações:*

Globalmente, os resultados numéricos obtidos no estudo comparativo das ferramentas numéricas acompanharam satisfatoriamente a tendência exibida nos resultados medidos experimentalmente. Contudo, algumas discrepâncias levantaram dúvidas sobre estas medições. Em alguns casos, foi simplesmente impossível acompanhar a magnitude dos valores experimentais, em qualquer um dos códigos FE testados. A título de exemplo, pode-se mencionar as forças do punção experimentais, para o caso HC260LAD LC3, cujo valor máximo esteve em média 30% acima do valor máximo das previsões numéricas. Portanto, repetiu-se o estudo de simulação numérica do processo de conformação do S-Rail, apresentado no Benchmark #02 do congresso Numisheet 2008, analisando o efeito da variabilidade de parâmetros de processo (diferentes condições de atrito e folga de freio) e parâmetros numéricos (diferentes modelos de material) para os casos HC260LAD LC1 e HC260LAD LC3. O objetivo foi avaliar o impacto dos parâmetros de processo e numéricos nos resultados para perceber se a causa raiz das diferenças entre os resultados numéricos e experimentais estaria do lado da construção do modelo numérico ou do lado das condições dos ensaios e medições experimentais. Para garantir que as formulações FE inerentes às ferramentas FEA não interferissem neste estudo, realizaram-se todas as simulações em apenas um software, a saber, o AutoForm R5.2. As variáveis analisadas foram as forças de conformação (forças do punção), escoamento e retorno elástico. Em termos das previsões de forças de conformação observou-se que estas são mais sensíveis às variações dos parâmetros de processo. Para o caso HC260LAD LC1, verificou-se uma variação de 57% na previsão das forças de conformação dentro das diferentes condições de atrito testadas. Já no caso HC260LAD LC3, o parâmetro mais influente foi a geometria do freio, sendo que a existência ou inexistência de folga levou a uma variação de 21% das forças de conformação previstas. Na avaliação da variável escoamento a tendência manteve-se. Comparando a influência dos diferentes parâmetros, verificou-se que as condições de atrito provocam uma variação do escoamento 5.2 vezes superior à variação provocada pelo modelo material no caso HC260LAD LC1. Já no caso HC260LAD LC3 o parâmetro “geometria do freio” gera uma variação de escoamento quase 3.5 vezes superior à variação gerada pelo modelo material. Finalmente, a tendência inverte-se para a previsão do retorno elástico, onde a influência dos parâmetros numéricos mostrou ser superior. No caso HC260LAD LC1, a variação do parâmetro “modelo material” produziu um desvio angular médio 2.7 vezes maior do que o produzido pela variação do parâmetro “condições de atrito”. No caso HC260LAD LC3, este rácio aumentou para 2.9. Porém, vale a pena notar que 88% da variação do retorno elástico gerada pelo “modelo material”, no caso HC260LAD LC1, e 86%, no caso HC260LAD LC3, devem-se exclusivamente à introdução de uma lei de encruamento cinemático. Assim, os dados obtidos nesta análise, apontam como a causa raiz mais provável para a discrepância entre valores numéricos e experimentais, razões associadas à geometria do freio.

*Estudo de Variabilidade dos Parâmetros de Simulação - Recomendações:*

O impacto da variabilidade dos parâmetros de simulação sobre os resultados obtidos foi claramente demonstrado. Este tipo de estudo é fundamental para se compreender a causa raiz de discrepâncias entre resultados numéricos e experimentais e é essencial para assegurar a robustez dos processos de estampagem validados em ambiente virtual. Como foi evidenciado, os parâmetros de processo têm uma grande influência sobre os resultados de conformabilidade geral obtidos nas simulações numéricas de processos de estampagem. Por isso, a questão da sua variabilidade deve ser meticulosamente avaliada durante a concepção do processo. Depois de assegurar a factibilidade do produto estampado e a factibilidade e robustez do processo de estampagem, é necessário atentar a variabilidade dos parâmetros numéricos para se conseguir resultados retorno elástico robustos e confiáveis. Este primeiro estudo, deve ser realizado para se entender se o retorno elástico deve ser compensado geometricamente ou se o conceito da ferramenta e/ou parâmetros de processo precisam ser modificados. Com base nestas premissas, avalia-se a robustez da resposta do retorno elástico à variabilidade do processo de fabrico antes de compensar a geometria das ferramentas. Visto que a modificação da geometria das ferramentas influencia directamente o escoamento do material que, por sua vez, afecta o retorno elástico, torna-se necessário realizar uma nova análise de robustez após a compensação do retorno elástico para assegurar que o esquema final de compensação seja repetível. Anteriormente, a variabilidade do processo não era tida em conta. A abordagem clássica consiste em introduzir margens de segurança e levar em conta os piores cenários. Desta forma, a incorporação da variabilidade e de ruído é reduzida a um problema determinístico onde o domínio de validade da simulação é estabelecido para um conjunto específico de variáveis e propriedades atribuídas durante o pré-processamento. O resultado esperado é um protótipo virtual que demonstre que é possível produzir a peça. Isto permite definir um ponto de processo. Porém, além de não garantir a robustez do processo e nada revelar acerca da variabilidade dos resultados, esta abordagem incorre no risco de obter soluções demasiadamente conservativas e dispendiosas. Em termos práticos, o que muitas vezes sucede é que, embora se obtenham peças com sucesso em ambiente virtual, em ambiente industrial peças com defeitos que precisam ser descartadas continuam a fazer parte do ciclo de produção. Isto ocorre porque, diferentemente do que é especificado no processo virtual, o processo real está sujeito à variabilidade e ao ruído. As forças da prensa não são constantes, a espessura do filme lubrificante não é constante, as propriedades mecânicas do material não são constantes. Esta variabilidade reflecte-se nos valores de conformabilidade e retorno elástico que diferem de peça para peça. Portanto, quando se parte para o processo de produção uma “janela de processo”, que leve em conta esta variabilidade, deve ser conhecida para garantir um processo de produção estável. Ao reproduzir-se o Benchmark #02 anulando o valor da folga existente nos freios constatou-se que os valores da força de conformação convergiram para as magnitudes pretendidas. Portanto, é provável que a discrepância existente entre os resultados numéricos e experimentais esteja relacionada com a geometria dos freios e as condições de travamento impostas na sua zona de actuação. É de todo legítimo questionar a informação experimental recebida, a qual não permite

correlacionar a situação real do ensaio com a situação ideal simulada. Esta é uma conclusão importante uma vez que o benchmark realizado está diretamente relacionado com a influência dos freios no control do efeito de retorno elástico tão presente nos processos de conformação de chapa da indústria automóvel. De facto, os resultados experimentais obtidos neste tipo de benchmarks são muitas vezes utilizados pelos desenvolvedores de softwares de estampagem FEA para melhorar as ferramentas numéricas e, neste caso particular, a precisão dos modelos de freios. Contudo, se estes resultados não forem totalmente confiáveis, os modelos numéricos calibrados com base nestes tampouco o serão. Por isso, resultados de modelos de freios virtuais, baseados na informação experimental deste benchmark, podem conduzir a conclusões questionáveis. Tanto para a indústria como para a comunidade académica, é essencial que o desenvolvimento e validação de modelos numéricos se baseia em testes experimentais robustos capazes de devolver resultados consistentes e confiáveis. Portanto, o domínio sobre os parâmetros de processo e o seu ajuste deve ter prioridade. Tendo em conta que a informação experimental é mais difícil de obter e tratar no caso de peças e processos mais complexos, é necessário usar de especial critério ao escolher os casos de estudo que servirão de benchmark para avaliar a precisão de ferramentas FEA, das suas formulações FE e leis constitutivas escolhidas para o modelo numérico. A questão da concepção de um processo de estampagem robusto que permita o controlo eficaz das suas variáveis e uma geometria compatível com a conformabilidade do material ganha outra força no caso dos materiais multi-camada e multi-material que, por natureza, são mais sensíveis a instabilidades de processo.

#### *Caracterização Experimental de Chapas Micro-Sandwich Hybrix - Observações:*

O âmbito deste projecto teve como base a aplicação do micro-sandwich Hybrix em componentes estampados para a indústria automóvel. Para avaliar a conformabilidade deste novo micro-sandwich avançado foi necessário caracteriza-lo experimentalmente. O objectivo foi desenvolver uma metodologia experimental robusta e simples, capaz de devolver dados confiáveis e ser facilmente implementada na indústria. Nesta fase, foram realizados testes em uma máquina universal de tração uniaxial e uma máquina de ensaios Nakazima. O principal desafio consistia em caracterizar a camada intermédia das chapas de Hybrix constituída por um compósito de fibras metálicas/poliméricas impregnadas em uma resina epoxídica. Para descrever numericamente o comportamento mecânico de um dado material é crucial utilizar modelos constitutivos adequados e identificar um conjunto de parâmetros constitutivos adequados. Quando se trata de materiais multi-camada e multi-material, conhecer de antemão os parâmetros constitutivos de cada constituinte, pode não ser suficiente nem possível. Mesmo quando o núcleo compósito fibras/matriz é tido como homogéneo e modelos constitutivos apropriados estejam disponíveis, a identificação correcta de parâmetros constitutivos tendo como base teste experimentais pode ser muito desafiadora. Em alguns casos, a caracterização experimental das chapas metálicas exteriores e do núcleo compósito, em separado, não são suficientes para garantir uma descrição precisa do comportamento

mecânico do micro-sandwich (uma vez que o comportamento mecânico nas interfaces coladas e o efeito de uma camada sobre a outra é desconhecido). Por isso, foi necessário seguir uma estratégia diferente para determinar os parâmetros mecânicos do material compósito desconhecido e, posteriormente, identificar os parâmetros constitutivos necessários. A metodologia desenvolvida baseou-se na determinação do comportamento mecânico da camada intermédia a partir do comportamento mecânico global do micro-sandwich e do comportamento mecânico das camadas metálicas exteriores. Assim, com simples ensaios de tração, comumente aplicados na indústria, conseguiu-se determinar as principais propriedades mecânicas para as 3 camadas do micro-sandwich, segundo as orientações 0°, 45° e 90° face à direção de laminagem da chapa. Os ensaios foram realizados numa máquina universal de teste Tinius Olsen, segundo a norma EN 10002-1: 2009. Adicionalmente, foram realizados ensaios Nakazima, em uma máquina universal de teste Ericshen (modelo 142-20), para 5 geometrias diferentes (20-30-45-60-100-180), segundo a norma ISO 12004. Com a instalação de um dispositivo GOM ARAMIS, munido de câmaras de alta resolução, foi possível registar a história de deformação dos provetes ao longo dos ensaios. Assim, foi possível desenhar alguns Diagramas de Limite de Conformação (FLD – Forming Limit Diagram) experimentais e determinar as forças de conformação envolvidas. A partir dos ensaios experimentais, obtiveram-se os parâmetros mecânicos necessários para a construção dos modelos constitutivos. Utilizando as ferramentas FEA comerciais AutoForm e PAM-STAMP 2G, reproduziram-se os ensaios mecânicos de tração uniaxial e Nakazima em ambiente virtual. Com base na metodologia adoptada, testaram-se diferentes configurações do micro-sandwich Hybrix. Embora a escolha do material para as chapas metálicas exteriores tenha sempre recaído sobre o AISI 304, procurou-se investigar e caracterizar o comportamento mecânico de chapas com configuração simétrica, isto é, onde as chapas metálicas exteriores apresentem a mesma espessura nominal (0.10mm e 0.15mm), e configuração assimétrica, isto é, onde as chapas metálicas exteriores apresentem diferentes espessuras nominais (0.15mm/0.30mm). Além disso, a composição do núcleo compósito também foi alterada, tendo sido testadas chapas com núcleo de fibras metálicas impregnadas em uma resina epoxídica dura e chapas com núcleo de fibras poliméricas impregnadas em uma resina epoxídica flexível. Inicialmente, os resultados obtidos para os ensaios de tração foram pouco consistentes em fornecer módulos de Young confiáveis. Ainda assim, a boa reprodutibilidade numérica dos resultados experimentais em termos de forças de conformação, perfis de maior deformação principal e conformabilidade geral demonstraram que a metodologia era apropriada e funcional para desenvolver modelos eficazes para a simulação de materiais micro-sandwich. Por isso, voltaram-se a realizar mais ensaios experimentais às chapas Hybrix correlacionando a informação obtida com a informação experimental das chapas metálicas antes do processo de fabrico do micro-sandwich, fornecidas pelo próprio fabricante, obtendo-se resultados muito mais consistentes e credíveis. Um dos aspectos mais importantes, que interfere na confiabilidade dos resultados, relaciona-se com a qualidade da matéria-prima. Se a qualidade das chapas não for garantida no seu processamento, em particular as propriedades de adesão das diferentes camadas, a qualidade dos



provetes será também severamente afetada. As configurações assimétricas mostraram uma qualidade inferior neste respeito, observando-se defeitos como rugas e delaminação. Por outro lado, as camadas metálicas são extremamente finas na configuração simétrica, estando mais propensas a efeitos de *tearing*. Por estes motivos, as FLC's experimentais não provaram suficientemente a sua robustez para serem utilizadas.

#### *Caracterização Experimental de Chapas Micro-Sandwich Hybrix - Recomendações:*

Os ensaios mecânicos realizados neste estudo foram fundamentais para a caracterização do comportamento mecânico de chapas micro-sandwich Hybrix quando deformadas plasticamente por processos de conformação. A conformabilidade e resistência destas chapas dependem principalmente das chapas metálicas exteriores de reduzida espessura. Portanto, este micro-sandwich não é apropriado para aplicações estruturais, mas deve ser antes utilizado em aplicações com baixos requisitos de resistência. Durante a conceção da geometria da peça deve-se levar em conta que a redução de espessura admissível das chapas metálicas exteriores é muito baixa. Todos os cantos, raios e saliências da geometria devem ser suavizados para se evitar o excesso de adelgaçamento e rotura. Zonas de compressão devem ser evitadas pois podem induzir a formação de rugas e, conseqüentemente, a delaminação do micro-sandwich. Conforme demonstrado nos ensaios Nakazima, é possível tirar partido da excelente conformabilidade das chapas Hybrix simétricas quando a deformação plástica é dominada pelo modo de estiramento biaxial. Contudo, a reduzida espessura das chapas metálicas exteriores torna estas chapas muito sensíveis ao aparecimento de fissuras nas "fronteiras de corte" quando deformadas plasticamente. Por isso, as operações de corte devem ser realizadas idealmente após as operações de conformação. Os ensaios mecânicos realizados às chapas Hybrix assimétricas apresentaram alguns fenómenos inesperados associados não só à configuração do material, mas também à falta de robustez no seu processo de fabrico. Por exemplo, observou-se que os provetes de tração encurvaram após os testes de tração uniaxial. Tal comportamento é explicado pelos diferentes estados de deformação e tensão equivalentes existentes em cada uma das chapas metálicas exteriores. Assim, a curvatura do provete dependerá da espessura e propriedades de cada uma das camadas do micro-sandwich. Portanto, a estampagem de chapas micro-sandwich assimétricas exigirá um estudo mais aprofundado no que toca aos fenómenos de recuperação elástica entre as diferentes operações. Sendo que o balanço das propriedades mecânicas entre as diferentes camadas poderia ser utilizado para reduzir o efeito de retorno elástico. Os ensaios Nakazima, por seu lado, revelaram o comportamento instável deste micro-sandwich com o aparecimento de rugas e delaminação em alguns dos provetes testados. Para isso, não terá só contribuído a substituição de uma skin metálica por outra com o dobro da espessura, mas também a composição da camada interior do micro-sandwich que correspondia a uma versão mais antiga e menos robusta do Hybrix. Portanto, o efeito conjugado das forças de conformação que aumentaram significativamente para vencer a resistência do microsandwich, gerando tensões de corte

ao longo da espessura mais elevadas durante a flexão do provete, e da camada interna de qualidade inferior, estão na base dos fenómenos observados. Ao longo deste estudo consolidou-se um conhecimento importante sobre a caracterização e modelação do comportamento mecânico do Hybrix, para a conceção de geometrias factíveis e processos de conformação robustos baseados em modelos numéricos confiáveis. Conclui-se que as propriedades mecânicas e o comportamento deste micro-sandwich tornam-no mais adaptado à produção de componentes estampados para acabamentos interiores e/ou painéis exteriores.

#### *Abordagens FEM Para Modelação e Simulação de chapas Micro-Sandwich - Observações:*

Seguidamente, reproduziram-se virtualmente os ensaios mecânicos realizados para uma validação preliminar dos modelos criados. Neste contexto, compararam-se dois tipos de modelos espaciais para a modelação do micro-sandwich, um baseado em elementos finitos 3D e outro baseado em elementos finitos 2D. Em relação à modelação constitutiva das chapas Hybrix, também foram avaliadas duas hipóteses. Em um caso, atribuíram-se propriedades mecânicas médias ao compósito micro-sandwich, como se se tratasse de uma chapa mono-camada e mono-material; a segunda estratégia teve em conta a modelação constitutiva de cada uma das camadas da chapa micro-sandwich. No que toca às estratégias de modelação constitutiva testadas, verificou-se que ambas asseguram uma boa previsão das forças de conformação face aos resultados experimentais. Além disso, os perfis numéricos de maior deformação principal em ambos os modelos também são muito semelhantes. Contudo, o modelo “mono-material” não consegue descrever o comportamento mecânico associado a cada camada e, conseqüentemente, o seu nível de adelgaçamento, limites de conformabilidade e retorno elástico associado. Por isso, tais modelos simplistas não são adequados para avaliar a factibilidade de um produto resultante da conformação de chapas Hybrix. Ainda assim, podem ser utilizados para a determinação de parâmetros mecânicos globais e a identificação de parâmetros constitutivos a partir de métodos inversos. Quanto às abordagens FEM, verificou-se que tanto os modelos 2D como 3D devolvem boas previsões em termos de forças de conformação. Em relação aos perfis de maior deformação principal, observou-se a existência de ruído para os modelos 2D nos estágios iniciais de conformação, bem como uma ligeira tendência para sobrestimar os valores de deformação nos ensaios Nakazima. Embora os modelos 3D ofereçam previsões mais próximas das medições experimentais, não servem como alternativa para um uso industrial intenso dado o seu elevado custo computacional. No caso da simulação de processos de conformação de chapas micro-sandwich com skins muito finas, a questão da eficiência numérica torna-se ainda mais importante se forem utilizados elementos finitos hexaédricos de dimensões equivalentes à espessura das chapas metálicas exteriores. Por último, compararam-se os resultados numéricos (forças e deformações) devolvidos pelos módulos multi-camada das ferramentas comerciais AutoForm R5.2 e PAM-STAMP 2G 2015.1, constatando-se previsões muito semelhantes. O AutoForm apresenta a possibilidade de introduzir no modelo material multi-camada informação experimental biaxial e melhorar assim a precisão dos resultados. Por outro lado, o PAM-STAMP 2G

mostrou-se mais eficaz na previsão de rugas, as quais constituem um defeito comum em processos de estampagem de chapas finas e particularmente importante de se avaliar no caso de serem micro-sandwich, uma vez que estão na origem de mecanismos de delaminação.

#### *Abordagens FEM Para Modelação e Simulação de chapas Micro-Sandwich - Recomendações:*

A reprodução virtual dos ensaios mecânicos realizados permitiu estabelecer uma primeira validação do modelo numérico para as chapas Hybrix. Numa primeira abordagem, foi possível constatar que a metodologia standard de caracterização experimental de chapas metálicas, com base em ensaios de tração uniaxial para 3 direções distintas (RD, TD e ND) e no levantamento das respectivas propriedades mecânicas globais do micro-sandwich, apenas é eficaz para a previsão das forças de conformação. A previsão correcta do comportamento mecânico de chapas Hybrix deformadas plasticamente só é possível com recurso a modelos espaciais multi-camada. No caso destes, recomenda-se a utilização de modelos baseados em elementos finitos 2D para a reprodução virtual dos ensaios de tração uniaxial e Nakazima, visto que o nível de precisão alcançado foi bastante satisfatório e o custo computacional associado bastante reduzido. O estudo numérico realizado também deixa claro que a informação experimental biaxial desempenha um importante papel na evolução das forças de conformação e nos estados de deformação e tensão instalados no provete Nakazima durante o seu funcionamento.

#### *Caso de Estudo: Comparação e Validação Experimental de Diferentes Modelos FEM na Simulação de Processos de Estampagem de Geometrias Complexas com Chapas Micro-Sandwich - Observações:*

Depois de conseguida uma primeira validação do modelo numérico para simulação de chapas Hybrix procurou-se estabelecer uma validação mais consistente a partir da simulação de um caso prático com uma das peças desenvolvidas pelo departamento de R&D do PCC Sodecia. Geralmente, chapas de espessuras reduzidas de aço inoxidável e chapas micro-sandwich de aço ou alumínio têm sido aplicadas na indústria automóvel essencialmente para a produção painéis exteriores ou para acabamentos interiores. Estas geometrias permitem um controlo mais eficaz das trajetórias de deformação e não apresentam uma redução significativa de espessura, sendo por isso mais indicadas para este tipo de materiais. Embora o grupo Sodecia não produza componentes deste tipo, o desafio estipulado no início deste projeto foi a aplicação deste micro-sandwich a um dos seus produtos com um o mínimo de alterações ao processo industrial atualmente implementado. Assim, este desafio trouxe dificuldades acrescidas, sendo nestas que reside o carácter inovador deste projeto. Neste âmbito, optou-se pela geometria de um sistema de enchimento de um tanque de combustível inicialmente concebido para ser estampado em alumínio. Embora se tenha conseguido a aprovação e comprometimento inicial da empresa Lamera AB para o estudo do comportamento das chapas Hybrix na produção de componentes estampados para a indústria automóvel, o fornecedor em questão não quis avançar para a produção do componente proposto, uma vez que a

factibilidade do produto não era garantida. Visto que a Lamera AB é o único produtor e distribuidor de Hybrix no mundo, seleccionou-se um novo micro-sandwich para realizar este estudo. Assim, a escolha recaiu sobre o micro-sandwich Litecore S, produzido pela empresa Thyssenkrupp AG e desenvolvido em parceria com o grupo Volkswagen. Os protótipos físicos foram produzidos nas instalações da empresa Quantal S.A, sendo utilizados o mesmo processo e ferramentas na simulação numérica com o software comercial PAM-STAMP 2015.1. O objectivo principal deste estudo comparativo foi avaliar a precisão e exactidão de 3 abordagens FEM disponíveis em softwares comerciais para modelar e simular processos de estampagem de chapas micro-sandwich na indústria automóvel. Tendo em conta os resultados obtidos, verificou-se que embora os modelos 3D sólidos sejam os mais precisos, o elevado custo computacional e complexidade no processo de geração da malha FE associados tornam-os inadequados para a prática industrial. Por outro lado, os modelos 2D cascas são altamente eficientes e oferecem bons resultados quando a geometria das ferramentas, os raios de entrada e folga existente facilitam o escoamento do material assegurando ao mesmo tempo bons níveis de estiramento uniformemente distribuído. Porém, quando a geometria da ferramenta é demasiadamente complexa e introduz estados de deformação severos, os resultados numéricos são afectados pela tecnologia do elemento finito.

No caso de estudo apresentado observou-se que:

- As forças de conformação previstas pelo modelo de cascas 2D no final da operação de estampagem são 22% maiores do que as previstas pelo modelo de sólidos 3D.
- Malhas de elementos casca 2D altamente refinadas sujeitas a trajetórias de deformação complexas induzem o aparecimento de picos nos perfis das deformações principais irrealísticos e, conseqüentemente, previsões incorretas quanto à percentagem de adelgaçamento e engrossamento da chapa micro-sandwich. Flutuações espúrias do valor máximo das tensões principais também foram registadas.
- O modelo de cascas 2D não foi capaz de reproduzir o aparecimento e colapso de rugas.

Seguindo uma abordagem FEM que combina elementos casca 2D e elementos sólidos 3D a precisão dos resultados melhorou significativamente:

- As forças de conformação previstas pelo modelo misto 2D/3D no final da operação de estampagem são 11% maiores do que as previstas pelo modelo 3D.
- Os perfis das deformações principais, espessura e valor máximo das tensões principais do modelo misto 2D/3D correlacionam-se muito bem com os valores previstos pelo modelo de sólidos 3D.
- O modelo misto 2D/3D foi capaz de reproduzir a formação e crescimento de rugas durante o processo e a localização de pontos de ruptura na peça

*Caso de Estudo: Comparação e Validação Experimental de Diferentes Modelos FEM na Simulação de Processos de Estampagem de Geometrias Complexas com Chapas Micro-Sandwich - Recomendações:*

Devido à facilidade de implementação dos modelos multi-camada baseados em elementos casca 2D nos códigos FE comerciais, esta tem sido a escolha natural dos desenvolvedores de ferramentas FEA para acrescentar novas potencialidades de simulação aos seus softwares. Nos últimos anos, tanto PAM-STAMP 2G como AutoForm integram módulos baseados em modelos de casca 2D para a simular processos de estampagem com materiais-multicamada. Estes módulos têm permitido conceber processos industriais ajustados à produção de componentes estampados com chapas micro-sandwich, tais como peças de acabamento interior e painéis exteriores (capot, guarda-lamas, interior de portas, etc.). Porém, estes módulos não são adequados para serem utilizados com geometrias muito complexas, acabando por limitar parte do trajeto de inovação dos novos automóveis. Dada a sua elevada eficiência, estes módulos podem e devem ser utilizados em estudos de factibilidade iniciais. Se forem usados de forma criteriosa, podem fornecer algumas indicações relativas à geometria da peça, tamanho e forma do esboço, curso das ferramentas e carga a aplicar, entre outros. Contudo, tais variáveis só podem ser devidamente ajustadas com a utilização de: *um modelo mais preciso na descrição da formabilidade da chapa e na deteção de instabilidades de processo* como, por exemplo, o aparecimento de rugas. Neste caso, a utilização de modelos mistos 2D/3D permite um estudo de factibilidade mais confiável e melhorar a robustez do processo de estampagem.

Este trabalho procurou consolidar mais o conhecimento científico em torno da temática dos materiais multi-camada colmatando, ao mesmo tempo, algumas necessidades industriais nesta área. Durante este projecto, foi desenvolvida uma metodologia experimental robusta para a caracterização de chapas micro-sandwich cujas propriedades do núcleo compósito são, à partida, desconhecidas. Esta metodologia foi aplicada no micro-sandwich Hybrix com bons resultados. Além de robusta, esta metodologia pode ser facilmente implementada na indústria. As ferramentas FEA disponíveis foram amplamente testadas quanto à sua eficácia computacional e à precisão dos resultados numéricos obtidos. Este estudo foi importante para se avaliar a confiabilidade dos resultados numéricos devolvidos pelos modelos espaciais baseados em elementos casca 2D na simulação de materiais multi-camada. Os módulos dedicados para a simulação de processos com materiais multi-camada não conseguem reproduzir atualmente fenómenos de delaminação. Este modo de falha está associado a esforços de tração normais e/ou esforços de corte. Os modelos numéricos baseados unicamente em elementos finitos de cascas 2D não conseguem comportar esta informação. Para poder reproduzir este efeito na simulação numérica precisam ser utilizados elementos sólidos 3D. Contudo, estes elementos não são utilizados por serem muito mais caros a nível computacional, tornando as simulações demasiadamente caras. Portanto, será necessário fazer um estudo mais aprofundado sobre os modelos espaciais mais adequados para reproduzir fenómenos de delaminação/descolagem, nomeadamente com o modelo misto 2D/3D já aqui referido. Do ponto de vista experimental, a deteção da delaminação também não é evidente. Mesmo após a ocorrência de falha, as camadas podem permanecer coladas e juntas pela ação de forças de *Van-der-Waals*. Neste âmbito, Liewald

and Hofmann (2017) investigaram recentemente os limites de conformabilidade de chapas micro-sandwich com base no controlo do fenómeno de delaminação (D-FLC) durante os ensaios Nakazima. Estudos como este podem ser muito úteis do ponto de vista industrial, já que a obtenção de uma FLC confiável é um aspeto bastante crítico nos materiais multi-camada. Além disso, a associação do efeito de delaminação com o estado de deformação biaxial também é um *input* fundamental para o modelo numérico. Outra linha de investigação importante, com especial relevância para a Sodecia, destina-se a aplicações automóvel para materiais multi-camada de elevada resistência. O processamento de chapas HSS e AHSS em estruturas multi-camada traz outros desafios, mas a sua introdução no *body-in-white* resultaria em automóveis ainda mais rígidos e mais leves, incrementando a sua segurança e contribuindo para a diminuição da sua pegada ecológica.



## 8. REFERÊNCIAS

1. Abed-Meraim, F., Trinh, V.D., Combescure, A. (2011) "A New Assumed Strain Solid-Shell Formulation 'SHB6' for the Six-Node Prismatic Finite Element." *Journal of Mechanical Science and Technology* 25:2345-2364.
2. Alves, J.L., *Simulação Numérica do Processo de Estampagem de Chapas Finas – Modelação Mecânica e Métodos Numéricos*, PhD Thesis, Escola de Engenharia, Departamento de Engenharia Mecânica, Universidade do Minho, 2003.
3. Banabic, D., Balan, T., Comsa, D.S. (2000) "A new yield criterion for orthotropic sheets metals under plane-stress conditions." *Proceedings of the 7<sup>th</sup> International Conference 'TPR2000'*, Cluj Napoca, Romania, 217-224
4. Banabic, D., Kuwabara, T., D. Balan, T., Comsa, D.S., Julean, D. (2003) "Non-quadratic yield criterion for orthotropic sheets metals under plane-stress conditions." *International Journal of Mechanical Sciences* 45:797-811.
5. Banabic, D., Aretz, H., Comsa, D.S., Paraianu, L. (2005) "An improved analytical description of orthotropy in sheet metallic sheets." *International Journal of Plasticity* 21:493-512
6. Banabic, D. "Sheet Metal Forming Processes – Constitutive Modelling and Numerical Simulation". Springer- Verlag Berlin Heidelberg, 2010.
7. Barlat, F., Lian, J. (1989) "Plastic behaviour and stretchability of sheet metals (Part I): A yield function for orthotropic sheet under plane stress conditions." *International Journal of Plasticity* 5:51-56.
8. Barlat, F., Lege, D.J., Brem, J.C. (1991) "A six-component yield function for anisotropic materials." *International Journal of Plasticity* 7:693-712.
9. Barlat, F., et al. (2000) "Constitutive modeling for aluminium sheet forming simulations." In: Khan, A.S., Zhang, H., Yuan, Y., (eds) *Plastic and viscoplastic response of materials and metalforming. Proceedings of the 8<sup>th</sup> International Symposium in Plasticity and its Current Applications*, Whistley, Canada, Neat Press, Fulton, MD, 591-593.
10. Barlat, F., Brema, J.C., Yoon, J.W., Chung, K., Dick, R.E., Legea, D.J., Pourboghra, F., Choi, S-H., Chu, E. (2003) "Plane stress yield function for aluminum alloy sheets – part 1: theory." *International Journal of Plasticity* 19:1297–1319.
11. Bishop, J.F.W., Hill, R. (1951) "A theory of the plastic distortion of polycrystalline aggregates under combined stress." *Philosophical Magazine* 42:414-427.



12. Bittencourt, E., Plasticidade Teórica e Computacional I, *Apontamentos da Sebenta da Disciplina de Pós-graduação "Tratamento de problemas não lineares na mecânica dos sólidos"*, Departamento de Engenharia Civil, Rio Grande do Sul, 2002, cap 5-7.
13. Bridgman, P. W. "Studies in Large Plastic Flow and Fracture - With Special Emphasis on the Effects of Hydrostatic Pressure". McGraw-Hill, New York, 1952.
14. Cazacu, O., Barlat, F. (2001) "Generalization of Druker's yield criterion in orthotropic sheet metals." *Journal of Materials Processing Technology* 168:1-9
15. Cazacu, O., Barlat, F. (2004) "A criterion for description of anisotropy and yield differential effects in pressure-insensitive metals." *International Journal of Plasticity* 20:2027-2045.
16. Chaparro, B.M., Alves, J.L., Menezes, L.F., Fernandes J.V. (2007) "Optimization of the phenomenological constitutive models' parameters using genetics algorithms." In: Banabic, D. (ed) *Advanced methods in material forming*, Springer, Heidelberg, 35-54.
17. Cosovici, G.A. (2006) "Implementation of the new yield criteria in the FE programs for sheet metal forming simulation". PhD Thesis, Cluj Napoca, Romania (in Romanian).
18. Drucker, D.C. (1949) "Relations of experiments to mathematical theories of plasticity." *Journal of Applied Mechanics* 16:349-357.
19. Drucker, D. C. (1951) "A more fundamental approach to stress-strain relations." Report All-58/13 to ONR (May 1951) G.D.A.M., Brown University. Also in the Proceedings of the First National Congress of Applied Mechanics. A.S.M.E. pp. 1487-1491.
20. Engelman, M. (2009). "Usability of the Fibrous Core Sandwich Material HYBRIX for Automobile Body Applications." Master of Science Thesis MMK 2009:47 MKN 012, KTH Industrial Eng. and Management, Sweden.
21. GENEVOIS, P. "Étude expérimentale et modélisation du comportement plastique anisotrope de tôles d'aciers en grandes transformation". PhD Thesis, Institut National Polytechnique de Grenoble, 1992.
22. Hill R. (1948) "A theory of the yielding and plastic flow of anisotropic metals." *Proceedings of the Royal Society London A* 193:281-297.
23. Hill, R. (1979) "Theoretical plasticity of textured aggregates." *Mathematical Proceedings of the Cambridge Philosophical Society* 85: 179-191.
24. Hosford, W.F. (1972) "A generalized isotropic yield criterion." *Journal of Applied Mechanics* 39:607-609.
25. Hosford, W.F. (1979) "On yield loci of anisotropic cubic metals." In: *Proceedings of the 7<sup>th</sup> North American Metalworking Conference (NMRC)*, SME, Dearborn, MI, 191-197.
26. Hosford, W.F. (1985) "Comments on anisotropic yield criteria." *International Journal of Mechanical Sciences* 27:423-427.

27. Hosford, W.F. (1993) "The mechanical of crystal and textured polycrystals." Oxford University Press, Oxford.
28. Hosford, W.F. (1996) "On the crystallographic basis of yield criteria." *Texture and microstructures* 26-27:479-493.
29. *Hybrix Brochure* (2009) in: [<http://www.aircraftinteriorsexpo.com>].
30. Jackson, K.P, Allwood, J.M., Landert, M. (2008) "Incremental forming of sandwich panels." *Journal of Materials Processing Technology* 204:290-303.
31. Jonhson, C.D., Kienholz, D.A. (1982). "Finite element prediction of damping in structures with constrained viscoelastic layers." *AIAA J* 20:1284-90.
32. Kant, T., Swaminathan, K. (2001) "Free Vibration of Isotropic, Orthotropic and Multilayer Plates Based on Higher Order Refined Theories." *Journal of Sound and Vibrations* 241: 319-327.
33. Kant, T., Swaminathan, K. (2008) "Analytical Solutions Using Higher Order Refined Theory for the Stability Analysis of Laminated Composite and Sandwich Plates." *Structural Engineering and Mechanics* 82:277-289.
34. Karafillis, A.P., Boyce, M.C. (1993) "A general anisotropic yield criterion using bounds and a transformation weighting tensor." *Journal of the Mechanics and Physics of Solids* 41:1859-1886.
35. Kilian, J.W., Lu, Y.P. (1984) "A finite element modeling approximation for damping material used in constrained damped structures." *Journal of Sound and Vibration* 97:352-4.
36. Kim, K.J., Kim, D., Choi, S.H., Chung, K., Shin, K.S, Barlat, F., Oh, K.H., Youn, J.R. (2003) "Formability of AA5182/polypropylene/AA5182 sandwich sheets." *Journal of Materials Processing Technology* 139:1-7.
37. Lian, J., Zhou, D. Baudelet, B. (1989) "Application of Hill's new theory to sheet metal forming – I. Hill's 1979 criterion and its application to predicting sheet forming limits." *International Journal of Mechanical Sciences* 31:237-244.
38. Liewald, M., Hofmann, D. (2017) "Investigations on Delamination Behavior of Sandwich Sheets". *Procedia Engineering*. 17th International Conference on Sheet Metal, SHEMET17, 183:71-76.
39. Logan, R. Hosford, W.F. (1980) "Upper-bound anisotropic yield locus calculations assuming (111) – Pencil glide." *International Journal of Mechanical Sciences* 22:419-430.
40. Martins, P., Rodrigues, J. "Tecnologia mecânica – tecnologia da deformação plástica". Vol. I *Fundamentos Teóricos*, 2005, pp.142, 194-200.
41. Mendelson S. "Plasticity: Theory and Application". Macmillan, New York, 1968.
42. Moreira, R.A.S., Rodrigues, J.D. (2004) "Constrained damping layer treatments: finite element modeling." *Journal of Vibration and Control* 10:575-95.
43. Moreira, R.A.S., Rodrigues, J.D. (2006) "A layerwise Model for thin soft core sandwich plates." *Computational and Structures* 84:1256-1263.

44. Moreira, R.A.S., Alves S. R. J., Valente R.A.F. (2010) "A solid-shell layerwise finite element for non-linear geometric and material analysis." *Composites Structures* 92:1517-1523.
45. Mulone, A. (2015) "Characterization of ultra-light metal-polymer sandwich composite material through dynamic mechanical thermal analysis and microstructural analysis of nickel metal coating obtained through pulse-electrodeposition." Master of Science in Materials Engineering and Nanotechnology, POLITECNICO DI MILANO - School of Industrial Engineering and Information, Italy.
46. Natal, J., Dinis, L.S., "Teoria da plasticidade" *Sebenta de Apontamentos*. Departamento de Engenharia Mecânica e Gestão Industrial, Faculdade de Engenharia, Universidade do Porto, 2004/2005, pp. 28-36.
47. Cho, M., Oh, J., Kim, J.S., Grédiac, M. (2008) "A Finite Element Formulation Based on an Enhanced First Order Shear Deformation Theory for Composite and Sandwich Structures." *Journal of Mechanical Science and Technology* 22:871-878.
48. Pandya, B.N., Kant, T. (1988) "Higher-Order Shear Deformable Theories for Flexure of Sandwich Plates-Finite Element Evaluations." *International Journal of Solid Structures* 24: 1267-1286.
49. Paraianu, L. (2006) "Modelling of the FLC using the large deformation theory." PhD Thesis, Cluj Napoca, Romania (in Romanian).
50. Pearce, R. (1968) "Some aspects of anisotropic plasticity in sheet metals." *International Journal of Mechanical Sciences* 10:995-1001
51. Rah, K., Van Paepegen, W., Habraken, A.M., Alves de Sousa, R.J., Valente, R.A.F. (2009) "Evaluation of different advanced finite element concepts for detailed stress analysis of laminated composite structures." *International Journal of Material Forming* 2:943-947.
52. Schwarze, M., Vladimirov, I.N., Reese, S. (2009) "On the implementation of the EAS and ANS concept into a reduced integration continuum shell element and applications to sheet forming." *International Journal of Material Forming* 2 :919-922.
53. Sidoroff, F. (1982) "Incremental constitutive equations for large strain elastoplasticity," *International Journal of Engineering Science* 20:19-26.
54. Suzuki, K., Kageyama, K., Kimpara, I., Hotta, S., Ozawa, T., Kabashima, S. (2003) "Vibration and damping prediction of laminates with constrained viscoelastic layers-numerical analysis by a multilayer higher-order-deformable finite element and experimental observations." *Journal of Mechanics of Advanced Materials and Structures* 10:43-75.
55. Teodosiu, C. "Dislocation modeling of crystalline plasticity, Large Plasticity Deformation of Crystalline Aggregates" Ed. C. Teodosiu, CISM Courses and Lectures N° 376, 1997.

56. Valente, R.A.F., Alves de Sousa, R.J., Natal Jorge, R.M. (2009) "Enhanced finite element formulation on the numerical simulation of tailor-welded hydroformed products." *International Journal of Material Forming* 2:927-929.
57. Vegter, D. Drent, P. Huetink J. (1995) "A planar isotropic yield criterion based on material testing at multi-axial stress state." In: Shen, S.F. Dawson, P.R. (eds) *Simulation of Materials Processing-theory, methods and applications*. AA Balkema, Rotterdam, pp.345-350.
58. Vegter, D. Van den Boogaard, A.H. (2006) "A plane stress yield function for anisotropic sheet material by interpolation of biaxial stress states." *International Journal of Plasticity* 22:557-580
59. Wendy, M. (2015) "The All New 2015 Chevrolet Colorado and GMC Canyon Cab Structure". *Great Designs in Steels Seminar*. In: [<https://www.autosteel.org>].
60. Woodthorpe, J., Pearce, R. (1970) "The anomalous behavior of aluminium sheet under balanced biaxial tension." *International Journal of Mechanics Sciences* 12:341-347.
61. Zhen, W., Cheung, Y.K., Lo, S.H, Wanji, C. (2008) "Effects of Higher Order Global-Local Shear Deformations on Bending, Vibration and Buckling of Multilayered Plates." *Composite Structures* 82 277-289.



## A. Anexo A – CINEMÁTICA DO MEIO CONTÍNUO

Nesta secção, o enfoque será atribuído a corpos que, ao nível macroscópico, apresentam uma distribuição contínua do material. O corpo em questão ocupa uma determinada região, no espaço tridimensional, definida em  $\mathbb{R}^3$ . A medida que o corpo se deforma a região ocupada por esse vai variando ao longo do tempo. O objetivo é, por isso, quantificar esta evolução.

No instante inicial  $t_0$  admite-se, por simplificação, que o corpo se encontra indeformado e relaxado (livre de tensões), ocupando a região  $\Omega_0$ . Esta é chamada de *configuração de referência*  $C_0$ . Qualquer *volume infinitesimal* de material correspondente ao corpo é tratado como um *ponto material*  $\wp \in \Omega_0$ . À medida que o corpo se move e se deforma, em resultado da ação de forças, passa a ocupar uma nova região  $\Omega$ . Sendo assim, no instante  $t$ , o ponto material  $\wp$ , que ocupava a posição  $\mathbf{x}_0$  passa a ocupar a posição  $\mathbf{x}$ , e o corpo assume uma nova configuração, a *configuração corrente*  $C$ .

Para definir o *movimento* do ponto material  $\wp$  é possível usar as suas coordenadas,

$$\mathbf{x} = \mathbf{x}(\mathbf{x}_0, t) \quad (\text{A.1})$$

Esta equação estabelece uma relação bi-unívoca entre  $\mathbf{x}_0$  e  $\mathbf{x}$  ou cada ponto  $\wp$  em  $\Omega_0$  corresponde um ponto  $\wp'$  em  $\Omega$ .

Sendo, no entanto, mais conveniente fazê-lo com a introdução do vetor *deslocamento*  $\mathbf{u}$ ,

$$\mathbf{u} = \mathbf{x} - \mathbf{x}_0 \quad (\text{A.2})$$

É importante satisfazerem-se certas condições para que a função vetor descreva adequadamente tal movimento. Primeiro, é preciso garantir que este vetor una unicamente dois pontos (assegurando uma direção). Segundo, é necessário garantir a preservação da orientação (assegurando sempre o mesmo sentido). Isto é possível por imposição do *Jacobiano*  $J$ , definido por

$$J = \det\left(\frac{\partial \mathbf{x}}{\partial \mathbf{x}_0}\right) \quad (\text{A.3})$$

Como positivo. Aqui,

$$\nabla_{\mathbf{x}} = \left(\frac{\partial \mathbf{x}}{\partial \mathbf{x}_0}\right) \quad (\text{A.4})$$

É chamado de **gradiente de transformação** (usualmente identificado pela letra **F**). Este gradiente avalia como ocorre a transformação na vizinhança de um ponto.

O facto de  $J$  ser positivo garante o **axioma da continuidade** ( $\det \mathbf{F} \neq 0$ ) e expressa a indestrutibilidade da matéria (um volume finito não pode ser transformado num volume nulo) e a impenetrabilidade da matéria (uma porção da matéria não pode penetrar outra). Isto é comprovado visto que

$$\det \mathbf{F} = \frac{dv}{dv_0} \quad (\text{A.5})$$

*Como o volume é sempre uma grandeza positiva,  $\det \mathbf{F}$  é sempre positivo e por consequência fica provado que  $\mathbf{F}$  é sempre invertível, sempre que a continuidade da matéria é preservada.*

No caso de se verificar *conservação da massa*  $\det \mathbf{F}$  representará a variação na densidade do material.

$$\det \mathbf{F} = \frac{\rho_0}{\rho} \quad (\text{A.6})$$

Em materiais incompressíveis, onde a transformação ocorre a volume constante, temos que:

$$\det \mathbf{F} = 1 \quad (\text{A.7})$$

É ainda importante reter que

$$\mathbf{F}^T \mathbf{F} = \mathbf{I} \quad (\text{A.8})$$

Ou

$$\mathbf{F}^T = \mathbf{F}^{-1} \quad (\text{A.9})$$

Logo  $\mathbf{F}$  é uma matriz ortogonal. Recorrendo à decomposição polar é possível decompor qualquer transformação  $\mathbf{F}$  de forma única num tensor ortogonal que representa uma rotação do corpo rígido ( $\mathbf{R}$ ) e um tensor simétrico positivo que representa uma *deformação pura* ( $\mathbf{U}$  ou  $\mathbf{V}$ ).

$$\mathbf{F} = \mathbf{R}\mathbf{U} \quad (\text{A.10})$$

$$\mathbf{F} = \mathbf{V}\mathbf{R} \quad (\text{A.11})$$

Onde  $\mathbf{R}^T \mathbf{R} = \mathbf{I}$  e  $\det \mathbf{R} = 1$ . A presente decomposição deve sempre ser lida da **direita para a esquerda** [Fig. A.1].

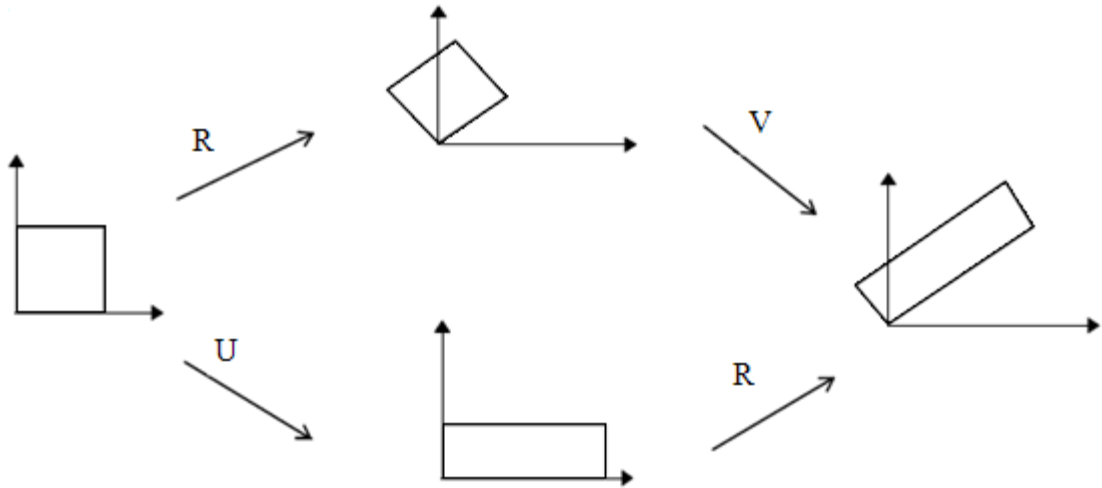


Fig. A.1 – Fenómenos de rotação de corpo rígido e deformação pura (Bittencourt, 2002).

O tensor  $\mathbf{U}$ , chamado de *tensor de deformação direito*, é aplicado sobre a configuração original do corpo, sendo por isso considerado uma grandeza lagrangeana. Já o tensor  $\mathbf{V}$ , chamado de *tensor de deformação esquerdo*, é aplicado sobre a configuração rodada, sendo por isso considerado uma grandeza euleriana.

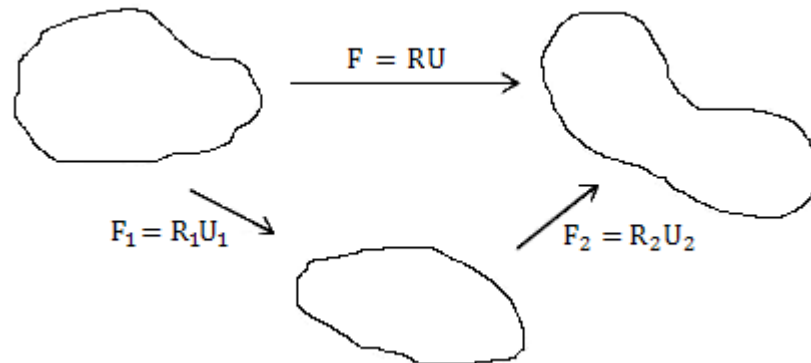


Fig. A.2 – Trajetória de deformação até configuração final (Bittencourt, 2002).

Perante a seguinte transformação composta [Fig. A.2] é possível inferir as seguintes relações:

$$\begin{aligned}
 d\vec{x}_2 &= \mathbf{F}d\vec{x}_0 \\
 d\vec{x}_1 &= \mathbf{F}_1d\vec{x}_0 \\
 d\vec{x}_2 &= \mathbf{F}_2d\vec{x}_1 = \mathbf{F}_2\mathbf{F}_1d\vec{x}_0 = \mathbf{F}d\vec{x}_0
 \end{aligned}
 \tag{A.12}$$

Logo:

$$\mathbf{F} = \mathbf{F}_2\mathbf{F}_1
 \tag{A.13}$$



Desta forma, perante grandes deformações, usa-se a decomposição multiplicativa dos gradientes de transformação.

Contudo, o gradiente de transformação contém informação respeitante quer a deformações quer a rotações. Isto torna a sua implementação complicada nas relações constitutivas que são desenvolvidas de forma a não prever tensões devido ao movimento do corpo livre (por exemplo, as rotações rígidas). No intuito de medir a deformação é importante estabelecer uma definição em termos da configuração indeformada (deformação lagrangeana). Para caracterizar a deformação pode-se pensar no comprimento  $d_s$  dum segmento que se encontra na nossa configuração corrente.

$$d_s^2 = d_{x_i} d_{x_i} = d_{\bar{x}}^T d_{\bar{x}} = d_{\bar{x}0}^T \mathbf{F}^T \mathbf{F} d_{\bar{x}0} \quad (\text{A.14})$$

Assim

$$\mathbf{C} = \mathbf{F}^T \mathbf{F} = \mathbf{U}^2 \quad (\text{A.15})$$

Esta matriz  $\mathbf{C}$  representa uma medida de deformação uma vez que relaciona o comprimento do segmento na configuração instantânea ( $d_s$ ) com o seu comprimento na configuração indeformada ( $d_{s0}$ ).  $\mathbf{C}$  é denominado tensor de **deformação de Cauchy-Green à direita**.

Porém, tanto  $\mathbf{U}$  como  $\mathbf{C}$  não são adequados para caracterizar a deformação, isto porque não fornecem um valor nulo quando não há deformação, fornecendo como resposta a matriz identidade. Para colmatar esta falha, os tensores empregues na prática são “regularizados”. Estes tensores podem ser agrupados segundo uma família denominada Hill.

A fórmula genérica é a seguinte

$$\mathbf{E} = \frac{1}{m} (\mathbf{U}^m - \mathbf{I}) \quad \text{para } m > 0 \quad (\text{A.16})$$

Dependendo da escolha de  $m$ , tem-se os diferentes tensores encontrados na prática. Um dos mais amplamente usados é o tensor de Green-Lagrange para  $m=2$ . Tendo presente (A.15), a expressão assume assim a forma

$$\mathbf{E}^{\text{GL}} = \frac{1}{2} (\mathbf{F}^T \mathbf{F} - \mathbf{I}) \quad (\text{A.17})$$

Ou, na forma indicial,

$$E_{ij}^{\text{GL}} = \frac{1}{2} (F_{mi} F_{mj} - \delta_{ij}) \quad (\text{A.18})$$

Assim, pela definição de  $\mathbf{F}$  e empregando as características de  $\delta_{ij}$  (delta de Kronecker), é possível reescrever Green-Lagrange como:

$$E_{ij}^{GL} = \frac{1}{2} \left[ \frac{\partial u_i}{\partial x_{0j}} + \frac{\partial u_j}{\partial x_{0i}} + \frac{\partial u_m}{\partial x_{0j}} \frac{\partial u_m}{\partial x_{0i}} \right] \quad (\text{A.19})$$

Esta é, pois, a forma mais usual de apresentação do tensor de deformação de Green-Lagrange.

Sendo que para *pequenas deformações* os infinitesimais de ordem superior perdem o significado a expressão assume outra forma

$$\varepsilon_{ij} = \frac{1}{2} \left[ \frac{\partial u_i}{\partial x_{0j}} + \frac{\partial u_j}{\partial x_{0i}} \right] \quad (\text{A.20})$$

Substituindo (A.15) em (A.17) é possível estabelecer a seguinte relação

$$\mathbf{I} + 2\mathbf{E}^{GL} = \mathbf{C} \quad (\text{A.21})$$

Tanto Green-Lagrange como Cauchy-Green à direita são tensores simétricos, possuindo, por isso, 3 valores próprios (valores principais) reais. Os vetores próprios (ou direções principais) das duas matrizes coincidem, já que a soma da matriz identidade não altera os vetores próprios do tensor Green-Lagrange. Estes tensores são Lagrangeanos, uma vez que medem a deformação a partir da configuração indeformada ( $\mathbf{U}$ ) do corpo ( $m>0$ ).

As relações estabelecidas até então permitem medir grandes deformações que se processem essencialmente no domínio elástico. Quando se trabalha com a teoria da elasticidade, as tensões são definidas a partir das configurações, inicial e final, não importando o caminho descrito pelas partículas durante o seu movimento. Porém, no processo de conformação de chapas finas, o comportamento plástico do material assume um significado que não pode ser desconsiderado, sendo fundamental conhecer-se a “história da deformação”. Para seguir o caminho da deformação é necessária uma formulação em taxas. Neste sentido, define-se o campo de velocidades associado ao movimento do ponto material  $\wp$  como

$$\vec{\mathbf{v}} = \vec{\mathbf{v}}(\vec{\mathbf{x}}, t) \quad (\text{A.22})$$

$$\mathbf{v} = \dot{\mathbf{x}} = \frac{\partial \mathbf{x}}{\partial t} \quad (\text{A.23})$$

A este campo de velocidade é possível corresponder um gradiente  $\mathbf{L}$

$$\mathbf{L} = \frac{\partial \mathbf{v}}{\partial \mathbf{x}} = \frac{\partial \left( \frac{\partial \mathbf{x}}{\partial t} \right)}{\partial \mathbf{x}} = \frac{\partial \left( \frac{\partial \mathbf{x}}{\partial t} \right)}{\partial x_0} \cdot \frac{\partial x_0}{\partial \mathbf{x}} = \dot{\mathbf{F}}\mathbf{F}^{-1} \quad (\text{A.24})$$

Este é conhecido como **gradiente espacial de velocidade** ou **gradiente de velocidade**. Desenvolvendo o termo da equação (A.24) é possível demonstrar que este gradiente é composto por uma parte simétrica e outra anti-simétrica

$$\mathbf{L} = \frac{1}{2}(\mathbf{L} + \mathbf{L}^T) + \frac{1}{2}(\mathbf{L} - \mathbf{L}^T) = \mathbf{D} + \mathbf{W} \quad (\text{A.25})$$

Onde  $\mathbf{D}$  é o **tensor velocidade de deformação** (parte simétrica) e  $\mathbf{W}$  é o **tensor de velocidade rotação** (parte anti-simétrica). Na forma indicial, estas matrizes são escritas da seguinte forma

$$D_{ij} = \frac{1}{2} \left[ \frac{\partial \dot{x}_i}{\partial x_j} + \frac{\partial \dot{x}_j}{\partial x_i} \right] = \frac{1}{2} \left[ \frac{\partial \dot{u}_i}{\partial x_j} + \frac{\partial \dot{u}_j}{\partial x_i} \right] \quad (\text{A.26})$$

$$W_{ij} = \frac{1}{2} \left[ \frac{\partial \dot{x}_i}{\partial x_j} - \frac{\partial \dot{x}_j}{\partial x_i} \right] = \frac{1}{2} \left[ \frac{\partial \dot{u}_i}{\partial x_j} - \frac{\partial \dot{u}_j}{\partial x_i} \right] \quad (\text{A.27})$$

Podemos definir a velocidade angular como:

$$\boldsymbol{\Omega} = \dot{\mathbf{R}}\mathbf{R}^T \quad (\text{A.28})$$

Enquanto  $\boldsymbol{\Omega}$  está livre do efeito de deformação, este não é o caso de  $\mathbf{W}$ . Estes tensores só serão iguais quando a transformação é uma rotação pura ( $\mathbf{F} = \mathbf{R}$ ).

Para se entender a função do tensor de deformação  $\mathbf{D}$ , tome-se um segmento qualquer em  $\mathbf{C}$ , e derive-se no tempo o quadrado do seu comprimento

$$\frac{d}{dt}(ds)^2 = \frac{d}{dt}(d\vec{x}^T d\vec{x}) = 2d\vec{x}^T \frac{d(d\vec{x}^T)}{dt} = 2d\vec{x}^T \mathbf{L} d\vec{x}$$

$$\frac{d}{dt}(ds)^2 = 2d\vec{x}^T (\mathbf{D} + \mathbf{W}) d\vec{x}$$

Como

$$d\vec{x}^T \mathbf{W} d\vec{x} = 0$$

Vem

$$\frac{d}{dt}(ds)^2 = 2d\vec{x}^T \mathbf{D} d\vec{x} \quad (\text{A.29})$$

Conclui-se que a taxa de variação do comprimento  $ds$  é calculada a partir da taxa de deformação  $\mathbf{D}$ . Derivando temporalmente o tensor de Green-Lagrange e multiplicando por 2, obtêm-se

$$2\dot{\mathbf{E}}^{\text{GL}} = \dot{\mathbf{F}}^T \mathbf{F} + \mathbf{F}^T \dot{\mathbf{F}} \quad (\text{A.30})$$

Da equação (A.24) é válido dizer-se que  $\dot{\mathbf{F}} = \mathbf{L}\mathbf{F}$ . Substituindo acima resulta em

$$2\dot{\mathbf{E}}^{\text{GL}} = \mathbf{F}^T \mathbf{L}^T \mathbf{F} + \mathbf{F}^T \mathbf{L} \mathbf{F} = \mathbf{F}^T (\mathbf{L}^T + \mathbf{L}) \mathbf{F} = \mathbf{F}^T (2\mathbf{D}) \mathbf{F} \quad (\text{A.31})$$

Que pode ser escrita como

$$\mathbf{D} = \mathbf{F}^{-T} \dot{\mathbf{E}}^{GL} \mathbf{F}^{-1} \quad (\text{A.32})$$

É importante ressaltar que o tensor taxa ou velocidade de deformação  $\mathbf{D}$  não é a mesma grandeza que a derivada temporal do tensor de deformação infinitesimal (A.20). Este é vertido por

$$\dot{\varepsilon}_{ij} = \frac{1}{2} \left[ \frac{\partial \dot{u}_i}{\partial x_{0j}} + \frac{\partial \dot{u}_j}{\partial x_{0i}} \right] \quad (\text{A.33})$$

Que difere de (A.26) onde se estabelece a derivada com relação às coordenadas espaciais  $X_i$  em vez de  $X_0$ . É verdade que quando as deformações são pequenas, ambas se confundem. Porém, unicamente (A.26) pode ser usada em *grandes deformações*.

Durante a elaboração do modelo constitutivo elastoplástico torna-se preponderante distinguir as contribuições elásticas e plásticas. Para isso, é norma recorrer ao processo de decomposição multiplicativa do gradiente de transformação  $\mathbf{F}$ . Introdz-se dessa forma uma configuração intermédia  $C^R$  [Fig. A.3] obtida por relaxamento total das tensões de natureza elástica na configuração  $C$ .

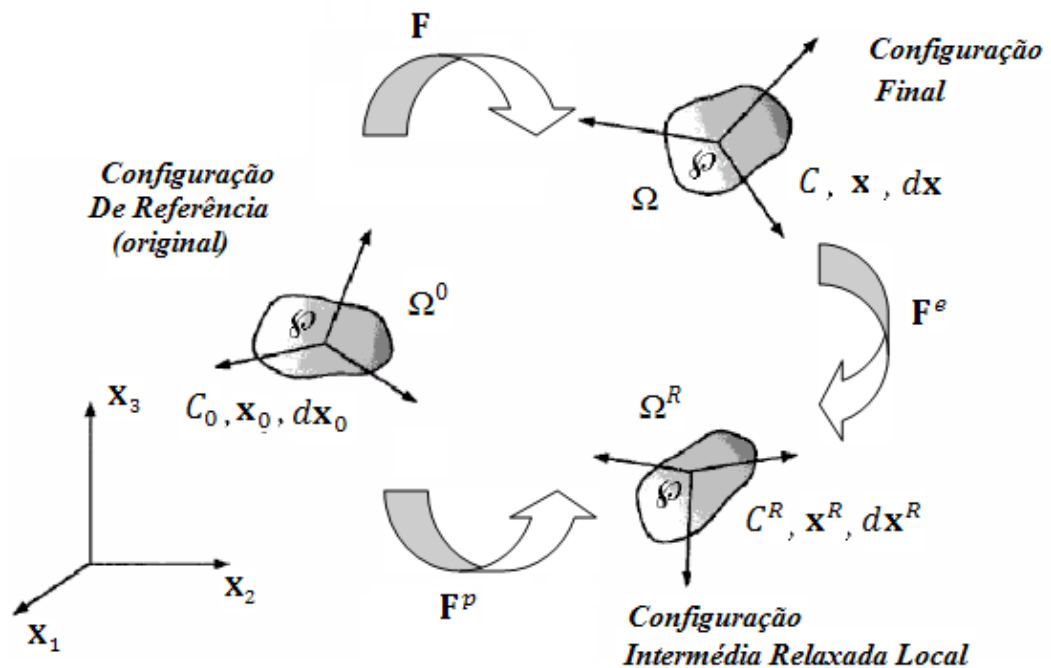


Fig. A.3 – Representação da configuração intermédia  $C^R$  (Alves, 2003).

Daí resulta

$$\mathbf{F} = \mathbf{F}^e \mathbf{F}^p \quad (\text{A.34})$$

Invocando a *decomposição polar* surge

$$\mathbf{F}^e = \mathbf{R}\mathbf{U} \quad (\text{A.35})$$

Ou,

$$\mathbf{F}^e = \mathbf{V}\mathbf{R} \quad (\text{A.36})$$

Admitindo-se válida a suposição de que em deformação plástica a frio de chapas metálicas a transformação elástica  $\mathbf{F}^e$  gera pequenas deformações quando comparadas com a unidade (embora possam ocorrer grandes rotações) (Teodosiu, 1997) tem-se que  $\mathbf{U} \approx \mathbf{V}$  (nestes casos, a discussão Euleriana/Lagrangeana perde o sentido, visto que as configurações de referência e instantânea se aproximam demasiadamente). Por sua vez,  $\mathbf{U}$  pode decompor-se como

$$\mathbf{U} = \mathbf{I} + \varepsilon^e, \quad \text{com} \quad |\varepsilon^e| \ll 1 \quad (\text{A.37})$$

Substituindo  $\mathbf{F}$  pela expressão da sua decomposição multiplicativa no gradiente de velocidade  $\mathbf{L}$  em (A.24) obtêm-se

$$\mathbf{L} = \mathbf{L}^e + \mathbf{L}^p \quad (\text{A.38})$$

Sendo que

$$\mathbf{L}^e = \dot{\mathbf{F}}^e \mathbf{F}^{e-1} \quad \text{e} \quad \mathbf{L}^p = \mathbf{F}^e \dot{\mathbf{F}}^p \mathbf{F}^{p-1} \mathbf{F}^{e-1} \quad (\text{A.39})$$

Que, tendo em conta a decomposição polar para  $\mathbf{F}^e$ , pode ser reescrito

$$\mathbf{L}^e = \dot{\mathbf{U}}\mathbf{U}^{-1} + \mathbf{U}\dot{\mathbf{R}}\mathbf{R}^T\mathbf{U}^{-1} \quad \text{e} \quad \mathbf{L}^p = \mathbf{U}\mathbf{R}\dot{\mathbf{F}}^p\mathbf{F}^{p-1}\mathbf{R}^T\mathbf{U}^{-1} \quad (\text{A.40})$$

Substituindo (A.37) em (A.40), desprezando os infinitesimais superiores  $\|\varepsilon^e\|^2$  para  $\mathbf{L}^e$ , e em  $\mathbf{L}^p$  os termos de ordem  $\|\varepsilon^e\|$ , obtêm-se (Sidoroff, 1982)

$$\mathbf{L}^e = \dot{\boldsymbol{\xi}} + \dot{\mathbf{R}}\mathbf{R}^T, \quad \text{com} \quad \dot{\boldsymbol{\xi}} = \dot{\varepsilon}^e + \varepsilon^e \dot{\mathbf{R}}\mathbf{R}^T - \dot{\mathbf{R}} \quad (\text{A.41})$$

$$\mathbf{L}^p = \mathbf{R}\dot{\mathbf{F}}^p\mathbf{F}^{p-1}\mathbf{R}^T \quad (\text{A.42})$$

Desta forma, é possível definir as contribuições elásticas e plásticas da parte simétrica e anti-simétrica do gradiente velocidade  $\mathbf{L}$ , isto é, do tensor velocidade ou taxa de deformação  $\mathbf{D}$  e do tensor velocidade de rotação  $\mathbf{W}$ .

$$\mathbf{D} = (\mathbf{L})^S = \mathbf{D}^e + \mathbf{D}^p \quad (\text{A.43})$$

$$\mathbf{W} = (\mathbf{L})^A = \mathbf{W}^e + \mathbf{W}^p \quad (\text{A.44})$$

As velocidades de deformação elástica e plástica resultam em

$$\mathbf{D}^e = \dot{\boldsymbol{\xi}} \quad \text{e} \quad \mathbf{D}^p = \mathbf{R}(\dot{\mathbf{F}}^p \mathbf{F}^{p-1})^S \mathbf{R}^T \quad (\text{A.45})$$

As velocidades de rotação elástica e plástica resultam em

$$\mathbf{W}^e = \dot{\mathbf{R}} \mathbf{R}^T \quad \text{e} \quad \mathbf{W}^p = \mathbf{R}(\dot{\mathbf{F}}^p \mathbf{F}^{p-1})^A \mathbf{R}^T \quad (\text{A.46})$$

Neste caso, a velocidade de rotação plástica  $\mathbf{W}^p$  é desprezável face à velocidade de rotação elástica  $\mathbf{W}^e$  podendo se considerar nula. Esta hipótese é válida quando se admite que as forças de corte que actuam na direção perpendicular ao plano da chapa são pouco significativas. O que tem todo o sentido ao se abordarem processos de conformação por deformação plástica de chapas finas.

O mesmo será dizer que

$$\mathbf{W} \approx \mathbf{W}^e = \dot{\mathbf{R}} \mathbf{R}^T \quad \text{com} \quad \mathbf{W}^p = 0 \quad (\text{A.47})$$

Podendo-se calcular assim a evolução da rotação elástica  $\mathbf{R}$  com o tempo

$$\dot{\mathbf{R}} = \mathbf{W} \mathbf{R} \quad (\text{A.48})$$

Com todos estes tensores definidos é agora possível, pela aplicação da expressão de Green-Lagrange (A.17), descrever a deformação do ponto  $\wp$  a partir de  $C_0$ .



## B. Anexo B – TEORIA DA PLASTICIDADE

Na modelação do comportamento plástico dos metais sujeitos a processos de conformação, procuram-se modelos constitutivos adequados, capazes de descrever, o mais fielmente possível, a resposta e o comportamento mecânico dos mesmos, quando sujeitos a diferentes trajetórias de solitação e deformação.

Durante a deformação plástica ocorrem fenómenos específicos de grande interesse, como é o caso do encruamento, da anisotropia plástica, da histerese elástica e do efeito de *bauschinger*, que invalidam as relações constitutivas tensão-deformação, determinadas para o regime elástico, já que introduzem uma maior complexidade matemática. Os modelos constitutivos que pretendem retratar a mecânica da deformação plástica podem inserir-se em duas correntes diferentes: os ‘tecnológicos’ ou fenomenológicos, que incorporam a experimentação, e os físicos, inteiramente baseados na textura cristalográfica, onde a deformação é analisada ao nível macroscópico (Rodrigues, 2005).

Nos modelos físicos, toda a informação relativa à textura cristalográfica é retirada a partir dos modelos de plasticidade de policristais TBH - Taylor-Bishop-Hill – sendo possível identificar a superfície de plasticidade, a sua evolução com a deformação, bem como a lei de comportamento plástico envolvida. Nestes modelos simula-se a evolução das deslocações segundo os planos de escorregamentos ativados pelo carregamento mecânico. Embora tais modelos consigam descrever o comportamento plástico com muita exatidão, visto que resultam de uma união estreita entre a evolução da textura e o processo de conformação, apresentam um elevado custo computacional que torna inaceitável o seu uso, face ao tempo e aos recursos informáticos necessários (Alves, 2003).

Nos modelos fenomenológicos, assume-se que o comportamento plástico do material é corretamente descrito por uma superfície de plasticidade que evolui com a deformação plástica, podendo descrever adequadamente os aspetos mais importantes do mesmo nos materiais policristalinos. Matematicamente esta superfície traduz-se como um potencial para um determinado estado de deformação.

A evolução da superfície de plasticidade ao longo do processo de deformação plástica resulta da sua expansão, que se admite isotrópica (encruamento isotrópico), ocorrendo também ocasionalmente uma deslocação desta superfície no espaço das tensões (encruamento cinemático). Estes pressupostos permitem descrever os efeitos cinemáticos resultantes da alteração de trajetória de deformação (efeito de *bauschinger*). Embora esta seja uma aproximação simplificada da lei de



comportamento dos materiais policristalinos, a evidência experimental corrobora a sua exactidão. A aplicação destes modelos, socorrendo-se duma análise por elementos finitos, revela ser numericamente muito mais eficiente do que os modelos de textura (Alves, 2003).

Em suma, para desenvolver um modelo matemático capaz de descrever o comportamento plástico do material é importante considerar três aspectos importantes:

- Um critério de cedência que indique o nível de tensão, em termos de tensor das tensões, de modo a analisar-se o início da deformação plástica.
- Uma lei de encruamento que descreva como o critério de cedência depende do grau de deformação plástica, depois de se iniciar a deformação plástica.
- Uma lei de plasticidade associada que defina a relação entre a tensão e deformação pós-plasticificação, comportando a deformação total, as componentes elástica e plástica.

## Critérios de plasticidade

O aparecimento do comportamento plástico é condicionado por um critério de plasticidade. Este, é formulado como  $\mathcal{F}(\boldsymbol{\sigma}) = 0$ , e define uma superfície no espaço das tensões que, sendo contínua, retrata todos os estados de tensão para os quais ocorre o início da deformação plástica. Na definição destes critérios é comum assumir-se que:

- Os estados hidrostáticos de tensão não só não provocam deformação plástica, como não influenciam o início do domínio plástico. Este pressuposto, apoiado pelos trabalhos de Bridgman (1952), determina que para materiais metálicos densos deve adoptar-se uma *superfície de plasticidade independente da pressão hidrostática*.

- Existe uma relação unívoca entre o tensor velocidade de deformação ( $L$ ) e um dado estado de tensão assegurada pela *convexidade da superfície de plasticidade* e a não existência de pontos singulares.

- Estes critérios encontram-se sempre ligados a uma *lei de plasticidade associada*, onde se adopta um potencial plástico para a superfície de plasticidade, e define-se que o tensor de velocidade de deformação é sempre ortogonal à mesma. Este pressuposto é denominado por regra da normalidade e, tal como os outros, deve ser sempre respeitado, como evidenciado pelo postulado de Drucker (1951).

Para uma melhor compreensão destes princípios é possível recorrer à representação geométrica da superfície de plasticidade. Como se trata de uma função de tensão, pode assumir-se como espaço para a respetiva representação, o espaço de tensões de *Haig-Westergaard*, em três eixos mutuamente ortogonais coincidentes com as direções principais de tensão [Fig. B.1].

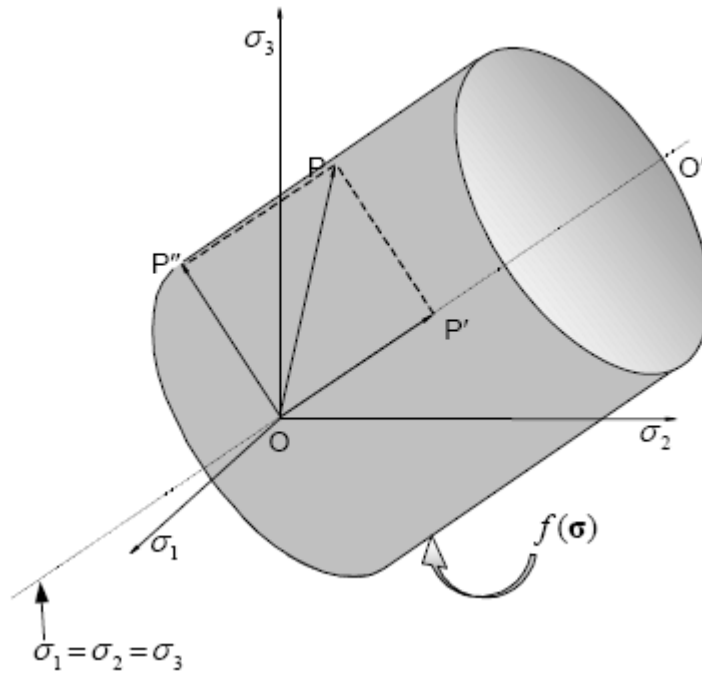


Fig. B.1 – Representação do espaço das tensões de Haig-Westergaard (Natal, 2004).

Considere-se um ponto material com um estado de tensão representado pelo ponto  $P$ , resultante de um incremento traduzido pelo vetor  $\overline{OP}$ . Este vetor é decomposto num vetor com direção  $OO'$  ( $\overline{OP'}$ ), que coincide com o eixo em que as três tensões principais tomam o mesmo valor ( $\sigma_1 = \sigma_2 = \sigma_3 = \sigma_m$ ), e num outro cuja linha de acção se encontra sobre o plano normal a  $OO'$  ( $\overline{OP''}$ ). Invocando o primeiro pressuposto, a pressão hidrostática não terá qualquer efeito na cedência do material, a qual dependerá apenas da intensidade, direção e sentido do vetor  $\overline{OP''}$ , ou seja, das tensões de desvio.

Visto que a função de cedência deve ser independente do referencial escolhido, isto é, deve sempre respeitar o princípio da objetividade, ela dependerá apenas do segundo e terceiro invariantes do tensor desviador  $\sigma'$

$$J_2 = \frac{1}{2} \text{tr}(\sigma'^2) = \frac{1}{2} \sigma'_{ij} \sigma'_{ji} \quad (\text{B.1})$$

$$J_3 = \frac{1}{3} \text{tr}(\sigma'^3) = \frac{1}{3} \sigma'_{ij} \sigma'_{jk} \sigma'_{ki} \quad (\text{B.2})$$

Outra representação geométrica possível consiste no rebatimento das projecções ortogonais dos eixos das tensões no plano normal a  $OO'$ . Na Fig. B.2 encontram-se representadas duas superfícies de cedência: uma corresponde, no espaço das tensões principais, a um cilindro e outra a um prisma. O plano de corte dos objectos geométricos, e que coincide com o plano do papel designa-se plano desviador. Quando este plano passa pela origem, e que por isso se caracteriza pela tensão hidrostática ser nula, é denominado plano  $\pi$  ou plano desviador (sinótico).

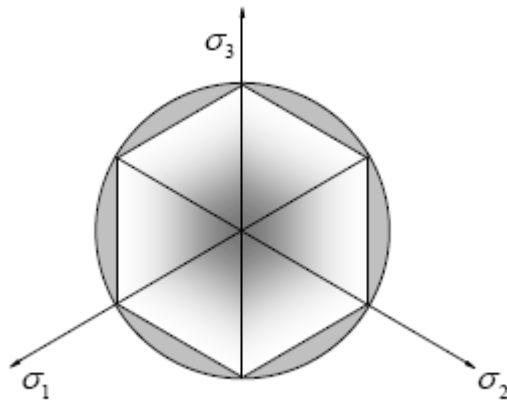


Fig. B.2 – Representação do plano desviador (Natal, 2004).

Atendendo à definição matemática da superfície de plasticidade e ao seu significado físico, é possível concluir que, sempre que se verificar a inequação  $\mathcal{F}(\boldsymbol{\sigma}) < 0$ , num determinado ponto do corpo material deformável, o corpo apresentará comportamento elástico nesse ponto. Se se verificar a igualdade  $\mathcal{F}(\boldsymbol{\sigma}) = 0$ , o comportamento será plástico. Quando se atinge esse estado o comportamento nesse ponto será condicionado pela variação de  $\mathcal{F}$  relativamente a  $\boldsymbol{\sigma}$ ,

$$d\mathcal{F} = \left( \frac{\partial \mathcal{F}}{\partial \boldsymbol{\sigma}} \right)^T d\boldsymbol{\sigma} + \dots \quad (\text{B.3})$$

em que  $\frac{\partial \mathcal{F}}{\partial \boldsymbol{\sigma}}$  é um vetor normal à superfície de cedência, encontrando as componentes do tensor das tensões e as respetivas variações [Fig. B.3].

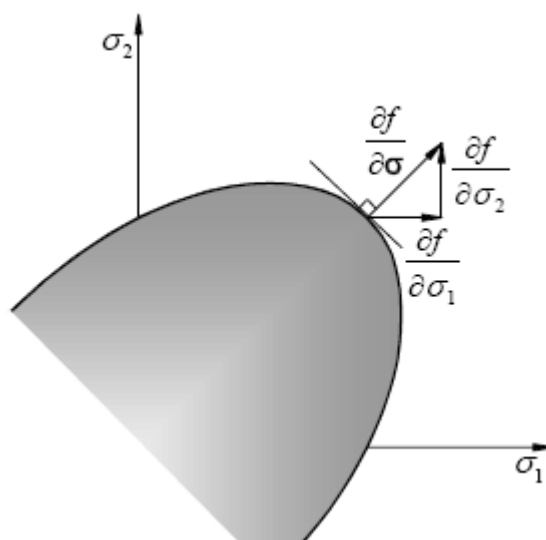


Fig. B.3 – Condição de ortogonalidade no espaço das tensões de  $\sigma_1 - \sigma_2$  (Natal, 2004).

Em suma, é possível concluir que:

- Se  $d\mathcal{F} < 0$ , vigora um estado de descarregamento elástico.

- Se  $d\mathcal{F} = 0$ , o estado de tensão atingiu a superfície de plasticidade e o material entra no regime plástico caso apresente um comportamento perfeitamente plástico.

- Se  $d\mathcal{F} > 0$ , o estado de tensão mantém-se sobre a superfície de plasticidade e esta altera-se.

Perante este comportamento diz-se que o material encrua.

Há que referir que não existe um critério fenomenológico universal. Isto porque estes, dependem dos mecanismos de rotura dos materiais, que vão variando consoante a gama a que estes pertencem. Desta forma, esta secção não visa apresentar todos os critérios de plasticidade existentes, pois a lista seria exaustiva e perder-se-ia o real objetivo deste capítulo na investigação e no tema global. Portanto, a informação que se segue procura abordar apenas os critérios de plasticidade investigados neste estudo de forma a fundamentar o seu uso e revelar o interesse que esses, em particular, apresentam neste trabalho. Como prática corrente da investigação procura-se estabelecer uma comparação entre os mesmos com o intuito de poder verificar, ou comprovar, qual, ou quais, se revelam mais adequados. Uma boa parte dos detalhes relacionados com os critérios de plasticidade apresentados a seguir são extensivamente abordados nas revisões bibliográficas de Alves (2003) e Banabic (2010).

### Critérios de Cedência para Materiais Isotrópicos

#### **Critério de Tresca (1864)**

Este critério foi postulado por Tresca em 1864 e, face a evidências experimentais, admite por hipótese, que a deformação plástica num ponto material, ocorre sempre que a tensão tangencial máxima atinge um determinado valor limite.

$$\tau_{\max} = \frac{\sigma_1 - \sigma_3}{2} \geq k \quad (\text{B.4})$$

Em que  $\sigma_1$  e  $\sigma_3$  são as tensões principais, com  $\sigma_1 \geq \sigma_2 \geq \sigma_3$ , e  $k$  um parâmetro característico do material a ser determinado experimentalmente e que pode ser função do encruamento.

Este critério encontra fundamentação fenomenológica nos conceitos de natureza físico-metalúrgica dos materiais metálicos. Quando se considera o mecanismo responsável pela deformação plástica, aceita-se que este se baseia na movimentação de defeitos, do tipo deslocações, no interior da rede cristalina. São as tensões de corte que originam a movimentação das deslocações e a, conseqüente, alteração da forma do corpo (Rodrigues, 2005). Graficamente, a expressão define,

no espaço tridimensional das tensões de *Haig-Westergaard*, um prisma hexagonal regular infinitamente longo, cujo eixo  $\sigma_1 = \sigma_2 = \sigma_3$ , é perpendicular ao plano desviador  $\pi$ .

### Critério de von Mises (1913)

O critério de plasticidade de von Mises assenta na observação de que a pressão hidrostática não provoca a cedência plástica do material. Assim, a conclusão tirada é que, naturalmente, apenas a energia elástica de distorção influencia a transição do estado elástico para o estado plástico, existindo um valor crítico de energia de distorção elástica para a qual se inicia a deformação plástica. Este critério pode ser expresso da seguinte forma,

$$(\sigma_1 - \sigma_2)^2 + (\sigma_2 - \sigma_3)^2 + (\sigma_1 - \sigma_3)^2 = 2Y^2 \quad (\text{B.5})$$

$\sigma_1$ ,  $\sigma_2$  e  $\sigma_3$  são as tensões principais e  $Y$  a tensão limite de elasticidade em tração uniaxial.

Tendo em conta a independência do referencial e do tensor hidrostático, este critério depende do segundo invariante das tensões de desvio. Enquanto Tresca admite um valor crítico constante para  $\tau_{\max}$ , von Mises considera um valor crítico constante para  $J_2$  [Fig. B.4].

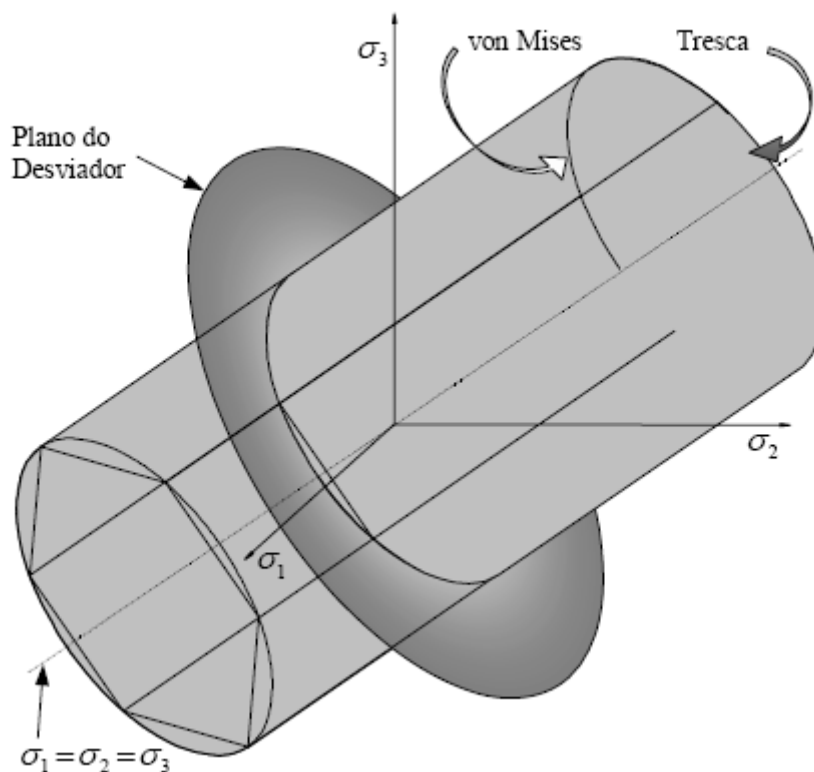


Fig. B.4 – Representação das superfícies limite de elasticidade no espaço de *Haig-Westergaard* (Natal, 2004).

É interessante notar que o critério de plasticidade de von Mises, constitui uma evolução, face ao critério de Tresca, já que considera a influência da tensão intermédia  $\sigma_2$ , sobre o limite de elasticidade. De facto, em situações de corte puro, isto é, em que  $\sigma_3 = -\sigma_1$  e  $\sigma_2 = 0$ , regista-se a diferença máxima entre os dois critérios. Nestes casos, a aplicação do critério de Tresca leva a uma tensão efectiva,  $\bar{\sigma}$ , 1,15 vezes superior à obtida pela aplicação do critério de von Mises, permitindo concluir que é, por isso, mais conservativo do que este último.

Tanto Tresca como von Mises constituem critérios inadequados à descrição do comportamento plástico que as chapas exibem durante os processos de estampagem. A representação geométrica de Tresca no plano  $\pi$ , revela a existência de pontos singulares (vértices do hexágono), que dificulta o cálculo de  $\partial f / \partial \sigma$ , impedindo a *convexidade da superfície plástica*. Von Mises resolve esse problema, mas continua longe de conseguir descrever o efeito da anisotropia na superfície de plasticidade, além de não introduzir o terceiro invariante do tensor desviador na sua formulação, o que impede a descrição do efeito da alteração da trajetória de deformação (já que se parte do princípio que as condições de entrada no domínio plástico são as mesmas, quer se considere as tensões de tração, ou compressão).

As chapas laminadas são exemplos de materiais anisotrópicos de comportamento ortotrópico, isto é, materiais com três planos de simetria de propriedade mutuamente ortogonais em cada ponto material. Assim, necessitam de critérios mais evoluídos, nomeadamente anisotrópicos. Porém, visto que estes se desenvolveram a partir dos critérios isotrópicos, uma pequena alusão a estes (Tresca e von Mises), acaba por ser de proveito. Na prática corrente, é norma empregar-se um sistema de eixos local (ou de ortotropia) utilizado na definição dos critérios de plasticidade, a partir da direcção de laminagem (RD) e das direcções transversa (TD) e normal (ND), respectivamente, no plano da chapa e na sua direcção normal (Alves, 2003).

### **Critérios de Cedência Clássicos para Materiais Anisotrópicos**

#### **Critério de Hill (1948)**

Em 1948, Hill (1948) propõe um critério válido para materiais anisotrópicos ortotrópicos, que surge como uma generalização do critério quadrático isotrópico de von Mises.

$$F(\sigma_{yy} - \sigma_{zz})^2 + G(\sigma_{zz} - \sigma_{xx})^2 + H(\sigma_{xx} - \sigma_{yy})^2 + 2L\tau_{yz}^2 + 2M\tau_{xz}^2 + 2N\tau_{xy}^2 = Y^2 \quad (\text{B.6})$$

Em que F, G, H, L, M e N são os parâmetros de anisotropia do material, e x, y e z os eixos principais de anisotropia. A forma tensorial desta expressão, que favorece em muito o cálculo algébrico, aparece na seguinte forma

$$\boldsymbol{\sigma} : \mathbf{M} : \boldsymbol{\sigma} = Y^2 \quad (\text{B.7})$$

Em notação indicial surge como

$$M_{ijkl}\sigma_{ij}\sigma_{kl} = Y^2 \quad (\text{B.8})$$

Sendo  $\mathbf{M}$  o tensor de 4ª ordem (e dimensão  $3 \times 3 \times 3 \times 3$ ) dos parâmetros de anisotropia de Hill, cujas propriedades são

$$M_{ijkl} = M_{jikl} = M_{klij} \quad e \quad M_{iikm} = 0 \quad (\text{B.9})$$

A igualdade  $M_{iikm} = 0$  advém da condição de incompressibilidade plástica, que no caso dos metais é aceitável, e permite substituir o tensor  $\boldsymbol{\sigma}$ , pelo seu desviador  $\boldsymbol{\sigma}'$ , ao se calcular a tensão equivalente. Por outro lado, a simetria do tensor  $\mathbf{M}$ , permite adotar a convenção de Voigt e produzir um tensor equivalente  $\mathbf{M}$  de 2ª ordem (e de dimensão  $6 \times 6$ ).

$$\begin{bmatrix} \sigma_1 \\ \sigma_2 \\ \sigma_3 \\ \sigma_4 \\ \sigma_5 \\ \sigma_6 \end{bmatrix} : \begin{bmatrix} G+H & -H & -G & 0 & 0 & 0 \\ -H & F+H & -F & 0 & 0 & 0 \\ -G & -F & F+G & 0 & 0 & 0 \\ 0 & 0 & 0 & 2L & 0 & 0 \\ 0 & 0 & 0 & 0 & 2M & 0 \\ 0 & 0 & 0 & 0 & 0 & 2N \end{bmatrix} : \begin{bmatrix} \sigma_1 \\ \sigma_2 \\ \sigma_3 \\ \sigma_4 \\ \sigma_5 \\ \sigma_6 \end{bmatrix} = Y^2 \quad (\text{B.10})$$

Para relacionar os coeficientes de anisotropia com as constantes do critério de plasticidade de Hill, pode-se considerar que o ensaio de tração se realiza segundo a direção  $x'$  que faz um ângulo  $\beta$  com a direção principal de anisotropia  $x$ . Nestas condições, é possível definir-se o coeficiente de anisotropia segundo a direção  $x'$

$$r_\beta = \frac{d\varepsilon_{y'}}{d\varepsilon_{z'}} \quad (\text{B.11})$$

Em que  $d\varepsilon_{y'}$  e  $d\varepsilon_{z'}$  são os incrementos de extensão segundo a direção perpendicular a  $x'$  e à espessura, respectivamente.

Estes incrementos de extensão podem ser obtidos através duma transformação dos incrementos de deformação segundo os eixos principais de anisotropia

$$d\varepsilon_{x'} = d\varepsilon_x \cos^2 \beta + d\varepsilon_y \sin^2 \beta + 2d\varepsilon_{xy} \cos \beta \sin \beta \quad (\text{B.12})$$

$$d\varepsilon_{y'} = d\varepsilon_x \sin^2 \beta + d\varepsilon_y \cos^2 \beta - 2d\varepsilon_{xy} \cos \beta \sin \beta \quad (\text{B.13})$$

Finalmente, vem o coeficiente de anisotropia segundo o eixo de solitação  $x'$

$$r_\beta = \frac{d\varepsilon_{y'}}{d\varepsilon_{z'}} = \frac{d\varepsilon_{y'}}{d\varepsilon_z} = \frac{[H + (2N - 4H - F - G)\sin^2 \beta \cos^2 \beta]}{F \sin^2 \beta + G \cos^2 \beta} \quad (\text{B.14})$$

Como no caso das chapas a direção de laminagem (RD) é geralmente um eixo principal de anisotropia, usa-se a expressão (B.14) para calcular os coeficientes de anisotropia segundo três direções, 0°, 45° e 90°

$$r_0 = \frac{H}{G}; \quad r_{45} = \frac{2N - (F + G)}{2(F + G)}; \quad r_{90} = \frac{H}{F} \quad (\text{B.15})$$

Daí determinam-se os parâmetros de Hill em função dos coeficientes de anisotropia

$$\begin{aligned} H &= r_0 \cdot G; & G &= \frac{1}{r_0 + 1}; & F &= \frac{H}{r_{90}} \\ L = M &= 1.5; & N &= \frac{1}{2} \cdot \frac{(r_0 + r_{90}) \cdot (2r_{45} + 1)}{r_{90} \cdot (r_0 + 1)}; \end{aligned} \quad (\text{B.16})$$

Também é possível demonstrar que os coeficientes de anisotropia se podem relacionar com as tensões de cedência pela seguinte relação

$$\frac{\sigma_0}{\sigma_{90}} = \sqrt{\frac{r_0(1 + r_{90})}{r_{90}(1 + r_0)}} \quad (\text{B.17})$$

Esta equação implica que a  $r_0 > r_{90}$  corresponde  $\sigma_0 > \sigma_{90}$  e vice-versa. Existe, portanto, uma relação de dependência entre  $\sigma_0$  e  $\sigma_{90}$ . Contudo, nem todos os materiais satisfazem esta condição. Estes materiais apresentam um comportamento anômalo classificado como *comportamento anômalo de segunda ordem*.

Interessa agora entender como tais coeficientes de anisotropia se relacionam com a anisotropia da chapa. Existem dois tipos de anisotropia presentes nas chapas laminadas que se destinam à estampagem; a *anisotropia planar* e a *anisotropia normal*. A anisotropia normal sugere uma variação das propriedades mecânicas segundo a espessura. Neste sentido, a anisotropia normal é de particular interesse na estampagem de chapas finas, já que é indicativa da resistência da chapa ao adelgaçamento, e, permite fazer uma avaliação da possível redução do perímetro do esboço plano, sem provocar fratura. A anisotropia planar resulta da variação da anisotropia normal com o ângulo medido em relação à direção de laminagem e está diretamente relacionada com a formação de orelhas de embutidura durante processo de conformação de embutidos axissimétricos.

Para quantificar a anisotropia segundo a espessura, define-se o coeficiente de anisotropia normal médio, que consiste em pesar igualmente os coeficientes de anisotropia para as três direções consideradas no plano

$$\bar{r} = \frac{r_0 + 2r_{45} + r_{90}}{4} \quad (\text{B.18})$$



Este coeficiente de anisotropia normal exerce forte influência na forma da superfície de plasticidade (Rodrigues, 2005).

Para os casos de tensão plana em que as direções principais do tensor das tensões coincidem com os eixos de anisotropia ( $\sigma_{xx} = \sigma_1$ ,  $\sigma_{yy} = \sigma_2$ ,  $\sigma_{zz} = \sigma_{zx} = \sigma_{yz} = \sigma_{zz} = 0$ ), o critério de Hill 1948 pode ser escrito em função das tensões principais, assumindo a seguinte forma

$$\sigma_1^2 - \frac{2r_0}{1+r_0}\sigma_1\sigma_2 + \frac{r_0(1+r_{90})}{r_{90}(1+r_0)}\sigma_2^2 = \sigma_0^2 \quad (\text{B.19})$$

Portanto, são necessários apenas três parâmetros mecânicos, nomeadamente  $r_0$ ,  $r_{90}$  e  $\sigma_0$ , para definir a cedência em tensão plana.

A equação (B.19) representa uma família de elipses dependentes dos parâmetros mecânicos  $r_0$  e  $r_{90}$ . A influência destes coeficientes de anisotropia sobre a superfície de plasticidade é demonstrada na Fig. B.5.

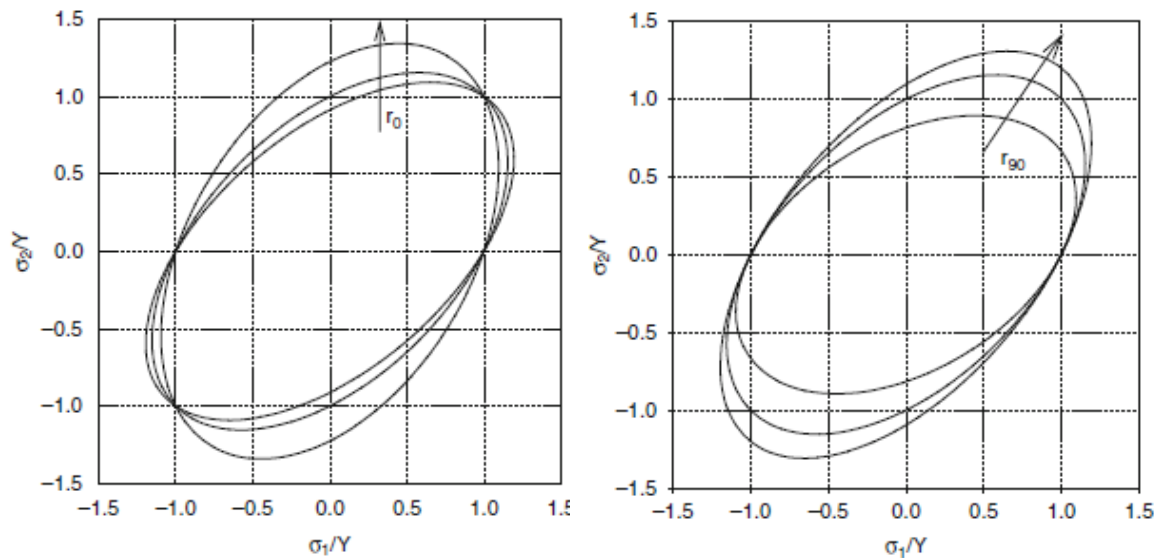


Fig. B.5 Influência dos coeficientes de anisotropia  $r_0$  e  $r_{90}$  sobre a superfície de plasticidade definida pelo critério de Hill 1948 (Banabic, 2010).

Considerando uma chapa com isotropia planar ( $r_0 = r_{90} = \bar{r}$ ) impõe-se, pela equação (B.17), que  $\sigma_0 = \sigma_{90}$  e a equação (B.19) pode ser reescrita como

$$\sigma_1^2 - \frac{2\bar{r}}{1+\bar{r}}\sigma_1\sigma_2 + \sigma_2^2 = \sigma_u^2 \quad (\text{B.20})$$

em que  $\sigma_u$  é a tensão de cedência uniaxial.

A influência dos parâmetros  $\bar{r}$  e  $\sigma_u$  na forma da superfície de plasticidade pode ser observada na Fig. B.6.

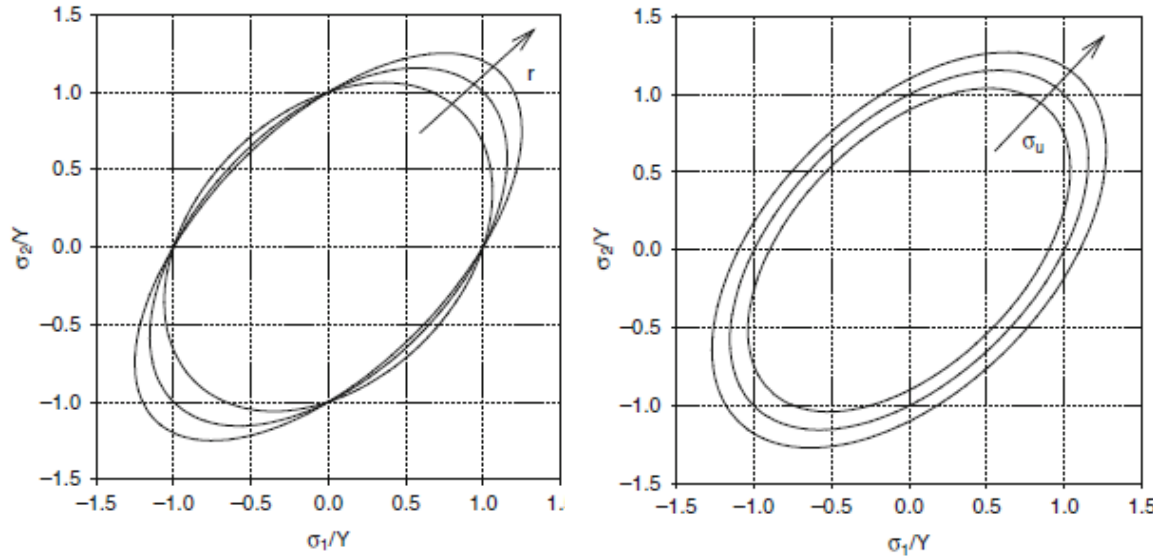


Fig. B.6 – Influência dos coeficientes de anisotropia  $\bar{r}$  e  $\sigma_u$  sobre a superfície de plasticidade definida pelo critério de Hill 1948 (Banabic, 2010).

Neste caso, quando  $\bar{r} < 1$ , a superfície de plasticidade prevista por Hill 1948 encontrar-se-á no interior da superfície de von Mises. Em contrapartida, se  $\bar{r} > 1$ , é a superfície de von Mises que ocupará o espaço interior da superfície de Hill. Porém, segundo Woodthorpe and Pearce (1970) e Pearce (1968), alguns materiais (em particular as ligas de alumínio) apresentam uma superfície de plasticidade localizada exteriormente a von Mises embora  $\bar{r} < 1$ . Este comportamento inesperado foi classificado de *comportamento anómalo de primeira ordem*. Esta limitação do critério de Hill 1948 levou ao desenvolvimento de novos critérios fenomenológicos a partir da década de 70, especialmente critérios não-quadráticos.

### Critério de Hill 1979

Em 1979, Hill propõe um critério de plasticidade não-quadrático expresso por uma função geral ou definido para quatro casos especiais. A formulação mais comum deste critério é denominada de *caso 4*. Diferentemente de Hill (1948), Hill (1979) só pode ser aplicado à conformação de chapas de comportamento ortotrópico, isto é, quando os eixos de anisotropia coincidem com as direções principais, sendo expresso matematicamente da seguinte forma

$$f|\sigma_2 - \sigma_3|^m + g|\sigma_3 - \sigma_1|^m + h|\sigma_1 - \sigma_2|^m + a|2\sigma_1 - \sigma_2 - \sigma_3|^m + b|2\sigma_2 - \sigma_1 - \sigma_3|^m + c|\sigma_3 - \sigma_1 - \sigma_2|^m = \sigma_e^m \quad (\text{B.21})$$

onde  $f$ ,  $g$ ,  $h$ ,  $a$ ,  $b$  e  $c$  são os coeficientes de anisotropia e o expoente  $m$  pode ser obtido pela expressão (B.21), escrita em função da tensão equibiaxial ( $\sigma_1 = \sigma_2 = \sigma_b$ ;  $\sigma_3 = 0$ ):

$$\left(\frac{\sigma_b}{\sigma_m}\right)^m = \frac{1}{2}(1+r) \cdot \left(1 + \frac{(2^{m-1}-2) \cdot (a-c)}{a + 2^{m-1} \cdot c + f}\right), \quad (\text{B.22})$$

Para o estado de tensão plana a expressão (B.21) assume a seguinte forma simplificada

$$c|\sigma_1 + \sigma_2|^m + h|\sigma_1 - \sigma_2|^m = \sigma_e^m \quad (\text{B.23})$$

Assumindo isotropia planar os eixos 1 e 2 podem ser orientados arbitrariamente no plano da chapa e os termos associados às tensões de corte tornam-se desnecessários. Neste caso, o critério de Hill pode ser expresso em função de apenas dois coeficientes,  $c$  e  $h$ , dependentes dos parâmetros  $r$  e  $m$

$$c = \frac{r}{2(1+r)}, \quad h = \frac{1+2r}{2(1+r)} \quad (\text{B.24})$$

O que possibilita reescrever a expressão (B.23)

$$|\sigma_1 + \sigma_2|^m + (1+2r)|\sigma_1 - \sigma_2|^m = 2(1+r)\sigma_u^m \quad (\text{B.25})$$

Por outro lado, a condição de convexidade exige que  $m > 1$ . Neste caso particular a equação (B.22) toma a forma

$$\left(\frac{\sigma_b}{\sigma_u}\right)^m = \frac{1+r}{2^{m-1}}, \quad (\text{B.26})$$

A resolução desta equação conduz geralmente a coeficientes de valor não-inteiro.

Como *vantagens* do critério de Hill 1979 destacam-se (Lian *et al.*, 1984):

- A descrição do comportamento anômalo dos materiais.
- A forma relativamente simples.
- Conduzir a uma expressão analítica da lei de plasticidade associada e deformação equivalente.

Como *desvantagens* do critério de Hill 1979 enumeram-se:

- Incapacidade de descrever o comportamento  $\frac{r_0}{r_{90}} \neq 1$  e  $\frac{\sigma_0}{\sigma_{90}} \neq 1$ .
- Uso de procedimentos numéricos, até para a solução mais simples, dado a existência de um valor não-inteiro para o coeficiente  $m$ .

Superfícies de plasticidade previstas por este modelo por vezes afastadas das superfícies experimentais determinadas pela teoria de Bishop-Hill (Bishop and Hill, 1951).

### Critérios de Cedência Baseados no Comportamento Plástico do Cristal

### Critério de Hosford 1979

A par do próprio Hill, Hosford (1979) investigou alternativas aos critérios de cedência quadráticos, apresentando um critério de cedência anisotrópico com a seguinte forma

$$F(\sigma_{22} - \sigma_{33})^a + G(\sigma_{33} - \sigma_{11})^a + H(\sigma_{11} - \sigma_{22})^a = Y^a \quad (\text{B.27})$$

onde  $F$ ,  $G$  e  $H$  são parâmetros anisotrópicos e em que  $a \neq 2$ . Este critério pode ser encarado como um caso particular do critério de Hill 1979 ( $a = b = c = 0$  e  $f = g$ ). A única diferença substancial face a Hill é que Hosford relaciona o seu critério com a estrutura cristalográfica do material (Logan and Hosford, 1980; Hosford, 1985; Hosford, 1993; Hosford, 1996). De acordo com ele as melhores aproximações à superfície de plasticidade obtêm-se quando se utilizam os valores  $a = 6$  e  $a = 8$ , respectivamente, para materiais que apresentam estruturas cristalinas do tipo CFC (Cúbica de Faces Centradas) e CCC (Cúbica de Corpo Centrado).

Para o estado de tensão plano a equação (B.27) assume a forma simplificada

$$r_{90}|\sigma_{11}|^a + r_0|\sigma_{22}|^a + r_0r_{90}|\sigma_{11} - \sigma_{22}|^a = r_{90}(r_0 + 1)\sigma_0^a \quad (\text{B.28})$$

A maior vantagem do critério de cedência Hosford 1979 é o alcance de uma boa aproximação face à superfície de plasticidade obtida pela teoria de Bishop-Hill ou obtida a partir de informação experimental por ajuste do parâmetro  $a$ .

### Critério de Barlat 1991 (Yld91)

Em 1991, Barlat propõe um novo critério de plasticidade anisotrópico, que corresponde a uma generalização do critério isotrópico apresentado por Hosford, em 1972, e que pode ser aplicado a qualquer estado de tensão (Barlat *et al.*, 1991).

O método consiste numa transformação linear  $\mathbf{L}$  do tensor das tensões. O tensor das tensões transformado  $\mathbf{s}$ , já não corresponde ao tensor das tensões do material anisotrópico inicial, mas, a um novo tensor num estado plástico isotrópico equivalente, e pode, por isso, ser diretamente introduzido no critério isotrópico de Hosford. Uma vez que se opera uma transformação sobre o tensor de tensões originais, não se torna necessário provar a convexidade deste critério que já está provada para o critério de Hosford 1972.

Este estado de tensão desviador  $\mathbf{s}$  designa-se por “Estado Plástico Isotrópico Equivalente”. E é definido como

$$\mathbf{s} = \mathbf{L} : \boldsymbol{\sigma} \quad \text{ou} \quad \mathbf{s} = \mathbf{L} : \boldsymbol{\sigma}' , \quad (\text{B.29})$$

Se a transformação operar sobre o tensor das tensões  $\boldsymbol{\sigma}$  ou  $\boldsymbol{\sigma}'$ , respetivamente.

$$\mathbf{s} = \mathbf{L} : (\boldsymbol{\sigma} - \mathbf{X}) \quad \text{ou} \quad \mathbf{s} = \mathbf{L} : (\boldsymbol{\sigma}' - \mathbf{X}), \quad (\text{B.30})$$

Se a transformação operar sobre o tensor das tensões efectivas,  $\boldsymbol{\sigma} - \mathbf{X}$ . Sendo que  $\mathbf{X}$  é o tensor das tensões inversas e  $\mathbf{L}$  um tensor de 4ª ordem, simétrico e desviador. A componente hidrostática de  $\mathbf{s}$  é nula e independente da componente hidrostática do tensor  $\boldsymbol{\sigma}$  (ou  $\boldsymbol{\sigma} - \mathbf{X}$ ), uma vez que o tensor transformador tem as seguintes propriedades

$$L_{ijkl} = L_{jikl} = L_{jilk}, \quad L_{ijkl} = L_{klij} \quad e \quad L_{ijkk} = 0 \quad (\text{B.31})$$

O tensor  $\mathbf{L}$ , proposto por Barlat, pode representar-se, para um material de comportamento ortotrópico e adoptada a convenção de Voigt, por:

$$\mathbf{L}|_{6 \times 6} = \begin{bmatrix} (c_2 + c_3)/3 & -c_3/3 & -c_2/3 & 0 & 0 & 0 \\ -c_3/3 & (c_3 + c_1)/3 & -c_1/3 & 0 & 0 & 0 \\ -c_2/3 & -c_1/3 & (c_1 + c_2)/3 & 0 & 0 & 0 \\ 0 & 0 & 0 & c_4 & 0 & 0 \\ 0 & 0 & 0 & 0 & c_5 & 0 \\ 0 & 0 & 0 & 0 & 0 & c_6 \end{bmatrix} \quad (\text{B.32})$$

Com 6 variáveis independentes  $c_1, c_2, c_3, c_4, c_5$  e  $c_6$ . Estes termos estão relacionados com a anisotropia do material e tem de ser obtidos por via experimental.

A representação esquemática do conceito de “Estado Plástico Isotrópico Equivalente” é apresentada na Fig. B.7.

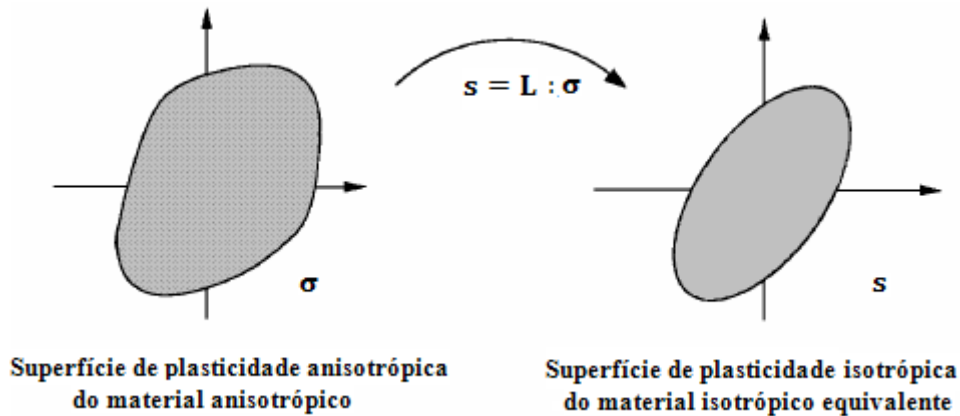


Fig. B.7 – Representação esquemática das superfícies plasticidade anisotrópica e “isotrópica equivalente” (Alves, 2003).

A formulação do critério de plasticidade Yld91 sobrevém como

$$\mathbf{s} = \mathbf{L} : (\boldsymbol{\sigma} - \mathbf{X}) \quad e \quad (\text{B.33})$$

$$|s_1 - s_2|^a + |s_2 - s_3|^a + |s_1 - s_3|^a = 2Y^{2a} \quad (\text{B.34})$$

Sendo que  $s_1, s_2, s_3$  são as tensões principais do tensor  $\mathbf{s}$ ,  $Y$  a tensão limite de elasticidade em tração uniaxial e  $a$  um parâmetro isotrópico.

O critério de cedência Yld91 é geral e flexível, prevê superfícies de plasticidade compatíveis com as determinadas pelas teorias dos policristais, é fácil de implementar num código FE e fornece uma boa estimativa da distribuição das tensões de cedência uniaxiais e dos coeficientes de anisotropia no plano da chapa. A sua maior desvantagem está relacionada com o procedimento de determinação da lei de plasticidade associada.

### Critério de Karafillis & Boyce (1993)

Karafillis e Boyce propuseram um critério de plasticidade cuja característica mais significativa seria a possibilidade de reproduzir diferentes famílias de superfícies de plasticidade isotrópica (Karafillis and Boyce, 1993). Este critério seria mais flexível do que todos os anteriores em reproduzir a isotropia do material e poderia ser ainda usado para modelar o “Estado Plástico Isotrópico Equivalente” introduzido por Barlat em 1991.

Baseados nos estudos de Hosford (1972) e Mendelson (1968), Karafillis & Boyce consideram que a isotropia que o material pode manifestar coloca a sua superfície de plasticidade entre dois limites bem definidos. A chamada fronteira limite inferior, coincide com a superfície de Tresca 1864, por outro lado, a fronteira limite superior corresponde a um hexágono (resultante da semi-soma dos dois maiores diâmetros dos círculos de Mohr), dentro do qual se inscreve o círculo de von Mises. Colocando todas essas superfícies sobre o plano desviador  $\pi$  é possível fazer a seguinte representação esquemática [Fig. B.8]

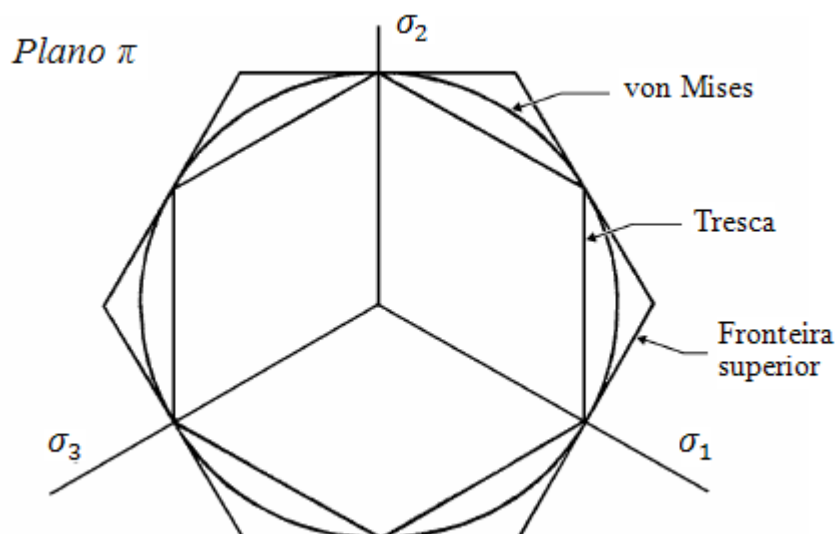


Fig. B.8 – Representação geométrica da superfície de plasticidade de von Mises com os respectivos limites, superior e inferior (Alves, 2003; Karafillis and Boyce, 1993).

O critério de Hosford 1972 é usado para descrever as superfícies de plasticidade existentes entre os critérios de Tresca e von Mises mediante a seguinte expressão

$$\Phi_1(\sigma') = (\sigma_1 - \sigma_2)^{2k} + (\sigma_2 - \sigma_3)^{2k} + (\sigma_3 - \sigma_1)^{2k} = 2Y^{2k} \quad (\text{B.35})$$

Sendo  $\sigma_1$ ,  $\sigma_2$  e  $\sigma_3$  as tensões principais do desviador  $\sigma'$ . O expoente  $k$  aparece como um parâmetro isotrópico inteiro positivo. Quando  $k$  toma o valor 1, a superfície reproduzida corresponde ao círculo de von Mises, quando  $k \rightarrow +\infty$ , a superfície obtida tende para o hexágono de Tresca. Valores intermédios de  $k$ , produzem superfícies de plasticidade intermédias, isto é, compreendidas entre a fronteira limite inferior (Tresca) e o círculo de von Mises (Fig. B.9 a)).

Por outro lado, as superfícies de plasticidade isotrópica compreendidas entre a superfície de von Mises e a fronteira limite superior, são descritas matematicamente recorrendo à expressão

$$\Phi_2(\sigma') = \sigma_1^{2k} + \sigma_2^{2k} + \sigma_3^{2k} = \frac{2^{2k} + 2}{3^{2k}} Y^{2k} \quad (\text{B.36})$$

Neste caso,  $k=1$  descreve a superfície de von Mises e a fronteira limite superior é representada quando  $k \rightarrow +\infty$  (Fig. B.9 b)).

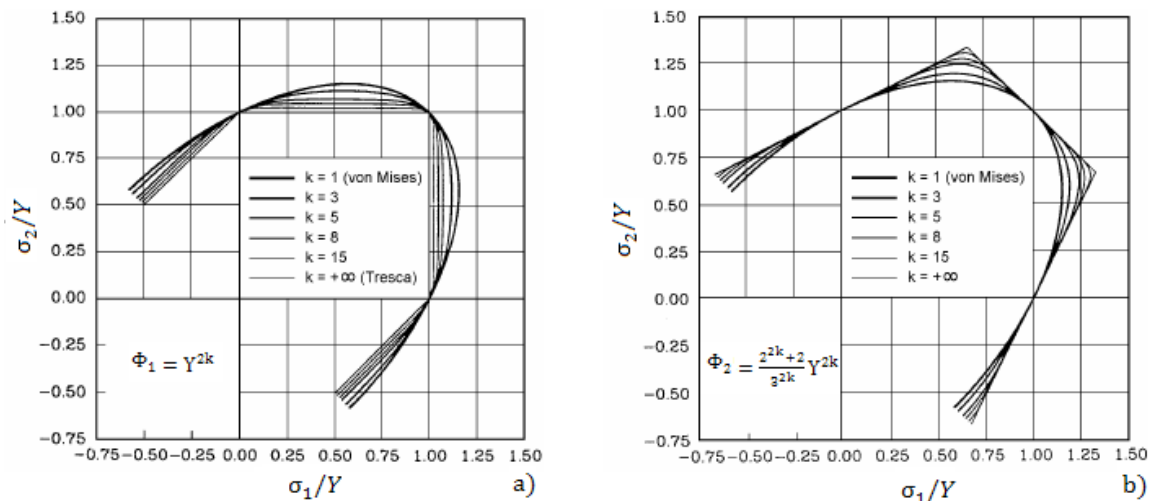


Fig. B.9 – Representação das diferentes superfícies de plasticidade existentes entre a) von Mises e a fronteira inferior e b) von Mises e a fronteira superior (Alves, 2003; Karafillis and Boyce, 1993).

Na sua forma final, a superfície de plasticidade isotrópica genérica apresentada por Karafillis and Boyce (1993) surge da combinação linear de (B.35) e (B.36) com o parâmetro isotrópico  $c \in [0,1]$ . Vem pois

$$\Phi(\boldsymbol{\sigma}') = (1 - c)\Phi_1(\boldsymbol{\sigma}') + c \frac{3^{2k}}{2^{2k-1} + 1} \Phi_2(\boldsymbol{\sigma}') = Y^{2k} \quad (\text{B.37})$$

Este critério de plasticidade genérico modela assim todas as superfícies de plasticidade isotrópicas compreendidas entre as fronteiras limites superior e inferior. O parâmetro  $c$  permite determinar o peso dado as funções  $\Phi_1$  e  $\Phi_2$  na função de cedência  $\Phi$ . Vê-se aqui que este critério define dois parâmetros ( $c$  e  $k$ ) para “ajustar” a superfície de plasticidade no espaço de tensões, o que, por sua vez, lhe confere mais flexibilidade em relação aos outros critérios isotrópicos.

Com o intuito de modelizar a superfície de plasticidade para materiais com comportamento anisotrópico Karafilis & Boyce adoptaram a metodologia, anteriormente apresentada, proposta por Barlat em 1991. Introduzindo o conceito de IPE (*Estado Plástico Isotrópico Equivalente*) no critério de plasticidade isotrópico generalizado, obtém-se as seguintes expressões

$$\Phi_1(\mathbf{s}) = (s_1 - s_2)^{2k} + (s_2 - s_3)^{2k} + (s_3 - s_1)^{2k} = 2Y^{2k} \quad (\text{B.38})$$

$$\Phi_2(\mathbf{s}) = s_1^{2k} + s_2^{2k} + s_3^{2k} + \frac{2^{2k} + 2}{3^{2k}} Y^{2k} \quad (\text{B.39})$$

$$\Phi(\mathbf{s}) = (1 - c)\Phi_1(\mathbf{s}) + c \frac{3^{2k}}{2^{2k-1} + 1} \Phi_2(\mathbf{s}) = Y^{2k} \quad (\text{B.40})$$

Nas quais  $s_1, s_2, s_3$  são as tensões principais do tensor  $\mathbf{s}$ ,  $Y$  a tensão limite de elasticidade em tração uniaxial.

Este critério é, por isso, uma extensão do critério Yld91, o qual considerava apenas as superfícies de plasticidade descritas por Hosford 1972 (tratando-se do caso particular,  $c=0$ ). Desta forma, o critério de Karafilis & Boyce 1993 estende-se a materiais anisotrópicos de comportamento não exclusivamente ortotrópicos. As superfícies previstas pelo critério de Karafilis-Boyce representam uma aproximação muito boa face às superfícies descritas pela teoria de Bishop-Hill e às superfícies determinadas a partir da informação experimental. A correlação com os dados experimentais é também muito boa quando comparada a variação das tensões de cedência à tração uniaxial e dos coeficientes de anisotropia no plano da chapa. Outra vantagem que este critério apresenta é que todos os parâmetros mecânicos necessários podem ser obtidos unicamente com testes de tração uniaxial. Uma desvantagem apontada ao critério de Karafilis-Boyce é que o procedimento de identificação do tensor operador é complexo e requer uma solução numérica. Porém, esta não é uma limitação significativa quando se implementa um critério de cedência num código de elementos finitos.

### **Critérios de Cedência Anisotrópicos Avançados**



### Critério de Cazacu & Barlat (2001)

O critério de Cazacu and Barlat (2001) assenta sobre duas extensões do critério proposto por Drucker (1949).

A primeira extensão resume-se à introdução da anisotropia do material no critério isotrópico de Drucker, mediante a conhecida transformação linear proposta por **L**, inicialmente proposta por Barlat *et al.* (1991). Em vez de se utilizarem os invariantes  $J_2$  e  $J_3$  do tensor das tensões, utilizam-se os invariantes  $J_2^s$  e  $J_3^s$  referentes ao tensor das tensões linearmente transformado **s**,

$$J_2^s = \frac{1}{2} \text{trs}^2 \quad \text{e} \quad J_3^s = \frac{1}{3} \text{trs}^3 \quad (\text{B.41})$$

Aplicando esses valores em Drucker 1949

$$(J_2^s)^3 - c(J_3^s)^2 = 27 \left( \frac{Y}{3} \right)^6 \quad (\text{B.42})$$

Para que a convexidade seja respeitada neste critério é necessário que  $-\frac{27}{8} \leq c \leq \frac{9}{4}$ .

Seguidamente, a segunda extensão do critério isotrópico de Drucker visa a sua generalização à ortotropia. Por tratamento matemático, os autores chegaram às expressões dos invariantes generalizados  $J_2^o$  e  $J_3^o$ , que constituem polinómios homogêneos do 2º e 3º graus das tensões, independentes da componente hidrostática do tensor das tensões e invariantes em relação a qualquer transformação envolvendo os planos de ortotropia.

$$J_2^o = \frac{a_1}{6} (\sigma_{xx} - \sigma_{yy})^2 + \frac{a_2}{6} (\sigma_{yy} - \sigma_{zz})^2 + \frac{a_3}{6} (\sigma_{xx} - \sigma_{zz})^2 + a_4 \tau_{xy}^2 + a_5 \tau_{xz}^2 + a_6 \tau_{yz}^2 \quad (\text{B.43})$$

$$\begin{aligned} J_3^o = & \frac{1}{27} (b_1 - b_2) \sigma_{xx}^3 + \frac{1}{27} (b_3 - b_4) \sigma_{yy}^3 + \frac{1}{27} [2(b_1 + b_4) - b_2 - b_3] \sigma_{zz}^3 - \frac{1}{9} (b_1 \sigma_{yy} - b_2 \sigma_{zz}) \sigma_{xx}^2 \\ & - \frac{1}{9} (b_3 \sigma_{zz} - b_4 \sigma_{xx}) \sigma_{yy}^2 - \frac{1}{9} [(b_1 - b_2 + b_4) \sigma_{xx} + (b_1 - b_3 + b_4) \sigma_{yy}] \sigma_{zz}^2 + \frac{2}{9} (b_1 - b_4) \sigma_{xx} \sigma_{yy} \sigma_{zz} \\ & - \frac{\tau_{xz}^2}{3} [2b_9 \sigma_{yy} - b_8 \sigma_{zz} - (2b_9 - b_8) \sigma_{xx}] - \frac{\tau_{xy}^2}{3} [2b_{10} \sigma_{zz} - b_5 \sigma_{yy} - (2b_{10} - b_5) \sigma_{xx}] \\ & - \frac{\tau_{yz}^2}{3} [(b_6 + b_7) \sigma_{xx} - b_6 \sigma_{yy} - b_7 \sigma_{zz}] + 2b_{11} \tau_{xy} \tau_{xz} \tau_{yz} \end{aligned} \quad (\text{B.44})$$

Os quais são directamente introduzidos no critério de Drucker 1949,

$$(J_2^o)^3 - c(J_3^o)^2 = 27 \left( \frac{Y}{3} \right)^6 \quad (\text{B.45})$$

Obtém-se daí a generalização deste critério à anisotropia ortotrópica.

O critério de Cazacu & Barlat 2001 envolve 18 parâmetros de anisotropia ( $a_1 \dots a_6, b_1 \dots b_{11}$  e  $c$ ) para estados triaxiais, e 11 para os estados planos de tensão. Para considerar o caso particular da isotropia basta devolver o valor unitário aos parâmetros de anisotropia, obtendo-se  $J_2^o = J_2$  e  $J_3^o = J_3$ , voltando o critério de Drucker 1949 à sua forma original.

Quando se trata de processos de conformação de chapa é aceitável admitir que estas se encontram sujeitas a um estado plano de tensão. Por isso, o critério de Cazacu & Barlat 2001 é usado com 11 parâmetros de anisotropia, que podem ser determinados à base das tensões limite de elasticidade  $Y_\alpha$  e dos coeficientes de anisotropia  $r_\alpha$ , obtidos a partir de ensaios de tração uniaxial realizados em 5 direcções diferentes, e da tensão limite de elasticidade  $\sigma_b$  ou coeficiente de anisotropia  $r_b$ , em tração biaxial. A partir da teoria da representação de funções tensor, Cazacu e Barlat tiveram êxito em descrever o comportamento tração/compressão assimétrico exibido por certas ligas com estrutura HC (Hexagonal Compacta) (Cazacu and Barlat, 2004). A maior vantagem deste critério de cedência consiste na sua capacidade de descrever com precisão o comportamento de tração/compressão de determinadas ligas de magnésio e titânio.

### Critério de Vegter (2006)

A partir de pontos da superfície de plasticidade determinados experimentalmente, Vegter *et al.* (1995, 2006) descreveu a superfície de plasticidade no primeiro quadrante recorrendo à interpolação de Bézier. Como tal, o critério de Vegter requer a determinação de três parâmetros para cada ponto de referência (as duas tensões principais  $\sigma_1$  e  $\sigma_2$  e o vetor de deformação  $\rho = \frac{d\varepsilon_2}{d\varepsilon_1}$ ), perfazendo um valor total de 17 parâmetros para a descrição total da anisotropia planar.

A expressão analítica do critério de Vegter é dada por

$$\begin{pmatrix} \sigma_1 \\ \sigma_2 \end{pmatrix} = (1 - \lambda)^2 \begin{pmatrix} \sigma_1 \\ \sigma_2 \end{pmatrix}_i^r + 2\lambda(1 - \lambda) \begin{pmatrix} \sigma_1 \\ \sigma_2 \end{pmatrix}_i^h + \lambda^2 \begin{pmatrix} \sigma_1 \\ \sigma_2 \end{pmatrix}_{i+1}^r \quad (\text{B.46})$$

para  $\sigma_e$  e o ângulo  $\varphi$  onde

$$\begin{pmatrix} \sigma_1 \\ \sigma_2 \end{pmatrix}_{i+1}^r = \sum_{j=0}^{m \cos} \begin{pmatrix} a_1^j \\ a_2^j \end{pmatrix}_i \cos(2j\varphi) \quad (\text{B.47})$$

é uma expansão trigonométrica associada ao ponto de referência;

$$R(\varphi) = \sum_{j=0}^{m \cos} b^j \cos(2j\varphi) \quad (\text{B.48})$$

é a interpolação cosseno da função  $R(\varphi)$ ;  $\varphi$ , é o ângulo entre as direções principais e os eixos ortotrópicos;  $\lambda$  é o parâmetro da função de Bézier;  $r$  é o índice que denota o ponto de referência;  $h$  é o índice que denota o ponto de ruptura;  $\begin{pmatrix} a_1^j \\ a_2^j \end{pmatrix}_i^r$  são os parâmetros da interpolação trigonométrica a serem determinados nos pontos de referência;  $b^j$  são os parâmetros da interpolação trigonométrica da função  $R$ .

A maior vantagem deste critério é a flexibilidade que possui associada ao elevado número de parâmetros. Como desvantagens podem ser apontadas a formulação matemática complexa, a qual dificulta o tratamento numérico e cálculo computacional, o número elevado de testes experimentais requeridos (tração uniaxial, tração biaxial, deformação plana e corte puro) e a necessidade de elevadas competências matemáticas do utilizador.

#### **Critério de Barlat 2000 (Yld2000-2d)**

Barlat *et al.* (2000) apresentam um novo critério de plasticidade anisotrópico especialmente direcionado para o estado plano de tensão (2D).

Considere-se a transformação linear definida pela expressão

$$\mathbf{X} = \mathbf{C} \cdot \mathbf{s} \quad (\text{B.49})$$

onde  $\mathbf{s}$  é o tensor tensão desviador e  $\mathbf{X}$  representa o tensor tensão linearmente transformado. Neste caso, são obtidos 7 coeficientes independentes para o estado plano de tensão. Contudo, apenas um coeficiente está disponível para  $\sigma_{45}$  e  $r_{45}$ . Neste sentido, Barlat *et al.* (2003) refere que, no contexto das transformações lineares, é possível obter coeficientes adicionais pela utilização de duas transformações respetivamente associadas a duas funções de cedência isotrópicas diferentes.

Assim, Barlat *et al.* (2003) propõem uma função de cedência expressa pela seguinte relação

$$\Phi = \Phi' + \Phi'' = 2\sigma_e^a \quad (\text{B.50})$$

onde

$$\Phi' = |S_1 - S_2|^a \quad (\text{B.51})$$

$$\Phi'' = |2S_2 + S_1|^a + |2S_1 + S_2|^a \quad (\text{B.52})$$

sendo  $S_1$  e  $S_2$  as tensões desviadoras principais e ' $a$ ' um expoente determinado com base na estrutura cristalográfica do material.

Aplicando a transformação linear a cada função isotrópica definida pelas equações (B.51) e (B.52) obtém-se a função de cedência

$$\Phi = \Phi'(X') + \Phi''(X'') = 2\sigma_e^a \quad (\text{B.53})$$

onde  $\sigma_e$  é a tensão equivalente e  $'a'$  um coeficiente do material e

$$\Phi' = |X'_1 - X'_2|^a \quad (\text{B.54})$$

$$\Phi'' = |2X''_2 + X''_1|^a + |2X''_1 + X''_2|^a \quad (\text{B.55})$$

e

$$\mathbf{X}' = \mathbf{C}' \cdot \mathbf{s} = \mathbf{C}' \cdot \mathbf{T} \cdot \boldsymbol{\sigma} = \mathbf{L}' \cdot \boldsymbol{\sigma} \quad (\text{B.56})$$

$$\mathbf{X}'' = \mathbf{C}'' \cdot \mathbf{s} = \mathbf{C}'' \cdot \mathbf{T} \cdot \boldsymbol{\sigma} = \mathbf{L}'' \cdot \boldsymbol{\sigma} \quad (\text{B.57})$$

$\mathbf{T}$  é a matrix que transforma o tensor de tensão Cauchy  $\boldsymbol{\sigma}$  no seu desviador  $\mathbf{s}$ :

$$\mathbf{T} = \begin{bmatrix} 2/3 & -1/3 & 0 \\ -1/3 & 2/3 & 0 \\ 0 & 0 & 1 \end{bmatrix} \quad (\text{B.58})$$

sendo  $C'$  e  $C''$  as transformações lineares.

No sistema de referência associado à simetria do material

$$\begin{bmatrix} X'_{11} \\ X'_{22} \\ X'_{12} \end{bmatrix} = \begin{bmatrix} C'_{11} & C'_{12} & 0 \\ C'_{21} & C'_{22} & 0 \\ 0 & 0 & C'_{66} \end{bmatrix} \begin{bmatrix} S_{11} \\ S_{22} \\ S_{12} \end{bmatrix} \quad (\text{B.59})$$

e

$$\begin{bmatrix} X''_{11} \\ X''_{22} \\ X''_{12} \end{bmatrix} = \begin{bmatrix} C''_{11} & C''_{12} & 0 \\ C''_{21} & C''_{22} & 0 \\ 0 & 0 & C''_{66} \end{bmatrix} \begin{bmatrix} S_{11} \\ S_{22} \\ S_{12} \end{bmatrix} \quad (\text{B.60})$$

Visto que  $\Phi'$  depende de  $X'_1 - X'_2$ , apenas 3 coeficientes permanecem independentes em  $C'$ . Em  $C''$  existem 5 coeficientes independentes. Assim, as duas transformações, perfazem um total de 8 coeficientes independentes.

Os valores principais de  $X_1$  e  $X_2$  de  $\mathbf{X}'$  e  $\mathbf{X}''$  são dados por

$$X_1 = \frac{1}{2} \left( X_{11} + X_{22} + \sqrt{(X_{11} - X_{22})^2 + 4X_{12}^2} \right) \quad (\text{B.61})$$

$$X_2 = \frac{1}{2} \left( X_{11} + X_{22} - \sqrt{(X_{11} - X_{22})^2 + 4X_{12}^2} \right) \quad (\text{B.62})$$

Os coeficientes de  $\mathbf{L}'$  e  $\mathbf{L}''$  podem ser expressos por

$$\begin{bmatrix} L'_{11} \\ L'_{12} \\ L'_{21} \\ L'_{22} \\ L'_{66} \end{bmatrix} = \begin{bmatrix} 2/3 & 0 & 0 \\ -1/3 & 0 & 0 \\ 0 & -1/3 & 0 \\ 0 & 2/3 & 0 \\ 0 & 0 & 1 \end{bmatrix} \begin{bmatrix} \alpha_1 \\ \alpha_2 \\ \alpha_7 \end{bmatrix} \quad (\text{B.63})$$

$$\begin{bmatrix} L'_{11} \\ L'_{12} \\ L'_{21} \\ L'_{22} \\ L'_{66} \end{bmatrix} = \begin{bmatrix} -2 & 2 & 8 & -2 & 0 \\ 1 & -4 & -4 & 4 & 0 \\ 4 & -4 & -4 & 1 & 0 \\ -2 & 8 & 2 & -2 & 0 \\ 0 & 0 & 0 & 0 & 1 \end{bmatrix} \begin{bmatrix} \alpha_3 \\ \alpha_4 \\ \alpha_5 \\ \alpha_6 \\ \alpha_8 \end{bmatrix} \quad (\text{B.64})$$

Para determinar os 8 coeficientes associados às transformações lineares são necessários 8 parâmetros de material. Os testes de tração uniaxial na direção de laminagem, diagonal e transversal, junto com os testes de tração biaxial fornecem apenas 7 parâmetros do material (3 tensões de cedência uniaxial, 3 coeficientes de anisotropia uniaxial e tensão de cedência biaxial). Barlat adoptou o coeficiente biaxial de anisotropia  $r_b$  como o oitavo parâmetro de material no procedimento de identificação dos parâmetros constitutivos.

#### **Crítério de Banabic-Balan-Comsa (BBC2000, 2003, 2005)**

No ano 2000, os membros do CERTETA iniciaram um projeto de pesquisa cujo principal objetivo era desenvolver um modelo capaz de fornecer uma descrição mais precisa da superfície de plasticidade comparativamente com os existentes nessa altura. Partindo do critério isotrópico de Hershey, foram adicionados coeficientes à formulação matemática original, para desenvolver um novo critério mais flexível. A última versão deste critério incorpora oito coeficientes, o que, por sua vez, conduz a um procedimento de identificação que utiliza oito parâmetros mecânicos (três tensões de cedência uniaxial, três coeficientes de anisotropia uniaxial, uma tensão de cedência biaxial e um coeficiente de anisotropia biaxial).

A primeira formulação do critério de cedência proposto por Banabic *et al.* (2000) aparece na seguinte forma

$$\bar{\sigma} = [a(b\Gamma + c\Psi)^{2k} + a(b\Gamma + c\Psi)^{2k} + (1 - a)(2c\Psi)^{2k}]^{\frac{1}{2k}} \quad (\text{B.65})$$

em que  $a$ ,  $b$ ,  $c$  e  $k$  são parâmetros do material, enquanto  $\Gamma$  e  $\Psi$  são funções do segundo e terceiro invariantes do tensor tensão transformado  $s' = \mathbb{L}\sigma$ , onde  $\mathbb{L}$  é um tensor de 4ª ordem.

Associando o sistema coordenado de referência (1,2,3) às direções de ortotropia tem-se

$$s'_{11} = d\sigma_{11} + e\sigma_{22}$$

$$\begin{aligned}
s'_{22} &= e\sigma_{11} + f\sigma_{22} \\
s'_{33} &= -(d+e)\sigma_{11} - (e+f)\sigma_{22} \\
s'_{12} &= g\sigma_{12} \\
s'_{13} &= s'_{13} = 0
\end{aligned} \tag{B.66}$$

onde  $d, e, f$  e  $g$  são as quatro componentes independentes do tensor  $\mathbb{L}$  para o estado de tensão plana.

As expressões das funções  $\Gamma$  e  $\Psi$  em termos de suas componentes de tensão são

$$\begin{aligned}
\Gamma &= M\sigma_{11} + N\sigma_{22} \\
\Psi &= \sqrt{(P\sigma_{11} + Q\sigma_{22})^2 + R\sigma_{12}^2}
\end{aligned} \tag{B.67}$$

onde

$$M = d + e; N = e + f; P = \frac{d-e}{2}; Q = \frac{e-f}{2}; R = g^2 \tag{B.68}$$

A convexidade da superfície de cedência descrita por (B.65) é garantida se  $a \in [0,1]$  e  $k$  for um número inteiro e positivo. A distribuição tensão de cedência uniaxial, da tensão de cedência equibiaxial e dos coeficientes de anisotropia no plano da chapa para direcções segundo uma inclinação  $\theta \in [0,90^\circ]$  para o critério de cedência BBC2000 é apresentada em Cosovici (2006).

A forma da superfície de cedência é definida pelos parâmetros de material  $a, b, c, d, e, f, g$  e  $k$ . O parâmetro  $k$  é definido em função do tipo da estrutura cristalográfica do material sendo  $k=3$  para ligas com estrutura CCC e  $k=4$  para ligas com estrutura CFC. Os restantes sete coeficientes são determinados de forma que o modelo consiga a melhor correlação possível entre os parâmetros mecânicos experimentais e os parâmetros mecânicos teóricos. Assim, é possível obter os seus valores pela resolução de um sistema de sete equações não-lineares.

Posteriormente, Banabic *et al.* (2003) apresentou uma melhoria ao seu modelo pela introdução de mais um parâmetro mecânico, o coeficiente de anisotropia biaxial. O novo critério proposto (BBC2003) passa a ter a seguinte forma:

$$\bar{\sigma} = [a(\Gamma + \Psi)^{2k} + a(\Gamma - \Psi)^{2k} + (1-a)(2\Lambda)^{2k}]^{\frac{1}{2k}} \tag{B.69}$$

onde  $k \in \mathbb{N} \geq 1$  e  $0 \leq a \leq 1$  são parâmetros de material, enquanto  $\Gamma, \Psi$  e  $\Lambda$  são funções dependentes das componentes planares do tensor tensão

$$\begin{aligned}
\Gamma &= \frac{M\sigma_{11} + N\sigma_{22}}{2} \\
\Psi &= \sqrt{\left(\frac{N\sigma_{11} + P\sigma_{22}}{2}\right)^2 + Q^2\sigma_{12}\sigma_{21}}
\end{aligned} \tag{B.70}$$

$$\Lambda = \sqrt{\left(\frac{R\sigma_{11} + S\sigma_{22}}{2}\right)^2 + T^2\sigma_{12}\sigma_{21}}$$

em que as quantidades  $M, N, P, Q, R, S$  e  $T$  também são parâmetros de material. Mais detalhes a respeito da variação da tensão de cedência uniaxial, da variação do coeficiente de anisotropia e do procedimento de identificação de parâmetros do critério de cedência BBC2003 podem ser encontrados em Banabic *et al.* (2003) e Paraianu (2006).

Assim como em BBC2000, os outros oito parâmetros constitutivos (além de  $k$ ) são determinados de forma que o modelo consiga a melhor correlação possível entre os parâmetros mecânicos experimentais ( $\sigma_0^{\text{exp}}, \sigma_{45}^{\text{exp}}, \sigma_{90}^{\text{exp}}, \sigma_b^{\text{exp}}, r_0^{\text{exp}}, r_{45}^{\text{exp}}, r_{90}^{\text{exp}}$  e  $r_b^{\text{exp}}$ ) e os parâmetros mecânicos teóricos ( $\sigma_0, \sigma_{45}, \sigma_{90}, \sigma_b, r_0, r_{45}, r_{90}$  e  $r_b$ ). É possível obter um valor para os parâmetros de material pela resolução numérica de um sistema de oito equações não-lineares. Contudo, para evitar soluções múltiplas, pode-se recorrer a uma estratégia de identificação mais eficiente impondo a minimização da seguinte função de erro

$$\begin{aligned} \mathcal{F}(a, M, N, P, Q, R, S, T) = & \left(\frac{r_0}{r_0^{\text{exp}}} + 1\right)^2 + \left(\frac{r_{45}}{r_{45}^{\text{exp}}} + 1\right)^2 + \left(\frac{r_{90}}{r_{90}^{\text{exp}}} + 1\right)^2 + \left(\frac{r_b}{r_b^{\text{exp}}} + 1\right)^2 + \left(\frac{\sigma_0}{\sigma_0^{\text{exp}}} + 1\right)^2 \\ & + \left(\frac{\sigma_{45}}{\sigma_{45}^{\text{exp}}} + 1\right)^2 + \left(\frac{\sigma_{90}}{\sigma_{90}^{\text{exp}}} + 1\right)^2 + \left(\frac{\sigma_b}{\sigma_b^{\text{exp}}} + 1\right)^2 \end{aligned} \quad (\text{B.71})$$

Como *vantagens* destes modelos enumeram-se

- Expressões simples para as funções de cedência.
- A boa precisão em descrever as superfícies de plasticidade e a distribuição planar das tensões de cedência uniaxial e dos coeficientes de anisotropia uniaxial.
- A forma da superfície de plasticidade segue de perto os resultados dos modelos de textura.
- O custo computacional em simulações de processos de conformação complexos não aumenta significativamente.
- Os modelos podem ser usados em casos mesmo quando não estão disponíveis todos os oito parâmetros mecânicos (por exemplo, 2, 4, 5, 6, ou 7).
- Os modelos podem ser reduzidos às formulações clássicas de Hill 1948 ou Barlat 1989.

Como *desvantagens* podem ser mencionadas

- A formulação do critério de cedência não mostra ser muito *user-friendly*.
- Os coeficientes da função de cedência não apresentam um significado físico direto.
- A generalização aos estados de deformação tridimensionais é difícil.

Uma nova versão deste critério (BBC2005) apresentada por Banabic *et al.* (2005) foi implementada no software comercial de elementos finitos Autoform. Segundo este modelo assume-se que a chapa

apresenta com um comportamento plástico ortotrópico e está sujeita a um estado plano de tensão. Nestas condições, a superfície de plasticidade é expressa pela equação

$$\Phi(\sigma_{\alpha\beta}, Y) := \bar{\sigma}(\sigma_{\alpha\beta}) - Y = 0 \quad (\text{B.72})$$

em que  $\bar{\sigma}(\sigma_{\alpha\beta}) > 0$  é a tensão equivalente do critério de BBC2005,  $Y > 0$  é o parâmetro de cedência e  $\sigma_{\alpha\beta} = \sigma_{\beta\alpha}$  ( $\alpha, \beta = 1, 2$ ) são as componentes planares do tensor tensão expressas no sistema referencial de ortotropia. Neste critério, qualquer quantidade representando uma tensão de cedência pode ser atribuída a  $Y$ . Por exemplo,  $Y$  pode ser uma tensão de cedência uniaxial  $Y_\theta$  determinada para uma direção que difere de um ângulo  $\theta$  em relação à direção de laminagem.

A lei de plasticidade associada à superfície de plasticidade de BBC2005 é descrita pela equação

$$\dot{\varepsilon}_{\alpha\beta}^p = \dot{\lambda} \frac{\partial \Phi}{\partial \sigma_{\alpha\beta}}, \quad \alpha, \beta = 1, 2 \quad (\text{B.73})$$

onde  $\dot{\varepsilon}_{\alpha\beta}^p = \dot{\varepsilon}_{\beta\alpha}^p$  ( $\alpha, \beta = 1, 2$ ) são as componentes planares do tensor velocidade de deformação (expressas na mesma base correspondente às componentes do tensor tensão) e  $\dot{\lambda} \geq 0$  é um multiplicador escalar.

Recorrendo à equação (B.72), conclui-se que as derivadas parciais da função  $\Phi$  em relação às componentes planares do tensor tensão, podem ser obtidas através das derivadas parciais da tensão equivalente

$$\frac{\partial \Phi}{\partial \sigma_{\alpha\beta}} = \frac{\partial \bar{\sigma}}{\partial \sigma_{\alpha\beta}}, \quad \alpha, \beta = 1, 2 \quad (\text{B.74})$$

A tensão equivalente requerida é dada pela seguinte expressão:

$$\bar{\sigma} = [a(\Lambda + \Gamma)^{2k} + a(\Lambda - \Gamma)^{2k} + b(\Lambda + \Psi)^{2k} + b(\Lambda - \Psi)^{2k}]^{\frac{1}{2k}} \quad (\text{B.75})$$

onde  $k \in \mathbb{N} \geq 1$  e  $a, b > 0$  são parâmetros de material, enquanto  $\Gamma$ ,  $\Psi$  e  $\Lambda$  são funções dependentes das componentes planares do tensor tensão

$$\begin{aligned} \Gamma &= L\sigma_{11} + M\sigma_{22} \\ \Lambda &= \sqrt{(N\sigma_{11} - P\sigma_{22})^2 + \sigma_{12}\sigma_{21}} \\ \Psi &= \sqrt{(Q\sigma_{11} - R\sigma_{22})^2 + \sigma_{12}\sigma_{21}} \end{aligned} \quad (\text{B.76})$$

em que as quantidades  $L, M, N, P, Q$  e  $R$  também são parâmetros de material.

As equações (B.74), (B.75) e (B.76) conduzem à expressão



$$\frac{\partial \Phi}{\partial \sigma_{\alpha\beta}} = \frac{\partial \bar{\sigma}}{\partial \Gamma} \frac{\partial \Gamma}{\partial \sigma_{\alpha\beta}} + \frac{\partial \bar{\sigma}}{\partial \Lambda} \frac{\partial \Lambda}{\partial \sigma_{\alpha\beta}} + \frac{\partial \bar{\sigma}}{\partial \Psi} \frac{\partial \Psi}{\partial \sigma_{\alpha\beta}} \quad \alpha, \beta = 1, 2 \quad (\text{B.77})$$

em que

$$\begin{aligned} \frac{\partial \bar{\sigma}}{\partial \Gamma} &= \frac{a}{\bar{\sigma}^{2k-1}} [(\Lambda + \Gamma)^{2k-1} - (\Lambda - \Gamma)^{2k-1}] \\ \frac{\partial \bar{\sigma}}{\partial \Lambda} &= \frac{1}{\bar{\sigma}^{2k-1}} [(\Lambda + \Gamma)^{2k-1} + (\Lambda - \Gamma)^{2k-1}] + b [(\Lambda + \Psi)^{2k-1} + (\Lambda - \Psi)^{2k-1}] \\ \frac{\partial \bar{\sigma}}{\partial \Psi} &= \frac{b}{\bar{\sigma}^{2k-1}} [(\Lambda + \Psi)^{2k-1} - (\Lambda - \Psi)^{2k-1}] \end{aligned} \quad (\text{B.78})$$

e,

$$\begin{aligned} \frac{\partial \Gamma}{\partial \sigma_{11}} &= L, & \frac{\partial \Gamma}{\partial \sigma_{22}} &= M, & \frac{\partial \Gamma}{\partial \sigma_{12}} &= 0, & \frac{\partial \Gamma}{\partial \sigma_{21}} &= 0, \\ \frac{\partial \Lambda}{\partial \sigma_{11}} &= \frac{N(N\sigma_{11} - P\sigma_{22})}{\Lambda}, & \frac{\partial \Lambda}{\partial \sigma_{22}} &= -\frac{P(N\sigma_{11} - P\sigma_{22})}{\Lambda}, \\ & & \frac{\partial \Lambda}{\partial \sigma_{12}} &= \frac{\sigma_{21}}{2\Lambda}, & \frac{\partial \Lambda}{\partial \sigma_{21}} &= \frac{\sigma_{12}}{2\Lambda}, \\ \frac{\partial \Psi}{\partial \sigma_{11}} &= \frac{Q(Q\sigma_{11} - R\sigma_{22})}{\Psi}, & \frac{\partial \Psi}{\partial \sigma_{22}} &= -\frac{R(Q\sigma_{11} - R\sigma_{22})}{\Psi}, \\ & & \frac{\partial \Psi}{\partial \sigma_{12}} &= \frac{\sigma_{21}}{2\Psi}, & \frac{\partial \Psi}{\partial \sigma_{21}} &= \frac{\sigma_{12}}{2\Psi} \end{aligned} \quad (\text{B.79})$$

a qual possibilita expressar a lei de plasticidade associada (B.73) como dependente das componentes do tensor tensão  $\sigma_{\alpha\beta}$  ( $\alpha, \beta = 1, 2$ ).

O procedimento de identificação dos parâmetros constitutivos  $a, b, L, M, N, P, Q$  e  $R$  consiste na resolução do seguinte sistema de oito equações não-lineares

$$\begin{aligned} \tilde{Y}_0 &= Y_0, \tilde{Y}_{45} = Y_{45}, \tilde{Y}_{90} = Y_{90} \\ \tilde{r}_0 &= r_0, \tilde{r}_{45} = r_{45}, \tilde{r}_{90} = r_{90} \\ \tilde{Y}_b &= Y_b, \quad \tilde{r}_b = r_b \end{aligned} \quad (\text{B.80})$$

onde:

- $\tilde{Y}_0, \tilde{Y}_{45}$  e  $\tilde{Y}_{90}$  são as tensões de cedência teóricas correspondentes à tração pura para as direcções de  $0^\circ, 45^\circ$  e  $90^\circ$  em relação à direcção de laminagem.
- $\tilde{r}_0, \tilde{r}_{45}$  e  $\tilde{r}_{90}$  são os coeficientes de anisotropia plástica uniaxial teóricos associados às direcções de  $0^\circ, 45^\circ$  e  $90^\circ$  em relação à direcção de laminagem.

- $\tilde{Y}_b$  é a tensão de cedência teórica correspondentes à tração biaxial para as direcções de 0° e 90° em relação à direcção de laminagem.
- $\tilde{r}_b$  é o coeficiente de anisotropia plástica biaxial teórico associado às direcções de 0° e 90° em relação à direcção de laminagem.

Portanto, este procedimento de identificação necessita de fórmulas matemáticas específicas para determinar cada um dos parâmetros mecânicos teóricos necessários.

Para calcular a tensão de cedência uniaxial teórica  $\tilde{Y}_\theta$  tem-se a seguinte expressão

$$\tilde{Y}_\theta = \frac{Y}{F(\theta)} \quad (\text{B.81})$$

com a qual se podem calcular os parâmetros  $\tilde{Y}_0$ ,  $\tilde{Y}_{45}$  e  $\tilde{Y}_{90}$  para  $\theta = 0^\circ, 45^\circ$  e  $90^\circ$ , respectivamente.

A função  $F(\theta)$  é dada por

$$F(\theta) = [a(\Lambda_\theta + \Gamma_\theta)^{2k} + a(\Lambda_\theta - \Gamma_\theta)^{2k} + b(\Lambda_\theta + \Psi_\theta)^{2k} + b(\Lambda_\theta - \Psi_\theta)^{2k}]^{\frac{1}{2k}} \quad (\text{B.82})$$

enquanto as quantidades  $\Gamma_\theta$ ,  $\Lambda_\theta$  e  $\Psi_\theta$  são definidas por

$$\begin{aligned} \Gamma_\theta &= L\cos^2\theta + M\sin^2\theta \\ \Lambda_\theta &= \sqrt{(N\cos^2\theta - P\sin^2\theta)^2 + \sin^2\theta\cos^2\theta} \\ \Psi_\theta &= \sqrt{(Q\cos^2\theta - R\sin^2\theta)^2 + \sin^2\theta\cos^2\theta} \end{aligned} \quad (\text{B.83})$$

O coeficiente de anisotropia plástica uniaxial teórico  $\tilde{r}_\theta$  pode ser determinado com base na expressão

$$\tilde{r}_\theta = \frac{[F(\theta)]^{2k}}{G(\theta)} - 1 \quad (\text{B.84})$$

com a qual se podem calcular os parâmetros  $\tilde{r}_0$ ,  $\tilde{r}_{45}$  e  $\tilde{r}_{90}$  para  $\theta = 0^\circ, 45^\circ$  e  $90^\circ$ , respectivamente.

A função  $F(\theta)$  é dada pela equação (B.82) ao passo que a função  $G(\theta)$  é dada por

$$\begin{aligned} G(\theta) &= a \left[ \frac{(N - P)(N\cos^2\theta - P\sin^2\theta)}{\Lambda_\theta} + L + M \right] (\Lambda_\theta + \Gamma_\theta)^{2k-1} \\ &\quad + a \left[ \frac{(N - P)(N\cos^2\theta - P\sin^2\theta)}{\Lambda_\theta} - L - M \right] (\Lambda_\theta - \Gamma_\theta)^{2k-1} \\ &\quad + b \left[ \frac{(N - P)(N\cos^2\theta - P\sin^2\theta)}{\Lambda_\theta} + \frac{(Q - R)(Q\cos^2\theta - R\sin^2\theta)}{\Psi_\theta} \right] (\Lambda_\theta + \Psi_\theta)^{2k-1} + \\ &\quad + b \left[ \frac{(N - P)(N\cos^2\theta - P\sin^2\theta)}{\Lambda_\theta} - \frac{(Q - R)(Q\cos^2\theta - R\sin^2\theta)}{\Psi_\theta} \right] (\Lambda_\theta - \Psi_\theta)^{2k-1} \end{aligned} \quad (\text{B.85})$$

Para calcular a tensão de cedência biaxial teórica  $\tilde{Y}_b$  recorre-se à equação

$$\tilde{Y}_b = \frac{Y}{F_b} \quad (\text{B.86})$$

endo que a função  $F_b$  é obtida por

$$F_b = [a(\Lambda_b + \Gamma_b)^{2k} + a(\Lambda_b - \Gamma_b)^{2k} + b(\Lambda_b + \Psi_b)^{2k} + b(\Lambda_b - \Psi_b)^{2k}]^{\frac{1}{2k}} \quad (\text{B.87})$$

onde

$$\begin{aligned} \Gamma_b &= L + M \\ \Lambda_b &= \sqrt{(N - P)^2} = |N - P| \\ \Psi_b &= \sqrt{(Q - R)^2} = |Q - R| \end{aligned} \quad (\text{B.88})$$

Por último, o parâmetro mecânico teórico  $\tilde{r}_b$  é dado pela expressão

$$\tilde{r}_b = \frac{F_b^{2k}}{G_b} - 1 \quad (\text{B.89})$$

em que a função  $F_b$  é dada pela equação (B.87) ao passo que a função  $G_b$  é dada por

$$\begin{aligned} G_b &= a \left[ \frac{N(N - P)}{\Lambda_b} + L \right] (\Lambda_b + \Gamma_b)^{2k-1} + a \left[ \frac{N(N - P)}{\Lambda_b} - L \right] (\Lambda_b - \Gamma_b)^{2k-1} \\ &+ b \left[ \frac{N(N - P)}{\Lambda_b} + \frac{Q(Q - R)}{\Psi_b} \right] (\Lambda_b + \Psi_b)^{2k-1} + b \left[ \frac{N(N - P)}{\Lambda_b} - \frac{Q(Q - R)}{\Psi_b} \right] (\Lambda_b - \Psi_b)^{2k-1} \end{aligned} \quad (\text{B.90})$$

As quantidades necessárias ao procedimento de identificação determinadas podem ainda ser apresentadas em uma forma mais conveniente pelas seguintes igualdades

$$\begin{aligned} [F(0^\circ)]^{2k} &= y_0^{2k}, \quad [F(45^\circ)]^{2k} = y_{45}^{2k} \\ [F(90^\circ)]^{2k} &= y_{90}^{2k}, \quad F_b^{2k} = y_b^{2k} \end{aligned} \quad (\text{B.91})$$

e

$$\begin{aligned} G(0^\circ) &= \frac{1}{r_0+1} y_0^{2k}, \quad G(45^\circ) = \frac{1}{r_{45}+1} y_{45}^{2k} \\ G(90^\circ) &= \frac{1}{r_{90}+1} y_{90}^{2k}, \quad G_b = \frac{1}{r_b+1} y_b^{2k} \end{aligned} \quad (\text{B.92})$$

em que

$$y_0 = \frac{Y}{Y_0}, \quad y_{45} = \frac{Y}{Y_{45}}, \quad y_{90} = \frac{Y}{Y_{90}}, \quad y_b = \frac{Y}{Y_b} \quad (\text{B.93})$$

representam valores de tensão de cedência experimentais normalizados.

Finalmente, com algum tratamento matemático, estas expressões podem ser reescritas em termos dos parâmetros constitutivos desconhecidos  $a, b, L, M, N, P, Q$  e  $R$  por

$$\begin{aligned}
& a(N + L)^{2k} + a(N - L)^{2k} + b(N + Q)^{2k} + b(N - Q)^{2k} = y_0^{2k} \\
& a \left[ \sqrt{(N - P)^2 + 1} + L + M \right]^{2k} + a \left[ \sqrt{(N - P)^2 + 1} - L - M \right]^{2k} + b \left[ \sqrt{(N - P)^2 + 1} + \sqrt{(Q - R)^2 + 1} \right]^{2k} \\
& \quad + b \left[ \sqrt{(N - P)^2 + 1} - \sqrt{(Q - R)^2 + 1} \right]^{2k} = (2y_{45})^{2k} \\
& a(P + M)^{2k} + a(P - M)^{2k} + b(P + R)^{2k} + b(P - R)^{2k} = y_{90}^{2k} \\
& a(N - P + L + M)^{2k} + a(N - P - L - M)^{2k} + b(N - P + Q - R)^{2k} + b(N - P - Q + R)^{2k} = y_b^{2k} \\
& a(P - M)(N + L)^{2k-1} + a(P + M)(N - L)^{2k-1} + b(P + R)(N + Q)^{2k-1} + b(P - R)(N - Q)^{2k-1} \\
& \quad = \frac{r_0}{r_0 + 1} y_0^{2k} \\
& a\sqrt{(Q - R)^2 + 1} \left\{ \left[ \sqrt{(N - P)^2 + 1} + L + M \right]^{2k-1} + \left[ \sqrt{(N - P)^2 + 1} - L - M \right]^{2k-1} \right\} \\
& \quad + b \left\{ \left[ \sqrt{(N - P)^2 + 1} + \sqrt{(Q - R)^2 + 1} \right]^{2k} - \left[ \sqrt{(N - P)^2 + 1} - \sqrt{(Q - R)^2 + 1} \right]^{2k} \right\} \\
& \quad = \sqrt{(N - P)^2 + 1} \sqrt{(Q - R)^2 + 1} \frac{r_{45} + 1/2}{r_{45} + 1} (2y_{45})^{2k} \\
& a(N - L)(P + M)^{2k-1} + a(N + L)(P - M)^{2k-1} + b(N + Q)(P + R)^{2k-1} + b(N - Q)(P - R)^{2k-1} \\
& \quad = \frac{r_{90}}{r_{90} + 1} y_{90}^{2k} \\
& a(N + L)(N - P + L + M)^{2k-1} + a(N - L)(N - P - L - M)^{2k-1} + b(N + Q)(N - P + Q - R)^{2k-1} \\
& \quad + b(N - Q)(N - P - Q + R)^{2k-1} = \frac{1}{r_b + 1} y_b^{2k} \tag{B.94}
\end{aligned}$$

As equações (B.94) formam um sistema de oito equações não-lineares cuja solução numérica é obtida através de um método de Newton.

Este sistema pode ser escrito na sua forma genérica como

$$f_i(a, b, L, M, N, P, Q, R) = 0, \quad i = 1, 2, \dots, 8 \tag{B.95}$$

onde

1.  $f_1 = a(N + L)^{2k} + a(N - L)^{2k} + b(N + Q)^{2k} + b(N - Q)^{2k} - y_0^{2k}$

$$\begin{aligned}
2. f_2 &= a \left[ \sqrt{(N-P)^2 + 1} + L + M \right]^{2k} + a \left[ \sqrt{(N-P)^2 + 1} - L - M \right]^{2k} + \\
& b \left[ \sqrt{(N-P)^2 + 1} + \sqrt{(Q-R)^2 + 1} \right]^{2k} + b \left[ \sqrt{(N-P)^2 + 1} - \sqrt{(Q-R)^2 + 1} \right]^{2k} - (2y_{45})^{2k} \\
3. f_3 &= a(P+M)^{2k} + a(P-M)^{2k} + b(P+R)^{2k} + b(P-R)^{2k} = y_{90}^{2k} \\
4. f_4 &= a(N-P+L+M)^{2k} + a(N-P-L-M)^{2k} + b(N-P+Q-R)^{2k} + b(N-P-Q+R)^{2k} = y_b^{2k} \\
5. f_5 &= a(P-M)(N+L)^{2k-1} + a(P+M)(N-L)^{2k-1} + b(P+R)(N+Q)^{2k-1} + \\
& b(P-R)(N-Q)^{2k-1} - \frac{r_0}{r_0+1} y_0^{2k} \\
6. f_6 &= a \sqrt{(Q-R)^2 + 1} \left\{ \left[ \sqrt{(N-P)^2 + 1} + L + M \right]^{2k-1} + \left[ \sqrt{(N-P)^2 + 1} - L - M \right]^{2k-1} \right\} + \\
& b \left\{ \left[ \sqrt{(N-P)^2 + 1} + \sqrt{(Q-R)^2 + 1} \right]^{2k} - \left[ \sqrt{(N-P)^2 + 1} - \sqrt{(Q-R)^2 + 1} \right]^{2k} \right\} - \\
& \sqrt{(N-P)^2 + 1} \sqrt{(Q-R)^2 + 1} \frac{r_{45} + 1/2}{r_{45} + 1} (2y_{45})^{2k} \\
7. f_7 &= a(N-L)(P+M)^{2k-1} + a(N+L)(P-M)^{2k-1} + b(N+Q)(P+R)^{2k-1} + \\
& b(N-Q)(P-R)^{2k-1} - \frac{r_{90}}{r_{90}+1} y_{90}^{2k} \\
8. f_8 &= a(N+L)(N-P+L+M)^{2k-1} + a(N-L)(N-P-L-M)^{2k-1} + \\
& b(N+Q)(N-P+Q-R)^{2k-1} - \frac{1}{r_b+1} y_b^{2k} \tag{B.96}
\end{aligned}$$

O critério de cedência BBC2005 também contempla formulações específicas. Por exemplo, pode ser reduzido ao critério de cedência de Hill 1948 pela escolha dos seguintes parâmetros constitutivos

$$Y = Y_0$$

$$k = 1$$

$$a = \frac{\sqrt{\frac{1+r_0}{r_0} \cdot \frac{1+r_{90}}{r_{90}} - 1}}{\sqrt{\frac{1+r_0}{r_0} \cdot \frac{1+r_{90}}{r_{90}} + 1}} \cdot \frac{1+r_0}{r_0} \left( 1 + \frac{r_0}{r_{90}} \right) \left( r_{45} + \frac{1}{2} \right)$$

$$b = \frac{a}{\sqrt{\frac{1+r_0}{r_0} \cdot \frac{1+r_{90}}{r_{90}} - 1}}$$

$$L = N = Q = \frac{1}{2\sqrt{a+b}}$$

$$M = P = R = \frac{1}{2} \sqrt{\frac{\frac{r_0}{1+r_0} \cdot \frac{1+r_{90}}{r_{90}}}{a+b}} \quad (\text{B.97})$$

Neste caso, o procedimento de identificação requer apenas como parâmetros mecânicos de entrada  $r_0, r_{45}$  e  $r_{90}$ .

O critério anteriormente proposto por Barlat and Lian (1989) pode ser obtido nas seguintes condições

$$Y = Y_0, \quad k = 3 \text{ ou } 4, \quad L = N = Q, \quad M = P = R \quad (\text{B.98})$$

Também neste caso, o procedimento de identificação requer apenas os parâmetros  $r_0, r_{45}$  e  $r_{90}$ .

Para situações de anisotropia normal ( $r_0 = r_{45} = r_{90} = r, Y_0 = Y_{45} = Y_{90} = Y$ ), o critério de BBC2005 pode também ser reduzido aos critérios de Hill 1948 e Barlat 1989 (dependendo do valor do expoente  $k$ )

$$k = 1 \text{ (Hill 1948)}, \quad k = 3 \text{ ou } 4 \text{ (Barlat 1989)},$$

$$a = \frac{1}{1+r}, \quad b = \frac{r}{1+r}, \quad L = N = Q = M = P = R = \frac{1}{2} \quad (\text{B.99})$$

Em muitos casos, o coeficiente de anisotropia biaxial  $r_b$  não é fornecido. Para contornar esta situação a estratégia mais conveniente passa por introduzir a seguinte condição na equação ((B.96).8)

$$N = P \quad (\text{B.100})$$

Se além do coeficiente de anisotropia biaxial  $r_b$  não for fornecida a tensão de cedência biaxial  $Y_b$ , devem-se introduzir nas equações ((B.96).4) e ((B.96).8) as seguintes condições

$$L + M = 2N, \quad N = P \quad (\text{B.101})$$

Se além do coeficiente de anisotropia biaxial  $r_b$  não forem fornecidas as tensões de cedência uniaxial  $Y_{45}$  e  $Y_{90}$ , devem-se introduzir nas equações ((B.96).2), ((B.96).3) e ((B.96).8) as seguintes condições

$$M = R, \quad L + M = 2N, \quad N = P \quad (\text{B.102})$$

## Sumário

A simplicidade matemática, os coeficientes com significado directo e o número reduzido de parâmetros mecânicos exigidos pelo procedimento de identificação do critério de cedência de Hill 1948, explicam a sua popularidade em aplicações industriais. Contudo, este critério não oferece uma

boa previsão da distribuição planar da tensão de cedência uniaxial e do coeficiente de anisotropia uniaxial. Por outro lado, não consegue prever a cedência para estados de tensão biaxial. Para ultrapassar as limitações de Hill 1948 devem-se utilizar os critérios de cedência anisotrópicos mais flexíveis. Como demonstrado anteriormente, o desenvolvimento de um critério de cedência anisotrópico passa pelas seguintes etapas:

*Métodos usados para transformar formulações isotrópicas em formulações anisotrópicas*

- Inclusão de novos coeficientes nos modelos isotrópicos: Hill 1948, Hill 1979, Hosford 1979
- Uso de transformações lineares: Barlat 1991, Karafillis-Boyce 1993
- Funções de representação: Cazacu-Barlat 2001
- Extensão do critério de cedência para fora dos eixos de ortotropia utilizando transformações de coordenadas: Barlat 1989

*Estratégias de identificação*

- Soluções analíticas: Hill 1948
- Procedimentos numéricos:
  - Newton-Raphson: Barlat 1989, Barlat 2000, BBC2005
  - Minimização da função de erro: BBC2000
  - Algoritmos genéticos: Chaparro *et al.* (2007)

No que respeita a modelação da anisotropia plástica, a escolha do critério mais adequado à descrição do comportamento mecânico de um material nem sempre é evidente, pelo que é necessário definir alguns fatores a levar em consideração:

- ✓ Precisão em determinar a superfície de plasticidade, tensão de cedência uniaxial e coeficiente de anisotropia plástica uniaxial.
- ✓ Eficiência computacional e facilidade de implementação nos códigos de simulação numérica.
- ✓ Flexibilidade do critério de cedência.
- ✓ Grau de generalidade.
- ✓ Número de parâmetros mecânicos necessários ao procedimento de identificação.
- ✓ Robustez do procedimento de identificação.
- ✓ Dificuldades experimentais associadas à determinação dos parâmetros mecânicos.
- ✓ Aceitação do critério de cedência na comunidade científica/industrial.

Os critérios de cedência avançados permitem descrever com precisão o comportamento anisotrópico dos materiais. Ao passo que conseguem descrever a variação da tensão de cedência uniaxial e do coeficiente de anisotropia plástica na chapa, também conseguem modelar as anomalias do comportamento anisotrópico de primeira e segunda ordem. Estes critérios já foram generalizados

para estados de tensão tridimensionais e permitem modelar os efeitos de assimetria da superfície de plasticidade de alguns materiais específicos com estrutura HC. Futuramente, a investigação nesta área será conduzida para o desenvolvimento de materiais com propriedades especiais (materiais superplásticos, materiais com memória de forma, etc.). A inclusão da evolução dos coeficientes nas funções de cedência permitirá a previsão das superfícies de plasticidade para carregamentos não-lineares. A modelação estocástica será mais amplamente utilizada para uma previsão mais robusta da superfície de plasticidade (que leve em conta a variabilidade dos parâmetros mecânicos). A combinação de modelos fenomenológicos com modelos microestruturais possibilitará uma melhor previsão da evolução dos parâmetros durante os processos tecnológicos (temperatura, velocidade de deformação, trajetória de deformação, evolução da microestrutura).

Por fim, espera-se que a cadeia de processo virtual seja descrita com mais precisão de modo a ser utilizada nos processos de fabricação reais. Os fatores mais importantes na escolha de um critério de cedência num código de elementos finitos são a precisão na descrição do comportamento anisotrópico do material e o seu custo na eficiência computacional do programa. A Tab. B.1 apresenta alguns dos critérios de cedência anisotrópicos implementados nos principais códigos FE comerciais.

Tab. B.1 – Critérios de cedência implementados nos códigos FE comerciais mais utilizados.

Software	Hill 1948	Hill 1990	Barlat 1989	Barlat 2000	Vegter	BBC2005
ABAQUS	X	X	X			
AUTOFORM	X	X	X			X
LS-DYNA	X	X	X	X		
OPTRIS	X		X			
PAM-STAMP	X	X	X	X	X	
STAMPAK	X	X				

## Leis de evolução

Nos materiais elastoplásticos susceptíveis de encruar o limite elástico modifica-se com o fluxo plástico. De facto, as superfícies de plasticidade iniciais deixam de modelar correctamente o comportamento plástico do material, sendo necessário associar aos critérios de plasticidade leis de evolução, geralmente designadas por leis de encruamento.

Na simulação dos processos de conformação de chapa supõe-se que a superfície de plasticidade se expande isotropicamente (encruamento isotrópico) e, eventualmente, se desloca (encruamento cinemático) em função do trabalho plástico (Alves, 2003). Fundamentalmente, as leis de encruamento dependem de variáveis internas do material, que determinam as características da



superfície de plasticidade (tamanho, forma e posição). É, portanto, necessário relacionar a tensão limite de elasticidade actual com a quantidade de deformação plástica sofrida pelo material desde o estado plástico inicial até ao actual. Em vista disso, é possível enveredar por dois métodos possíveis.

O primeiro recorre ao conceito de trabalho plástico  $W^P$  como variável interna a adotar nas leis de encruamento macroscópicas.

$$W^P = \int \boldsymbol{\sigma} : d\boldsymbol{\varepsilon}^P \quad (\text{B.103})$$

O segundo método recorre ao conceito de deformação plástica equivalente integrada  $\bar{\boldsymbol{\varepsilon}}_e^P$  ou, mais habitualmente, deformação plástica equivalente  $\bar{\boldsymbol{\varepsilon}}^P$

$$\boldsymbol{\varepsilon}_e^P = \int d\boldsymbol{\varepsilon}_e^P \quad \text{e} \quad d\boldsymbol{\varepsilon}_e^P = \left( \frac{2}{3} d\boldsymbol{\varepsilon}'^P : d\boldsymbol{\varepsilon}'^P \right)^{\frac{1}{2}} \quad (\text{B.104})$$

$$\bar{\boldsymbol{\varepsilon}}^P = \int \dot{\bar{\boldsymbol{\varepsilon}}}^P dt \quad \text{e} \quad \bar{\sigma} \cdot \dot{\bar{\boldsymbol{\varepsilon}}}^P = \boldsymbol{\sigma} : \dot{\boldsymbol{\varepsilon}}^P \quad (\text{B.105})$$

As leis de evolução devem ser associadas aos critérios de plasticidade através do potencial plástico  $\mathcal{F}$  que, sendo uma função de carregamento, representa a aplicação das tensões. Este é dado por:

$$\mathcal{F}(\boldsymbol{\alpha}_k, \alpha_k) = \bar{\sigma}(\boldsymbol{\alpha}_{k_1}, \alpha_{k_1}) - Y(\boldsymbol{\alpha}_{k_2}, \alpha_{k_2}) \quad (\text{B.106})$$

Trata-se, portanto, dum potencial que é função de variáveis tensoriais  $\boldsymbol{\alpha}_k$  e escalares  $\alpha_k$ , onde  $\bar{\sigma}$  e  $Y$ , são a tensão equivalente e a tensão de escoamento associadas ao critério de plasticidade e à(s) lei(s) de evolução. Para que haja plastificação é importante que  $\mathcal{F} = 0$  se verifique a todo instante, o que é garantido pela equação  $\dot{\mathcal{F}} = 0$ , conhecida por condição de coerência plástica. Desta forma, impõe-se que, no domínio plástico, o estado de tensão num dado ponto material se situe *sempre* sobre a superfície de plasticidade, mantendo-se a relação  $\bar{\sigma} = Y$ .

### Leis de encruamento isotrópico

No âmbito do encruamento isotrópico assume-se que tanto a anisotropia plástica que se desenvolve durante a deformação, como o efeito de *Bauschinger*, são fenómenos que podem ser desprezados. Consequentemente, este modelo de encruamento caracteriza-se por uma expansão uniforme da superfície de plasticidade inicial, isto é, sem alterar a sua forma (já que se despreza o efeito da anisotropia plástica). Por outro lado, os centros das superfícies de plasticidade inicial e actualizada mantêm-se coincidentes, isto é, admite-se que a superfície não se desloca durante a evolução da deformação plástica (já que se despreza o efeito de *Bauschinger* evidenciado aquando da inversão de trajetória).

Este modelo de encruamento é, portanto, mais adequado para processos de deformação plástica onde as trajetórias de deformação são monotónicas e as extensões elevadas. No caso das trajetórias de deformação não serem monotónicas, descreve a atualização de superfícies de plasticidade que admitem a propriedade  $\mathcal{F}(\boldsymbol{\sigma}) = \mathcal{F}(-\boldsymbol{\sigma})$  em qualquer instante. O encruamento isotrópico modela a expansão isotrópica da superfície da plasticidade em função, por exemplo da deformação plástica equivalente  $\bar{\epsilon}^p$ . Como expresso anteriormente pela condição de coerência, a evolução da tensão equivalente  $\bar{\sigma}$  depende da tensão limite de elasticidade em tração uniaxial  $Y$ . Assim, várias leis matemáticas foram desenvolvidas para descrever a curva tensão – deformação uniaxial  $Y = f(\epsilon)$ , e descrever desta forma o encruamento isotrópico sofrido pelo material.

O tipo de encruamento, definido pelo grau da função do encruamento isotrópico, depende do módulo de encruamento isotrópico, definido por

$$H' = \partial Y / \partial \bar{\epsilon}^p, \quad (\text{B.107})$$

Entre as mais importantes e eficazes neste sentido, destacam-se as leis de Swift (1947) e Voce (1948), implementadas no modelo constitutivo utilizado.

A lei de Swift,

$$Y = C(\epsilon_0 + \bar{\epsilon}^p)^n, \quad (\text{B.108})$$

Revela-se mais apropriada na descrição do comportamento mecânico de materiais que exibem encruamento isotrópico sem saturação, como por exemplo, os aços. Já a lei de Voce,

$$Y = Y_0 + (Y_{\text{sat}} + Y_0) \cdot [1 - \exp(-C_Y \bar{\epsilon}^p)], \quad (\text{B.109})$$

É mais favorável à descrição do comportamento mecânico de materiais que exibem encruamento isotrópico com saturação, o que acontece no caso das ligas de alumínio, por exemplo.

### **Leis de encruamento cinemático**

O modelo de encruamento cinemático assume que, durante o processo de deformação plástica, a superfície de plasticidade preserva as suas dimensões e a sua forma, sofrendo, contudo, translações de corpo rígido no espaço das tensões. Com isso, procura-se modelar fenómenos como o amaciamento transiente ou efeito de Bauschinger associados a mudanças de trajetória de deformação.

O encruamento cinemático modela a evolução da posição do centro da superfície de plasticidade no espaço das tensões, e é descrito pelo tensor das tensões inversas  $\mathbf{X}$  e pelas leis que regem a sua evolução. Neste sentido, também é possível contextualizar dois modelos importantes.

O primeiro, proposto por Prager em 1955, é dado pelas seguintes equações

$$\dot{\mathbf{X}} = k\mathbf{D}^P \quad \text{ou} \quad \dot{\mathbf{X}} = k\dot{\boldsymbol{\varepsilon}}^P \quad (\text{B.110})$$

Trata-se assim dum modelo de encruamento linear, em que a superfície de plasticidade se desloca linearmente na direção definida pelo tensor velocidade de deformação plástica  $\mathbf{D}^P$ .

Porém, se o estado de tensão equivalente associado ao tensor das inversas  $\mathbf{X}$  for superior ao valor do estado de tensão equivalente associado ao tensor das tensões  $\boldsymbol{\sigma}$ , o que pode ocorrer em grandes deformações, o conceito de estado de tensão efetivo ( $\Sigma = \boldsymbol{\sigma} - \mathbf{X}$ ) deixa de ter sentido físico. Do ponto de vista físico, o centro da superfície de plasticidade inicial ( $\boldsymbol{\sigma} = 0$ ) passa a ficar fora da superfície de plasticidade atualizada, o que, de imediato, invalida um dos requisitos que prova a convexidade da superfície.

Este modelo revela-se inconsistente em estados planos e triaxiais, e inadequado no caso de deformações cíclicas ou alterações bruscas nas trajetórias de deformação. Para superar tais limitações, Lemaître & Chaboche 1985 propuseram uma lei de encruamento não-linear com saturação, matematicamente descrita pela equação

$$\dot{\mathbf{X}} = C_X \left[ \frac{X_{sat}}{\bar{\sigma}} (\boldsymbol{\sigma}' - \mathbf{X}) - \mathbf{X} \right] \dot{\boldsymbol{\varepsilon}}^P, \quad \text{com} \quad \mathbf{X}(0) = 0 \quad (\text{B.111})$$

Onde  $X_{sat}$  caracteriza o valor de saturação da norma do tensor das tensões inversas  $\|\mathbf{X}\|$  e  $C_X$  a velocidade de aproximação ao valor de saturação. Fisicamente esta lei traduz a tendência para coaxialidade entre os tensores  $\boldsymbol{\sigma}' - \mathbf{X}$  e  $\mathbf{X}$ , sendo que a diferença entre estes assegura um efeito de memória da história de deformação. Esta lei de encruamento cinemático é a mais utilizada, em associação com as leis de encruamento isotrópico de Swift e Voce.

### Atualização da superfície de plasticidade

Depois de consideradas as leis de encruamento isotrópico e cinemático, torna-se necessário implementá-las no potencial plástico  $\mathcal{F}$ , generalizando a formulação da condição de coerência (B.106) que possibilita agora descrever a evolução da superfície de plasticidade inicial. Surge assim

$$\mathcal{F}(\boldsymbol{\sigma}' - \mathbf{X}, \mathbf{L}, \alpha_k) = \bar{\sigma}(\boldsymbol{\sigma}' - \mathbf{X}, \mathbf{L}, \alpha_{k_1}) - Y(\alpha_{k_2}) = 0 \quad (\text{B.112})$$

Sendo que  $\boldsymbol{\sigma}'$  e  $\mathbf{X}$  aparecem, respectivamente, como tensor das tensões desviadoras e das tensões inversas;  $\mathbf{L}$  como matriz dos parâmetros anisotrópicos;  $\alpha_{k_1}$  e  $\alpha_{k_2}$ , como o conjunto de parâmetros escalares intervenientes no critério de plasticidade e no modelo de encruamento isotrópico, respectivamente. Pode-se observar que enquanto a lei de encruamento isotrópico aparece de forma

explícita, ocupando o termo  $Y(\alpha_{k_2})$ , a lei de encruamento cinemático é implementada de forma oculta, à custa do conceito de estado de tensão efetivo.

## Lei de plasticidade

Após definir a lei de plasticidade, que rege a evolução da superfície de plasticidade, convém esclarecer sua relação com a deformação plástica exibida pelo material. Com isso em mente, é possível optar por uma lei de plasticidade dita associada ou dita não-associada.

A lei de plasticidade associada caracteriza-se por uma função capaz de descrever não apenas a superfície de plasticidade, mas também o potencial plástico. O potencial plástico é a função utilizada para determinar a velocidade de deformação plástica. Consequentemente, se  $\mathcal{F}$  for a função descritiva da superfície de plasticidade e  $\mathcal{G}$  do potencial plástico, ter-se-á  $\mathcal{F} = \mathcal{G}$ , para as leis de plasticidade associadas. Neste caso, o mesmo potencial serve à descrição do comportamento plástico em termos de cedência e de deformação plástica.

Se  $\mathcal{F} \neq \mathcal{G}$ , a lei é não associada. Por outras palavras, não é possível usar o mesmo potencial para descrever comportamento plástico em termos de estados de tensão e de deformação. Neste caso, admite-se que, se elevada, a pressão hidrostática pode induzir à deformação plástica do material. Embora esta última hipótese dê mais flexibilidade aos modelos constitutivos, as leis de plasticidade associadas originam resultados concordantes com observações experimentais para a generalidade dos materiais metálicos (Genevois, 1992). Por outro lado, em solos, a aplicação de leis de plasticidade não-associada em simulações numéricas, conduzem a resultados mais realistas.

A seguinte figura representa geometricamente a lei associativa e não associativa.

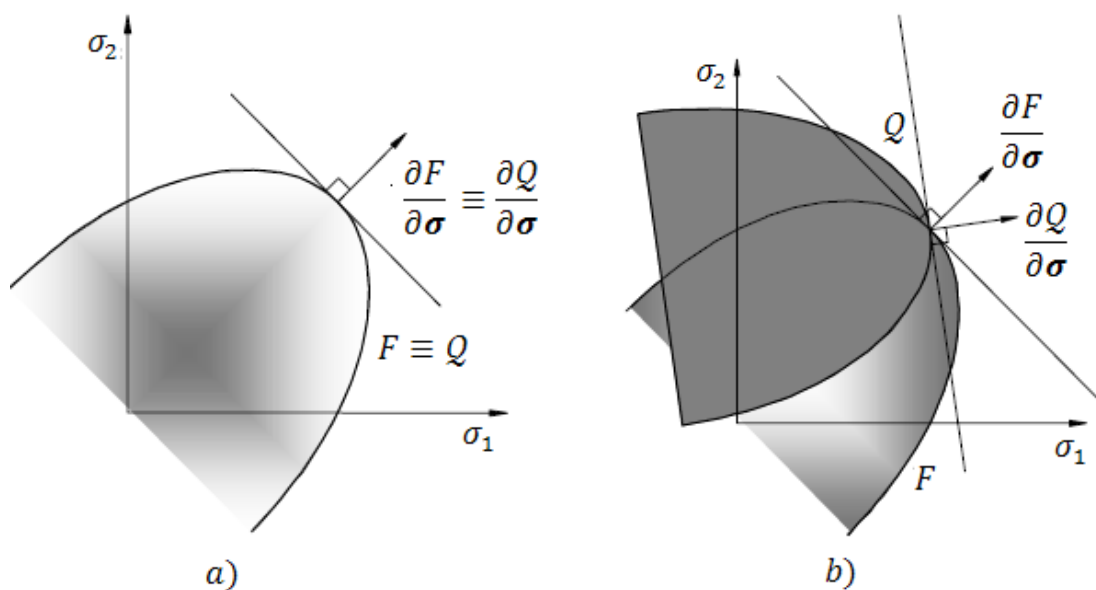


Fig. B.10 – escoamento plástico fazendo uso duma lei a) associada b) não-associada (Natal, 2004).

Levando em conta a condição de coerência plástica,  $\mathcal{F} = \mathcal{G} = 0$  define o potencial plástico e o tensor de velocidade de deformação plástica traduz-se pela seguinte expressão matemática

$$\hat{\mathbf{D}}^P = \lambda \frac{\partial \mathcal{G}}{\partial (\hat{\boldsymbol{\sigma}}' - \hat{\mathbf{X}})} = \lambda \frac{\partial \mathcal{F}}{\partial (\hat{\boldsymbol{\sigma}}' - \hat{\mathbf{X}})} = \lambda \frac{\partial \bar{\sigma}}{\partial (\hat{\boldsymbol{\sigma}}' - \hat{\mathbf{X}})} \quad (\text{B.113})$$

Sendo que  $\hat{\mathbf{D}}^P$  é dado pela lei da normalidade, o vetor que representa a velocidade de deformação plástica será sempre normal à superfície de plasticidade no ponto de carregamento  $(\hat{\boldsymbol{\sigma}}' - \hat{\mathbf{X}})$ . O escalar  $\lambda$  é designado de multiplicador plástico e determina a intensidade do vetor.

Para simplificar o tratamento matemático, pode-se considerar a grandeza tensorial auxiliar  $\hat{\mathbf{V}}$ , tal que

$$\hat{\mathbf{V}} = \frac{\partial \bar{\sigma}}{\partial (\hat{\boldsymbol{\sigma}}' - \hat{\mathbf{X}})} \quad (\text{B.114})$$

Que possibilita, por sua vez, reescrever (B.113)

$$\hat{\mathbf{D}}^P = \lambda \hat{\mathbf{V}} \quad (\text{B.115})$$

onde  $\hat{\mathbf{V}}$  é deduzido em função do critério de plasticidade adotado no modelo constitutivo.

O multiplicador plástico pode ser determinado a partir da condição de coerência, sendo, na sua forma final, traduzido pela expressão matemática

$$\lambda = \dot{\epsilon}^P = \frac{\hat{\mathbf{V}} : (\hat{\boldsymbol{\sigma}}' - \hat{\mathbf{X}})}{H'} \quad (\text{B.116})$$

## Formulação da lei elastoplástica

O processo de deformação plástica de chapas metálicas enformadas a frio caracteriza-se por grandes deformações e rotações elastoplásticas. Facto pelo qual, se usa uma lei elastoplástica definida mediante uma superfície de plasticidade, uma lei que rege a evolução desta e uma lei de plasticidade.

O modelo constitutivo elastoplástico formulado comporta elasticidade isotrópica e plasticidade anisotrópica. Sendo que, para continuar a respeitar o princípio da objetividade, esta lei deve ser formulada em relação à configuração relaxada local  $C^R$ . Para rodar os tensores para a configuração relaxada local  $C^R$ , recorre-se às equações seguintes

$$\hat{\boldsymbol{\sigma}} = \mathbf{R}^T \boldsymbol{\sigma} \mathbf{R} \quad (\text{B.117})$$

$$\hat{\mathbf{D}} = \mathbf{R}^T \mathbf{D} \mathbf{R} \quad (\text{B.118})$$

onde  $\hat{\boldsymbol{\sigma}}$  e  $\hat{\mathbf{D}}$ , são, respetivamente, os tensores tensão e velocidade de deformação, definidos na configuração relaxada local, sendo lagrangeanos na sua orientação e obedecendo ao princípio da indiferença material.

Importante será salientar que as deformações elásticas são muitíssimo reduzidas. Parte-se, portanto, duma lei de comportamento elástico isotrópico aplicável a pequenas deformações, e faz-se a extensão deste formalismo a grandes deformações, para chegar à lei do comportamento elastoplástico. Para traduzir a transformação elástica que ocorre entre a configuração relaxada local  $C^R$  e a configuração corrente  $C$  em pequenas deformações, é possível recorrer à seguinte formulação hipoeelástica

$$\dot{\boldsymbol{\sigma}} = C^e : \dot{\boldsymbol{\varepsilon}}^e \quad (\text{B.119})$$

em que  $\dot{\boldsymbol{\sigma}}$  é o tensor velocidade de tensão,  $C^e$  o tensor das constantes elásticas (conhecido por módulo elástico) e  $\dot{\boldsymbol{\varepsilon}}^e$  é o tensor da velocidade das deformações elásticas. Esta lei apresenta-se sob a forma diferencial e é, por isso, propícia ao carácter incremental da deformação plástica.

Na configuração corrente  $C$ , esta lei assume a seguinte forma

$$\dot{\boldsymbol{\sigma}}^J = C^e : \dot{\boldsymbol{\varepsilon}}^J \quad (\text{B.120})$$

em que  $\dot{\boldsymbol{\sigma}}^J$  é a derivada objetiva de Jaumann do tensor das tensões  $\boldsymbol{\sigma}$  e  $\dot{\boldsymbol{\varepsilon}}^J$  é a derivada objetiva de Jaumann do tensor das deformações  $\boldsymbol{\varepsilon}^e$

Para fazer a extensão desta lei às grandes deformações é necessário, como já referido anteriormente, definir as variáveis na configuração relaxada local  $C^R$ , podendo-se reescrever a equação (B.119)

$$\dot{\hat{\boldsymbol{\sigma}}} = \hat{C}^e : \hat{\mathbf{D}} \quad (\text{B.121})$$

O módulo elástico isotrópico  $\hat{C}^e$  é dado, em notação indicial, pela expressão

$$C_{ijkl}^e = \hat{C}_{ijkl}^e = \lambda \delta_{ij} \delta_{km} + \mu (\delta_{ik} \delta_{jm} + \delta_{im} \delta_{jk}) \quad \text{com } i, j, k, m = 1, 2, 3, \quad (\text{B.122})$$

em que  $\delta$  é o símbolo de *Kronecker*, e  $\mu$  e  $\lambda$  os coeficientes de *Lamé*, que podem ser determinados através do módulo de *Young*  $E$  e do coeficiente de *Poisson*  $\nu$ ,  $K$  é o módulo de compressibilidade:

$$\mu = G = \frac{E}{2(1+\nu)}, \quad \lambda = \frac{\nu E}{(1+\nu)(1-2\nu)} \quad e \quad K = \lambda + \frac{2\mu}{3} \quad (\text{B.123})$$

Embora esta relação seja isotrópica e objectiva, ela não é adequada para o uso em grandes deformações elásticas. Isto dá-se, porque, neste caso, uso da derivada de Jaumann conduz a

resultados absurdos. Por outro lado, ela é inconsistente com o conceito de hiperelasticidade, ou seja, não é possível estabelecer uma “densidade de energia de deformação” que resulte neste formato.

Porém, tais inconvenientes são ultrapassados, quando se consideram pequenas deformações elásticas e transformações isocóricas, o que acontece geralmente no caso dos metais.

Substituindo (B.122) em (B.121), e separando as componentes hidrostáticas e desviadora do tensor velocidade de deformação, obtém-se

$$\dot{\sigma}_{ij} = \lambda D_{kk} \delta_{ij} + 2\mu D_{ij} = \left( \lambda + \frac{2\mu}{3} \right) D_{kk} \delta_{ij} + 2\mu D'_{ij} \quad (\text{B.124})$$

Esta equação é fundamental no desenvolvimento dos módulos elastoplásticos. Para determinar o módulo elastoplástico tangente recorre-se à forma hipoeástica da lei de Hook dada, no referencial de ortotropia, pela expressão

$$\dot{\boldsymbol{\sigma}} = \hat{\mathbf{C}}^e : \hat{\mathbf{D}}^e \quad (\text{B.125})$$

Para o subsequente desenvolvimento do módulo elastoplástico tangente é necessário ter em conta:

- A decomposição do vetor velocidade de deformação nas partes elástica e plástica, dada pela equação

$$\hat{\mathbf{D}} = \hat{\mathbf{D}}^e + \hat{\mathbf{D}}^p, \quad (\text{B.126})$$

- A condição do carregamento plástico e a condição de coerência

$$\mathcal{F}(\bar{\sigma}, Y) = \bar{\sigma}(\hat{\boldsymbol{\sigma}}' - \hat{\mathbf{X}}, \hat{\alpha}_k) - Y(h) = 0 \quad e \quad \dot{\mathcal{F}} = 0, \quad (\text{B.127})$$

- A lei de plasticidade associada

$$\hat{\mathbf{D}}^p = \lambda \hat{\mathbf{V}}, \quad (\text{B.128})$$

- As leis de encruamento cinemático de Prager e Lemaître & Chaboche, respetivamente

$$\dot{\mathbf{X}} = k \mathbf{D}^p \quad e, \quad (\text{B.129})$$

$$\dot{\mathbf{X}} = C_X \left[ \frac{X_{sat}}{\bar{\sigma}} (\boldsymbol{\sigma}' - \mathbf{X}) - \mathbf{X} \right] \dot{\varepsilon}^p, \quad \text{com} \quad \mathbf{X}(0) = 0 \quad (\text{B.130})$$

Levando em consideração a decomposição do vetor velocidade de deformação e a lei da plasticidade associada, a lei hipoeástica pode ser reescrita como

$$\dot{\boldsymbol{\sigma}} = \hat{\mathbf{C}}^e : (\hat{\mathbf{D}} - \alpha \lambda \hat{\mathbf{V}}) \quad (\text{B.131})$$

A separação das componentes hidrostática e desviadora do tensor tensão, apresentada na equação (B.124), conduz à seguinte expressão

$$\hat{\sigma} = K \text{tr}(\hat{\mathbf{D}}) \hat{\mathbf{I}} + 2\mu(\hat{\mathbf{D}}' - \alpha \lambda \hat{\mathbf{V}}) \quad (\text{B.132})$$

sendo  $\alpha$  o parâmetro que traduz a condição de carregamento elástico ou elastoplástico do material. A formulação do comportamento plástico deve fazer-se no espaço das tensões efetivo  $\hat{\sigma}' - \hat{\mathbf{X}}$ , tornando-se necessário recorrer às leis de encruamento cinemático para a determinação do módulo elastoplástico.

### Lei de Prager

A dedução do tensor das tensões efetivo, faz-se pela subtração da lei de encruamento cinemático à parte desviadora do tensor velocidade de tensão (B.132). No caso de Prager, obtém-se

$$\hat{\sigma}' - \hat{\mathbf{X}} = 2\mu \hat{\mathbf{D}}' - (k + 2\mu) \lambda \hat{\mathbf{V}} \quad (\text{B.133})$$

Da condição de coerência  $\dot{\mathcal{F}} = 0$  deduz-se

$$\dot{\mathcal{F}}(\bar{\sigma}, Y) = \dot{\sigma} - \dot{Y} = \hat{\mathbf{V}} : (\hat{\sigma}' - \hat{\mathbf{X}}) - H' \dot{\varepsilon}^P \quad (\text{B.134})$$

Como  $\hat{\mathbf{V}}$  é desviador,  $\dot{\lambda} = \dot{\varepsilon}^P$  pode-se escrever

$$\dot{\lambda} = \dot{\varepsilon}^P = \frac{2\mu \hat{\mathbf{V}} : \hat{\mathbf{D}}'}{(k + 2\mu) \hat{\mathbf{V}} : \hat{\mathbf{V}} + H'} \quad (\text{B.135})$$

Substituindo (B.135) em (B.133), e após algum tratamento matemático, chega-se à seguinte expressão

$$\hat{\sigma} = \hat{C}^e : \hat{\mathbf{D}} - \alpha \frac{4\mu^2}{(k + 2\mu) \hat{\mathbf{V}} : \hat{\mathbf{V}} + H'} (\hat{\mathbf{V}} \otimes \hat{\mathbf{V}}) : \hat{\mathbf{D}}' \quad (\text{B.136})$$

Concluindo, a adoção da lei de Prager conduz-nos à seguinte expressão para a determinação do módulo elastoplástico tangente

$$\hat{C}^{ep} = \hat{C}^e - \alpha f_0 (\hat{\mathbf{V}} \otimes \hat{\mathbf{V}}) \quad , \quad f_0 = \frac{4\mu^2}{(k + 2\mu) \hat{\mathbf{V}} : \hat{\mathbf{V}} + H'} \quad (\text{B.137})$$

### Lei de Lemaître & Chaboche

Aplicando a mesma metodologia para o caso do encruamento cinemático de Lemaître & Chaboche 1985, desenvolvem-se as seguintes expressões



$$\dot{\hat{\boldsymbol{\sigma}}}' - \dot{\hat{\mathbf{X}}} = 2\mu(\hat{\mathbf{D}}' - \alpha\lambda \hat{\mathbf{V}}) - C_x \left[ \frac{X_{sat}}{\bar{\sigma}} (\boldsymbol{\sigma}' - \mathbf{X}) - \mathbf{X} \right] \dot{\hat{\boldsymbol{\varepsilon}}}'^p, \quad (\text{B.138})$$

$$\lambda = \dot{\hat{\boldsymbol{\varepsilon}}}'^p = \frac{2\mu \hat{\mathbf{V}} : \hat{\mathbf{D}}'}{2\mu \hat{\mathbf{V}} : \hat{\mathbf{V}} + C_x \hat{\mathbf{V}} \left[ \frac{X_{sat}}{\bar{\sigma}} (\boldsymbol{\sigma}' - \mathbf{X}) - \mathbf{X} \right] + H'} e \quad (\text{B.139})$$

$$\hat{\boldsymbol{\sigma}} = \hat{C}^e : \hat{\mathbf{D}} - \alpha \frac{4\mu^2}{2\mu \hat{\mathbf{V}} : \hat{\mathbf{V}} + C_x \hat{\mathbf{V}} \left[ \frac{X_{sat}}{\bar{\sigma}} (\boldsymbol{\sigma}' - \mathbf{X}) - \mathbf{X} \right] + H'} (\hat{\mathbf{V}} \otimes \hat{\mathbf{V}}) : \hat{\mathbf{D}}' \quad (\text{B.140})$$

Finalmente, chega-se ao módulo elastoplástico tangente

$$\hat{C}^{ep} = \hat{C}^e - \alpha f_0 (\hat{\mathbf{V}} \otimes \hat{\mathbf{V}}) , \quad f_0 = \frac{4\mu^2}{2\mu \hat{\mathbf{V}} : \hat{\mathbf{V}} + C_x \hat{\mathbf{V}} \left[ \frac{X_{sat}}{\bar{\sigma}} (\boldsymbol{\sigma}' - \mathbf{X}) - \mathbf{X} \right] + H'} \quad (\text{B.141})$$